Granular Dynamic Theory and Its Applications

Aixiang Wu
Yezhi Sun

Metallurgical Industry Press

Springer

Aixiang Wu
Yezhi Sun

Granular Dynamic Theory and Its Applications

Aixiang Wu
Yezhi Sun

Granular Dynamic Theory and Its Applications

With 207 figures

Metallurgical Industry Press

Springer

AUTHORS:

Prof. Aixiang Wu,
Civil & Environment Engineering School,
University of Science and Technology Beijing,
100083,China
E-mail:wuaixiang@126.com

Dr.Yezhi Sun,
School of Resources & Safety Engineering,
Central South University,
410083,China
E-mail:sunyezhi999@sohu.com

Based on an original Chinese edition:
《散体动力学理论及其应用》(Santi Donglixue Lilun Jiqi Yingyong), Metallurgical Industry Press, 2002.

ISBN 978-7-5024-4300-9	Metallurgical Industry Press,Beijing
ISBN 978-3-540-75821-1	Springer Berlin Heidelberg New York
e-ISBN 978-3-540-75822-8	Springer Berlin Heidelberg New York

Library of Congress Control Number: 2007937707

Co-published by Metallurgical Industry Press, Beijing and Springer-Verlag GmbH Berlin Heidelberg

Springer is a part of Springer Science+Business Media
Springer.com

Cover design: Frido Steinen-Broo, Estudio Calamar, Spain
Printed on acid-free paper

Foreword

The behavior of granular material in every engineering project has important implications. The failure of the stability of bridges, dams, slopes of excavation, etc. is often caused by the dynamics of the granules, so it is essential to know the fundamental properties of granules if these need to be manipulated and controlled in a positive direction.

This book is a comprehensive treatise, which examines the essential features of granules. After dealing with the physical and mechanical properties of granules, the authors have classified the granules in various grain groups. These granule groups were tested both in the laboratory as well as on site for their strength and behavior in different situations. During the experimental work the authors discovered that if the granules were vibrated in an appropriate manner, then they would flow without any external impediment, and blockages caused by the broken ores forming arches or other obstructions could be avoided.

This concept of the application of induced vibration led to the development of the Vibrating Ore-drawing Machine (VOM). Since its first introduction in China in 1974, the vibrating ore-drawing technology has progressed a long way. Thanks to the joint research cooperation between industry and academic institutions such as Central South University, many of the initial teething problems have been solved. Now, most metal mines and some surface mines in China and other countries have adopted VOM in their ore-loading chutes or in feeders. With the establishment of VOM, mining companies in China experience the benefits of lower installation as well as maintenance costs, lower man-power requirements, higher safety records, as well as increased productivity.

The authors of this book acknowledge that there is still scope for further development of VOM so that its application is more flexible and can be implemented in most if not every situation. They have suggested some future research work that could be carried out to achieve this objective.

It has been my honor as well as pleasure to be associated with the compilation of this book, which in my opinion will be useful to all research workers as well as to the field personnel involved with ore loading operations. Above all, this book is a comprehensive study of granular behavior and this information supplied will ensure the trouble free flow of ore to its loading points.

The striving wish of all engineers is to make sure that productivity and safety records are maintained at their highest levels. With this in mind, I am confident that the contents of this book will add to the knowledge of all practicing engineers, not only in the field of mining, but also in all engineering operations.

Professor Gour C Sen
University of Wollongong
AUSTRALIA

Preface

In recent years, much interest has focused on the physics of granular media: assemblies of macroscopic particles such as sand, gravel, ore, powders, or pharmaceutical pills that interact primarily through contact forces. Granular materials are ubiquitous in a wide range of industrial processes and complex systems. The properties of flowing granular matter are dominated by rapid inelastic collisions between the grains, which quickly dissipate the kinetic energy unless it is replenished by gravity, external vibration, or interstitial gas flow. Granular flows have revealed a host of behaviors that are unexpected from ordinary fluids, such as non-Newtonian boundary layers, propagating density waves, and avalanches. Furthermore, if a mixture of the material is stirred, shaken or rotated, different particle sizes or masses typically segregate into different regions of the confining container, in contrast with the homogenizing effect of ordinary fluids under stirring.

The applications of vibration effect in industry involve the disposal of granular materials and improving or controlling granular flow by all kinds of vibrating-aided devices. Mechanical vibration effect is widely used to compact and process granules (powder) in such industrial sectors as construction, hydropower, railway, highway and etc.

In China vibrating ore-drawing technology has been rapidly developed since the first vibrating ore-drawing machine was successfully developed in 1974. It has been widely used in all kinds of stopes, ore passes and ore bins. According to a national survey, the number of all kinds of inertial vibrating ore-drawing machines used in China has exceeded 5000, which brought substantial economic efficiency and social efficiency at home and abroad. Standardization and serialization work has begun as more vibrating machines are continually appearing and are often modified to suit different situations. China is definitely in a leading position in the field of vibrating ore drawing in the world at the conclusion of its national key project "technique and device of continuous mining in underground mines". Theoretical investigations are widespread and have been extended into the field of sandy soil, slurry, and etc. Some of the examples are: the mechanism of the action of stress wave on granules, granular mechanics characteristic in vibrating field, flow form of vibrated granules, vibrating drag reduction of high concentration slurry transported by pipeline, fractal behavior when granules vibrate and vibrating liquefaction characteristic of saturated granules.

Study of granular dynamics started in Central South University in 1980's. Recently a series of experimental and theoretical researches have been carried out. The principal author of this book has been engaged in theoretical research and practice of granular dynamics for an extensive period of time. This book is a good generalization of his research findings. It primarily probes into the granular dynamic characteristics, the vibrating liquefaction, the wave theory, the vibrating aided flow, the vibrating drag reduction, and the fractal behavior, etc.

The research is sponsored by China's national natural science foundation. Research topics include the granular dynamic effect and its mechanism of action under vibration, DSA-1 type vibrating direct shear device, the action mechanism of vibration for the slurry transportation and storage, the mechanism of vibrating loosen and compaction for the high moisture content fine granular materials, the wave propagation and its mechanism of action in the granular media, and so on.

Any suggestions and critical comments are sincerely welcomed.

The authors are indebted to many professors and experts of School of Resource and Safety Engineering, Central South University, China for their assistance and suggestions.

The authors wish to thank Xiong Zhengming who is a professor of South Institute of Metallurgy for his assistance in some of the chapters.

The authors give sincerely thanks to Dr. Li Jianhua who is an engineer in Fifth Building Company in Guangdong Province for providing a vast number of useful statistics.

The authors wish to acknowledge Zeng Xiaoqing who is PhD of Central South University and professor Gour C Sen of University of Wollongong, Australia for their assistances and suggestions.

Aixiang Wu and Yezhi Sun
January, 2007

Acknowledgements

The authors would like to acknowledge the financial support for this work provided by the National Science Fund for Distinguished Young Scholars of China (50325415), National Natural Science Foundation of China (50574099) and National Key Fundamental Research and Development Program of China(2004CB619205).

Contents

Introduction

Anything comprising a great quantity of similar grains is termed as the granular medium (in general, it is called granules), such as the broken ores, sands, slurry, fine coals, cements, corns, etc. Especially, the broken ores and sands are usually applicable in this study[1 ~ 4]. With the development of modern engineering techniques, the fields involving the granular dynamics are rapidly increasing. The so-called dynamical forces are mainly produced by seismism, rock-burst, wind's vibration, wave, mechanical vibration, blasting, etc. In engineering practices scientists and engineers are deeply concerned with two issues, one is the prevention of vibrating hazards and the other is the use of vibrating energy.

With the construction of highways, high-rise buildings, bridges, dams and other big geotechnical engineering projects as well as the exploitation of big metal and coal mines, the stability of the building foundation, the dumping site of mines, and big tailings dams must be ensured[5~19]. The natural hazards, such as landslip, mud-rock flow, seismic activity, etc., often take place, which make the buildings collapse, the surfaces subside, the dams and bridges be destroyed. These cause both the economic loss and many casualties. Therefore, the seismic dynamics, the foundation dynamics of motive power machine, the soil dynamics, and the structural dynamics are also applicable as the occasion requires[20~36]. The basic prerequisite of these studies is to understand the propagation law of stress wave in rocks and soils, and the dynamic characteristics of rocks and soils under the vibration. These studies offer the method for engineering designs and suitable precautionary measures to prevent and reduce the hazards.

The vibrating energy is used widely. Recently, this method has been developed rapidly in order to consolidate yielding soil foundation by vibration and impact[37~41]. In addition, all kinds of vibrating ramming compactors, vibrating tamper, etc., play an important part in many civil engineering projects. On the other hand, many vibrating machines are widely used to discharge, transport or deal with the granules. According to the relevant statistics[2, 5], in China more than 5000 vibrating ore-drawing machines are used to deal with the granules in the mines of metallurgy, chemical engineering, manufacture of building materials, nuclear industry, etc., as well as other sections of water conservancy, shipping, traffic, etc. At the same time, thousands of vibrating machines of electromagnetic, hydraulic and pneumatic are used in various projects. Therefore, the cases of the granules acted by the motive power machines in varieties of engineering projects are very universal.

All the above mentioned problems of engineering projects relate to the interaction between the wave and granules, the granular strength in the vibrating situation, the changes of the cohesion C and the angle of internal friction φ, etc. These basic mechanical parameters must be obtained by corresponding measuring techniques. Taking the design of vibrating bunker as an example, if there is no corresponding development of measuring techniques, it is impossible to develop the new granular mechanics and dynamics and to design for the engineering practice. It does not matter how the design method is advanced and acceptable, if the measuring techniques are not reliable, every parameter for the design calculation cannot be obtained precisely.

The measuring techniques are not only important for the engineering practice, but also play a crucial part in the research and development of scientific theory[2, 9]. The soil mechanics belongs to the granular mechanics. For example, the Darcy's law, the Moore-Coulomb strength theory, the nonlinear stress-strain relation, etc., are based on the measuring results[42~49]. In addition, the famous ore-drawing ellipsoidal theory and its corresponding computational formulae in ore-drawing science are also obtained by the experiments[50, 51]. Therefore, the granular mechanics and dynamics are based on the measuring techniques and experiments.

Since the invention of the first ore-drawing machine in 1974 in China, the ore-drawing technique has been rapidly developed, and applied widely in variety of stopes, chute raises and ore bins[2, 5]. Although the handling techniques of granules, such as ore-drawing technique, have been studied extensively, and lots of in-situ industrial experiments have been done, there are still many things are worth doing in the theoretical study[47~53]. For example, the mechanism of stress wave in granular media, the change of mechanical properties in the vibrating situation, the vibrating liquefaction of saturated granules, the vibrating aided flow in flowing field, the vibrating drag reduction of high concentration slurry, the granular fractal behavior, etc., are worth studying further[54~65]. Therefore, the studies of the granular dynamic measuring techniques and the dynamic theory have great theoretical and practical significances.

This book states from the broken ores, then extends to the studies of sands, slurry and other granular media. So the study of granular dynamics is very extensive and comprehensive, and is not restricted to the broken ores only. Based on the theories of granular mechanics, soil mechanics, soil dynamics and the findings of previous researches, this book strives towards perfection.

Firstly, this book briefly introduces basic mechanical properties of granular media, including the granular basic compositions, its concepts and classification, the granular shear strength and the deformation characteristics. Then it introduces the granular dynamic testing techniques, such as the dynamic triaxial test, the large scale vibrating table test, the resonance column triaxial test, and the dynamic single shear test. In addition, the DSA-1 type vibrating direct shear instrument has been developed, and many dynamic experiments were done with it. Based on these experiments, the granular dynamic shearing and its differential mechanical model, as well as the granular dynamic characteristics have been studied, including the mechanism of granular dynamic shear strength, the deformation characteristic of granular dynamic shear strength, the granular dynamic yield criterion and dynamic stress-strain relation, the excited response of granular ores under vibration, the granular dynamic strength and its cyclic effect, the dynamic strength of several kinds of granular media, the propagation law of wave in the elastic granular medium, the wave propagation and dissipation in viscoelastic granular medium, etc. Subsequently, the vibrating liquefaction of saturated granules is studied, including the evolution of liquefaction problem, the effective stress principle and mechanical mechanism of vibrating liquefaction, the experimental instrument of granular vibrating liquefaction, the liquefaction experiments, the main factors influencing the granular vibrating liquefaction, the granular liquefaction evaluation, the wave mechanism of saturated granular liquefaction and compaction phenomenon, etc. Using the wave theory and the experimental results, the influence of three body waves on hydraulic pressure in pores and granules are analyzed in detail. This study revealed that the mechanism of hydraulic pressure increment and the wave mechanism of vibrating liquefaction have creative effects. The flowing granular media is regarded as weak transverse isotropic substance, and on this assumption the phase velocity expressions of wave P, SH and SV are deduced. Also the propagation specialties of waves in the flowing granular media have been analyzed. It is thought that the mechanism of the aided flow by vibration is explained fully first time in this book. By the use of two-phase flow theory of liquid-solid, the mechanism of vibrating drag reduction of densely concentrated slurry is studied. The reflection and transmission of stress wave, which attenuate in the vertical direction of the pipeline, are also analyzed. In the meantime, utilizing multigrid technique the influence of vibrating wave on the change of flow form of laminar flow is studied. The mechanism of vibrating drag reduction of densely concentrated slurry in pipeline is explained fully firstly. Utilizing fractal geometry, the fractal behavior of granules, pores and seepage, the fractal behavior of granules with vibrating, the self-organized behavior of granular piles and the self-organized criticality of saturated granular liquefaction are studied systemically. Moreover, utilizing Visual C++ (6.0), their fractal figures have been created. In terms of the character of vibrating liquefaction, the concept the self-organized criticality of saturated granular liquefaction is put forward comprehensively. Utilizing the dissipation structure theory, the evolutionary process of vibrating liquefaction in saturated granules is analyzed. According to the synergetics, the equation of liquefaction evolution is deduced, and the evolutionary process is analyzed by dynamics. Finally, the application of granular dynamics in engineering is also discussed in detail, such as the vibrating ore-drawing technique.

The authors' research findings of many years are summarized in this book. There are also some new viewpoints introduced. For example, utilizing the wave theory, this book interprets the mechanism of vibrating liquefaction, the mechanism of vibrating aided flow and the mechanism of vibrating drag reduction; and puts forward the concept of "self-organized criticality of saturated granular liquefaction".

1

Basic Physical and Mechanical Properties of Granular Media

1.1 Granular Basic Property, Conception and Classification

Granular medium is a kind of aggregate that is formed by many granules related to one another. In terms of water content and stickiness, it can be divided into ideal and nonideal medium. When the medium has water content and stickiness, it is called an ideal granular medium; otherwise, it is called a nonideal granular medium. The granular media commonly studied are often nonideal, such as, broken ores, clays, sands, slurry and other granular or powdery materials.

The main characteristics of granular media are loosening, complexity and mutability. The granular media are different from rocks and soils[66~73]. Rocks and granular media are all composed of particles and pores. The former have the powerful coupling force, and they can be separated into continuous media, but the latter have low intensity and more complexity. In addition, the granular media are also different from the soils. The main characteristic of the soil is its fertility. It can offer essential nutrition to plants and weeds. However, the granular medium is mainly an engineering conception. For example, the broken ores in stopes are mining resources; the granular soils which bear the load of such construction as houses, bridges, roads and dams are called foundation; in tunnels, culverts and underground constructions, the granular media are in the surroundings; whereas in embankments, earth dam, the railroad bed and other earthen structures, the granular media are construction materials.

1.1.1 *Basic concept of granular medium*

1.1.1.1 Density

The density is the granular mass per volume, and its expression is:

$$\rho_s = \frac{m_s}{V_s} \tag{1.1}$$

where ρ_s is the granular density, kg/m^3; m_s is the granular mass, kg; V_s is the granular volume, m^3。

According to different stacked conditions, the granular density can often be divided into free stacking density and dynamic compaction stacking density. The ratio of compaction density and free density is called the coefficient of compactness, and its expression is:

$$K_m = \frac{\rho_m}{\rho_d} \tag{1.2}$$

where K_m is the coefficient of compactness; ρ_d is the free stacking density, kg/m^3; ρ_m is the compaction stacking density, kg/m^3.

1.1.1.2 Granular structure

The granular structure is a kind of special arrangement of granules and pores. The granular structure which only can been seen by the optical microscope or the electronic microscope is called microstructure; and the structure which can be seen by naked eyes or an ordinary magnifying glass is called macrostructure, such as stratifications, fractures, big pores, and granules, etc. On the basis of its granules arranging and coupling, the granular structure can be divided into the following three types:

(1) Single-grain structure. It is the structure of the broken ores or sands, which have no coupling force among the particles, or when the force is so weak that it is negligible. According to the array of granules, this structure can be further divided into loose structure and compact structure (as shown in Fig. 1.1). The loose structure can be converted to compact one by static load or vibrating load. The compaction degree of single-grain structure depends on its mineral component, particle shape, degree of uniformity, and degree of sedimentation, etc. The sandy soils composed of laminar minerals are mostly loose; and the ones composed of circular particles is more compact than the sandy soils composed of angular particles. The more nonuniform is the particles, the more compact is its structure. The granular structure that is formed quickly is looser than the one formed slowly.

(2) Honeycombed structure. The granules that are coupled to each other by the form of side-side or side-face are known to have the honeycombed structure (sometimes called cellular structure or flocculent structure), which makes the granules have a special property related closely to the intention and distortion, such as the cellular porosity, viscidity and elasticity. Please refer to Fig. 1.2.

(3) Glomerogranular texture. Some granules assemble by the form of face-face when the big stack aggregation becomes apparent.

With the change of such external conditions as the load and temperature, the granular structure will alter. The coupling force of the granules will increase if the granular media desiccate. Acted by pressure and shear, the honeycombed structure can transform into a parallel directional structure, and the granular intention and

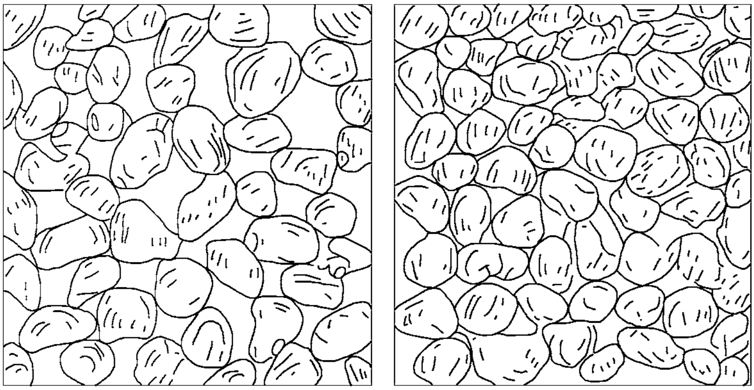

(a) (b)

Fig. 1.1 Single-grain structure

(a) Loose; (b) Compact

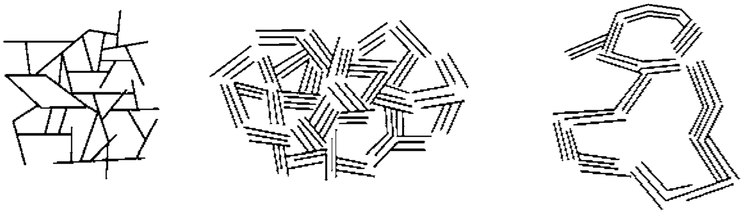

(a) (b) (c)

Fig. 1.2 Honeycombed structures

(a) Single-grain,side-side or side-face flocculation;

(b) Clay granules or side-face flocculation; (c) Side-side flocculation

compressibility may also change.

1.1.1.3 Porosity factor, porosity ratio and compaction degree

The porosity factor of granular media is the ratio of pores volume and the total volume of granular media in loose condition. Namely:

$$n=\frac{V_s-V_z}{V_s}\times 100,\ \% \tag{1.3}$$

where n is the porosity of granular media, %; V_s is the total volume of granular media; V_z is the total volume of solid particles.

The porosity of granular media can also be expressed by the porosity ratio. The porosity ratio is the ratio of pores volume and granules volume in loose condition. Namely:

$$e=\frac{V_s-V_z}{V_z}\times 100,\ \% \tag{1.4}$$

where e is the porosity ratio of granular media, %.

The relation between the porosity factor and the porosity ratio is:

$$n = \frac{e}{1+e} \quad \text{or} \quad e = \frac{n}{1-n}$$

An important characteristic of granular media is that there are many pores among the granules. The porosity factor of a granular medium differs with its granular structure. The porosity factor is large for angular irregularly shaped granular media and small for round regularly shaped granular media. It is large for single-grain structure and small for the flocculent structure and glomerogranular texture.

The properties of granular media having same porosity but different granular size-grade distribution and shapes are different. So it is not sufficient to know its porosity factor and porosity ratio only. The compaction degree must be also known, so that the looseness, compaction and structure stability of granular media can be worked out.

As shown in Table 1.1[54], the compaction degree of granular media is the degree that the granular media can be compacted by an external force. In general, the ratio of the granular volume after compaction and the total volume in its original loose state is termed as the compaction degree of granular media, and its expression is:

$$K_{ys} = \frac{V_{ys}}{V_s} \tag{1.5}$$

where K_{ys} is the compaction degree of granular media; V_{ys} is the granular volume after compacted.

Also, the compaction degree can be expressed by the porosity ratio:

$$K_{ys} = \frac{e_{max} - e}{e_{max} - e_{min}} \tag{1.6}$$

where e_{max} is the maximum porosity ratio which is in absolutely free and loose state; e_{min} is the minimum porosity ratio which is in completely compacted state; e is the natural or appreciably compacted porosity ratio.

Table 1.1 The compaction degree of granular media

Grade	K_{ys}	Standard average blow count $N_{63.5}$
Very compact	$K_{ys} \geqslant 0.67$	35～50
Compact	$0.67 > K_{ys} \geqslant 0.33$	10～29
Loose	$0.33 > K_{ys} \geqslant 0.20$	5～9
Very loose	$K_{ys} < 0.20$	<5

1.1.1.4 Bulk property of granular media

When rock is crashed, its volume will increase. This property is termed as the bulk property of granular media. The ratio of the bulk volume and the original rock volume is called loosening coefficient, which can be expressed as:

$$K_s = \frac{V_k}{V_t} \tag{1.7}$$

where K_s is the loosening coefficient; V_k is the volume of broken ores, m^3; V_t is the original rock volume, m^3.

The relationship between the compaction degree and the loosening coefficient is:

$$K_{ys} = \frac{K_y}{K_s} \tag{1.8}$$

where K_y is the loosening coefficient after compacted; K_s is the loosening coefficient before compacted.

The loosening coefficient can be further divided into the initial loosening coefficient and the secondary loosening coefficient. They are discussed as follows:

(1) Initial loosening coefficient. The bulk increase of the caved ores is called the initial loosening. The ratio of the volume of broken ores to its original rock volume is called the first loosening coefficient. In terms of different conditions, the first loosening coefficient can be described as:

a. For deep-hole blasting, the initial loosening coefficient is 1.25～1.32;

b. For vertical blast-hole, the initial loosening coefficient is 1.15～1.25;

c. For expansion chamber blasting, the initial loosening coefficient is 1.12～1.14.

(2) Secondary loosening coefficient and ultimate loosening coefficient. After the initial loosening of broken ores, due to continuous ore-drawing the ores in stope will generate the secondary loosening. The expression of the secondary loosening coefficient is:

$$K_e = \frac{V_c - V_e}{V_e} + 1 = \frac{V_c}{V_e} \tag{1.9}$$

where K_e is the secondary loosening coefficient; V_e is the volume before secondary loosening, m^3; V_c is the volume after secondary loosening, m^3.

Both practices and experiments show that the loosening coefficient is a constant if the blasting parameters and the properties of the broken ores remain unchangeable. In general, this loosening coefficient is leading to the so-called ultimate loosening coefficient. The value of the ultimate loosening coefficient is equal to the product of the initial loosening coefficient and the secondary loosening coefficient. Namely:

$$K_j = K_s K_e \tag{1.10}$$

where K_j is the ultimate loosening coefficient; K_s is the first loosening coefficient.

1.1.2 *Moisture content and its property of granular media*

The moisture content of a granular medium is the amount of water in the specified granular medium. In general, it can be expressed as the ratio of the water mass and the dried granular media. Namely:

$$M = \frac{m_s - m_g}{m_g} \times 100, \quad \% \tag{1.11}$$

where M is the moisture content; m_s is the mass of granular media with water, kg; m_g is the mass of dried granular media, kg.

The properties of granular media are not only decided by the absolute moisture content, but also by the moisture form and structure, and the physical or chemical components within. The water molecule is a kind of polar molecule (as shown in Fig. 1.3). Because of the negative electric charge on the surface of the granular media, the water molecules among the granules will be affected by the surface electric charge and electric field. According to the degree of static electric attraction, the water within the granular media can be divided into four types, i.e. tightly bound water, loosely bound water, capillary water and free water (as shown in Fig. 1.4).

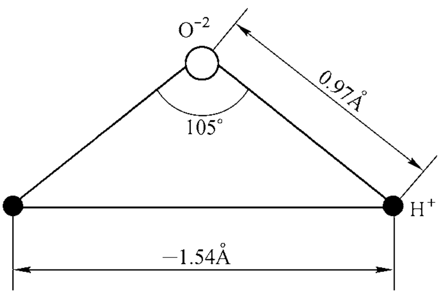

Fig. 1.3 Polar molecule of water

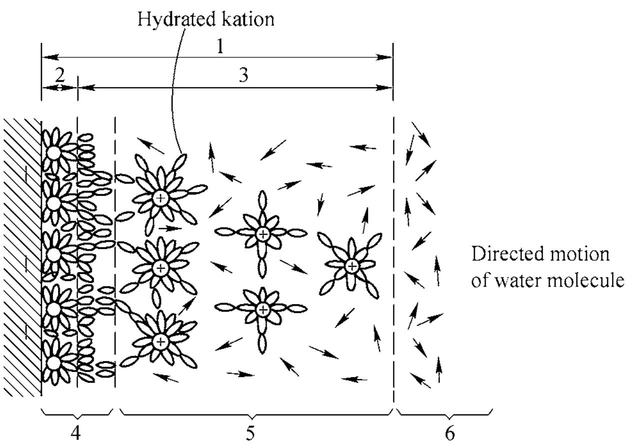

Fig. 1.4 Formation of bound water

1—Electric double layer; 2—Adsorbed layer; 3—Diffused layer; 4—Adsorbed bound water; 5—Seepage adsorbed water; 6—Free water

1.1.2.1 Tightly bound water

Tightly bound water abuts on the surface of granular media, and static electric attraction on the surface of granules is the strongest. This attraction adsorbs hydrating ions and polar water molecules on the surface of granules, and an immobile layer forms. Tightly bound water has no dissolution ability and cannot transmit hydrostatic pressure. The water tightly bounds on the surface of granules whose property is similar to solid, its density is about 1.2～2.4 g/cm^3 and freezing point is −78℃. If dried granular media are exposed to naturally moist air, its mass will increase and it will adsorb the tightly bound water until the maximum hygroscopic moisture content is reached. The finer the granule is, the larger the surface area of granules. The tightly bound water layer is also called adsorbed layer or immobile layer.

1.1.2.2 Loosely bound water

Loosely bound water is a water film that abuts on the periphery of a tightly bound surface. In this water film, incoming water molecules and the hydrating ions would be absorbed by the static electric attraction. It still can't transmit the hydrostatic pressure, but the loosely bound water in thicker film can move slowly towards the nearly thinner film. The loosely bound water layer is called diffusion layer. The electric double layer is comprised of the immobile layer, the diffusion layer and the negative electric charge on the surface of granules (shown in Fig.1.5). The electric potential on the surface of granules is called heating power electric potential. The influence factors of heating power electric potential include the mineral component of granules and the dispersed degree of granules. When it is balanced by the tightly bound water, the electric potential on the surface of immobile layer turns into electricity ξ, namely, zeta potential. It will continually absorb water molecule and the hydrating ions until the influence disappears wholly.

1.1.2.3 Capillary water

Capillary water is a kind of free water affected by the surface tension in the interface between water and air. The surface tension in the interface of curved liquid surface and granules reacts upon the granules, and makes the granules squeeze each other. This surface tension is called capillary pressure. Because of the action of capillary pressure, a kind of pseudo-cohesive force comes into being in the granular media. In engineering practice, the risen height of this capillary significantly influences the moisture proof of a building foundation and the frost heave of a roadbed.

1.1.2.4 Free water

Free water is also called gravitational water, which is not affected by the electric charge or the electric field on the surface of granules. It has the same property as

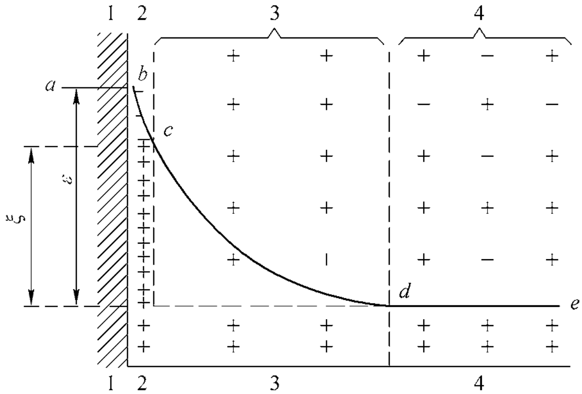

Fig. 1.5 Structure of electric double layer and its change of electric potential

1-1-Inner layer; 2-2-Immobile layer; 3-3-Diffusion layer; 4-4-Free liquid; *a-b*-Electric potential of granule surface; *d-e*—Electric potential of liquid surface; *bcd* curve—Potential difference on the interface of solid and liquid, the electric potential in the interface is called heating power electric potential and is equal to ε; *cd* curve—Potential difference between the immobile layer and the diffused layer; the electric potential on the immobile is called zeta potential ξ

common water. In addition, it can pass on hydrostatic force, its freezing point is 0℃, and has dissolution ability.

1.1.3 *Grain size, grading and classification of granular media*

1.1.3.1 Grain size of granular media

Grain size of a granular medium is denoted by the size (the unit is mm) of the above or below sieve pore on certain granules when these granules are sieved. In terms of grain size, granular media can be divided into various groups, such as gravels, sands, powder and sticky granules. The typical standard of classification of grain groups is shown in Table 1.2.

Table 1.2 Typical standard of classification of grain groups

Name of grain groups		Range of grain size /mm
Boulders or block rocks		>200
Screes or crushed stones		200～20
Conglomerates or sharp grits	Coarse	20～10
	Middle	10～5
	Fine	5～2
Sands	Coarse	2～0.5
	Middle	0.5～0.25
	Fine	0.25～0.10
	Very fine	0.10～0.05

Continues Table 1.2

Name of grain groups		Range of grain size /mm
Powder grains	Coarse	0.05~0.01
	Fine	0.01~0.05
Sticky grains		<0.005

1.1.3.2 Grading and classification of granular media

The grading of granular media is the relative content of different size granules, and this is identified by the percent of certain size granules in the sample. The grading is performed by the stepwise sieving with sifters of different pore diameters. Therefore, a sample can be divided into a few groups, and every group includes all granules of certain range from minimum granules to maximum granules. The distinction of grading is carried out by the size of sieve pores through which some granules can pass. In general, the grading analysis is to draw a chart that denotes the mass percent of some granules which can pass through the sieve pores from the total granule mass. It is shown in Fig. 1.6, in which the abscissa is the size of the sieve pores and the ordinate is the mass percent. In the grading analysis of granular media, the group of all granules from a_{max} to $0.8a_{max}$ is called the maximum granular group, where a is the size of granules.

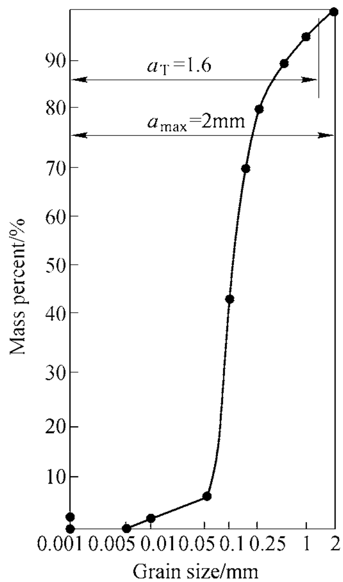

Fig. 1.6 Curve of grading of granular media

According to the uniformity degree of granules, the grading of granular media can be divided into good grading and poor grading. When the ratio of maximum and minimum granules $a_{max}/a_{min}>2.5$, the grading is a good grading; when $a_{max}/a_{min} \leqslant 2.5$, it is a poor grading.

As for every kind of granular medium, there exists a kind of typical granules. In general, as for the good grading granular media, the following size should be considered as the typical size:

(1) If the content of maximum granular group less than 10%, then 0.8-times the maximum size is used, namely:

$$a_T = 0.8a_{max}$$

(2) If the content of maximum granular group more than 10%, then the maximum size is used, namely:

$$a_T = a_{max}$$

As for the poor grading granular media, the average size of granules is used for the most typical size, namely:

$$a_T = \frac{a_{max} + a_{min}}{2}$$

In terms of the size of granules, the classification of granular media is shown in Table 1.3. In addition, the classification of mineral grains is shown in Table 1.4; and the classification of bulk solids and sands is shown in Table 1.5.

Table 1.3 Classification of granular media

Name	Size/mm
Massive granular media	>160
Middle granular media	160～60
Small clod	60～10
Grainy media	10～0.5
Powdery media	0.5～0.05
Mote media	<0.05

Table 1.4 Classification of mineral grains

Name	Size/mm
Gravels	>20
Grits	20～2
Coarse sands	2～2.5
Middle sands	0.5～0.25
Fine sands	0.25～0.05
Coarse powdery sands	0.05～0.01
Fine powdery sands	0.01～0.05
Clays	<0.005

Table 1.5 Classification of bulk solids and sands

Name	Size and mass proportion
Broken stones	>10 mm, >50%
Grits	>2 mm, >50%
Gravels	>2 mm, >25%
Coarse sands	>0.5 mm, >50%
Middle sands	>0.25 mm, >50%
Fine sands	>0.1 mm, >75%
Powdery sands	>0.1 mm, <75%

1.1.4 *Natural angle of repose*

According to the property of granular media, it is a state between solids and liquids. The flowability of granular media is limited, and it only retains its shape when the angle of interfaceslope to the horizontal plane is within a certain limit (shown in Fig. 1.7). This limiting angle β_c is called natural angle of repose. At present, the definition of natural angle of repose is still in dispute. In general, the natural angle of repose is regarded as the maximum inclination angle of slope to the horizontal plane when the granular medium has accumulated natural moisture in certain condition.

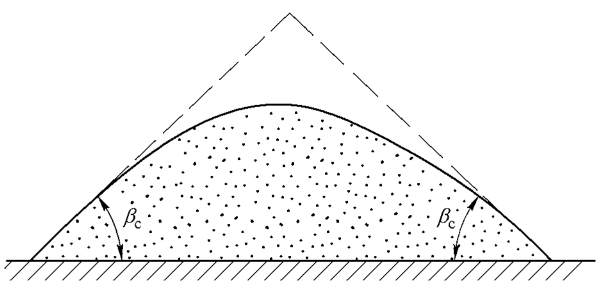

Fig. 1.7 Stacking state of granules

1.1.4.1 Measuring methods of natural angle of repose

Method of loading simulated measuring box

Loading simulated measuring box is a kind of device for measuring natural angle of repose simulating in-situ static pressure, which is shown in Fig. 1.8. When measuring, granules are firstly put into box 1 and flattened. Then, pressure piston 2, on which poises 3 are placed, is activated. Subsequently, sliding door 4 is open, and because of the action of gravity and the static pressure granules 5 will flow and the slope forms. Lastly, the angle of the slope of the pile, which is the natural angle of repose β_y(°), is measured. This angle can be calculated by:

$$\tan\beta_y = \frac{h_m}{l_p} \tag{1.12}$$

where h_m is the aperture of the open door, mm; l_p is the spreading length of the granules in the pile, mm.

Method of bottomless cylinder

This practice shows that the ratio of the diameter and the height of an bottomless cylinder should be 1:3, and the diameter of cylinder must be more than 4～5 times of the maximum diameter of the granules. For example, when the diameter of the granules is less than or equal to 15 mm, the diameter of the cylinder can be 60 mm or 85 mm, and the height of cylinder can be 180 mm or 225 mm. The diagram of a bottomless cylinder is shown in Fig. 1.9.

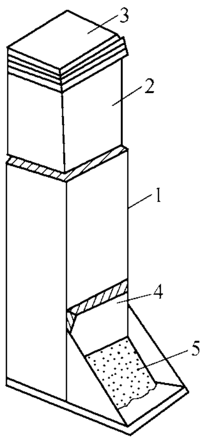

Fig. 1.8 Method of loading simulated measuring box

1—Box; 2—Pressure piston; 3—Poise; 4—Strobe; 5—Granules

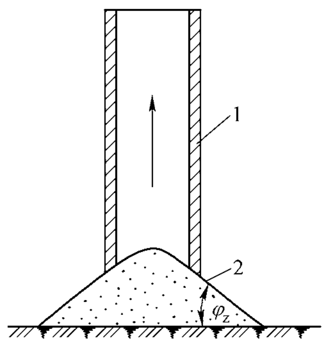

Fig. 1.9 Method of open-ended cylinder

1—Open ended cylinder; 2—Granules

When measuring, the bottomless cylinder is placed on the plane and is filled with granules from the top. Then, the cylinder is lifted vertically very slowly by manual work or by a pulley block, and the granules will form a cone. The included angle of the cone face to the horizontal plane is the natural angle of repose φ_z(°), which is calculated by:

$$\tan\varphi_z = \frac{2h_{zd}}{d_{zd}} \tag{1.13}$$

where h_{zd} is the height of the cone, mm; d_{zd} is the bottom diameter of the cone, mm.

Method of rotary box

The structure of the rotary box is shown in Fig. 1.10. There are two transparent glass plates on opposite sides of a rotary box, in order to observe and measure the angle. The specification of this rotary box is: height×width×length=20 cm×20 cm×40 cm.

When measuring, the granules are put into the box, which is rotated 90° to upright position round the axis. Then the granules are leveled off, and the box is returned to its level position, meantime, the granules will form a slope. The included angle of this slope to the horizontal plane is the natural angle of repose.

Method of falling in a measuring device

The structure of the measuring device is shown in Fig. 1.11. The specification of this device is: height × width × length=700 cm × 150 cm × 200 cm. In measurement, the granules are put into the box and leveled off. Then the bottom sliding door is opened slowly and the granules will flow freely out and form a pile in the box. The included angle of this pile slope to the horizontal plane is the natural angle of repose.

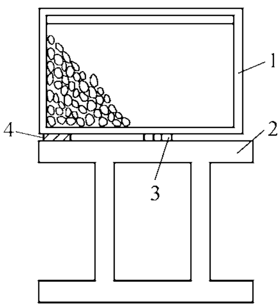

Fig. 1.10 Method of rotary box

1—Box; 2—Frame of box;
3—Rotary axis; 4—Fixation plate

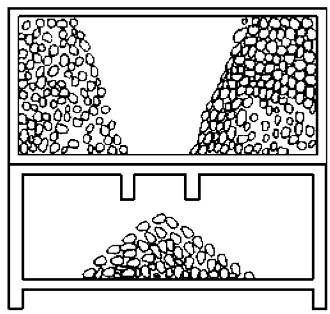

Fig.1.11 Method of falling measuring device

1.1.4.2 Influence factors of the natural angle of repose

Granular size and measuring device

With the increment of granular size (1 mm to 80 mm), the natural angle of repose will decrease (as shown in Fig. 1.12). Fig. 1.12 also shows that the natural angle of repose decreases quickly with the increase of small granules. When the granular size reaches 80 mm, the nature angle of repose becomes steady. In addition, the measured values of natural angle of repose differ with the measuring devices (shown in Table 1.6).

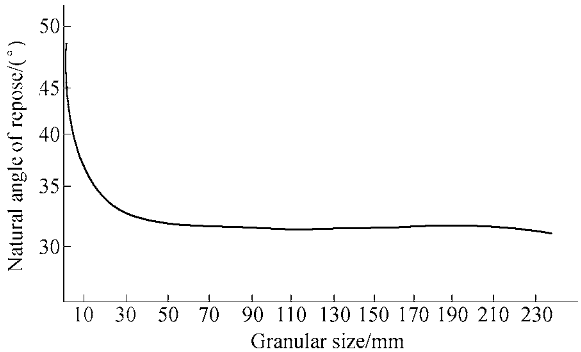

Fig. 1.12 Relationship of granular size and natural angle of repose

Table 1.6 The nature angle of repose measured by different devices

Grading	Name of devices			
	Loading simulated measuring box	Open-ended cylinder	Rotary box	Falling measuring device
Fine granules	35°28′	34°00′	38°10′	42°12′
Middle granules	34°46′	33°54′	37°36′	41°24′
Coarse granules	33°40′	30°49′	36°48′	40°48′
Mixed granules	34°35′	32°17′	37°00′	41°00′

Moisture content of granules

With the increment of moisture content in granules, the cohesion among the granules will increase. Therefore, the natural angle of repose will increase with the increment of moisture content in granules. When the moisture content reaches the saturated degree, the pores of the granular media are filled with water so that the friction decreases significantly and results in the decrease of natural angle of repose. This phenomenon is shown in Table 1.7.

Table 1.7 Relation of nature angle of repose and moisture

Name of granules	Natural angle of repose/(°)		
	Dried	Wet	Wettest
Scree	32～45	36～48	30～40
Sands	28～35	30～40	22～27
Sandy clay	40～50	35～40	25～30

1.1.5 *Granular angle of internal or external friction and cohesive force*

1.1.5.1 Angle of external friction

The angle of external friction is the included angle of slope to the horizontal surface when the granules begin to slip. The tangent of the angle of external friction is called the coefficient of external friction.

In mining engineering, in order to make the granules slide along the slope, the inclination angle α must be more than the angle of external friction φ_w. A measuring device for angle of external friction is shown in Fig. 1.13.

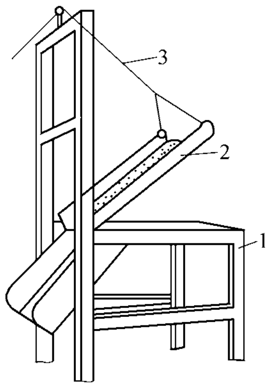

Fig. 1.13 Measuring device of the angle of external friction

1—Frame ; 2—Rotating trough; 3—Line

In measurement, granules are placed in a rotating trough 8~10 cm from its rotary axis. Then the trough is lifted slowly and uniformly through pulling a line. Once the granules begin to slip downwards, the lifting of trough is stopped. The included angle of the slope to the horizontal surface is measured. It is the angle of external friction, which is calculated by:

$$\sin \alpha_w = \frac{h_x}{l_x} \tag{1.14}$$

where α_w is the angle of external friction, (°); h_x is the lifted height of rotary trough, mm; l_x is the length of rotary trough, mm.

If the density is 3.4 t/m^3 and the rigidity f =14~16, the angle of external friction of magnetite quartzite is shown in Table 1.8.

Table 1.8 Angle of external friction of magnetite quartzite

Grading/mm	Angle of external friction /(°)			
	Timber surface		Iron surface	
	Common moisture	Wettest	Common moisture	Wettest
+160	28.0		23.0	
−160+80	32.0		26.0	
−80+40	32.5	27.0	26.5	24.5
−40+20	34.0	30.0	27.5	25.0
−20+8	35.0	34.0	28.5	26.0
−8+5	37.0	46.0	30.0	40.0
−5	45.0	51.0	34.0	43.0

Table 1.8 shows that the smaller the size of the granules is, the larger the angle of external friction is and vice versa. The moisture content of the granular media has strong influence on the angle of external friction. When the moisture content of the granular media reaches a certain degree, the angle of external friction would decrease significantly. In this situation, the granules will probably generate "granular flow". Therefore, the moisture content has a critical value. In addition, the angle of external friction relates to the smoothness of the interface. Different in contact with each other materials have different angle of external friction (as shown in Table 1.9).

Table 1.9 Angle of external friction of different interface

Contacting material	Steel and iron ores	Steel and granites	Steel and sandstone	Granite porphyry and granites	Board and Stone plate	Concrete slab and Stone plate
Coefficient of friction	0.42	0.45	0.38	0.66	0.46~0.6	0.76

1.1.5.2 Granular angle of internal friction

Granular angle of internal friction is the included angle of direct stress acted on the shearing face and the resultant stress when the granular media without cohesion is sheared. Granular angle of internal friction can be measured by the experimental method of shear strength. With the obtained experimental results, a figure of direct stress σ–shearing force τ can be drawn. The included angle of the shear strength curve and the abscissa σ is called internal friction angle, and the tangent of internal friction angle φ is called coefficient of internal friction f. Namely:

$$f = \tan\varphi = \frac{\tau}{\sigma} \tag{1.15}$$

If the granular media are of the nonideal granular composition, because of the cohesion C the coefficient of internal friction should be the ratio of the difference between the shear force and the cohesion ($\tau - C$) and the direct stress σ, namely:

$$f = \tan\varphi = \frac{\tau - c}{\sigma} \tag{1.16}$$

There is always a kind of internal friction when the granules contacting each other move relatively within themselves. According to this condition, the internal friction can be divided into sliding internal friction, static internal friction and rolling internal friction. The interface does not slip relatively, but there is a tendency of slipping because of the action of force. This kind of force obstructing the relative motion of granules is called static internal friction. When one part of the granules move along another part of the granules, the force obstructing the slipping motion is called slip internal friction. When one part of granules rolls along another part of granules, the force obstructing this rolling motion is called roll internal friction. The above three kinds of internal frictions have the corresponding coefficients of internal friction and the angles of internal friction respectively. In general, the angle of internal friction is the static angle of internal friction.

1.1.5.3 Factors influencing the angle of internal friction

There are some factors which have great influence on the angle of internal friction of granular media, such as loosening, moisture, shape, composition, roughness, shear velocity, etc. With the increment of looseness coefficient, the angle of internal friction, the coefficient of internal friction and cohesion will decrease (shown in Table 1.10 and Fig. 1.14). On the other hand, with the increment of compaction degree, the angle of internal friction will increase. If the displacement among the granules increases, the shear force also increases. Therefore, it is helpful for granular aided flow to increase the looseness coefficient and the pore ratio and to decrease the compaction degree.

Table 1.10 Relation between the angle of internal friction, cohesion and looseness coefficient

Looseness coefficient	1.30	1.35	1.45	1.55	1.65	1.75
Angle of internal friction/(°)	46	45	43	40	38	36
Cohesion/MPa	0.5	0.26	0.20	0.05	0	0

With the increment of moisture content in granular media, the cohesion caused by capillarity and the shear strength will increase rapidly. However, when the granular media reach a saturated degree the cohesion caused by capillarity will disappear, and the angle of internal friction will also decrease rapidly. As for the same grading, the round granules have smaller angle of internal friction, but the coarse granules have bigger angle of internal friction. When the shear velocity is high, the angle of internal friction will be small.

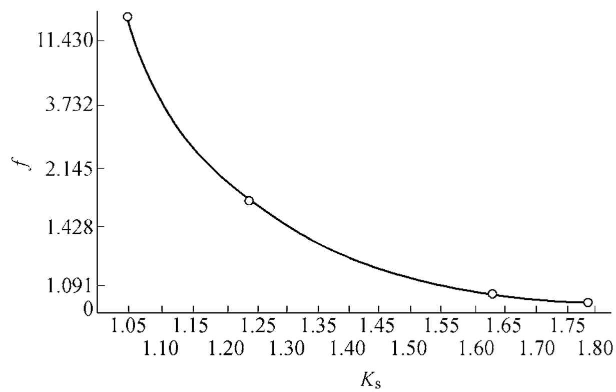

Fig. 1.14 Relation of the coefficient of internal friction f and the looseness coefficient K_s

In a word, the angle of internal friction has great influence on the flowability of granular media. Therefore, the angle of internal friction is an important mechanical parameter.

1.1.5.4 Cohesion of granular media

Even though there is no pressure, granular media still have certain rigidity and shear ability when there are water and sticky materials present among the granules. This initial shear ability is called the cohesion of granular media, which determines the shear strength of the granular media together with the angle of internal friction.

The cohesion of granular media is dependent on the quantity of sticky granules, moisture content and the degree of compaction. In addition, it is also related to the capillarity of pores water. When the quantity of sticky granules and the moisture content increase, the granular media will be solidified, as a result the cohesion will increase. The cohesion also has a great influence on the flowability of granular media. The cohesion can be measured when the angle of internal friction is measured.

When granular media is stored, the property of losing adhesion and becoming solidified is called cohesive property. With the given size of hopper opening, if there is no any boulder and granules can flow freely, it indicates that the cohesion is smaller or nothing. On the contrary, if a cohesive arch forms in the hopper opening, it means the cohesion is higher. Some researchers utilize the exposed area of the cavity in the hopper opening to judge the cohesive degree. For example, as for certain granular medium (the moisture is 1.7%～11% and the percent of sticky granules is 0%～40%), the cohesive degree is shown in Table 1.11.

Table 1.11 Measured results of cohesive degree

Percent of sticky granules/%	Number of experiments	Moisture for maximum cohesion/%	Maximum exposed area of cavity in hopper opening /10^{-2} m^2	Limiting value of moisture causing cohesion/%
0	5	1.9～2.3	2.8	2.0～2.5
3	4	2.0～3.0	4	6.0
6	5	1.7～2.4	5	7.0
9	5	1.7～3.0	7	7.5
12	5	1.7～3.5	12	8.0
15	4	2.0～4.0	18	8.5
20	5	2.0～5.0	24	9.0
30	5	2.0～5.0	32	10.0
40	6	3.0～6.0	42	11.0

Table 1.11 shows that as long as there is some moisture content, the cohesion will increase with the increment of percent of sticky granules. With the increment of moisture, the cohesion also increases significantly. However, when the moisture content reaches a specific degree, the cohesion will decrease. Depending on the

percentage of sticky granules, the moisture limit is 5%~11%. The cohesive property has significant influence on the granular flow. The sticky granules hardly flow through the hopper opening, they form an arch or a cavity, so the efficiency of discharge decreases. This condition will cause safety problems in mines and reduce the yield of undiluted ores.

1.2 Granular Shear Strength and Deformation Characteristic

1.2.1 *Granular shear strength*

Granular strength, *viz*. the breaking strength, is mainly dependent on its shear strength. Granular tensile strength is also related to the shear strength, but the compressive strength is dependent on the strength of grains and the pressure in the contact points.

The following method is used to ascertain the granular shear strength. Granules are put into the opening of a serrated block composed of two parts—top and bottom. The bottom part is fixed and the top part is allowed to move along I—I section by applying shear force F_s (as shown in Fig. 1.15). Force F acts on I—I section vertically. The horizontal displacement is measured by a gauge. Sometimes, the bottom part can move, but the top part does not move.

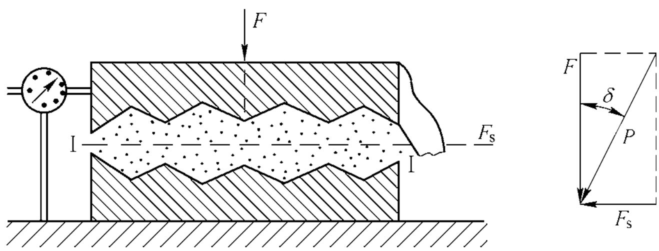

Fig. 1.15 Testing of the granular shear strength

In the course of the experiment the force F is kept constant meanwhile the force F_s is added gradually until a part of the granules just starts to slip relative to another part of the granules. By applying different force F the same experiment is repeated, and for each experiment the limiting value of the shear force, which is the resultant force F_s of the granular shear strength, is obtained.

The results of the experiments are shown in Fig. 1.16, which indicates the relationship between shear strength F_s and normal force F. The curve is so flat (except at the beginning section) that it can be represented by a straight line. It approximately obeys the Coulomb Law, and the shear force is equal to the sum of the internal friction and the cohesion. It can be expressed by the following formula:

$$F_s = Ff + cA \tag{1.17}$$

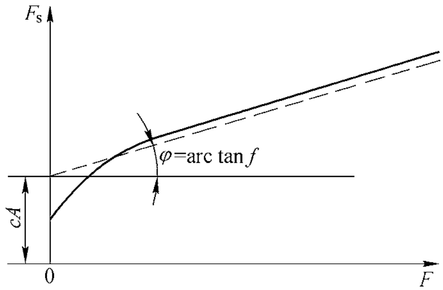

Fig. 1.16 Relation between the shear strength and the normal pressure

where f is the coefficient of internal friction of granular media, which is equal to the tangent of the angle of internal friction, *viz*, $f = \tan\varphi$ or $\varphi = \arctan f$; c is unit cohesion, *viz*, the cohesion on the granular unit; A is the shear area.

The shear strength can be expressed by the ratio of shear force F_s and the shear area A:

$$\tau = \frac{F_s}{A} = \tan\varphi + c = \sigma' \tan\varphi \tag{1.18}$$

where $\sigma' = \sigma_0 + \sigma$ is the equation of normal pressure, *viz*, the pressure caused by the internal cohesion; $\sigma = \dfrac{F}{A}$ is the pressure perpendicular to the shear surface; $\sigma_0 = \dfrac{c}{\tan\varphi}$ is the viscous pressure.

Since the design strength of granular materials is optimal, but the conditions of different granular media differ in numerous ways, it is difficult to evaluate them precisely. In practice the shear strength is measured by some widely accepted experiments. The commonest experiment is the triaxial compression test.

Granular medium is not a rigid plastic body, and it is liable to deform due to the shear force. Meantime, it has obvious body deformation as well as the shear deformation. This phenomenon is called shear expansion. Shear expansion, which is related closely to the granular physical and mechanical properties, is unique to a granular medium. With the increase of axial strain, the granules will move relative to each other and slip on the contact points, so that the granular structure can take on more load and the axial load will be increased continuously until the granular medium is broken up. A part of the elastic energy is accumulated through the confining pressure and the axial surface. When the granules are broken, the accumulated elastic energy is released in the form of vibration and heat.

For most granular media, such as sands, broken ores and coarse soils, etc., the cohesion is very small, so the main factors which influence the shear strength are friction, shear expansion, realignment and granular breaking process, etc.

1.2.1.1 Friction among granules

In the course of shearing, the equilibrants with external load are the direct stress acted on the contact surface and the friction resistance. For the frictional granular materials the mechanism of shear strength rests with the frictional phenomenon among the granules. Therefore, the dominant influence factor on the shear strength is obviously the friction component.

1.2.1.2 Shear expansion

In the course of shearing, a part of energy will dissipate by volume expansion process. Some researchers argue that the shear strength can be evaluated by abating this part of energy. After the volume expansion (or compaction), the interlocking state of granular medium will change towards more stable state, and its structure will take on more load. With the shear deformation, not only a part of essential energy will dissipate in the visual change of volume, but also some unobservable structure changes occur along with the change of volume. This resultant effect is called shear expansion effect.

1.2.1.3 Realignment

With the development of shear deformation, granules will slip or rotate between each other. This phenomenon is called granular realignment. This realignment continuously changes toward new structure state till the peak value of strength appears. The result of realignment certainly strengthens the load bearing capacity. Therefore, the difference of principal stress increases continuously with the increase of axial strain. Because of this realignment, the granular volume will change. But this phenomenon is regarded as the effect of shear expansion. However, the direct structure change of the granular deformation, i.e., the structure change assuming more load bearing capacity, is regarded as the effect of realignment.

1.2.1.4 Granular breakdown

Granular breakdown seems to be the phenomenon of primary change of the granular grading when a part of granules are destroyed or separated. Only from this apparent phenomenon of grading change, it is difficult to understand the relationship between the granular breakdown and shear strength. Moreover, the granular breakdown has many forms from the breakdown of contacting points to the whole granule separating into two parts. Up to now, it is not clear the mechanisms which are related to the influence of granular breakdown on the granular mechanical characteristics. For example, what kind of collapsing mode of granular media is most important to the shear strength and deformation characteristics?

Once the granular medium is broken down, the primary loading structure of the granular medium is also destroyed. Consequently, the load of the contact points among the granules will be realigned. Since the stress concentration of contact points is reduced, the loading of contact points is evenly distributed and a more stable structure forms, but the cohesion among the granules will be weaker. This provides a more easy motion of the granules, which obstructs the effect of the shear expansion instead. Therefore, this is the main reason for the reduction of the angle of internal friction.

1.2.2 *Granular deformation characteristics*

Granular deformation is most universally applicable in geotechnical engineering. Whether the granular media act as the foundations for supporting engineering structures or the roadbeds of earth slope, or act as an engineering material, such as dyke, earthfill of retaining wall, etc., the granular deformation must be controlled within certain limit, otherwise, the engineering structures will be unstable or even destroyed. The granular deformation is more complex than any other engineering materials, and many factors can lead to granular deformation. These factors are:

(1) Under pressure granular media will have volume compaction, deformation and solidification, and when the pressure is reduced granular media will expand. Because granular media commonly do not bear tensile force, it is not usually considered.

(2) Because of the change of moisture content, the water in granular media will be affected by freezing and thawing process, so that granular media will be deformed.

(3) Because of the change of moisture content, granular media will have either dry shrinkage or water swelling, causing the unstability of structure with extra deformation, such as settlement of structure due to saturated granular media.

(4) Because of the change of chemical environment, the interaction between granules and water will change, so the granular deformation characteristic will be influenced.

Amongst the above factors the change of pressure is the most important item and is well studied. Granular medium is different from other elastic engineering materials, and its deformation is changed horizontally parallel with the stress and is not a constant. However, its behavior is also the same in certain aspects in comparison with other engineering materials, *viz*, the granular deformation (or strain) and the load intensity (or stress) are the two sides of the same problem. Strictly speaking, there is neither deformation separated from intensity nor intensity without deformation in the granular medium. They interact, namely, sometimes the deformation is expounded elaborately in certain degree of intensity but sometimes the intensity is defined in terms to certain deformation. Therefore, the two are usually inseparable.

1.2.2.1 Granular compressive deformation

In laboratories the compressive deformation of granular media is often tested and researched by consolidometer. In consolidometer, the sides of the granular media are confined and do not register deformation, only having compressive deformation vertically. This is one-dimensional deformation, which is also called specialized compressive deformation.

However, there are many other compressive deformations in engineering practice. In many engineering cases, there are some lateral deformations as well as partial confined deformation, such as the deformation of soil mass below the foundation and in the earth-retaining structure. Therefore three-dimensional deformation should be considered. In addition, there is a kind of compressive deformation generated entirely without lateral confinement in granular media. For example, this kind of compressive stress must be considered when the layer of soils is excavated to achieve the critical height.

In the broad sense compressive deformation can occur in two-dimensional or three-dimensional conditions. The compressive deformation of one-dimension and the deformation without lateral confinement are special examples. All of these deformations are the examples of generalized compressive deformation.

1.2.2.2 Indexes of compressive deformation and their interrelation

Relationship of compressive coefficient of volume κ_V, compressive modulus K_s and compressive coefficient α

The compressive coefficient of volume κ_V is the change of volume caused by unit pressure (p) under the condition of lateral confinement. In practice, it is often denoted by the factor of porosity (n), which substitutes the change of volume.

$$\kappa_V = \frac{\Delta n}{\Delta p} \tag{1.19}$$

In order to express exactly the relationship of stress-strain in the course of compaction, the change of porosity ratio e is used, so that the result of compressive experiments is denoted by the curve of e-p, which is often substituted by an approximate line (shown in Fig. 1.17). Therefore, the following formula can be obtained,

$$e_1 - e_2 = \alpha(p_2 - p_1) \tag{1.20}$$

where α is the compressive coefficient.

Because of the change of granular porosity ratio $\Delta n = \dfrac{\Delta e}{1+e_1}$, and $\Delta p = \dfrac{\Delta e}{\alpha}$, thereby,

$$\kappa_V = \frac{\alpha}{1+e_1} \tag{1.21}$$

The compressive modulus of granular media is the ratio of stress σ_z and the corresponding strain ε_z under the compressive condition of lateral confinement. It is expressed by,

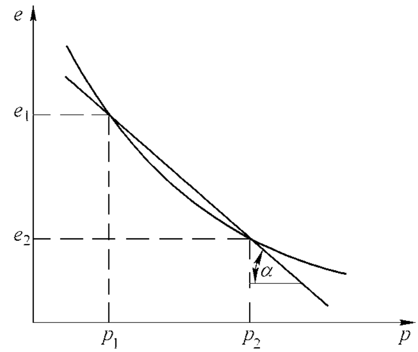

Fig. 1.17 Curve of e–p

$$E_s = \frac{\sigma_z}{\varepsilon_z} \tag{1.22}$$

In the compressive experiments, $\sigma_z = p_2 - p_1 = \Delta p$ and $\varepsilon_z = \dfrac{\Delta e}{1+e_1}$.

According to the compressive law, $\alpha = \dfrac{\Delta e}{\Delta p}$, thereby:

$$K_s = \frac{\Delta p}{\dfrac{\Delta e}{1+e_1}} = \frac{1+e_1}{\alpha} \tag{1.23}$$

Therefore, $K_s = \dfrac{1}{\kappa_V}$, which is the reciprocal of compressive coefficient of the volume. According to engineering experience, when $K_s < 4$ MPa, the compaction is called high compressibility; when $40 \leqslant K_s \leqslant 150$ MPa, it is called middle compressibility; and when $K_s > 150$ MPa, it is called low compressibility.

Relationship between the deformation modulus E and the compressive modulus K_s

Granular deformation modulus E is the ratio of stress-strain for the isotropic granular media without lateral confinement in semi-infinite space. And granular compressive modulus K_s is the ratio of stress-strain under the condition of entire lateral confinement. Theoretically E and K_s can be converted into each other. In terms of the generalized Hooke's law, the strain along x axis ε_x comprises $\dfrac{\sigma_x}{E}$, $-\mu\dfrac{\sigma_y}{E}$, and $-\mu\dfrac{\sigma_z}{E}$ caused by σ_x, σ_y and σ_z respectively. The negative sign denotes lengthening, and μ is granular poisson's ratio. Because the sample is tested without lateral dilation, so $\varepsilon_x = \varepsilon_y = 0$, thereby,

$$\varepsilon_x = \frac{\sigma_x}{E} - \mu\frac{\sigma_y}{E} - \mu\frac{\sigma_z}{E} = 0 \tag{1.24}$$

Assuming that β_0 is the coefficient of lateral pressure, *viz*, $\sigma_x = \sigma_y = \beta_0 \sigma_z$, so that the relationship of β_0 and μ is:

$$\beta_0 = \frac{\mu}{1-\mu} \tag{1.25}$$

or

$$\mu = \frac{\beta_0}{1+\beta_0} \tag{1.26}$$

2

Granular Dynamic Testing Techniques

2.1 Outline

In soil dynamics field, extensive studies have been done on the granular dynamic characteristics. Soil dynamics has gained a great advancement ever since its beginning of development in Germany in 1930s. The study on soil dynamics has brought three sub-disciplines into the world. They are blasting dynamics, seismic dynamics and power machinery elementary dynamics[6~12].

With the advancement of soil dynamics, granular dynamic characteristic testing devices and techniques have been developed. According to different conditions, geotechnical dynamic testing methods can be divided into four types[6~9]:

(1) Indoor test. Its characteristic is that all kinds of conditions can be artificially controlled, so that the granular dynamic characteristics can be tested. Because the testing conditions can be idealized and standardized, this kind of testing is mostly used to identify the elementary geotechnical dynamic parameters, or to carry out multifactor simulation tests under complicated stress or boundary conditions (such as liquefaction).

(2) In-situ simulation test. It is used to simulate the granular dynamic response influenced by the factual power machinery or devices, such as the rigidity test of the groundwork affected by various kinds of dynamics, dynamic deformation and dynamic strength tests and so on.

(3) In-situ test. It is mainly used to measure the entire dynamic characteristics of the granular layer, such as the measurement of various kinds of wave velocities, the attenuation coefficient and the natural period, etc.

(4) Prototype measurement, such as the measurement of characteristics of factual dam body and dam foundation, foundation and groundwork under natural and artificial seismic actions.

The methods of granular indoor dynamic test involve dynamic direct shear test, dynamic triaxial test, dynamic single shear test, dynamic torsion ring shear test, vibrating table test and resonance column test. The characteristics of each test method can be seen from Table 2.1.

Table 2.1 Classification of the methods of granular dynamic indoor test

Test method	Main content	Open question
Dynamic direct shear test	The container similar to ordinary direct shear apparatus is placed on the vibrating table. Vertical load and shear load act alternately on it singly or synchronously	Stress can not be better controlled. The sample can not be sealed properly
Dynamic triaxial test	Cylindrical sample are concreted by the action of both axial and side directions. Then exciting force is exerted on them so that the shear force of the sample on the shear plane has periodical change	Stress condition has great difference from the onsite practical situation
Dynamic single shear test	A quadrate sample which is sealed in the rubber membrane is made within the sample container. The vertical pressure is exerted on it so that a pair of side walls of the container has the alternating motion by the action of the alternating shear force	The sample is not uniformly shaped. Side pressure can not be controlled
Dynamic torsion ring shear test	The sample is a hollow column whose inside has different heights. A fixed alternating torsional moment is exerted on the sample's plane by the action of certain side pressure. The shearing stress is well-distributed. The stress state can be controlled. The onsite stress condition can be better simulated	The preparation of the sample and its sealing are difficult. The operation is also difficult
Vibrating table test	A sealed sand container full of saturated sand sample is placed on the vibrating table. Then a forced vibration is exerted on it. The frequency and amplitude of the vibration are adjusted according to the requirements. The transformation of the pore water pressure and stress strain must be measured at the same time	The boundary condition and the condition of the sample's active forces are not consistent with the practical stress state completely
Resonance column test	The tailor-made device is used to excite a cylindrical rock and soil sample so that the level torsional vibration and vertical vibration can be produced. The resonance of the first vibration mode is obtained at the same time. Then the frequency of resonance and amplitude values are measured. Finally according to the theory of elasticity the shear wave velocity, rigidity (modulus), corresponding amplitude value of the shearing strain and damping coefficient are calculated	The operation is complicated. The influential factors on the result are more. The practical state is difficult to be simulated. There are difficulties in processing the test data

West countries have similar test devices as listed in Table 2.1. However their devices have a certain disparity with ours. Since the development of soil dynamics has only a history of a little more than 50 years, and some test devices and techniques have been developed recently, they leave much to be desired. With the advancement of electronic instruments and techniques, and the continuous availability of high-tech products, the dynamic testing techniques of rock and soil have bright future. For example, electrohydraulic servo large vibrating table has been applied, resonance column testing machines have passed the examination by experts by the end of 1980s' in China, computer technology and sensor technology have gradually been popularized in soil tests. Since rock and soil dynamic test technology is a new subject and its study started very late in China, it is in the stage of rapid development.

2.2 Dynamic Triaxial Test

Dynamic triaxial test is developed from triaxial test. They both have many common characters. Dynamic triaxial test is to utilize the similar axial stress condition, and then to exert simulant dynamic principal stress on the sample. Finally it is to measure the dynamic response that the sample shows under the action of dynamic load[7~11].

In the earlier dynamic triaxial test, the level of axial stress basically is kept the same, but by changing vertical axial pressure periodically the sample in the test undergoes a cyclic major principal stress in the axial direction; thereby in the sample the cyclic normal stress and shearing stress are accordingly generated within the sample. This is the so-called constant side pressure dynamic triaxial test. Where σ'_0 is the given ambient pressure; σ_1 is the cyclic major principal stress; and σ_d is the dynamic stress. The load is exerted on the sample by the semi-peak amplitude. $\sigma'_0 \pm \sigma_d/2$ is the normal stress generated on the 45° inclined plane inside the sample. $\sigma_d/2$ is the value of the dynamic shearing stress on the same inclined plane.

Since 1970s' the variable side pressure type of dynamic triaxial test has been developed in order to overcome the shortcoming of the constant side pressure type of dynamic triaxial test that cannot be used to obtain the major stress ratio (σ_1/σ_3). This variable type testing technique can exert the alternant dynamic load that has two axial directions and whose phase difference is 180° on the sample. In this way, the normal stress on any inclined plane inside the sample is kept invariable. The shearing stress on the inclined plane changes its signs alternately so that the seismic shearing stress on the soil layers when sandy soils are liquefied can be simulated without limit of stress ratio (σ_1/σ_3).

2.2.1 *Test contents*

(1) Measure granular dynamic characteristic indexes, such as dynamic modulus, dynamic damping ratio, dynamic strength and so on.

(2) Measure the strength of resisting liquefaction of sandy soils.

(3) Study the influence of some factors on the granular dynamic characteristics.

2.2.2 *Types of the dynamic triaxial instruments and the specification of the sample*

According to different methods of generating and exerting dynamic load, the dynamic triaxial instruments in China can be classified as:

(1) Dynamic triaxial instrument of electromagnetic excitation;

(2) Dynamic triaxial instrument of inertial excitation;

(3) Dynamic triaxial instrument of hydraulic excitation;

(4) Dynamic triaxial instrument of pneumatic excitation.

The sizes of the samples are usually smaller. There are several kinds of specification such as ϕ38 mm×76 mm, ϕ 60 mm×120 mm, ϕ100 mm×200 mm, etc.

2.2.3 *Scheme of the tests*

The magnitude of the indexes of the granular dynamic characteristic depends on a certain dynamic condition, granular condition, stress condition and drainage condition. So when a certain specific problem needs to be solved and the indexes of the granular dynamic characteristic need to be supplied, the practical condition should be simulated as much as possible according to the above four aspects.

2.2.3.1 Dynamic condition

The wave pattern, direction, frequency, amplitude and duration time of the dynamic action should be simulated as much as possible. In seismic analysis, according to the method of Seed, the wave pattern of seismic random variation can be simplified into the equivalent action of the harmonic. The amplitude value of shearing stress of the harmonic wave is $\tau_s = 0.65\ \tau_{max}$. The equivalent circular number N_S of the harmonic wave can be ascertained according to the scale of the seismic magnitudes. The frequency from 1 Hz to 2 Hz is used. The direction of seism is considered according to the level shearing wave. This method is most widely used in the dynamic triaxial tests at present in China.

2.2.3.2 Granular condition

It is mainly to simulate the practical granularity, humidity, density and structure of the researched granules. For in situ soil sampling these cannot be disturbed in the course of making the sample. For prepared soil samples the humidity and density need to be considered. For saturated sandy soils the main simulated soil character condition is the density of the sample, which is controlled through the actual density of sandy soils in the landfill or in a dam body. If the actual density changes in a certain range, several kinds of typical density conditions should be controlled.

Without directly measured density data, the density can be controlled according to the relative density corresponding to the blow numbers of the penetration test according to the status of the field. All the above are easy to achieve in the tests. But in the sandy soils there are too much coarse granular materials, the simulation becomes a problem worth studying with the limitation of the size of vibrating triaxial instrument sample. It is widely accepted by the researchers that the content of the coarse granular materials is a key factor. If the coarse granular materials in the granules can form a steady framework and the coarse granular materials only have the function of filling the holes, the granular character mostly depends on the characteristic of coarse granular materials. From the viewpoint of liquefaction the risk is less. On the contrary, if the content of the granular materials is not enough to form a steady framework and the coarse granular materials only can disperse in refined granular material, the granular character mostly depends on the characteristic of the refined granular materials. There is more risk of liquefaction.

2.2.3.3 Stress conditions

The actual granular stress states under the movable and immovable condition are simulated. In the dynamic triaxial test σ_1, σ_3 and their transformations are usually applied to express the following: the consolidation stress before the seism is σ_{1c} and σ_{3c}; the stress during the seism is σ_{1c} and σ_{3c}. At first, for the level ground (as shown in Fig. 2.1a) because the action of the seism propagates in the direction of plane shearing wave, on the plane of any depth h before the seism, the stress is $\sigma_c = \sigma_0 = \gamma h$, $\tau_c = 0$; during the seism the stress is $\sigma_e = \sigma_0$, $\tau_e = \pm\tau_d$. As stated before, the stress state can be simulated by the stress on the 45° plane if solidification is the same in the dynamic triaxial test. Namely, when $\sigma_{1c} = \sigma_{3c} = \sigma_0$ the normal stress on the 45° plane is $\sigma_c = \sigma_0$, the tangential stress on the 45° plane is $\tau_e = 0$. During the action of the seism, $\sigma_{1e} = \sigma_{1c} \pm \sigma_d /2$, $\sigma_{3e} = \sigma_{3c} \pm \sigma_d /2$, and the normal stress on the 45° plane is $\sigma_e = \sigma_0$, $\tau_e = \tau_d = \pm\sigma_d /2$. The transformation of stress state can be simulated by so called bi-directional excitation triaxial instrument. But when the problems of the stress and transformation are studied it can be substituted by the equivalent applied stress state in order to use the simplex excitation triaxial instrument. Namely, $\sigma_{1c} = \sigma_{1c} \pm \sigma_d$, $\sigma_{3c} = \sigma_{3c}$; an equal stress is $\pm 1/2\ \sigma_d$. On this occasion, the final stress state on the 45° plane is still $\sigma_e = \sigma_0$, $\tau_e = \tau_d = \pm\sigma_d /2$. At the same time, because the equal stress $\pm\sigma_d /2$, which is not directly exerted, does not change the granular strength and the size of the transformation, the total effect is the same as the practical result when the two directions have the stress transformation. The theory and practice have proved the correctness of this processing method. Secondly for the sloping ground (shown in Fig. 2.1b), on the plane of any depth z under the ground the stress before the seism is $\sigma_c = \sigma_0 = \gamma h$, $\tau_e = \tau_0$; during the seism the stress is $\sigma_e = \sigma_0$, $\tau_e = \tau_0 \pm \tau_d$. This kind of stress state should be simulated in the dynamic triaxial test by using stress transformation on the 45° plane when the biasing solidification occurs. Namely, when $\sigma_{1c} > \sigma_{3c}$ and $\sigma_0 = 1/2\ (\sigma_{1c} + \sigma_{3c})$, the normal stress on the 45° plane is $\sigma_e = \sigma_0$; tangential stress is $\tau_e = \tau_0 = (\sigma_{1c} - \sigma_{3c})/2$. During the seism, $\sigma_{1e} = \sigma_{1c} \pm \sigma_d\ /2$, $\sigma_{3c} = \sigma_{3e} \pm \sigma_d\ /2$; the normal stress on the 45° plane is $\sigma_e = \sigma_0$; tangential stress is $\tau_e = \tau_0 \pm \sigma_d\ /2$. This kind of stress state is easily be simulated by using the triaxial instrument of the bi-directional excitation. It can also be simulated by using the dynamic triaxial instrument of the simplex excitation on the similar plane, but biased solidification is needed, namely $\sigma_{1c} > \sigma_{3c}$ and $\sigma_0 = (\sigma_{1c} + \sigma_{3c})/2$. At the same time, on the 45° plane $\sigma_e = \sigma_0$, $\tau_c = \tau_0 = (\sigma_{1c} - \sigma_{3c})/2$. During the seism the applied stress in the test is $\sigma_{1c} = \sigma_{1c} \pm \sigma_d$ and $\sigma_{3c} = \sigma_{3e}$. The equal stress indirectly exerted is $\pm \sigma_d\ /2$. On this occasion, the final stress on the 45° plane is still $\sigma_e = \sigma_0$ and $\tau_e = \tau_0 \pm \tau_d \pm \sigma_d\ /2$. Finally, for the more complicated stress state (as shown in Fig. 2.1c), such as the condition that before the seism on any plane $\sigma_c = \sigma_0$ and $\tau_c = \tau_0$ and during the seism $\sigma_e = \sigma_0 \pm \sigma_d$, $\tau_c = \tau_0 \pm \tau_d$, the triaxial instrument of simplex excitation cannot simulate. Only the triaxial instrument of bi-directional excitation can be applied. Before the seism $\sigma_{1c} > \sigma_{3c}$ and $\sigma_0 = 1/2(\sigma_{1c} + \sigma_{3c})$; on this occasion on the 45° plane $\sigma_c = \sigma_0$, $\tau_c = \tau_0 = 1/2(\sigma_{1c} - \sigma_{3c})$. During the seism, $\sigma_{1e} = \sigma_{1c} \pm \sigma_{1d}\ /2$, $\sigma_{3e} = \sigma_{3c}\ \pm \sigma_{3d}\ /2$; on this occasion on the 45° plane $\sigma_e = \sigma_0 \pm \sigma_d = \sigma_0 \pm (\sigma_{1d} + \sigma_{3d})/2$, $\tau_e = \tau_0\ \pm \tau_d = \tau_0 \pm (\sigma_{1d} - \sigma_{3d})/2$.

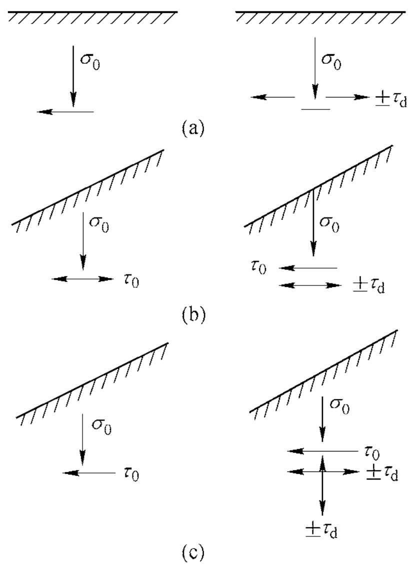

Fig. 2.1 Three kinds of stress states on the ground

2.2.3.4 Drainage condition

The influence of the granular different drainage boundary on the actual velocity of the pore pressure development under the action of seism is simulated. As before, the sand pipe draining a part of water is installed towards the pore pressure pipe. Then the drainage condition can be controlled through changing the length of the sand pipe and the coefficient of permeability of sandy soils. But under the condition of instruments and equipments available, considering the temporary action of seism and the application safety of the test results, the dynamic triaxial tests are usually done under the condition of non-draining.

2.3 Large Scale Vibrating Table Test

Large scale vibrating table has been developed recently. It is an indoor large scale dynamic test equipment studying exclusively for the prediction of the soils' liquefaction[6~9]. It has many significant advantages:

(1) It can overcome the shortcoming that occur in small scale tests, such as the influence caused by the different forms of the application of force mechanism, the influence of the surface of the sample, etc.

(2) Large scale samples can reduce the influence of the boundary conditions of small-scale instruments. In this way samples can vibrate in a "free field" condition. Moreover, the character of samples during vibration as well as after vibration can be directly observed with naked eyes.

(3) It can offer convenience for using large scale samples to simulate the stress condition of natural layers, i.e. solidification can be achieved; the incumbent effective pressure upper wing converts can be simulated.

(4) It can utilize electrohydraulic servo machines to closely simulate the actual action of seismic waves. This kind of action is to input certain random waves into soil layers from bottom to top or to produce harmonic vibration with a given characteristic parameters. In this way, the soil layers are sheared by the action of input level acceleration. As a result whether liquefaction occurs it can be observed in the range of a limited duration of seismism or cyclic numbers of vibration.

The length to height ratio of samples should be more than 10 in order to ensure that the samples are in the state of "free field" while vibration. The vibration must be similar to the situation that shearing wave inputs vertically upwards from base rocks during the seism. On this occasion, the sample is covered with a sealed film of rubber. The air pressure is exerted in order to simulate the effective pressure on the liquefaction layers. The side walls of the samples should be inclined from the base to the top surface in order to eliminate the boundary influence on the samples and to allow free generation of shearing deformation. An appropriate method should be chosen to prepare soil samples in order to control the homogeneity and representativity of the samples.

However, the large scale vibrating table test is not a perfect method in practice, because the preparation of large scale samples is very uneconomical and the reaction on the stress ratio of the diversity caused by different methods of preparation may reach 200%[9].

2.4 Resonance Column Triaxial Test

The resonance column triaxial test is to exert longitudinal vibration or torsional vibration on the soil column (solid or hollow) under the condition of a certain humidity, density and stress, then gradually change the driving frequency and cut power so as to measure the attenuation of the vibration curve. According to the resonance frequency, the size of the sample and the limitation conditions on its end, the dynamic modulus E_d or G_d of the sample are calculated. According to the attenuation curve the damping ratio λ is calculated.

The resonance column technology was introduced into soil test very early (Japan, 1938), but it was not widely applied or greatly developed until the beginning of 1960s'. Especially in recent years it has been widely applied in many countries (USA, Japan, Germany, etc.) to measure the dynamic modulus of soil and the damping indexes. In China, such equipments for resonance column test have been indigenously made or introduced and the study on it has begun. The first locally made GZ-1 type machine for resonance column test was developed successfully by Engineering Mechanics Institute of Chinese Academy of Sciences. The resonance column equipment developed by Automatization Institute of Nanking has been modified and used in the Water Conservancy Institute of Science of Nanking. The advantage of this kind of instrument is that the dynamic characteristic of the soil in the strain range of $10^{-6}\sim10^{-3}$ can be studied. But it is very difficult for the dynamic triaxial test to obtain accurate exact results under the condition of low strain (less than 10^{-4})[7~10].

2.4.1 *Operating principle of the resonance column test*

Briefly, the resonance column test is to utilize some tailor-made devices to excite a cylindrical rock and soil sample. This is to generate a plane torsional vibration or vertical vibration and to achieve the resonance vibration of the first vibration type. Under the condition of this kind of resonance vibration the frequency of the resonance vibration and amplitude value are measured. Then according to the theory of elasticity, the velocity of shearing wave, shearing rigidity (modulus) and the corresponding shearing strain amplitude value, etc. are calculated. The test can be divided into two parts of excitation and measurement of vibration. Fig. 2.2 shows the sketch map of the resonance column system.

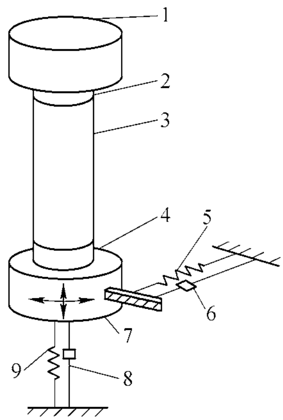

Fig. 2.2 The sketch map of resonance column system

1—The mass of the cover disk of rigidity; 2—The cover disk of the passive end; 3—Sample; 4—The base disk of the driving end; 5—The torsion vibration spring with mass; 6—The torsion vibration damping instrument without mass; 7—A part of the device with slight vibration connected on the base disk for rigidity; 8—The longitudinal damping instrument without mass; 9—The longitudinal spring without mass

2.4.2 *Test condition*

The resonance column method is a special one used to measure the elasticity modulus and damping coefficient of rock and soil. The two parameters usually depend on the strain amplitude value of the vibration, the effective stress state of confining pressure, the porosity ratio of soil, etc. Even the ambient temperature and test time can influence the measured data. So the availability of the results of the resonance column test for the actual project depends on how to control these parameters during the test. In principle, the special conditions of geotechnical engineering must be strictly simulated in the resonance column test. In simulating test, the type and various constants of the test instrument are the most important factors.

The actual rigidity and mass of the resonance column must exactly accord with the mechanism shown in Fig. 2.2. Therefore, the instrumental constant of every part must be limited. Suppose that: m_p is the mass of the cover disk of passive end, including the parts connected by rigidity on it; m_A is the mass of the base disk of the active end, including the parts connected by rigidity on it; K_{SL}, K_{ST} are respectively the spring constant of the longitudinal vibration and the level torsional vibration; f_{OL}, f_{OT} are respectively the resonance frequency of the instrument during the longitudinal excitation and the level torsion; J_A, J_P are respectively the inertia moment of the active end's base disk and the passive end's cover disk and both of them include the parts connected by rigidity; ADC_L, ADC_T are respectively the damping coefficient of the instrument during the vibration and the level torsional vibration; F_{CF}, T_{CF} are respectively the ratio of the applied exciting force during the longitudinal excitation and the level torsional excitation (or torsion moment) to the electrical current input into the excitation system; LCF_A, RCF_A are respectively the calibration coefficient of the sensor under the condition of the longitudinal vibration and the level torsional vibration corresponding to the base disks of the active end (the subscript is A) and the passive end (the subscript is P).

2.4.3 *Damp of system*

In a word, there are two methods to measure damping constant: (1) utilizing the hysteresis curve of the steady-state vibration to calculate; (2) utilizing the attenuation curve of the amplitude of damping free vibration and according to the following expression to calculate the logarithmic attenuation coefficient δ:

$$\delta = \frac{1}{n}\ln\frac{A_1}{A_{n+1}} \tag{2.1}$$

where A_1 is the amplitude value of the first cycle after the electric source of the resonance system is cut off; A_{n+1} is the amplitude value of the $(n+1)$th cycle.

Both of the above methods are applicable to measure the damping coefficient of the resonance system. In theory, the two methods can get the same result. But in practice, because of the influence of the experimental error and the system error the results of both methods are only approximate to each other. The hysteresis curve of the steady-state vibration method is much easier to use. The attenuation curve of the amplitude value of free vibration method is usually used to verify a few abnormal situations. How to choose the two methods is independent of the longitudinal vibration or the level torsional vibration adopted. When the hysteresis curve of the steady-state vibration method is adopted the value of electric current of the sensor at the active end or the passive end needs to be measured under every resonance frequency.

2.4.4 *Measurement of elastic modulus*

The elastic modulus E of rock and soil measured by the resonance column method is called as"the member modulus", because according to the test principle the sample is dealt with as an elastic member with axial vibration. Usually it is measured by the longitudinal excitation. However the shearing modulus of rock and soil is measured by plane torsional vibration. More specifically, the member modulus and shearing modulus should be defined as a modulus of homogenous linear viscoelastic sample (equivalent to Voigt model). The ideal sample may have resonance under the action of the given exciting force (or the moment of force).

In the resonance column test, the hysteresis curve of the steady-state vibration is used to describe the relation between stress and strain. However the above two kinds of modulus is equivalent to the slope angle of a straight line across the end point of the hysteresis curve. According to the measured frequencies of the longitudinal vibration and the level torsional vibration of the system, the member modulus and the shearing modulus can be obtained by the following calculation. The absorption of the resonance column system in the vibrating energy can be used to measure the damping characteristic of soils. It is usually expressed by member damping ratio D_L and shearing damping ratio D_T and is critical in a single-degree freedom vibration system. These two kinds of damping ratio can be calculated by the following expressions:

$$D_L = 0.5(\eta\omega / E) \tag{2.2}$$

where η is the viscosity coefficient of the member vibration, N • s/m^2; ω is the frequency of the resonance circle, rad/s; E is the member modulus, Pa.

$$D_T = 0.5(\mu\omega / G) \tag{2.3}$$

where μ is the viscosity coefficient under the condition of torsional vibration; G is the shearing modulus, Pa.

The damping ratio obtained by the above two methods is equivalent to the elastic strain energy of the coverage included by the hysteresis curve divided by 4π. The strain energy is stored internally when the sample has the most strain. In the viscoelastic theory the characteristics of the modulus and the damping are expressed by a composite modulus. For example, composite member modulus is that:

$$E^{*} = E(1 + 2iD_L) \tag{2.4}$$

The composite shearing modulus is that:

$$G^{*} = G(1 + 2iD_T) \tag{2.5}$$

where $i = \sqrt{-1}$.

2.5 Dynamic Single Shear Test

Dynamic single shear is also called as dynamic simple shear. A special shearing chamber is used to apply shearing stress on every point of the soil sample uniformly so that the strain can be equable. Virtually it is close to simple shear action[6~12].

The dynamic single shear testing can be divided into rigid case type and piled loop type, which are achieved by making the shear chamber with a rigid case or a piled loop. The single shear chamber is made of rigid metal hinges. Each pair of the hinge joints are placed facing each other. When it has the rotary inversion the original rectangular cross section of the rigid plate will be changed into rhombic cross section and is sloping in both sides. In this way, the shearing strain of the same angle will be generated in the sample. The operating principle of the piled loop type is the same to that. The only difference is that its shearing chamber is made of thin ferrules piled together and the man-made displacement on the shear plane is substituted by the whole volume angular strain. The dynamic single shear is mainly used to decide the liquefaction potential. It has three advantages over the dynamic triaxial method. Firstly, the dynamic action condition provided by it is closer to the process of liquefaction generated in the course of the seism in natural soil layers. Secondly, according to the actual situation, whether the original shear stress should be exerted on the sample can be decided. Thirdly, the dynamic single shear test can also measure the dynamic elastic modulus, the dynamic strength, and the damping coefficient of the soils, etc.

It should be noticed that due to the complicated condition of the dynamic test a dynamic parameter is usually measured by several test methods. In addition, a set of dynamic test device can synchronously measure many dynamic parameters or simulate many test vibrating conditions. Each device has its advantages and applied range, and no one device is absolutely ideal or universal. Various kinds of dynamic testing methods of rocks and soils are shown in Table 2.2.

Table 2.2 Granular dynamic testing methods and characteristics

Range of the dynamic strain magnitude		10^{-6}—10^{-5}—10^{-4}—10^{-3}—10^{-2}—10^{-1}—10^{1}		
Mechanical characteristic		Elasticity and viscoelasticity	Elasto-plasticity	Stability
Engineering phenomena		Wave propagation and vibration	Dehiscence and sinking unhomogeneously	Compaction, liquefaction, landslip and flowing
Measurement of parameters		Wave velocity, dynamic elastic modulus, dynamic shear modulus, Poisson ratio and damping ratio		Dynamic strength C and φ
Indoor testing methods	Dynamic triaxial	$10^{-6}\sim10^{-4}$		
	Dynamic single shear	$10^{-6}\sim10^{-4}$		
	Resonance column	$10^{-5}\sim10^{-3}$		
	Vibrating table	$10^{-3}\sim10^{-1}$		
Field testing methods		In-situ wave velocity method	$10^{-6}\sim10^{-4}$	
		Vibrating model test	$10^{-5}\sim10^{-2}$	
		Observation of pulsation	$10^{-6}\sim10^{-4}$	
Prototype observation and actual observation			$10^{-6}\sim10^{1}$	

It can be seen from Table 2.2 that when $\varepsilon > 10^{-2}$ the destructive deformation happens in granules during liquefaction and flowing process. Thereby, the vibrating table testing method is used to measure the granular dynamic parameters, and other testing methods are not so suitable. But the large-scale vibrating table is the laboratory large-scale dynamic testing device, which has been developed within last ten years to study the liquefaction potential of soils. It mainly simulates the seismic waves. The preparation of large-scale samples is not very economical. Moreover the stress ratio of the samples caused by various preparation methods can differ by 200%. So it can be seen that while simulating the granular flowing and liquefaction caused by dynamic machines the vibrating table method is not very appropriate. Under the condition of the available techniques in existence, the direct shear method is an effective method to measure the granular strength and the value C and φ under the action of dynamic machines.

The dynamic direct shear in Table 2.1 is used to simulate the alternative shear stress of the seism in soil dynamics. Soil dynamics mainly concerns retaining wall and foundation design. In addition, soil dynamics is also mainly concerned about the characters of rocks and soils before they yield. The granular disposal study mainly focuses on the condition of yielding and flowing, while soil dynamics does not concern about the flowing after soils yield, which is just right the conjunct part of the engineering subject of granular materials disposal and soil dynamics.

Both dynamic single shear test and dynamic triaxial test have their own advantages. The advantage of dynamic single shear test over dynamic triaxial test is mainly that the condition of the dynamic action provided by it is much closer to the process of liquefaction of the natural soil layers during the seism. Moreover, this type of test can consider whether the original shear stress should be exerted on the sample in terms of the physical circumstances. So the liquefaction test has been the chief function of the dynamic single shear instruments since they were developed.

The elastic constants of soils such as dynamic elastic modulus, dynamic strength, damping coefficient, etc. can be measured by using dynamic single shear instruments. But when the elastic constants are measured the sample does not carry the axial stress but the shear stress only. Hence the corresponding strain measured is also not axial. Therefore, it is more appropriate for it to be used to measure directly the shear modulus (rigidity). But the dynamic triaxial and the dynamic single shear are different in their applied stress condition, so when analyzing the results of both tests they should be discriminated. Because in the dynamic triaxial test the maximum shear stress on the sample is generated on the 45° slope plane not on the level plane, the stress ratio ($\sigma_d /2\sigma_3$) is greater than the stress ratio on the level plane in the dynamic single shear test. It is supposed that the ratio of both is C_r. According to the study provided by Finn and others, the values of C_r are shown in Table 2.3. Considering the multiway vibratory force on the liquefaction soil layers during seism, the dynamic single shear can only simulate the unidirectional vibration. The comparative test results of Finn and others show that the difference is very small.

Table 2.3 Relation between C_r and β_0

Authors	C_r	$\beta_0 = 0.4$	$\beta_0 = 1.0$
Finn etc. (1970)	$C_r = \frac{1+\beta_0}{2}$	0.7	1.0
Seed, Peacock (1971)	(variable)	0.55～0.72	1.0
Castro (1975)	$C_r = \frac{2(1+2\beta_0)}{3\sqrt{3}}$	0.69	1.15

In the field of granular materials disposal, many researches have been conducted on the characteristics of granular static dynamics at home and abroad. The device used mostly is Jenike's direct shear instrument (as shown in Fig. 2.3)[1～12]. The soviet researchers did much work in studying the granular dynamic characteristics. But the reported information is limited to the research results such as the transformation of the value of C and φ, the attenuation of the vibration wave, etc. The analytical process, the methods of study and the test facilities are not described. Roberts, et al, have determined the influence of mechanical vibration on the strength and fluidity of the crushed material whose diameter is less than 1mm. They have made great contribution to this special field. However, in China there are only a few studies carried out on the granular dynamic characteristics.

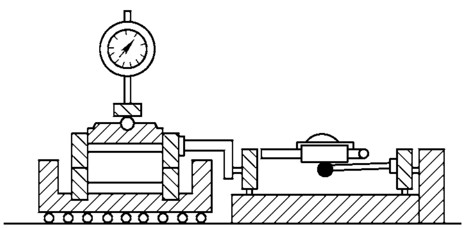

Fig. 2.3 Typical static direct shear instrument

There is a great development in dynamic testing techniques of rocks and soils, but the study on the granular dynamic characteristics concerned about the field of granular disposal is not sufficient. Especially in China, it is still a new field. Therefore, researchers engaging in the study on rocks and soils must have the courage to exploit this new field, develop new devices and adopt new technology to discover the laws of granular dynamic characteristic transformation in order to give impetus to the in-depth development of relevant theory and applications.

2.6 DSA-1 Type Vibrating Direct Shear Instrument

2.6.1 *Outline*

In many national economic sectors all types of vibrating machines are widely used to do some work such as granular compaction by repeated shaking, granular discharging, granular transportation, etc. DSA-1 type vibrating direct shear instrument is a kind of instrument whose main function is to produce mechanical vibration, and whose main object is to loose rocks and soils. It is used to study the granular dynamic characteristic in vibrating field. The instrument is designed to produce reliable results with advanced techniques[2].

With the rapid development of science and technology some new technologies, such as computer technology and sensor technology, are widely applied into many fields. In this instrumental testing system, computer technology and sensor technology substitute for all kinds of time consuming activities, such as burette, indicating gauge, dynamometer link, manual count, charting and calculating. It automatically collects, records, calculates and processes the testing data. Multi-level automatic loading has substituted the original loading by handwheel or lifting jack. There is also the automatic equivalent strain shear gauge on the sample. Thereby, the precision of the testing data is improved, data processing velocity is faster, manual power is saved and labor intensity is alleviated. Thus the superiority of testing technology of geotechnical engineering has achieved. The main frame of the burette instrument adopting combined type design can combine at any time according to different testing contents. The instrument's relevant parameters are adjustable within a wide range, moreover, the adjustment is flexible and convenient. It can create many vibrating fields needed for the test, having the level or vertical vibration of the top box or the whole box. It has not only the function of static direct shear instrument but also that of dynamic one. After the shearing force box is dismantled it can be acted as a multifunctional vibrating table to conduct granular vibration liquefaction and other model tests. In general, the machine has multifunction and can meet the requirements of various kinds of testing.

2.6.2 *Instrumental functions and chief technical criteria*

The instrument is mainly used to test such dynamic parameters as the stress-strain curve in the course of granular shearing, dynamic and static shearing strength, the angles of internal and external friction and the internal cohesion, etc. It can also determine the degree of influence of the factors such as amplitude, frequency, moisture and granular size on the granular dynamic characteristics.

2.6.2.1 Chief technical criteria of the shearing instrument

(1) The maximum vertical stress: 1.0 MPa;
(2) The minimum vertical stress: 0.01 MPa;
(3) The maximum thrust force of the level shear: 10 kN;
(4) The specifications of the sample: ϕ95 mm×60 mm, ϕ185 mm×100 mm;
(5) The shearing velocity: 0.0025~25.000 mm/min;
(6) The shearing displacement: 0~20 mm;
(7) The method of excitation: level or vertical excitation;
(8) The range of frequency: 5~500 Hz;
(9) The range of amplitude: 0~±5 mm;
(10) The wave type: sine wave, cosine wave.

2.6.2.2 Chief instruments and apparatus used in the experimental investigation

(1) DXC-TY signal disposal instrument;
(2) DHF-4 charge amplifier;
(3) YD series acceleration sensor;
(4) Personal computer;
(5) BLR pulling force and pressure sensor;
(6) ZQ-Y hydraulic pressure sensor;
(7) CF-152 magnetic tape machine;
(8) Laser printer;
(9) LZ3 function recording instrument;
(10) WCY-2 displacement sensor;
(11) YD-15 dynamic resistance strain gage;
(12) SF-2 sweep signal generator;
(13) GF-300 power amplifier;
(14) JZ-20 vibration exciter;
(15) YE charge amplifier;
(16) Mechanical type vibration measurer;
(17) Precise differential detector;
(18) Soil moisture tachymeter;
(19) Precise pressure gauge;
(20) Contacting type speed indicator;
(21) Dial gauge;
(22) Stopwatch;
(23) Measuring tube;
(24) Bench scale;
(25) Slide gauge and ruler;

(26) Triphase alternating current constant voltage power supply;
(27) Count micro instrument.

2.6.3 *Structure of the instrumental system*

DSA-1 type vibrating direct shear instrument is made up of five subsystems, namely shearing system, excitation system, vibration measuring system, shearing force and displacement measurement system, and vertical loading system.

2.6.3.1 Shear system

This is a main frame of the vibrating direct shear instrument including the motor for driving, the transmission case, the ram, and the shear box device, etc. Every part is laid on the worktable according to the tri-dimensional form in order to make every part to work normally and keep the operation safe and convenient.

Shear box

According to requirement the granular sample needed for shearing is filled into the shear box whose specifications are $\phi 95$ mm and $\phi 185$ mm. The shear boxes of two specifications are designed to have the same base disk in order to make the placement of shear box more convenient.

a. Choosing of shear mode. The measurement of the granular strength has two control modes: one is the stress control mode; the other is the strain control mode. The former is to measure the corresponding strain by controlling a certain increment of the stress within a limited time in the course of the test. The latter is to measure the corresponding stress with the transformation by controlling a certain deformation of the sample within a limited time in the course of the test. The strain control mode can measure the strength of peak value and the final value more accurately. At present this mode is widely adopted. Therefore, the chosen shear mode is the strain control mode here.

b. Choosing of shear box shape. The sample's shape depends on the shape of the shear box container, which has two shapes, namely, the square and the circular. The practical experience shows that every shape has its own advantages and disadvantages. The comparison is shown in Table 2.4[9].

The circular shear box has obvious advantages and is widely applied. This type of shear box is designed into circular shape. The external shape of it is inequilateral eight-square. This will be of great advantage to apply shearing force and to measure shear displacement. Also, this can reduce the weight of shear box and save copper materials.

Table 2.4 The comparison of the shear boxes with different shape

Items	Square	Circular
Sample preparation	It can only be cut into shape, more difficult to prepare	It can be cut into the shape with a cutting ring, easier to prepare
Transfer and distribution of shearing stress	The distribution of the shearing stress is more homogeneous on two side under stress, but inhomogeneous in the middle of the sample	The distribution of the shearing stress of two semicircles on the sheared plane by the direct shear is inhomogeneous, but more homogeneous in the middle of the sample
Shearing strain (displacement)	The shearing displacement on every point of the sample is different	The shearing displacement on every point of the sample is more similar

Layout of the shear direction and the excitation direction

There have three layout modes, which are shown in Fig. 2.4. The reference of the layout is the direction of the shear force F_s. The excitation force $p(t)$ is perpendicular or parallel to it, or assumes a certain angle with it. The excitation force $p(t)$ is alternative, so:

$$p(t)=p\cos\omega t \tag{2.6}$$

where p is the amplitude of the excitation force generated by vibration exciter.

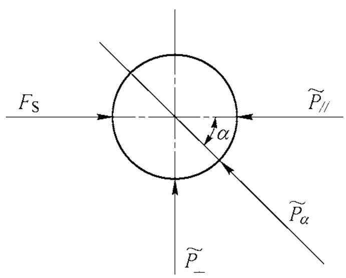

Fig. 2.4 Relation of the shear direction and the excitation direction

Suppose that the resulting force along the direction of the shearing force F_s is $p(t)$,

a. if F_s is parallel to $p(t)$:

$$p(t)=F_s+p\cos\omega t \tag{2.7}$$

b. if F_s and $p(t)$ have an included angle α:

$$p(t)=F_s+p\cos\omega t\cdot\cos\alpha \tag{2.8}$$

c. if F_s is perpendicular to $p(t)$:

$$p(t) = p\cos\omega t \cdot \cos(\pi/2) = F_s \tag{2.9}$$

According to the above analysis, by using the first two layout modes the excitation force and the shearing force influence each other. The force measured by the force sensor is the resulting force including the alternative component of stress, which brings some difficulties to measure accurately the shearing strength. If the vertical layout is adopted then the force measured is the shearing force, so it is better to adopt the layout mode in which the shear direction is perpendicular to the excitation direction.

Exertion of shear force

The motor drives gearbox through the coupling shaft, and then drives the thruster, which is made up of the system of worm gear and worm screw, by the chain. Finally by the force sensor and thrust bearing runner shearing force is exerted on the shear box with the direction across the contact plane of the top and lower shear box.

The advance or retreat of the thruster depends on the manipulation of the switch on the control panel over the co-rotating and reversion of the electric machine. The full speed of the thruster is the key to achieve the equivalent strain velocity shear. The thrust force should be uniform and homogeneous. Moreover the noise should be low and the variation range of the velocity should be wide in order to meet the requirement of different tests. This purpose is attained through using a 25-grade gearbox. By manipulating two control levels A and B, different combinations between these two can generate different shear velocities. The variation range of the velocity of the thruster is shown in Table 2.5.

The conventional direct shear instrument usually exerts shearing force by using a handwheel to push or using lift jack to load. It is obvious that equivalent strain velocity shear is difficult to achieve if the rotating velocity of the handwheel is manually controlled; the variation range of the velocity is very unstable and limited; the labour intensity is very high and the operation is inconvenient; and the influence of human factors on the results of the test is significant. In order to overcome these disadvantages , Nanking Soil Instrument Factory, a well known old factory producing geotechnical engineering testing instruments in China, has recently developed DJ-1 type electrodynamic equivalent strain direct shear instrument. This is a static direct shear instrument and the specification of the shear box is 61.8 mm and its shear velocity has two controls, namely, 1.2 mm/min and 2.4 mm/min. However, DSA-1 type vibrating direct shear instrument is superior considering the size of shear box or the variation of applying velocity. It can lighten the labour intensity and improve the precision of the test. So it represents the advanced technical level.

Table 2.5 The range of shearing velocity (mm/min)

		A grade				
		1	2	3	4	5
B grade	I	0.0025	0.0130	0.0650	0.3300	1.6000
	II	0.0053	0.0250	0.1300	0.6500	3.2500
	III	0.0103	0.0530	0.2500	1.3000	6.5000
	IV	0.0205	0.1030	0.5300	2.5000	12.7500
	V	0.0400	0.2050	1.0300	5.2500	25.0000

Mode of open slot and air pressure counterforce device

a. Mode of open slot: a small gap is left between the top and bottom shear boxes in order to decrease the influence of lateral confinement on the shearing strength when large granular shear takes place. Here an open slot of screw mode is adopted. The regulating range of the height of the open slot is 0～10 mm.

b. Air pressure counterforce device: when air pressure is applied it exerts a downward vertical pressure on the sample and an upward counterforce on the top shear box. The counterforce is transferred to the bottom shear box through the open slot screw and a guiding box. The ball bearings are placed and grease is daubed between the guide bars and the top shear box in order to decrease frictional resistance as much as possible. This is shown in Fig. 2.5.

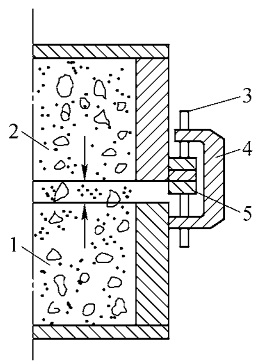

Fig. 2.5 Structural diagram of open slot and air pressure counterforce device

1—Bottom box; 2—Top box; 3—Open slot screw; 4—Guiding box; 5—Guiding bar

2.6.3.2 Excitation system

The system is used to generate plane or vertical periodical forced vibration. When the whole box vibrates the excitation component is directly connected with the bottom plate on which the shear box is fixed. When the top box vibrates, both excitation and shear force act on the top box. If the excitation component and the top box are fixed, they will influence each other. Here the excitation component is connected to the top box through a specially designed spherical slip hinge in order to ensure high accuracy of the measured shear force, which is shown in Fig. 2.6. When the vibration exciter is stopped and the bottom plate is fixed the static shear can be generated, having the functions of general static direct shear instrument. When the level excitation happens a rubber plate spring as an elastic cell is adopted or the bottom plate of the shear box has the reciprocal level motion along the guiding slot with ball bearings. When the vertical excitation happens rubber block acts as an elastic cell. Two adopted excitation types are electromagnetic type and mechanical type.

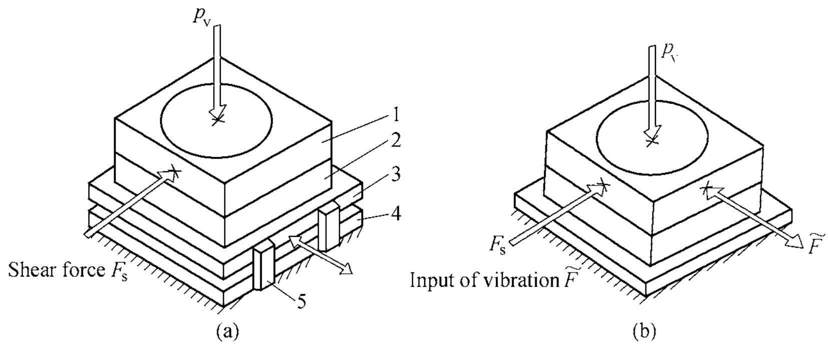

Fig. 2.6 Schematic diagram of vibrating exertion

(a) Vibration of the whole box; (b) Vibration of the top box

1—top box; 2—bottom box; 3—top soleplate; 4—bottom soleplate; 5—flat spring

Electromagnetic type

The sweep signal generator, the power amplifier, and the vibration exciter, etc. are included. The range of vibration frequency is 5～500 Hz. The range of amplitude is 0～±3 mm. The excitation force is 200 N. This type can carry through multifunctional excitation such as sine, cosine scanning, etc. It has such characteristics as high frequency, low amplitude, credible operation, regulating parameters flexibly, etc. It is mostly used to generate level vibration field.

Mechanical type

It is made up of the speed regulator, the regulated electric machine, and the mechanical vibration exciter, etc., Two methods can be used to regulate the frequency. One is to change the rotating velocity of the regulated electric machine by changing the parameters of the speed regulator. The range of regulation is 120～1200 r/min. The other is to change the transmission ratio i (i=1～4) by using belt pulleys of four specifications in order to widen the range of frequency modulation as much as possible. The amplitude regulation is achieved by changing the eccentric gap of the eccentric wheel. The range of regulation is 0～±5 mm.

The chief characteristics of the mechanic vibration exciter are low frequency, high amplitude and great excitation force. It can generate a level or vertical vibration field. The cost of this system is low. However the electromagnetic vibration exciter will cost highly to generate a high excitation force.

Two excitation types have different characteristics. Moreover concerning the regulation range of the frequency, amplitude, excitation force parameters, etc., both types can supplement each other. Thereby the capability of the whole excitation system is improved; the regulation range of the parameters is widened; and the favorable conditions are created so as to simulate the vibration fields generated by all kinds of dynamic machines.

2.6.3.3 Measurement system of vibration

The computer is used to control the measurement of vibration mode. This measurement system of vibration includes YD series acceleration sensor, DHF charge amplifier, DXC-TY signal processor, computer, laser printer, and etc.

The analytical functions of the instrument includes the amplitude spectrum, the auto power spectrum, the cross power spectrum, the autocorrelation and cross correlation functions, the transmissibility, the coherency function, the direct FFT, the frequency response function, the impulse response function, and the frequency domain mean, etc.

The measurement system of the vibration can measure rapidly and accurately, display, print and output vibration parameters. This can also supply a lot of complete information for analysis and calculation and feed back in time so as to control and regulate the vibration field. The whole system has many superiorities over that made up of the conventional ray oscillograph, such as ease of operation, full functions, and accurate and reliable testing results, etc.

2.6.3.4 Measurement system of shearing force and displacement

This system is made up of the shearing force and displacement sensors, the static resistance strain gauge, and x–y function recording instrument, etc. Depending on different tests the BLR-1 type of pulling force and pressure sensor of strain resistance mode, whose measuring ranges are 0～0.30 kN, 0～2 kN, 0～5 kN and 0～10 kN, should be confidently chosen to measure the shearing force. The sensor has a simple structure, high intensity, reliable measuring results, better resistance to impact and superior static and dynamic properties. The sensor used in measuring the shear displacement is WCY-2 strain type displacement sensor, whose measuring range is 0～20 mm and has a good resolution. The secondary instruments are the dynamic resistance strain gauge and x–y function recording instrument, which has better magnifying capability and the ability of recording continuously, factually and accurately during the entire shearing stress-strain process.

Currently for the direct shear tests in geotechnical engineering the dynamometer link is used to measure the shearing force; the dial test indicator is used to measure the shear displacement. The shearing stress-strain curve is recorded manually. These types of detection with highly intensive labor are influenced by human factors. It has poor testing precision and limited range of measuring capacity (the stress measured is usually less than 1.2 kN). If the dynamometer link and the dial indicator are substituted by dynamometer and displacement sensor, the above shortages can be overcome. Moreover, the testing techniques will be transformed from manual testing to auto testing.

2.6.3.5 Vertical loading system

There are two loading methods used to exert all kinds of stable positive stress:

(1) Balanced weight loading. It can accurately exert stable positive stress. The specifications of the common weights are 0.5 kg, 1.0 kg and 3.0 kg. The total mass is 30 kg. All kinds of force needed for testing can be obtained, which can be used for the level vibration in low-pressure range.

(2) Air pressure loading. In the process of vertical vibration, if the balanced weight loading is still used to exert the positive stress, the positive pressure is the resultant force of the alternative inertia force generated by the mass of weights. Hence a subsidiary shearing force will be generated, which results in difficulties in determining the granular shear strength. If the air pressure loading method is used, the air pressure can be loaded into a pressure bag of the sample's upper part; its counterforce can be transported to the base of the box in order to exert stable positive stress.

This air pressure loading system uses compressed air as pressure source. The initial pressure is 15 MPa, which can be controlled within the required range by using pressure reducing and regulating device, and then it is transmitted to the sample.

2.7 Shear Technique of DSA-1 Type Vibrating Direct Shear Instrument

2.7.1 *Size of sample and maximum granular diameter*

In the granular static shear test the size of shearing force box depends on the size of the sample, which is relative to the maximum granular diameter[2]. It is assumed that D is the diameter of the sample; h is the height of the sample, $d_{\max}$ is the maximum granular diameter of the granules; $D/d_{\max}$ is the ratio of diameter to diameter; $h/d_{\max}$ is the ratio of height to diameter.

In order to find a reasonable ratio of diameter to diameter a certain scientific research institution in China used the direct shear instrument of $\phi 250 \text{ mm} \times 80 \text{ mm}$ to do the testing research. The results are shown in Table 2.6[17].

Table 2.6 The ratio of diameter to diameter and the shear strength index

	Maximum granular diameter d_{max}/mm				
Shear strength index	5	10	15	20	25
C/MPa	0.6	0.5	0.5	0.6	0.5
φ/(°)	26	26	25	26	31
D/d_{max}	50	25	16.7	12.5	10

The results of the test show that when $D/d_{max} \geqslant 12.5$ the influence of the ratio of diameter to diameter on the strength is low; when $D/d_{max} \leqslant 12.5$ the strength increases rapidly, which shows that the size of the instrument is too small and the constraining force has obvious influence.

In order to find a reasonable ratio of diameter to diameter, another scientific research institution also used the direct shear instrument of ϕ500 mm×500 mm and ϕ500 mm×300 mm to do the test with gravel rock materials of different large granular upper limit (the relative density is 0.8; the testing materials is in the dry state). The results of the test are shown in Fig. 2.7 and Fig. 2.8.

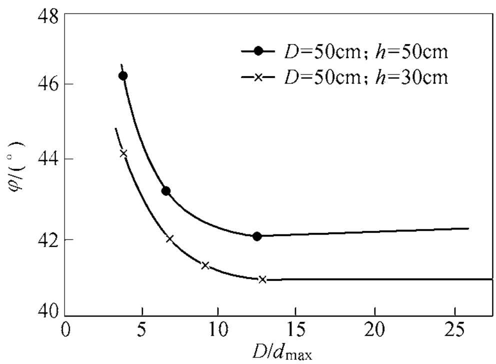

Fig. 2.7 Figure of the relation of ϕ(°)~D/d_{max}

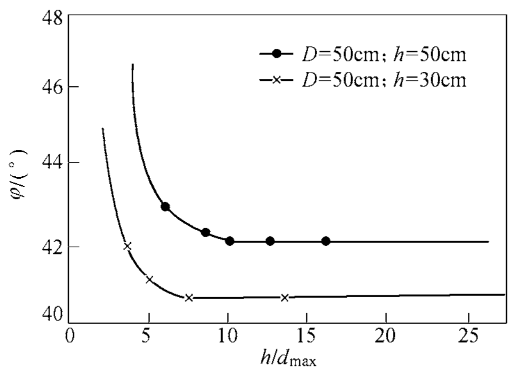

Fig. 2.8 Figure of the relationship of ϕ (°)~h/d_{max}

The above figures show that when the ratio of diameter to diameter is the same the strength of the sample changes according to the ratio of height to diameter. So the relationship between the maximum granular diameter and the size of the sample is determined by both the ratio of diameter to diameter and height to diameter.

The four samples used in this test are: L_1, L_2, L_3 and L_4. The maximum granular diameters of them are respectively 1 mm, 5 mm, 10 mm and 15 mm. The sizes of the samples are ϕ185 mm×100 mm and ϕ95 mm×60 mm. The shear box of ϕ185 mm uses L_1, L_2, L_3 and L_4 whose D/d_{max} = 185~12.3 and h/d_{max} = 100~6.6. The shear box of ϕ95 mm uses L_1 and L_2, whose D/d_{max} = 95~19 and h/d_{max} = 60~12.

2.7.2 *Preparation of sample*

The preparation of the sample in the vibrated granular shear test can refer to the following three methods.

2.7.2.1 Impacting compact method

The testing materials are layered, impacted and compacted to a dry unit weight needed for the test. This method is appropriate for the viscous granules to use this method.

2.7.2.2 Static pressure method

Positive pressure is exerted through lifting jack so that the testing materials are layered and compacted to a dry unit weight necessary for the test. This method is inconvenient to release air. Because large granules are very unhomogeneous and the applied force is not uniform under the static pressure state, this method is rarely used.

2.7.2.3 Shaker ramming method

For nonviscous granules the shaker ramming method is used to make the granules to achieve the needed dry unit weight.

In the contrast test of the static and dynamic shear, the samples are needed to have the same maximum dry unit weight before the shear in order to make the results of the test comparable. The shaker ramming method is almost used all over the world to achieve the maximum dry unit weight. Here the vibration time t and the amplitude A are the fundamental parameters for the shaker ramming method.

After the sample is filled in, the weights are placed to provide vertical pressure p_v in order to prevent the granules from bouncing and to decrease the granular separation. Then a vibration for 4 min is exerted (usually f = 30 Hz, A = 0.27 mm, p_v = 8.847kPa). By now the dry unit weight of the sample becomes stable. Even though the vibration time is increased continuously, the length of the sample does not basically change.

Besides the above listed $L_1 \sim L_4$ the testing materials in the test include calcite L_5 whose maximum granular diameter is 12 mm and tailings L_6 whose maximum granular diameter is 2 mm. The sample is graded by using sieving method. The rapid test method and dry weighing method are used to measure moisture where the latter is more common. The fundamental state of testing materials is shown in Table 2.7. The category size fraction of the tailings is shown in Fig. 2.9.

Table 2.7 Testing materials

Code	Name	d_{min}/mm	d_{max}/mm	Loose absolute density /kN • m^{-3}	Moisture/%
L_1	Iron powder ore	0	1	21.8	0~20 chosen
L_2	Iron ore	2.5	5	21.5	Air-dry
L_3	Iron ore	8	10	21.4	Air-dry
L_4	Iron ore	13	15	19.4	Air-dry
L_5	Calcite	10	12	15.4	Air-dry
L_6	Tailing	0	2	15.5	0~30 chosen

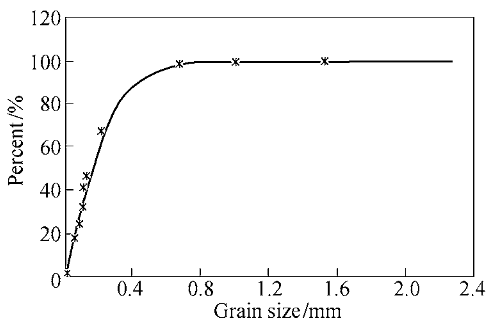

Fig. 2.9 Distribution diagram of the size category fraction of the tailings

2.7.3 *Choice of the size of open slot*

In the process of granular dynamic shear, slippage, tumbling and shear dissipation of the granules in shear box are different from the practical situation. In engineering practice the shear is applied by granular pressure, so the granular displacement is mostly rolling and tumbling, and shear dissipation is less pronounced. In the direct shear instrument, the sample shear belongs to the whole lateral confinement situation. Moreover because of the constraining action when the shear plane fixes the granular rolling and tumbling, the shear dissipation is larger and accompanies obvious shear-expansion phenomenon, which causes higher strength. In order to overcome this disadvantage, a certain slot should be open on the shear's top and bottom boxes before the shearing.

The purpose of opening a slot is to make the direct shear instrument change from the whole lateral confinement to part lateral confinement which is close to the practical situation. If the size of the open slot is too small the influence of the constraining action will not be eliminated; if it is too big, the sample is easily squeezed out. So in China most of institutions take the maximum granular diameter as the base of the size of open slot[12～17]. The size of the open slot $h = (1/2.5 \sim 1/7)\ d_{max}$.

2.7.4 *Shear velocity*

Shear velocity is one of the factors which influence the shear strength. The granular shear strength increases with the increment of shear velocity. For the viscous granules, there are two factors that shear velocity influences shear strength. One factor is the influence of shear velocity on the generation, transfer and dissipation of the pore water pressure. High shear velocity inhibits the transfer and dissipation of pore water pressure, so shear strength becomes high; and vice versa. The other is the granular creep deformation property. The coupling strength between granules and the viscous flow strength of the adhesive water are directly proportional to the velocity of the viscous deformation. So under the condition of higher shear velocity and shorter shear time the measured coupling strength may increase correspondingly. The result of their combined action reflects on the influence of shear velocity on shear strength.

The DSA-1 vibration-type direct shear instrument has 25 adjustable levels. So it can be adjusted to meet the requirements of quick shear (3～5 min, even 30～50 s shear dissipation), consolidated quick shear and slow shear (1～4 h shear dissipation) in geotechnical engineering test. Moreover, the test of the influence of shear velocity on shear strength can be done. In the present tests the quick shear velocity, namely shear velocity is 2.5 mm/min, is used to make the shear dissipation of the sample within 3～5 min.

2.7.5 *Choice of failure criteria*

The determination of the failure criteria relates to the failure mechanism of the sample and the purpose of the test. In granular direct shear test the present failure criteria has[10, 17]: (1) the ultimate strength criteria; (2) the shear deformation criteria; and (3) the shear expansion criteria.

The relation of the stress and strain of the granules in the process of shear is shown in Fig. 2.10.

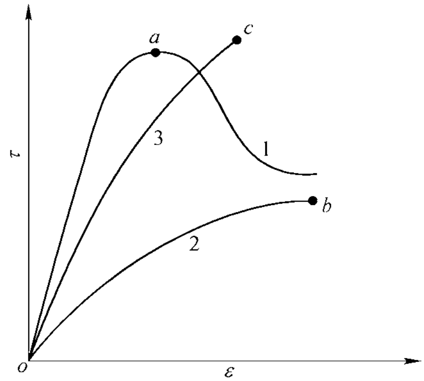

Fig. 2.10 Relation curve of stress and strain

2.7.5.1 Brittle failure

Before the failure the stress and strain of the sample increase correspondingly. When the strain is small the stress increases rapidly. After attaining the peak strength (shown in Fig. 2.10, point *a* of line 1), the granules suddenly are sheared to failure. After the failure, though the strength decreases the ultimate value of the strength still exists.

2.7.5.2 Failure by plastic flow

In the course of shear the stress increases with the increment of strain until every point of the sample cannot resist higher shear force. When the shear intensity is kept constant the deformation increases continuously, then a plastic flow appears. The strength of the failure (or termed as the stable value) by the plastic flow is shown by the point *b* in the line 2 of Fig.2.10.

2.7.5.3 Half brittle failure

As shown by the line 3 of Fig.2.10, the stress-strain curve increases by degrees at all times. In one hand it is approximated to the characteristic of brittle failure, being sheared to failure only when the strain value is low. On the other hand it has the characteristic of the failure by plastic flow but differs from ideal plastic flow and only has the ultimate shear strength value (shown by the point *c* in Fig. 2.10).

In our dynamic shear test the relation between the stress and the strain is basically analogous to the curve 1, 2. In the granular disposal engineering granules should overcome the ultimate shear strength in order to flow. So according to the theory of ultimate equilibrium, the peak value or the value of the stability on the curve τ–ε is chosen as the failure value. If there is no peak value, the shearing stress as shear deformation is 1/15 the size of the shear box is considered as the failure value.

2.7.6 *Procedures of test*

(1) Turn on the power switch; preheat the signal generator, the power amplifier, the dynamic resistance strain gage, the x–y plot instrument, the charge amplifier, the signal processor, the computer, and the printer, etc.

(2) By the open slot screws on the shear box, regulate the size of the open slot (h = (1/4)d_{max}) and align the top and bottom plates of the shear box so that they are parallel, then fix the position by using a fixed pin.

(3) After mixing the weighed testing materials, divide them into 2～3 layers and then fill them into the shear box. The positions of the layers must be staggered with the place of the open slot. Finally level off the surface and measure the height of the sample.

(4) Place the porous disk, the pressure plate and the weight for consolidation on the surface of the sample.

(5) According to the requirement fix the vibration sensor, preset the charge amplifier, the signal processor, the computer, etc. in order to make the measurement system of vibration in preparation for the test.

(6) Set the dynamic resistance strain gage to zero; preset the dynamic resistance strain gage, the x–y plot instrument, etc. in order to make the measurement system of the force and displacement in preparation for the work.

(7) Preset the frequency factor and the wave selection of the signal generator; regulate the grade switch of the power amplifier to the "loading" grade, then regulate slowly the "gain" knob in order to make the output electric current (or the voltage) to achieve a predetermined value.

(8) Consolidate the vibration 4min; turn off the "gain" knob of the power amplifier; regulate the grade switch to "electrical source switching-on" and then the vibration stops. Press the "advance" knob on the control cabinet in order to have only a very small slit between the thrust cone and the shear box; then stop.

(9) Unload the weights for consolidation; measure the height of the sample; according to the test plan place the vertical pressurizing weights (or place the topping to input the air pressure); carefully pull out the positioning pin.

(10) Fix the displacement sensor and make it and the shear box to have a slight contact; set the x–y plot instrument to zero.

(11) According to step 7 exert vibration and make the x–y plot instrument under the state of "record"; press the "advance" knob on the control cabinet; finish the three operation procedures according to the sequence.

(12) Open the measurement system of the vibration; test and monitor the

vibrating field in the course of shear; show and print the results of the measurement; store it into the magnetic tape machine.

(13) Notice the working of every instrument. If abnormal phenomenon happens, deal with it in time. After the shear dissipation of the sample, make the x–y function recording under the state of "raising pen"; close the excitation system and push-in system; control the "cancel" knob on the control cabinet; and once the thrust cone resets, press "stop" knob.

(14) Undo the displacement sensor; remove the vertical pressure; take out the testing materials to release the shear box; and then clean up the residues between the shear boxes to prepare the next new test.

(15) When the static shear test is done, close the excitation system and the measurement system of the vibration. The other procedures are the same as the above.

(16) When the mechanical excitation is used, close the electromagnetic excitation system. The other procedures are the same as the above.

2.7.7 *Matters need attention when using instruments*

(1) Frequently examine whether the fixing screws of the instruments loosen or fall off.

(2) Use level meter to calibrate the shear boxes in order to keep the surface of the boxes level and to make the axes of the thrust cone across the midline of the surface of the open slot of the shear box.

(3) Keep the space between the surfaces of the shear boxes clean. Apply lubricating oil on the contact surfaces frequently.

(4) When the air pressure loading is used, examine the sealing performance of the system in order to prevent air leaking from the pressurizing box and the joint.

(5) When high pressure loading is exerted, switch off the low-pressure valve. Otherwise the components of low-pressure instrument will be damaged.

(6) The machine must be stopped while gearbox shifting. If shaft A and B can not shake, manually turn the axis-connect to the machine or turn the electric machine.

(7) Use No.20 machine oil into the gearbox. The height of the added oil must not reach beyond the next row of gear shafts in order to make the surfaces of the next row gears lubricate.

(8) Strictly operate the electrical measurement instruments according to the operating instructions in order to ensure the correctness of every input parameter.

(9) The cables of the electrical measurement system must be connected correctly to the electric power line, especially the cables for inputting and outputting. Otherwise the instruments may be damaged.

2.7.8 *Calibration of measurement system*

2.7.8.1 Calibration of force sensor

Place vertically the BLR pulling force and pressure sensor. Then gradually increase the vertical loading, namely increase the number of weights. The mass of the weights should be accurate to 0.5%. After every time the loading is increased, record the displacement of the pen of the x–y plot instrument until the required loading is reached. Then gradually take off the loading, record the displacement of the pen and the value of the attenuation grade of the dynamic resistance strain gage and the x–y plot instrument. If the values of two calibrations are close to each other, choose the average value of two readings; draw the relation curve of the shear force (namely calibrating vertical loading) and the displacement of the pen for recording; perform regression analysis by using the computer. The slope ratio of the curve is the calibration coefficient K_S, here assuming that the attenuation coefficient of the dynamic resistance strain gage is K_y, and the attenuation coefficient of the function instrument is K_n (2 kN sensor).

(1) $K_y = 10$ $K_n = 50$ MV
Calibration equation: $y = 0.487x+0.321$
Coefficient of correlation: $R = 0.99$
Standard deviation: $S_l = 7.984\times 10^{-2}$
Calibration coefficient: $K_S = 0.487$
(2) $K_y = 3$ $K_n = 50$ MV $K_S = 0.151$
Calibration equation: $y = 0.151x–0.343$
Coefficient of correlation: $R = 0.99$
Standard deviation: $S_l = 0.858\times 10^{-2}$
(3) $K_y = 30$ $K_n = 50$ MV $K_S = 1.456$
Calibration equation: $y = 1.456x+1.866$
Coefficient of correlation: $R = 0.99$
Standard deviation: $S_l = 4.024\times 10^{-2}$

2.7.8.2 Calibration of displacement sensor

The basic instrument for the displacement calibration is the precise differential calculator, whose measurement ranging is 0～25 mm and its accuracy is 0.5 μm. The calibration to meet the various accuracy needs is shown in Table 2.8.

The instrument, with a high accuracy in displacement measurement, producing small error and stable indicating value, meets the requirement of AA grade accuracy. So it can be the basic component of calibrating instrument of displacement and the displacement base to examine all kinds of mechanical, pneumatic and dynamoelectric micrometer.

Table 2.8 Grade of the accuracy of the calibration

	Grade of the accuracy	A/μm	AA/μm	AAA/μm
Indicating accuracy	0~25 mm	±2	±1	±0.5
	0~10 mm	±1	±0.5	±0.5
	0~5 mm	±0.5	±0.5	±0.5
	Error	0.8	0.6	0.4
	Stability of the indicating value	0.2	0.2	0.2

The measuring head of the precise differential calculator contacts opposite to the displacement sensor and the axes of them are positioned as much as possible on the same line. Then rotate the turning wheel of the measuring head in order to make the displacement sensor gradually change position. Measure and record the reading of the measuring head and the displacement of the pen of x–y plot instrument when every grade of displacing happens until the needed numerical value is reached. In the meantime keep a record of the grades of the strain gauge and the function instrument. Repeat this process three times and then choose the average value. Use computer to do regression analysis and draw a curve of the relation between the input displacing and the displacement of the recording pen. The slope ratio of the curve is the calibration coefficient K_x. The results of the calibration are as follows:

(1) $K_y = 30$ $K_n = 5$ MV $K_x = 9.183\times10^{-3}$
Calibration equation: $y = 9.183\times10^{-3}x + 1.208\times10^{-1}$
$R = 0.99$ $S_1 = 7.780\times10^{-3}$
(2) $K_y = 30$ $K_n = 10$ MV $K_x = 1.825\times10^{-2}$
Calibration equation: $y = 1.825\times10^{-2}x + 5.544\times10^{-2}$
$R = 0.99$ $S_1 = 3.310\times10^{-2}$
(3) $K_y = 10$ $K_n = 50$ MV $K_x = 3.233\times10^{-2}$
Calibration equation: $y = 3.233\times10^{-2}x – 6.794\times10^{-2}$
$R = 0.99$ $S_1 = 1.614\times10^{-2}$
(4) $K_y = 30$ $K_n = 50$ MV $K_x = 9.256\times10^{-2}$
Calibration equation: $y = 9.256\times10^{-2}x + 1.954\times10^{-1}$
$R = 0.99$ $S_1 = 3.384\times10^{-2}$

2.7.8.3 Calibration of vibration sensor

The measurement system of vibration still uses the precise differential calculator as the base of input displacement and the mechanical measuring vibration instrument as the medium. At first, calibrate the mechanical measuring vibration instrument, then use the precise differential calculator to input the standard displacement into the mechanical measuring vibration instrument and record its magnification times K_a, then take the recording strip to the microscope to read the number, finally record the magnification times K_b of the microscope and its reading. Repeat this three times and choose the average value, then do the regression analysis of the recorded data and draw a curve of the relation between the input standard displacement and the reading of the microscope. The results of the calibration coefficient K_1 are:

(1) The magnification times of the mechanic measuring vibration instrument: $K_a = 4$

The magnification times of the microscope: $K_b = 100$

The total magnification times: $K_c = 400$

Calibration equation: $y = 2.390 \times 10^{-3}x + 5.44 \times 10^{-2}$

$R = 0.99$ $\quad S_1 = 5.116 \times 10^{-2}$

$K_1 = 2.390 \times 10^{-3}$

(2) $K_a = 10$ $\quad K_b = 100$ $\quad K_c = 100$

Calibration equation: $y = 1.059 \times 10^{-3}x - 4.495 \times 10^{-2}$

$R = 0.99$ $\quad S_1 = 8.575 \times 10^{-2}$

$K_1 = 1.059 \times 10^{-3}$

(3) $K_a = 10$ $\quad K_b = 100$ $\quad K_c = 200$

Calibration equation: $y = 5.733 \times 10^{-3}x - 5.701 \times 10^{-3}$

$R = 0.99$ $\quad S_1 = 1.432 \times 10^{-3}$

$K_1 = 5.733 \times 10^{-3}$

So based on these, the computer measuring system of vibration is calibrated. Use simultaneously the mechanical measuring vibration instrument and the computer measuring system of vibration to monitor a vibration signal and record the preset parameters; then the result is output by the computer. Take the recording strip of the mechanical instrument to the microscope to read the numbers. Use the calibration curve of the mechanical measuring vibration instrument to recalculate them into the standard displacement. Repeat this three times, and then calculate the average value of them. Use computer to make regression analysis of the recorded results and draw a curve of the relation between the standard displacement and the displacement result output by the computer. Thereby get the calibration coefficient K_d. The scanning signal generator can show the frequency of the excitation. In the meantime the computer will also output it. So the curve of the relation between the input acceleration and the velocity of the computer and the calculation coefficient K_g can be recalculated. The results of the calibration are:

(4) Input frequency: $f = 30$ Hz

Magnification times of the mechanic measuring vibration: $K_a = 20$

State of the computer: I

a. Calibration equation of the displacement:

$y = 1.395\times10^{-3}x–1.032\times10^{-1}$

$R = 0.99$ $S = 1.302\times10^{-2}$

b. Calibration equation of the acceleration:

$y = 7.776\times10^{-3}x–4.707\times10^{-1}$

$R = 0.99$ $S = 5.980\times10^{-2}$

(5) $f = 60$ Hz $K_a = 20$

State of the computer: II

a. Calibration equation of the displacement:

$y = 4.565\times10^{-3}x + 1.083\times10^{-2}$

$R = 0.97$ $S = 7.967\times10^{-3}$

b. Calibration equation of the acceleration:

$y = 2.729\times10^{-3}x–9.086\times10^{-2}$

$R = 0.97$ $S = 4.583\times10^{-2}$

(6) $f = 20$ Hz $K_a = 10$

State of the computer: III

a. Calibration equation of the displacement:

$y = 3.526\times10^{-3}x + 2.706\times10^{-1}$

$R = 0.97$ $S = 9.098\times10^{-2}$

b. Calibration equation of the acceleration:

$y = 3.046\times10^{-3}x–2.226\times10^{-1}$

$R = 0.99$ $S = 2.803\times10^{-2}$

2.7.9 *Treatment of the test data*

There are many methods to express the correlation between test data. The methods such as scatter diagram, table and curve etc. are simple and visualized. But they cannot reflect in-depth internal relation between the terms, so they are used only under the proper condition. Mathematical expression or empirical formula can avoid these disadvantages. It can provide in-depth internal law of the terms. Usually the regression analysis is used to get the empirical formula.

2.7.9.1 Principle of methods

Suppose that the test variable quantities X and Y have linearity correlation. By performing N times tests, get observation data (x_1, y_1); (x_2, y_2);...; (x_N, y_N). Its mathematical model is:

$$y=a+b+\varepsilon \tag{2.10}$$

where a, b are the unknown coefficients, $\varepsilon=y_i–a–bx_i$.

When the residual sum of squares $Q=\sum_{i=1}^{N}\left(y_i-\hat{y}_i\right)^2$ is minimum, there is:

$$\hat{a}=\overline{y}-\hat{b}\overline{x}\ ;\quad \hat{b}=\sum_{i=1}^{N}(x_i-\overline{x})(y_i-\overline{y})/\sum_{i=1}^{N}(x_i-\overline{x})^2 \tag{2.11}$$

where

$$\overline{x} = \frac{1}{N}\sum_{i=1}^{N} x_i;\ \ \overline{y} = \frac{1}{N}\sum_{i=1}^{N} y_i \tag{2.12}$$

Thereby get the monadic equation of linear regression with the minimum residual sum of squares as follows:

$$\hat{y} = \hat{a} + \hat{b}x \tag{2.13}$$

The estimated value R of the coefficient of correlation ρ of x and y is:

$$R = \sum_{i=1}^{N}(x_i - \overline{x})(y_i - \overline{y}) / \sqrt{\sum_{i=1}^{N}(x_i - \overline{x})^2 \sum_{i=1}^{N}(y_i - \overline{y})^2} \tag{2.14}$$

Choose the statistical F to perform the correlative significance test:

$$F = \frac{R^2}{1 - R^2}(N - 2) \tag{2.15}$$

With a given significance level, compare the value of F with critical value F_α (1, N-2); if $F > F_\alpha$, reject the former hypothesis. This shows $\rho \neq 0$ and the linearity correlation between the variables is evident; whereas it is not so evident.

Moreover when the residual standard deviation S is minimum, it provides an index for appraising the effect of the regression:

$$S = \sqrt{\frac{Q}{N - 2}} \tag{2.16}$$

When a non-linearity relation exists between the variables, the right curve model should be chosen to do the regression. Only by this way an accurate result can be obtained. By substituting the variables a curvilinear regression should be converted into a linear regression. For example:

Exponential function: $y = ax^b$;

Suppose $V = \ln y$, $u = \ln x$, $c = \ln a$, then obtain $V = c + bu$;

Parabola: $y = a + x^2/b$;

Suppose $V = y$, $u = x^2$, $c = 1/b$, then obtain $V = a + cu$.

2.7.9.2 Program function

(1) Include several kinds of curvilinear regression analysis: the line, the curve of exponential function, the log curve, the exponential curve, the reciprocal exponential curve, the parabola, the hyperbola and the S shape curve (shown in Table 2.9).

(2) Use a table form to output the coefficient of correlation, the regression equation, the standard deviation, and the statistic F value, etc.

(3) Predict according to the chosen curve model.

(4) Describe automatically the scatter diagram of the original data and the regression curve diagram. The form of the coordinate and the size of the diagram can be changed. A multicolor pen can be use to describe different regression curves, which are compared each other.

Table 2.9 Types of regression curve and codes (K)

K	Name of curve	Mathematical model	K	Name of curve	Mathematical model
1	Line	$y=a+bx$	5	Reciprocal exponential curve	$y = ae^{b/x}$
2	Curve of exponential function	$y = ax^b$	6	Parabola	$y = a + x^2/b$
3	log curve	$y = a + b\ln x$	7	Hyperbola	$1/y = a + 1/x$
4	Exponential curve	$y = ae^{bx}$	8	S shape curve	$1/y = a + b^{-x}$

2.7.9.3 Calculation example

A regression analysis of the results of the relational curve of shear force F_s and shear displacement x in the granular dynamic shear test is done. The diameter of the testing materials (magnetic iron ore) is $d_{\max} = 5$ mm; frequency is f=60 Hz; amplitude is A=0.08 mm; position pressure is σ=6.117 kPa. The testing data are shown in Table 2.10. The results of the regression analysis are shown in Table 2.11.

Table 2.10 Original data

I	$x(I)$	$y(I)$
1	0.05	30.00
2	0.10	43.00
3	0.27	60.00
4	1.00	57.00
5	1.50	60.00
6	2.00	60.00
7	2.50	61.00
8	3.00	63.00
9	3.50	64.00

Table 2.11 Results of regression analysis

No	Type	R	a	b	Equation (y=)	S	F0.1	F0.05	F0.01	F
1	$y=a+bx$	0.728	45.538	6.332	$45.538+6.332x$	8.404	3.59	5.59	12.20	7.55

Continues Table 2.11

No	Type	R	a	b	Equation (y=)	S	F0.1	F0.05	F0.01	F
2	$y=ax^b$	0.878	55.919	0.140	$55.919x-0.14$	0.128	3.59	5.59	12.20	23.48
3	$y=a+b\ln x$	0.898	56.949	6.488	$56.949+6.481nx$	5.331	3.59	5.59	12.20	29.17
4	$y=ae^{bx}$	0.682	44.011	0.232	44.011exp0.132x	0.196	3.59	5.59	12.20	6.07
5	$y=ae^{b/x}$	−0.985	62.727	−0.036	62.727exp(−0.036/x)	0.045	3.59	5.59	12.20	236.06
6	$y=a+x^2/b$	0.601	49.391	0.651	$49.391x^2/0.651$	9.689	3.59	5.59	12.20	3.95
7	$1/y=a+b/x$	0.986	0.015	0.001	$1/(0.015+0.001/x)$	0.001	3.59	5.59	12.20	238.08
8	$1/y=a+be^{-x}$	0.763	0.014	0.011	1/[0.014+0.01exp(−x)]	0.004	3.59	5.59	12.20	9.76

According to the table of the regression analysis, when the seventh curve form, hyperbola function, is used to regress, the correlation coefficient R = 0.986, the statistic F=238.08. It is obvious that $F>F$ 0.01$>F$ 0.05$>F$ 0.1 and the standard deviation S = 0.001, which shows that the result of the regression is very evident. So it is ideal of using hyperbola function model $1/y=a+b/x$ to reflect the relation between F_s and x. Moreover, when the fifth curve form, reciprocal exponential function, is used to regress the result takes second place, but it is also very evident. The regression of relationship between the predicted value and the original value is shown in Fig. 2.11 and Fig. 2.12. The effect of parabolic regression is the worst.

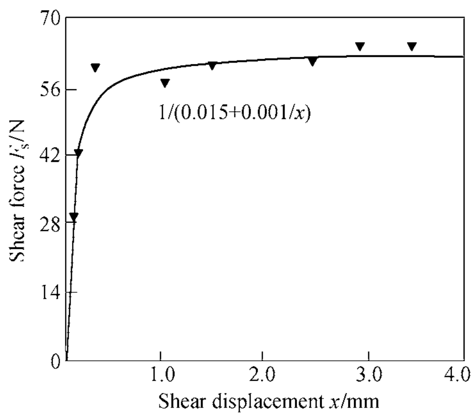

Fig. 2.11 Regression curve of hyperbolic function

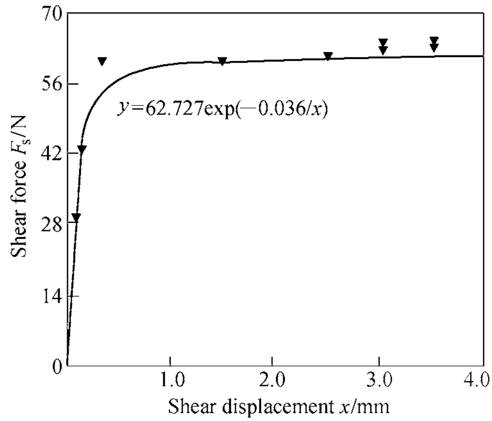

Fig. 2.12 Regression curve of reciprocal exponential function

3

Granular Dynamic Shearing and Its Differential Mechanical Model

3.1 Experimental Principle

The basic theory of the granular mechanics is the theory of ultimate equilibrium[1~12]. The ultimate equilibrium is a state in which the shear strength τ reaches the maximum, and can overcome the friction F_f and cohesion C in the entire or partial granular media. Fig.3.1 gives the stress conditions at point N in the flow boundary of a body. The forces acting on the point N include vertical stress σ_v (comprising normal stress σ and shear stress τ), internal friction F_f (equal to $\sigma\tan\varphi$, φ is the angle of internal friction) caused by the normal direct stress and cohesion C. The shear stress τ makes the granules move, but $\sigma\tan\varphi + C$ can obstruct the granular movement. Once the ultimate equilibrium is disturbed, the granular medium will be unstable, and the destruction of stability will make the granular medium begin to yield and flow.

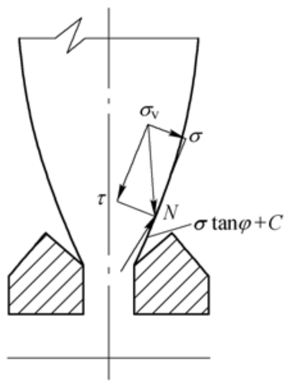

Fig. 3.1 Stress system of certain point in the flow boundary of granular medium

If the granular medium reaches its state of ultimate equilibrium, the stress circle called the limiting stress circle and the envelope line of the shear are necessary tangent (as shown in Fig. 3.2a). The shear force of tangent point N is equal to the shear strength. In Fig. 3.2 the included angle of the failure surface and the acting surface of the maximum principal stress can be deduced as follows:

$$2\alpha = 90^\circ + \varphi$$

Therefore

$$\alpha = 45^\circ + \varphi/2 \tag{3.1}$$

And in terms to the geometrical relation of ΔABN, the following expression can be obtained:

$$\sin\varphi = \frac{AN}{AB} = \frac{\sigma_1 - \sigma_3}{\sigma_1 + \sigma_3 + 2C\cdot\tan^{-1}\varphi} \tag{3.2}$$

After conversion, obtain:

$$\begin{cases} \sigma_1 = \sigma_3\tan^2(45^\circ + \varphi/2) + 2C\cdot\tan(45^\circ + \varphi/2) \\ \sigma_3 = \sigma_1\tan^2(45^\circ - \varphi/2) - 2C\cdot\tan(45^\circ - \varphi/2) \end{cases} \tag{3.3}$$

In addition, in terms to Hooker's law the equation of the line BN is:

$$\tau = C + \sigma\tan\varphi \tag{3.4}$$

All the above expressions of ultimate equilibrium can act as the criterion of granular breakage. They indicate that the shear stress leading to the granular breakage is not in reality the maximum shear force loaded onto the granular media. However, when the corresponding relation between normal stress and shear stress is close to the maximum stress which the granular media can withstand, i.e., when the stress at the tangent point of the envelope line of the shear strength and the Mohr's diagram of stress is in the state of ultimate equilibrium, the granular media will be damaged. Consequently, we can simply analyze the stress state of shear box in the shear experiment.

The shear stress of shear breakage is τ under the action of vertical load σ. This stress is the point N on the curve of shear strength, which is the tangent point of the limiting stress circle and the line BN (shown in Fig. 3.2). The limiting stress circle intercepts the abscissa in point 1 and 3, so the maximum principal stress and the minimum principal stresses are σ_1 and σ_3 respectively. The directions of the two principal stresses can be ascertained by the following method. Because the principal shear surface is being horizontal, it is possible to draw a horizontal line NP through the point N, and linking the line $1P$ and the line $3P$ (the two lines are the directions of maximum and minimum principal stresses respectively). It is reflected in Fig. 3.2b by the shaded area of a triangle in the sample of the shear

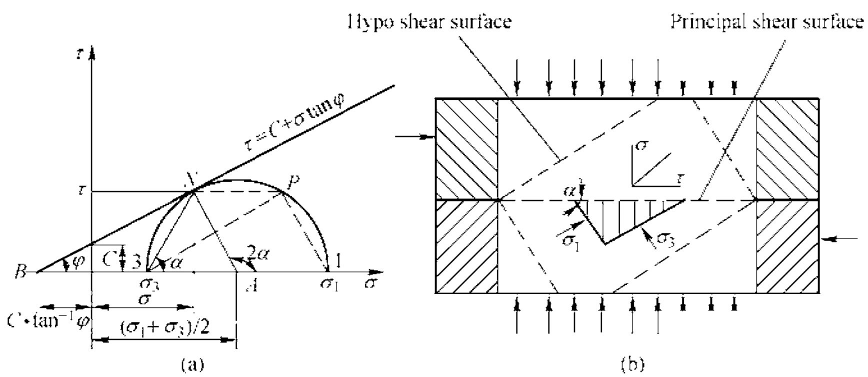

Fig. 3.2 Stress state in the shear surface

box.When the shear box is moving, the sides of box experience a horizontal pressure, and the interfaces between the top box and the bottom box form two slip surfaces of $90^\circ - \alpha$ or α, namely hypo shear surfaces. The two surfaces move towards the center from the two sides, and the shear area is shaped until the sample is broken.

Introduction of vibration will cause the change of granular stress state in shear box. The granular dynamic shear strength τ_d is controlled by:

$$\tau_d = F(\sigma_1, \sigma, f, A, \rho, \omega_c, d) \tag{3.5}$$

where σ_1 is the principal consolidation stress; σ is the direct stress corresponding to the shear yield; f is the frequency; A is the amplitude of vibration; ρ is the granular density; ω_c is the granular moisture content; and d is the average size of granules.

Utilizing the developed vibrating direct shear device, the granular media are sheared when the vibration is exerted. Changing the experimental conditions as mentioned, in this chapter, the granular dynamic characteristics can be probed when the granular dynamic shear strength τ_d, C and φ are regarded as the basic mechanical parameters.

3.2 Whole Box Vibrating Shearing Experiment

3.2.1 *Granular shearing relation between stress-strain*

Fig.3.3 shows the typical figure of experimental results obtained from iron ores when the size of granules d_{max} is 10 mm. Curve A is the static relation curve of shear force F_s and shear deformation x when the direct stress σ=8.847 kPa. Curve B is the curve of vibrating shear process with the same direct shear force as A, when the frequency f=60 Hz and the amplitude of vibration A= 0.080 mm. It is obvious that the vibration causes the granular shear strength to decrease, and the relation between dynamic and static shear forces is approximately F_{sd}/F_{sj}=4/7 when the granular medium is yielded.

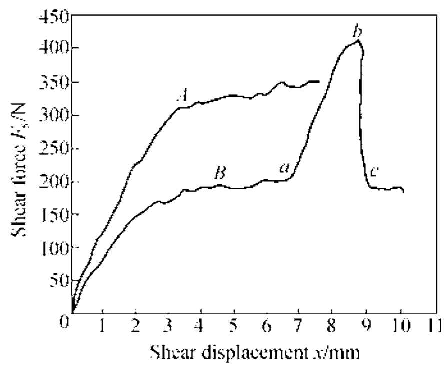

Fig. 3.3 Relation of stress-strain of iron ores

The curve B begins to yield before reaching point a. After it reaching point a, the exciter is switched off, here the sample re-solidifies and the shear force increases to a higher level than the curve a without vibration. The reason is that the action of vibration heightens the solidifying strength. If the vibrator is switched on again, the shear force will decrease to the level a just before.

The relationship between the shear stress and strain in the whole experimental process shows the analogous regularity. Therefore, as for the granular dynamic characteristics, the general conclusion is that the shear force can be increased rapidly because of the action of the shear deformation velocity $\dot{x}$. Because of the friction in the granular bin, the shear force increases linearly, indicating plastic flow begins and in the end the yield point appears. When the relative horizontal distance between the top shear box and the bottom one expands further, the sample will be damaged. Fig.3.4 shows the experimental results of dynamic and static state of iron ores when the size of granules is less than 1 mm, under the conditions of f= 60 Hz, A=0.080 mm and the shear box of ϕ185. In another word, whether it is the dynamic or static shear stress, the relation between stress-strain of the sample is analogous, and the introduction of vibration will cause the reduction of rigidity and shear strength.

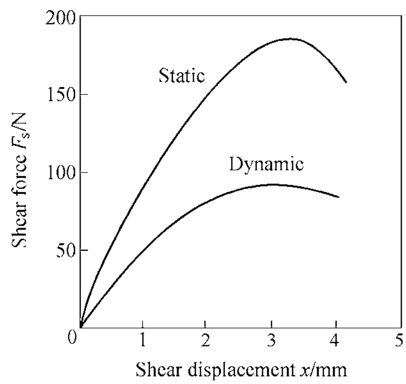

Fig. 3.4 Comparative figure of dynamic and static state

3.2.2 *Test of shear strength* τ, *cohesion C and angle of internal friction* φ

In terms of Coulomb's Law, there is the equation of $\tau = C + \sigma\tan\varphi$. For different direct stresses σ, the shear strengths are tested, and then C and φ are confirmed when the granular medium is vibrated.

The experimental data in Fig.3.5 and Fig.3.6 are conducted regression analysis, and the results are shown in Table 3.1.

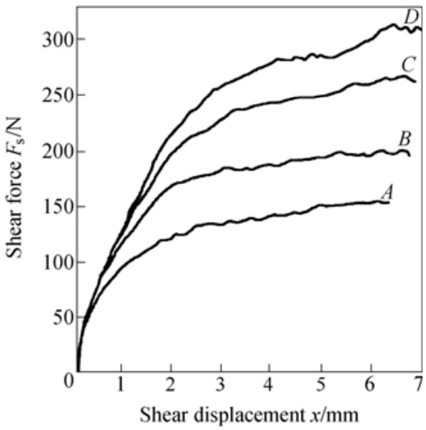

Fig. 3.5 Experimental curve of x-F_s with static shear

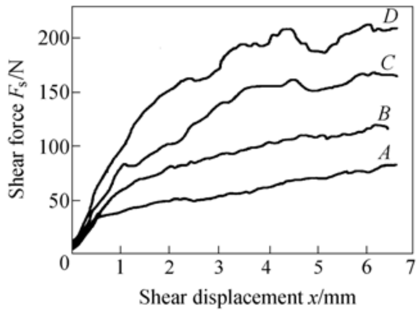

Fig. 3.6 Experimental curve of x-F_s with dynamic shear

f=30 Hz, A=0.120 mm, horizontal vibration, shear box of ϕ185, magnetite of d_{max}=5 mm, σ_A=3.390 kPa, σ_B=3.117 kPa, σ_C=8.847 kPa, σ_D=11.207 kPa

Table 3.1 Values of C and φ of regression analysis

State	No.	regression equation of τ-σ	φ/(°)	C/kPa
J①	4J	τ=0.697σ+3.346	33.874	3.346
D②	4D	τ=0.667 σ+0.045	33.766	0.045

① J denotes static state; ② D denotes dynamic state.

The curve of τ-σ is shown in Fig. 3.7, and other experimental results are analogous, such as Fig.3.8, which is the figure of experimental results of iron ores when d_{max}=15 mm. Because of the vibration the value of φ decreases by 1° ~3° , the value of C decreases by 50% or more. That is to say that mechanical vibration clearly improves the flowability of granules.

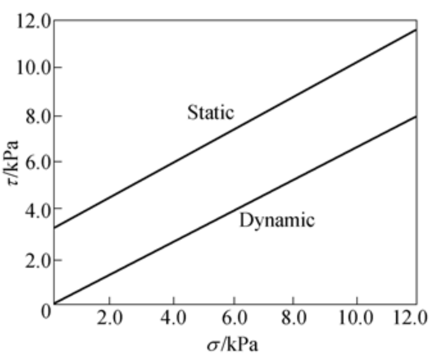

Fig. 3.7 Relation curve of τ-σ

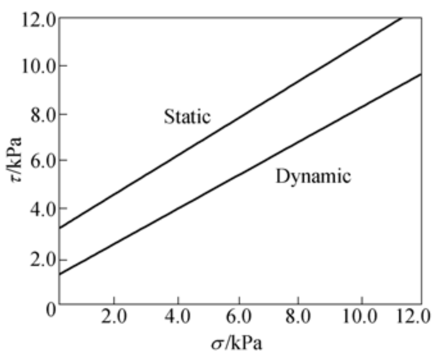

Fig. 3.8 Relation curve of τ - σ

3.2.3 *Influence of amplitude of vibration on shear strength*

The property of shear strength has been studied when the frequency f is fixed and the amplitude of vibration A is variable. Fig.3.9 is the typical figure of the experimental results with iron ores when f=30 Hz and d_{max}=5 mm. It denotes the static state when A=0.

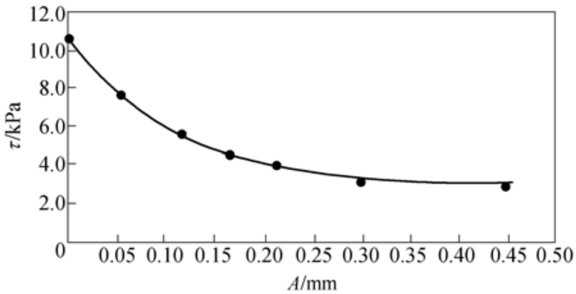

Fig. 3.9 Relation between the amplitude of vibration and the shear strength

The introduction of vibration causes the rapid fall-off of τ, which decreases gradually along with the increment of A. However, when A increases to a certain value, about 0.15～0.25, the curve tends to be smoother. τ will approach to a constant value in the end, which indicates that A has extreme value. The results of other experiments are analogous.

3.2.4 *Influence of frequency on shear strength*

When A is confined within a small range, about 0.08 mm, and frequency f is changeable, the experimental results of iron ores with d_{max}=5 mm are shown in Fig.3.10. In this figure f=0 denotes the static state.

When the state is changed from static to dynamic, τ decreases in equal steps. With the increment of f, although the value of τ decreases slightly, on the whole it inclines to be steady. Compared with the amplitude of vibration, the influence of high frequency on the dynamic strength is not significant. The experimental result of calcspar with d_{max}=10 mm is analogous.

3.2.5 *Influence of moisture content on shear strength*

Under the dynamic conditions of f=30 Hz, and A=0.01 mm, the experimental results of iron ores when the granular size is less than 1mm are shown in Fig.3.11.

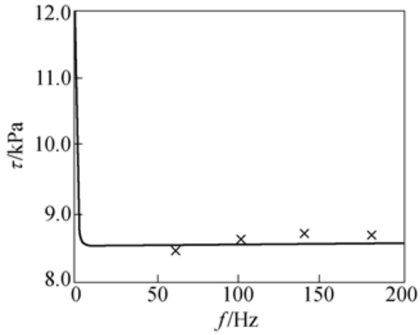

Fig. 3.10 Relation between frequency and shear strength

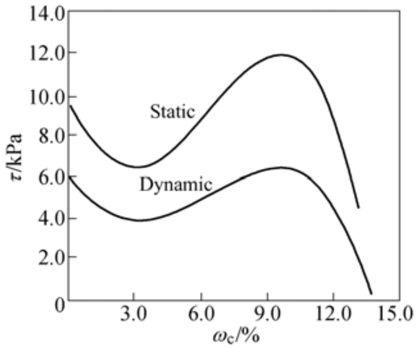

Fig. 3.11 Relation between moisture content and shear strength

With the increment of moisture content, the shear strength will firstly decrease and then increase, When the moisture content ω_c is about 10% the value of τ reaches the peak value. When the moisture content ω_c is about 13%, the vibrating liquefaction of the granular medium occurs and the shear strength is close to zero. However, under the static state with the same condition, the sample still has large strength (shown in Fig.3.12). The experimental results of tailings also show the same pattern, so controlling optimum moisture content is very important in practice.

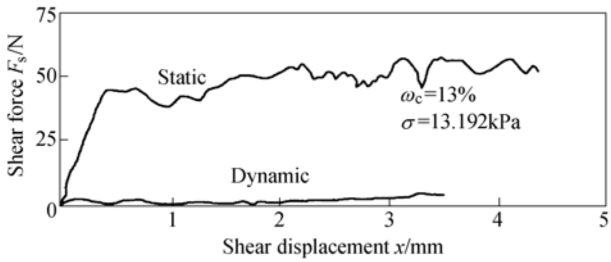

Fig. 3.12 Different curves of x-F_s on the static and dynamic experiments

3.2.6 *Influence of granular size on shear strength*

Adopting four groups of iron ores, the comparison between static and dynamic load experiments has been conducted under the same condition. The results are:

(1) With the increment of granular size, the angle of internal friction φ shows a tendency of increasing but the slope is very small. The slope of φ in static state is slightly more than the one in dynamic state. In addition, for the same size the all values of φ in static state are more than the values in dynamic state (shown in Fig.3.13).

(2) The influence of granular size on shear strength τ is not very obvious, and there is no noticeable trend of either increase or decrease. The reason is that shear strength is influenced by many factors. For example, the smaller granules have bigger surface area and more contact points, so that the cohesion and friction are bigger. Although the bigger granules have smaller surface area, the granular interlocking force is higher, so that τ shows a fluctuation in certain range of granular size (shown in Fig.3.14).

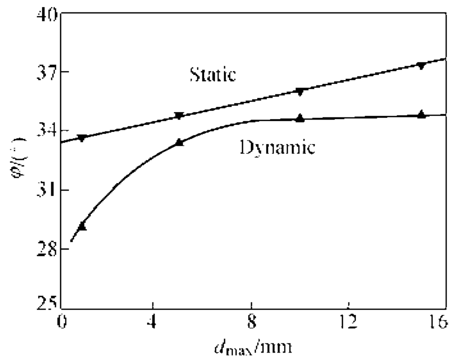

Fig. 3.13 Relation between d_{max}-φ

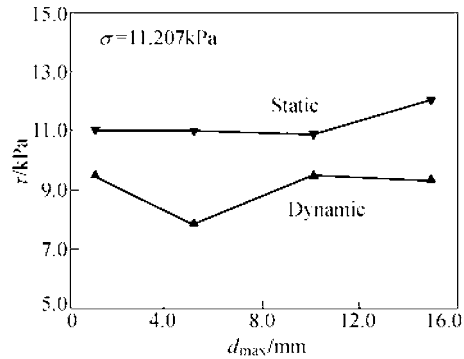

Fig. 3.14 Relation between d_{max}-τ

(3) The granular size has influence on the curve of x-F_s. The curve of x-F_s in the course of shearing is shown in Fig.3.15. In fact, this curve of x-F_s is not a smooth curve. Because of the granular dislocation in the course of shearing, the stress will release or increase, so that the curve shows somewhat wavy. The bigger the granular size is, the more the wavy characteristic will be.

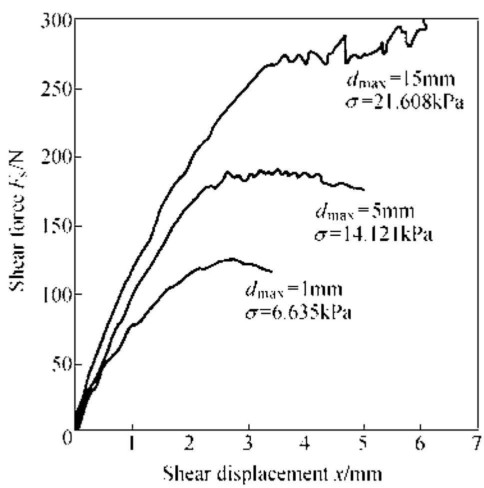

Fig. 3.15 Influence of d_{max} on the curve of x-F_s

3.2.7 *Influence of exciting method on shear strength*

Adopting horizontal and vertical methods of excitation respectively, the comparative static and dynamic experiments are done under two different conditions. The experimental results show that the result of vertical vibration fairly agrees with the result of horizontal vibration. For the vertical vibration, the dynamic shear strength is τ_d/τ_j=1/3～2/3, and a typical curve of x-F_s is shown in Fig.3.16. Although the directions of vibration are different, all granules can be activated, and the vibrations from different directions have uniform effect to improve the granular flowability.

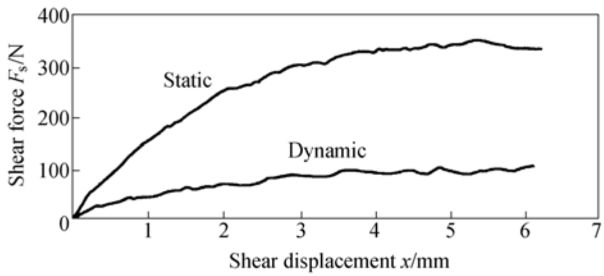

Fig. 3.16 Curves of x-F_s when vibration is activated

Shear box of ϕ185; σ=25 kPa; f=17 Hz; A=±1.200 mm; d_{max}=5 mm; iron ores

3.2.8 *Influence of granular discharge in the course of shearing*

Through the opening of the shear box in the bottom, during the course of shearing the change of stress is observed when a given amount of sample materials are discharged from the shear box. The typical experimental results are shown in Fig. 3.17 and Fig. 3.18. The shear box with diameter of ϕ185 mm is adopted, and the sample material is iron ores of d_{max}=5 mm.

Fig. 3.17 is the relation curve between x and F_s under the dynamic conditions. Point a is the peak point, and point b indicates that the sample have already been destroyed and the shear force begins to reduce. 5.5% of sample materials is discharged at point b. F_s decreases by 52% from point b to point c. After point c the opening is switched off, F_s begins to ascend to point d. From point d to point e another 20% of the sample materials are discharged. Compared with point b, F_s in point e decreases by 88%. At point e the opening is closed once more. Meanwhile F_s begins to ascend again. It is good that line 0a is approximately parallel to line *ef*, and line *bc* is approximately parallel to line *de*. These indicate that the discharge of a small quantity of sample materials causes the increment of porosity factor and the abrupt reduction of F_s. Because of the air pressure load, the direct stress retains dynamic equilibrium, and the sample materials solidify again under the vibration; F_s also ascends correspondingly to the original level before discharge. In another words, the granular discharge will cause rapid reduction of stress.

Fig. 3.18 is the static curve of x-F_s when the sample materials are vertically sheared. The discharged sample materials are about 1.8% from 1 to 2, and F_s decreases by 45%. The discharged sample materials are about 10.2% from 3 to 4, and F_s then decreases by 73.2%. It should be noted that after point 4 if the discharge is stopped, the sample materials begin to solidify again, but the degree of the solidification is far less than the one in Fig.3.17 under the vibration. Therefore, the value of F_s at point 5 is far less than the one at point 1.

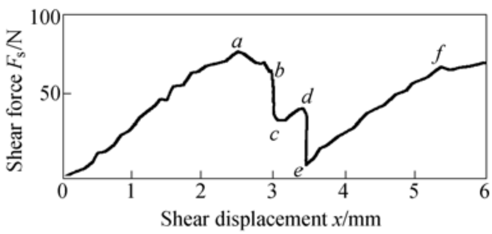

Fig. 3.17 Curve of x-F_s when vertically vibrating

f=17 Hz; A=±1.2 mm

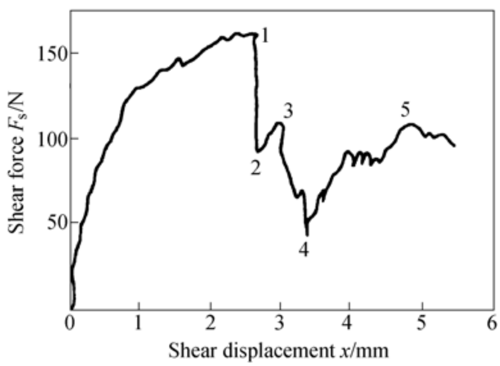

Fig. 3.18 Static curve of x-F_s

when vertically shearing

3.3 Top Box Vibrating Shearing Experiment

3.3.1 *Curve of stress-strain for top box shearing*

For the top box shear, there are three kinds of materials which are used for the side of the box, such as steel plate ST, wood plate TM and rubber plate RB. The sample material is the calcspar with d_{max}=5 mm;the shear box is of ϕ185 mm; σ=9.537 kPa;the dynamic conditions are f=60 Hz and A=0.080 mm. The relations between shear stress F_s and shear strain x are shown in Fig. 3.19, Fig. 3.20 and Fig. 3.21.

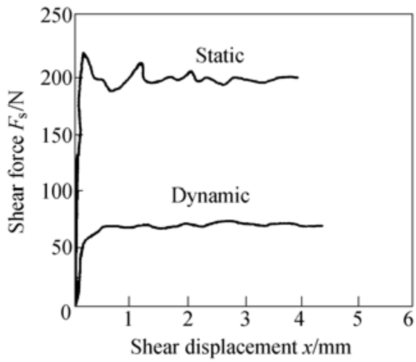

Fig. 3.19 Curve of x-F_s for steel plate

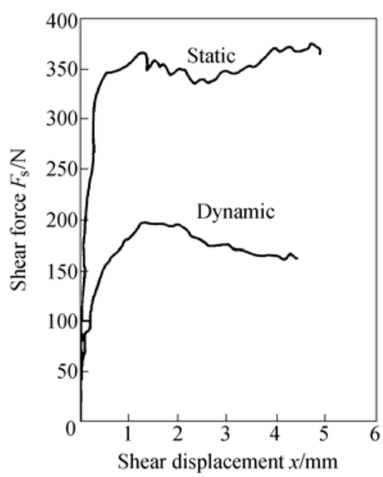

Fig. 3.20 Curve of x-F_s for wood plate

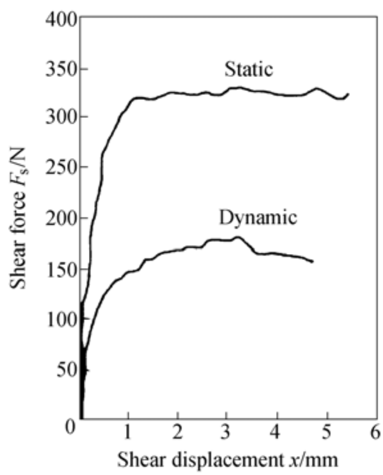

Fig. 3.21 Curve of x-F_s for rubber plate

The dynamic shear strength is far less than the static shear strength, and the introduction of vibration causes the reduction of granular rigidity[2,61~65]. In addition, if the side materials are different, the curves of x-F_s are also different. For the rigidity of the side materials, steel plate ST > wood plate TM > rubber plate RB, the curves of x-F_s correspond to them obviously. If the rigidity of the side materials is high, the granules will be destroyed under very small deformation, then will remain stable condition. The surface roughness of the side materials also has great influence on the shear force. Steel plate is the smoothest, rubber plate takes second place, and wood plate is the roughest. It has been found that the highest roughness corresponds to the highest shear force. For the steel plate, the curve of x-F_s shows that during the course of static shearing it has the peak value like a pulse. Many other experimental results show similar trend. The reason is that the rigidity of the steel plate is high and the surface is very smooth.

Fig. 3.22 is the figure showing comparative experimental results between static and dynamic loading when the steel plate is used for the side material. In this figure, F_{sd}/F_{sj}=0.25, and the dynamic curve of x-F_s has no peak value similar to the static curve. During the course of dynamic shearing the vibration exciter is closed at point a, so F_s rapidly ascends and reaches the peak value. If it is unblocked again, line F_s will descend to the original level. It indicates that the vibration can reduce the shear strength and improve the granular flowability.

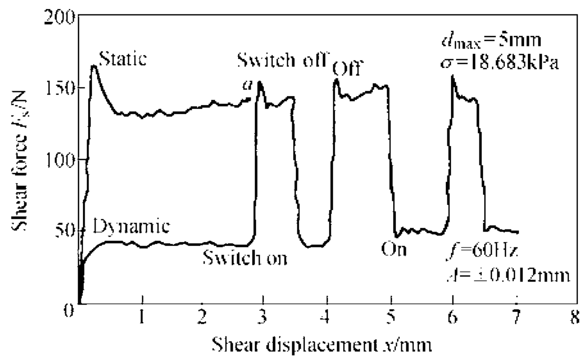

Fig. 3.22 Curve of static and dynamic comparative experimental result

3.3.2 *Change of the shear strength of sides* τ, *the angle of external friction* φ_w *and the cohesion C*

The parameters in the following two experiments are: the shear box is of ϕ185 mm; the sample material is magnetite with d_{max}=5 mm; f=60 Hz, and A=0.070 mm; the direct pressures are σ_A=3.082 kPa, σ_B=3.811 kPa, σ_C= 9.537 kPa, and σ_D=11.530 kPa.

The curves of x-F_s for the static and dynamic side shearing are shown in Fig. 3.23 and Fig. 3.24. The relative experimental data are carried out by regression analysis (shown in Table 3.2), and the curves of regression analysis are shown in Fig. 3.25.

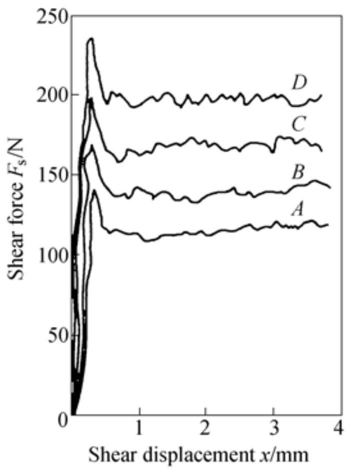

Fig. 3.23 Static side shear curve of x-F_s

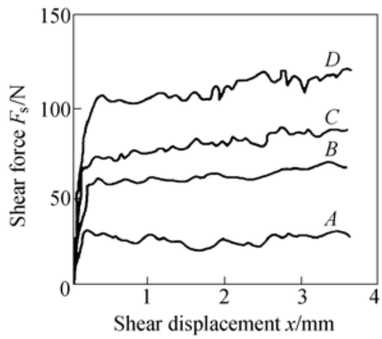

Fig. 3.24 Dynamic side shear curve of x-F_s

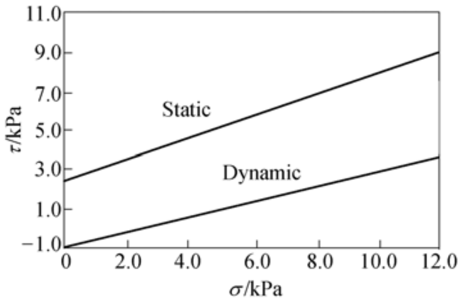

Fig. 3.25 Relative curve of static and dynamic τ-σ for ST

Table 3.2 Static and dynamic experimental values of φ_w and C

No.	State	Regression equation of τ-σ	φ_w/(°)	C/kPa
36J	J	τ=0.4911σ+3.093	23.157	3.093
36D	D	τ=0.489σ−0.303	19.238	−0.303

In contrast to the static state, the dynamic values of C and φ are reduced significantly. These results agree with the ones of the whole box shearing experiment.

3.3.3 *Static and dynamic shear experiment for different side materials*

The surface roughness of different side materials is: wood plate TM > rubber plate RB > steel plate ST. Under the same trial conditions the experimental results correspond to the characteristics of the materials respectively. The results are shown in Table 3.3.

Table 3.3 Static and dynamic comparative experimental values of φ_w and C

No.	State	Regression equation τ-σ	$\varphi_w/(^\circ)$	C / kPa
38J	J	τ=0.913σ+7.054	42.412	7.054
40D	D	τ=0.403σ+2.730	21.937	2.730
38J	J	τ=0.904σ+3.407	42.109	3.407
40D	D	τ=0.591σ+0.374	30.479	0.374

The corresponding regression curves are also shown in Fig. 3.26 and Fig. 3.27 respectively. The static and dynamic experimental results are shown in Table 3.2 and Fig. 3.25 respectively. Fig. 3.28 is the comparative figure of the difference between static and dynamic internal friction $\Delta\varphi$.

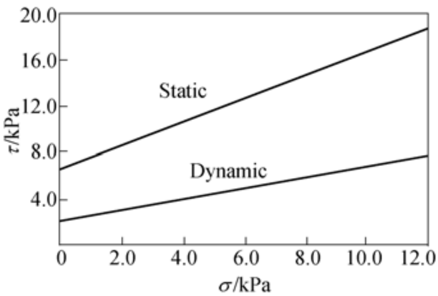

Fig. 3.26 Curve of static and dynamic τ-σ for TM

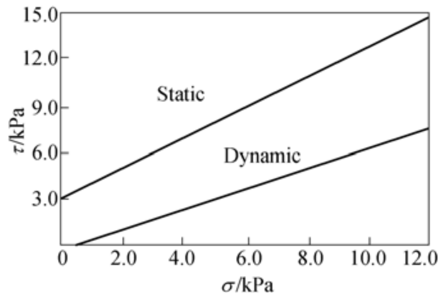

Fig. 3.27 Curve of static and dynamic τ-σ for RB

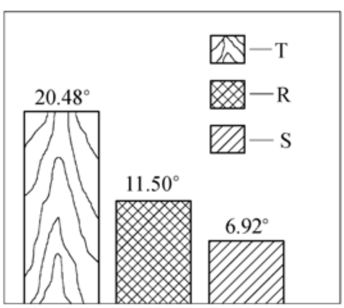

Fig. 3.28 Comparative figure of the difference between static and dynamic internal friction $\Delta\varphi$

The experimental results show that the roughness of side materials is an important factor. The bigger the roughness is, the more will be the shear strength, C, φ and the difference between static and dynamic internal friction. It indicates that the vibration has significant influence on the granular flowability along the sides.

3.3.4 *Influence of the amplitude of vibration*

Changing the amplitude of vibration A, the variation of τ is observed when the frequency f=60 Hz. The experimental condition is that the sample materials are iron ores; the shear box is of ϕ185 mm; the side material is steel plate; and A=0, indicating static state. The experimental results are shown in Fig. 3.29.

Fig.3.29 shows that the curve goes down gradually until it is in equilibrium, and A still has ultimate value. This agrees with the results of the whole box vibration.

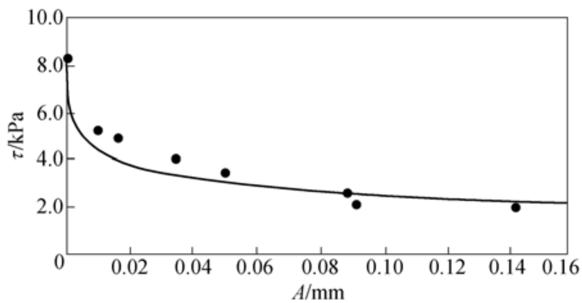

Fig. 3.29 Relation between amplitude of vibration and shear strength

3.3.5 *Influence of frequency*

When A is confined to a small range, about 0.08 mm, and the frequency f is changeable, the experimental result of magnetite is shown in Fig. 3.30, where the side material is steel plate; the granular size is $d_{\max}$=5 mm; and the shear box is of ϕ185 mm; It indicates the static state when f=0. The experimental result, which is similar to the result of the whole box hearing vibration, indicates that f has an extremum.

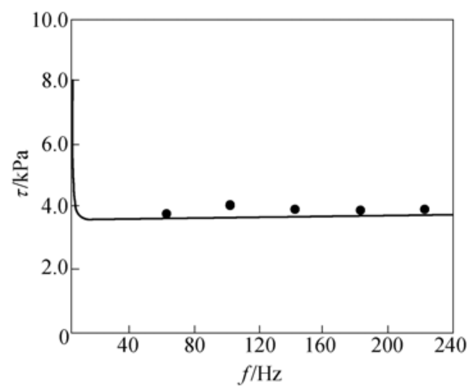

Fig. 3.30 Relation between frequency and shear strength

3.3.6 *Influence of moisture*

The sample material is the magnetite with d_{max} =1 mm; the direct pressure is σ= 3.811 kPa; and the side material is steel plate. The experimental results are shown in Fig.3.31, from which it is known that firstly τ decreases, then increases along with the increment of moisture, and in the end reaches the peak value when the moisture content is close to 10%. Because of the influence of liquefaction, τ is nearly equal to zero when the moisture content is close to 13%. However, under the same conditions τ still has a fairly high value for the static state.

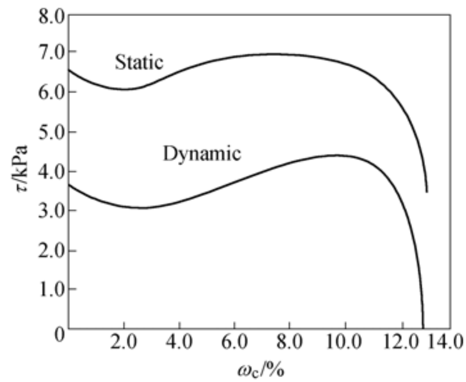

Fig. 3.31 Influence of moisture on shear strength

3.4 Differential Mechanical Model of Dynamic Shear

3.4.1 *Modeling prerequisites*

The physical basic of modeling is the DSA-1 vibrating direct device. There are two kinds of method to analyze the deformation and flowability of complex granular media. One is the method of continuous media, and the other is the method of special or discontinuous media[61].

Because the method of continuous media is convenient to do theoretical analysis and experimental simulation, at present most of researches are based on the method of continuous media. The model of continuous media assumes that the granular property can be expressed by the space-time function. The modeling prerequisite is that:

(1) The granules on the shear surface are isotropic, and the granular property is almost unchangeable in the direction of vibration during the course of shearing.

(2) Comparing to the granular size, the amplitude of vibration on the shear surface is very small, and the application of vibration does not generate pre-shear.

(3) The granular material is regarded as viscoelastic body, which has coulomb damping and viscous damping.

(4) Because of the influence of vibration, the granules in shear box in fact will move along with the direction of the force. The reciprocal effect will not be considered.

3.4.2 *Granular shear coulomb-elastic model*

Many experiments and researches show that in either static state or dynamic state, the characteristic of stress-strain is similar in form. Because of the application of vibration, the granular rigidity and coulomb's friction will decrease, so that the shear strength is tended to decrease. During the course of shearing, the deformation of sample experiences three stages: rigid, elastic and plastic one(shown in Fig. 3.32).

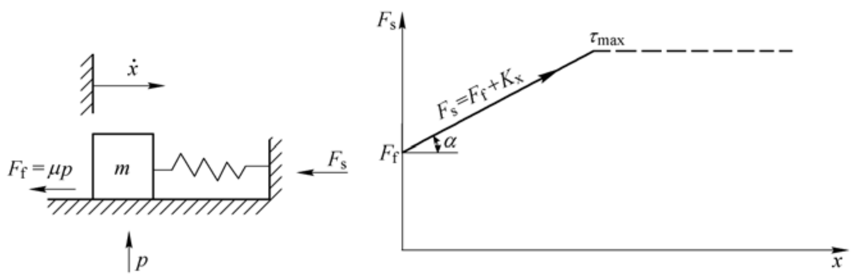

Fig. 3.32 Simple coulomb-elastic model

(1) Rigid stage. The displacement x is unchangeable until the shear force F_s reaches a certain pre-determined value F_f, which is called a rigid point. The value of this rigid point increases proportionally with the increment of direct pressure and the reduction of porosity ratio. In addition, the introduction of vibration will reduce the value of rigid point significantly, *viz*, by the coulomb's force one can obtain that:

$$F_s \leqslant F_f \qquad x=0 \tag{3.6}$$

(2) Elastic stage. F_s increases proportionally with the increment of x; moreover, these two have a good linear relation, which begins at the rigid point F_f and ends at the yield point F_{smax}. Consequently,

$$F_s = F_f + K_x \tag{3.7}$$

where K_x is granular shear rigidity, which increases proportionally with the increment of direct pressure and the reduction of porosity ratio, but decreases proportionally with the application of vibration.

(3) Plastic stage. When the shear force F_s reaches the yield point, the plastic

stage begins. The curve of x-F_s is nearly a straight line. This provides:

$$F_s = F_{smax}; \quad x = x_{max} \tag{3.8}$$

In the model $\dot{x}$ is the shear velocity, f is the coefficient of friction and p is the direct pressure. F_f and K_x are two important parameters characterizing the value of shear strength. When the other factors, such as direct pressure, granular composition and porosity ratio, are certain, the vibration will cause the reduction of F_f and K_x to a great extent and this indicates that the granular flowability is improved.

3.4.3 *Differential mechanical model of dynamic shear when the shear box vibrates wholly*

During the course of dynamic shearing, the granules vibrate within the shear box. If the top box and the bottom box are regarded as a whole, then the shear box and the sample have the same state of motion. Fig.3.33 is the differential mechanical model of dynamic shear.

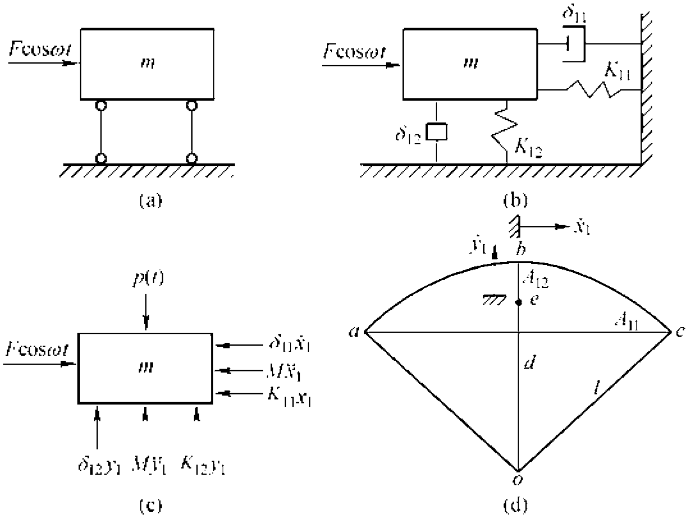

Fig. 3.33 Differential mechanical model of dynamic shear

The total mass of the top box and the bottom box is m, and the exciting force generated by exciter is $F\cos\omega t$. Under the action of exciting force, the spring will vibrate to and fro. This motion is divided into the horizontal and vertical components, which is shown in Fig.3.33b. Assuming the displacements are X_1 and Y_1 respectively, the restoring forces of springs are $K_{11}x_1$, $K_{12}y_1$, where K_{11} and K_{12} are the horizontal rigidity and the vertical rigidity respectively; damping forces are $\delta_{11}x_1$ and $\delta_{12}y_1$, where δ_{11} and δ_{12} are the horizontal and vertical damping coefficients respectively. $p(t)$is the generalized exciting force along the vertical direction. The vibrating differential equation is established as follows:

$$\left.\begin{aligned} m\frac{\mathrm{d}^2x_1}{\mathrm{d}t^2}+\delta_{11}\frac{\mathrm{d}x_1}{\mathrm{d}t}+K_{11}x_1 &= F\cos\omega t \\ m\frac{\mathrm{d}^2y_1}{\mathrm{d}t^2}+\delta_{12}\frac{\mathrm{d}y_1}{\mathrm{d}t}+K_{12}y_1 &= p(t) \end{aligned}\right\} \tag{3.9}$$

Firstly, the horizontal vibration is studied. Assuming that $\frac{K_{11}}{m}=p^2, \frac{\delta_{11}}{m}=2n, \frac{F}{m}=q$, Which are substituted into the first equation of formula(3.9), the following is obtained:

$$\frac{\mathrm{d}^2x_1}{\mathrm{d}t^2}+2n\frac{\mathrm{d}x_1}{\mathrm{d}t}+p^2x_1=q\cos\omega t \tag{3.10}$$

This is a second order linear inhomogeneous differential equation with constant coefficients. The solution of this equation comprises the general solution of the homogeneous differential equation and the particular solution of the inhomogeneous differential equation. Due to the damping, free vibration will disappear soon after the vibration begins, so only the particular solution is discussed as follows:

$$x_1=A_{11}\cos(\omega t-\varphi) \tag{3.11}$$

where A_{11} is the amplitude of vibration along the direction of x_1; φ is the phase angle.

Substituting x_1, its first derivative and its second derivative into Eq.(3.10), A_{11} and φ can be resolved by:

$$A_{11}=\frac{q}{\sqrt{(p^2-\omega^2)+4n^2\omega^2}} \tag{3.12}$$

$$\tan\varphi=\frac{2n\omega}{p^2-\omega^2} \tag{3.13}$$

Supposing $\omega/p=Z$, $n/p=\zeta$, they are substituted in Eqs. (3.12) and (3.13), therefore,

$$A_{11}=\frac{F}{K_{11}}\frac{1}{\sqrt{(1-Z^2)^2+(2\zeta Z)^2}} \tag{3.14}$$

$$\varphi=\tan^{-1}\frac{2\zeta Z}{1-Z^2} \tag{3.15}$$

That is to say, the horizontal vibration of the system of the whole box including the sample is also a simple harmonic motion, where the angular frequency is ω, and the amplitude of vibration is A_{11}. The phase angle φ is determined by the property of the system, where the mass is m, the rigidity of elastic system is K_{11} and the damping coefficient of spring is δ_{11}, and the property of exciting force, whose amplitude of force is F and angular frequency is ω, but does not relate to its initial conditions.

The motion law of vertical vibration relates closely to the horizontal vibration. In Fig.3.33d, the line *ob* is the equilibrium position when the spring is vertical, and the positive and negative points of *b* along x_1 are points *a* and *c* respectively. Assuming that *l* is the length of the spring, and A_{12} is the vertical amplitude of the vibration, the following expressions are obtained which give their geometric relationships:

$$oa=ob=oc=l \tag{3.16}$$

$$ad=dc=A_{11} \tag{3.17}$$

$$be=ed=A_{12} \tag{3.18}$$

because $$\mathrm{bd}=2\mathrm{A}_{12}=\mathrm{l}-\mathrm{od}$$

so $$\mathrm{A}_{12}=\frac{1}{2}(\mathrm{l}-\sqrt{\mathrm{l}^2-\mathrm{A}_{11}^2}) \tag{3.19}$$

The phase from *d* to *c* for the horizontal vibration is half of the periodic time, but the phase from *b* to *d* for the vertical vibration is a full periodic time. Therefore, if the frequency of horizontal vibration is ω, the frequency of vertical vibration will be 2ω with an advance of $\pi/2$. By testing with a vibration meter, the established model is proved to be true. When the frequency of the horizontal vibration is 20Hz, the measured frequency of vertical vibration is 40Hz. The motion law of the vertical vibration can be expressed as:

$$y_1 = A_{11}\cos(2\omega t+\frac{\pi}{2}-\varphi) \tag{3.20}$$

$$viz.:\ y_1=\frac{1}{2}(l-\sqrt{l^2-A_{11}^2})\sin(2\varphi t-\varphi) \tag{3.21}$$

When l=35 mm, the relation curve between $x_1=A_{11}\cos(\omega t-\pi/2)$and $y_1=A_{12}\cos 2\omega t$ is shown in Fig.3.34, and the relation between their amplitude of vibration is shown in Fig.3.35.

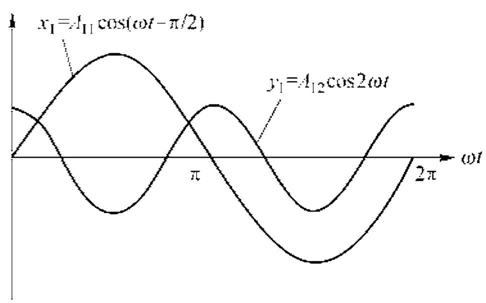

Fig. 3.34 Law of horizontal and vertical vibration

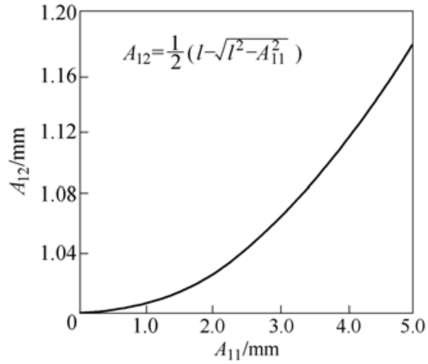

Fig. 3.35 Relation between A_{11} and A_{12}

The relation between A_{11} and A_{12}, whose values are far different, is nonlinear. When the amplitude of vibration for horizontal vibration is small, such as A_{11}=0.5 mm, the amplitude of vibration for vertical vibration is also very small, that is $A_{12}=1.78\times10^{-3}$ mm. Since $A_{11}/A_{12}=280.89$, *viz.*, $A_{11}\gg A_{12}$, it could be considered that there is only horizontal vibration and the vertical vibration can be ignored.

3.4.4 *Differential mechanical model of dynamic shear when the shear box vibrates partially*

In fact, there is a shear slot filled with the granules between the top box and the bottom box. The vibration is transmitted to the top box by the granular medium. Thus, on one hand, the top box moves along with the bottom box and produces absolute displacements x_2 and y_2. On the other hand, because of the granular viscoelastic plasticity the top box has the relative displacements x_r and y_r. Moreover, the following relations exist: $x_r=x_2-x_1$, $y_r=y_2-y_1$, where x_1 and y_1 are the input displacements ascertained by the whole vibrating model. Based on the differential mechanical model of dynamic shear (shown in Fig.3.36), the law of motion of the top box and the sample materials is studied. By the use of a viscous element, an elastic element and a plastic element, the model of the granular viscoelastic plasticity can be established.

The motion equation of the bottom box is similar to the whole vibration, and the input displacements are:

$$x_1=A_{11}\cos\omega t \tag{3.22}$$

$$y_1=A_{12}\sin2\omega t \tag{3.23}$$

In terms of the supposition of isotropy of the granular medium in the shear box, the granular horizontal and vertical rigidity and the damping coefficient are the same. According to Fig.3.36b, the mechanical analysis of the top box can be

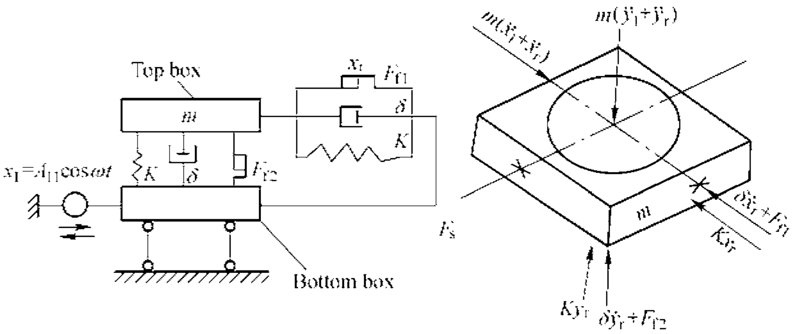

(a) (b)

Fig. 3.36 Vibrating mechanical model of a part of the shear box

done. The inertia forces: $m(\ddot{x}_1+\ddot{x}_r)$and $m(\ddot{y}_1+\ddot{y}_r)$;the elastic forces: Kx_r and Ky_r; the viscous forces: $\delta\dot{x}_r$ and $\delta\dot{y}_r$; the Coulomb forces: F_{f1} and F_{f2}. Firstly, the relative displacements x_r and y_r act as independent variables, and the differential equation of the motion of top box is obtained:

$$m\left(\frac{d^2x_1}{dt^2}+\frac{d^2x_r}{dt^2}\right)+\delta\frac{dx_r}{dt}+Kx_r+F_{f1}=0 \tag{3.24}$$

$$m\left(\frac{d^2y_1}{dt^2}+\frac{d^2y_r}{dt^2}\right)+\delta\frac{dy_r}{dt}+Ky_r+F_{f2}=0 \tag{3.25}$$

After transforming, they become:

$$m\frac{d^2x_r}{dt^2}+\delta\frac{dx_r}{dt}+Kx_r+F_{f1}=mA_{11}\omega^2\cos\omega t \tag{3.26}$$

$$m\frac{d^2y_r}{dt^2}+\delta\frac{dy_r}{dt}+Ky_r+F_{f2}=4mA_{12}\omega^2\sin 2\omega t \tag{3.27}$$

where m is the total mass of the top box; K is the granular dynamic rigidity; δ is the granular viscous damping coefficient; F_{f1} and F_{f2} are the horizontal and vertical Coulomb forces respectively.

The horizontal vibrating Eq.(3.26)is firstly studied. The Coulomb force F_{f1} is an alternating force, whose direction reverses the direction of motion. The Coulomb force, which is a function of time t, is a square wave whose amplitude is $\pm F_{f1}$ ($F_{f1}=\mu p$, μ is coefficient of friction, p is the direct pressure) and angular frequency is ω. It is shown in Fig.3.37. The function of the Coulomb force is as follows:

$$F_{f1}(t)=\begin{cases} F_{f1}, & 0<t<T/2 \\ -F_{f1}, & T/2<t<T \end{cases} \tag{3.28}$$

where T is the moving period, $T=2\pi/\omega$.

The periodic function can be expanded by Fourier's series:

$$f(t)=\frac{a_0}{2}+a_1\cos\omega t+a_2\cos 2\omega t+\cdots+b_1\sin\omega t+b_2\sin 2\omega t+\cdots$$

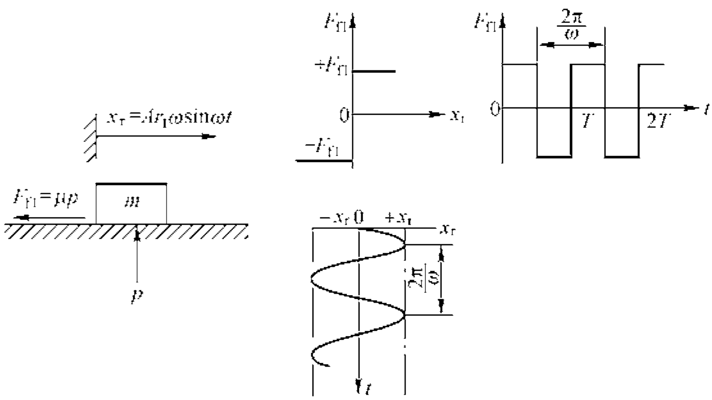

Fig. 3.37 Change of Coulomb force subjected by simple harmonic motion

$$=\frac{a_0}{2}+\sum_{n=1}^{\infty}(a_n\cos n\omega t+b_n\sin n\omega t) \tag{3.29}$$

The coefficients of Fourier's series a_0, a_n and b_n can be ascertained by Euler's formula:

$$a_0=\frac{2}{T}\int_0^T f(t)\mathrm{d}t \tag{3.30}$$

$$a_n=\frac{2}{T}\int_0^T f(t)\cos n\omega t\mathrm{d}t \quad n=1,2,3,\cdots \tag{3.31}$$

$$b_n=\frac{2}{T}\int_0^T f(t)\sin n\omega t\mathrm{d}t \quad n=1,2,3,\cdots \tag{3.32}$$

Eq.(3.28) is substituted into Euler's formula, then it is integrated to obtain:

$$\left.\begin{aligned} a_0&=0 \qquad a_n=0\\ b_n&=\frac{4F_{\mathrm{f}1}}{n\pi} \quad n=1,3,5\cdots\end{aligned}\right\} \tag{3.33}$$

The expression of Fourier's series of the Coulomb force is:

$$F_{\mathrm{f}1}(t)=\frac{4F_{\mathrm{f}1}}{\pi}(\sin\omega t+\frac{1}{3}\sin 3\omega t+\frac{1}{5}\sin 5\omega t+\cdots) \tag{3.34}$$

$F_{\mathrm{f}1}(t)$is a symmetrical odd function of half-wave. In general, a single non-linear problem is usually approximately expressed by the first item of Fourier's series as the amplitude of vibration of higher harmonic term can be omitted. Therefore, we can substitute an equivalent linear viscous force F_{E} for the non-linear Coulomb friction, consequently,

$$\frac{4F_{\mathrm{f}1}}{\pi}\sin\omega t=\delta_{\mathrm{E}1}A_{\mathrm{r}1}\omega\sin\omega t$$

$$\text{or}\quad F_{\mathrm{f}1}(t)=\frac{4F_{\mathrm{f}1}}{\pi}\sin\omega t=\delta_{\mathrm{E}1}x_{\mathrm{r}}=F_{\mathrm{E}}$$

$$viz.: \quad \delta_{E1} = \frac{4F_{f1}}{\pi\omega A_{r1}} \tag{3.35}$$

where A_{r1} is the amplitude of horizontal relative motion; δ_{E1} is the coefficient of horizontal equivalent viscous damping. By the same method the coefficient of vertical equivalent viscous damping δ_{E2} can be deduced:

$$\delta_{E2} = \frac{2F_{f2}}{\pi\omega A_{r2}} \tag{3.36}$$

where A_{r2} is the amplitude of the vertical relative motion.

The damping of the whole system is the total of viscous damping δ and the equivalent damping caused by Coulomb friction $\delta_{E1}(\delta_{E2})$.

The damping ratio of horizontal vibration: $\zeta_1 = \dfrac{\delta + \delta_{E1}}{\delta_{cr}}$

$$viz.: \quad \zeta_1 = \frac{\delta\pi\omega A_{r1} + 4F_{f1}}{2m\pi\omega\omega_n A_{r1}} \tag{3.37}$$

The damping ratio of vertical vibration: $\zeta_2 = \dfrac{\delta + \delta_{E2}}{\delta_{cr}}$

$$viz.: \zeta_2 = \frac{\delta\pi\omega A_{r2} + 2F_{f2}}{2m\pi\omega\omega_n A_{r2}} \tag{3.38}$$

where $\delta_{cr} = 2m\omega_n$ is the critical damping coefficient, ω_n is the natural frequency. Assuming that the frequency ratio of horizontal vibration is $r_1 = \omega/\omega_n$, and the frequency ratio of vertical vibration is $r_2 = 2\omega/\omega_n$, the differential equations of the motion of top box are:

$$\frac{d^2 x_r}{dt^2} + 2\zeta_1\omega_n \frac{dx_r}{dt} + \omega_n^2 x_r = A_{11}\omega^2 \cos\omega t \tag{3.39}$$

$$\frac{d^2 y_r}{dt^2} + 2\zeta_2\omega_n \frac{dy_r}{dt} + \omega_n^2 y_r = 4A_{12}\omega^2 \sin 2\omega t \tag{3.40}$$

Resolving these two differential equations, one can get:

$$x_r = A_{r1}\cos(\omega t - \varphi_1) \tag{3.41}$$

$$y_1 = A_{r2}\sin(2\omega t - \varphi_2) \tag{3.42}$$

Moreover, the ratio of the input amplitude of motion and the relative amplitude of the motion of top box, and their phase difference can be expressed by:

$$\frac{A_{r1}}{A_{11}} = \frac{r_1^2}{\sqrt{(1-r_1^2)^2 + (2\zeta_1 r_1)^2}} \tag{3.43}$$

$$\frac{A_{r2}}{A_{12}} = \frac{r_2^2}{\sqrt{(1-r_2^2)^2 + (2\zeta_2 r_2)^2}} \tag{3.44}$$

$$\varphi_1 = \tan^{-1}\frac{2\zeta_1 r_1}{1-r_1^2} \tag{3.45}$$

$$\varphi_2 = \tan^{-1}\frac{2\zeta_2 r_2}{1-r_2^2} \tag{3.46}$$

The damping of vibrating system probably has many types, such as viscous damping, coulomb damping, fluid damping and structural damping. The properties of various damping are different and complex. For example, for the elastic body of continuous media, the structural damping hasn't been understood completely. For the viscous granular media, the damping characteristic is more complex, and it is probably combined with many other factors, such as the friction among the granules, the plastic deformation of contacting points and the fluid damping at the boundary. Moreover, its characteristic is distinctly non-linear, and it is difficult to obtain analytical solution by any precise method. In the above analysis it is considered synthetically the influence of viscous damping and coulomb damping, and the establishment of the model provides an acceptable approximate solution. The following are two typical examples.

(1) Viscous damping. Assuming that coulomb damping is zero, and there only exists viscous damping, so the damping ratio $\zeta_1=\delta/\delta_{cr}$ is a constant. The solutions of Eqs.(3.39)and(3.40)are the same with that of Eqs.(3.44)and (3.46)in form.

(2) Coulomb damping. Assuming that viscous damping is zero, namely, $\delta=0$, and there is only coulomb damping. Consequently,

$$\zeta_1 = \frac{2F_{f1}}{m\pi\omega\omega_n A_{r1}} \quad \text{or} \quad \zeta_1 = \frac{2F_{f1}}{\pi k A_{r1} r_1} \tag{3.47}$$

$$\zeta_2 = \frac{2F_{f2}}{m\pi\omega\omega_n A_{r2}} \quad \text{or} \quad \zeta_2 = \frac{2F_{f2}}{\pi k A_{r2} r_2} \tag{3.48}$$

So the amplitude ratio of relative motion can be obtained:

$$\frac{A_{r1}}{A_{11}} = \pm\sqrt{\left(\frac{r_1^2}{1-r_1^2}\right) - \left[\frac{4F_{f1}}{\pi F_{s1}\left(1-r_1^2\right)}\right]^2} \tag{3.49}$$

$$\frac{A_{r2}}{A_{12}} = \pm\sqrt{\left(\frac{r_2^2}{1-r_2^2}\right)^2 - \left[\frac{4F_{f2}}{\pi F_{s2}\left(1-r_2^2\right)}\right]^2} \tag{3.50}$$

$$\varphi_1 = \tan^{-1}\left[\frac{4F_{f1}}{-\frac{\pi A_{r1}}{A_{11}} F_{s1}(1-r_1^2)}\right] \tag{3.51}$$

$$\varphi_2 = \tan^{-1}\left[\frac{4F_{f2}}{-\frac{\pi A_{r2}}{A_{12}} F_{s2}(1-r_2^2)}\right] \tag{3.52}$$

where $F_{s1}=KA_{11}$, is the horizontal equivalent static force; $F_{s2}=KA_{12}$ is the vertical equivalent static force.

From Eqs.(3.49)and(3.50), it is known that if A_{r1} and A_{r2} have real number solutions, the following equations must be applicable:

$$\frac{F_{f1}}{F_{s1}} < \frac{\pi r_1^2}{4} \tag{3.53}$$

$$\frac{F_{f2}}{F_{s2}} < \frac{\pi r_2^2}{4} \tag{3.54}$$

Generally speaking, the above conditions are achieved easily when the friction is small. However, for the low frequency $r \ll 1.0$, the above conditions are difficult to achieve. For the resonance state, *viz.*, when r=1.0, the amplitude of vibration does not have a fixed value because the energy dissipation is less than the energy input during the same period.

The above analysis shows that the horizontal motion of the top box and the sample is simple harmonic motion, whose angular frequency is ω and the vertical motion is also a simple harmonic motion, whose angular frequency is 2ω. The state of vibration is determined by the property of the exciting system, such as the amplitude of vibration and frequency, and the property of the granular medium, such as the mass, the dynamic rigidity and the damping coefficient. Based on numerous experimental results and the physical models, the established differential mechanical model of granular dynamic shearing has the properties of simple structure and obvious physical meaning. Considering the influence of viscoelastic plasticity, the characteristics of a sample under vibration conditions can be described correctly, and these provide a theoretical foundation for the study of the granular dynamic characteristics in the vibration field.

3.5 Vibrating Spectrum Analysis of Dynamic Shearing and Model Verification

In order to understand clearly the spectrum of vibrating signal, the time period of vibration or the related function is transformed into a function described in the frequency domain by the Fourier's series. This method is called the spectrum analysis.

3.5.1 *Fourier's series*

The function $f(t)$, whose period is T, can be expanded into the Fourier's series of complex number:

$$f(t) = \sum_{n \to -\infty}^{\omega} C_n e^{i\omega_n t} \tag{3.55}$$

where $\omega_n = \dfrac{2n\pi}{T}$; $n = 0, \pm 1, \pm 2, \cdots, \pm\infty$; $C_n(\omega) = \dfrac{1}{T}\int_{-T/2}^{T/2} f(t) e^{-i\omega_n t} dt$; C_n is the complex function of the amplitude of vibration.

3.5.2 *Auto power spectrum density function G_{xx}*

Power spectrum can be calculated by two methods. One method is that the Fourier transformation of signal is calculated first, then the square of absolute value is taken into consideration and the power spectrum is obtained. The other method is to calculate the power spectrum using the correlation function. The autocorrelation function is transformed by Fourier transformation, obtaining that:

$$G_{xx}(\omega)=\frac{1}{2\pi}\int_{-\infty}^{\infty}R(\tau)\mathrm{e}^{-i\omega\tau}\mathrm{d}\tau=\frac{1}{2\pi}\int_{-\infty}^{\infty}R(\tau)\mathrm{e}^{-i2xf\tau}\mathrm{d}\tau \tag{3.56}$$

where

$$R(\tau)=\lim_{T\to\infty}\frac{1}{T}\int_{0}^{T}y(t)y(t+\tau)\mathrm{d}t \tag{3.57}$$

where $y(t)$is the sample function; τ is the time difference.

The spectrum analysis can provide the power of signal, *viz*., the frequency distribution of energy, and analyze the main frequency of signal spectrum. At present, the vibrating signal can only be analyzed entirely by computer.

3.5.3 *Model verification*

The structure of entire vibration and frequency spectrum

The sensor is installed on the bottom plate along the vertical and horizontal direction. The measured signal indicates the whole vibration, *viz*., the input vibration. The sample is iron ores, whose size is 5 mm.

The signal of time domain when the vibration is input horizontally, is shown in Fig. 3.38. The entire structure of the time domain of signal is steady and regular, and the differences between the peak values are not significant. The absolute value of the ratio between the positive and negative maximum of vibrating acceleration is approximately equal to 1, *viz*., $a_{\max}/a_{\min}=1$. The auto power spectrum, when the vibration is input horizontally, is shown in Fig. 3.39, in which the vibrating motion is a simple harmonic motion. The frequency is singular (f=20 Hz), so that the vibrating energy is concentrated in this frequency. This conclusion agrees with the entire model.

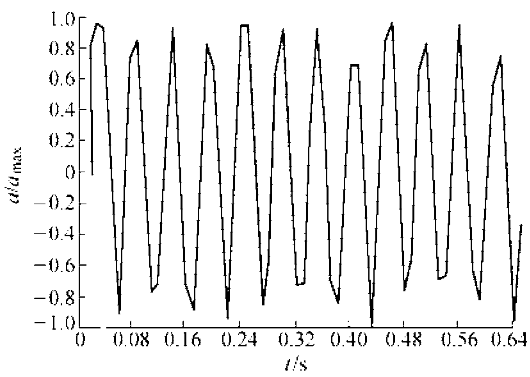

Fig. 3.38 Signal of time domain of horizontal vibration

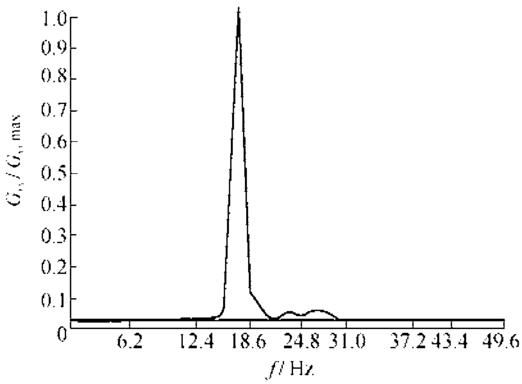

Fig. 3.39 Auto power spectrum of horizontal vibration

The signal of time domain when the vibration is input vertically is shown in Fig. 3.40. Comparing with Fig.3.38, it is obvious that this figure is more irregular and unsteady. Moreover, a_{max}/a_{min} =0.30, so the difference between them is large. The auto power spectrum, when the vibration is input vertically, is shown in Fig. 3.41. The main frequency is about 2 times of the one of horizontal vibration, *viz.*, 40 Hz. However, at the same time there is the presence of harmonic wave of low frequency with low energy, which is about 20% of the power of main frequency. Due to the non-linearity of elastic system and the gravity, the vertical vibration wave formation is poor, and the ratio between the vertical vibration energy of top box and the horizontal input vibration of the bottom box is: $G_{xx\max}\perp/G_{xx\max}//=0.361$. Therefore, the amplitude of vertical vibration is considerably less than the one of horizontal vibration.

Vibrating structure of a section and frequency spectrum

The sensors are installed on the bottom plate and the top box respectively, so that the vibrating signal of a section can be analyzed. The signals of time domain and the auto power spectrum of horizontal vibration of top box are shown in Fig. 3.42 and

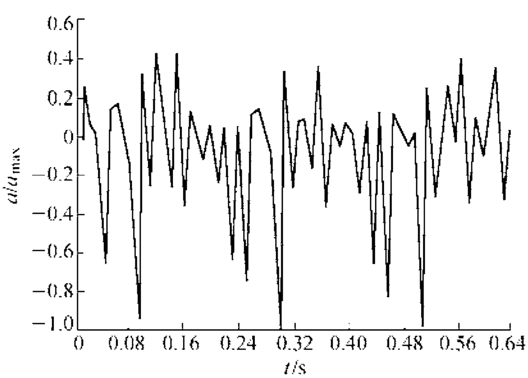

Fig. 3.40 Signal of time domain of vertical vibration

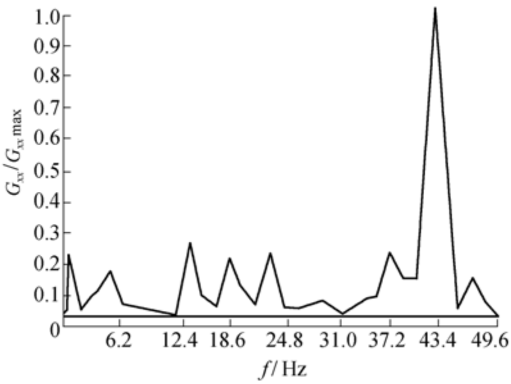

Fig. 3.41 Auto power spectrum of vertical vibration

Fig. 3.43, in which a_{max}/a_{min}=0.367. The two figures are irregular, and the main frequency is 20 Hz, but there are also other frequencies and the ratio between the vertical vibration energy of the top box and the horizontal input vibration of the bottom box is: G_{xxmax}top$\perp/G_{xxmax}$bottom//=0.360. It can be concluded that the vibration energy is attenuated significantly through the granular media. The conclusion made from model consists with this.

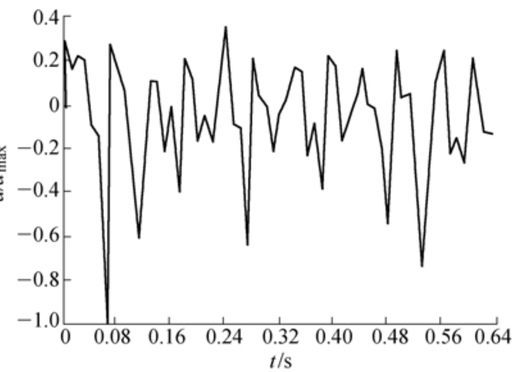

Fig. 3.42 Horizontal vibrating signal of time domain of the top box

The signal of time domain and the auto power spectrum of vertical vibration of top box are shown in Fig. 3.44 and Fig. 3.45, where a_{max}/a_{min}=0.653. These two graphical traces are very irregular, and the main frequency is 40 Hz. In the component of resonant vibration, the vibration energy of frequency 20 Hz is about 70% of the vibration energy of main frequency. In addition, the ratio between the vertical vibration energy of the top box and the horizontal input vibration of the bottom box is: $G_{xxmax}\perp/G_{xxmax}$//=0.243, which verifies again that the amplitude of vertical vibration is very small.

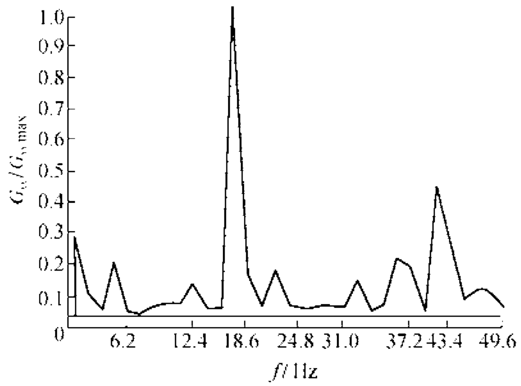

Fig. 3.43 Horizontal vibrating auto power spectrum of the top box

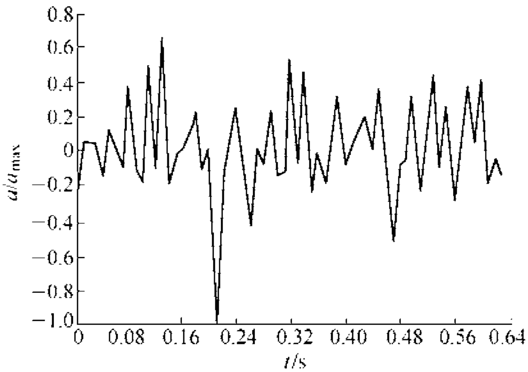

Fig. 3.44 Vertical vibrating signal of time domain of the top box

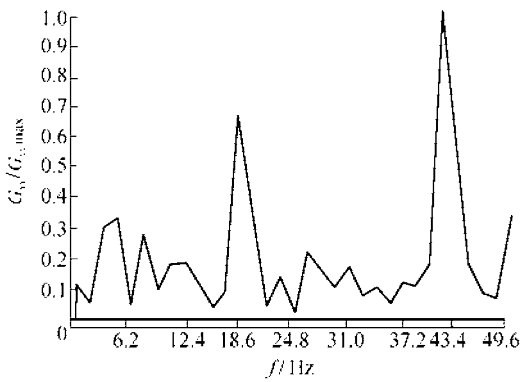

Fig. 3.45 Vertical vibrating auto power spectrum of the top box

In a word, due to the influences of the non-linearity of the vibrating spring and the viscous damping and coulomb damping of the granules, the vibrating wave is subjected to distortion and attenuation. However, all conclusions derived from the models are consistent with the experimental results.

4

Granular Dynamic Characteristics and Wave Law

4.1 Mechanism of Granular Dynamic Shear Strength

4.1.1 *Fundamental principle of modern tribology*

4.1.1.1 Classic frictional law

Da Finch, an Italian scientist, was the first to study the behavior of friction in 1508; then in 1780 Coulomb delivered the classic Frictional Law[2, 3, 42].

(1) The frictional force is proportional to the normal load on the contact surfaces, irrelevant to the nominal contact area between substances, namely:

$$F_f = fp \tag{4.1}$$

where F_f is the frictional force; f is the coefficient of friction; p is the normal load.

(2) The direction of the frictional force is opposite to the direction of relative motion on the contact surfaces.

(3) The frictional force is impertinent to the relative sliding velocity between the contact surfaces.

(4) The static frictional force is higher than the dynamic one.

The classic tribology laws can be applied in general engineering practice with certain limitations.

4.1.1.2 Modern frictional theories

Frictional theories have achieved significant developments since nearly 500 years ago. Examples of these are the mechanical theory, the attraction theory of molecules, the theory of cohesive friction, the molecular-mechanical theory, etc. The molecular-mechanical theory among them put forward by Soviet scientist, Kragelskii, is the most significant.

(1) Friction is a complex process in accordance to the molecular-mechanical

theory. It not only overcomes the mutual interaction between molecules, but also overcomes the resistance of mechanical deformation.

$$F_z=\tau_h A_h+\tau_j A_j \tag{4.2}$$

where F_z is the total frictional force; τ_h is unit action force between molecules; A_h is the real contact area of molecular acting force; τ_j is the unit mechanical acting force; A_j is the real contact area under mechanical action.

(2) The coefficient of friction is changeable. It is the comprehensive characteristic of materials' properties and environmental conditions.

(3) The coefficient of friction is related to the real area of contact. The frictional force is in direct proportion to the real area of contact.

(4) The coefficient of friction is relevant to the sliding velocity on the surfaces, it is generally accepted that the coefficient will decrease with the increase of sliding velocity.

(5) The frictional coefficients of most metals decrease with the increase of temperature.

(6) If there are various films on the contact surfaces, the frictional coefficient and the abrasion will decrease.

(7) The surface roughness affects the frictional coefficient, and the mechanical deformation enhances the coefficient of friction on rough surfaces. On the other hand, very sticky surfaces for the molecules may support tensile stress to enlarge the frictional coefficient. Appropriate roughness is the decisive factor for the minimum coefficient of friction.

(8) The coefficient of static friction is pertinent to the static contact period; the longer the contacting duration, the larger the static coefficient.

4.1.2 *Concept of the granular dynamic shear strength*

The ultimate shear strength, when the granules resist the shear sliding action subjected by the outside forces, is called the granular shear strength. The shear strength under the dynamic load is called the granular dynamic shear strength. From the point of view of the applied mechanics, there are three necessary and sufficient conditions to separate dynamic force from static one:

(1) The action of force is cyclic;

(2) The action of force produces the wave deformation on the applied body or the reciprocating motion of particles;

(3) The action of force is accompanied with the alternative accelerations.

The dynamic shear strength can be reflected by the effect or reactions of the three conditions, and they can be summed up as the dynamic strength and the dynamic deformation.

From numerous experiments and investigations, the dynamic shear strength is the same as the static one in nature and they are only clearly different in quantities.

There are several basic shear theories, such as Coulomb's Law, the total stress law, the effective stress law and Moor-Coulomb strength standards. Due to the simplicity and practicality, Coulomb's theory has been applied widely. The theory postulated by Coulomb, a French engineer, shows that the shear strength is a linear function of the normal stress within the range of a limited pressure. The formulae are listed below:

$$\tau = \sigma \tan\varphi \quad \text{(for sandy soil)} \tag{4.3}$$

$$\tau = C + \sigma \tan\varphi \quad \text{(for clay)} \tag{4.4}$$

where τ is the shear strength; σ is the normal stress on shear surfaces; C is cohesive force; φ is the angle of internal friction.

4.1.3 *Mechanism of granular dynamic shear strength*

For the granular media, their properties rely on the prevailing conditions. Eq. (4.4) has shown that the shear strength is equal to the sum of the internal friction and the cohesion.

4.1.3.1 Internal friction

The internal friction is the resistance preventing the relative motion or its trend between granules. The frictional force is produced between the static granules and the moving ones or between the moving granules with different velocities. Thus the friction relates with the relative motion. Granules can also produce internal friction in terms of the modern theories of friction. Its reasons are listed below[87~95].

(1) Resistance of mechanical action F_1 (as shown in Fig. 4.1).

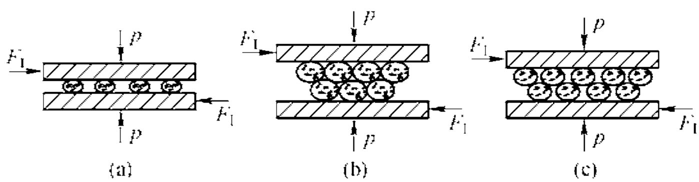

Fig. 4.1 Engaging action between granules

(a) Smooth surface; (b) Weak engaging surface; (c) Strong engaging surface

1) Some granules are engaged into the others' convex and concave surfaces, and produce macro biting-force components F_{11}.

2) The seeming smooth surface, where the particles inlay into each others' surfaces, is actually rough, that produce micro biting-force components F_{12}.

3) Granules are broken up under high stress action. Extra strength is generated from the re-arrangement of consumed energy of the granules, called extrusion re-arrangement components F_{13}.

(2) Adsorption of molecules F_2.Mutual action between the molecules produces the resistance on the contact surfaces. The longer is the attraction duration and

larger is the contact area, the bigger will be the adsorption of molecules.

The real contact area is clearly less than the possible contact area of surface. The reason is that the irregular shapes and sizes of the appearance of granular media subject particles to contact with each other at some points or in a small part of the surface area. The internal friction features the mechanical resistance. The higher is the granular density, the deeper will be the biting depth and also the stronger is the biting force. Macro biting-force constantly accompanies with the shear-expansion effects. The frictions of the granules are divided into two patterns according to the formation of motion, the sliding friction and the rolling friction.

4.1.3.2 Cohesion F_2

From Eq. (4.4), it can be concluded that the shear strength is equal to the cohesion when normal load is zero. It is thought that the cohesion C is the initial shear resistance without the normal load according to the knowledge of physics. As experiments have stated, C is an objective existence whether the granules are composed of dried particles or sticky fine ores with moisture. C is the combination of two components:

$$C=C_1+C_2 \tag{4.5}$$

where C_1 is the resistance from mutual biting of granules; C_2 is the cohesion due to the united effect of condense and colloid.

(1) The resistance C_1. It is the initial resistance from mutual biting of roughness of granules and dislocation of arrangements. C_1 always presents in any granular media, which is different from the conclusion that C_1 doesn't exist in non-clay sandy soil in soil mechanics. Numerous experiments and other academic sources have proved this statement[89~93].

(2) Cohesive Force C_2. The causes of its production are listed below.

1) The cohesion of attraction of molecules between the water films among granules and the neighboring granules is termed as the initial cohesion. The initial cohesion will expand with the compaction of the granules and the reduction of distance between the granules.

2) The adhesive force from the cementation of chemical compound in granular media is termed as the solidification cohesion. The cementing materials include clay minerals, sulphide minerals, chemical cementing materials and organic compounds, etc. Part of the adhesion will be lost if the initial granular structure is disturbed[19].

Simply, the granular shear strength is a combination of the following strength components:

$$\begin{aligned}\tau&=C+\sigma\tan\varphi=C+F=C_1+C_2+F_1+F_2\\&=C_1+C_{21}+C_{22}+F_{11}+F_{12}+F_{13}+F_2\end{aligned} \tag{4.6}$$

where F is the internal friction; F_1 is the mechanical resistance; F_2 is the adsorption of molecules; C_{21} is the initial cohesion; C_{22} is the solidification cohesion; F_{11} is macro biting-force; F_{12} is micro biting-force; F_{13} is the component of extrusion and re-arrangement. Other symbols have been already described.

In fact, the composition of shear strength is complicated; it is also difficult to separate the components from each other. Granular media differ in composition and proportion for each composition in various conditions. For example F_{13} can be taken as zero under low stress; in dry granules of granular media C_{12} can be taken as zero. Eq. (4.6), which is supported by the Coulomb's Law, is the common formula of shear strength. However, Coulomb's Law has not given very explicit explanations, and only can be applied within limited pressure. Some researchers have stated that shear strength appears to have nonlinear relationships in the initial stage of low pressure and in the stage of high pressure. Hence, Coulomb's Law has its limitations in treating granular media[1,13]. However the basic formula of Coulomb's Law is still widely applied in theoretical researches and in engineering practices as it can meet the precision demands in solving common strength problems.

4.2 Various Characteristics of Granular Dynamic Shear Strength

Properties of dynamic shear strength of granular media are very complicated. They are related to such elements as the stress and strain situations, the history of stress action, the size distribution of granules, the properties of surface, the density, the moisture content, the pore pressure, the loading velocity, the temperature and the characteristics of load, etc[77~94]. They may interact with each other sometimes. Their formats of quantitative functions are difficult to determine, but with the development of theories and measuring methods, some aspects of inferences have been preliminarily delineated, and a few important breakthroughs have been made. This section will discuss several main elements of influence on shear strength.

4.2.1 *Influence of types, shapes and size distributions of mineral granules*

The individual components of granular minerals affect shear strength greatly. As soft granules can be smashed into pieces under even low stress, its internal friction is low under certain pressure. The shear strength of clay minerals of granular media is higher than that of minerals exclude clay. More granules are embedded deeply into each other's concave surfaces that make the internal friction larger because of their irregular shapes of granules and their rough surfaces. The strength index of shapes of irregular granules is better than that of spherical shapes. The contact areas among granules and the biting-force become relatively larger after enlarging the sizes of granules. This simultaneously causes the mechanical frictional resistance to rise and to increase the coefficient of internal friction. The size of the granules has no significant influence on the shear strength, and small granules have larger area and more contact points. Though single point has little biting-force, the total biting-force is still remarkable because of the adsorption of molecules and the cohesive force can generate a part of the biting-force. So the total shear strength does not change. The samples with nonuniform size distribution (i.e. raw ore) have bigger internal angle of friction than samples with uniform size distribution (i. e. graded ore). This is due to the particles of different grades mesh and their combining with each other to increase the total contact points and contact area. This in turn makes the mechanical resistance and adsorption properties of the molecules larger, creating a relatively high internal friction.

4.2.2 *Influence of the porosity ratio or the density*

The magnitude of porosity ratio directly influences the granular shear strength. The decrease of porosity ratio will lead to the compaction of granular media. The "ineffective" granules which originally situated in the relatively large space with no stress on its sides will turn into "effective" granules if be pressed by other particles under higher density condition. C_1, C_2, F_1, F_2 will improve while the biting points and the embedded depth increase, at the same time the compactness of granules become larger. When the porosity ratio increases C_1, C_2, F_1, F_2 will quickly decrease with the enhancement of distance between the granules, because the attraction of molecules are in inverse proportion to the cube of distance between granules. F_2 will partly decrease with the drop of embedding rate; moreover, the sliding frictional motion in compact situations will become joint motion of sliding and rolling friction of granular media. In bulk and soft medium, the rolling friction is less than the sliding friction. The shear strength will rapidly drop in composite action of several aspects of elements. In the long run, porosity ratio is a sensitive and comprehensive factor. In practice, this principle is used for allowing the broken ores to gradually loose and discharging a part of broken ores, which have kept up for a long time in ore passes or ore-bins.

4.2.3 *Influence of moisture content*

The variation of granular strength is related to moisture content. The shear strength is relatively high when moisture content ω_c is zero. The shear strength decreases inversely when ω_c increases a little, the minimum trough point of the strength curve will appear. After this point the shear strength increases with the increase of ω_c , until the peak appears, then the curve drops abruptly, accompanying with the appearance of vibration liquefaction. When ω_c is equal to zero, the cohesion C_2 tends to zero. Thus the shear strength mainly comprises mechanical resistance F_1 of internal friction, the attraction of molecules F_2 and the initial resistance of internal cohesion C_1. If ω_c increases a little, a coat of water film will cover surfaces of the granules, and lubricate the granules causing the drop of internal friction F, when the trough point of the shear strength appears. If ω_c increases further, F will drop further, and tend to become extreme under the lubrication action; then it seems to become constant. But C_2 will rise and reach to its maximum point; simultaneously the shear strength reaches its maximum value. If ω_c increases a little more, the attraction among molecules will decrease, and then it will disappear. Due to C_2 decreasing, the shear strength will also drop. When ω_c increases nearly to its saturation, F and C will transmit into pore water and disappear under vibration action. At the same time, the vibrating liquefaction will occur, and the shear strength will approach zero.

Dry unit weight γ_d has the same performance as the shear strength C. Some researchers have made experiments with sandy soil and coal under static situation. The results shown in Fig. 4.2 demonstrate validity of this experiment and its theoretical analysis. It can be said that, when ω_c of granular media is below 4%, it possesses good fluidity; if ω_c is between 8% and 12%, it has the worst fluidity and is easy to agglomerate, and may cause blockage in the ore pass, which should be avoided as much as possible. By increasing ω_c more, the vibrating liquefaction can remove the blockage.

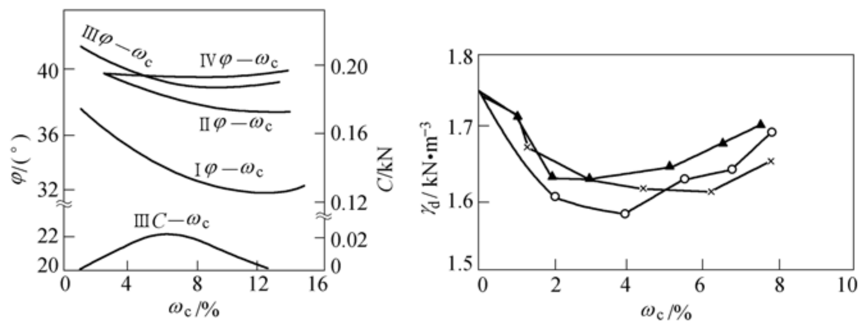

Fig. 4.2 Relationships between ω_c and γ_d, between C and φ

4.2.4 *Influence of vibrating velocity on shear strength*

The vibrating velocity of shear box is $v=2\pi HfA_{11}$. It comprehensively reflects the influence of input amplitude of vibration A_{11} and the frequency f, which indicates the amount of energy of the shear box and the granular media. The vertical amplitude of vibration A_{12} is very small since the horizontal amplitude of vibration is below 0.5 mm. The input motion and the relative motion under the conditions of certain granular characteristics have the relationship of direct proportion quantities according to the analysis carried out on model. Moreover, the input amplitude of vibration is easier to measure than the relative amplitude of vibration. For the sake of simplicity, only the horizontal motion is taken into consideration from the input parameters of motion. Fig. 4.3 states the typical experimental results related to the relationships between the vibrating velocity and the shear strength.

Fig. 4.3a corresponds to whole box vibration, which shows that τ clearly decreases with the increase of input vibrating velocity, and the trend of smooth decrement of the curve. Fig. 4.3b corresponds to the vibration of upper box, which shows the same trend of decrement as in Fig. 4.3a. At that time the input amplitude of vibration is equal to the relative amplitude of vibration and the existence of extreme value has been indicated, both curves are being the same in nature. Through the regression analysis of eight kinds of curves, their optimum function formula is given below:

$$\tau = a\exp(-bv) \tag{4.7}$$

where a and b are the regression constants.

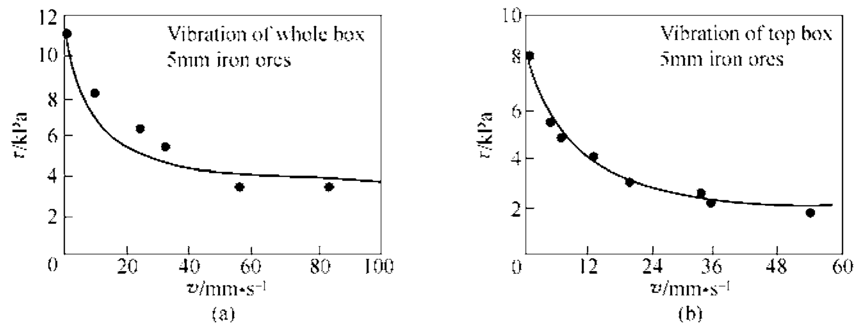

Fig. 4.3 Relationships between the vibrating velocity v and the shear strength τ

The consistent behaviors of the experimental results can be seen by analyzing Fig. 4.4, where τ_j is corresponding to the static shear strength at the circumstances of v=0; τ_c is the extreme shear force, which proves the effect of vibration action on the decrease of shear strength. It can be concluded by the following pertinent formula:

$$\tau = \tau_c + a\exp(-2\pi b A_{11} f) \tag{4.8}$$

where $f=\omega/2$, Hz; a and b are constants, which are determined by the degree of compactness and by the direct stress to a certain given granules respectively. When f is equal to zero (or $A_{11}=0$), the static shear strength is:

$$\tau_j = \tau_c + a \tag{4.9}$$

If expressed by the ratio of dynamic and static shear stress, the relationship is:

$$\frac{\tau}{\tau_j} = 1 - \frac{a}{\tau_j}(1 - \exp(-2\pi b A_{11} f)) \tag{4.10}$$

The constant a represents the initial decreasing value of the dynamic shear stress, determined probably by the maximum decreasing range of dynamic shear stress, b can be comprehended as a constant of vibrating velocity, and its amount determines the decreasing velocity of the shear force.

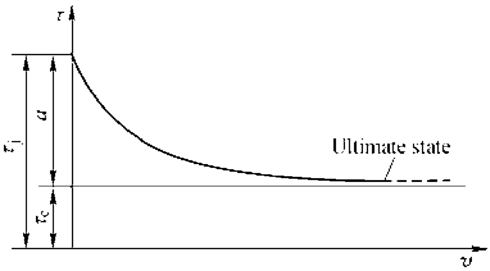

Fig. 4.4 Variety regularity of shear strength

4.3 Granular Dynamic Yield Criterion and Relation of Dynamic Stress-strain

4.3.1 *Granular dynamic yield criterion*

Numerous engineering practices and theoretical researches have indicated that the properties of granular media will change under the vibration action. The mechanism of shear strength reduction in the vibration field includes:

(1) The static friction is changed into dynamic friction while the dynamic coefficient of friction is below the static one.

(2) The cohesion decreases under vibration action; the relative motion between two vibrated granules will make the initial embedded degree reduce, so that the initial obstruction resistances should be very small. In addition, the initial cohesion C_{21} from the mutual action of water molecules and the solidification cohesion C_{22} from granules' gluing intimately relate to the duration of contact, the distance between the granules and the granular structure. Vibration action shortens the duration of contact, and also enlarges the distance between the granules; furthermore, vibration can affect or destroy the stability of the granular initial structure, so that C_{21} and C_{22} will not exist. A number of experiments have demonstrated that dynamic cohesion is about half of static cohesion or even less.

(3) Vibration action is feasible to reduce the frictional force for the upper box shear because vibration shortens the interlocked duration of macro and micro biting actions between neighboring granules or between granules and the side walls (i. e. the steel plate). That can reduce the area of contacting surfaces to the greatest extent.

(4) Vibration input leads to the increase of porosity ratio on the shear face for the whole box vibration since vibration input produces the relative motion of granules near the face, which brings up the "effects of shear-expansion" in the sample. The increase of porosity ratio will cause the all-round decrease of every

component of shear strength.

For the sake of simplification in analysis, every mechanism of dynamic shear strength decrease can be considered as equivalent to the increase of porosity ratio. That is to say that only the increase of porosity ratio can provide the same effect. Then it can be analyzed by the yield concept that was put forward by Hvorslev, and improved by Roscoe, etc. Hvorslev and others have pointed out that the shear strength under the yield is the function of effective direct stress and the porosity ratio (or density) on yield surfaces when they studied the static characteristics of clay. They connected the shear strength τ, the direct stress σ, the porosity ratio e to form a cubic space in the course of spoiling of sample; they also produced Hvorslev yield face as shown in Fig. 4.5. A random point under the yield face does not mean that the sample has yielded. The sample starts to yield when the stress reaches the random point on the yield face. The critical porosity ratio curve defines the boundary of Hvorslev yield face. The critical porosity ratio represents the extreme situation in the sample as beyond that the increase of shear deformation will not cause further variation of porosity ratio. CVR curve is the only curve which makes all loading orbit gathered in the e-σ-τ space.

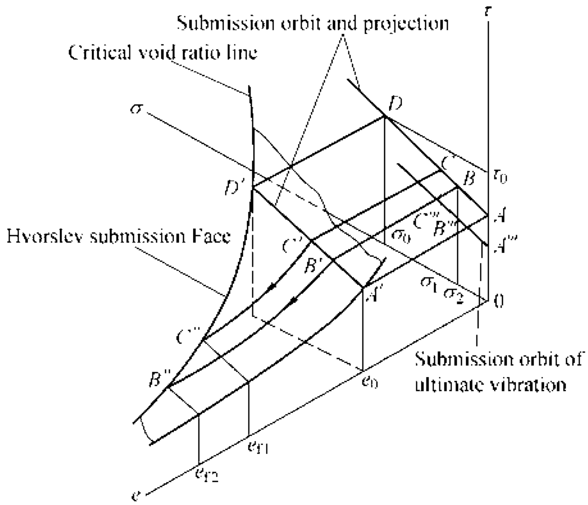

Fig. 4.5 Hvorslev yield face and the dynamic character of sample

The Hvorslev yield face can also be applied to dynamic environment because equivalent effect of vibration comprehensively leads to the increase of porosity ratio. As Fig. 4.5 has stated, the sample in the shear box has been solidified, and its principal stress is σ_0, while shear stress is τ_0 and corresponding porosity ratio is e_0. D_1 denotes this sample's situation. Under static conditions, when the direct stress ranges from σ_1 to σ_2, which are corresponding to C_1 and B_1 points on the yield face, the projections of B_1 C_1 D_1 to σ-τ face produce yield orbit of the material under certain solidification conditions. The porosity ratio of the sample on the shear face will increase and its situation will vary along line C_1C_2 if vibrated during the course of loading direct stress σ_1. The direct stress σ_2 has also the same regularity, which will vary along line B_1B_2. Given a certain direct stress, void ratio will increase until its extreme value is reached with the exertion of mechanical vibration. e_{f1} and e_{f2} express the extreme porosity ratio under σ_1 and σ_2 action respectively, which determines the two points of extreme vibration yield orbit. This determines the possible extreme value of shear stress decrement. It also states that the continuous increase of vibration intensity cannot result in the corresponding decrease of shear strength.

Yield can be obtained at a random face of Hvorslev Face fixed by static conditions and critical porosity ratio under the dynamic load action. As an example, the yield orbit exists between line BC and line B_3C_3 on σ-τ face. To a given granular media, the corresponding locations of yield situation on the yield surface are determined by vibration velocity (including amplitude and frequency), the direct stress loading, etc.

4.3.2 *Granular dynamic stress-strain relations*

In analysis of the dynamic response of granular structure, the relationship between dynamic stress-strain and the corresponding dynamic modulus and damp under the dynamic load must be known. Under the action of dynamic load the granular media show various dynamic stress-strain relationships if the strain amplitude is different. If the amplitude increases, the stress-strain demonstrates the following three states in turn, elastic, hysteretic elastic and non-linear relationships[67~74].

4.3.2.1 Elastic dynamic stress-strain relation

In theory the pure elastic dynamic stress-strain relation is that the stress and strain always change proportionally and synchronously under the dynamic load, namely, in the course of loading the strain can occur in time and in the course of discharge the strain could restore in time. Therefore, if the dynamic stress σ_d is equal to zero the strain is also equal to zero, if the dynamic stress reaches the peak value σ_{d0}, the stress is also reaches the peak value ε_{d0} without phasic difference. To draw the relationship of one stress-strain circle in the coordinate system of σ_d-ε_d , a beeline is obtained(as shown in Fig. 4.6). Fig. 4.6 shows that the elastic stress-strain varies along the beeline, and the slope of this line, E_d, is the granular dynamic elastic modulus,then

$$E_d = \frac{\sigma_{d0}}{\varepsilon_{d0}} \tag{4.11}$$

The relational expression of dynamic stress-strain is:

$$\left.\begin{aligned}\sigma_{\mathrm{d}} &= \sigma_{\mathrm{d}0}\sin\omega t\\ \varepsilon_{\mathrm{d}} &= \varepsilon_{\mathrm{d}0}\sin\omega t\end{aligned}\right\}\tag{4.12}$$

where ω is the angular frequency of cyclic stress.

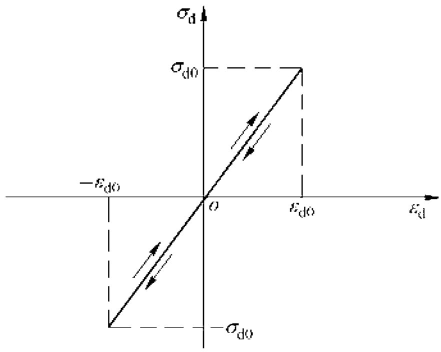

Fig. 4.6 Elastic dynamic stress-strain relation

4.3.2.2 Hysteretic elastic stress-strain relation

Most granular media are triphasic (solid, liquid and gas), and show the viscous damping characteristic under the dynamic loading action. This granular medium is also termed as a viscoelastic body or hysteretic elastic body. In general, under the dynamic loading action the dynamic strain lags behind the dynamic stress. Namely, the momentary dynamic stress and strain have a phenomenon of constant phase lag. By taking a cycle of stress-strain, a figure is drawn in the coordinate system of σ_{d}-ε_{d} , so a curve of stress-strain in this cycle is obtained (shown in Fig. 4.6). This curve shown in Fig. 4.7b is a closed curve like an approximate ellipse, and it is termed as the hysteresis loop. The characteristic of this relationship of dynamic stress-strain is that: when the cyclic stress reaches the amplitude $\sigma_{\mathrm{d}0}$, the cyclic strain is still less than the amplitude $\varepsilon_{\mathrm{d}0}$. Once the strain reaches to the amplitude $\varepsilon_{\mathrm{d}0}$, the cyclic stress is less than $\sigma_{\mathrm{d}0}$. If the cyclic stress is equal to zero, the cyclic strain is not and vice versa. The relationship between dynamic stress-strain can be expressed as:

$$\left.\begin{aligned}\sigma_{\mathrm{d}} &= \sigma_{\mathrm{d}0}\sin\omega t\\ \varepsilon_{\mathrm{d}} &= \varepsilon_{\mathrm{d}0}\sin(\omega t-\delta)\end{aligned}\right\}\tag{4.13}$$

where δ is the phase angle of stress lag.

The parameters of ideal elastic hysteresis, such as E and E' (E is the elastic modulus; E' is the loss modulus) do not change with the amplitude of stress. While the amplitude of stress is stable, the shape and size of hysteresis loop do not change with the increment of vibration number. When the amplitude of stress changes, the hysteresis loop will similarly zoom out or zoom in without shape change. The hysteresis hoop drawn by Eq. (4.13) is an ellipse, and when the amplitude of

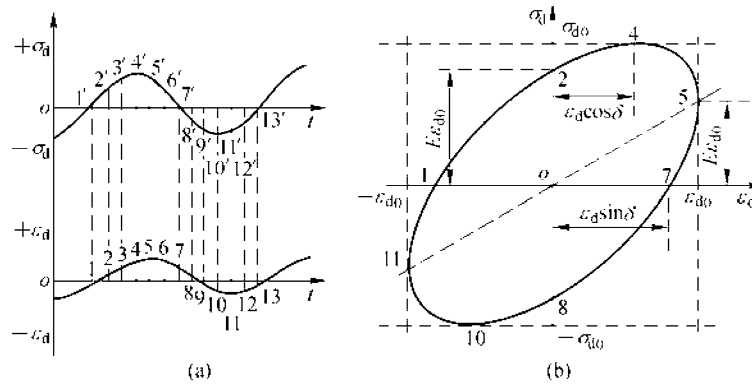

Fig. 4.7 Dynamic stress-strain of elastic hysteresis

strain changes the eccentricity will be constant. Moreover, the point of amplitude of strain will move up and down along a line through the origin. The slope of this line is the granular elastic modulus E (shown in Fig. 4.7 by a dotted line).

The experimental results show the granular medium is approximately a viscoelastic body, if the magnitude of strain is not very high (less than 10^{-4}). We can utilize the slope of the two top ends of the hysteresis loop to substitute the average dynamic modulus E_d. The area of hysteresis loop indicates that the energy dissipation in the unit granular volume when the stress-strain cycles a round, and reflects the magnitude of the granular viscous damp. Assuming that the dissipation energy is ΔW in a stress-strain cycle, then:

$$\Delta W = \int_{-\varepsilon_{d0}}^{\varepsilon_{d0}} \sigma_d(t) \mathrm{d}\varepsilon_d(t) \tag{4.14}$$

4.3.2.3 Non-linear dynamic stress-strain relation

The experimental results show that when the granular amplitude of strain is large (in general, more than 10^{-4}), the granular dynamic stress-strain relationship will not always keep a linear relationship. With the increment of the amplitude of stress, the amplitude of strain increases much more, and the hysteresis loop of stress-strain inclines toward the strain axis correspondingly more and more and becomes wide (shown in Fig. 4.8). The characteristics of hysteresis loop are: 1) The shape of hysteresis loop is changeable with the change of amplitude of strain, and the width of hysteresis loop augments continuously, namely, the granular viscous damp increases with the increment of amplitude of strain, or the phase of strain lags as the stress gradually increases; 2) The connecting line of the top ends of hysteresis loops for the difference amplitudes of stress is a curve termed as the skeletal curve of stress-strain. When the amplitude of stress increases, the slope of the connecting line between the top of hysteresis loop and the origin decreases, namely, the granular dynamic secant modulus gradually decreases.

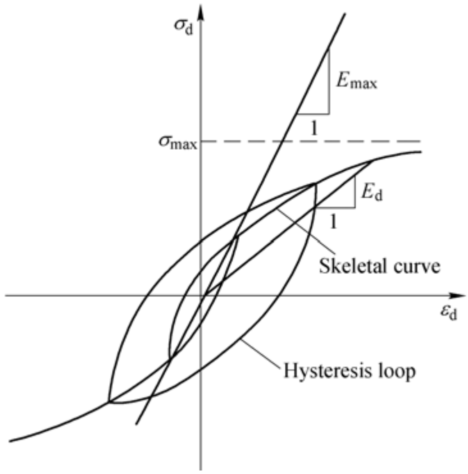

Fig. 4.8 Non-linear relation between dynamic stress-strain

Expressions of the equivalent elastic modulus E_d and the equivalent shear modulus G_d

The equivalent elastic modulus E_d is defined as the slope of the connecting line between the top of hysteresis loop and the origin, namely, it is the secant modulus in the skeletal curve corresponding to the amplitude of stress, which is denoted by $E_d = \dfrac{\sigma_a}{\varepsilon_a}$ in Fig. 4.8.

The equivalent dissipation coefficient η is the ratio of the dissipation energy ΔW in a stress-strain cycle (corresponding to the area of hysteresis loop for strain) and the maximum of storing elastic strain energy W with load:

$$\eta = \frac{1}{2\pi}\frac{\Delta W}{W}$$

A number of experimental data show that the skeletal curve of stress-strain under the cyclic loading action is similar to a hyperbola (as shown in Fig. 4.8), and its expression is:

$$\sigma_d = \frac{\varepsilon_d}{a + b\varepsilon_d} \tag{4.15}$$

where σ_d and ε_d are amplitudes of the cyclic stress and strain respectively, *viz*., the abbreviation of σ_{d0} and ε_{d0}. So that the equivalent elastic modulus E_d becomes

$$E_d = \frac{\sigma_d}{\varepsilon_d} = \frac{1}{a + b\varepsilon_d} \tag{4.16}$$

In aseismatic engineering, the granules of foundation are loaded in the action of shear wave propagating from the bedrock to the earth's surface. Therefore, in dynamic analysis the dynamic shear stress τ_d and the dynamic shear strain γ_d can be computed directly, and the equivalent shear modulus G_d is:

$$G_d = \frac{\tau_d}{\gamma_d} = \frac{1}{a + b\gamma_d} \tag{4.17}$$

A number of experiments show that σ_d-ε_d and τ_d-γ_d have the same changing regularity, and

$$G_d = \frac{E_d}{1+\mu} \tag{4.18}$$

The above maximum dynamic shear modulus G_{max} must be measured under the condition of very small shear strain, but that will not be accurate enough. So the following empirical formulae are often used to solve this problem:

For clay soils:

$$G_{max} = 3230\frac{(2.97-e)^2}{1+e}(OCR)^k(\sigma_0')^{0.5} \tag{4.19}$$

For pure angular sands:

$$G_{max} = 3230\frac{(2.97-e)^2}{1+e}(\sigma_0')^{0.5} \tag{4.20}$$

For pure round sands(e<0.8):

$$G_{max} = 6930\frac{(2.17-e)^2}{1+e}(\sigma_0')^{0.5} \tag{4.21}$$

where e is the granular porosity ratio; σ_0' is the average effective principal stress, kPa; OCR is the granular over-consolidation ratio; k is a constant related with the plastic index of viscous granular media I_p, it is shown in Table 4.1.

Table 4.1 Value of constant k

Plastic index I_p	0	20	40	60	80	≥100
k	0	0.18	0.30	0.41	0.48	0.50

Expression of the equivalent damping ratio λ (γ_d)

In dynamic analysis the granular damp is often denoted by the equivalent λ (γ_d), which substitutes for the equivalent dissipation coefficient η. The damping ratio λ is the ratio of the real damping coefficient c and the critical damping coefficient c_{cr}. The relation between dissipation coefficient η and λ is:

$$\lambda = \frac{\eta}{2} = \frac{1}{4\pi}\frac{\Delta W}{W} \tag{4.22}$$

The experimental results verify the relationship between the granular damping ratio and the dynamic strain and that could be expressed as

$$\lambda = \lambda_{max}\frac{\gamma_d/\gamma_j}{1+\gamma_d/\gamma_j} \tag{4.23}$$

where λ_{max} is the damping ratio while $\gamma_d \to \infty$, *viz*., the maximum damping ratio.

4.4 Excited Response of Granular Ores under Vibrating Field

In many fields of granules, vibrating equipment has been used to some extent[1~4]. Especially, the vibrating ore-drawing technology has been widely applied in various stopes, ore passes, ore bins and bunkers. According to the statistics[1,5], in China there are more than 5,000 various vibrating machines, and the technology is still being improved and expanded continuously. Although lots of technological studies and in-situ experiments have been done to consummate the vibrating ore-drawing technology[5, 61~65], more work need to be done on the vibrating ore-drawing mechanism and its theories. This section will discuss the granule's excited response with the dynamic theories[29~31, 96~98].

4.4.1 *Brief introduction to the excitation system*

There are many kinds of vibrating exciters, one of which is the double-axe exciter[5]. Its mechanical model is shown in Fig. 4.9. On its two parallel axes there is an eccentric body, whose eccentric mass is m_0 and eccentric distance is e. The two axes rotate in synchronism and opposite directions motivated by two identical gears. When the initial center of mass in the two eccentric bodies lies in the same side of the axes line and the force is perpendicular to the axes line, the exciting force which changes along with time in terms of the cosine law will be generated. Its expression is:

$$p(t)=2m_0e\omega^2\cos\omega t=p\cos\omega t \tag{4.24}$$

where $p=2m_0e\omega^2$ is the amplitude of exciting force; ω is the radian frequency; t is the time.

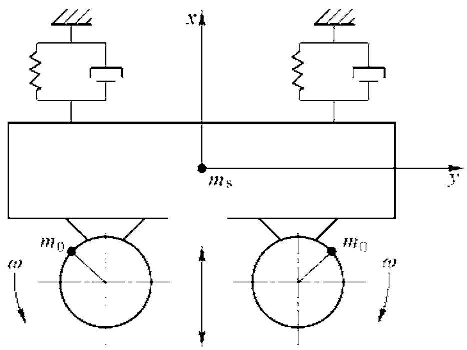

Fig. 4.9 Mechanical model of exciter with double axes

4.4.2 *Mechanical model of excited response of granular ores*

While being excited, granular ores will be vibrated with damping. If the excitation ends, the vibration will finally stop because of the energy dissipation[5~8]. There is viscosity among granular ores due to water content and other factors. Hence a viscous damping mechanical model can be created which is shown in Fig. 4.10. Because the exciting force $p(t)$ of the exciter with double axes is a harmonic exciting force, the excited kinetic equation of granular ores is:

$$\boldsymbol{m}\ddot{\boldsymbol{u}} + \boldsymbol{c}\dot{\boldsymbol{u}} + \boldsymbol{k}\boldsymbol{u} = \boldsymbol{p}(t) \tag{4.25}$$

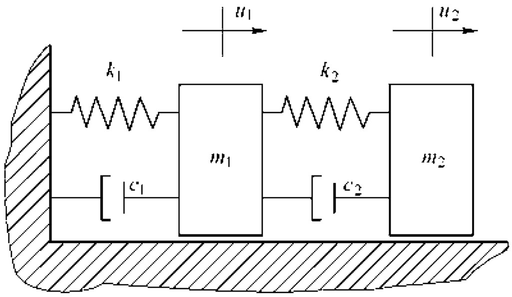

Fig. 4.10 Viscous damping mechanical model of granular ores
m_1, m_2—Granular masses; k_1, k_2—Elastic elements;
c_1, c_2—Viscous elements; u_1, u_2—Displacements

where $\boldsymbol{m}$ is the mass matrix; $\boldsymbol{c}$ is the damping matrix; $\boldsymbol{k}$ is the vector of stiffness; $\boldsymbol{p}(t)$ is the vector of exciting force; $\boldsymbol{u}$ is the vector of displacement.

In addition, when t=0 the initial vector of displacement and velocity are:

$$\left.\begin{aligned} \boldsymbol{u}_{t=0} &= \boldsymbol{u}_0 \\ \dot{\boldsymbol{u}}_{t=0} &= \dot{\boldsymbol{u}}_0 \end{aligned}\right\} \tag{4.26}$$

In order to obtain the dynamic response, Eq. (4.25) should be solved under the initial conditions of Eq. (4.26); and the vectors of displacement, velocity and acceleration must be determined first. The three coefficients of matrix $\boldsymbol{m}$, $\boldsymbol{c}$ and $\boldsymbol{k}$ of Eq. (4.25), which is a kinetic coupled equation set, probably have nonzero coupling terms. The coupled equation set could be changed into the non-coupled equation set through the normal modal method. The kinetic equation of its main coordinate is:

$$\boldsymbol{M}\ddot{\boldsymbol{U}} + \boldsymbol{C}\dot{\boldsymbol{U}} + \boldsymbol{K}\boldsymbol{U} = \boldsymbol{\Phi}^T \boldsymbol{p}(t) = \boldsymbol{P}(t) \tag{4.27}$$

where $\boldsymbol{M}$ is the modal mass matrix; $\boldsymbol{C}$ is the modal damping matrix; $\boldsymbol{K}$ is modal stiffness matrix; $\boldsymbol{\Phi}$ is the modal matrix; $\boldsymbol{P}(t)$ is the modal force matrix; $\boldsymbol{U}$ is the modal displacement matrix.

4.4.3 *Excited response of granular ores*

Eq. (4.27) is the kinetic equation of viscous damping mode of granular ores, so the modal damping matrix $\boldsymbol{C}$ can be assumed as

$$\varphi_r^T \boldsymbol{C} \varphi_s = 0, r \neq s \tag{4.28}$$

where φ_r is the mode of r; φ_s is the mode $\boldsymbol{s}$. Eq. (4.27) will be changed into the non-coupled equation through the modal coordinates, so it becomes non-coupled modal equation set,

$$\ddot{\boldsymbol{U}}_r + 2\xi_r \omega_r \dot{\boldsymbol{U}}_r + \omega^2 \boldsymbol{U}_r = \frac{1}{\boldsymbol{M}_r} \boldsymbol{P}_r(t) \quad r = 1, 2, \cdots, N \tag{4.29}$$

where ξ_r is the modal damping factor; ω_r is the natural radian frequency. Then the solution of the Eq. (4.27) is:

$$\boldsymbol{U}_r(t) = \left(\frac{1}{\boldsymbol{M}_r \omega_{\mathrm{d}r}}\right) \int_0^t \boldsymbol{P}_r(\tau) \mathrm{e}^{-\xi_r \omega_r (t-\tau)} \sin \omega_{\mathrm{d}r}(t-\tau) \mathrm{d}\tau + \boldsymbol{U}_r(0) \mathrm{e}^{-\xi_r \omega_r t} \cos \omega_{\mathrm{d}r} t + \left(\frac{1}{\omega_{\mathrm{d}r}}\right) [\dot{\boldsymbol{U}}_r(0) + \xi_r \omega_r \boldsymbol{U}_r(0)] \mathrm{e}^{-\xi_r \omega_r t} \sin \omega_{\mathrm{d}r} t \quad 0 \leqslant \tau \leqslant t \tag{4.30}$$

where
$$\omega_{\mathrm{d}r} = \omega_r \sqrt{1 - \xi_r^2} \tag{4.31}$$

Utilizing the Wilson mode-acceleration method, from Eq. (4.25) the approximate expression of vibration displacement $\boldsymbol{u}(t)$ is given by:

$$\tilde{\boldsymbol{u}}(t) = \frac{\boldsymbol{p}(t)}{\boldsymbol{k}} - \frac{\boldsymbol{c}}{\boldsymbol{k}} \sum_{r=1}^{n} \varphi_r \dot{\boldsymbol{U}}_r(t) - \frac{\boldsymbol{m}}{\boldsymbol{k}} \sum_{r=1}^{n} \frac{1}{\omega_r^2} \varphi_r \ddot{\boldsymbol{U}}_r(t) \quad n \leqslant N \tag{4.32}$$

where N is the number of equations; n is the approximate number of equations whose mode has been cut off.

The system of viscous damping granular ores is excited by the harmonic exciting force $p(t) = p\cos\omega t$ of the exciter with double axes. Therefore, Eq. (4.27) becomes:

$$\ddot{\boldsymbol{U}}_r + 2\xi_r \omega_r \dot{\boldsymbol{U}}_r + \omega_r^2 \boldsymbol{U}_r = \frac{1}{\boldsymbol{M}_r} \boldsymbol{p}_r \cos \omega t \tag{4.33}$$

For single-degree-of-freedom system,the complex frequency response of Eq. (4.31) is:

$$\ddot{\bar{U}}_r + 2\xi_r \omega_r \dot{\bar{U}}_r + \omega_r^2 \bar{U}_r = \omega_r^2 \frac{p_r}{K_r} \mathrm{e}^{i\omega t} \tag{4.34}$$

and the steady solution of response is:

$$\bar{U}_r = \frac{\boldsymbol{p}_r / \boldsymbol{K}_r}{\sqrt{(1 - r_r^2)^2 + 4\xi_r^2 r_r^2}} \cos(\omega t - \alpha_r) \tag{4.35}$$

where

$$\tan \alpha_r = \frac{2\xi_r r}{1 - r_r^2} \tag{4.36}$$

The complex frequency response of physical coordinate $\boldsymbol{u}$ is:

$$\bar{\boldsymbol{u}}(t) = \sum_{r=1}^{N} \frac{\varphi_r \varphi_r^T \boldsymbol{p}}{K_r} \left[\frac{1}{1 - r_r^2} + i(2\xi_r r_r)\right] \mathrm{e}^{i\omega t} \tag{4.37}$$

From the complex frequency response of physical coordinate $\boldsymbol{u}$, the steady solution of displacement response $\boldsymbol{u}(t)$ of granular ores under the harmonic exciting force is given by

$$\boldsymbol{u}(t) = \sum_{r=1}^{N} \frac{\varphi_r \varphi_r^T \boldsymbol{p}}{K_r} \left[\frac{1}{\sqrt{(1 - r_r^2)^2 + i(2\xi_r r_r)}}\right] \cos(\omega t - \alpha_r) \tag{4.38}$$

4.4.4 *Step-by-step integration method of granular excited response*

4.4.4.1 Computational formulae

From Eq. (4.27), the acceleration at time t_i and the excited kinetic equation at time $t_i + \Delta t_i$ are given:

$$\ddot{\boldsymbol{U}}_i = \frac{1}{\boldsymbol{M}}(\boldsymbol{P}_i - \boldsymbol{C}\dot{\boldsymbol{U}}_i - \boldsymbol{K}\boldsymbol{U}_i) \tag{4.39}$$

$$\boldsymbol{M}\ddot{\boldsymbol{U}}_{i+1} + \boldsymbol{C}\dot{\boldsymbol{U}}_{i+1} + \boldsymbol{K}\boldsymbol{U}_{i+1} = \boldsymbol{P}_{i+1} \tag{4.40}$$

From time t_i to time $t_i + \Delta t_i$, the mean value of acceleration is:

$$\ddot{U}(\tau) = \frac{1}{2}(\ddot{U}_i + \ddot{U}_{i+1}) \tag{4.41}$$

Integrating the above formula twice gives:

$$\dot{U}_{i+1} = \dot{U}_i + \frac{\Delta t_i}{2}(\ddot{U}_i + \ddot{U}_{i+1}) \tag{4.42}$$

$$U_{i+1} = U_i + \Delta t_i \dot{U}_i + \frac{\Delta t_i^2}{4}(\ddot{U}_i + \ddot{U}_{i+1}) \tag{4.43}$$

The matrix that expresses the Eq. (4.40), Eq. (4.42) and Eq. (4.43) is:

$$\begin{bmatrix} \boldsymbol{K} & \boldsymbol{C} & \boldsymbol{M} \\ 0 & 1 & -\Delta t_i/2 \\ 1 & 0 & -\Delta t_i^2/4 \end{bmatrix} \begin{Bmatrix} \boldsymbol{U}_{i+1} \\ \dot{\boldsymbol{U}}_{i+1} \\ \ddot{\boldsymbol{U}}_{i+1} \end{Bmatrix} = \begin{bmatrix} 0 & 0 & 0 \\ 0 & 1 & \Delta t_i/2 \\ 1 & \Delta t_i & \Delta t_i^2/4 \end{bmatrix} \begin{Bmatrix} \boldsymbol{U}_i \\ \dot{\boldsymbol{U}}_i \\ \ddot{\boldsymbol{U}}_i \end{Bmatrix} + \begin{Bmatrix} \boldsymbol{P}_{i+1} \\ 0 \\ 0 \end{Bmatrix} \tag{4.44}$$

And then the following recursion relation is given:

$$\begin{Bmatrix} \boldsymbol{U}_{i+1} \\ \dot{\boldsymbol{U}}_{i+1} \\ \ddot{\boldsymbol{U}}_{i+1} \end{Bmatrix} = \frac{1}{1+\frac{\eta}{2}+\frac{\xi}{4}} \begin{bmatrix} (1+\eta/2) & \Delta t_i(1+\eta/2) & \Delta t_i^2/4 \\ -\xi/2\Delta t_i & (1-\xi/4) & \Delta t_i/2 \\ -\xi/4t_i^2 & -(\xi+\eta)/\Delta t_i & -(\eta/2+\xi/4) \end{bmatrix} \begin{Bmatrix} \boldsymbol{U}_i \\ \dot{\boldsymbol{U}}_i \\ \ddot{\boldsymbol{U}}_i \end{Bmatrix} +$$
$$\frac{1}{\boldsymbol{M}+\frac{\boldsymbol{C}\Delta t_i}{2}+\frac{\boldsymbol{K}\Delta t_i^2}{4}} \begin{bmatrix} \Delta t_i^2/4 & -C\Delta t_i/4 & (\boldsymbol{M}+C\Delta t_i/2) \\ \Delta t_i/2 & (\boldsymbol{M}+\boldsymbol{K}\Delta t_i^2/4) & -\boldsymbol{K}\Delta t_i/2 \\ 1 & -\boldsymbol{C} & \boldsymbol{K} \end{bmatrix} \begin{Bmatrix} \boldsymbol{P}_{i+1} \\ 0 \\ 0 \end{Bmatrix} \tag{4.45}$$

where

$$\left.\begin{aligned} \xi &= \frac{\boldsymbol{K}\Delta t_i^2}{\boldsymbol{M}} \\ \eta &= \frac{\boldsymbol{C}\Delta t_i}{\boldsymbol{M}} \end{aligned}\right\} \tag{4.46}$$

Fig. 4.11 is the computational flow chart of the above step-by-step integration method.

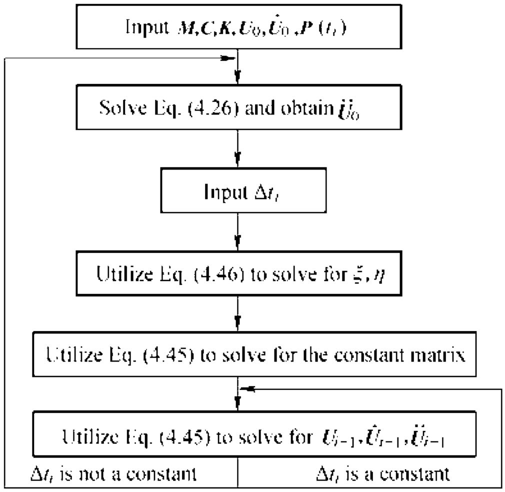

Fig. 4.11 Computational flow chart of the step-by-step integration method

4.4.4.2 Computational example

Problem: Utilize the step by step integration method to solve the undamped free vibration response given by: K=M=2, C=0, $P(t)$=0, initial conditions: $U(0)=1$, $\dot{U}_0 = 0$.

Choose the proper step length, and integrate it in the range $0 \leqslant t \leqslant 3.0$ s.

When Δt_i=0.3 s (constant), utilize the step by step integration method and program to compute and the results are shown in Table 4.2. U_t=cos t_i is the accurate solution. From Table 4.2 there is little error between the computational values utilized the step by step integration and the accurate value, hence the computation is successful.

Table 4.2 Results of the computational example

i	t_i	$\ddot{u}_i$	$\dot{u}_i$	u_i	$\cos(t_i)$
0	0.0	−1.00000	0.00000	1.00000	1.00000
1	0.3	−0.95599	−0.29340	−0.95599	0.95533
2	0.6	−0.82720	−0.56078	0.82720	0.82534
3	0.9	−0.62626	−0.77880	0.62626	0.62161
4	1.2	−0.37020	−0.92827	0.37020	0.36236
5	1.5	−0.08155	−0.99603	0.08155	0.07074
6	1.8	0.21427	−0.97612	−0.21427	−0.27720
7	2.1	0.49123	−0.87029	−0.49123	−0.50485
8	2.4	0.72495	−0.68786	−0.72495	−0.73739
9	2.7	0.89486	−0.44489	−0.89486	−0.90407
10	3.0	0.98601	−0.16276	−0.98601	−0.98999

4.5 Granular Dynamic Strength and Cyclic Effect

4.5.1 *Granular dynamic strength*

The granular dynamic strength is the required dynamic stress corresponding to a designated failure strain ε_f in N action circles. Obviously, if the magnitude of the failure strain is variable, the corresponding dynamic strength will also vary, therefore, the dynamic strength relates closely to the failure criterion. Designating the failure strain reasonably is the basis of discussing the dynamic strength. For the experiments of saturated granular media with or without drainage facilities, the failure criterion can denote the developing degree of pore water pressure, and is termed as the pore pressure criterion. In addition, if the deformation begins to be strong in the course of loading action, the failure criterion is termed as the yield failure criterion. If the ultimate equilibrium condition is considered as the failure criterion, it is termed as the equilibrium condition criterion[83~90]. In general, the granular dynamic strength is denoted by the relation of the vibrating number N_f when the granular media reach the above certain criterion and the dynamic stress σ_d, *viz.*, the curve of σ_d-N_f, which is called the curve of granular dynamic stress (shown in Fig. 4.12).

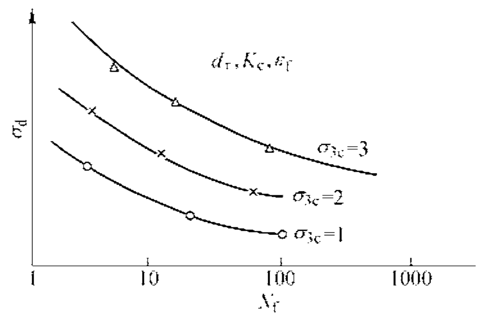

Fig. 4.12 Curve of σ_d-N_f

There are three factors influencing the granular dynamic strength, granular property, static stress state and dynamic stress. So besides the various failure criterions, the granular dynamic strength curve must indicate the initial static stress state (i.e., the initial shear force ratio τ_0/σ_{3c}, the consolidation stress σ_{1c}, σ_{3c} and σ'_v, the ratio of consolidation stress, etc.) and the granular properties (i.e., the density, moisture and structure). The experimental results show that when the ratios of consolidation stress $K_c=\sigma_{1c}/\sigma_{3c}$ are the same, the curve of σ_d-N_f raise with the increment of the average consolidation principal σ_m (or σ_{3c}). However, in

Fig. 4.13 for the same consolidation stress ratio K_c, in spite of the magnitude of σ_{3c}, the experimental points basically fall on the same curve of σ_d/σ_{3c}-N_f. Moreover, the bigger the stress ratio K_c is, namely, the bigger the initial shear force τ_0 is, the higher the curve of dynamic strength is. For the dynamic triaxial test, the dynamic shear curve describe the relation between the N_f and the ratio of τ_d=1/2σ_d on the 45° surface and σ_{3c} (or σ_m). The larger the granularity is, the higher the dynamic strength is; the larger the density is, the higher the dynamic strength is. The dynamic strength changes approximately linear with the relative density D_r (shown in Fig. 4.14).

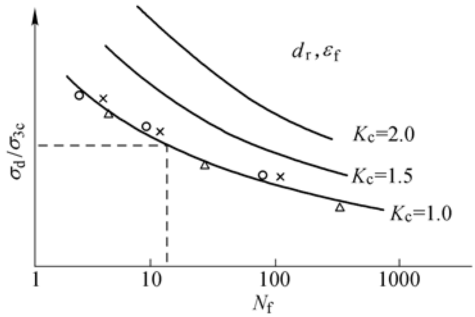

Fig. 4.13 Curve of σ_d/σ_{3c}-N_f

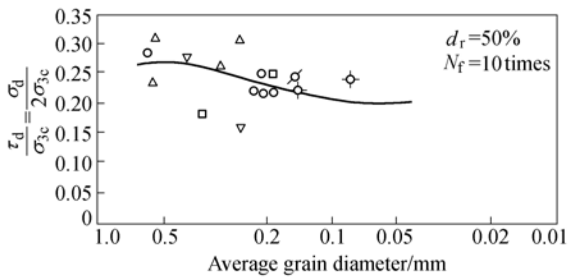

Fig. 4.14 Relation between the dynamic strength and the average grain diameter

According to the above curve of the dynamic strength for the saturated granular medium, the shear index C and φ can be obtained. According to the index of total stress strength, the dynamic strength ratio $(\sigma_d/\sigma_{3c})_N$ can be obtained from Fig. 4.13 at a certain relative density d_r, stress ratio K_c and cycle index of stress N. Then, for a certain σ_{3c}, the corresponding σ_{1c} can be obtained in terms of the value of K_c. Subsequently, σ_d which is corresponding to the σ_{3c} and σ_{1c} is obtained in terms of the value of $(\sigma_d/\sigma_{3c})_N$. According to the sum of σ_d and σ_{1c}, the principal stress for the dynamic failure situation $\sigma_{1d}=\sigma_{1c}+\sigma_d$ and $\sigma_{3d}=\sigma_{3c}$ can be obtained, and a Mohr's circle is drawn. For different σ_{3c}, different Mohr's circles are drawn, and their enveloping curve is then obtained (shown in Fig. 4.15). By the longitudinal intercept and the slope of enveloping curve, two parameters of shear strength under the dynamic action, *viz*., the dynamic cohesion C_d and the coefficient of dynamic internal friction tan φ_d. For different N_f, K_c and d_r, all these parameters can be obtained. For example, for the sands the value of tan φ_d will increase with the increment of K_c or d_r, or the decrease of N_f. Furthermore, in order to obtain the dynamic effective index, also can utilize the curve of p_d/σ_{3c}-σ_d/σ_{3c} (shown in Fig. 4.16) to get the σ_d first and the corresponding p_d will be obtained then. According to $\sigma'_{1d}=\sigma_{1c}+\sigma_d-p_d$ and $\sigma'_{3d}=\sigma_{3c}-p_d$ the Mohr's circles and their enveloping curve are drawn (shown in Fig. 4.17), and the index of granular effective stress strength C'_d and $\tan'\varphi_d$ under the dynamic situation are obtained.

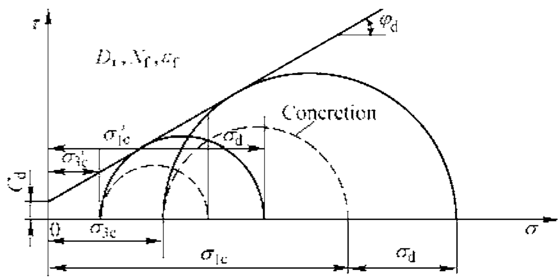

Fig. 4.15 Mohr's circle and enveloping curve

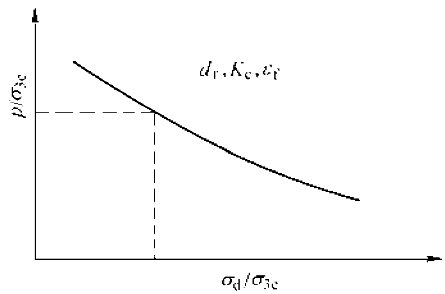

Fig. 4.16 Curve of p_d/σ_{3c}- σ_d/σ_{3c}

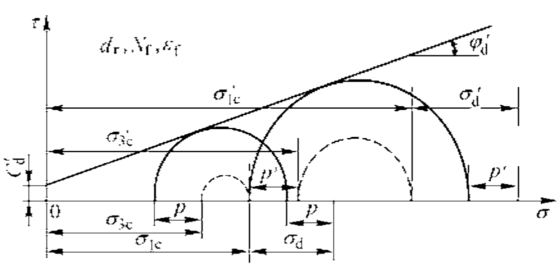

Fig. 4.17 Mohr's circle and enveloping curve

4.5.2 *Cyclic effect*

The granular dynamic strength and cyclic effect under the cyclic loading action can be proved by experiments. Firstly, the sample is consolidated under the uniform confining pressure σ_3, and, the static pressure is exerted gradually up to σ_s ($\sigma_s > \sigma_3$, but less than the static failure strength σ_f) with drainage. Then measure the corresponding strain and exert N times cyclic stress whose amplitude is σ_{d0}^1, and measure the ultimate strain. Repeat the above experiment under the same conditions, and the amplitude of cyclic stress for every experiment is to be increased gradually to σ_{d0}^2 and σ_{d0}^3, consequently, the curve of stress-strain in Fig. 4.18 is obtained. The dynamic stress in the point where the slope of the stress-strain curve changes abruptly is termed as the dynamic strength σ_{df}, which is of the initial static stress σ_s and the loading cycle number N.

If σ_s and other conditions are stable, a series of stress-strain curves (as shown in Fig. 4.19a) can be obtained after changing N. If the initial static stress is the same, the dynamic strength decreases with the increment of vibrating number and becomes close to the static strength or less than. If the initial static stress is variable but N is constant, the stress-strain curve is shown in Fig. 4.19b. Therefore, if the vibrating number is the same, the dynamic strength will decrease with the increment of initial static stress.

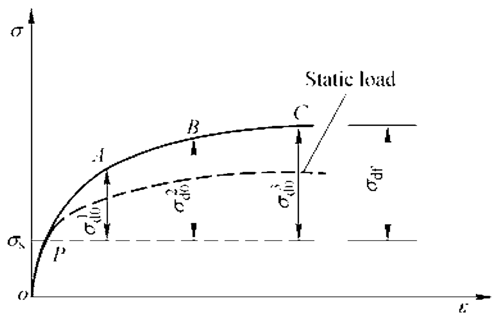

Fig. 4.18 Curve of stress-strain when cycle index is N

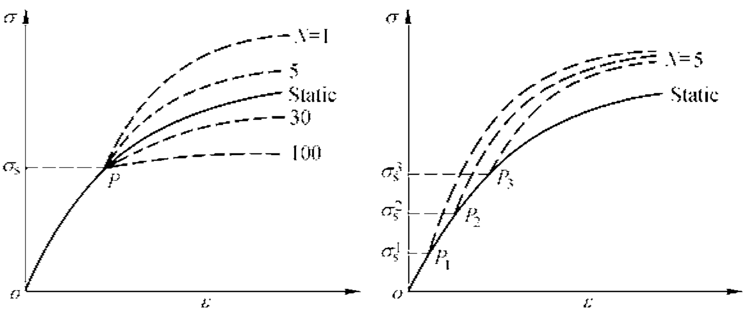

(a) (b)

Fig. 4.19 Curve of stress-strain

(a) When the cycle index N is different;(b) When the initial static stress is different

Fig. 4.20 shows the relationship of two ratios: the ratio of σ_s+ σ_{df} and the static strength σ_f and the ratio of the initial static stress σ_s and the static strength σ_f. In this figure part (a) reflects the experimental results of several compact unsaturated granular media and part (b) shows that of several saturated granular media. Easy to know that:

(1) The granular dynamic strength under the cyclic load is more complex than the static stress, and rests with the cycle index N and the magnitude of the initial static stress.

(2) The granular dynamic strength decreases with the increment of cycle index. Fig. 4.20 shows that when $N\approx100$, $\sigma_s+\sigma_{df}\approx\sigma_f$, and when $N>100$, $\sigma_s+\sigma_{df}<\sigma_f$. The influence of cycle index of dynamic load on the granular strength is termed as the cyclic effect of dynamic load. Fig. 4.20b shows that the cyclic effect of saturated granular media is more remarkable than the unsaturated one. When $N=50$, $\sigma_s+\sigma_{df}$ is approximately equal to σ_f, so for different granular media the cycle indexes are also different. The dynamic effect of cyclic load is: when the cycle index is less, the effect of loading velocity is predominant and $\sigma_s+\sigma_{df}>\sigma_f$; when the cycle index increases, the effect of loading velocity will be gradually balanced out by the cyclic effect. Lastly the cyclic effect is predominant and $\sigma_s+\sigma_{df}<\sigma_f$. When $\sigma_s/\sigma_f= 0.67$, equivalently the safety factor of static design is 1.5, the ratio value of $(\sigma_s+\sigma_{df})/ \sigma_f$ can be obtained at the point of intersection between the line and the corresponding strength curve.

(3) If the sample is subjected by unidirectional shear force under the dynamic loading, the dynamic load only change the magnitude of shear force but not the direction. This kind is called the unidirectional loading experiment. On the other hand, under the dynamic loading action the force not only changes the magnitude, but also the direction, that is called bi-directional loading experiment, which is shown in Fig. 4.20b by the dotted line. For the bidirectional loading experiment, the granular dynamic strength obviously decreases with the reduction of the initial stress ratio, and somewhat lower than that of the unidirectional loading experiment. If the initial stress ratio is zero, the sample is bearing the two-way shear, and the dynamic strength will decrease further.

In Fig. 4.20, when $50<N<100$, $\sigma_s+\sigma_{df}>\sigma_f$, the reason is that the cyclic load is given rapidly, and the granular strength under the quick loading increases obviously with the increment of the load velocity. This situation is called the loading velocity effect. In the Fig. 4.20a, if the period of cyclic load is 1s, the initial static stress $\sigma_s=0$ and the loading time is 0.25 s, the loading velocity effect is about 1.4 times. For the saturated granular media shown in Fig. 4.20b, the loading velocity effect is comparatively stronger and about 1.55 times.

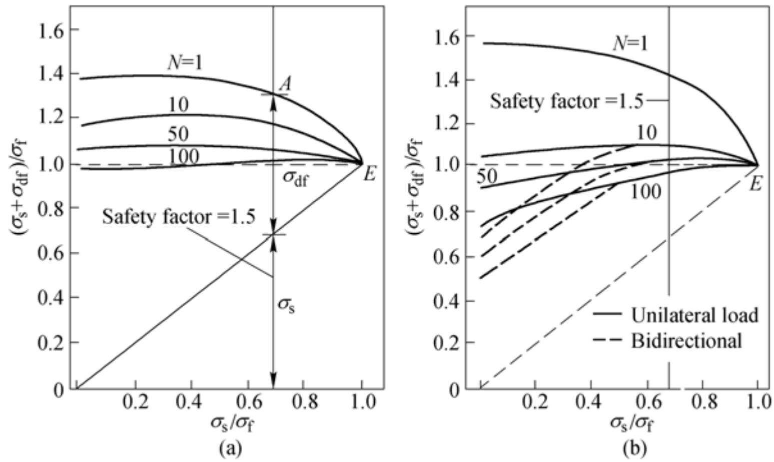

Fig. 4.20 Relation between the dynamic strength and the initial static stress (period of cyclic load is 1s)

(a) For unsaturated granular media;(b) For saturated granular media

4.6 Dynamic Strength of Several Kinds of Granular Media

4.6.1 *Shear strength of dry sands under the cyclic action*

Both Barkan (in 1948) and Mogami (in 1953) reported their experimental results of dry sands conducted by direct shear apparatus on the vibrating table[67,68]. The former used the horizontal vibrating table and obtained the relation curve (shown in Fig. 4.21) of the horizontal acceleration ratio η (a_h/g, where a_h is the horizontal acceleration, g is gravitational acceleration) and the frictional coefficient of dry sands (where the ratio of τ_f and a_v is adopted).

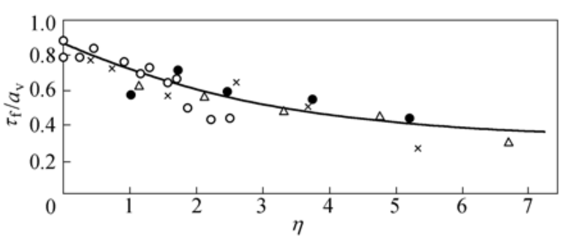

Fig. 4.21 Experimental results for the horizontal vibrating shear by Barkan

Fixing the axial inertia type vibrating triaxial apparatus on the vertical vibrating table, Chang Yaping studied the shear strength of dry sands in 1960 s[68]. The initial stress state of the sample is the confining pressure σ_3 and the axial pressure σ_1. Using the vertical acceleration of vibrating table a_v, the amplitude of cyclic stress σ_{ac} can be obtained by the law of inertia:

$$\sigma_{ac} \approx \frac{a_v}{g}\sigma_1 \tag{4.47}$$

The failure criterion is the occurrence of sample's shear failure. When the sample is destroyed the effective angle of internal friction φ'_c is given by:

$$\sin\varphi'_c = \frac{\sigma_1 + \sigma_{ac} - \sigma_3}{\sigma_1 + \sigma_{ac} + \sigma_3} \tag{4.48}$$

The experimental results are shown in Fig. 4.22 and Table 4.3, where $\tan\varphi'_c$ / $\tan\varphi'_s$ is the ratio of the dynamic and static frictional coefficients and N_f is the cycle index. It can be observed that the frictional coefficient of compact sands begins to decrease after vibration; the frictional coefficient of loose sands increases slightly in the initial stages, then decreases, but the frictional coefficient of dry sands only decreases about 10% after being vibrated for a long time.

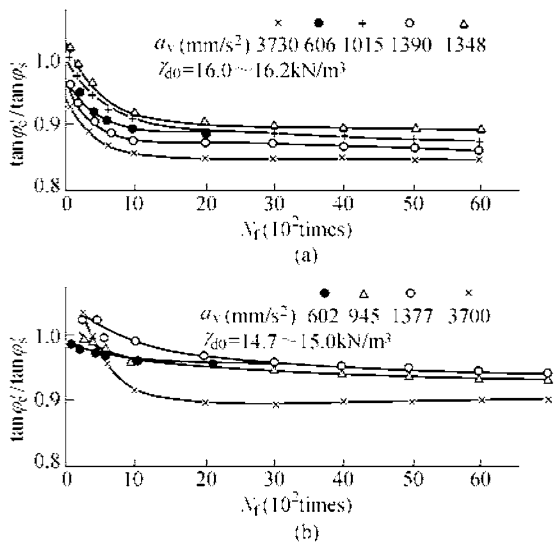

Fig. 4.22 Experimental results of shear strength of dry sands under the vibration

(a) For compact sands; (b) For loose sands

Table 4.3 Experimental results of shear strength of dry sands under the vibration[68]

γ_{d0} /kN • m^{-3}	$N_f \leqslant 10^2$		N_f=(20~70)×10^2		a_v/g
	$\frac{\tan\varphi'_c}{\tan\varphi'_s}$	$\varphi'_c - \varphi'_s$/(°)	$\frac{\tan\varphi'_c}{\tan\varphi'_s}$	$\varphi'_c - \varphi'_s$/(°)	
16.0~16.2	0.92~1.0	−2~0	0.84~0.89	−5~−3	0.06~0.37
14.7~15.0	1±α (α is very small)	0+α (α is very small)	0.90~0.94	−3~−2	0.06~0.37

For dry sands, $c'_c=0$, $u=0$, then

$$\tau_f=\tau_s+\tau_c=(\sigma_c+\sigma_s)\tan\varphi'_c \tag{4.49}$$

For the experiment of vertical vibrating table, $\tau_c=0$, then

$$\tau_f=(\sigma_s-\sigma_c)\tan\varphi'_c \tag{4.50}$$

where σ_c is the amplitude of inertia vibrating normal stress related to the vertical acceleration a_v.

For the experiment of horizontal vibrating table, $\sigma_c=0$, then

$$\tau_f=\tau_s+\tau_c=\sigma_s\tan\varphi'_c \tag{4.51}$$

where τ_c is the amplitude of inertia vibrating shear stress related to the horizontal acceleration a_h.

For the shear strength in the experiment of horizontal vibrating table, if τ_c is ignored , which increases with the increase of σ_c, a lower frictional coefficient could be obtained according to the following formula:

$$\frac{\tau_s}{\sigma_s}=\frac{\tau_s+\tau_c}{\sigma_s}=\tan\varphi'_c \tag{4.52}$$

For the experiment of vertical vibrating table, if the vertical acceleration $a_v \geqslant g$, τ_f tends to zero as σ_s-σ_c also tends to zero.

4.6.2 *Dynamic deformation and strength of gravel materials*

In engineering, the gravel materials whose particle diameters in general more than 2.00 mm can be divided into the gravel materials of natural foundation and the artificially broken rocks. In general, the former particles are rounding and the size distribution is very wide, but the latter particles always are angular. The gravel materials are certainly the main constructional materials for rock-fil dams, and they are also often used in back filling soils around the structure and in the earthfill of foundation. These gravel materials have great compactness, dynamic strength and rigidity after being rolled. Moreover, they have good water permeability. Taken as the permeable material, they can avoid the granular liquefaction when an earthquake occurs.

Contrast to the clays and the sandy soils, it is difficult to conduct the gravel materials experiments of deformation and strength characteristics, even though the static experiments are not easy to perform. Therefore, there are only a few measured data of deformation of dynamic strength available. The in-situ practical experiments are applying elastic wave. According to the velocity of elastic wave, the elastic modulus for micro-deformation can be measured, and the filling experiment can control the compactness when the gravel materials are being rolled. In addition, limited by the size of the experimental apparatus, it is difficult to do the laboratory experiment using the in-situ large size gravel materials. For example, for the triaxial test, the upper limiting value of particle diameter must be 1/8～1/5 of the sample. In general, the sample diameter is about 30～50 cm, so the maximum diameter of sample is limited to about 10 cm. Therefore, some granules whose diameter is beyond a certain value are excluded. However, the sample for experimental purpose must approach the original natural state, e.g., the in-situ saturated state, the drainage under the dynamic load, etc.

4.6.2.1 Dynamic deformation characteristics of gravel materials

Using a large triaxial equipment (where the diameter of sample is 300 mm and the height is 70 mm), the dynamic deformation of the broken rocks and the rounded gravel are measured. This triaxial equipment has been modified, that the force transducer with axial load is installed in the pressure chamber. A supersensitive non-contact type displacement meter is used, so that it can improve the measurement accuracy and measure the physical index in a strain range from 10^{-6} to 10^{-3}. The wet sample is divided into five layers and put into the die with every layer consolidated by a vibrator until the porosity ratio is about e=0.3～0.5. After compacting the saturated granular media, the dynamic load is applied without drainage and its frequency is about 0.1 Hz. The load is carried on ten times and a hysteresis curve of stress-strain is drawn. Then the secant shear modulus and the hysteresis damping ratio is obtained. The hysteresis curve of stress-strain is shown in Fig. 4.23.

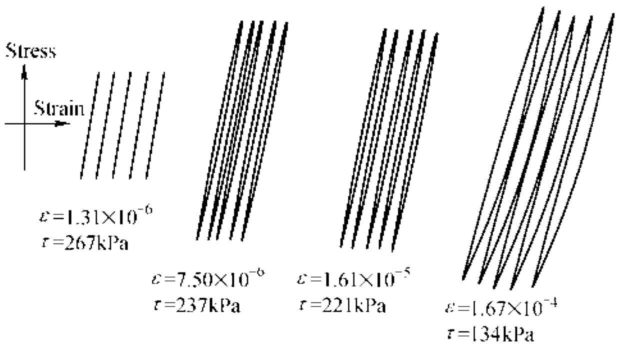

Fig. 4.23 Hysteresis curve of stress-strain for gravel materials

4.6.2.2 Dynamic strength characteristics of gravel materials

Using the cylindrical sample whose diameter is 50 mm and height is 100 mm, the dynamic strength of three kinds of broken rocks has been studied by the dynamic triaxial test. The maximum diameters are 101.6 mm, 63.5 mm and 19.1 mm respectively. By the use of an oil jack, the materials are consolidated in the die to make a compact sample,whose porosity ratio are e=0.30～0.45. Under saturated condition, the sample is compacted with the average principal stress of 90～380 kPa. Then a static shear force is applied followed by a dynamic stress whose frequency is 1 Hz acting 100 times without drainage. The experimental results of dynamic strength show that when the initial shear force ratio was less than 0.7, the dynamic strength has the tendency to reduce, and the reduction percent varies for different materials. This phenomenon is also seen in the test of other granular materials.

4.6.3 *Shear strength of saturated sands under the cyclic action*

Due to the influence of shear expansion and compaction under the cyclic action, the pore water pressure in the saturated sands will change no matter with drainage or not. It is the main factor influencing the granular shear strength under the cyclic action. If the cohesion factor is not considered and the shear strength is measured in conventional cyclic triaxial test, the condition of the failure stress must obey the following:

For compression failure:

$$\frac{\sigma_{10}+\sigma_{\mathrm{ac}}-\sigma_{30}}{2}=\frac{\sigma_{10}+\sigma_{\mathrm{ac}}+\sigma_{30}}{2}\sin\varphi_{\mathrm{c1}} \tag{4.53}$$

or

$$\frac{\sigma'_{10}+\sigma'_{\mathrm{ac}}-\sigma'_{30}}{2}=\left(\frac{\sigma'_{10}+\sigma_{\mathrm{ac}}+\sigma'_{30}}{2}-\Delta u_{\mathrm{f}}\right)\sin\varphi'_{\mathrm{c1}} \tag{4.54}$$

for tensile failure:

$$\frac{\sigma_{30}-\sigma_{10}+\sigma_{\mathrm{ac}}}{2}=\frac{\sigma_{30}+\sigma_{10}-\sigma_{\mathrm{ac}}}{2}\sin\varphi_{\mathrm{c2}} \tag{4.55}$$

or

$$\frac{\sigma'_{30}-\sigma'_{10}+\sigma_{\mathrm{ac}}}{2}=\left(\frac{\sigma'_{30}+\sigma'_{10}-\sigma_{\mathrm{ac}}}{2}-\Delta u_{\mathrm{f}}\right)\sin\varphi'_{\mathrm{c2}} \tag{4.56}$$

Presently, the failure criterion is that the axial strain ε_{a} reaches a certain ultimate value of $\varepsilon_{\mathrm{af}}$ or $\Delta\varepsilon_{\mathrm{af}}$. The corresponding amplitude of cyclic stress σ_{ac} and the cycle index N_{f} are the two indexes reflecting the cyclic strength of the test specimen. σ_{ac} is also termed as the cyclic pressure, and it relates to the cycle index N_{f}, $\varepsilon_{\mathrm{af}}$ (or $\Delta\varepsilon_{\mathrm{af}}$), and the ratio of initial principal stress $K_0=\sigma_{10}/\sigma_{30}$ (or $K_0=\sigma'_{10}/\sigma'_{30}$).

Fixing the inertia vibrating triaxial apparatus on the vertical vibrating table, in 1960's Chang Yaping did the saturated sands experiments of triaxial shear force with drainage and in consolidation without drainage[68]. In these experiments the appearance of shear surface in sample is considered as the failure criterion. At that time the axial strain is about 20%. The experimental results are portrayed by Fig. 4.24 and Table 4.4, where $\tan\varphi'_{\mathrm{c}}/\tan\varphi'_{\mathrm{s}}$ is the ratio of static and dynamic effective frictional coefficients and N_{f} is the vibration number. Compared with the dry sands, the results are alike. If the vibration number is less than 100, then $\tan\varphi'_{\mathrm{c}}/\tan\varphi'_{\mathrm{s}}\approx 1$, *viz.*, $\varphi'_{\mathrm{c}}\approx\varphi'_{\mathrm{s}}$.

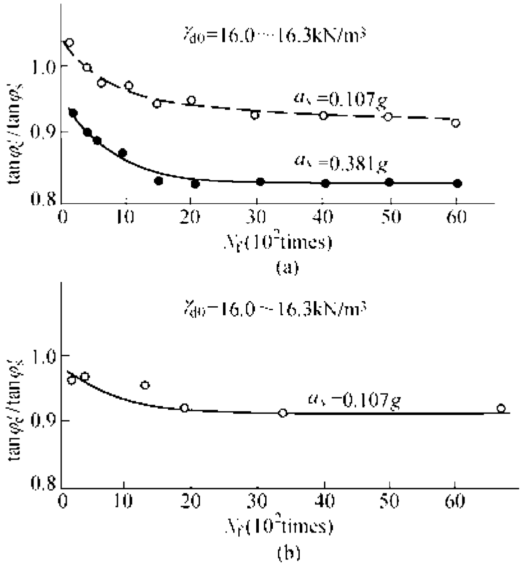

Fig. 4.24 Experimental results of effective shear strength of saturated sands under vibration

(a) Drainage;(b) Consolidation and no drainage

Table 4.4 Experimental result of effective shear strength of saturated sands under the vibration[68]

Experimental method	γ_{d0} /kN • m^{-3}	$N_f \leqslant 10^2$		$N_f=(20\sim70)\times10^2$		a_v/g
		$\dfrac{\tan\varphi'_c}{\tan\varphi'_s}$	$\varphi'_c-\varphi'_s$ /(°)	$\dfrac{\tan\varphi'_c}{\tan\varphi'_s}$	$\varphi'_c-\varphi'_s$ /(°)	
With drainage	16.0~16.3	0.93~1.04	−2~1.2	0.83~0.92	−5~−2	0.1~ 0.38
With consolidation and without drainage	16.0~16.3	0.96	−1	0.91	−2.5	0.107

In general, the shear strength of saturated sands under the cyclic action without drainage is only studied for the short-term cyclic action. For the long-term cyclic action, the saturated sands would be drainable. The shear strength of saturated sands under the short-term cyclic action or under the seismic action is the most important, and it is often related with the granular liquefaction. The research method is mainly the cyclic triaxial consolidated undrained test. Firstly, the test specimen is consolidated under the initial stresses, which are σ'_{10} and σ'_{30}, then the axial cyclic stress is applied with its amplitude of σ_{ac}. The experimental results are often described by the relation curve of σ_{ac}-N_f. If the change of pore water pressure Δu_f is not considered, *viz.*, σ_{10} and σ_{30} in Eq. (4.53) and Eq. (4.55) are substituted by σ'_{10} and σ'_{30} respectively, or Δu_f in Eq. (4.54) and Eq. (4.56) is deleted, then the total stress condition for the sample failure in consolidated undrained test can be expressed by the following equations:

for compression failure:

$$\frac{\sigma'_{10} + \sigma_{ac} - \sigma'_{30}}{2} = \frac{\sigma'_{10} + \sigma_{ac} + \sigma'_{30}}{2} \sin \varphi cu_{c1} \tag{4.57}$$

for tensile failure:

$$\frac{\sigma'_{30} - \sigma'_{10} + \sigma_{ac}}{2} = \frac{\sigma'_{30} + \sigma'_{10} - \sigma_{ac}}{2} \sin \varphi cu_{c2} \tag{4.58}$$

where $\sin\varphi cu_{c2}$ is the angle of internal friction of cyclic total stress.

In the analysis of granular seismic stability, the seismic shear strength is denoted by the stress state of surface failure after seismic activity. In the cyclic triaxial consolidated undrained test, the effective angle of internal friction φ'_c under the cyclic action and the static effective angle of internal friction φ'_s are almost the same in the saturated granular medium. Thus it is easy to ascertain the failure surface of test specimen (θ=45° $\pm\varphi'_c/2$, where the positive sign denotes the compression failure and the negative means the tensile failure), the initial normal effective pressure σ'_{f0}, the initial shear stress τ_{f0} and the amplitude of cyclic stress τ_{fc}. In 1980s Wang Wenshao suggested that "the state of seismic total stress" on the surface failure of test specimen can be indicated by σ'_{f0} and $\tau_{fs}=\tau_{f0}+\tau_{fc}$. He used the curve of $\sigma'_{f0}-\tau_{fs}$ to substitute the shear strength curve of "the seismic total stress" (shown in Fig. 4.25).

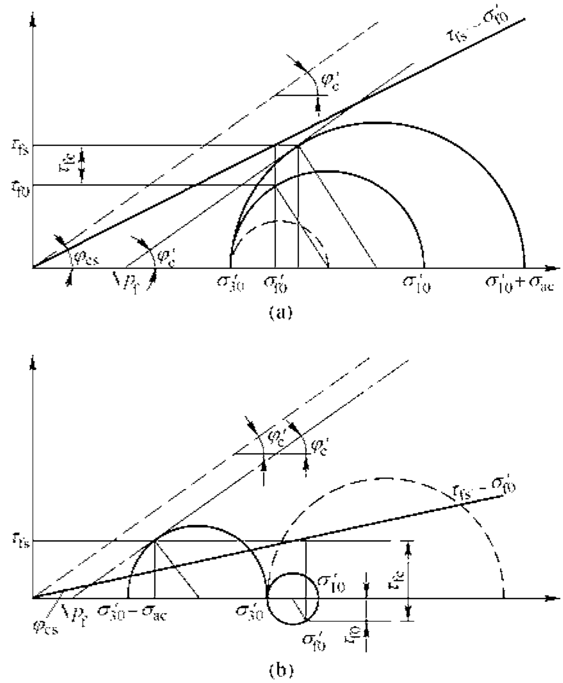

Fig. 4.25 Shear strength curve in the cyclic triaxial consolidated undrained test of saturated sands of "the seism total stress"

(a) For compression failure;(b) For tensile failure

4.6.4 *Shear strength of cohesive soil under the cyclic action*

The shear strength of cohesive soil under the cyclic action is often not easy to measure accurately and express clearly due to many complex factors, such as cohesion, internal friction angle, pore water pressure. So generally most researchers take the relation among the cyclic pressure σ_{ac}, the cycle index N_f and the axial stress to study the cohesive soil strength index under the cyclic action, then to compare it with the corresponding static pressure σ_{af}.

In 1960s Seed and his collaborators reported their experimental results of cohesive soil strength under the seismic action. The experiment was a triaxial undrained test. Firstly, the static pressure of sample $\sigma_{af}=\sigma_{1f}-\sigma_{30}$ was measured, and then several values of $\sigma_{as}=\sigma_{1s}-\sigma_{30}(\sigma_{1s}<\sigma_{1f})$ less than the value σ_{af} were chosen to be the initial pressure of the sample (before seismic action). When the axial strain was stable, the cyclic stress σ_{ac}, about 20%~50% of the axial total stress, was exerted till the sample was broken, and the cycle index N_f was recorded. The experimental results could be expressed by the relation curve of the cyclic pressure ratio σ_{ac}/σ_{af} and N_f and the relation curve of σ_{ac}/σ_{af} and the ratio of initial static pressure σ_{as}/σ_{af} respectively in Fig. 4.26 and Fig. 4.27.

Because of the relation between τ, shear force on the failure surface, and the difference of principal stresses $\sigma_a(\sigma_a=\sigma_1-\sigma_3)$, *viz.*,

$$\tau=\frac{\sigma_a}{2}\cos\varphi' \tag{4.59}$$

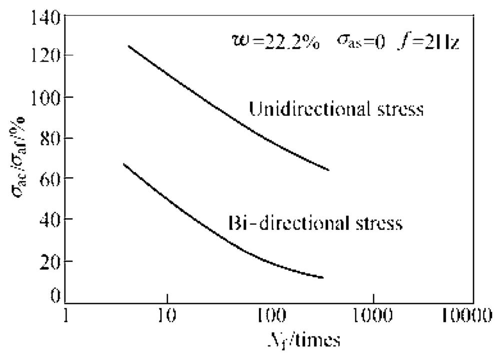

Fig. 4.26 Relation between cyclic pressure ratio and cycle index in saturated cohesive soil

so

$$\left.\begin{aligned}\tau_f&=\frac{\sigma_{af}}{2}\cos\varphi'\\ \tau_s&=\frac{\sigma_{as}}{2}\cos\varphi'\\ \tau_c&=\frac{\sigma_{ac}}{2}\cos\varphi'\end{aligned}\right\} \tag{4.60}$$

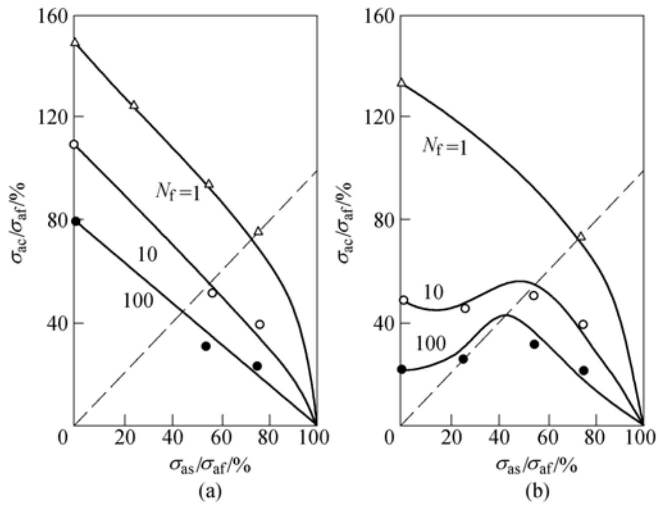

Fig. 4.27 Relation between cyclic pressure ratio and ratio of initial static pressure in saturated cohesive soils

(a) For unidirectional stress;(b) For bi-directional stress

where τ_f, τ_s, τ_c are the static shear strength, the initial shear force and the cyclic shear force respectively.

Therefore, two equations can be obtained:

$$\left.\begin{aligned}\frac{\sigma_{ac}}{\sigma_{af}} = \frac{\tau_c}{\tau_f}\\ \frac{\sigma_{as}}{\sigma_{af}} = \frac{\tau_s}{\tau_f}\end{aligned}\right\} \tag{4.61}$$

The main factors influencing the dynamic strength of cohesive soil are shear velocity and alternative load. The cohesive soil strength of bearing alternating load could be obtained by shear experiments, such as triaxial shear test, pure shear test and torsional shear test. Because of the alternating load, the dynamic strength of saturated cohesive soil will decrease. However, the precise definition of dynamic strength of bearing alternating load has not found yet. But generally, it can be indicated by the stress $\tau_s+\tau_{df}$, which corresponds to the accumulated strain γ_c, where τ_{df} is the amplitude of alternative load, and τ_s is the initial shear force.

Which one is more remarkable? Is it dynamic strength or static strength? It is due to the effects of two factors—shear velocity and alternative load. While alternating load is not exerted so many times, the velocity effect is significant, namely, the dynamic strength is more remarkable than the static strength (shown in Fig. 4.31). In addition, Fig. 4.28 shows that the initial shear force is also important. Under alternating load, the dynamic strength is further decreased.

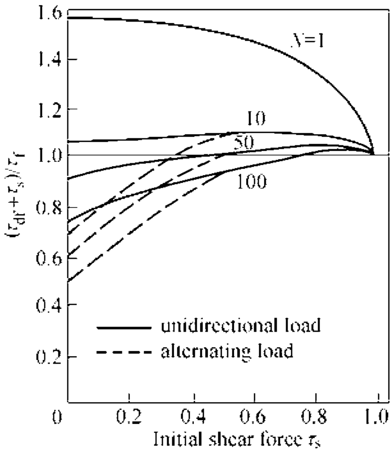

Fig. 4.28 Relation between dynamic strength and initial shear force

Unlike sands, the dynamic strength of cohesive soil is greatly affected by alternating load period (shown in Fig. 4.29). The dynamic strength of cohesive soil also changes with soil types. The lower in plasticity, the weaker the strength is.

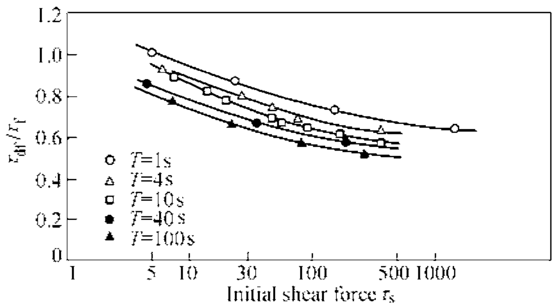

Fig. 4.29 Influence of period on dynamic strength

In 1969 Taylor and his collaborators performed the cyclic triaxial undrained test of the cohesive soil. They found the relationship among the peak value of shear force $\hat{\tau}$ and the cycle index N_f and the amplitude of cyclic stress ε_{ac}:

$$\hat{\tau} = a + b\sigma'_m \tag{4.62}$$

$$\sigma'_m = \frac{1}{3}(\sigma'_1 + \sigma'_2 + \sigma'_3) \tag{4.63}$$

where σ'_m is the average effective principal stress; a and b are two empirical coefficients indicated by the viscosity and friction characteristic respectively.

4.7 Laws of Wave Propagation in Elastic Granular Medium

The granular media are aggregates of particles with similar characters, like clays, sands, broken coals, cements, corns, and other granular or powdery materials. There are many fields referring to the granular mechanism, such as foundation stability in vibration, the landslide and mudflow control, the granular discharge, the ore-drawing, etc. Researchers have performed lots of work in such fields as granular microstructure and constitutive relation, shear mechanical model, vibrating compaction, elastic wave propagation, etc. This section is mainly about the wave equations of elastic wave and its energy and the laws of Rayleigh wave and Love wave.

4.7.1 *Wave equations of elastic wave in granular media*

4.7.1.1 Wave equations of elastic wave in the granular isotropic medium

If the value of strain $\varepsilon<10^{-4}$, the granular deformation is considered as the elastic deformation. Assuming that the granular media are the isotropic elastic media firstly, and establish an equilibrium equation in the granular micro-unit, then make use of Hooke's law to obtain the following wave equation set:

$$\left.\begin{aligned}(\lambda+G)\frac{\partial e}{\partial x}+G\nabla^2 u_x=\rho\frac{\partial^2 u_x}{\partial t^2}\\(\lambda+G)\frac{\partial e}{\partial y}+G\nabla^2 u_y=\rho\frac{\partial^2 u_y}{\partial t^2}\\(\lambda+G)\frac{\partial e}{\partial z}+G\nabla^2 u_z=\rho\frac{\partial^2 u_z}{\partial t^2}\end{aligned}\right\}\tag{4.64}$$

where u_x, u_y and u_z are displacements along the directions of x, y, z respectively; λ is the Lame constant; G is the shear modulus; ρ is the granular density; e is the volume strain for micro-unit; ∇^2 is Laplacian operator. In addition,

$$e=\frac{\partial u_x}{\partial x}+\frac{\partial u_y}{\partial y}+\frac{\partial u_z}{\partial z};\quad \nabla^2=\frac{\partial^2}{\partial x^2}+\frac{\partial^2}{\partial y^2}+\frac{\partial^2}{\partial z^2}$$

Elastic wave transmits in the granular media in two ways, *viz*., two body waves, wave P and wave S. Their common form of wave equation can be abbreviated as follows:

$$\frac{\partial^2\psi}{\partial t^2}=a^2\nabla^2\psi\tag{4.65}$$

where a is the wave velocity.

For wave P:

$$a=v_{\mathrm{P}}=\sqrt{\frac{\lambda+2G}{\rho}}=\sqrt{\frac{E(1-\mu)}{\rho(1+\mu)(1-2\mu)}}\tag{4.66}$$

For wave S:

$$a=v_{\mathrm{S}}=\sqrt{\frac{G}{\rho}}=\sqrt{\frac{E}{2\rho(1+\mu)}}\tag{4.67}$$

where v_{P} is the velocity of wave P; v_{S} is the velocity of wave S; μ is the Poisson's ratio.

The velocity ratio between waves P and S is

$$\frac{v_P}{v_S}=\sqrt{\frac{\lambda+2G}{G}}=\sqrt{\frac{2(1-\mu)}{1-2\mu}} \tag{4.68}$$

When Poisson's ratio μ is about 0~0.5, the relation is

$$v_P > \sqrt{2}v_S \tag{4.69}$$

The relation between the velocity ratio v_P/v_S and the Poisson's ratio is shown in Fig. 4.30.

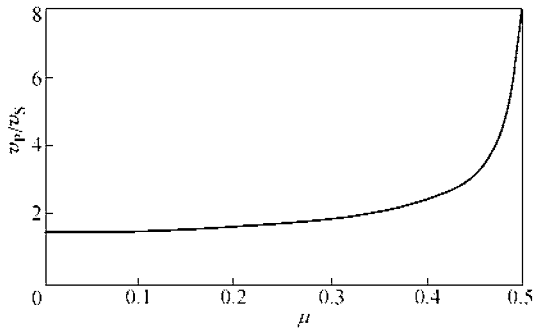

Fig. 4.30 Relation between v_P / v_S and μ

4.7.1.2 Wave equations of elastic wave in the granular transverse isotropic medium

Due to the compactness of deposition, granular media (i.e., foundation, sandy beach, sand desert) often show the transverse isotropy. That is to say, the granular medium has isotropic property in the horizontal direction, but has anisotropy in the vertical direction. The propagation of elastic wave in the transverse isotropic media is more complex, and the wave equation set is:

$$\left.\begin{aligned}
\rho\frac{\partial^2 u_x}{\partial t^2}&=\frac{\partial}{\partial x}\left(C_{11}\frac{\partial u_x}{\partial x}+C_{12}\frac{\partial u_y}{\partial y}+C_{13}\frac{\partial u_z}{\partial z}\right)+\\
&\quad C_{66}\left(\frac{\partial^2 u_y}{\partial x\partial y}+\frac{\partial^2 u_x}{\partial y^2}\right)+C_{44}\left(\frac{\partial^2 u_x}{\partial z^2}+\frac{\partial^2 u_z}{\partial x\partial z}\right)\\
\rho\frac{\partial^2 u_y}{\partial t^2}&=\frac{\partial}{\partial y}\left(C_{12}\frac{\partial u_x}{\partial x}+C_{11}\frac{\partial u_y}{\partial y}+C_{13}\frac{\partial u_z}{\partial z}\right)+\\
&\quad C_{44}\left(\frac{\partial^2 u_z}{\partial z\partial y}+\frac{\partial^2 u_y}{\partial z^2}\right)+C_{66}\left(\frac{\partial^2 u_x}{\partial x\partial y}+\frac{\partial^2 u_y}{\partial x^2}\right)\\
\rho\frac{\partial^2 u_z}{\partial t^2}&=\frac{\partial}{\partial z}\left(C_{13}\frac{\partial u_x}{\partial x}+C_{13}\frac{\partial u_y}{\partial y}+C_{33}\frac{\partial u_z}{\partial z}\right)+\\
&\quad C_{44}\left(\frac{\partial^2 u_x}{\partial x\partial z}+\frac{\partial^2 u_z}{\partial x^2}\right)+C_{44}\left(\frac{\partial^2 u_y}{\partial y\partial z}+\frac{\partial^2 u_z}{\partial y^2}\right)
\end{aligned}\right\} \tag{4.70}$$

where $C_{66} = 1/2\ (C_{11}+C_{12})$; C_{11}, C_{12}, C_{13}, C_{33} and C_{44} are the five independent elastic constants; in order to make the meaning of these elastic constants clear, Anderson (1967) and Gatmiri (1992) have defined them as follows:

$$C_{11} = \frac{E_{\mathrm{h}}(1-\mu_{\mathrm{hv}}\mu_{\mathrm{vh}})}{\Delta}, \qquad C_{12} = \frac{E_{\mathrm{h}}(1-\mu_{\mathrm{hh}}^2)}{\Delta}$$

$$C_{13} = \frac{E_{\mathrm{h}}(1+\mu_{\mathrm{hh}}\mu_{\mathrm{vh}})}{\Delta}, \qquad C_{33} = \frac{E_{\mathrm{v}}(1-\mu_{\mathrm{hh}}^2)}{\Delta}$$

$$C_{44} = G_{\mathrm{v}}, \qquad \Delta = (1+\mu_{\mathrm{hh}})(1-\mu_{\mathrm{hh}}-2\mu_{\mathrm{hv}}\mu_{\mathrm{vh}})$$

where E_{v} and E_{h} are the vertical and horizontal Young's modulus respectively; G_{v} is the vertical shear modulus; G_{h} is the horizontal shear modulus; μ_{hh} is the Poisson's ratio of lateral deformation in the horizontal direction caused by the horizontal stress; μ_{vh} is the Poisson's ratio of lateral deformation in the horizontal direction caused by the vertical stress; μ_{hv} is the Poisson's ratio of lateral deformation in the vertical direction caused by the horizontal stress.

Because wave S can be divided into the vertical component SH and the horizontal component SV, the above equation set can be divided into two parts. One part includes wave P as well as wave SV:

$$\left.\begin{aligned} & C_{11}\frac{\partial^2 u_x}{\partial x^2} + C_{44}\frac{\partial^2 u_x}{\partial z^2} + (C_{13}+C_{44})\frac{\partial^2 u_z}{\partial x \partial z} - \rho\frac{\partial^2 u_x}{\partial t^2} = 0 \\ & (C_{13}+C_{44})\frac{\partial^2 u_x}{\partial x \partial z} + C_{13}\frac{\partial u_y}{\partial y} + C_{33}\frac{\partial^2 u_z}{\partial z^2} + C_{44}\frac{\partial^2 u_z}{\partial x^2} - \rho\frac{\partial^2 u_z}{\partial t^2} = 0 \end{aligned}\right\} \tag{4.71}$$

And the other part only includes wave SH:

$$C_{44}\frac{\partial^2 u_y}{\partial z^2} + C_{66}\frac{\partial^2 u_y}{\partial x^2} - \rho\frac{\partial^2 u_y}{\partial t^2} = 0 \tag{4.72}$$

4.7.2 *Wave energy and its dissipation in granular media*

4.7.2.1 Wave energy in the granular isotropic medium

Wave energy in the granular isotropic medium includes elastic strain energy and kinetic energy. Wave exerts some force to the granular medium while propagating. Wave P exerts the direct stress and wave S exerts the shear force to a granular micro-unit. In the rectangular coordinate system, the direct strain energy E_{P} and the shear strain energy E_{S} for the micro-unit are:

$$\left.\begin{aligned} E_{\mathrm{P}} &= \frac{1}{2}\iiint(\sigma_{xx}\varepsilon_{xx} + \sigma_{yy}\varepsilon_{yy} + \sigma_{zz}\varepsilon_{zz})\mathrm{d}x\mathrm{d}y\mathrm{d}z \\ E_{\mathrm{S}} &= \frac{1}{2}\iiint(\tau_{xy}\gamma_{xy} + \tau_{yz}\gamma_{yz} + \tau_{xz}\gamma_{xz})\mathrm{d}x\mathrm{d}y\mathrm{d}z \end{aligned}\right\} \tag{4.73}$$

where σ and τ are the direct stress and the shear force respectively, similarly ε and γ are the direct strain and shear strain and all subscripts denote the directions.

So the total strain energy is:

$$E_{PS} = E_P + E_S = \frac{1}{2}\iiint(\sigma_{xx}\varepsilon_{xx} + \sigma_{yy}\varepsilon_{yy} + \sigma_{zz}\varepsilon_{zz} + \tau_{xy}\gamma_{xy} + \tau_{yz}\gamma_{yz} + \tau_{xz}\gamma_{xz})\mathrm{d}x\mathrm{d}y\mathrm{d}z \tag{4.74}$$

Assuming that the particle displacement caused by the stress wave is $s(u_x, u_y, u_z, t)$, the kinetic energy of micro-unit is:

$$E_K = \frac{1}{2}\rho\iiint\left[\left(\frac{\partial u_x}{\partial t}\right)^2 + \left(\frac{\partial u_y}{\partial t}\right)^2 + \left(\frac{\partial u_z}{\partial t}\right)^2\right]\mathrm{d}x\mathrm{d}y\mathrm{d}z \tag{4.75}$$

So the total wave energy of the granular micro-unit is

$$E = E_P + E_S + E_K = \frac{1}{2}\iiint\left\{\sigma_{xx}\varepsilon_{xx} + \sigma_{yy}\varepsilon_{yy} + \sigma_{zz}\varepsilon_{zz} + \tau_{xy}\gamma_{xy} + \tau_{yz}\gamma_{yz} + \tau_{xz}\gamma_{xz} + \rho\left[\left(\frac{\partial u_x}{\partial t}\right)^2 + \left(\frac{\partial u_y}{\partial t}\right)^2 + \left(\frac{\partial u_z}{\partial t}\right)^2\right]\right\}\mathrm{d}x\mathrm{d}y\mathrm{d}z \tag{4.76}$$

The above are the ideal formulae deduced by the classic elastic energy. Moreover, the energy dissipation is not considered here. However, they can intuitively express the energy (or mechanical energy) relation in granular media.

4.7.2.2 Elastic wave dissipation in the granular transverse isotropic media

There is two kinds body waves could transmit in the granular media, the longitudinal wave and the transverse wave. The longitudinal wave is the compressional wave propagating outwards from the vibration source and is called wave P. The direction of particle movement is the same as the wave propagation. The transverse wave is the shear wave propagating outwards from the vibration source and is called wave S. The direction of particle movement is vertical to the direction of wave propagation.

Wave propagation in the granular transverse isotropic media attenuates layer by layer. The broken ore in the vibrating ore-drawing is an example. Loose broken ores are drawn from the stopes while loose ellipsoid extends continuously (as shown in Fig. 4.31). If the granular medium has been layered, the vibrating energy would gradually attenuate due to the wave refraction and reflection on the layers' interfaces, as like Fig. 4.32 shows. Vibrating energy attenuation obeys the well-known Snell law[2]:

$$\frac{\sin\alpha}{v_{P1}} = \frac{\sin\beta}{v_{S1}} = \frac{\sin\gamma}{v_{P2}} = \frac{\sin\theta}{v_{S2}} \tag{4.77}$$

where v_{P1} and v_{P2} are the velocities of wave P for the layer 1 and layer 2 respectively; v_{S1} and v_{S2}, the velocities of wave S for the layer 1 and layer 2 respectively; α is the angle of incidence; β is the angle of reflection of wave S; γ is the angle of refraction of wave P; θ is the angle of refraction of wave S.

With the change of position and time, the wave energy (or the mechanical energy) will weaken gradually because a part of the mechanical energy turns into heat energy, chemical energy or electric energy. The wave dissipation in the vibrating ore-drawing is an example (shown in Fig. 4.31). The main reasons of dissipation of wave energy in the broken ores are:

(1) The spatial dissipation of wave energy. Part of energy transmits to the dead zone and the pillars uselessly.

(2) The plastic deformation of media. When the strain reaches to a certain degree (i.e., more than $10^{-4} \sim 10^{-2}$), the broken ores will have the plastic deformation. Because of the nonreversibility of plastic deformation, the wave energy will attenuate during the course of propagation.

(3) The viscosity of broken ores. Because of the existence of powdery ores, water and cohesive ores, the broken ores has the viscosity, which will cause the attenuation of vibrating energy.

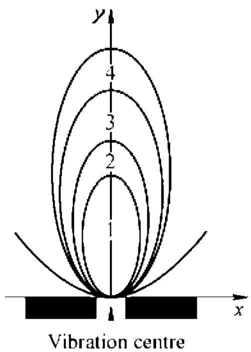

Fig. 4.31 Granular secondary loosening

(4) The friction among granules. The wave propagation causes the relative motion between the particles, which will cause the friction. Therefore, the vibrating property will be absorbed.

(5) The refraction and reflection of wave on the interfaces. As shown in Fig. 4.32, a part incident energy will be reflected, and transmitted energy is obviously

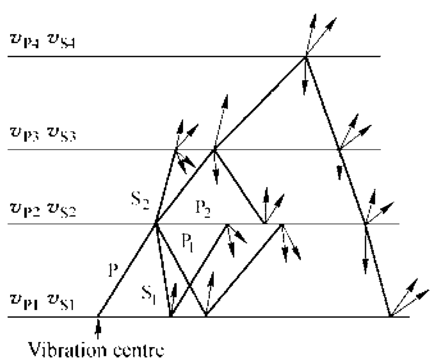

Fig. 4.32 Refraction and reflection of wave

less than incident energy. Many times of refraction and reflection will lead to the energy attenuation gradually.

(6) The influence of drawed ores' loosening. Take wave S as an example. Assuming that the wave velocity is v_S, and the incident wave is the only interfering source and is a harmonic wave, thereby:

$$f_1(t,x) = Ae^{i\omega(t+x/v_{S1})} \tag{4.78}$$

then the reflected wave is also a harmonic wave:

$$D_1(t,x) = \alpha Ae^{i\omega(t-x/v_{S2})} \tag{4.79}$$

The amplitude of the reflected wave is αA, which is α times of the incident wave, but the waveform does not change. Therefore, the energy flows of the incident wave and the reflected wave in the interface respectively are:

$$\left.\begin{aligned} Q_{\text{incident}} &= v_{S1}\rho_1\left[f_1(t)\right]^2 = v_{S1}\rho_1\left(i\omega Ae^{i\omega t}\right)^2 \\ Q_{\text{reflect}} &= v_{S1}\rho_1\left[D_1(t)\right]^2 = v_{S2}\rho_{S2}\left(i\omega ae^{i\omega t}\right)^2 \end{aligned}\right\} \tag{4.80}$$

so the ratio of the reflected energy and the incident energy is:

$$\frac{Q_{\text{reflect}}}{Q_{\text{incident}}} = \alpha^2 \tag{4.81}$$

Assuming that the energy transmission coefficient λ_0 is the ratio of energy flow between the refracted wave and the incident wave and according to the law of conservation of energy, one can get that: $Q_{\text{incident}}=Q_{\text{reflect}}+Q_{\text{transmission}}$. Transform it, then:

$$\lambda_0 = 1-\alpha^2 = 1-\left(\frac{1-K}{1+K}\right)^2 \tag{4.82}$$

where $K=\rho_1 v_{S1}/\rho_2 v_{S2}$ is the wave impedance ratio.

It can be seen from Eq. (4.82) that when the density difference of media is more bigger, *viz.*, whether $K \ll 1$ or $K \gg 1$, λ_0 approaches to zero, and more energy will not transmit. It can be seen from Fig. 4.31 and Fig. 4.32 that the loosening ellipsoid continuously extends during the course of drawing ores. The closer is the ore mass to the discharge gate, the looser the ores become. So, the relation of the densities of the first four layers is $\rho_1<\rho_2<\rho_3<\rho_4$. Namely, the vibrating wave propagates from the low density layer to the higher one. The density difference is the source of transverse isotropy. Besides the energy dissipation which is caused by granular property, the density difference is the key factor which leads to the attenuation of vibrating energy. It can be concluded that the attenuation of wave energy is more serious when the ores are drawn than that when the discharge lip is closed. This conclusion is also substantiated by the results of experiments as shown in Table 4.5.

Table 4.5 The attenuation coefficients(m^{-1})

Testing condition	Lip closed	Lip opening, hard discharge	Lip opening, stable discharge
Calcspar	0.39～0.52	0.52～0.68	0.57～0.72
Scree	0.35～0.48	0.53～0.62	0.51～0.67
Fine iron ore	0.43～0.50	0.54～0.70	0.60～0.74

4.7.3 *Wave equation of Rayleigh wave in granular media*

4.7.3.1 Wave equation of Rayleigh wave in the granular isotropic medium

Wave P and wave S are the two kinds body waves that can transmit in infinite elastic medium. In 1887, Rayleigh found that in the semi-infinite space, such as soil foundation, sands beach, sand desert, etc., there is a kind of surface wave, which is generated by the interference between wave P and wave S. Subsequently, this kind of wave is known as Rayleigh wave[90]. Rayleigh wave propagates along the surface of a medium, and attenuates quickly with the increment of the depth. While Rayleigh wave propagates, the motion path of elastic particle is an ellipse whose long axis is vertical to the ground and the motion direction is opposite to the wave propagation (shown in Fig. 4.33). The Rayleigh wave's propagating velocity is less than the velocity of wave S in the same medium, and its vertical component of displacement is larger than the horizontal component on the ground surface[128~134]. Because the propagation range of this kind wave is very wide, so it can be dealt with as a two-dimensional problem, and its wave equation set is:

$$\left.\begin{aligned}(\lambda+G)\frac{\partial e}{\partial x}+G\nabla^2 u_x-\rho\frac{\partial^2 u_x}{\partial t^2}=0\\(\lambda+G)\frac{\partial e}{\partial z}+G\nabla^2 u_z-\rho\frac{\partial^2 u_z}{\partial t^2}=0\end{aligned}\right\}\tag{4.83}$$

In order to divide the expansion and compaction from the rotation, using the potential function ϕ and ψ ,the following are obtained:

$$\left.\begin{aligned}u_x&=\frac{\partial\phi}{\partial x}+\frac{\partial\psi}{\partial z}\\u_z&=\frac{\partial\phi}{\partial z}-\frac{\partial\psi}{\partial x}\end{aligned}\right\}\tag{4.84}$$

hence the above equation set is turned into:

$$\left.\begin{aligned}\rho\frac{\partial}{\partial x}\left(\frac{\partial^2\phi}{\partial t^2}\right)+\rho\frac{\partial}{\partial z}\left(\frac{\partial^2\psi}{\partial t^2}\right)=(\lambda+2G)\frac{\partial}{\partial x}(\nabla^2\phi)+G\frac{\partial}{\partial z}(\nabla^2\psi)\\\rho\frac{\partial}{\partial z}\left(\frac{\partial^2\phi}{\partial t^2}\right)-\rho\frac{\partial}{\partial x}\left(\frac{\partial^2\psi}{\partial t^2}\right)=(\lambda+2G)\frac{\partial}{\partial z}(\nabla^2\phi)-G\frac{\partial}{\partial x}(\nabla^2\psi)\end{aligned}\right\}\tag{4.85}$$

The Eq. (4.85) shows that Rayleigh wave is the superposition of waves P and S.

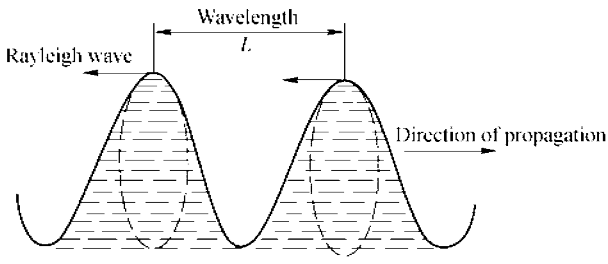

Fig. 4.33 Rayleigh wave

4.7.3.2 Wave equation of Rayleigh wave in the granular transverse isotropic medium

In general, the granular media of natural sediment can be regarded as the transverse isotropic medium. There is a difference between the vertical modulus and the horizontal modulus, which relates to granular kind, consolidation stress, over-consolidation ratio, etc. The wave equation set can then be expressed by (the plane problem):

$$\left.\begin{aligned}\rho\frac{\partial^2 u_x}{\partial t^2} &= C_{11}\frac{\partial^2 u_x}{\partial x^2} + C_{44}\frac{\partial^2 u_x}{\partial z^2} + (C_{13}+C_{44})\frac{\partial^2 u_z}{\partial x \partial z} \\ \rho\frac{\partial^2 u_y}{\partial t^2} &= (C_{13}+C_{44})\frac{\partial^2 u_x}{\partial x \partial y} + C_{33}\frac{\partial^2 u_y}{\partial y^2} + C_{44}\frac{\partial^2 u_y}{\partial x^2}\end{aligned}\right\} \tag{4.86}$$

Rayleigh wave in the isotropic media is mainly influenced by the shear modulus G. There are two shear modulus for Rayleigh wave in the transverse isotropic media: one is the vertical shear modulus G_V; the other is the horizontal shear modulus G_H. Moreover, in terms of the characteristics of Rayleigh wave, it attenuates gradually along the direction of y, and do not along the x.

4.7.4 *Love wave in the granular medium*

Love wave is generated by the intensified interference caused by the polygenous perfect reflection of shear wave SH on the free surface and interfaces of different layers in half-space structure. It belongs to plane wave, which has diffusibility and does not relate to the compressional wave velocity. It only relates to the granular thickness, mass density of the layer and the velocity of shear wave[135,136].

Love wave has no vertical component, and its propagating velocity relates to the frequency of vibration. The following signs with an apostrophe denote that they relate to the property of medium in the semi-infinite space, but the signs without an apostrophe denote that they relate to the property of surface layer. For the wave SH, it obeys the following wave equations:

$$\nabla^2 u_z = \frac{1}{v_S}\frac{\partial^2 u_z}{\partial t^2}, \qquad \nabla^2 u_z' = \frac{1}{v_S'}\frac{\partial^2 u_z'}{\partial t^2} \tag{4.87}$$

Love wave has the following characteristics relating to the wave velocity:

(1) When $v_s > v_s'$, Love wave propagates along the surface layer and its velocity is nearly equal to v_s, at the same time, partial energy radiates toward the underlayer. When the frequency increases to a certain level, the wave energy all confined into the surface layer, but the vibration in the underlayer attenuates rapidly with the depth. That is to say, when the frequency of vibration tends to infinity the velocity of Love wave is closed to the velocity of transverse wave in the surface layer.

(2) When $v_s < v_s'$, some energy radiates into the underlayer, so only when

the velocity of transverse wave in the surface layer is less than the underlayer, the Love wave will be formed.

To study the diffusion curve and the displacement distribution of Love wave, the diffusion wave equation on the surface in half-space structure needs to be established in analytical method and discuss its properties. However, when there are too many layers or the wavelength is too short it is difficult to solve the problem in this way. Xia Tangdai utilized the finite-element and half-finite-element method and the finite-element-analytical method to establish the diffusion equation of Love wave in the layer foundations. He systemically studied the Love wave for difference type of foundation, and gained very good results[135].

4.8 Wave Propagation and Dissipation in Viscoelastic Granules

In geotechnical engineering, usually only the elastic property and inertia property of granules are hotly studied, and it is thought that the mechanical behavior of the media materials can be fully described by Hooke's law. According to the classic elastic solid theory, the elastic displacement x follows this partial differential equation[125~127]:

$$(\lambda + 2G)\,\mathrm{grad}(\mathrm{div}x) - G\mathrm{curl}(\mathrm{curl}x) = \rho\frac{\partial^2 x}{\partial t^2} \tag{4.88}$$

where λ is Lame elastic constant; ρ is the density of granular media; t is time; G is the shearing module.

In fact in granules, the amplitude of plane wave will attenuate and free vibration of elastomers will disappear, i.e., there will be energy dissipation. The dissipation derives from two ways, scattering and absorbing. Scattering mainly takes place in granular media or pores, and absorbing is mainly caused by the viscosity and heat exchange of granular media. Besides the attenuation of amplitude, wave propagation in the viscoelastic granular media has an obvious characteristic which will leads to wave dispersion and absorption. This section analyzes the law of wave propagation and attenuation in granular media in terms of viscoelastic property.

4.8.1 *Viscoelastic model and constitutive relation*

4.8.1.1 Maxwell model

Maxwell model comprises a spring and a dashpot plunger in series (Fig. 4.34). This model simultaneously has the properties of solid and viscous fluid, and the deformation rate tends to be a constant with the increase of time. This viscoelastic model belongs to viscous fluid, and its constitutive equation is:

$$\sigma + \frac{\eta}{E}\frac{\mathrm{d}\sigma}{\mathrm{d}t} = \eta\frac{\mathrm{d}\varepsilon}{\mathrm{d}t} \tag{4.89}$$

where σ is the stress; ε is the strain; E is the elastic modulus; η is the viscosity coefficient.

4.8.1.2 Kelvin model

Kelvin model is a spring parallel connected with a dashpot plunger (Fig. 4.35). This model simultaneously has the properties of elastic solid and viscous fluid, and the viscoelastic granular medium belongs to the elastic solid, and its constitutive equation is:

$$\sigma = E\varepsilon + \eta\frac{\mathrm{d}\varepsilon}{\mathrm{d}t} \tag{4.90}$$

4.8.1.3 Standard linear solid model

Kelvin model cannot explain the sudden change of strain under stress and indicate the residual strain after the stress disappears, and Maxwell model have not the property of creep. These two models are both inadequate for describing many kinds of the properties of viscoelastic media. Therefore, the standard linear solid model, which has the properties of the sudden change of strain, the residual strain and the creep, should be established. This model is a tertiary solid model comprising Kelvin model and a spring in series (shown in Fig. 4.36). It has the property of instantaneous elasticity and quasi-elasticity. The normal form of constitutive equation of standard linear solid model is:

$$\sigma + p_1\frac{\mathrm{d}\sigma}{\mathrm{d}t} = q_0\varepsilon + q_1\frac{\mathrm{d}\varepsilon}{\mathrm{d}t} \tag{4.91}$$

where $p_1 = \dfrac{\eta}{E_1 + E_2}, q_0 = \dfrac{E_1E_2}{E_1 + E_2}, q_1 = \dfrac{E_1\eta}{E_1 + E_2}$.

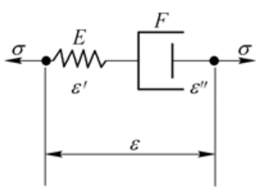

Fig. 4.34 Maxwell model

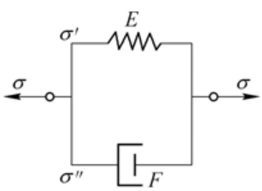

Fig. 4.35 Kelvin model

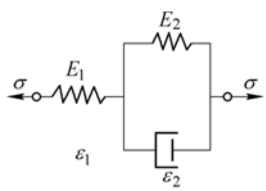

Fig. 4.36 Standard linear solid model

4.8.2 *Wave equation in the viscoelastic granular media*

While there is minor deformation, the viscoelastic fundamental equations are given as follows:

the strain-displacement equation is:

$$\varepsilon_{ij}(x_i,t)=\frac{1}{2}[u_{i,j}(x_i,t)+u_{j,i}(x_i,t)] \tag{4.92}$$

the three-dimensional constitutive equation is:

$$\sigma_{ij}(x_i,t)=\delta_{ij}\lambda(t)\bullet \mathrm{d}\varepsilon_{kk}+2G(t)\bullet \mathrm{d}\varepsilon_{ij} \tag{4.93}$$

and the dynamic equation is:

$$\sigma_{ij,j}(x_i,t)+f_i=\rho\frac{\partial^2 u_i(x_i,t)}{\partial t^2} \tag{4.94}$$

where δ_{ij} is the Kronecker mark; i, j, k corresponds to axis x, y, z; f_i is the body force component; $\lambda(t)$ and $G(t)$ are viscoelastic functions; u is the displacement.

A three-dimensional wave equation can be deduced from the above basic equations:

$$[\lambda(t)+G(t)]\bullet \mathrm{d}\theta_{,i}+G(t)\mathrm{d}\nabla^2 u_i+f_i=\rho\frac{\partial^2 u_i}{\partial t^2} \tag{4.95}$$

where

$$\left.\begin{aligned}\theta_{,i}&=u_{j,ji}\\ \nabla^2 u_i&=u_{i,jj}\end{aligned}\right\} \tag{4.96}$$

Assuming that the body force is negligible, so Eq. (4.95) can be rewritten as

$$[\lambda(t)+G(t)]\bullet \mathrm{d}\theta_{,i}+G(t)\cdot \mathrm{d}\nabla^2 u_i=\rho\frac{\partial^2 u_i}{\partial t^2} \tag{4.97}$$

i.e.

$$\left.\begin{aligned}\rho\frac{\partial^2 u_x}{\partial t^2}&=[\lambda(t)+G(t)]\cdot \mathrm{d}\left(\frac{\partial\theta}{\partial x}\right)+G(t)\cdot \mathrm{d}\nabla^2 u_x\\ \rho\frac{\partial^2 u_y}{\partial t^2}&=[\lambda(t)+G(t)]\cdot \mathrm{d}\left(\frac{\partial\theta}{\partial y}\right)+G(t)\cdot \mathrm{d}\nabla^2 u_y\\ \rho\frac{\partial^2 u_z}{\partial t^2}&=[\lambda(t)+G(t)]\cdot \mathrm{d}\left(\frac{\partial\theta}{\partial z}\right)+G(t)\cdot \mathrm{d}\nabla^2 u_z\end{aligned}\right\} \tag{4.98}$$

Above expressions are the wave equations in viscoelastic granular media, and here θ is the volume strain.

For the simple harmonic plane wave in the viscoelastic granular media, the longitudinal and transverse waves' velocities can be deduced:
the velocity of longitudinal wave:

$$v_{\mathrm{P}}=\mathrm{Re}\sqrt{\frac{\lambda^*(i\omega)+2G^*(i\omega)}{\rho}} \tag{4.99}$$

the velocity of transverse wave:

$$v_{\mathrm{S}}=\mathrm{Re}\sqrt{\frac{G^*(i\omega)}{\rho}} \tag{4.100}$$

where Re is the real part of complex number; λ^*, G^* correspond to λ and G in the viscoelastic granular media.

4.8.3 *Wave attenuation and energy dissipation in the viscoelastic granular media*

In the viscoelastic granular media, because of the non-ideal elastic deformation the energy dissipation of vibrating wave is different from that in perfect elastic media. This is mainly related to the factors such as the characteristics of granular media, the frequency of vibration, etc.

4.8.3.1 Wave attenuation in the viscoelastic granular media

Suppose that $\boldsymbol{P}$ is the propagation vector and $\boldsymbol{A}$ is the attenuation vector, the relation of $\boldsymbol{P}$, $\boldsymbol{A}$ and material parameter can be expressed by:

$$\left.\begin{aligned}&\boldsymbol{P}\cdot\boldsymbol{P}-\boldsymbol{A}\cdot\boldsymbol{A}=\mathrm{Re}(k^2)\\&\boldsymbol{P}\cdot\boldsymbol{A}=|\boldsymbol{P}||\boldsymbol{A}|\cos\gamma=-\frac{\mathrm{Im}(k^2)}{2}\end{aligned}\right\}\tag{4.101}$$

The phase velocity and the maximum attenuation of generalized plane wave are:

$$\boldsymbol{v}=\omega\boldsymbol{P}/|\boldsymbol{P}|^2 \text{ and } |\boldsymbol{A}|$$

While $\boldsymbol{A}\neq 0$ and $\gamma\neq\pi/2$, consequently,

$$\left.\begin{aligned}&|\boldsymbol{P}|=\left\{\frac{1}{2}\left\{\mathrm{Re}(k^2)+\left\{[\mathrm{Re}(k^2)]^2+\frac{[\mathrm{Im}(k^2)]^2}{\cos^2\gamma}\right\}^{\frac{1}{2}}\right\}\right\}^{\frac{1}{2}}\\&|\boldsymbol{A}|=-\frac{1}{2}\frac{\mathrm{Im}(k^2)}{|\boldsymbol{P}|\cos\gamma}=\left\{\frac{1}{2}\left\{-\mathrm{Re}(k^2)+\left\{[\mathrm{Re}(k^2)]^2+\frac{[\mathrm{Im}(k^2)]^2}{\cos^2\gamma}\right\}^{\frac{1}{2}}\right\}\right\}^{\frac{1}{2}}\end{aligned}\right\}\tag{4.102}$$

where γ is the inclination between $\boldsymbol{P}$ and $\boldsymbol{A}$; Im is the imaginary part of complex number; $k=\omega/v$ is the wave number; v is the wave velocity.

If the attenuation coefficients of viscoelastic longitudinal wave and transverse wave are α_{P} and α_{S} respectively, then:

$$\left.\begin{aligned}&\alpha_{\mathrm{P}}=-\omega\,\mathrm{Im}\sqrt{\frac{\rho}{\lambda^*(i\omega)+2G^*(i\omega)}}\\&\alpha_{\mathrm{S}}=-\omega\,\mathrm{Im}\sqrt{\frac{\rho}{G^*(i\omega)}}\end{aligned}\right\}\tag{4.103}$$

It can be seen from the Eq. (4.102) and Eq. (4.103) that the propagation vector, the attenuation vector and the attenuation coefficients of longitudinal and transverse wave are related to the angular frequency and the wave number. Because the wave number depends on the angular frequency, the wave attenuation is related to frequency. The higher the frequency is, the more the attenuation is. In the experiment granular materials used are screes and calcspars, and the vibration source is the mechanical vibrating table. The experimental results are shown in Fig. 4.37 and Fig. 4.38. The auto-power spectrum figures show that the proportion of high-frequency wave(energy) will gradually decrease with the wave propagation, but the proportion of low-frequency wave will gradually increase. It is consistent with the theoretical conclusions of the Eq. (4.102) and Eq. (4.103). Therefore, it is better to choose low-frequency vibration considering the propagation efficiency.

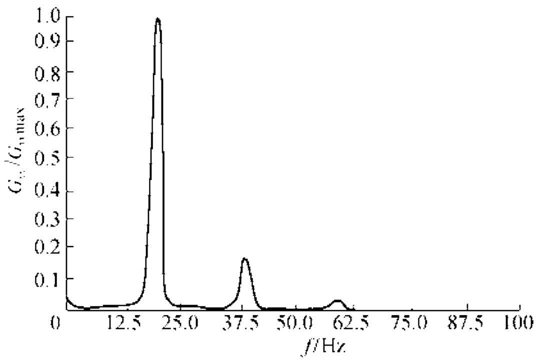

Fig. 4.37 Auto-power spectrum figure of screes

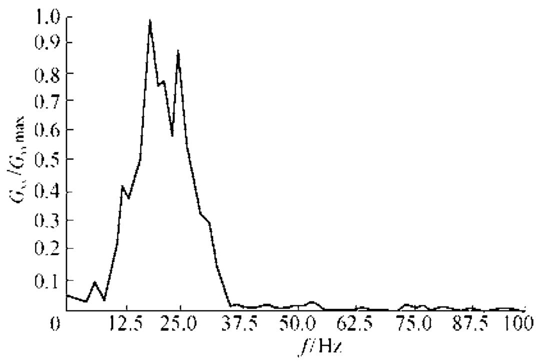

Fig. 4.38 Auto-power spectrum figure of calcspars

4.8.3.2 Selective absorption of frequency

Besides the attenuation property, granules also show the selectively absorption of frequencies. The simplest way to describe the absorption band is using the granular permeation factor:

$$\exp\left[-\left(\frac{f}{f_1}\right)^q \frac{x}{x_1}\right]$$

where f is frequency; f_1 is a constant reference frequency; x_1 is a constant; x is wave propagation distance in granules; q is a parameter on which the verge steepness of absorption band is decided; supposing that x_1 is given, then f_1 is the frequency when amplitude attenuates to 1/e on the distance of $x = x_1$; e is the natural base number. In Fig. 4.39, a set of curves is drawn. They describe the transformations of the following function when parameter value q is changed.

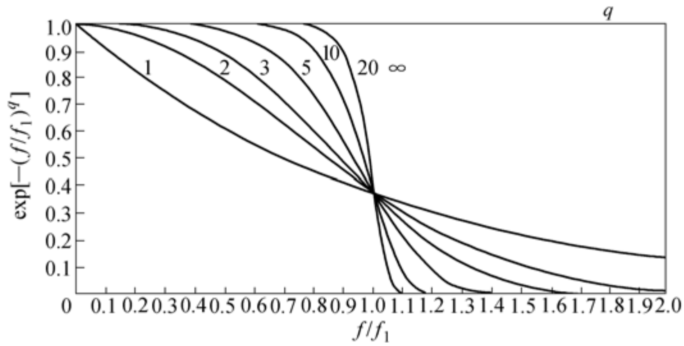

Fig. 4.39 Frequency band figure of spectrum absorbed by granular media

These curves express frequency bands of spectrums which are possibly absorbed by granules. When q becomes higher the verge steepness of the absorption band will increase. However, when q increases infinitely, frequencies less than f_1 will freely penetrate; and others will be perfectly absorbed.

4.8.3.3 Energy dissipation by friction

During the course of wave propagation the relative sliding friction will be caused among granules by the stress. The energy dissipation ΔW is proportional to the relative sliding degree ΔU and sliding surface S. The relation is expressed as:

$$\Delta W \propto \Delta U \cdot S$$

Because the relative sliding degree ΔU is proportional to the wave strain amplitude ε, and the dissipation rate $1/Q$ is proportional to ε as well, then the relation is expressed as:

$$\delta Q^{-1} \propto \delta\varepsilon$$

where δ is the phase angle between stress and strain. In addition, because of the granular sliding viscoelastic modulus $E(\omega)$ decreases with the increase of strain amplitude ε, and the velocity V correspondingly decreases with the increase of strain amplitude ε. The above-mentioned relations can be expressed as:

$$\delta E(\omega) \propto -\delta\varepsilon \qquad \delta V \propto -\delta\varepsilon$$

Observations in the laboratory show that when the strain in sandstone is greater than 10^{-6} ($\varepsilon > 10^{-6}$), Q and the velocity are irrespectively related to the strain ε. However, when the strain is less than 10^{-6} ($\varepsilon < 10^{-6}$), Q is not related to the strain ε. It indicates that energy dissipation is not very obvious if the strain amplitude is less than 10^{-6}.

5 Vibrating Liquefaction of Saturated Granules

5.1 Liquefaction Problem

Liquefaction of saturated granules (e.g. broken rocks, sandy soil and tailings, etc.) is a phenomenon that granules show some characters similar to liquid phase and lose carrying capacity completely under the action of dynamic load. Something like seismic wave, vehicle running, machine vibration, piling, explosion, etc. could lead to liquefaction of saturated granules[6~9]. Vibration can partly, even fully, break saturated granules down. Vibration results in acting some kind force of inertia and disturbances on particles, which is responsible for the change from solid state into liquid state[2,54]. Vibrating liquefaction is a harmful phenomenon in the field of civil engineering, however its prevention and control have been provided.

The phenomenon of liquefaction influences greatly the human activities. Sometimes it is ruinous that causes serious property lost. Hence human race have already attached importance to it since long time ago. In the Song Dynasty of China, Shen Kuo, a scientist, described the liquefaction effect of sandy soil in his famous encyclopedia *Meng Xi Bi Tan*[137]: "In Fuyan an army lost many soldiers when they were passing through a sandy river, that was named *Fanhe* by Yue's people and quick sands by northern Chinese. In my first time to across the *Wudinghe* river, we encountered quick sands. People and horses passed through quick sands like walking on a curtain, because quick sands shook in a large field. In some areas when the troops and chariots stepped on, they sank immediately, and there were at least hundreds of soldiers sank and lost. Some people also called this phenomenon as flowing-sands." The description above provides lively picture of the liquefaction of saturated sandy soil.

There are many people having studied or studying the liquefaction of saturate granules in the world[138~173]. In 1925, Terzaghi put forward the effective stress theory, which is important for subsequent researchers to explain the liquefaction phenomenon. In 1936, Casagrande put forward the concept of the critical porosity ratio, and in 1970's he put forward the concept of the flowing structure in terms of the research findings of Castro who was his doctoral student. In 1954, Moslov, a Soviet Union scientist, put forward the permeation theory of the stability of dynamic failure and the concept of the critical acceleration. In China Wang Wenshao summarized the liquefaction forms as the sand boil, the flow slide and the cyclic mobility, and explained their mechanisms. This work mainly refers to flow slide. If not specified otherwise, the liquefaction described here only denotes the flow slide.

The liquefaction always acts with some external phenomena, such as the eruption of water and sands from the ground, the instability of foundation, the large area landslide, the building falling apart by vibration, etc[155~163]. The problem about liquefaction is a hot issue in geotechnical engineering. In the last decades, with the development of soil dynamics, a number of problems have been discussed extensively, such as the mechanism of liquefaction, its influencing factors, the criterion of liquefaction probability, the preventive methods of liquefaction, etc. In the meantime, significant progress has been gained on this topic[146~172].

5.1.1 *Gradual progress of the critical porosity ratio*

In 1925, Terzaghi founded the principles of soil mechanics and put forward the effective stress theory for the granular shear strength, and this theory is important for subsequent researchers to explain the liquefaction phenomena[68,155~167].

In 1936, Casagrade believed that, in course of the shear deformation, there are shear-expansion (for dense material) and shear-compaction (for loose material) in the non-cohesive soil, and there is a critical density between these two[68,150~158]. In its critical state, the soil mass has no volume deformation if it flows or has big shear deformation. When its density is less than the critical density for the saturated non-cohesive soil medium, the pore water can't discharge in time during the course of continuous shearing. Also the pore water pressure will increase and the shear strength of effective stress will decrease, hence the medium will be unstable, even generate a flow slide. On the other hand, in any other situations there is no hazard of flow slide. Casagrande used the compression curve for non-cohesive soil, i.e. the relationship between the pressure and the porosity ratio, to explain the mechanism of increment of pore water pressure and its relationship with the critical density during the course of shearing in saturated loose sands.

In 1948, Terzaghi, et al, put forward the concept of the critical porosity ratio e_{cr} in the book *Practical Soil Mechanics* in terms of the Casagrande's theory. The critical porosity ratio is a kind of porosity ratio corresponding to the critical density. The researchers thought that the critical porosity ratio e_c relates to the normal stress σ_n on the shear surface[68,157~163]. In 1948, in the book *Ground-work of Soil Mechanics*, Taylor probed into the detail of the test measurement methods of the critical porosity ratio of sandy soil, and compared three test measurement methods, such as the original test measurement method of Casagrande, Fidler's test measurement method in 1940, viz, the constant σ_3 method, and the test measurement method of constant volume. Moreover, Taylor believed that the experimental methods have strong influences on the critical porosity ratio, and the experimental methods relate closely to the liquefaction of sandy soil under the sudden impacting force. Although, he doubted whether the experimental results can show the true critical porosity ratio.

Table 5.1 Experimental results of the critical porosity ratio

σ_3 and σ_{3P} (6.9 kPa)	Value of e_{cr} by different methods		
	Casagrande method	Constant σ_3 method	Constant volume method
15	0.84	0.81	0.77
30		0.74	0.69
60	0.74	0.69	0.65
120		0.63	0.59

Notes: $\sigma_3 = \sigma_1$ (p=0) is the beginning ; σ_{3P} is the value of σ_3 (p=0) in the peak dot $(\sigma_1/\sigma_3)_{max}$.

In 1922, Close, et al, described the seismic hazard of the loess area that happened in 1920 in Gansu, China. The soil clods and the soil on the earth's surface spewed like the flowing water, forming many whirlpools and turbulence like the vortex swirl formed by the rapid flow[68]. In 1950, Terzaghi thought that the reason of this phenomenon is that the violent impact of seism destroys the structure of loess, in which cementation of particles is weak.

In 1948, Terzaghi, et al, put forward the concept of the spontaneous liquefaction. For the spontaneous liquefaction, the structure of sandy soil is breaking down, at the same time there is a sudden temporary rise in pore water pressure. The sandy soil is temporarily in the state of flowing and stopping; the concentration of liquids is very high; the bearing capacity is close to zero. Once the flow stops, a new sedimentary texture forms, and its density will not ever be more than the one of original state. The researches considered that the critical porosity ratio cannot be used to forecast this spontaneous liquefaction, and more attention should be given to the failure of structure of sandy soil.

5.1.2 *Theory of the critical acceleration*

Based on Barkan's experimental results of vibrating compaction of sandy soil (1948), the relationship curve between the ratio of vibrating velocity $\eta = a/g$ and the porosity ratio of sandy soil e was drawn in Fig. 5.1 and Moslov (1954) put forward the concept of the critical acceleration a_{cr}[68]. For a certain porosity ratio n ($n = \dfrac{e}{1+e} \times 100\%$), when the sands are vibrated or impacted in the vessel (such as tube and box), they can be compacted (i.e., n decreases) only when the acceleration a is larger than critical value a_{cr}. There is no compaction if $a<a_{cr}$. Moreover, there is some kind relationship between a_{cr} and n. Because of the action of vibrating compaction, the pore water must be discharged from the saturated sands, so Moslov put forward the permeation theory of dynamic failure of stability in the saturated sands.

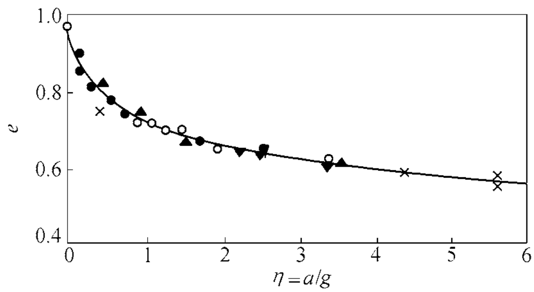

Fig. 5.1 Relation between acceleration and porosity ratio

5.1.3 *Theory of initial liquefaction*

In 1966, Seed, et al, published their research findings after Niigata seism took place and put forward a concept of the initial liquefaction. They utilized the cyclic triaxial test to simulate the saturated sands of foundation, and studied the liquefaction under the horizontally cyclic shearing action of seismic wave[68,155~161]. Seed's definition of the initial liquefaction and the corresponding relation between the ratio of cyclic shear force and the cycle index N_L were widely cited to predict the seismic liquefaction of saturated sands, and established some empirical correlations among the static sounding, the standard penetration test, the relative density and earthquake scale[68].

Seed often regarded the initiation of liquefaction $(p=\sigma_3)$ and the amplitude of axial stress ε_{ac} or the ultimate value of stress ε_a (e.g., $\varepsilon_{ac}=\pm 2.5\%$ or $\varepsilon_a=5\%$) as the parameters of liquefaction and failure criteria of saturated sands. These two parameters often appear simultaneously, and in his book he frequently used the liquefaction and failure at the same time. His criteria was cited by other researchers. However, when the initial liquefaction is tested in the laboratory, it is obviously influenced by the preparation process of test specimen. For example, in Fig. 5.2 the $\sigma_{ac}/2\sigma_0'-N_{L/f}$ curves of experimental results are obtained by eight kinds of different methods. Although the density is the same (d_r=50%), and the consolidation pressure is also the same (σ_0'=55.2 kPa), but the eight curves differ greatly from each other[68]. Therefore, the relationship between the cyclic shear force and the cycle index for the initial liquefaction is not unique, and the influence of in-situ soil composition must be considered.

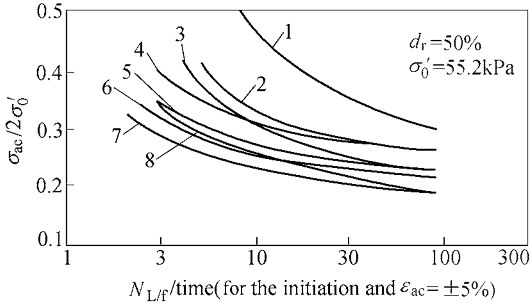

Fig. 5.2 Results of cyclic triaxial test for different methods

1—For high frequency vibration with moisture; 2—For impaction with moisture; 3—For ramming with moisture; 4—For low frequency vibration without moisture; 5—For high frequency vibration with out moisture; 6—For wet sands from water; 7—For wet sands from air; 8—For ramming without moisture

5.1.4 *Theory of cyclic liquefaction*

In 1979, Casagrande thought that the transient phenomenon ($p=\sigma_3$) for Seed's cyclic triaxial test would not occur in practical operation[68,160~166]. Based on the experimental results, he proved that the distribution of relative density after the cyclic triaxial test is vastly different; so he put forward the concept of cyclic liquefaction, which was popularly called cyclic mobility. He considered that the cyclic liquefaction is a kind reflection for the dilative sandy soil. This is true only if the peak value of pore water pressure in each cycle instantaneously rises and is equal to the ambient pressure under the action of cyclic load of triaxial test. But the actual liquefaction (or Abbr. liquefaction) is some kind reflection of flow slide when the saturated loose sands are impacted and the strength basically is lost.

In addition, based on his concept of the critical porosity ratio put forward during 1935~1938, and the research findings of partial failure of Fort Peck Dam, Casagrande further put forward the supposition of the flow structure of sands liquefaction. He thought that this structure only appear while flowing. Therefore, he improved his former experimental method of critical porosity ratio test and put forward the loading method of dead-load increments in the consolidated triaxial test without drainage. Using this method the flow structure will appear.

5.1.5 *Dynamic triaxial test of liquefaction*

In 1960s Wang Wenxi considered that Moslov, et al, used the cylinder or sand box as the experimental conditions of soil vibrating liquefaction do not conform to the actual stress state in sandy foundation or slope. He suggested that the experiment should use a special triaxial compression apparatus of dynamic load to perform adequately[68,156~161]. Utilizing the inertia vibrating triaxial apparatus fixed on the vertical vibrating table,which is developed by China Academy of Science of Water Conservancy and Hydroelectricity, one kind of fine sands or mud is consolidated and vibrated without drainage (where the ambient pressure is σ_3, the axial pressure is σ_1, and the pore water pressure p=0). The amplitude of dynamic stress: $\sigma_{ac} = (a_v / g)$ σ_1, where a_v and g are the acceleration amplitude of vertical vibrating table and the gravitational acceleration respectively. He found that under the action of vibration without drainage the maximum mean pore water pressure ratio u/σ_3 is influenced by the following factors: the consolidation stress ratio σ_1/σ_3, the ambient consolidation stress σ_3, the vibrating acceleration a_v and the dry unit weight of soil γ_d (shown in Fig. 5.3).

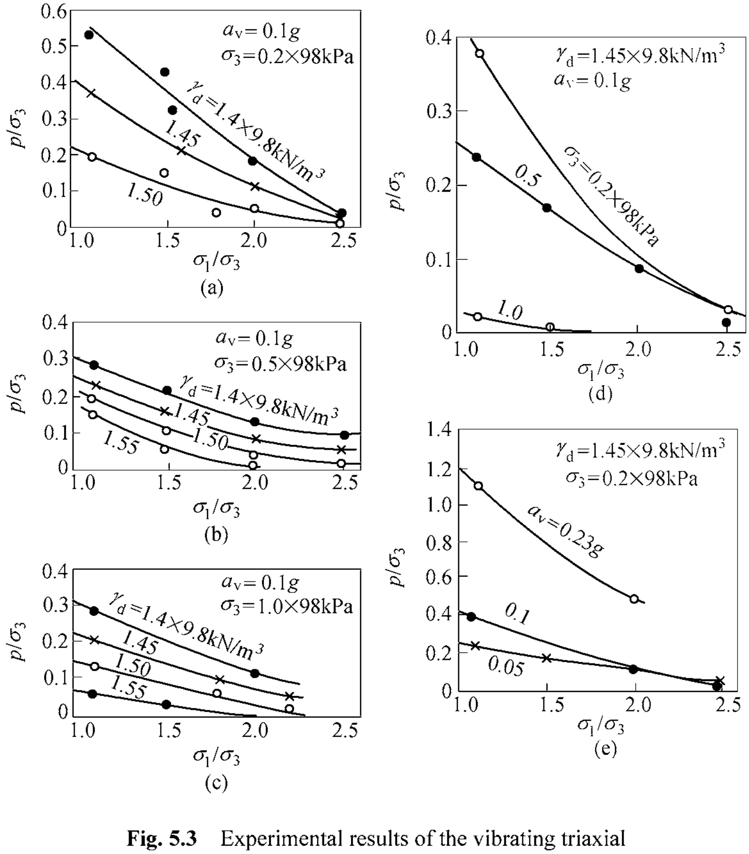

Fig. 5.3 Experimental results of the vibrating triaxial test with consolidation without drainage

The consolidation triaxial vibrating test without drainage only measures the change of pore water pressure caused by the vibration in the enclosed surrounding for the saturated sands, but actual situation is often different. Therefore, in 1963, Wang Wenshao put forward the diffusion and dissipation of pore water pressure system where the saturated sands were vibrated. Later (in 1964, 1980 and 1981)[68, 161,167], he further improved his theory. In fact, he improved Moslov's one-dimensional dynamic permeation theory and extended it to the three-dimensional problem, where the basic volume compatible equation is:

$$\frac{1}{\gamma}(k \operatorname{grad} p_{\mathrm{d}}) = -\frac{\partial n}{\partial t} \tag{5.1}$$

where p_{d} is the supplementary pore water pressure caused by the vibration; $\frac{\partial n}{\partial t}$ is the rate of change of the porosity ratio in the saturated sandy soil.

According to the characteristics of the soil vibrating compaction and spring, and considering the re-distribution of stress, the following relations are established: without the residual spring:

$$\frac{\partial n}{\partial t} = \alpha \frac{\partial}{\partial t}(p_{\mathrm{d}}^* + \sigma_{\mathrm{mo}} - p_{\mathrm{d}}) \tag{5.2}$$

with the residual spring:

$$\frac{\partial n}{\partial t} = \beta \frac{\partial}{\partial t}(\sigma_{\mathrm{mo}} - p_{\mathrm{d}}) \tag{5.3}$$

where p_{d}^* is the supplementary pore water pressure caused by the vibration in the closed position; α and β are the soil compaction coefficient and spring coefficient; σ_{mo} is the original mean general normal stress.

In addition, the following indicator function can be used to judge whether there is the existence of residual spring:

$$A = \frac{\partial}{\partial t}\left(p_{\mathrm{d}} - \sigma_{\mathrm{mo}} - \frac{p_{\mathrm{d}}^*}{1 - \dfrac{\beta}{\alpha}} \right) \tag{5.4}$$

5.2 Effective Stress Principle and Mechanical Mechanism of Vibrating Liquefaction

5.2.1 *Effective stress principle*

The effective stress principle is very important in the soil mechanics[155~165]. A certain horizontal plane whose area is A in the granular medium is considered (shown in Fig. 5.4). The stress acting on the plane is σ, which is generated by the inter-action of the granules weight, the hydrostatic pressure and the external load P, and σ is termed as the general stress. One part of this stress is carried by the intergranular contacting surface, and it is termed as the effective stress; the other part is carried by the pore water and gas, as the pore water pressure. To analyze the part above the *a-a* section, it is assumed that the normal stress acting on the contacting surface is σ_{s}, the total area of all contacting surfaces is A_{s}, the pore water pressure is p_w and the corresponding area is A_w, the gas pressure is p_a and the corresponding area is A_a. The following formula is obtained according to the soil equilibrium condition:

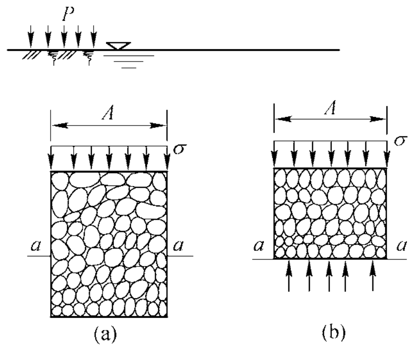

Fig. 5.4 Effective stress principle

$$\sigma A = \sigma_s A_s + p_w A_w + p_a a_a \tag{5.5}$$

For the saturated granules, both p_a and A_a are zero in above formula, hence:

$$\sigma A = \sigma_s A_s + p_w A_w = \sigma_s A_s + p_w (A - A_s)$$

or

$$\sigma = \frac{\sigma_s A_s}{A} + p_w \left(1 - \frac{A_s}{A}\right) \tag{5.6}$$

Bishop believed that A_s/A is generally about 0.01～0.03, so:

$$\sigma = \frac{\sigma_s A_s}{A} + p_w \tag{5.7}$$

where $\frac{\sigma_s A_s}{A}$ is the effective stress which is often expressed as $\bar{\sigma}$, if the pore water pressure p_w is expressed as p, Eq. (5.7) is simplified to:

$$\sigma = \bar{\sigma} + p \tag{5.8}$$

For the partial saturated soil, the following formula can be obtained based on Eq. (5.5):

$$\sigma = \frac{\sigma_s A_s}{A} + p_w \frac{A_w}{A} + p_a \frac{A - A_w - A_s}{A} = \bar{\sigma} + p_a - \frac{A_w}{A}(p_a - p_w) - p_a \frac{A_s}{A} \tag{5.9}$$

If $p_a \frac{A_s}{A}$ is ignored, the effective stress formula for the partial saturated soil is:

$$\bar{\sigma} = \sigma - p_a + \beta\ (p_a - p_w) \tag{5.10}$$

where $\beta = A_w / A$, which is ascertained by the granular type and the degree of saturation.

Simply, the effective stress principle can be concluded that:

(1) The effective stress of granules $\bar{\sigma}$ is equal to the difference between the total stress σ and the pore water pressure p.

(2) The effective stress of granules controls the granular deformation and the

strength.

5.2.2 *Mechanical mechanism of vibrating liquefaction*

5.2.2.1 Mechanical mechanism of vibrating liquefaction for the granular structure's disintegration

The low and middle dense saturated granules will cause the granular structure's sudden disintegration under the unidirectional or repetitive shear force, so the granules in fact will suspend in the pore water[168~173]. If the ground is horizontal, the granular structure's sudden disintegration can make the effective stress decrease to zero while the saturated granules become the "flowing sands" .The state of the flowing sands depends on the critical gradient of upward seepage $i_{cr} = \frac{\rho_s - 1}{1+e}$, where ρ_s is the granular density; e is the porosity ratio.

The experimental results of cyclic shearing without drainage for different amplitude of shear stress are shown in Fig. 5.5, where γ is the shear strain, τ_d is the shear stress, and p_d is the pore water pressure. If the liquefaction is caused by the cyclic shear stress, the granular structure will have sudden disintegration; at that time the shear strain and the pore water pressure will increase suddenly. Before the liquefaction take place the increments of the shear strain and the pore water pressure can be ignored. In the cyclic shear test without drainage the irreversible change of granular structure will cause this formation and the increment of excess pore pressure. It is probably related to the intergranular microscopic slip. When the cyclic shear stress generates this irreversible change of granular structure, the structure will tend to shrink. However, the volume of saturated granules without drainage is unchangeable. The granular framework has this tendency of shrinkage, but in fact it also has the properties of invariability, so this contraction leads to the increase of pore water pressure.

5.2.2.2 Mechanical mechanism of vibrating liquefaction for the low-plastic cohesive soil

Both in-situ investigation and the simulation experiments show that the liquefaction occurs not only in the sandy soil but also in the low plastic or cohesive soil (containing a vast amount of sand, powder particles and a little cohesive particles). Some laboratory testing data show that the pore pressure and the strain of the saturated low-plastic cohesive soil are similar to the dense sands under cyclic load[169~173]. For the occurrence of strain, it develops earlier but its velocity gradually decreases and tends to become zero. That is to say, during the course of the cyclic loading the saturated low-plastic cohesive soil does not behave similar to the loose or middle-dense saturated sands which have the structure's sudden disintegration when the shear strain and the pore water pressure suddenly increase.

Especially, for the low-plastic cohesive soil and for the low cyclic load ratio, the development of pore pressure is similar to the dense sands. According to the characteristics of the development of pore pressure and strain for the saturated low-plastic cohesive soil they also have certain shear strength and shear modulus after the initiation of liquefaction.

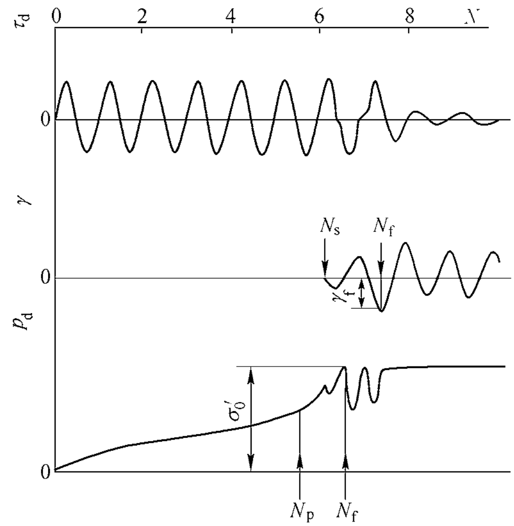

Fig. 5.5 Cyclic simple shear test without drainage

5.2.2.3 Cyclic stress without drainage after the increase of pore water pressure

For the compact saturated non-cohesive soil, the pore pressure can also gradually increase to the level that the cyclic pore pressure ratio is equal to 100% under the condition that the cyclic shear stress is slightly less than the static strength. The reason is that even if for the compact soil, the tendency of nonreversible change of the granular structure is also shrinkable when the shear stress is low. Only when the shear strain is more than a limited value, the soil begin to expand, so the pore pressure which has increased begins to decrease and the effective stress bounces back correspondingly. Therefore, the compact saturated non-cohesive soil still has certain shear strength after the initiation of liquefaction, and that the effective stress is equal to zero is only an instantaneous phenomenon. That is to say, they still have certain shear modulus after the initiation of liquefaction.

Based on P. De. Alba's experiment (in 1976), the relative density of homogeneous fine sands is 80%, the maximum strain of the liquefaction is 10% for 10 stress cycles. But when the relative density is 72%, 57% and 92%, the corresponding maximum shear strain is 15%, 25% and 5%. He considers that when the original relative density is less than 46%, the continuous liquefaction with big strain will occur under the cyclic. When the original relative density is more than 46%, the liquefaction with limited strain will occur. This liquefaction is also termed as the cyclic liquefaction (A. Casagrande, 1975), the cyclic mobility (G. Castro, 1975) or the initiation of liquefaction with limited strain (H. B. Seed, 1976)[169~173].

5.3 Experiments of Liquefaction

5.3.1 *Experimental device for granular vibrating liquefaction*

A set of additional device for experiment has been designed to study the problems relating to the vibrating liquefaction of fine-ores and tailings on the basis of DSA-1 type direct shear apparatus, including the model of a straight tube, model of curved tubes and model of a sandbox[2,56].

5.3.1.1 Model of a straight tube

The size of the model is ϕ 50 mm×300 mm(length). This model is a transparent circular plexiglass tube and has been adopted to observe the motion of granules easily during the course of vibration. The pore water pressure within the granules in the plexiglass tube is transmitted via the sensor of pore water pressure, amplified by dynamic resistance-strain apparatus, and then monitored by a *x*-*y* function recorder, which is used to delineate the change of pore water pressure in the course of vibration liquefaction.

5.3.1.2 Model of curved tube

This model is the combination of an elbow of 90° and circular plexiglass tubes connected to the elbow's ends. The size of the model is 2×50 mm (diameter)× 150 mm(length). It is applied to study the effect of vibration on pore water within granules and the blockage created by the curved tubes.

5.3.1.3 Model of a sandbox

The sandbox is also made up of plexiglass whose thickness is 10 mm. The size is 280 mm×280 mm×300 mm. Experiments with the Sandbox is divided into two parts: one is to test the whole sandbox subjected to vibration, namely, the whole sandbox is placed on the vibration platform in order to observe the physical changes and the degree of subsidence due to liquefaction; the other is to test the platform's influence on the sandbox. In this situation, the sandbox is fixed, a metal plate whose size is 3 mm×25 mm×30 mm is inserted into the sandbox to investigate the corresponding effects of vibration and the conditions of liquefaction.

5.3.2 *Experiments of the model of straight tube*

Some fine-ores and tailings that contain water were inserted into the straight tube, which was then vibrated. At the same time the movements in the pipe was observed, and the change of pore water pressure in sample granules was noted. Dynamic pore water pressure is a prime factor to judge the liquefaction phenomena and provides the following characters of its transition[2,3]:

(1) With the vibration, the pore water pressure increases rapidly with the filling density. It tends to be stable (as shown in Fig. 5.6). This indicates that the granular liquefaction has taken place under the vibration.

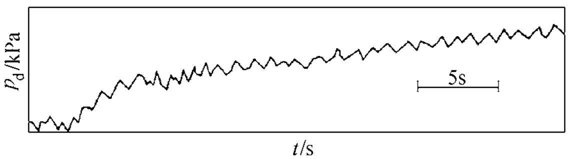

Fig. 5.6 Change of pore water pressure

Water content of tailing: ω_c=35%; Unit weight: γ=19.0 kN/m^3;

Frequency: f=20 Hz; Amplitude of vibration: A=±1 mm; Acceleration: a=1.579g

(2) The pore water pressure rises quickly; moreover, it shows that the oscillation property, which has certain frequency and amplitude related to the character of the vibration source (as shown in Fig. 5.7).

(3) The change of acceleration significantly influences the change of pore water pressure. The increase of acceleration leads to high increment of pore water pressure. The experiments show that when the acceleration increases by 4 times, the maximum pore water pressure increases by 4.7 times, and the wave amplitude increases by 4.3 times (shown in Fig. 5.8). The increment of vibration acceleration indicates that the samples gain more shock wave energy.

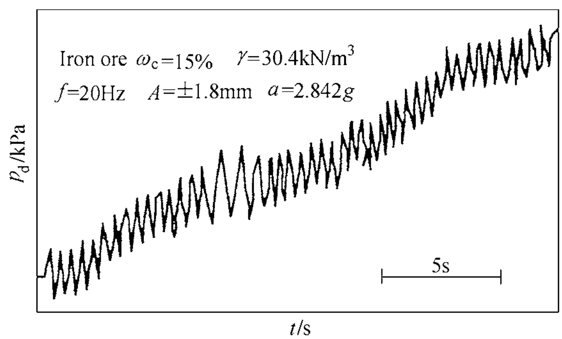

Fig. 5.7 Fluctuation of pore water pressure

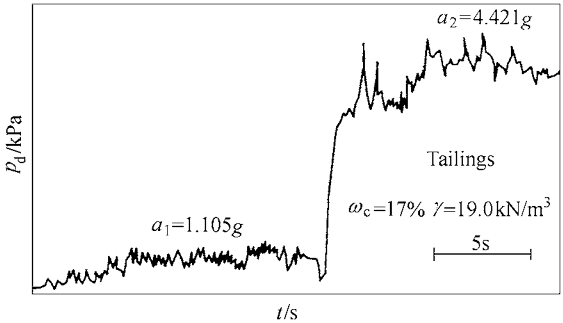

Fig. 5.8 Influence of acceleration on pore water pressure

5.3.3 *Experiments of the model of curved tube*

The elbow of the tube is the place blockage takes place frequently because of rather large resistance to granules' flow. It is a common experience that elbows present difficulties to granular movement in pipe transportation. Two aspects of experimental research have been performed for this purpose. One is the dynamic pore water pressure measured under vibration action, and the delineation of probability of vibrating liquefaction. The other is to artificially block the angled curved tube in order to obtain a certain unit weight of the granules in the curved tube; then the effect of vibration on blockage clearance is observed. The experimental circumstances are listed below[2,56]:

(1) The change of pore water pressure in test is similar to that of the experiments of the straight tube model (shown in Fig. 5.9).

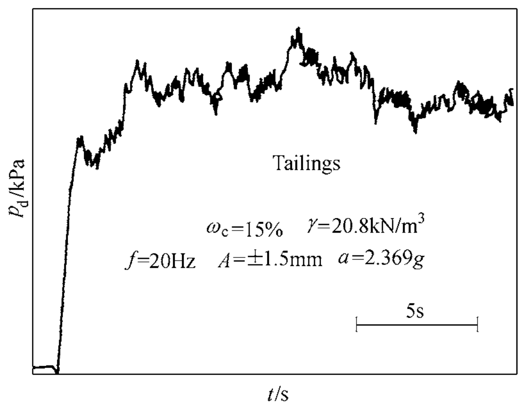

Fig. 5.9 Change of pore water pressure in the curved tube

(2) The effect of vibration on the blockage of curved tube.

In order to get certain dry unit weight, granules are compacted into the tube.

As marked the two ends with A and B, There is an empty passage near the end A facing in vertical direction. Vibration at different directions has been respectively applied (shown in Fig. 5.10). VD_1 is vertical to the axis of the end A, and parallel to the axis of the end B, VD_2 is vertical to axis of end B and parallel to that of the end A.

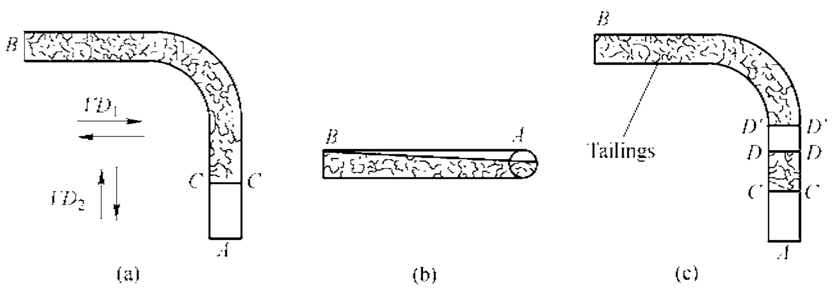

Fig. 5.10 The blockage clearance by vibration in an angled tube

(a) Before clearance; (b) In clearance; (c) After clearance

1) The clearance of the blockage by liquefaction

Each one of the vibration directions of VD_1 or VD_2 can liquefy the granular sample quickly. The sample turns into a suspended liquid state and flows from the face CC to the end A. It will form a near horizontal slope in a short time (shown in Fig. 5.10b), and then the blockage at the elbow will be cleared. Different vibration directions can bring various effects toward the clearance of blockage.

2) The clearance of blockage by "transportation"

Because of longer duration of blockage, the granular water content has been gradually decreased and is unable to meet the requirements of liquefaction criteria. At this point the liquefaction method cannot be used to clear blockage.

As experiments have stated, VD_1 direction of vibration cannot dislodge the blockage even though the vibration duration is longer than 2 minutes. The face CC is still stable. On the other hand, VD_2 direction of vibration averagely needs only 25 seconds to make the column between the face CC and the face DD to move, then the face $D'D'$ to move as well. The motion gradually extends to the elbow. Fig. 5.10c has shown that "transportation" action of vibration has removed the blockage at the elbow.

5.3.4 *Sandbox experiments*

5.3.4.1 Vibration experiments of whole box

The settling velocity of natural subsidence within 2 hours is 0.015 mm per minute, while the average settling velocity is 2.125 mm/min within the initial 4 minutes under vibration action. The latter is 141 times as much as the former. The declining rate gradually tends to become stable with the lapse of time. It appears that there is no linear relationship as shown in Fig. 5.11 shows. The increase of subsidence symbolizes higher density of tailings. When the height of tailings h_1 falls, the height of covering water face rises. However, each has its own extreme value and approaches an asymptote figure.

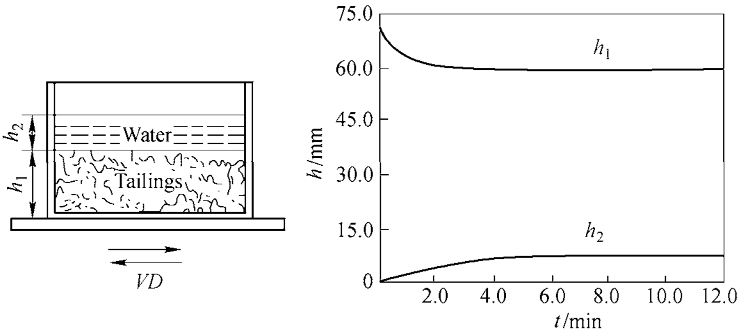

Fig. 5.11 Relationship between the subsidence of tailings by vibration and time

(a) Vibration experiments of whole box; (b) Experimental results

5.3.4.2 Experiments of sandbox-vibration board

When moisture content in the tailings is 10 percent

From the results of shear experiments, the shear strength of tailings is fairly high and has good stability. Vibration can cause subsidence of sand mass and make cracks occur on its surface. While the vibrating action is ceased, a stable pore with smooth wall will emerge in the tailings. In subsidence area, with the pore formed by vibration board as its center, the tailings' density is increased. so it is difficult to dislodge the tailings. The subsidence area is a revolving paraboloid with its center caved in on the whole sand surface (shown in Fig. 5.12).

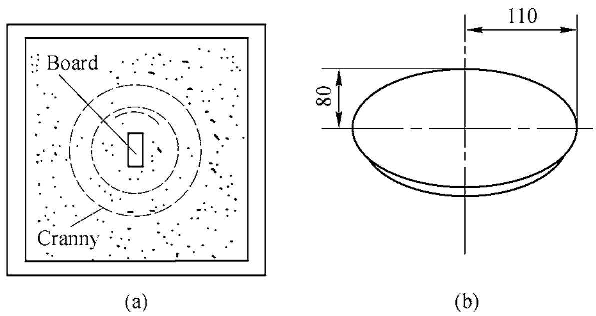

Fig. 5.12 Vibrating subsidence area of tailings

ω_c=10%; γ=15.5 kN/m^3; f=20 Hz; A=±3 mm; a=4.70g; t=8 min

When the moisture content in tailings is 18 percent

A clearly visible motion area emerges in the tailings under the intense agitation by the vibration board, causing considerable turmoil in tailings which then sink gradually. The moisture in the tailings flows up and gathers at the upper part of the sandbox and the tailings will become more compact with extended vibration duration. The visible motion area will become rather smaller, and a stable motion zone will form around the vibration board (shown in Fig. 5.13a). The scope of motion zone relates to the vibrating acceleration, and these two are proportional (shown in Fig. 5.13b). Fig. 5.14 shows that the scope of the wave propagation and its influence.

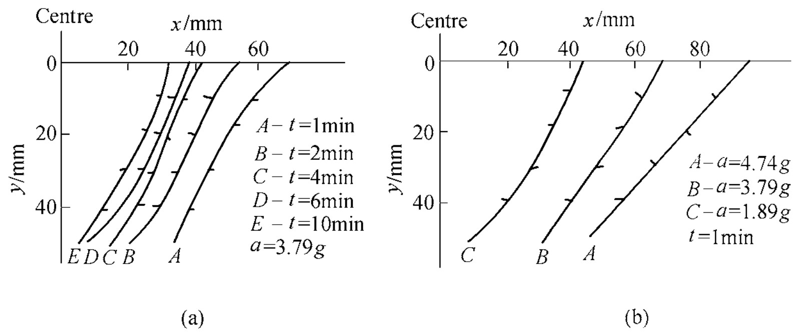

Fig. 5.13 Influencing scope of vibration

Tailings: ω_c=18%; γ=18.8 kN/m^3; f=20 Hz; t—Time; a—Acceleration

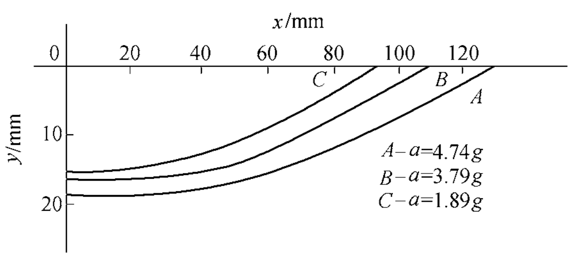

Fig. 5.14 Radius of vibrating subsidence area

5.4 Main Factors Influencing the Granular Vibrating Liquefaction

The vibrating liquefaction of saturated granules is usually affected by many factors. Researchers have done many experiments and have conducted theoretical researches. Synthetically, the factors that influence the vibrating liquefaction of saturated granules are mainly[7,155~173]:

(1) The initial stress. Mainly refers to the shear stress and normal stress

before the loading and their combined effects.

(2) The granular characteristics. Mainly refers to the structure characteristic, the characteristic of granules and the characteristic of density.

(3) The restraining pressure and the boundary deformation.

(4) The dynamic load and the drainage. The dynamic conditions are mainly the direction of loading force, the wave types, the amplitude of vibration, duration, etc. The drainage conditions are the path of seepage, permeability, boundary condition, etc.

(5) Other factors. For example, the earlier history of stress, the process of granular formation, the inherent gas content, etc.

5.4.1 *Initial stress*

The granular initial stress is very important for the occurrence of the vibrating liquefaction. In the lateral confinement test on the horizontal surface, the stress state is often denoted by the overlying effective pressure σ'_{v0}. The bigger is σ'_{v0}, the smaller is the probability of liquefaction. Moreover, the relation between σ'_{v0} and the critical acceleration is linear. Under the experimental condition of tri-axial test, the initial state of stress is often expressed as the initial consolidation stress ratio $K_c = \sigma_{1c} / \sigma_{3c}$ and the initial shear stress ratio τ_0 / σ_0 The bigger K_c is, the stronger the ability of anti-liquefaction is. When the consolidation ratio K_c>1.0, the granular media are consolidated by deviatoric stress. At this stage the inner granules have a certain initial shear stress and its strength is slightly more than the strength when K_c=1 (the initial shear stress is zero). When K_c=1, vibration makes the direction of the shear stress changeable again and again; but when K_c>1, the shear stress doesn't change direction but magnitude. It is believed that if K_c is far more than 1, the initial shear stress will be very large. Under the dynamic stress, the shear stress is probably more than the residual shear strength, and the strength of anti-liquefaction will even decrease further. Therefore, the influence of shear stress can be divided into two different situations. When $\sigma_d / 2\sigma_{3c} > 0.5(K_c - 1)$, the shear stress will be reversed once in each dynamic loading cycle, and the initiation of liquefaction will occur. On the other hand, when $\sigma_d / 2\sigma_{3c} < 0.5(K_c - 1)$, the dynamic and static stress don't change the direction of shear stress, namely, the maximum principal stress is still the static axial stress, and the hydraulic pressure under the cyclic load will not increase to such a high level that could cause the initial liquefaction. In addition, Lee and Seed believed that for different relative densities d_r the dynamic shear stress (especially the horizontal and initial shear stress) ratio probably increase, decrease or unchanged (shown in Fig. 5.15). Using the maximum shear strain to express the strength, if the initial shear stress increases, the strength will increase and does not relate to d_r and shear strain[6~9].

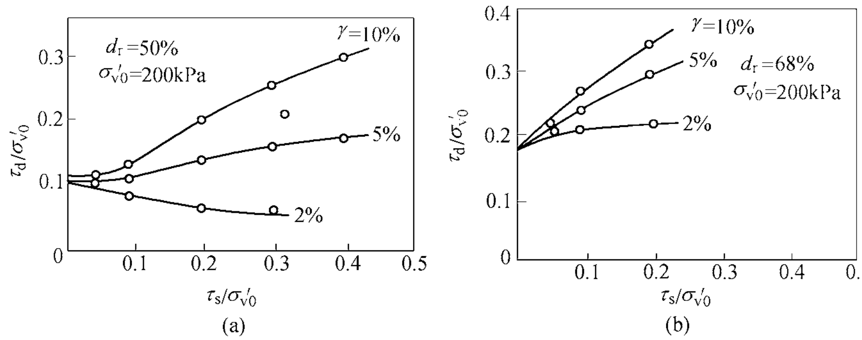

Fig. 5.15 τ_s/σ'_{v0} vs τ_d/σ'_{v0}

5.4.2 *Granules' properties*

In Haicheng's earthquake (in 1975, earthquake magnitude: 7.3) and Tangshan's earthquake (in 1976, earthquake magnitude: 7.8) happened in China, the liquefaction of the foundation soil had widely generated. According to the investigation data, liquefaction mainly occurred in non-compact sandy soil, low-plastic cohesive soil(such as ancient river-way and floodplain), coastal region, shallow sea, etc. Japan earthquake record shows that liquefaction phenomena mostly occurred in new alluvium and un-compacted sandy fillings. Furthermore, in 1977 S. N. Hoose reported that the new delta deposit is also very sensitive to cause liquefaction; but the soil which have a great deal of sticky granules and the prepleistocene sediments often have no liquefaction tendency[167~173].

In the past decades researchers had done many liquefaction experiments in the laboratory using uniform graded fine sands[156~164]. The experiments show that this type of sand has the lowest ability of anti-liquefaction (e.g., K. L. Lee & J. A. Fitton, in 1969; H. B. Seed & W. H. Peacock, in 1971; R. T. Wong, etc, in 1975). It is reported that the under-water gravels of earthen dam will liquefy under the action of seism load[173]. The investigations of many earthquake disasters show that the landslip of protective layer of earth dam's inclined wall is caused by the liquefaction of under-water gravels during the seism process. The investigations also show that even in the area where earthquake intensity is not very high (e.g., 6 or 7 scales) the landslip will take place. In addition, the coarse materials (diameter> 5 mm), the fine granules (diameter =0.5~0.1 mm) and the clay content (diameter < 0.1 mm) obviously influence the characteristic of liquefaction. Particularly while the clay content is high the ability of anti-liquefaction significantly decrease. However, there are many different opinions about the influence of granular diameter on the liquefaction. In 1975, R. T. Wong, etc., thought that the high ability of anti-liquefaction of the coarse gravels and sands in laboratory results was probably caused by the compliance effect of film[173].

The parameters such as non-uniformity coefficient, mean grain size and sticky particles' content are decisive factors influencing granules' characters. Lots of findings show that the bigger are the granules, the higher is the dynamic stability[6~8]. Therefore, the possibility of liquefaction will increase in terms of the following sequence: coarse granules, middle granules, fine granules, powdery granules. The granules in the same grade face the difficulty to liquefy when the non-uniformity coefficient is in excess of 10. However, the content of the granules that lack middle sizes of granules or pebbles and other large granules is not enough to form a stable framework. The media whose main component is fine granules have lower ability of anti-liquefaction, and the liquefaction of Miyun's dam is a typical example that its main components are sands and gravels. When the content of sticky granules increase to a certain degree (e.g., in excess of 10%), the granular stability will increase. Therefore, the light loams commonly have higher dynamic stability than the sandy soil. However, the light mild clays will also liquefy under the strong earthquake effect (e.g., the liquefaction of light mild clays occurred in the Tangshan's earthquake)[7].

Regarding the granular structure characteristics, the granules' ability of anti-liquefaction is different for various arrays and cementations. The granules with the stable array sand and better cementation have good ability of anti-liquefaction. Because of the influences of the age of deposition, the history of stress and strain, etc. of the undisturbed soil are more difficult to liquefy than the manipulated soil. The shear force of anti-liquefaction of the undisturbed soil is about 1.5~2 times, averagely 1.75 times, and more than that of the manipulated soil. Ancient soil layers are more difficult to liquefy than the new soil layers, and soil suffered from earthquake is more difficult than the soil not suffered[6~8].

Generally, relative density d_r, porosity ratio e, dry specific gravity γ_d, etc. are main factors for the granules' liquefaction. However, there is also a problem, so called re-liquefaction. There remain some loose and unstable areas in the soil after an earthquake. Subsequently, it will re-liquefy after a new earthquake which has lower intensity. However, if the soil suffered a series of minor post-earthquakes it will have rather higher stability after the first liquefaction and consolidation[7,159~165].

5.4.3 *Constraining force and border deformation*

According to the cyclic tri-axial test results of pure sands (K. L. Lee & H. B. Seed, 1967)[173], the cyclic shear stress generating the initial liquefaction in a given number of cycles is approximately proportional to the initial containing force which is about 1~15 kg/cm^2. At present, various simple shear test and torsion ring shear test have been designed. In general, they are more practical to simulate the in-situ situation than the tri-axial test. The cyclic torsion ring shear test shows that the *ability of anti-liquefaction will increase with the increment of initial static pressure coefficient* K_0 under a certain initial vertical effective stress (P. De. Alba, 1976). In addition, the experiment also shows that the ability of anti-liquefaction is proportional to the initial mean effective pressure $\bar{\sigma}_0' = \dfrac{1+2K_0}{3}\sigma_{v0}'$ (where σ_{v0}' is the initial vertical effective pressure). Fig. 5.16 is the experimental results conducted in sands. In China Shi Zhaoji et al. believed that the relation between the liquefaction stress σ_d and the principal stress σ_1 is linear, and it can be expressed as: $\sigma_d = A + B\sigma_1$, where A and B are the only parameters relating to granular properties.

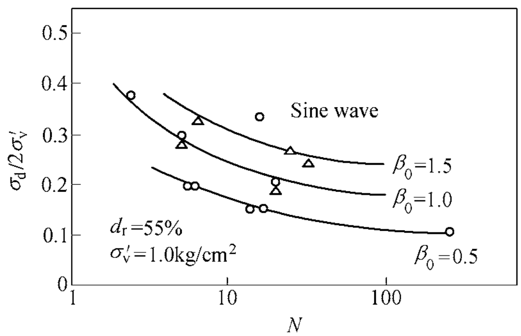

Fig. 5.16 Relation between cyclic stress ratio and cycle index

The constraining pressure is generated by the edges, which can be variable (such as the tri-axial test), or which can be rigid (such as the simple shear test whose shear box is made of metal). Under the flexible boundary, when the pore water pressure rises, the water film around the granules will be extruded, so the liquefaction will be delayed. This compliance effect of water film is very important for the experiment of liquefaction. During the course of the experiment of liquefaction, the pressure difference of water film will change significantly.

5.4.4 *Dynamic load and drainage*

The dynamic load parameters are waveform, amplitude, frequency, duration, direction, etc[6~9].

Many experiments show that the influence of waveform on the liquefaction is obvious[7]. In China Xie Dingyi, Wu Zhihui, et al. put forward six wave effects in terms of the experimental results, such as big wave effect, head wave effect, continuous effect, buffering effect, strengthening effect and accelerating effect. In America Shen Zhigang, L. F. Harder, J. L. Vrymoed, W. J. Bennett et al. believed that the bigger impulsion of stress would generate larger increment of pore water. The smaller impulsion of stress will generate a destructive effect which is not proportional to its magnitude while it appears after the bigger impulsion of stress.

The smaller impulsion will increase the intensity of liquefaction while it appears before the bigger impulsion of stress.

The duration of dynamic action has great influence on the development of liquefaction, which can be proved by the repeated factual seism and laboratory tests. Even though the amplitude of vibration is not very large, only if the duration of vibration is long enough, sandy soil will also probably be liquefied. It must be taken a fairly long time for granules' structure destruction and increment of pore pressure and deformation to reach the maximum limit. Furthermore, the area of soil liquefaction often gradually increases with the increment of time. So, under a certain depth, soil would be liquefied after vibrating for some time even if it is stable now. At present, in the laboratory researches the time of vibration is often indicated by different vibrating cycle index.

According to the expression of acceleration is $a = 4\pi^2 f^2 A$, where f is the frequency and A is the amplitude of vibration, the acceleration can be obtained through the combination of the frequency and the amplitude of vibration. The experiments show that if the acceleration is constant, there is no big difference of granular dynamic response under the conditions of low-frequency with high-amplitude or low-amplitude with high-frequency. However, the conclusion is not so sure while the frequency is very low. This is due to the motion of pretty big amplitude which will lose dynamic characteristics. The experiments also show that for a certain density (n=41%), with the increment of vibrating frequency the critical acceleration of granules will decrease, and when the frequency approaches to its natural frequency the critical acceleration will decrease even further. So the influence of frequency cannot be neglected.

Regarding the direction of vibration, many experiments show that the horizontal and vertical actions are similar, but for the angle of 45° the granules will have relatively bigger deformation and the lower shear strength.

The drainage of granules is affected by such factors as the permeability, the seepage path and the boundary condition[6~8]. In general, since the action time is short, the pore water cannot discharge in time and the pressure of pore water cannot dissipate, so the experiments of liquefaction are often operated without drainage. However, if the action time is long and the water permeability is good, the pore water pressure can dissipate during the course of the vibration, and the increment and the dissipation of pore water pressure will appear simultaneously, so the peak of pore water pressure would be reduced and the ability of anti-liquefaction increase.

5.4.5 *Other factors*

There are other factors influencing the granular liquefaction, such as stress history, granules' formation, blocked bubbles, etc.

Generally, the granules do not have regular structure. In 1976 Load's research showed that the preparation method of sample and the granular structure have great influence on the saturated granules liquefaction with the action of cyclic load. In 1976 Seed pointed out that the stress condition and vibration amplitude would change a lot in sand samples with the same density in a given number of cycles due to the difference of samples preparation methods. Therefore, in laboratory test the granules' orientation and structure must be carefully simulated.

The granules probably generate some strains because of the seism. In order to identify the influence of the earlier history of strain, in 1970 Fitton studied the newly deposited sands under the simple shear conditions. He found that the earlier strain has great influence on liquefaction. In 1976 Seed pointed out that even though the earlier strain did not change the granules' density greatly, it would also make the liquefaction stress increase by 1.5 times. In 1975 Focht believed that the severe earlier strain would lead to the more liquefaction increment.

In addition, if the pore water pressure increases in the granular media which have blocked bubbles, air compression will dissipate a part pressure. Therefore, the blocked bubbles are helpful for reducing the probability of liquefaction.

5.5 Discriminatory Analysis of Granular Liquefaction Potential

The discriminatory analysis of liquefaction potential is very important for most practical applications[155~173]. In order to solve the problem of analysis, a series of methods have been postulated, such as the reliability evaluation, the critical porosity ratio, the vibrating stable density, the simple energy, the critical acceleration, the shear wave velocity, etc. The reliability evaluation and the simple energy methods are introduced in following section.

5.5.1 *Reliability evaluation method*

Fig. 5.17 is a typical liquefaction curve, where u is the pore water pressure, σ_0' is the effective consolidation pressure, τ/σ_0' is the stress ratio, n is the cycle index. For different values of p/σ_0', such as 1.0, 0.7, 0.3 and 0.05, the trend of change is similar. Fig. 5.18 shows the relationship between τ/σ_0' and p/σ_0' when n=20. It shows that the liquefaction occurs when τ/σ_0' is more than or equal to 0.3 and p/σ_0' is equal to 1.0. There is no liquefaction on other occasions. The liquefaction intensity ratio R_1 is defined as:

$$R_1 = \left(\frac{\tau}{\sigma_0'}\right)_{\text{critical}} \Bigg/ \left(\frac{\tau}{\sigma_0'}\right)_{\text{dynamic}} \tag{5.11}$$

if $R_1 > 1.0$, no liquefaction; $R_1 < 1.0$, liquefaction.

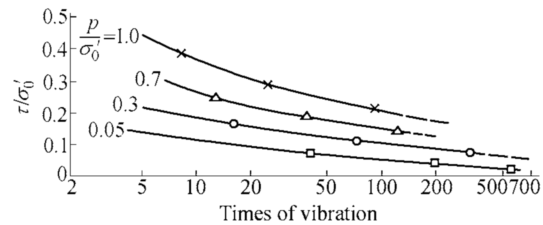

Fig. 5.17 Experimental results of sands liquefaction

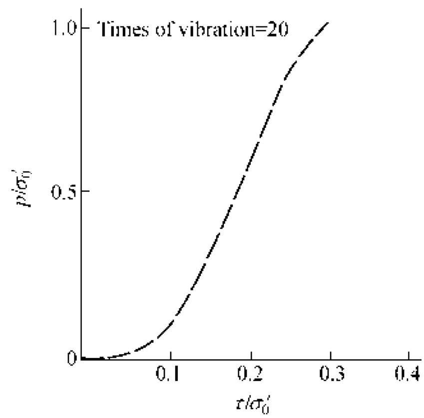

Fig. 5.18 Pore pressure ratio vs stress ratio

According to the change of pore water pressure and R_1, Fig. 5.17 can be obtained, and it can be divided into three phases:

(1) Non-liquefaction phase. $R_1>3.2$, during this stage $p/\sigma_0' \approx 0$, the sample will not be liquefied.

(2) Partial-liquefaction phase. $1.0<R_1<3.2$, during this stage $1.0> p/\sigma_0' >0$, the granules are subjected to partial liquefaction.

(3) Entire liquefaction phase. $R_1<1.0$, during this stage $p/\sigma_0'=1.0$, the sample will be broken and macro-liquefaction occurs.

The experimental studies show that when the pore pressure ratio is more than 0.6～0.7, the liquefaction will obviously influence the sample's properties, and the sample's deformation will increase[163～167]. The in-situ measurements and computational analysis also show that 0.6～0.7 is a characteristic value, and when the pore pressure is more than this value it will influence the granular motion characteristics, such as the waveform, the amplitude, frequency, etc. On the other hand, the laboratory tests show that when the pore pressure ratio is less than 0.3, the influence of pore pressure on the sample's deformation is small and negligible. Therefore, in terms of the influence of pore pressure on the sample's characteristic the curve of Fig. 5.19 can be divided into three phases.

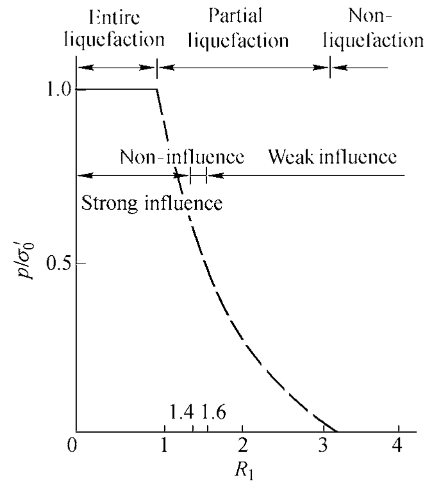

Fig. 5.19 Influence of pore pressure ratio

(1) Non-influence phase of pore pressure, p/σ_0'<0.3, R_1=1.6;
(2) Weak-influence phase of pore pressure, p/σ_0'<0.3, R_1=1.6;
(3) Strong-influence phase of pore pressure, 0.65<p/σ_0'<1.0, R_1<1.4

5.5.2 *Simple energy method*

Considering that the seismic energy will dissipate gradually in the course of the propagation due to the damping of rocks and soil, the total seismic energy E_1 in the unit soil can be quantified as[59]:

$$E_1(E,R)=\theta E/R^2 \tag{5.12}$$

where θ is a constant; E is the total seismic energy; R is the distance from the seismic source.

But the total dissipation of seismic specific energy in each unit of foundation soil so called ΣE_D is:

$$\Sigma E_D=\lambda_1(N)\cdot\theta\times10^{4.8+1.5M}/R^2 \tag{5.13}$$

where M is the Richter's earthquake magnitude; $\lambda_1(N)$ is the modified function of energy dissipation; N is the standard number of blows.

After deducting the relation between the pore pressure ratio and the seismic dissipation specific energy σ_0' is found to be:

$$\frac{p_d}{\sigma_0'}=\alpha\left[\frac{F_1(K_c)\cdot F_2(D_r)\cdot\lambda(N)\cdot\theta\times10^{4.8+1.5M}}{\sigma_0'R^2}\right]^\beta \tag{5.14}$$

where α and β are the test parameters; $F_1(K_c)$ is the correction factor reflecting the change of deviation stress; $\lambda(N)$ is the energy dissipation function; $F_2(D_r)$ is the correction function of relative density.

Assuming that:

$$\eta(N)=\frac{\alpha^{1/\beta}\sigma_0'\times 10^{-4.8}}{F_1(K_c)F_2(D_r)\lambda(N)\theta} \tag{5.15}$$

Eq. (5.14) can be simplified as:

$$\frac{p_d}{\sigma_0'}=\left[\frac{10^{1.5M}}{\eta(N)R^2}\right]^{\beta} \tag{5.16}$$

According to the situation of soil liquefaction, the critical equation when the foundation soil reach the state of the initial liquefaction could be expressed as:

$$\frac{p_d}{\sigma_0'}=1.0 \tag{5.17}$$

so the critical liquefaction function $\eta_L(N)$ is:

$$\eta_L(N)=\frac{10^{1.5M}}{R^2} \tag{5.18}$$

For Eq. (5.18) $10^{1.5M}/R^2$ is also the seismic specific energy function $T(M, R)$, so the discriminant of liquefaction is:

$$\frac{T(M,R)}{\eta_L(N)}\geqslant .0 \tag{5.19}$$

where the seismic specific energy function has a well-known function: $T=\frac{10^{1.5M}}{R^2}$, but $\eta_L(N)$ is still an undetermined function.

In order to obtain the function $\eta_L(N)$, the empirical regression method in the seismologic engineering is often used. Based on many seismic liquefaction data and their regression analysis, the seismic specific energy T can be worked out, then the figure of T-N can be drawn (shown in Fig. 5.20, where N is the standard number of blows). Fig. 5.28 shows that the liquefaction area and non-liquefaction area is separated by a line. In terms of the definition for liquefaction, this line is the critical liquefaction line η_L. Through regression analysis, the following expression is given:

$$\eta_L(N)=\frac{N^5}{900} \tag{5.20}$$

In terms of Eq.(5.20) and Eq.(5.19), the empirical equation of simple energy method for the discriminatory analysis of soil liquefaction potential is given:

$$\frac{T(M,R)}{\eta_L(N)}=\frac{900\times 10^{1.5M}}{R^2N^5}\geqslant 1 \tag{5.21}$$

Based on the empirical equation Eq. (5.21) of simple energy method, the Tangshan's seismic data (in China in 1976) are used to assess liquefaction potential and to judge the reliability of this equation. Table 5.2 is the measured data of Tangshan's seism. By utilizing these measured data the empirical equation Eq. (5.21) of simple energy method has been used. It is then compared with the measured liquefaction potential, and the results are show by the last two rows in Table 5.2.

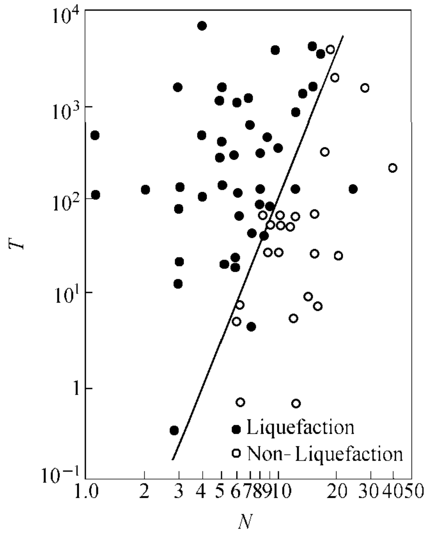

Fig. 5.20 *T-N*

Table 5.2 Utilizing the empirical equation of simple energy method to assess liquefaction potential[59]

Place	Epicentral distance /km	Kind	Depth /m	Number of blows N	In-situ	Computing result
Wangtan 1	81	Fine sands	2.3	6	Liquefaction	8.84
Wangjuntong	117.4	Fine sands	6.38	12	Non-liquefaction	0.13
Wangtan 2	79	Fine sands	3.6	19	Non-liquefaction	0.03
Qilihai	90.6	Fine sands	3.9	10	Non-liquefaction	0.55
Wangzhuang	116.4	Fine sands	8.7	8	Liquefaction	1.02
Yuzhuang	66.4	Fine sands	5.3	9	Liquefaction	1.73
Boge	44	Powdery sands	5.3	1.1	Liquefaction	1×10^5
Xiangyang	25	Middle sands	9.3	51	Non-liquefaction	2×10^{3}
Fangezhuang	22	Fine sands	2.61	10	Liquefaction	9.32
Changjiatuo	21	Fine sands	5.12	4	Liquefaction	998
Yanzhuang	15	Powdery sands	6.8	10.5	Liquefaction	15.71
Jingzhuang	9	Powdery sands	5.4	5	Liquefaction	1782
Donghuantuo	14	Fine sands	13.52	64	Non-liquefaction	2×10^{3}
Douhe	17.8	Powdery sands	6.4	18	Non-liquefaction	0.75
Dongtuozi	9.6	Fine sands	8.35	31	Non-liquefaction	0.17

5.6 Wave Mechanism of Saturated Granular Liquefaction and Compaction Phenomenon

5.6.1 *Wave propagation in saturated granular media*

5.6.1.1 Related suppositions

According to the following suppositions, this research work will obtain the wave propagation formula for saturated granular media[174~189]:

(1) The wavelengths are far longer than the sizes of the pores, and the framework of granules is a kind of the ideal elastic porous continuous medium. In addition, granules could be compressed;

(2) While flowing in granular media the pore water could be compressed, in a broad sense obeying the Darcy's Law;

(3) The strains of the liquid phase and the solid phase are small, and both strains are less than 10 ^{6};

(4) Granules have the statistical isotropy and uniformity, and the liquid phase is continuous, i.e., the pores are connected to each other;

(5) The influence of temperature is not considered.

5.6.1.2 Wave propagation formula of saturated granular media

While vibrating the following basic related formulae in granular media can be obtained[190~198]:

the relation of stress-strain:

$$\sigma_{ij} = \lambda e \delta_{ij} + 2G\varepsilon_{ij} - \delta_{ij}\alpha p_{\mathrm{f}} \tag{5.22}$$

the continuous equation of seepage:

$$-\dot{p}_{\mathrm{f}} = M\dot{w}_{i,i} + \alpha M\dot{U}_{i,i} \tag{5.23}$$

the granular movement equation:

$$\sigma_{ij,j} = \rho\ddot{U}_i + \rho_{\mathrm{f}}\ddot{w}_i \tag{5.24}$$

the liquid movement equation:

$$-p_{\mathrm{f},i} = \rho_{\mathrm{f}}\ddot{U}_{\mathrm{i}} + m\ddot{w}_i + \frac{\eta}{k_{\mathrm{p}}}\dot{w}_i \tag{5.25}$$

where σ_{ij} is the general stress of granular unit; λ, G are Lame constants of solid framework; α, M denote compressional constants of granules and pores fluid respectively; ε_{ij} is the strain of granular framework; e is the volume strain of granular framework; η is the viscosity coefficient of fluid; k_{p} is the seepage coefficient; p_{f} is the pore pressure; δ_{ij} is Kroneccher mark; ρ is the general density of saturated granules; w is the fluid displacement relative to solid framework; U is the displacement of solid framework; $m=a\rho_{\mathrm{f}}/n$, a is the distortion parameter, n

is the pore ratio.

According to the above equations, the following wave equations of saturated granules is given:

$$\left.\begin{aligned} &G\nabla^2 U + (\lambda + G + \alpha^2 M)\mathrm{grad}(\mathrm{div}U) + \alpha M \mathrm{grad}(\mathrm{div}w) = \rho\ddot{U} + \rho_{\mathrm{f}}\ddot{w} \\ &\alpha M \mathrm{grad}(\mathrm{div}U) + M\mathrm{grad}(\mathrm{div}w) = \rho\ddot{U} + \frac{\rho_{\mathrm{f}}}{n}\ddot{w} + \frac{\eta}{k_{\mathrm{p}}}\dot{w} \end{aligned}\right\} \tag{5.26}$$

where ∇^2 is the Laplace arithmetic operators.

5.6.1.3 Wave velocity

Concerning the wave in saturated granular media, under conditions of no dissipation the following equation will be deduced[192~199]:

$$\begin{pmatrix} w \\ U \end{pmatrix} = \begin{pmatrix} \mathrm{grad}\phi_1 \\ \mathrm{grad}\phi_2 \end{pmatrix} = \mathrm{grad}\phi \tag{5.27}$$

where ϕ is a potential function. Regarding wave P (i.e. compressional wave without rotation), the potential vector equation is:

$$[\boldsymbol{R}]\nabla^2\phi - [\boldsymbol{M}]\ddot{\phi} = 0 \tag{5.28}$$

where $[\boldsymbol{R}]$ and $[\boldsymbol{M}]$ indicate the stiffness matrix and the mass matrix respectively.

While matrix $[\boldsymbol{R}]^{-1}[\boldsymbol{M}]$ is positively definite and symmetrical, it has two positive real characteristic values, which are expressed as v_{P1}^2 and v_{P2}^2 respectively. In the reference system of characteristic vectors, the Eq.(5.28) can be expressed as:

$$\nabla^2\phi^* - \begin{pmatrix} \frac{1}{v_{\mathrm{P1}}^2} & 0 \\ 0 & \frac{1}{v_{\mathrm{P2}}^2} \end{pmatrix} \tag{5.29}$$

where $\phi*$ is ascertained by ϕ according to the change of reference system. The velocity expression of wave P can be written as:

$$\left.\begin{aligned} v_{\mathrm{P1}} &= \sqrt{\frac{\lambda + 2G}{\rho_{\mathrm{S}}(1-n)}} \\ v_{\mathrm{P2}} &= \sqrt{\frac{K_{\mathrm{f}}}{n\rho_{\mathrm{f}}}} \end{aligned}\right\} \tag{5.30}$$

where ρ_{S} is the density of granules; K_{f} is the volume modulus of pore fluid.

Without dissipation, the shear wave S obeys:

$$\begin{pmatrix} w \\ U \end{pmatrix} = \begin{pmatrix} \mathrm{curl}\ \psi_1 \\ \mathrm{curl}\ \psi_2 \end{pmatrix} = \mathrm{curl} \tag{5.31}$$

where ψ is a potential function. So, the shear potential functions are:

$$\left.\begin{aligned}&\nabla^2\psi_1-\frac{1}{v_S^2}\ddot{\psi}_1=0\\&\psi_2=0\end{aligned}\right\}\tag{5.32}$$

where the v_S can be expressed by:

$$v_S=\sqrt{\frac{G}{(1-n)\rho_S}}\tag{5.33}$$

From the above analysis and deduction, it can be shown that there are two kinds compressional waves and one kind shear wave in saturated porous granular media. The three kinds of body waves are the solid body wave P_1 (the wave velocity v_{P1}), the fluid body wave P_2 (the wave velocity v_{P2}), and the shear wave S (the wave velocity v_S).

5.6.1.4 Wave attenuation

Under the general condition with dissipation, the equation of potential vector is:

$$[\boldsymbol{R}]\nabla^2\phi=[A]\dot{\phi}+[\boldsymbol{M}]\ddot{\phi}\tag{5.34}$$

where $[A]$ is the damping matrix.

Assuming that wave P is a kind of simple harmonic wave propagating along X axis, then

$$\left.\begin{aligned}\phi_1&=\phi_{10}\exp[i(kx-\omega t)]\\\phi_2&=\phi_{20}\exp[i(kx-\omega t)]\end{aligned}\right\}\tag{5.35}$$

where ϕ_{10} and ϕ_{20} are two constants; ω is the angular frequency; k is the wave number.

Considering dissipation there are two solutions in the equation: k_{P1} and k_{P2}, which satisfy the expression of complex number given below:

$$k_{Pi}(\omega)=\mathrm{Re}\,k_{Pi}(\omega)+i\,\mathrm{Im}\,k_{Pi}(\omega)\tag{5.36}$$

where the imaginary part of the equation is the attenuation coefficient α_{Pi}, but the real part is related with v_{Pi}:

$$(\mathrm{Re}\,k_{Pi}(\omega))v_{Pi}(\omega)=\omega\tag{5.37}$$

As to the shear wave, it can be dealt with by the same method. Making the characteristic frequency f_c normalize, the normalized attenuation coefficient of compressional wave and shear wave could be obtained:

$$f_c=\frac{n\eta}{2\pi\rho_f k_P}\tag{5.38}$$

$$\left.\begin{aligned}\alpha_P&=\frac{2\pi f_c}{v_P}\\\alpha_S&=\frac{2\pi f_c}{v_S}\end{aligned}\right\}\tag{5.39}$$

5.6.2 *Wave mechanism of vibrating liquefaction*

The above analysis and deduction indicate that there are three kinds of body wave.

They are the solid compressional wave P_1, the fluid compressional wave P_2 and the shear wave S. They can propagate through the granular media as saturated granules are vibrated. This experiment shows that the pore water pressure has an oscillating characteristic as shown in Fig. 5.7, which is the result of the three waves' joint action. From the expression of wave velocity it can be seen that the velocity of compressional body wave is faster than that of shear wave, and the velocity v_{P1} of solid compressional wave P_1 is faster than the velocity v_{P2} of fluid compressional wave P_1. In fact, the process of wave propagation is the one that the vibration propagates ahead in the medium, so that the solid framework is under stress and gains energy in preference to fluid. Because of this adsorptive action, there is certain thickness of water film on the surface of the granules, i.e. bound water. The solid framework is under stress and gains energy, because the velocity v_{P2} of fluid's body wave is slower than the velocity v_{P1} of solid body wave. Then the bound water will be compressed by granular framework and cannot be discharged quickly. In the meantime, a part of the load is supported by neutral pressure so that the pore water pressure increases. This part of pressure increment is generated from the compression of bonding water by granules.

A part of force on the unit granules in vibration is caused by shear wave S. The propagating direction of shear wave S is vertical to the vibrating direction. Fig. 5.21 shows the ideal state of unit granules under stress. Before vibrating, the unit of granules is subjected by the effective principal stress σ_0' and $\beta_0\sigma_0'$ (β_0 is the static stress coefficient of granules). While vibrating, because of the action of wave S the unit is repetitively sheared by the shearing stress, which is periodic and continually changes in magnitude and direction. At the same time, this action reduces the viscosity force among granules. When the magnitude of the shearing stress is beyond a certain number, the original coupling intensity and structural state of granules is destroyed and the granules are separated from each other.

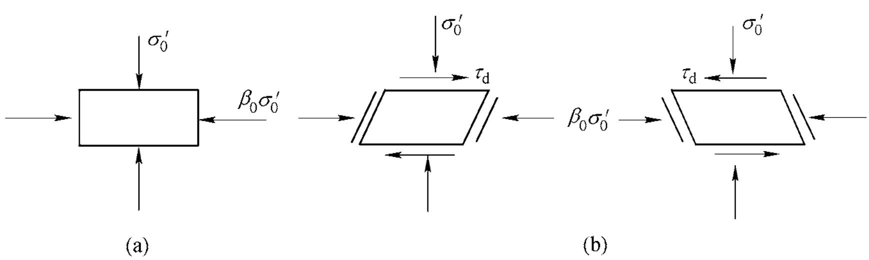

Fig. 5.21 State of granular unit under shear stress
(a) Before vibration; (b) In vibration

From the above analysis it can be seen that the granular framework imposes vertical stress and shear stress which are fluctuating in magnitude and direction because of the vibrating stress wave's movement. The granules have different mass, the granular array states are also different in various points, so, in vibration field, every point has different primary stress and different transferred dynamical loading intensity. Therefore, the granules have varied active forces with different magnitude, direction and actual influence, and a new stress field is created in every granular contact point. In addition, when the magnitude of the shearing stress is beyond certain number the shearing action reduces the viscosity force among granules. Then the original connecting intensity and the structural state of granules will be destroyed and the granules will be separated from each other. At that time the original pressure (effective pressure) transmitted by the granular contact points will be transferred to pore water to bear, so that the pore water pressure will increase abruptly. The increase of pore water pressure is caused by the combination of transferring pressure and the original pressure in the granules.

Due to the action of certain excess hydrostatic pressure the pore water tends to be discharged; at the same time, the granules will sink because of the gravity. Therefore, when the structure is destroyed in some time or even instantly, the sinking of granules will be obstructed by the upward discharge of pore water, the granules will partly or fully float (at that time the pore water pressure is equal to the effective overburden pressure). Then the shearing strength will be lost partly, even wholly, so that the granules are distorted in a certain degree or liquefied completely. In consequence, with the gradual discharge of pore water, the pore water pressure will decrease gradually. Then the granules will sink down gradually and pile up over again, and the pressure is transferred to the newly formed granular framework from pore water. At that time the saturated granules are stable again, i. e. they are now close-grained.

5.6.3 *Compaction phenomenon*

As mentioned in the previous section, the granules have experienced two steps that the pressure is transmitted from particles to pore water, and then from pore to particles. The two processes are different from each other but mutually related. Thus the original structure of the granules is lost; they have to rearrange themselves under new stresses. The newly formed structure is the reciprocal arrangement of coarse particles, and the fine particles filling into the pores between coarse particles. The result is the reduction of void ratio and the improvement of the degree compaction. The mechanical properties of the particles will improve because of the intimate association of the particles and the enlargement of the frictional force.

Moisture in saturated granules attains energy not only from vibrators but also from the vibration process of particles. The two media, water and granules, will have different effects in the same vibration. When the difference between their kinetic energy is above the moisture absorption capacity of the particles, the free water and capillary water will be separated out from particles' pores. The pressure of excess pore water will be gradually enhanced, making the pore water flow from the high-pressure area to the low-pressure area (i.e. the top part of granules). Eventually the pores between the particles will decrease and the density of the granules will improve.

Gas in the saturated granules derives from two sources. One is the influence of the capillary water to form hermetic gas in gaps between the particles. Fluid mechanics have shown that the existence of hermetic gas increasingly mitigates permeability of saturated granules and is resistant to the motion of free water. The other is that some dissolved gases (such as oxygen, carbon dioxide, etc.) constantly prevailing in the granules are gathered together into air bubbles and are extricated under certain temperature and pressure. Particles under vibration will produce heat due to friction during motion. In particular a part of the vibration energy will be transformed into heat, at the same time the dynamic stress will be generated from the corresponding kinetic energy of the particles and water. In these circumstances hermetic bubble will be moved, or the activity of the dissolvable gases in the water can improve this situation. The gases will be released out of the water, so that the volume of the granules will decrease and the resistance against pore water will reduce. Thus permeation of pore water will increase, which in turn will accelerate the condensation of the granules. With the experiments carried out in the laboratory, it can be clearly seen that many gas bubbles release out of the saturated sample.

Both longitudinal and transverse waves can propagate in the granular media in vibration. The stress wave reflects and refracts in the medium with compression effect and energy consumption. A part of this kinetic energy is converted into the potential energy of the granules. When this kind energy reaches a certain value, plastic deformation has done and elastic deformations gradually appear, and the energy of stress wave propagates outwards to compact nearby granules. Finally, the energy of the vibration is converted into potential energy of plastic deformation.

By simplifying the granules as a pile of spherical models with uniform radius "r" and connected with each other, the spherical bodies can be considered as homogeneous material statistically, and form a cubic pile as shown in Fig. 5.22a. Here each spherical ball is connected to six neighboring balls. The cubic body shown in Fig. 5.22b is considered as a model to calculate the void ratio. Its total volume is $8r^3$, while its internal tangent sphere volume is $4/3\,\pi r^3$, the void ratio can be calculated from:

$$e_1 = \frac{8r^3 - \frac{4}{3}\pi r^3}{\frac{4}{3}\pi r^3} = 0.91 \tag{5.40}$$

While a stress wave acts on the spheres, the compression wave with maximum propagation velocity firstly reaches the sphere and then shakes the tailings' structure to draw them close to each other in the x or y direction. The following shear wave will oscillate the sphere from side to side with powerful energy, then a compacted texture can be obtained (refers Fig. 5.22c). Each sphere element in the second layer will plunge into the space between four spheres of the first layer. Similarly, by dissecting a sphere from the model, its side length is $4/\sqrt{2}r^3$; its volume is $32/\sqrt{2}r^3$. There are six hemispheres and eight 1/8th spheres where each sphere's volume is $4/3\pi r^3$, so the porosity ratio is:

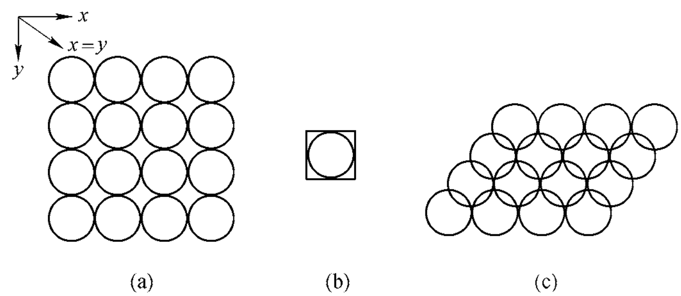

Fig. 5.22 Various arrangement patterns of sphere body

(a) Cubic pile; (b) Cell; (c) Compacted texture

$$e_2 = \frac{\frac{32}{\sqrt{2}}r^3 - 4\left(\frac{4}{3}\pi r^3\right)}{4\left(\frac{4}{3}\pi r^3\right)} = 0.35 \tag{5.41}$$

The reduction of unit thickness of tailings particles with two different arrangements is calculated from:

$$\Delta = \frac{e_1 - e_2}{1 + e_1} = \frac{0.91 - 0.35}{1 + 0.91} = 0.293 \tag{5.42}$$

That is to say that the thickness can be reduced probably by 29.3%.

The above analysis has confirmed that the vibration wave and the rearrangements of tailing particles can sharply reduce the granular porosity ratio. Although the real granules are much more complicated than the ideal sphere, it is obvious that theoretically the vibration have very good compaction effect. Laboratory researchers have also demonstrated that vibration can significantly reduce the height of tailings due to the compactness.

5.6.4 *Expectations of Application*

Three methods listed below can be adopted to apply vibration to granular materials, such as tailings:

(1) Burying air tube in advance, intermittently pump compressed air into the tube in a certain frequency to vibrate the granular materials.

(2) Application of a relatively large concrete agitator for vibration similar to

that in civil engineering field.

(3) The source of vibration is an immersed electric mechanical vibrator encased in steel materials.

The space in underground mine is limited, so there are great demands for equipment's weight and size to operate by hand or by small machinery to attain higher vibration intensity. But relatively large machine is advantageous to tailings' chamber. For operation convenience, it is always desirable to dehydrate the tailings as quickly as possible. The vibration methods compared to that of naturally obtained, not only greatly enhance dehydration speed, but also compact tailings' densely to improve its strength. A quick drainage of filling water can shorten the mining cycle and improve the efficiency.

In addition, simple drainage engineering can greatly lower the pressure of saturated fill materials in stope and would be rather less dangerous of tailings' overflow. Since water can be gathered on the upper part of the tailings, this will be helpful to accelerate the drainage. The direct effect of vibration on tailings' body in the tailings' chamber can accelerate the drainage and the subsidence of tailings. This will increase the volume of the stope, and lengthen its service time. Moreover, by increasing the shear strength of tailings, it will reduce the pressure of the tailing dam and enhance the safety of the tailing pond. And the potential economic benefit is very considerable.

6

Granular Flowability Theory and Vibrating Aided Flow

6.1 Basic Theory of Ellipsoid

Firstly, the withdrawal of the single hopper is studied[50,51]. Fig. 6.1 shows the single hopper solid ore-drawing model. There is a shutter fitted at the bottom of the hopper opening. Before ore-drawing, homogeneous are ores filled into the model. Put down a horizontal layer of color bands II of a certain height. After filling to the level layer A-A', stop filling ores and then fill the waste rocks to a certain height. Open the shutter of the hopper to withdraw the ores. In course of ore-drawing it is shown that not all ores and waste rocks move and that only a part of the ores and waste rocks on the top of the hopper opening are in the state of motion. The above phenomenon can be clearly seen by observing the movement of color bands through the glass at the opposite side of the model. In the process of the ore-drawing, the color bands which are symmetrical about the axis ox of the hopper are bent continuously downwards. When the granule P on the intersection point of the level layer A-A' and the axis reaches the hopper opening, 100 percent clean ores have been drawn. A large number of observations show that the space of the drawn ores in the model is approximately an ellipsoid, and is called as the withdrawal ellipsoid 1. The hopper-like body enveloped by the curve AoA' is called as the withdrawal hopper. The concave hopper formed by the level layers on the level layer A-A' is called as the moving hopper 3. After moving the boundary every color band is linked, and the formed ellipsoid of rotation is called as the loosening ellipsoid 4.

6.1.1 *Withdrawal ellipsoid*

The withdrawal ellipsoid, which is also termed as the withdrawal body, is the volume V of the ores with a certain size drawn from the hopper. The ores of this volume do not flow from a random body in the scope, but from a body of an ellipsoid. Namely, the space taken by the drawn ores in the scope is an ellipsoid whose underside is cut by the plane of the withdrawal hopper and symmetrical about the axis of the withdrawal hopper (refer to Fig. 6.1). This can be shown by the experiment of an ore-drawing model. At first, fill ores into the model, lay the labeled granules with numbers according to a certain designated position and keep records in detail. After finishing the filling, begin to draw ores. Every time a certain amount of ores V_1, V_2, …, V_5 are drawn, record the drawn labeled granules. Then according to the drawn and labeled granules, describe the special position occupied by V_1, V_2, …, V_5 in the model, then obtain the withdrawal ellipsoid (as shown in Fig. 6.2). Its volume is:

$$V = \frac{2\pi}{3}ab^2 + V_x = \frac{2}{3}\pi a^3(1-\varepsilon^2) + V_x \tag{6.1}$$

$$V_x = \pi\int_{x=0}^{x=na} y^2 \mathrm{d}x = \pi\int_{x=0}^{x=na}(a^2 - x^2)\frac{b^2}{a^2}\mathrm{d}x = \frac{1}{3}\pi a^3(1-\varepsilon^2)(3n-n^3) \tag{6.2}$$

where V is the volume of the ellipsoid, cm^3 or m^3; a is the semi-major axis of the ellipsoid, cm or m; b is the semi-minor axis of the ellipsoid, cm or m; ε is the eccentricity of the ellipsoid; $n=x/a$.

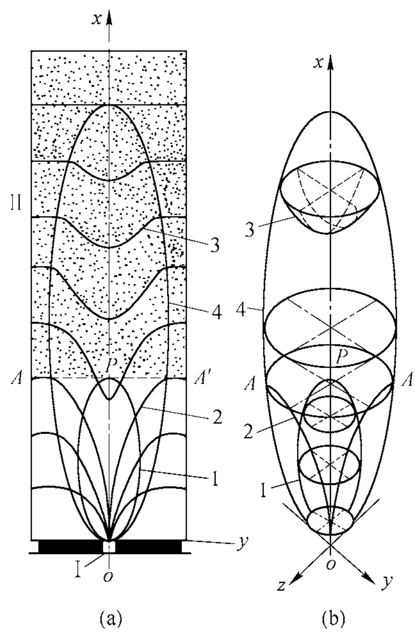

Fig.6.1 Withdrawal ellipsoid, withdrawal hopper, moving hopper and loosening ellipsoid
(a) Longitudinal diagram; (b) Tri-dimensional space diagram;
A-A' —Surface of contact between the ores and waste ores; I—Ore-drawing hopper; II—Color band;
1—Withdrawal ellipsoid; 2—Withdrawal hopper; 3—Moving hopper; 4—Loosening ellipsoid

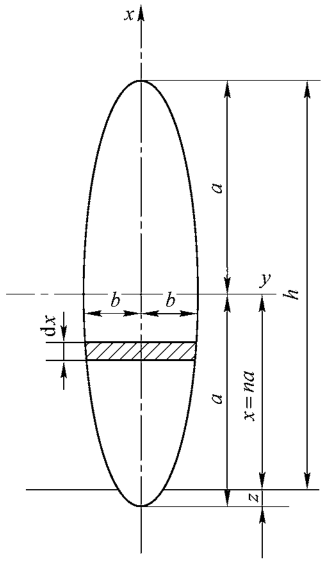

Fig. 6.2 Withdrawal ellipsoid

For convenient to use, a is expressed by the height h of the cut ellipsoid and the radius r of the withdrawal hopper. Therefore obtain:

$$a=\frac{h}{2}\left[1+\frac{r^2}{h^2(1-\varepsilon^2)}\right]$$

$$n=\frac{x}{a}=\frac{1-\dfrac{r^2}{h^2(1-\varepsilon^2)}}{1+\dfrac{r^2}{h^2(1-\varepsilon^2)}}$$

By derivation, lastly obtain:

$$\begin{aligned}V&=\frac{\pi}{6}h^3(1-\varepsilon^2)+\frac{\pi}{2}r^2h\\&\approx 0.523h^3(1-\varepsilon^2)+1.57r^2h\end{aligned}\tag{6.3}$$

6.1.2 *Loosening ellipsoid*

It is shown in Fig. 6.3 that when the volume V_f are drawn from the hole of the hopper at the bottom, the volume of the original V_f is filled by the granules from the scope of $2V_f$. Because during the granules' downward shift granules have the secondary loosening, the factual filled space is: $K_c(2V_f-V_f)=K_cV_f$, where K_c is the secondary loosening coefficient. So the residual space in the scope of $2V_f$ is: $\Delta_2=2V_f-K_cV_f$. The rest can be deduced by analogy, and they fill the vacancies in the proper order: nV_f, $\cdots$, $4V_f$, $3V_f$, $2V_f$, so:

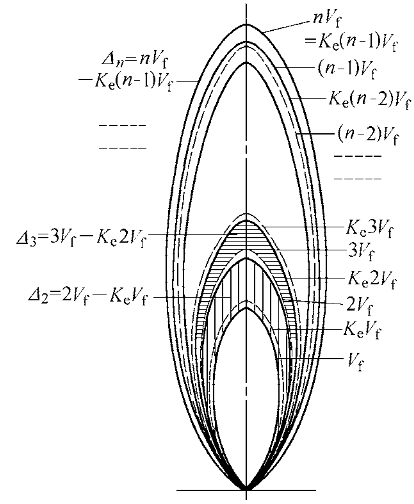

Fig. 6.3 Process of forming the loosening ellipsoid

$$\Delta_n=nV_f-K_c(n-1)V_f=0$$

From the above, obtain that

$$nV_f(K_c-1)=K_cV_f$$

where nV_f is the loosening body (V_s), namely the range of movement after drawing the granules. Because the form of the loosening body is approximated to an ellipsoid, so it is called the loosening ellipsoid. The relation between the loosening and the withdrawal ellipsoid is:

$$V_s=\frac{K_c}{K_e-1}V_f \tag{6.4}$$

From the above expression the coefficient of the secondary loosening can be derived. Namely:

$$K_e=\frac{V_s+K_eV_f}{V_s} \tag{6.5}$$

or

$$K_e=\frac{V_s}{V_s-V_f} \tag{6.6}$$

According to the experiment, it is obtained that K_c=1.066~1.10. After the ores are blasted, loosening is generated and the volume increases, causing the initial loosening. Suppose that the coefficient of the initial loosening is K_c. The loosening generated in the process of ore-drawing is the secondary loosening, whose coefficient is K_e. It can be found out from the experiment that under certain circumstances when the ores' condition and the drilling and blasting parameters are invariable the limitation of the loosening coefficient of ores K_f is a constant. The value of K_f is the arithmetic product of the coefficient of the first loosening (K_c) and the coefficient of the secondary loosening (K_c), namely K_f=K_cK_c. The moving speed in every section in the agitated field is different, correspondingly the loosening degree in every section is different. Because at present the problem about the relation between the secondary loosening and the moving speed is still not solved, only the average coefficient (K_e) of the secondary loosening is used. The meaning of the average coefficient of the secondary loosening is that once the granules begin to move, the loosening degree in every section is the same. It can be found out from Fig. 6.1 that the volume of the withdrawal hopper on every horizontal layer is the volume filled up by the above granules. Because of K_e, the volume of the withdrawal hopper becomes smaller and smaller with the height increases. At last an enclosed loosening body forms. Therefore, it can be established that the formation of the enclosed loosening body is due to the secondary loosening.

The boundary of the loosening body is the boundary of the granular moving field. It can be seen from Fig. 6.1 that the distance of the downword shift of the granules in the moving field in every section is different, thereby it can be concluded that the moving velocity in every section is different. On the same horizontal plane the velocity on the moving axis is the maximum. The closer to the boundary the smaller the velocity is. The velocity on the boundary is zero. It can be seen from the moving axis that the velocity is low at the top and high at the bottom. From the moving trace it can be established.

6.1.3 *Withdrawal hopper*

The hopper formed due to the plane of contact of the loose ores continuously descending and bending in the process of ore-drawing by the single hopper is called the withdrawal hopper. When its top point reaches the hopper opening, namely the point o, the intersection of the ore-rock contact plane and the flowing axis *ox*, reaches the hopper opening shown in Fig. 6.4. Before this moment, only clean ores will be drawn. If the ore-drawing continues the rocks will appear. The formed hopper AoA' is called the withdrawal hopper, which is symmetrical about the flowing axis *ox*.

The process of forming withdrawal hopper can be explained by using the principle mentioned previously that relevant position is invariable in the process of the transition of the withdrawal ellipsoid. It is shown in Fig. 6.4 that after drawing the quantity of clean ores V the withdrawal ellipsoid V and the moving ellipsoid Ⅰ, Ⅱ, Ⅲ, Ⅳ, Ⅴ under the condition of all heights are formed. Suppose that the ore-rock contact plane A-A' and the withdrawal ellipsoid have a tangential point o, then it and all moving ellipsoid intersect at the point 1, 2, 3, 4, 5 respectively. Because of the drawing of the granule V, the top of the withdrawal body is bound to reach the hopper opening. The point of intersection 1, 2, 3, 4, 5 of every moving ellipsoid and the plane of contact are also bound to descend to $1'$, $2'$, 3′ , 4′ , 5′ . Thus 1-1′ , 2-2′ , 3-3′ , 4-4′ , 5-5′ are the moving trace of every point respectively when every moving ellipsoid moves according to the principle that the granules relevant position is invariable. The line formed by connecting 1′ , 2′ , 3′ , 4′ , 5′ is the generating line of the withdrawal hopper. This also can be explained as that the line formed by connecting the points which are situated on any horizontal layer with the same moving time (or the same drawing quantity). It is the curve of the moving hopper. Also that the generating line of the withdrawal hopper is the connecting line of granules between the horizontal layer and the new position during the pure ores *V* are being drawn out.

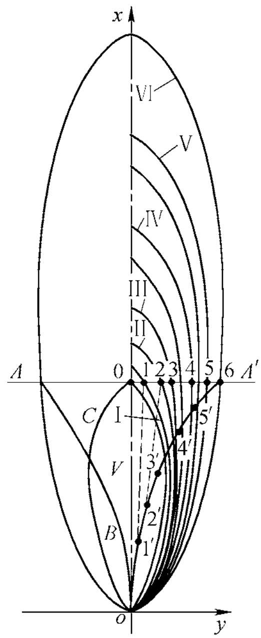

Fig. 6.4 Process of forming withdrawal hopper

C—Withdrawal ellipsoid; *B*—Generating line of withdrawal hopper;
I , II , III, IV , V —Moving ellipsoid with different height;
VI—Loosening ellipsoid

6.1.3.1 Characteristics of withdrawal hopper

(1) Form of withdrawal hopper.The form of the withdrawal hopper depends on the curvature of the generating line of the hopper. Its radius of curvature is large and determined by the following factors: 1) If the ore-drawing layer is higher, the radius of curvature is smaller and the inter-junction of the generating line and the ore-rock contact plane is smoother; 2) If the granular flowability is better, the eccentricity of the withdrawal body is smaller and the radius of curvature of the generating line is bigger.

(2) Volume of withdrawal hopper. When using single hopper to draw ores,

the volume of the withdrawal hopper, the volume of the withdrawal ellipsoid and the volume of the drawn clean ores are approximately equal, namely:

$$V_l \approx V \approx V_f \tag{6.7}$$

where V_l is the volume of the withdrawal hopper; V_f is the volume of the drawn clean ores.

The reason is that when these three are approximately equal the granules will generate the secondary loosening in the course of ore-drawing and the volume of the drawn clean ores is obtained by conversion according to the mass of ores.

(3) Maximum radius R and height h of withdrawal hopper. The height of the withdrawal hopper is equal to the height of the ore layer. Its radius is equal to the radius of the transverse section of the loosening ellipsoid and the contact plane of the ore-rock. Its value can be solved by the following method.

According to the elliptical equation:

$$y^2=(a^2-x^2)(1-\varepsilon^2)$$

Suppose

$$a=\frac{H_s}{2} \qquad x=\frac{H_s}{2}-h \qquad R=y$$

It can be obtained that:

$$R=\sqrt{(H_s-h)h(1-\varepsilon_s^2)} \tag{6.8}$$

where ε_s is the eccentricity of the loosening ellipsoid; h is the height of the withdrawal ellipsoid, namely the height of the ore layer.

6.1.3.2 Relationship between loosening ellipsoid and withdrawal ellipsoid

The quantitative relation between loosening ellipsoid and withdrawal ellipsoid is determined according to Eq. (6.4). If the coefficient of the secondary loosening is known, the relation between these two is also determined. Choose K_e=1.066~1.100, then:

$$V_s=(11\sim16)V \tag{6.9}$$

The relation between the height of the loosening ellipsoid and the withdrawal ellipsoid can be obtained from Eq. (6.9). Suppose $V_s=15V$, then:

$$V_s=15\left[\frac{\pi}{6}h^3(1-\varepsilon^2)+\frac{\pi}{2}hr^2\right] \tag{6.10}$$

Moreover

$$V_s\approx\frac{\pi}{6}(1-\varepsilon_s^2)H_s^3 \tag{6.11}$$

where ε_s is the eccentricity of loosening ellipsoid; H_s is the height of loosening ellipsoid. And then:

$$H_s=\sqrt[3]{\frac{6V_s}{\pi(1-\varepsilon_s^{\ 2})}} \tag{6.12}$$

$$V\approx\frac{\pi}{6}h^3(1-\varepsilon^2) \tag{6.13}$$

Thereby:

$$V_s = 15V = 15\left[\frac{\pi}{6}h^3(1-\varepsilon^2)\right] \tag{6.14}$$

Substituting Eq. (6.14) into Eq. (6.12) gives:

$$H_s = 2.46h\sqrt[3]{\frac{1-\varepsilon^2}{1-\varepsilon_s^2}} \tag{6.15}$$

And suppose that $\sqrt[3]{\frac{1-\varepsilon^2}{1-\varepsilon_s^2}}$ is approximately equal to 1, then:

$$H_s=2.46h\approx 2.5h \tag{6.16}$$

This expression shows that the height of the loosening ellipsoid is as much as two and half times of the height of the withdrawal ellipsoid.

It can also be seen from the above that the quantitative relation between the loosening ellipsoid and the withdrawal ellipsoid on the height and the volume is obtained under the condition of the coefficient of the secondary loosening K_e= 1.071. If the coefficient of the secondary loosening is different then the quantitative relationship between them is also different.

6.1.4 *Moving trace*

It is shown in Fig. 6.5 that any granule in the moving field takes $A_0(x_0, y_0, z_0)$ and when the hopper hole draws the volume V_f, it will move to the point $A(x, y, z)$. The moving trace of the point A_0 can be obtained by using the transition theory of the moving body.

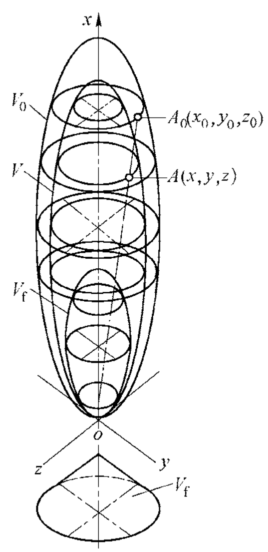

Fig. 6.5 Granular moving trace

The surface equation of the moving body across the point A is:

$$y^2+z^2=KH^{-n}(H-x)x \tag{6.17}$$

The surface equation of the moving body across the point A_0 is:

$$y_0{}^2+z_0{}^2=KH_0{}^{-n}(H_0-x_0)x_0 \tag{6.18}$$

Dividing Eq. (6.17) by Eq. (6.18) gives:

$$\frac{y^2+z^2}{y_0^2+z_0^2}=\frac{H^{-n}(H-x)x}{H_0{}^{-n}(H_0-x_0)x_0} \tag{6.19}$$

According to the characteristics of the withdrawal body, then:

$$\frac{x}{x_0}=\frac{H}{H_0}=\frac{H-x}{H_0-x_0} \tag{6.20}$$

Substituting Eq. (6.20) into Eq. (6.19) gives:

$$y^2+z^2=\left(\frac{x}{x_0}\right)^{2-n}(y_0^2+z_0^2) \tag{6.21}$$

Because of the symmetry, the granules should not have circumferential motion during course of moving towards the hopper hole. Thus there is no doubt that the point $A_0(x_0, y_0, z_0)$ and $A(x, y, z)$ are in a common plane across the axis x. Therefore the following relationship can be obtained:

$$\frac{z_0}{y_0}=\frac{z}{y} \tag{6.22}$$

Substituting Eq. (6.22) into Eq. (6.21) gives:

$$\left.\begin{aligned} y^2&=\left(\frac{x}{x_0}\right)^{2-n}y_0^2\\ z^2&=\left(\frac{x}{x_0}\right)^{2-n}z_0^2\end{aligned}\right\}\quad\text{or}\quad\left.\begin{aligned} y&=\left(\frac{x}{x_0}\right)^{1-\frac{n}{2}}y_0\\ z&=\left(\frac{x}{x_0}\right)^{1-\frac{n}{2}}z_0\end{aligned}\right\} \tag{6.23}$$

This expression is the granular moving trace equation.

6.2 Influence of Water Content on Granular Flowability

It is very important to increase the granular disposal productive capacity, decrease labor intensity, improve working and safety conditions, and create better economic benefit and social benefit that to study the factors influencing the granular flowability and to improve the granular flowability[56~65].

The production practices in mines show that the change of water content has significant influence on granular flowability. With certain water content the granules can be successfully drawn, but with another different water content the materials are often blocked up. When water content is in the state of saturation, ore-running accidents often happen.

The water content is related to granularity and the granular distribution. When the granular size is bigger and the content of the fine materials is less, the influence of water content on granular flowability is less; On the contrary, the influence is greater. The size range of fine materials is usually 0～5 mm. When the mass fraction of fine materials reaches about 8%, granules show a very obvious binding property. Jenike, a well-known scholar in America, thinks that fine materials have decisive effect on granular flowability, and without the binding of fine materials coarse materials have not sufficient shearing strength[64]. So the contents of fine materials and water content have the leading effect on granular flowability.

6.2.1 *Mechanical analysis when drawing granules from hopper*

The discharge lip is the "throat" of the hopper, which is the weak links in the course of production and it is also the place where blockages incidents often happen.

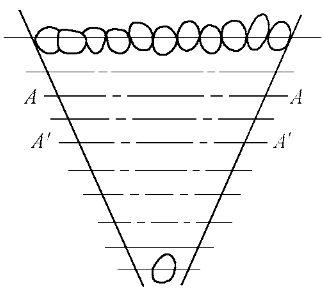

Fig. 6.6 Granular flow schematic diagram in hopper

Considering granular flow in a hopper with square cross section (shown in Fig. 6.6), during the flowing granules are bound to generate relative displacement and subsequent realignment in order to adapt to the reduction of the cross section of the hopper. In the course of granules displacing relatively and squeezing each other, considerable frictional resistance will generate and consequently the energy will be dissipated. This frictional resistance (namely internal friction) can be expressed as:

$$F_1 = pf_1k\gamma \tag{6.24}$$

where F_1 is the resistance of unit volume materials which is generated because of the reduction of the area of cross section; p is the positive pressure between materials and walls of the hopper; f_1 is the friction coefficient between granules; k is a constant relevant to granular form; γ is the shrinkage ratio of average area of hopper ($\gamma = A - A' \;/A$, A is the area of cross section at the materials entry point, A' is the sectional area when materials descend to a certain height).

It can be seen from Eq. (6.24) that the value of the internal friction depends on three factors, f_1, p and γ.

In the course of the granules' flow in the hopper there is a frictional force between materials and the walls of the hopper (namely external friction). The resistance of per unit area is directly proportional to the coefficient of friction between the materials and the walls of the hopper and the positive pressure of the materials on the walls of the hopper. So external friction can be expressed by using the resistance of per unit volume materials. Therefore the following equation is obtained:

$$F_2 = \frac{pf_2\eta s\Delta y}{A\Delta y} = pf_2\eta\frac{s}{A} \tag{6.25}$$

where F_2 is the external frictional force of the per unit volume materials; f_2 is the frictional coefficient between the materials and the hopper walls; η is an inclination factor, the ratio of the positive pressure on inclining hopper wall p' to positive pressure p; s is the perimeter of the hopper; Δy is vertical displacement. The total frictional force F of granular materials is:

$$F = \int_0^y F_1 \mathrm{d}y + \int_0^y F_2 \mathrm{d}y + \int_0^y pf_1k\gamma \mathrm{d}y + \int_0^y pf_2\eta\left(\frac{s}{A}\right)\mathrm{d}y \tag{6.26}$$

When granules contain a certain amount of fine materials, they tend to stick to each other or stick on the hopper wall due to the moisture. Thus they will generate resistance to granular movement. In the similar way, the cohesive force c of granular materials is:

$$c = \int_0^y c_1k\gamma \mathrm{d}y + \int_0^y c_2\left(\frac{s}{A}\right)\mathrm{d}y \tag{6.27}$$

where c_1 is the cohesive resistance between the granular materials; c_2 is the cohesive resistance of the materials on unit area of hopper wall.

Suppose that the influence of the mechanical applied force, such as vibration, on the granular flowability mainly finds a way in decreasing frictional force and cohesive force, not in exerting any pressure on granular flow, then only the component force of the mass of materials in flow direction $W_{\dot{y}}$ is the dynamic force impelling granular flow[64]. It is obvious that if continuous flow of materials in the hopper needs to be kept, the following condition must be obeyed: $W_{\dot{y}} > F + c$.

Namely:

$$W_{\dot{y}} > \int_0^y p\left[f_1k\gamma + f_2\eta\left(\frac{s}{A}\right)\right]\mathrm{d}y + \int_0^y\left[c_1k\gamma + c_2\left(\frac{s}{A}\right)\right]\mathrm{d}y \tag{6.28}$$

Eq. (6.28) shows that when the weight of the materials is more than the sum of the cohesive force between the materials and the hopper wall, cohesive force between the materials, external frictional force between the materials and the hopper wall and the internal frictional force between the materials, then materials will continuously flow. On the contrary, when the resistance is more than or equal to mass of the materials, materials will stop flowing, as a result the phenomenon of arching and blockage will appear.

6.2.2 *Influence of moisture on granular frictional resistance and cohesion*

Moisture in the granules can be divided into three kinds, molecular water, capillary water and gravity water. The molecular water is tightly absorbed onto the granular surface because of an electrical field formed by the granules' electric charges. The thickness of the granular molecular water film has an important influence on the granular cohesive force. In addition, the quantity of moisture evaporation also has a certain amount of influence on the granular cohesive force. Capillary water and gravity water belong to the free water. Gravity water is present in the bigger pores between the granules and has the general characteristics of water. Under the action of water pressure it flows in the state of penetration. Capillary water is present in the smaller pores between the granules. Its flow is caused by the combined action of the capillary force and the water pressure. By experiments, the height h_m of water raised by capillary pore can be expressed as:

$$h_m = \frac{1}{10D} \tag{6.29}$$

where D is granular diameter of materials, mm.

For the materials whose granular diameter is 0.1 and 0.01 mm, the height h_m of water raised by capillary pore is respectively 1 m and 10 m. All three kinds of water among the granules have influences on the granular flowability.

The angle of external friction or the coefficient of external friction is the relative value expressing the value of resistance in the course of materials gliding along the hard hopper wall. A study shows that if water content ratio is different then the coefficient of external friction has great variations. At the beginning the coefficient of external friction correspondingly increases with the increment of water content ratio. When the water content ratio increases to a certain limit the coefficient of external friction also has a maximum value. Thereafter, with the increment of moisture the coefficient of external friction shows a tendency to decrease. The reason for this is as follows. At the beginning the increased moisture of materials is easily absorbed by the granules, so the adsorbability between the granules and the hopper wall increases. With the increment of the absorbed moisture the adsorbability increases to a saturation point, namely corresponding to the maximum coefficient of external friction. If the moisture cannot be absorbed by the granules, the excess moisture is present in the form of free water and provides lubrication between the granules and the hopper wall, so the granules easily slip along the hopper wall, therefore the coefficient of external friction decreases. When the water content ω_c is 8%~10%, all the coefficients of external friction of all kinds of materials within the hopper wall show the maximum. Here the flowability of the materials along the hopper wall is the worst.

The coefficient of internal friction or the angle of internal friction is the relative value expressing the value of resistance between the granules in the course of the materials' motion. The law of the influence of water content ω_c on the internal friction angle is shown by the curve Ⅰ, Ⅱ, Ⅳ and Ⅴ in Fig. 6.7[2]. With the increment of water content, the angle of internal friction shows a tendency to decrease. When ω_c is equal to zero the friction between granules appears as dry friction. When ω_c slightly increases, a layer of water film is formed on the granular surface. As the water film provides lubrication between the granules, therefore the internal frictional force decreases. When ω_c increases continuously the internal frictional force decreases to a minimum value.

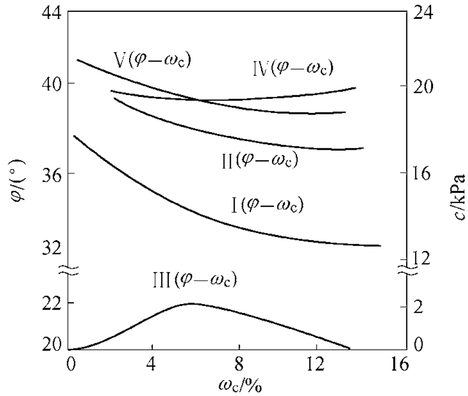

Fig. 6.7 Relationship of water content ω_c, cohesive force c, and internal friction angle φ

I —Fine coal; II—The content of granules of coal whose diameter is more than 2 mm is 30%; III、V—Raw coal; IV—The content of granules of coal whose diameter is more than 2 mm is 100%

The curve III in Fig.6.7 also shows the influence of water content ω_c on the cohesive force c. The cohesive force is mainly composed of molecular applied force within the granular water film and cementation applied force of chemical compounds in granules. The cohesive force has influence on the granular flowability and even make the granules gradually lose motion capability. Therefore, the cohesive force is the most harmful factor to cause blockage.

When water content ω_c is equal to zero, there is no water film between granules, so there is no cohesive force. Practical experiences have proved that after drying fine ores that have a very strong cohesiveness at the bottom of the mine-car, they will completely lose the cohesiveness. With the increment of the moisture content, a water film is formed between the granules, and then surface tension is generated on the gas-water interface. At the same time, gelatinous substance between granules and aquatic crystallisation generated by moisture will generate cohesive action. Therefore, cohesive force gradually increases, indicating the existence of maximum limit. After the moisture in the granules reaches the saturated state the water film between the granules and the surface tension will be destroyed. Therefore, the cohesive force will decrease continuously. So when dealing with incidents of gravity shaft blockage, using the method of filling water into the gravity shaft is based on the above results.

As mentioned before, when the component force of the granular mass on its flow direction is more than the shear resistance, the granules will keep on a state of continuous motion. Eq. (6.28) shows that the shear resistance is composed of frictional force and cohesive force, but it is very difficult to determine them. So by considering them very carefully, and using dynamic direct shear device[2,64], the relation between granular shear strength τ and water content ω_c can be obtained by experiments (shown in Fig. 6.8 and Fig. 6.9)[64].

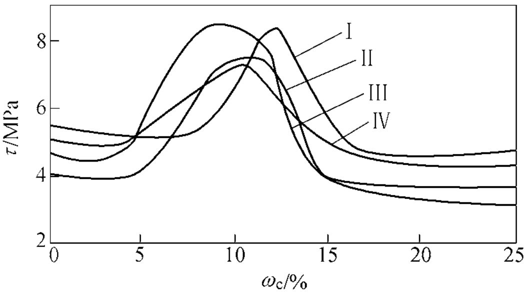

Fig. 6.8 Relation between shearing strength τ of different materials and water content ω_c

I —Sandrock; II —Sandy shale; III—Argillaceous shale; IV—Mineraldressing tailings

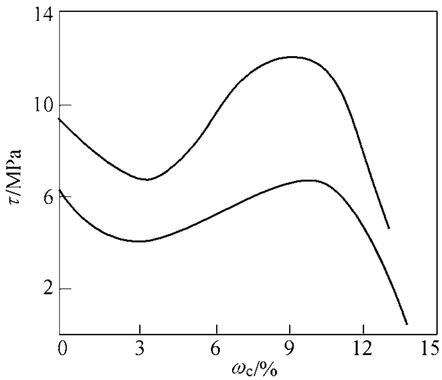

Fig. 6.9 Relation between shearing strength τ of dynamic and static comparative test and water content ω_c

Fig. 6.8 is the results of static shearing tests of different granular materials. Fig. 6.9 is the results of comparative tests of static and dynamic shear. A great deal of experimental investigation show that with the increment of water content ω_c the shear strength τ decreases at the beginning and later increases; τ has the extreme value when the water content reaches a certain limit, then it shows a decreasing tendency. The mechanism is the same as that of the influence of water content on frictional force and cohesive force. It is noticeable that in Fig. 6.9 when ω_c is about 13% the sample in the course of static shear still has a certain shearing strength, but shear strength τ of dynamic shear is almost zero. The reason for this is that in the state of saturated water, because of vibrating action, the granular materials generate vibrating liquefaction. Consequently, vibrating force destroys the contact between the granules, and the former contact stress between the granules is transferred to the pore water causing pore water pressure to increase rapidly and making granules in the state of suspending. The granular materials show the characteristic approximating to the fluid body and then the shearing strength is lost. Therefore, under the condition of both high fine materials and water content vibration is an effective method to deal with the blockage of gravity shaft and bunker.

Simply, the influence of moisture on granular flowability has the following laws: when the water content ω_c is 3%~4%, granular shearing strength τ is low and granular flowability is better; when the water content ω_c is 8%~12%, granular shearing strength τ has the maximum value, here the granular flowability is worse and blockage accidents easily happen; when water content ω_c increases to saturated state, granular shearing strength τ has the decreasing tendency and granular flowability is improved, especially when the granular shearing strength τ is zero under the action of vibration the granular flowability is the best. In production practice, it is very important for improving the granular flowability to control appropriate water content. But the incidents of blockage due to the water content should be avoided. If blockage incident happens, the solving method is filling water into the gravity shaft or exerting vibration in vibratory ore drawing case.

6.3 Influence of Vibration on Granular Flowability

The granular media are composed of a great number of granules. For a single granule, it has the characteristic of solid state. But because of the influence of granule's own weight, for the whole granular media it has the flowability. It is out of question that its flowability is limited because its internal frictional force is very high.

The granules in a container can exert horizontal pressure on the container wall. But the pressure value is less than the vertical pressure at the same depth, and this can be expressed as:

$$P_H = P_V K_C$$

where P_H is the pressure in the horizontal direction (namely lateral direction); P_V is the pressure in the vertical direction; K_C is the coefficient of the lateral pressure.

The coefficient of lateral pressure K_C is the function of granular internal friction angle φ_n. According to the theory of granules, the computation expression of this value can be derived by[5]:

$$K_C = \frac{1-\sin\varphi_n}{1+\sin\varphi_n} = \tan^2\left(45° - \frac{\varphi_n}{2}\right) \tag{6.30}$$

For different internal friction angle φ_n the value of its corresponding coefficient of lateral pressure K_C is listed in Table. 6.1.

Table 6.1 Angle of internal friction φ_n and the value of its corresponding coefficient of lateral pressure K_C

φ_n/(°)	K_C	φ_n/(°)	K_C
30	0.333	44	0.180
32	0.307	45	0.172
34	0.283	46	0.163
35	0.271	48	0.147
36	0.260	50	0.132
38	0.238	55	0.099
40	0.217	60	0.072
42	0.198	65	0.049

The coefficient of the granular lateral pressure K_C is: $0<K_C<1$, but for solid it is 0, for liquid it is 1. It can be seen from Table. 6.1 that the bigger the granular angle of internal friction is, the larger the internal friction between granules is, the worse the granular flowability will be, the smaller K_C is, consequently the smaller the pressure in the level direction is. On the contrary, with the enhancement of the granular flowability, the value of K_C increases and the horizontal pressure more approximates to vertical pressure. This shows that granules have the characteristic of transforming from a non-flow state to a flow state.

The transformation of the angle of internal friction φ_n shows the alteration of the granular flowability. So the angle of the internal friction φ_n is the basic physical quantity characterizing the granular flowability.

The angle of internal friction can be obtained by shearing tests. In the tests different vertical pressures are exerted on samples and then corresponding shearing resistances are obtained. Therefore a set of values of direct stress σ and shearing stress τ can be obtained, and then the coordinates σ-τ are drawn in a graph (shown in Fig. 6.10). So the curve of the granular shearing strength can be obtained. The included angle of the curve and the horizontal ordinate σ is called as the angle of internal friction. The tangent of the angle of internal friction is called as the coefficient of internal friction.

Fig. 6.10 shows the curve of a non-ideal granular shearing strength. The non-ideal granules have cohesive force C. So the coefficient f_n of internal friction is:

$$f_n = \tan \varphi_n = \frac{t - C}{\sigma} \tag{6.31}$$

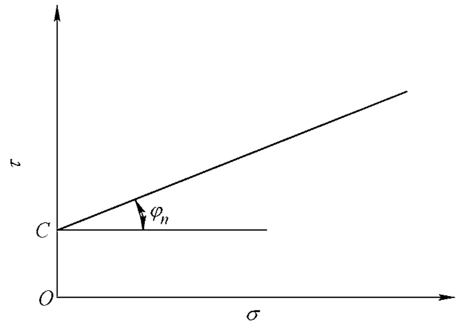

Fig. 6.10 Curve of granular shearing strength

The angle of the internal friction φ_n is the angle of static internal friction when the contact plane between the granules does not slip under the action of force, but has the tendency of slippage. It is influenced by some other factors such as the granular composition, form, porosity, moisture content, and shearing velocity, etc. For specific granules the angle of static internal friction can be regarded as a fixed value. But when the vibration is exerted on granules the angle of internal friction will change.

The energy of vibration obtained by the vibrated granules can be measured by its acceleration. The granules with acceleration can generate inertia force. This inertia force relates to intensity of vibration and is also proportional to granular mass. Granular inertia force appears as interaction force between the granules. Because the granular form, size and position are different, and every granule has a few of contact points with adjacent granules, the number, magnitude and direction of interaction force between the granules are random. For a granule, the active force is three-dimensional. The resultant force of the active forces, whose magnitude are different, is likely to pass the granular mass center or to depart from the mass center so as to make the granule lose balance. Therefore slippage or rolling motion happens among the granules. As a large number of granules lose balance, a relative motion is generated between the granules. The transition from static friction to dynamic friction makes the granular shearing strength decrease.

Within the effective propagation range of vibration energy, especially within the strong vibration area, such as the ore granules at the bottom of the recovery tunnel which only receive triple lateral confinement, a larger value of acceleration can be obtained. Under the condition of strong disturbance of dynamic force, the granules will be loose and the granular shear strength will decrease remarkably.

Moreover, during the course of propagation of vibration energy in the form of wave, the granules will generate shearing deformation and compression deformation. A new stress is generated on the contact point between the granules. Contact stress is another reason for the decrement of granular shear strength.

The increment of the vibrated granular flowability is of great advantage to achieve the open flow of discharged granules. If the granules are ores in the course of vibrating ore-drawing, the capability of ores withdrawal can be heightened and the loss of ores can be reduced.

It should be emphasized that improvement of granular flowability under the action of vibration happens in the course of granular withdrawal under the condition of normal vibration, namely the granules is withdrawn under the condition of not all-around lateral confinement. If the opening is closed so as not to withdraw granules while vibration is exerted, the granular porosity ratio will decrease and then granules will be compacted. Therefore granular flowability can not be improved.

Fig. 6.11 shows the relation between porosity ratio e of dry sandy granules under the action of normal pressure and vibration acceleration a. In the figure η is the ratio of vibration acceleration a to gravitational acceleration g.

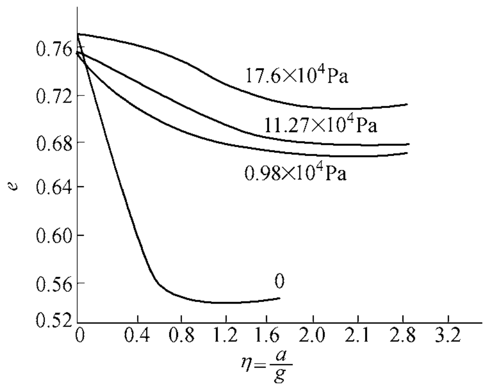

Fig. 6.11 Curve of granular vibration compaction under the action of different normal pressure

It can be seen from Fig. 6.11 that under the action of the same vibration the internal friction force between granular materials increases with increment of normal pressure that makes the granular motion difficult. Therefore the degree of granular vibration compaction decreases. The curves also show that under the action of a given normal pressure when the vibration acceleration exceeds a certain limiting value the degree of granular vibration compaction will become stable.

For fine materials with water under the action of vibration, the "vibrating liquefaction phenomenon" is likely to happen. The reason is that under the action of vibration, the pore water pressure of the saturated granules increases rapidly, as a result they lose shearing strength and enter into a suspended state. When the pore water is gradually discharged, the pore water pressure disappears gradually; fine materials will gradually settle down and deposit. Then they rearrange themselves to be a more close-grained state. The smaller and the more homogeneous the granular materials is, the easily the liquefaction happens. The vibrating liquefaction is of great advantage to withdraw and carry the stored saturated fine materials.

6.4 Wave Propagation and Mechanism of Vibrating Aided Flow in the Flow Field

There are many granular aided flow methods. Among them vibrating aided flow is widely applied because of its practicality, convenience and efficiency. The technology of vibrating ore-drawing is the application of vibrating aided flow in the mining industry. In 1957, the first vibrating ore-drawing equipment in the world was successfully developed in Russia. In the middle of 1970's, the technology of vibrating ore-drawing mechanism began to be applied in China. The first vibrating ore-drawing equipment in China was successfully developed in 1974[1]. The vibrating ore-drawing makes the passing coefficient of the discharge lip decrease from over 3.0 to about 1.5, but a steady flow of the ores can still be kept. Even if the passing coefficient of the discharge lip is only 1.2, generally the discharge lip blocking would not happen[2]. For drawing viscous fine-ores the laboratory experiments as well as practical results indicate that installation of vibrating walls, vibrating brackets or vibrating bedplates, etc. are all effective measures for aiding flow. They have a distinct effect on avoiding the formation of a steady granular arch barrier and the phenomenon of ore pipe flow[2,5].

The worldwide application researches on the technology of vibrating ore-drawing are close to perfection. However, there are still many researches to do some basic theory, such as the propagating and attenuating characteristics of vibrating waves in flowing granular ores, the influence of vibrating waves on the mechanical characteristic of granular ores, etc. This chapter will analyze the propagating law of vibrating waves in flowing granules and the mechanism of the vibrating aided flow by utilizing wave mechanics.

6.4.1 *Experiments*

6.4.1.1 Experimental apparatus

The experimental apparatus are shown in Fig. 6.12. The variable experimental parameters are:

(1) The exciting frequency (20～60 Hz);

(2) The amplitude of vibration ($\leqslant$4 mm);

(3) The degree of open-and-close of the hopper opening;

(4) The lay position of acceleration sensor in the sample materials;

(5) The sample materials.

6.4.1.2 Measuring apparatus

These consist of a portable DXC-TY dynamic signal-meter and a YD series piezoelectric type acceleration sensor.

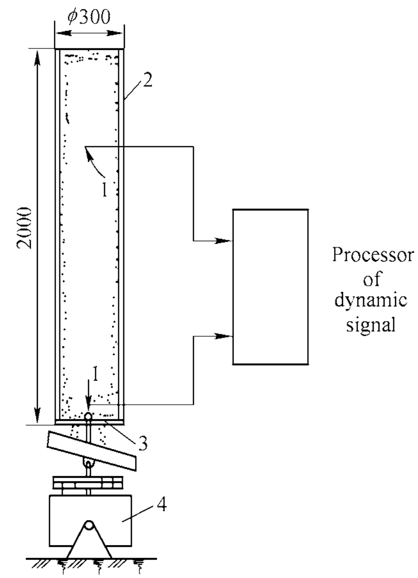

Fig. 6.12 Layout diagram of experimental apparatus and the measuring system

1—YD series accelerometer; 2—Plexiglass cylinder; 3—Vibrating plate; 4—Vibrating table

6.4.1.3 Measuring method

By choosing YD series accelerometers which are compatible to the sample materials in the geometric size and mass, these are placed in the pre-calculated positions in the sample materials. The response signal of the accelerometers is the vibrating acceleration of the granules.

6.4.1.4 Sample materials

The sample materials are shown in Table 6.2.

Table 6.2 Sample materials

Name	Characteristic	Loose specific gravity ρ_g/t • m^{-3}	Cohesiveness
Calcite	1~1.5 cm cube	1.46	No
Scree	1~1.5 cm ovoid	1.54	No
Iron powdery ores	≤0.5 mm fine powder	1.97	Strong

6.4.1.5 Analysis of experimental results

The experimental apparatus is a plexiglas cylinder installed on an upright bracket. The vibrating table vibrates the granular samples in the cylinder by a steel plate, which has an opening. The following are the experimental results:

(1) The vibration effect in the initial phase. The opening is switched on, and then the vibrating table begins to vibrate. The signal of the granular wave received by the sensor is extremely erratic (shown in Fig. 6.13). It shows the relation between time t and acceleration a (a_{max}=75.00 m/s^2, a_{min}=−19.92 m/s^2). The ordinate value is $J \times a_{max}$, where J is a ratio of acceleration. It indicates that the positive acceleration value changes continuously and that the granular samples are looser and have the obvious pulsation phenomena. The signals indicate that the granular samples are in a dynamic process: the structure is destroyed, the new structure is formed and then destroyed again. Moreover, as a whole the effect of vibration is that the granules are continuously loosening.

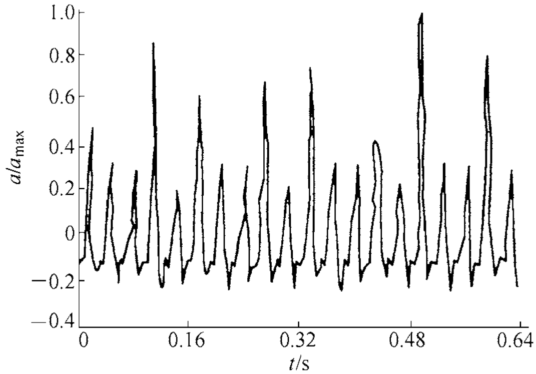

Fig. 6.13 Granular disordered signal of wave

(2) The vibration effect in the steadily flowing phase.If the opening can easily discharge the ores, after a certain time the granular wave signal received by the sensor will become uniform (shown in Fig. 6.14). The curve of the wave signal has the same interpretation as that in Fig. 6.13 (a_{max}=38.87 m/s^2, a_{min}= −23.44 m/s^2). The positive and negative accelerations are more uniform, but the differences of the absolute value are obvious. In this time the granules are looser, and have a steady rheologic state and a steady loose density. The intensity of vibration must be increased if further loosening is required.

(3) The vibration effect in the constraining flowing phase. When the granular sample reaches a steady loose density, the opening is closed. The granular wave acceleration signal received by the sensor experiences an opposite process of the initial vibration phase. The granules are continuously compacted, and the positive acceleration of granules continuously decreases, but the inverse acceleration gradually increases. The ratio of the positive to inverse acceleration decreases continuously and becomes a constant value (shown in Fig. 6.15, a_{max}=11.22 m/s^2, a_{min}=−10.55 m/s^2). At this time, the signals' small differences show that the granular sample is more compact, and there is a steady vibrating density. If the granules need to be compacted further, the vibrating intensity must be increased.

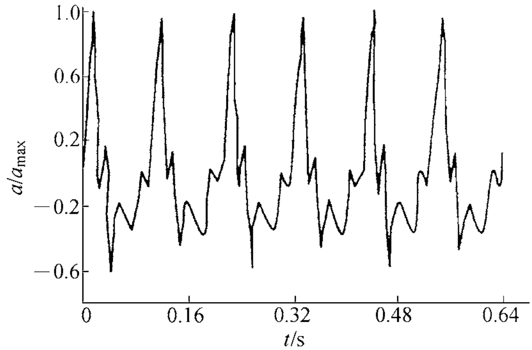

Fig. 6.14 Granular steady-difference signal of wave

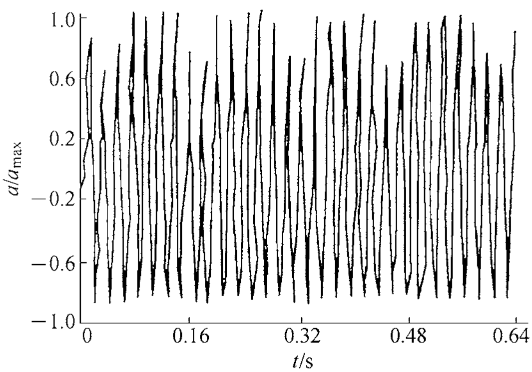

Fig. 6.15 Granular signal of wave with small-difference

6.4.2 *Wave propagation in granular flowing field*

6.4.2.1 Body wave in granular flowing field

The body wave in the granular media has two components, wave P and wave S. If the appropriate coordinate plane (x, o, y) is chosen the wave propagation direction n will always be parallel to the plane (shown in Fig. 6.16). The wave is not dependent on z coordinate. For the longitudinal wave (wave P), the displacement vector is perpendicular to the wave front; so the wave propagation direction will always be parallel to the plane (x, o, y). For the transverse wave (wave S), the displacement vector is parallel to the wave front. The displacement vector of wave S can be resolved into two components. One component is parallel to (x, o, y) plane, and the other one is perpendicular to the plane. The former one is called wave SV (erective polarized shearing wave) and the latter is called as wave SH (level polarized shearing wave). Wave P and wave SV form the motion in the plane

(plane strain problem); wave SH forms the motion outside the plane[136].

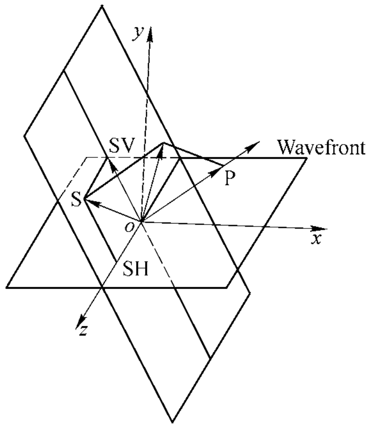

Fig. 6.16 Body wave in the granular medium

6.4.2.2 Propagation characteristics of wave P and wave SV

If the granular state in the flowing field is an ellipsoid and then it is thought that the granular media are weak transverse isotropic media. So the velocity expressions of wave P and wave SV are[200~226]:

$$\left.\begin{aligned} v_{\mathrm{P}} &= (1/2\rho)\{2C_{44} + (C_{11} - C_{44})\sin^2\theta + (C_{33} - C_{44})\cos^2\theta + \\ &\quad \{[(C_{11} - C_{44})\sin^2\theta + (C_{33} - C_{44})\cos^2\theta]^2 + [(C_{13} + C_{44})^2 - \\ &\quad (C_{11} - C_{44})(C_{33} - C_{44})]\sin^2\theta\}^{1/2}\} \\ v_{\mathrm{SV}} &= (1/2\rho)\{2C_{44} + (C_{11} - C_{44})\sin^2\theta + (C_{33} - C_{44})\cos^2\theta - \\ &\quad \{[(C_{11} - C_{44})\sin^2\theta + (C_{33} - C_{44})\cos^2\theta]^2 + [(C_{13} + C_{44})^2 - \\ &\quad (C_{11} - C_{44})(C_{33} - C_{44})]\sin^2\theta\}^{1/2}\} \end{aligned}\right\} \tag{6.32}$$

where ρ is the density of granular media; θ is phasic angle; C_{11}, C_{13}, C_{33}, C_{44} and C_{66} are five independent elastic constants.

According to the above expression, the follows can be obtained:

$\gamma = (C_{66} - C_{44})/2C_{44}$; $\varepsilon = (C_{11} - C_{33})/2C_{33}$;

$$\delta^* = [2(C_{13} + C_{44})^2 - (C_{33} - C_{44})(C_{11} + C_{33} - 2C_{44})]/2C_{33}^2$$

For the weak transverse isotropic media, the anisotropy parameters γ, δ^* and ε are small. If the value of the angle θ is fixed, then the parameters are approximately linearized. Therefore, the velocity expressions of wave P and wave SV are:

$$\left.\begin{aligned} v_{\mathrm{P}}(\theta) &= \alpha_0[1 + \delta\sin^2\theta\cos^2\theta + \varepsilon\sin^4\theta] \\ v_{\mathrm{SV}}(\theta) &= \beta_0[1 + \alpha_0^2(\varepsilon - \delta)\sin^2\theta\cos^2\theta/\beta_0^2] \end{aligned}\right\} \tag{6.33}$$

where

$$\alpha_0 = (C_{33}/v)^{1/2};\quad \beta_0 = (C_{44}/\rho)^{1/2};$$

$$\delta = [(C_{13}+C_{44})^2-(C_{33}-C_{44})^2] / [2C_{33}(C_{33}-C_{44})]$$

For most kinds of granular media, the values of γ, δ and ε have the same order of magnitude. For wave P, if angle θ is smaller, because $\sin^2\theta\cos^2\theta$ is larger than $\sin^4\theta$, its anisotropy is mainly dependent on δ. Fig. 6.17 (ε=0.2, δ=0.2) and Fig. 6.18 (ε=0.2, δ =–0.2) are the wavefronts of radiant wave P in a homogeneous weak transverse isotropy media. In the figures, V_{NMO} is the NMO (normal move out) velocity .It will be seen from these two figures that when $\varepsilon=\delta$ the wavefront of wave P is an ellipse, but when $\varepsilon\neq\delta$ the wavefront is not an ellipse. When the anisotropy is not large, the wavefront of the wave P is approximated to an ellipsoid. It will be known from the velocity expression of wave SV that in most cases its wavefront is not an ellipsoid; only when $\varepsilon=\delta$ its wavefront will turn into an ellipsoid.

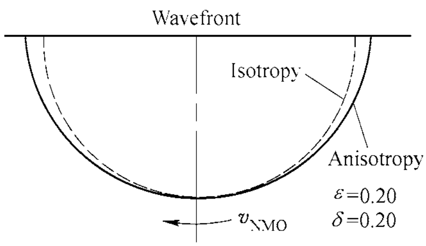

Fig. 6.17 Wavefront of wave P when $\varepsilon=\delta$

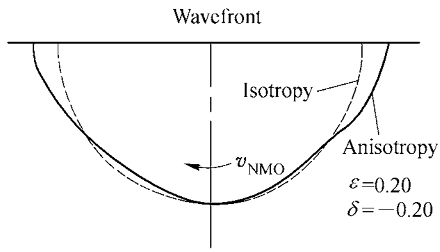

Fig. 6.18 Wavefront of wave P when $\varepsilon=-\delta$

In order to make the study easier, the local characteristics of the wavefront of wave P near some specific radial will be described by the corresponding equivalent ellipsoid. The relation of its radial velocity $v(\varphi)$ and the equivalent ellipsoid' s viewing vertical velocity v_1 and viewing horizontal velocity v_2 is:

$$\frac{1}{v^2(\varphi)}=\frac{\cos^2\varphi}{v_1^2}+\frac{\sin^2\varphi}{v_2^2}v(\varphi) \tag{6.34}$$

If the equivalent ellipsoid contacts with the actual wavefront on a specific radial, the same phase velocity will be obtained. Therefore, when the radial angle φ is changed the viewing vertical velocity v_1 of the corresponding equivalent ellipsoid and its viewing horizontal velocity v_2 will also be changed.

The phase velocity of the ellipsoid has already been proved that[226~237]:

$$v^2(\theta)=v_1^2\cos^2\theta+v_2^2\sin^2\theta \tag{6.35}$$

Therefore, if in the above expression the assumed phase velocity is equal to the corresponding actual phase velocity of the radial, an equivalent ellipsoid of the specific radial of weak transverse isotropy media has been formed.

In order to solve v_1 and v_2 when $v(\varphi)$、 φ and θ are known, according to Eq. (6.34) and Eq. (6.35) the following can be obtained:

$$v_1^2=v^2(\varphi)\cos(\varphi-\theta)\cos\varphi/\cos\theta \tag{6.36}$$

$$v_2^2=v^2(\varphi)\cos(\varphi-\theta)\sin\varphi/\sin\theta \tag{6.37}$$

Therefore, the equivalent ellipsoid of the actual wavefront of weak transverse isotropic media is commonly expressed by Eq. (6.34) and (6.35). Local characteristic of the radial is also described by them.

6.4.2.3 Propagation characteristic of wave SH

According to the definition of γ, it can be rewritten as[238~254]:

$$\gamma = [v_{SH}(\pi/2) - \beta_0]/\beta_0 \tag{6.38}$$

Therefore, γ is the anisotropy parameter of wave SH. The expression of the phase velocity of wave SH is:

$$v_{SH}(\theta) = \beta_0[1 + \gamma\sin^2\theta] \tag{6.39}$$

It is the same as the parameter of wave P when $\varepsilon=\delta$, so the wavefront is bound to be an ellipsoid.

The equation of the phase velocity of wave SH is rewritten as:

$$v^2(\theta) = v_v^2\cos^2\theta + v_h^2\sin^2\theta \tag{6.40}$$

where θ is the phasic angle, v_v is the vertical velocity and v_h is the horizontal velocity.

Suppose that $v_z=v\cos\theta$ and $v_x=v\sin\theta$, then:

$$(v_x^2 + v_z^2)^2 = (v_z v_v)^2 + (v_x v_h)^2 \tag{6.41}$$

Suppose that $v_z=v\cos\varphi$ and $v_x=v\sin\varphi$, then:

$$\left(\frac{v_x}{v_h}\right)^2 + \left(\frac{v_z}{v_v}\right)^2 = 1 \tag{6.42}$$

The above expressions show that the wavefront of wave SH is an ellipsoid whose transverse axis is V_h and whose vertical axis is v_v.

6.4.3 *Mechanism of vibrating aided flow*

It can be seen from the propagation law of the body wave that waves P, SV and SH are present in weak transverse isotropic media[244~250]. Wave P, whose wavefront is elliptical or approximately elliptical, propagates along the axis y. The granular state in the flowing field is a withdrawal ellipsoid or a loosening ellipsoid, so to a certain degree the wavefront will couple with the granular ellipsoid. The elliptical eccentric ratio of the wave front (Fig. 6.17) is less than that of the granular ellipsoid in the direction of the axis y (shown in Fig. 6.1). Moreover, the propagating process of the wave accompanies by the propagation of the stress and the energy. So the granular elliptical eccentric ratio will decrease with the vibration. Since the wave SH propagates along the axis z, its wavefront is also an ellipse. The wavefront approximately couples with the ellipsoid in the direction of the axis z of the granular ellipsoid. Because of being acted by the shear force, the viscosity resistance and the internal friction between the granular ores will decrease, which is in favor of the granular loosening. Since the wave SV propagates along the axis x, its wavefront is not an ellipsoid. The wave front will degenerate into a circle only when $\varepsilon = \delta$.Because of being acted by the shear force, the granular ellipsoid will stretch outwards along the axis x, and the eccentric ratio of the ellipse in the direction of the axis y will reduce. It is known from the elliptical theory that the granular loosening coefficient will increase because of the reduction of the eccentric ratio, which leads to a better flowability.

In the ore-drawingology, the granular flowability is appraised by the comparative coefficient[50,51]. The comparative coefficient is the ratio between the withdrawal volume of the ores by vibrating and the withdrawal volume of the ores by gravity force under the corresponding conditions. The simulated experiment shows that if the height of the withdrawal is in the range of 12～25 meters the comparative coefficient will increase from 1.17 to 1.42. Namely, under this condition the withdrawal volume of the ores by vibrating is 1.17～1.42 times as big as that of withdrawal of the ore by gravity force.

The comparative coefficient is related to vibrating parameters of the vibrating ore-drawing machines, such as the vibrating frequency, amplitude, and exciting force, etc. Under the condition that the lumpiness of the loose granular ores is in the range of 5～6 millimeters, when the relation between comparative coefficient and the amplitude is studied, the frequency is fixed at 13 Hz; when the relation between comparative coefficient and the frequency is studied, the amplitude is fixed at 2.5 cm. The results of this study are shown in Table 6.3. The results of the experiment show that the comparative coefficient increases at a slow rate with the increment of vibrating frequency and amplitude. Namely, withdrawal volume of ore drawing by vibration will slowly increase with the increment of vibrating frequency and amplitude.

Table 6.3 Relation of frequency, amplitude and comparative coefficient

Frequency/Hz	Comparative coefficient	Amplitude /mm	Comparative coefficient
10	1.00	2.0	1.00
13	1.00	2.5	1.00
17	1.10	3.0	1.09
20	1.30	3.5	1.20

It can be seen from the above table that when the vibrating frequency and amplitude are small, the vibration effect on granular flowability is also small. It is known from the physics that the density of the wave energy flow is:

$$I = \frac{1}{2}\rho v A^2 \omega^2 \tag{6.43}$$

where ρ is the media density, v is the velocity of wave S, A is the amplitude and ω is the angular frequency.

The density of the wave energy flow will increase with the increment of the amplitude and the angular frequency. During the course of vibration the wavefront of the wave P and the wave SH will couple with the granular ellipsoid to some degree, so under the condition that the amplitude and frequency are low, the effect on the granular flowability is less because of the minimum form changes of the granular ellipsoid by vibration.

When the amplitude and frequency gradually increase, the wave energy density will also increase. At this stage, the following reasons, the longitudinal wave stress and the shearing stress act on the granular media; the wavefront of the wave P and the wave SH are not coupled with the granular ellipsoid; the granules have got more energy and active ability which will transform the shape of the granular ellipsoid to some degree; the wavefront of the wave SV is not an ellipse so as to cause the shearing stress which make the granular ellipsoid expand outward along the axis x, the eccentric ratio decreases and correspondingly the granular coefficient increases. In addition, when the vibrating energy propagates outward in the form of a wave and shearing and compressing deformations of the granular ores take place, a new stress will be generated at each others' contact points of the granules. Because of the contact stress the granular viscosity resistance and internal friction will be decreased. Consequently the granular shearing strength will decrease. This decrease of the internal friction is represented by the decrease of the internal friction angle and the internal friction coefficient (Table 6.4), so that the granular ores have better flowability.

Table 6.4 Inner friction angle and inner friction coefficient in flow field

Material name	Inner friction angle (static) /(°)	Inner friction angle (dynamic) /(°)	Inner friction coefficient (static)	Inner friction coefficient (dynamic)
Hematite	40~45	30~35	0.84~1.00	0.52~0.70
Broken ores	45	35	1.00	0.70
Anthracite	27~45	27~30	0.51~1.00	0.51~0.57
Gravel	30~45	30	0.57~1.00	0.57
Limestone	40~45	30~35	0.84~1.00	0.57~0.50

7

Vibrating Drag Reduction of High Density Slurry Transported by the Pipeline

7.1 Simple Introduction of Drag Reduction Methods

Because the pipeline transportation has many advantages in technique, economy, administration, environmental conservation and productive capacity, it has a rapid development in many fields in recent years. In order to improve the transportation efficiency and to save energy, the study on the mechanics of drag reduction mechanics has attracted more and more attentions. Many drag reduction methods are available so that the mechanics of drag reduction has become an independent subject. At the early stage, the study on drag reduction was focused on the decrease of the drag force of the fire fighting system in order to increase the height of the spray; the draining of sewage water in sewer pipes and floodwater, the watercraft and weapons propelling under water, etc. The drag reduction techniques are concerned with saving energy and improving efficiency. Moreover the drag reduction phenomenon has a close relation with the basic law of generation of the boundary shear edge. So in recent years the study on drag reduction phenomenon has made a great progress. At present, the drag reduction techniques have been extended into offshore petroleum exploration, exploitation, the long-distance pipeline transportation of crude petroleum and solid material slurry.

At present the applications of the drag reduction techniques to the pipeline transportation are mainly to transport petroleum, crude petroleum, coal slurry, ores, slurry and slurry of other solid materials. But according to the drag reduction mechanism, the pipeline transportation of petroleum and crude petroleum is different from that of coal slurry and slurry of other materials. The former is one phase system and belongs to the pipeline transportation of Newton' s system, while the latter is two-phase or multiphase system and belongs to the pipeline transportation of non-Newton' s system. So the drag reduction of materials in pipeline transportation is more complicated.

7.1.1 *Drag reduction by macromolecular solution*

In 1949 Toms made the experiment of dissolving a little poly methacrylic acid methyl ester into the organic solution of hydraulic flow. Consequently the internal flow and the drag force decreased greatly. After that macromolecular solution has been used to reduce the drag force. The main characteristics of macromolecular used to reduce drag force is that their rated molecular weight are as much as one million. Besides this it must have the single long chain molecular structure and good dissolubility.

There are some assumptions about the mechanical figure of macromolecular solution for drag reduction: firstly, considering that the macromolecular causes drag reduction because the macromolecular generates slippage in the boundary region; secondly, considering that macromolecular solution delays the transition of laminar flow in the near wall region to hydraulic flow; thirdly, considering that the macromolecular solution changes the viscosity of the fluid body. Macromolecular solution drag reduction is effective only on hydraulic flow and not on laminar flow. Even if the fluid core of internal flow or external flow is in the state of hydraulic flow, only when macromolecular solution flows in the boundary region, can the drag reduction be achieved. If it flows in the fluid core region, it is not effective. Drag reduction of several general macromolecular materials is shown in Table 7.1.

Table 7.1 Name and effective concentration range of several general macromolecular materials

Name of material	Name of product	Dissolvent	Mass fraction ($\times 10^{-6}$)	Rated molecular mass ($\times 10^{-6}$)
Guar Gum	J-2FP	Water	60	0.2
Locust Bean Gum		Water	260	0.31
Karaya Gum		Water	780	9.5
Hydroxyethylcellulose	Cellasige QP-1500	Water	200	
	Cellasige QP-30000	Water	220	
	Cellasige QP-52000	Water	160	
Sodium Carboxymethylecelluose	CMC	Water	440	0.2~0.7
Polycthy Lene Oxide	Polyox WSR-35	Water	70	0.2
	Polyox WSR-205	Water	44	0.6
	Polyox Coagulant	Water	12	2.5
Polyacrylamide	Separan NP10	Water	20	1
	Separan NP20	Water	25	2
	Separan NP30	Water	29	2~3
	Polyhall	Water	130	

7.1.2 *Drag reduction by elastic membrane*

At the beginning of 1960s, derived from delphinus bionics, Kramer put forward a special method namely the drag reduction of elastic membrane[255~257]. In this method, a layer of elastic membrane is stuck onto the rigid boundary in order to make the combination of the physical constant of elastic material with the mechanics index very perfect. So that when the boundary layer of the laminar flow waves, the surface of the elastic membrane will wave synchronistically. In this state of synchronous wave the velocity of flow on the boundary surface will be more than zero; moreover the velocity gradient on the boundary surface will decrease. Thereby, the shear force on the boundary will decrease and the generated energy caused by the shear force will decrease, so that the coefficient of the drag force will decrease.

When drag reduction by elastic membrane is applied in practice, there is a difficulty in the pipeline processing technology. Moreover, the capability of the armored layer resisting attrition is poor in materials transportation by the pipeline, so the transportation cost will increase.

7.1.3 *Drag reduction by fibrous material*

Paper pulp is a typical fibrous material[60]. It is recognized that fibrous material could reduce drag force based on the discovery that transporting paper pulp can reduce drag force under a certain condition. Experiments have shown that when transporting paper pulp by a certain pipe diameter, the drag force will increase with the increment of velocity of flow; after increasing further to some point, the drag force will reach the maximum value. By increasing the velocity of flow continuously, however the drag force will decrease; after decreasing to some point, the drag force will then continuously increase. This is shown in Fig. 7.1.

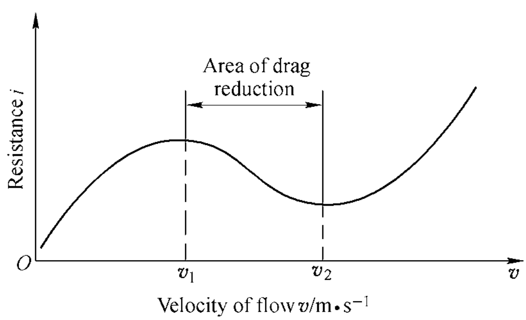

Fig. 7.1 Diagram of curves of i-v of paper pulp

Because the cheap fibrous material is difficult to find, the probability of applying this drag reduction method into practice is little. In addition, the paper pulp with fibrous material will bring further problems, such as dehydration, sewage, and environmental protection, etc. Hence its practical value is very small.

7.1.4 *Drag reduction by pendular water ring*

In China, with the aim of solving the drag reduction of tailings filling slurry, the researcher Han Wenliang et al. put forward the drag reduction of pendular water ring and conducted a vast amount of experimental researches. Their results showed that this method was only applicable to laminar flow not to turbulent flow.

In the drag reduction of pendular water ring, the high viscosity fluid is partly displaced by the low viscosity fluid. In this way the shear deformation of high viscosity fluid will be partly displaced by that of low viscosity fluid and the viscosity of boundary layer will reduce. Thereby a successful drag reduction is achieved. In many fields drag reduction by pendular water ring is widely applied, such as the hovercraft, mechanical air bearing, etc.. The effect on drag reduction is considerably obvious.

7.1.5 *Drag reduction by high pressure gas injection*

By a lot of experimental researches Heywood and Richaidson et al. think that if gas is injected into the laminar flow the effect of the drag reduction is better.The drag reduction of high pressure gas injection belongs to the problem of triphase flow.Its drag reduction mechanism has not been known at present.Generally thinking, after injecting gas the internal structure of the slurry substance will be changed. Then micro-bubbles between the slurry and pipe wall have the function of a "lubricant", thereby to decrease the frictional resistance of the slurry substance.

7.1.6 *Vibrating drag reduction*

In 1984, Kano carried out a research on the effect of vibration on the slug flow transportation with 90° bent pipe and straight pipe whose length was 5 m on a vertical plane. The result showed that the effect of vibration on slug flow were the pressure loss on bent pipe decreasing by 20% and power dissipation in straight pipe decreasing by 16.7%. Yang Lun did the same experiment, which showed that the vibrating drag reduction was effective. Dr. Chen Guanwen in Central South University studied the vibration drag reduction problem of liquid-solid biphase flow by experiments. The experiments showed that for high density transportation the vibrating drag reduction was very effective[255]. All these researchers also studied the mechanism of vibrating drag reduction initiatively. The writers think that their work on drag reduction filled upsome unknown areas in this research field, enriched the mechanism of drag reduction mechanics and pioneered the new application area for vibrating technology. Since the new drag reduction technology is a new topic, their study on vibrating drag reduction is only the primary research. So a lot of works need to be done.

This book contributes further research findings on the vibrating drag reduction, widens the application area of the vibrating drag reduction and puts forward new schemes about vibrating drag reduction.

7.1.7 *Other drag reduction methods*

Besides the above, there are some other drag-reduction methods, such as moulded hull drag reduction, fine sand slurry drag reduction, etc. Moulded hull drag reduction is used to research the effect of the streamline of the substance on keeping the boundary layer of laminar flow. In the early days, researchers paid a lot of attention to this field in order to find the drag reduction method of flow. Fine sand slurry drag reduction was discovered when people researched on the macromolecular drag reduction. By experimental research, it is shown that the mechanism of fine sand slurry drag is similar to that of the macromolecular drag reduction.

7.2 Experiment of Vibrating Drag Reduction of High Density Slurry Transported by the Pipeline

The successful application of the vibrating drag reduction technology in granular media shows that the effect of vibration on the movement of granular media is significant. The vibrating ore-drawing technology is an example of a successful application of this technology. The transportation experiment of the gas-solid two-phase pipeline flow also shows that it is favorable to decrease the transportation energy dissipation that the external dynamic force excites the pipeline to vibrate. The vibrating drag reduction experiments prove that vibration also has an obvious effect of drag reduction on high density slurry substance.

7.2.1 *Experimental system of vibrating drag reduction*

Though an external force, vibrating drag reduction technology excites the pipeline vibration in order to decrease transportation dissipation within the slurry substance[60,255]. The experimental system of vibrating drag reduction includes transportation system, cooling system and vibrating system. The experiment uses two vibrating motors as vibration source and utilizes synchronous vibration principle to make the pipeline generate harmonic vibration in order to achieve drag reduction.

7.2.2 *Dynamics principle of vibrating drag reduction*

The dynamics principle model of the experimental system of vibrating drag reduction is shown in Fig. 7.2. Two vibrating machines are fixed on the same side of the axes of the pipeline. Moreover the connecting line of mass centers of eccentric blocks on two vibrating machines must be parallel with the axes of the pipeline on the vertical plane. In its two parallel axes there is an eccentric block respectively, whose eccentric mass is m_0 and the eccentric distance is e. The two axes revolve synchronously but in opposite direction through a pair of same gears. When the initial center of the mass in two eccentric bodies lies in the same side of the axes line and the force is perpendicular to the axes line, the exciting force which changes along with time in terms of the cosine law is generated.Its expression is:

$$F_t = F\cos\omega t \tag{7.1}$$

where F is the amplitude of the exciting force, moreover $F=2m_0e\omega^2$; m_0 is eccentric mass of eccentric blocks; ω is the radian of frequency; t is the time.

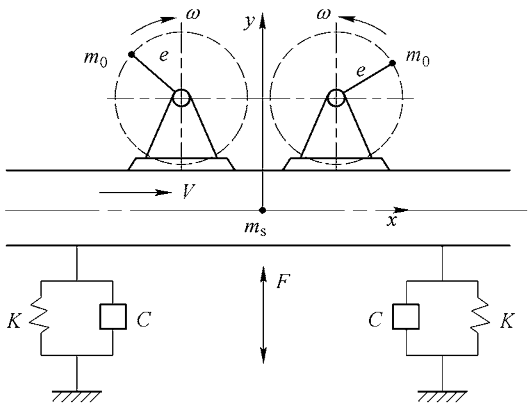

Fig. 7.2 The dynamics principle model of the experimental system of vibrating drag reduction

F can be controlled by regulating the rotational speed of vibrating motors and the included angle of the eccentric blocks of vibrating motors. Under the action of the excitation force,the pipeline vibrates to-and-fro on the vertical plane. Supposing that the rigidity of the system is K and the damping is C, the differential equation of the systematic vibration is:

$$m\frac{\mathrm{d}^2y}{\mathrm{d}t^2}+C\frac{\mathrm{d}y}{\mathrm{d}t}+Ky=F\cos\omega t \tag{7.2}$$

where $m=m_s+2m_0$, m_s is mass of the forced vibration; m_0 is eccentric mass of the eccentric block of single vibrating motor.

Assume that:

$$P^2 = \frac{K}{m}$$

$$2n = \frac{C}{m}$$

$$q = \frac{F}{m}$$

Eq. (7.2) can be rewritten as:

$$\frac{d^2 y}{dt^2} + 2n\frac{dy}{dt} + P^2 y = F\cos\omega t \tag{7.3}$$

Because of the damping, the free vibration disappears rapidly. So only the special solution needs to be discussed. That is:

$$y = A\cos(\omega t - \phi) \tag{7.4}$$

After Eq. (7.4) is substituted into Eq. (7.3), the following expressions of (7.5), (7.6), and (7.7)can be obtained.

Amplitude of the system:

$$A = \frac{q}{\sqrt{\left(P^2 - \omega^2\right)^2 + 4n^2\omega^2}} \tag{7.5}$$

Vibration velocity of the system:

$$\frac{dy}{dt} = -A\omega\sin(\omega t - \phi) = A\omega\cos\left[(\omega t - \phi) + \frac{\pi}{2}\right] \tag{7.6}$$

Vibration acceleration of the system:

$$\frac{d^2 y}{dt^2} = -A\omega^2\sin(\omega t - \phi) = A\omega^2\cos[(\omega t - \phi) + \pi] \tag{7.7}$$

where, vibration period:

$$T = \frac{2\pi}{\omega} \tag{7.8}$$

and vibration frequency:

$$f = \frac{1}{T} = \frac{\omega}{2\pi} \tag{7.9}$$

7.2.3 *Analysis of experimental results of drag reduction*

The experiments adopted tailings of Dahongshan as transportation materials where five kinds of densities are used, namely C_W=53.9%, 60.7%, 63.8%, 67.2%. The results by analyzing are shown in Table 7.2, where τ_{w1}, i_{m1} in the table respectively expresses the value of the shear stress of sidewall and dissipation of drag force in the course of general transportation; τ_w, i_m respectively expresses the value of shear stress on the sidewall and the dissipation of drag force under the action of vibration; $\Delta\tau_w / \tau_{w1}$ and $\Delta i_m / i_{m1}$ express the effect of the vibrating drag reduction.

It can be seen from Table 7.2 that:

(1) Whether $\Delta\tau_w / \tau_{w1}$ or $\Delta i_m / i_{m1}$ is used to express the effect of vibrating drag reduction, when the transportation velocity of the slurry substance of every

concentration is 1 m/s, the effect of the vibrating drag reduction is the best.

(2) With the increment of transportation concentration, the dissipation of friction resistance is a major part of the dissipation of resistance and (though appears as $\Delta\tau_w / \tau_{w1}$) is more close to $\Delta i_m / i_{m1}$.

(3) When the transportation velocity $v \leqslant 2.5$ m/s and the transportation density is no more than 63.8%, the better effect of the vibrating drag reduction can be obtained.

(4) When $v > 2.5$ m/s, the transportation concentration can reach more than 67.2%. Namely, with the same effect of the vibrating drag reduction, the higher concentration slurry material can be transported.

Table 7.2 Experimental results of vibrating drag reduction under the condition of several transportation concentrations

C_w/%	Experimental scheme	Transportation velocity v/m · s^{-1}				
		1.0	1.5	2.0	2.5	3.0
53.9	$\Delta i_m / i_{m1}$	17.5	13.2	11.5	10.3	9.5
	$\Delta\tau_w / \tau_{w1}$	50.0	29.0	16.0	10.9	9.6
60.7	$\Delta i_m / i_{m1}$	16.3	12.9	12.7	11.6	10.8
	$\Delta\tau_w / \tau_{w1}$	30.5	26.5	19.4	14.6	10.1
63.8	$\Delta i_m / i_{m1}$	11.5	10.3	11.9	9.8	—
	$\Delta\tau_w / \tau_{w1}$	40.0	34.8	33.3	—	—
67.2	$\Delta i_m / i_{m1}$	6.8	6.2	5.7	5.3	5.1
	$\Delta\tau_w / \tau_{w1}$	15.4	11.4	10.3	7.4	6.3

7.2.4 *Vibrating drag reduction rate*

Typical expressions of the vibrating drag reduction rate are as follows:

(1) Expressed by viscidity:

$$\gamma_\mu = \frac{\mu_1 - \mu_2}{\mu_1} \times 100\% = \frac{\Delta\mu}{\mu_1} \times 100\% \tag{7.10}$$

(2) Expressed by the coefficient of friction resistance:

$$\gamma_f = \frac{f_1 - f_2}{f_1} \times 100\% = \frac{\Delta f}{f_1} \times 100\% \tag{7.11}$$

(3) Expressed by the shear stress of side wall:

$$\gamma_\tau = \frac{\tau_{w1} - \tau_{w2}}{\tau_{w1}} \times 100\% = \frac{\Delta\tau}{\tau_{w1}} \times 100\% \tag{7.12}$$

where τ_{w1}, τ_{w2} are the shear stress of side wall before and after the drag reduction respectively; μ is viscidity of the slurry.

In the above expressions those whose subscripts are 1 are the correlation coefficients before the drag reduction and whose subscripts are 2 are the correlation coefficients after the drag reduction.

Because the high density slurry substance is mostly non-settleable isotropic body, both the dissipation of the granular settling resistance and the dissipation of the granular impacting resistance are small. The total resistance mostly appears as the dissipation of shear viscous resistance on sidewall. The drag reduction rate can be calculated from Eq. (7.12).

By theoretical derivation Chen Guangwen obtained the following expression of drag reduction rate[255]:

$$\gamma_{\mathrm{m}} = \frac{A\omega\rho_{\mathrm{m}}v}{\frac{8}{3}\tau_0 + \eta\frac{16v}{D}} \times \frac{I_1\left(\sqrt{\frac{\omega}{2v}}R\right)}{I_0\left(\sqrt{\frac{\omega}{2v}}R\right)} \times 10^{-2} \tag{7.13}$$

where A is amplitude; ω is angular frequency; ρ_{m} is density of slurry substance; v is kinematical viscosity of slurry substance; R is internal radius of the pipeline; τ_{w1} is shear stress of sidewall before drag reduction, D is the internal diameter of the pipeline. The value of $I(x)$ can be calculated from Bessel Function Table.

7.3 Mechanism of Vibrating Drag Reduction of High Density Slurry

7.3.1 *Mode of motion of solid granules in fluid flow*

At present it is generally thought that the mode of solid granules motion in fluid flow mainly depends on the characteristics of fluid. According to the relation between the concentration distribution of two-phase flow and its average flow velocity, the mode of motion of solid granules in fluid flow can be divided into four states.

7.3.1.1 Homogeneous suspension flow

Here all granules are in the suspension state. The distribution of density on whole fracture is homogeneous.

7.3.1.2 Unhomogeneous suspension flow

Here all granules are in the state of suspension and granular settling does not occur. The larger granules in the pipeline move close to the bottom. The small granules move on the whole fracture plane.

7.3.1.3 Unhomogeneous flow with sliding bed

Here part of the granules slide along the bottom of the pipeline. Concentration distribution is very unhomogeneous.

7.3.1.4 Flow state with a settling layer at the bottom of the pipeline

Here flow velocity is low enough to allow some solid granules to settle at the bottom of the pipeline. Thereby the effective fracture of the pipeline decreases; concentration distribution is unhomogeneous.

7.3.2 *Analysis of vibrating stress wave in the pipeline*

It is generally thought that high density slurry is a kind of ideal Bingham plastic formation and has a fluid core area as well as a non-fluid core area. The concentration gradient does not exist in the fluid core area, but in the non-fluid core area. Because the high density slurry has this characteristic, the wave reflection and transmission will be bound to happen when vibrating stress wave propagates in the slurry. For convenience of study, it is assumed that in the vertical direction of the axes of the pipeline there are three kinds of slurry with different concentrations and density, which are shown in Fig. 7.3.

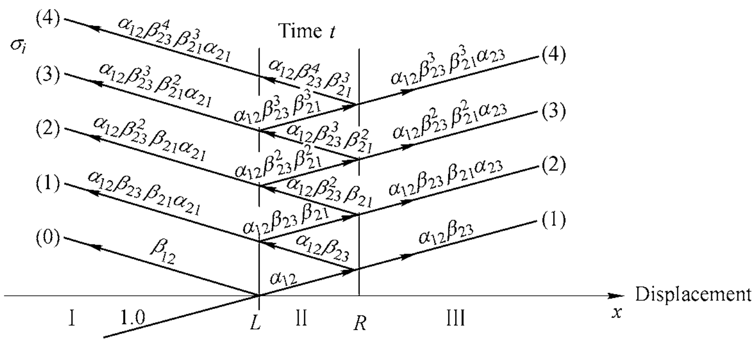

Fig. 7.3 Figure of Langrange x-t

Assume that the stress impulse is $\sigma_i = \sigma_0 f(t), t \geq 0$, wave incidence, inflection and transmission will occur through the plane L and R. A simple analysis shows that:

Wave impedance in the area I, II and III are:

$$R_1 = \rho_1 C_1 A_1;\ R_2 = \rho_2 C_2 A_2;\ R_3 = \rho_3 C_3 A_3 \tag{7.14}$$

where ρ_1, ρ_2 and ρ_3 are slurry density for the zones I, II and III respectively; A_1, A_2 and A_3 are the cross sectional area for the zones I, II and III respectively; C_1, C_2 and C_3 are wave propagation velocity for the zones I, II and III respectively.

When the stress wave propagates from the area I to II, its coefficient of reflection β_{12} and coefficient of transmission α_{12} are:

$$\beta_{12} = \frac{R_2 - R_1}{R_2 + R_1} \tag{7.15}$$

$$\alpha_{12} = \frac{2R_2}{R_2 + R_1} \times \frac{A_1}{A_2} \tag{7.16}$$

When stress wave propagates from the area II to I, its coefficient of reflection β_{21} and coefficient of transmission α_{21} are:

$$\beta_{21} = \frac{R_1 - R_2}{R_2 + R_1} \tag{7.17}$$

$$\alpha_{21} = \frac{2R_1}{R_2 + R_1} \times \frac{A_2}{A_1} \tag{7.18}$$

Similarly, when stress wave propagates from the area II to III, its coefficient of reflection β_{23} and coefficient of transmission α_{23} are:

$$\beta_{23} = \frac{R_3 - R_2}{R_2 + R_3} \tag{7.19}$$

$$\alpha_{23} = \frac{2R_3}{R_2 + R_3} \times \frac{A_2}{A_3} \tag{7.20}$$

Again, when stress wave propagates from the area III to II, its coefficient of reflection β_{32} and coefficient of transmission α_{32} are:

$$\beta_{32} = \frac{R_2 - R_3}{R_2 + R_3} \tag{7.21}$$

$$\alpha_{32} = \frac{2R_2}{R_2 + R_3} \times \frac{A_3}{A_2} \tag{7.22}$$

After stress wave reflects and transmits repeatedly, the transmission stress wave in the area I is:

$$\sigma_1 = \left[1 + \beta_{12} + \alpha_{21}\beta_{23}\alpha_{12} \sum_{k=1}^{n} \left(\beta_{21}\beta_{23} \right)^{k-1} \right] \sigma_i \tag{7.23}$$

Similarly, the transmission stress wave in the area II is:

$$\sigma_2 = \left[\alpha_{12} + \alpha_{12} \sum_{k=1}^{n} \beta_{23}^{k}\beta_{21}^{k} + \alpha_{12} \sum_{k=1}^{n} \left(\beta_{23}\beta_{21} \right)^{k-1} \right] \sigma_i \tag{7.24}$$

Again, the transmission stress wave in the area III is:

$$\alpha_3 = \left[\sum_{k=1}^{n} \alpha_{12}\alpha_{23} \left(\beta_{21}\beta_{23} \right)^{k-1} \right] \sigma_i \tag{7.25}$$

By analyzing σ_1, σ_2, σ_3, it can be found that:

$$\sigma_1 > \sigma_2 > \sigma_3 \tag{7.26}$$

Thus, the stress wave gradually attenuates while propagating along the vertical direction of the pipeline; so the stress borne by the granules in the vertical direction gradually decreases. Because the stress on the upper layer granules is smaller than the stress on the under-layer granules, the longitudinal wave generated by the vibration forces under-layer granules slightly move upwards.Thereby the concentration gradient of the slurry decreases in the vertical direction of the axes of the pipeline and becomes more homogeneous.As a result, the dissipation of viscous resistance of the slurry decreases; the shear stress on the sidewall decreases; and the effect of drag reduction is achieved.

7.3.3 *Effect of the pipeline vibration on flow velocity gradient of side wall*

In the above analysis, it is thought that longitudinal wave makes the slurry' s concentration gradient in the vertical direction of the axes of the pipeline decrease and the slurry becomes very homogeneous. This transformation will cause the velocity of the slurry' s movement in the pipeline and the fluid velocity of the laminar boundary layer of the pipeline wall to redistribute. The transformation is an important reason for the decrement of the resistance dissipation of high density slurry transportation.

According to the laminar boundary layer theory, the expression of distribution of flow velocity u_{δ_1} in the laminar boundary layer before the drag reduction is:

$$u_{\delta_1}=\frac{u_1^{*2}}{v}y^2+\frac{u_1^{*2}}{v}\left(1-3\frac{\delta_1}{R}\right)y \tag{7.27}$$

where u_1^{*} is the velocity of friction resistance before the drag reduction; δ_1 is the thickness of laminar boundary layer before the drag reduction; R is the radius of the pipeline; and v is the kinematic coefficient of viscosity.

When $\delta_1 << R$, namely $\delta_1/R\approx 0$, flow velocity gradient of the sidewall before the drag reduction is:

$$\left.\frac{\mathrm{d}u_{\delta_1}}{\mathrm{d}y}\right|_{y=0}=\frac{u_1^{*2}}{v}\left(1-3\frac{\delta_1}{R}\right) \tag{7.28}$$

approximating to:

$$\left.\frac{\mathrm{d}u_{\delta_1}}{\mathrm{d}y}\right|_{y=0}=\frac{u_1^{*2}}{v} \tag{7.29}$$

According to the laminar boundary layer theory, the expression of distribution of flow velocity u_{δ_2} in the laminar boundary layer after the drag reduction is:

$$u_{\delta_2}=u_{\delta_1}+Ak\left|\frac{I_0(kr)}{I_0(kR)}\right|\mathrm{e}^{i\left(\xi+\frac{\pi}{2}\right)}\Bigg| \tag{7.30}$$

where I_0 is a zeroth order Bessel function; A is the amplitude of sidewall; i is imaginary number; r is the distance between any points to the pipe center; $k=2\pi/\lambda$; $\xi=k(x-ct)$, c is the wave velocity and t is the time.

Substituting expression (7.27) into expression (7.30)gives:

$$u_{\delta_2}=\frac{u_1^{*2}}{v}y^2+\frac{u_1^{*2}}{v}(1-3\frac{\delta_1}{R})y+Ak\left|\frac{I_0(kr)}{I_0(kR)}\right|\mathrm{e}^{i\left(\xi+\frac{\pi}{2}\right)}\Bigg| \tag{7.31}$$

Using the above expression to differentiate y, obtain that:

$$\left.\frac{\mathrm{d}u_{\delta_2}}{\mathrm{d}y}\right|_{y=0}=2\frac{u_1^{*2}}{v}y+\frac{u_1^{*2}}{v}\left(1-3\frac{\delta_1}{R}\right)+Ak^2\frac{I_1(kr)}{I_0(kR)}\times\left.\frac{\mathrm{d}r}{\mathrm{d}y}\right|\mathrm{e}^{i\left(\xi+\frac{\pi}{2}\right)}\Bigg| \tag{7.32}$$

Because $r = R - y$, $dr/dy = -1$. When $y = 0$, substitute $r = R$ into Eq. (7.32) and suppose y=0, so the pipeline vibrates the flow velocity gradient of the side wall is:

$$\left.\frac{\mathrm{d}u_{\delta_2}}{\mathrm{d}y}\right|_{y=0} = \frac{u_1^{*2}}{v} - Ak^2 \frac{I_1(kR)}{I_0(kR)} \times \left.\frac{\mathrm{d}r}{\mathrm{d}y}\right| \mathrm{e}^{i(\xi+\frac{\pi}{2})} \Bigg| \tag{7.33}$$

In terms of the character of Bessel function, it can be known that:

$$I_1(kR) < I_0(kR)$$

and

$$0 < \left|\mathrm{e}^{i(\xi+\frac{\pi}{2})}\right| = \left|\cos\left(\xi + \frac{\pi}{2}\right)\right| \leqslant 1$$

comparing Eq.(7.29) with Eq. (7.33)gives:

$$\left.\frac{\mathrm{d}u_{\delta_2}}{\mathrm{d}y}\right|_{y=0} < \left.\frac{\mathrm{d}u_{\delta_1}}{\mathrm{d}y}\right|_{y=0} \tag{7.34}$$

This expression shows that the pipeline vibration makes velocity gradient of the sidewall slurry lower than that before the drag reduction.

According to the two-phase flow theory, before the drag reduction the shear stress of sidewall is:

$$\tau_{w1} = \mu\left(\left.\frac{\mathrm{d}u_{\delta_1}}{\mathrm{d}y}\right|_{y=0}\right) \tag{7.35}$$

where μ is the viscosity of slurry.

While the pipeline vibrates, the shear stress of sidewall is that:

$$\tau_{w2} = \mu\left(\left.\frac{\mathrm{d}u_{\delta_2}}{\mathrm{d}y}\right|_{y=0}\right) \tag{7.36}$$

According to the expression (7.34) then:

$$\tau_{w2} = \mu\left(\left.\frac{\mathrm{d}u_{\delta_2}}{\mathrm{d}y}\right|_{y=0}\right) < \tau_{w1} = \mu\left(\left.\frac{\mathrm{d}u_{\delta_1}}{\mathrm{d}y}\right|_{y=0}\right) \tag{7.37}$$

From Eq. (7.37) it can be seen that the pipeline vibration causes the velocity gradient of the slurry of the sidewall and the shear stress of the sidewall to decrease. The decrement of the shear stress of sidewall indicates the decrement of the resistance dissipation. Thereby the purpose of the vibrating drag reduction is achieved.

7.3.4 *Relation between boundary layer of slurry and drag reduction*

In 1930 s, Nikuradse, Reichardt, et al. conducted the fluid flow experiment in the pipeline whose internal wall was smooth and used the following dimensionless variable to express:

$$\left.\begin{aligned} u^+ &= \frac{u}{u^*} \\ y^+ &= \frac{yu^*}{v} \end{aligned}\right\} \tag{7.38}$$

where u^+ is the dimensionless velocity; y^+ is the dimensionless distance; u^* is the velocity of friction resistance; y is the normal distance when the pipeline wall is regarded as initial point; v is the kinematic coefficient of viscosity. The relation between u^+ and y^+ is shown in Fig. 7.4.

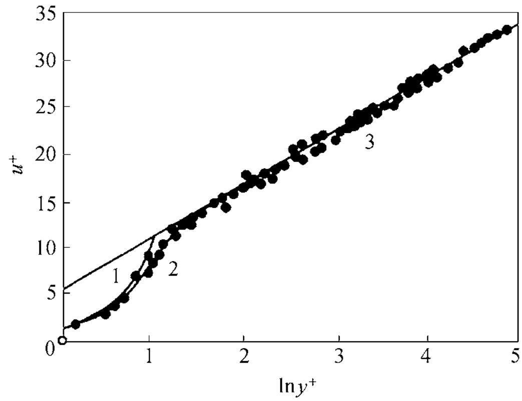

Fig. 7.4 Distribution of dimensionless flow velocity of smooth pipeline
1—Linear distribution of laminar boundary layer;
2—Transition section; 3—Prandtl distribution of turbulent flow

The experiment[256] shows that mean flowing velocity radius theory of Prandtl turbulent flow (shown in the line 3 of Fig. 7.4) is not suitable to the area close to the wall. Only when $y^+>70$, the flow area belongs to the complete hydraulic flow area. Within the range of $10<y^+<70$, this is so-called the laminar boundary layer.

From the kinematical point of view, it is not easy to determine the thickness of the boundary layer by using the experimental method. Its thickness δ^+ is determined by the following expression:

$$\delta^+ = \frac{\delta u^*}{v} \approx 11.6 \text{ 或 } \delta \approx \frac{11.6v}{u^+} \tag{7.39}$$

In the course of slurry transportation by the pipeline, the main characteristics of the pipeline laminar boundary layer are:

(1) The thickness and the distribution of flow velocity of the laminar boundary layer keep invariable along the flow direction. Namely, they are uniform and homogeneous.

(2) The distribution of flow velocity of the laminar boundary layer obeys the parabola law. Within the range of medium Reynolds number, it can be replaced by a straight line.

v(3) Reynolds number of the laminar boundary layer is approximate to a constant and invariable. Moreover:

$$Re = \frac{u_\delta \delta}{v} = \delta^+ \frac{u^* \delta}{v} = \delta^{+2} \approx 135 \tag{7.40}$$

(4) The stability of the laminar boundary layer nearly relates to drag reduction. The simple discussion is as follows:

When the viscous fluid moves in the pipeline, the effect of the viscosity mostly centralizes in the laminar boundary layer. So the drag reduction of the viscous fluid in the pipeline nearly relates to the stability of the laminar boundary layer.

Hou Huichang thinks that the thickness of the neutral stability area in the laminar boundary layer is $\delta \approx 5.5$. So within the range of $0 < y^+ < 5.5$, the fluid body is in the state of an absolutely stable laminar flow; within the range of $5 \sim 5.5 < y^+ < 11.6$, the motion state of fluid body is unstable and the change of the laminar flow will be likely to happen.

The study on the stability of the laminar boundary flow shows that in the course of the fluid body motion an intermittent vibration will exist in the laminar boundary layer. The characteristic value of the neutral vibration in the laminar boundary layer is:

Dimensionless wavelength is $\alpha = 2\pi\delta / \lambda \approx 0.625$, or $\lambda^+ = \lambda u^* / v \approx 107$.

The dimensionless wave velocity is $c^+ = c / u_\delta \approx 0.520$, ratio of the thickness of the laminar boundary layer to wavelength is $\delta / \lambda \approx 0.1$

So neutral exciting frequency is $n = c / \lambda \approx 0.5 \sim 2.0$ Hz, wavelength is $\lambda = 0.1 \sim 0.5$ cm, and the wavelength has the stability.

In order to achieve viscous drag reduction the internal structure of the laminar boundary layer must be changed and the range of the condition of stability of laminar boundary layer must be broaden. The main methods include:

(1) To decrease the flow velocity gradient of the area close to the sidewall in the laminar boundary layer in order to decrease the shear stress of fluid body on the sidewall.

(2) To increase the thickness of the laminar boundary layer in order to make the interfacial flow velocity in laminar boundary layer increase.

(3) To increase the neutral stable Reynolds number of the laminar boundary layer.

(4) To increase the characteristic value of neutral turbulence and to postpone the turn of flow form in the laminar boundary layer.

7.4 Analysis of the Influence of Vibrating Wave on the Flow State Change of the Laminar Flow by Utilizing Multigrid Technique

From the above analysis the presence of the periodical neutral perturbation in the laminar boundary layer can be known. The perturbation forces the laminar boundary layer to generate the change. The vibration method is used to generate stress wave in order to restraint the change; thereby the vibrating drag reduction is achieved. A multigrid technique is utilized to analyze the change of laminar flow[262], and this is described as follows.

7.4.1 *Governing equation and the boundary condition*

It is the author' s belief that the flow of the laminar boundary layer of high density slurry accords with the following expressions:

$$\left.\begin{aligned}&\frac{\partial u}{\partial t}+\frac{\partial uu}{\partial x}+\frac{\partial uv}{\partial y}-\frac{1}{Re}\left(\frac{\partial^2 u}{\partial x^2}+\frac{\partial^2 u}{\partial y^2}\right)+\frac{\partial p}{\partial x}=0\\&\frac{\partial v}{\partial t}+\frac{\partial uv}{\partial x}+\frac{\partial vv}{\partial y}-\frac{1}{Re}\left(\frac{\partial^2 v}{\partial x^2}+\frac{\partial^2 v}{\partial y^2}\right)+\frac{\partial p}{\partial y}=0\\&\frac{\partial u}{\partial x}+\frac{\partial v}{\partial y}=0\end{aligned}\right\}\tag{7.41}$$

where u and v are the components of velocity in the direction of x and y respectively; p is pressure; Re is Reynolds number.

The laminar boundary layer has a standard analytical solution, namely the Pliseuille flow, written as:

$$\left.\begin{aligned}&u_0(x,y,t)=1-y^2\\&v_0(x,y,t)=0\\&p_0(x,y,t)=-\frac{2}{Re}x+\text{const.}\end{aligned}\right\}\tag{7.42}$$

where x, y are the displacement in the direction of axis x and axis y respectively. When the neutral perturbation exists, then:

$$\left.\begin{aligned}&u=u_0+u'\\&v=v_0+v'\\&p=p_0+p'\end{aligned}\right\}\tag{7.43}$$

where u' ,v' are the perturbation velocities; p' is a perturbation pressure.

By substituting Eq.(7.43) into Eq.(7.41) and deleting the superscript of the perturbation component, the perturbation form of the governing equation is simplified to:

$$\left.\begin{aligned}&\frac{\partial u}{\partial t}+\frac{\partial u_0 u}{\partial x}+v\frac{\partial u_0}{\partial y}+\frac{\partial uu}{\partial x}+\frac{\partial uv}{\partial y}-\frac{1}{Re}\left(\frac{\partial^2 u}{\partial x^2}+\frac{\partial^2 u}{\partial y^2}\right)+\frac{\partial p}{\partial x}=0\\&\frac{\partial v}{\partial t}+\frac{\partial u_0 v}{\partial x}+\frac{\partial uv}{\partial x}+\frac{\partial vv}{\partial y}-\frac{1}{Re}\left(\frac{\partial^2 v}{\partial x^2}+\frac{\partial^2 v}{\partial y^2}\right)+\frac{\partial p}{\partial y}=0\\&\frac{\partial u}{\partial x}+\frac{\partial v}{\partial y}=0\end{aligned}\right\}\tag{7.44}$$

Use the boundary condition without slip, namely:

$$\left.\begin{aligned} u(x,-1,t) = v(x,-1,t) = 0 \\ u(x,1,t) = v(x,1,t) = 0 \end{aligned}\right\} \tag{7.45}$$

By choosing a section of the pipeline with a wavelength, suppose that L is the wavelength of the perturbation wave, the periodic boundary condition at its two ends is:

$$\left.\begin{aligned} u(x,y,t) = u(x+L,y,t) \\ v(x,y,t) = v(x+L,y,t) \\ p(x,y,t) = p(x+L,y,t) \end{aligned}\right\} \tag{7.46}$$

7.4.2 *Second order universal implicit array of difference*

Use equidistant crisscross grid to discrete the whole calculating area (as shown in Fig. 7.5). The center of the grid is the point P; the left and right side are point u; the upper and down side are v.

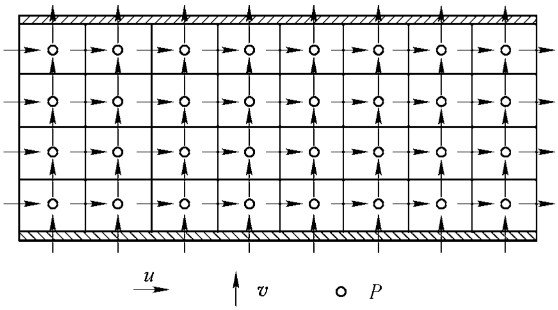

Fig. 7.5 Interlaced grid structure

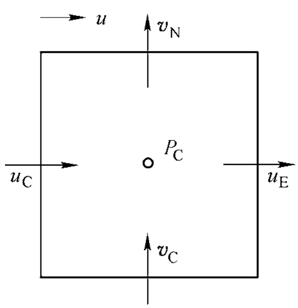

Fig. 7.6 Difference of continuity equation

Make the momentum equation in the direction x and direction y discrete, so the continuity equation is discrete (as shown in Fig. 7.6). Its expression becomes:

$$F_E u_E - F_C u_C + G_N v_N - G_C v_C = S_m \tag{7.47}$$

where:

$$F_E = F_C = \frac{1}{\Delta x}$$
$$G_N = G_C = \frac{1}{\Delta y} \tag{7.48}$$
$$S_m = 0$$

7.4.3 *Disposal of boundary condition*

The periodic boundary condition can be written as:

$$\left.\begin{aligned} u_{1,j} &= u_{n_i-1,j},\quad u_{n_i,j} = u_{2,j} \\ v_{1,j} &= v_{n_i-1,j},\quad v_{n_i,j} = v_{2,j} \\ p_{1,j} &= p_{n_i-1,j},\quad p_{n_i,j} = p_{2,j} \end{aligned}\right\} \tag{7.49}$$

where n_i is the largest label of the grid point in the direction x; i, j is the direction of x, y axis.

If the interlaced grid is used, the boundary condition of the wall plane is:

$$v_{i,2} = v_{i,n_j} = 0 \tag{7.50}$$

where n_j is the largest label of the grid point in the direction y.

7.4.4 *Fourth order universal implicit array of difference*

Using the fourth order or more than fourth order array of difference, for the change of the laminar flow, can effectively overcome the problems of manual viscosity and dispersion. The array of difference is shown in Fig. 7.7.

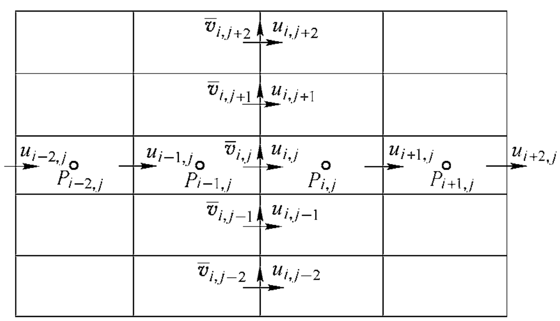

Fig. 7.7 Fourth order array of difference

Make the N-S equations set (7.44) discrete, and then obtain the general form of equations set for fourth order array of difference:

$$\left.\begin{aligned} & A_{\rm EE}u_{\rm EE} + A_{\rm E}u_{\rm E} + A_{\rm W}u_{\rm W} + A_{\rm WW}u_{\rm WW} + A_{\rm NN}u_{\rm NN} + A_{\rm N}u_{\rm N} + A_{\rm S}u_{\rm S} + A_{\rm SS}u_{\rm SS} \\ & -A_{\rm C}u_{\rm C} + D_{\rm WW}P_{\rm WW} + D_{\rm W}P_{\rm W} + D_{\rm WW}P_{\rm WW} + D_{\rm N}P_{\rm N} - D_{\rm C}D_{\rm C} = S_{\rm u} \\ & B_{\rm EE}v_{\rm EE} + B_{\rm E}v_{\rm E} + B_{\rm W}v_{\rm W} + B_{\rm WW}v_{\rm WW} + B_{\rm NN}v_{\rm NN} + B_{\rm N}v_{\rm N} + B_{\rm S}v_{\rm S} \\ & +B_{\rm SS}v_{\rm SS} - B_{\rm C}v_{\rm C} + E_{\rm SS}P_{\rm SS} + E_{\rm S}P_{\rm S} + E_{\rm N}P_{\rm N} - E_{\rm C}D_{\rm C} = S_v \\ & F_{\rm EE}u_{\rm EE} + F_{\rm E}u_{\rm E} + F_{\rm W}u_{\rm W} - F_{\rm C}u_{\rm C} + G_{\rm NN}v_{\rm NN} + G_{\rm N}v_{\rm N} \\ & +G_{\rm S}v_{\rm S} - G_{\rm C}v_{\rm C} = S_{\rm m} \end{aligned}\right\} \tag{7.51}$$

where:

$$\left.\begin{aligned} u_{\rm EE} &= u_{i-2,j},\quad u_{\rm E} = u_{i-1,j} \\ u_{\rm WW} &= u_{i-2,j},\quad u_{\rm W} = u_{i-1,j} \end{aligned}\right\} \tag{7.52}$$

7.4.5 *Distribution iteration, linearity distribution iteration, Gauss iteration*

The difference equation of the nonstationary N-S equation (7.41) can be simply written as:

$$\left.\begin{aligned} Q_{\tau h}u+\delta_x p&=f_1\\ Q_{\tau h}v+\delta_y p&=f_2\\ \delta_x u+\delta_y v&=f_3 \end{aligned}\right\} \tag{7.53}$$

where
$$Q_{\tau h}=\delta_\tau^- +\bar{u}\delta_x+\bar{v}\delta_y-\frac{1}{Re}\Delta h \tag{7.54}$$

δ_τ^- is the euler reverse difference of time τ; δ_x and δ_y are the central differences of x and y; Δh is the discretized Laplace difference operator.

Using the vector form to express Eq. (7.53), then:

$$\begin{bmatrix} Q_{\tau h} & 0 & \delta_x\\ 0 & Q_{\tau h} & \delta_y\\ \delta_x & \delta_y & 0 \end{bmatrix}\begin{bmatrix} u\\ v\\ p\end{bmatrix}=\begin{bmatrix} f_1\\ f_2\\ f_3\end{bmatrix} \tag{7.55}$$

Distribution iteration is a method that trying to use a transformation to change the characteristic of an equation. Suppose that:

$$\begin{bmatrix} u\\ v\\ p\end{bmatrix}=M\begin{bmatrix} \omega_1\\ \omega_2\\ \omega_3\end{bmatrix}=\begin{bmatrix} 1 & 0 & -\delta_x\\ 0 & 1 & -\delta_y\\ 0 & 0 & Q_{\tau h} \end{bmatrix}\begin{bmatrix} \omega_1\\ \omega_2\\ \omega_3\end{bmatrix} \tag{7.56}$$

Eq. (7.55) can be rewritten as:

$$\begin{bmatrix} Q_{\tau h} & 0 & \delta_x\\ 0 & Q_{\tau h} & \delta_y\\ \delta_x & \delta_y & 0 \end{bmatrix}\begin{bmatrix} u\\ v\\ p\end{bmatrix}=\begin{bmatrix} Q_{\tau h} & 0 & \delta_x\\ 0 & Q_{\tau h} & \delta_y\\ \delta_x & \delta_y & 0 \end{bmatrix}\begin{bmatrix} 1 & 0 & -\delta_x\\ 0 & 1 & -\delta_y\\ 0 & 0 & Q_{\tau h} \end{bmatrix}\begin{bmatrix} \omega_1\\ \omega_2\\ \omega_3\end{bmatrix} \tag{7.57}$$

Multiplying the two matrixes, and then substituting the result into Eq. (7.56) gives:

$$\begin{bmatrix} Q_{\tau h} & 0 & 0\\ 0 & Q_{\tau h} & 0\\ \delta_x & \delta_y & -\Delta h \end{bmatrix}\begin{bmatrix} \omega_1\\ \omega_2\\ \omega_3\end{bmatrix}=\begin{bmatrix} f_1\\ f_2\\ f_3\end{bmatrix} \tag{7.58}$$

By using the coefficient matrix Eq. (7.58) and the traditional iteration method to solve with solving repeatedly, and then substituting the results into Eq.(7.56), the new u, v and p will be achieved. The distribution iteration figure is shown in Fig. 7.8.

When $\Delta y \ll \Delta x$ or $\Delta x \ll \Delta y$, a linear distribution iteration is needed, namely all grids on the same line need to be solved synchronously. The linear distribution iteration is shown in Fig. 7.9.

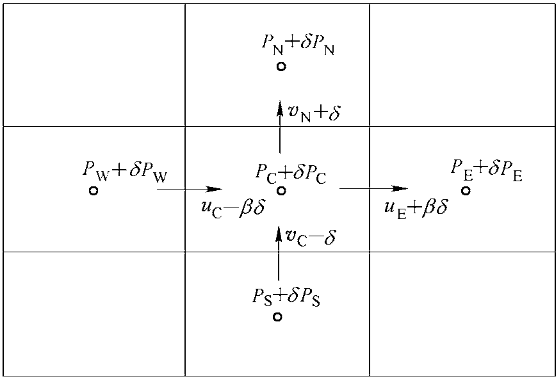

Fig. 7.8 Distribution iteration figure

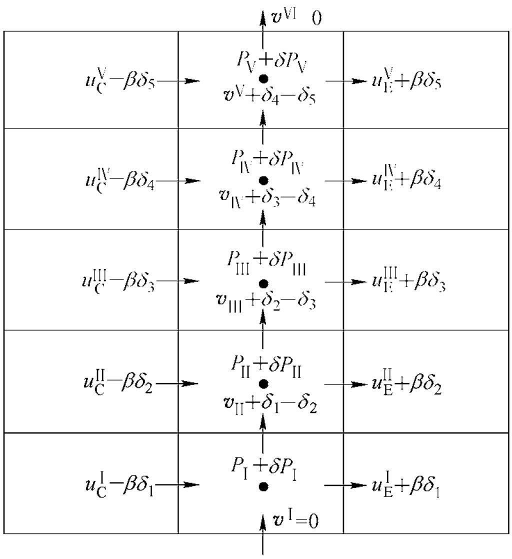

Fig. 7.9 Linear distribution iteration diagram

The specific procedures of the linear distribution iteration are as follows:

(1) Freeze P and carry on slack iteration along the direction of line y, then obtain u;

(2) Freeze P and carry on slack iteration along the direction of line y, then obtain v ;

(3) Regulate all u and v in the grids along the direction of line y in order to meet the continuity equations of all grids.

By using Gauss iteration the following matrix form of the discrete N-S expression; is obtained:

$$\begin{bmatrix} A_C & 0 & -D_C \\ 0 & -B_C & -E_C \\ -F_C & G_C & 0 \end{bmatrix} \begin{bmatrix} u_C \\ v_C \\ P_C \end{bmatrix} = \begin{bmatrix} (\tilde{S}_u)_C \\ (\tilde{S}_v)_C \\ (\tilde{S}_m)_C \end{bmatrix} \tag{7.59}$$

where:

$$\left.\begin{aligned} (\tilde{S}_u)_C &= (S_u)_C - \big(A_E u_{i+1,j} + A_W u_{i-1,j} + A_N u_{i,j-1} + \\ &\quad A_S u_{i,j-1} + D_W P_{i-1,j}\big) \\ (\tilde{S}_v)_C &= (S_v)_C - \big(B_E v_{i+1,j} + B_W v_{i-1,j} + B_N v_{i,j+1} + \\ &\quad B_S v_{i,j-1} + E_S P_{i,j-1}\big) \\ (\tilde{S}_m)_C &= -\big(F_E u_{i+1,j} + G_N v_{i,j+1}\big) \end{aligned}\right\} \tag{7.60}$$

Gaussian elimination can be used to solve Eq. (7.59) directly.

7.4.6 *Half-coarsing multigrid*

Half-coarsing multigrid is coarsening only along the direction y and yet it keeps the former grid distance along the direction *x* invariable (shown in Fig. 7.10).

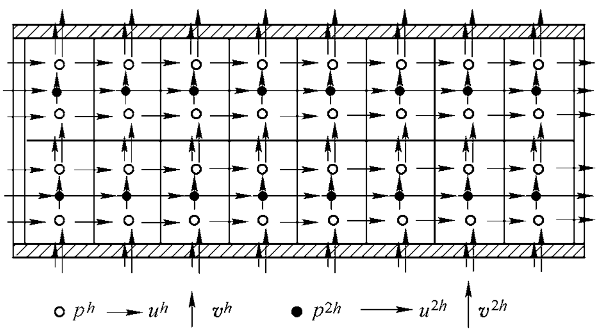

Fig. 7.10 Half-coarsing multigrid

The FAS format of a double-layer grid can be simply described as:

(1) Make the fine grid iteration:

$$L_h u^h = f^h \tag{7.61}$$

(2) Solve along the coarse grid:

$$L_{2h} u^{2h} = L_{2h} I_h^{2h} u^h + \tilde{I}_h^{2h} (f^h - L_h u^h) \tag{7.62}$$

(3) Make modification along coarse grid:

$$u^h \leftarrow u^h + I_{2h}^h \left(u^{2h} - I_h^{2h} u^h\right) \tag{7.63}$$

7.4.7 *Linear theory and initial value of time evolvement*

The expression described the increment of disturbance energy of the most unstable component in the linear theory is:

$$E = \frac{1}{2}\int_{-1}^{1} \mathrm{d}y \int_{0}^{L} \left(u^2 + v^2\right) \mathrm{d}x \tag{7.64}$$

and the increment expression of the general disturbance energy is:

$$E(t) = E_0 \mathrm{e}^{2\omega_1 t} \tag{7.65}$$

or

$$\ln\left[\frac{E(t)}{E_0}\right] = 2\omega_1 t \tag{7.66}$$

where E_0 is the disturbance kinetic energy when $t = 0$, ω_I is the disturbance angular frequency.

7.4.8 *Numerical calculation results*

By choosing three different Reynolds numbers: Re =2000, 7500, 20000, the characteristic values of the most unstable disturbance components corresponding with the Reynolds numbers are shown in Table 7.3. $\omega_\mathrm{R}, \omega_\mathrm{I}$ are real part and imaginary part of the characteristic values respectively.

Table 7.3 Characteristic values of the most unstable disturbance component

Re	ω_R	ω_I
2000	0.312100050	0.01979860
7500	0.24989154	0.00223497
20000	0.20966415	0.00330604

The parameters of numerical calculation are as follows:

Time step:

$$\Delta t = \frac{T_0}{500} = \frac{L}{\omega_\mathrm{R}} / 500 \tag{7.67}$$

Length of the pipeline: $L = 2\pi$

Number of grid points along the direction x: n_i=34

Number of grid points along the direction y: n_j=66 and 130

Here the array of difference uses second order time advance and spatial fourth order difference. By using the multi-grid FAS format and linear iteration, the convergence on every time step is expediated. The effect of the convergence shown in Fig. 7.11 is perfect .

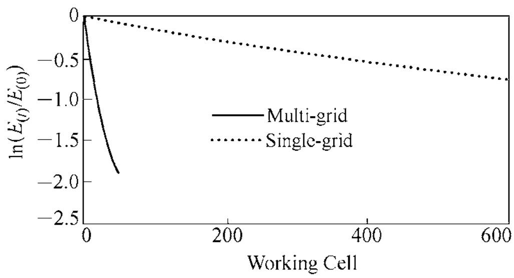

Fig. 7.11 Convergence effect of multigrid

According to the characteristic of the change in the laminar boundary layer, the vibration is exerted in order to make the frequency of vibrating wave similar to the frequency of the neutral disturbance wave, but the direction of wave is reverse. Thereby the change in the laminar boundary layer can be restricted; the disturbance amplitude decreases, and the energy dissipated by the disturbance of the laminar flow decreases.Furthermore the formation of an erratic flow is suppressed. Thus the laminar boundary layer becomes more stable. Consequently, the vibrating drag reduction is achieved.

7.4.9 *The effect of the pipeline vibration on thickness of laminar boundary layer*

From the effect of vibration on the change of the laminar flow, it can be seen that the neutral disturbance exists in the laminar boundary layer under the normal conditions in the course of transportation. Some researches have shown[259~266] that the relationship between the length of disturbance and the thickness of laminar boundary layer is:

$$\frac{\delta_1}{\lambda_1} \approx \frac{0.625}{2\pi} = 0.0995 \tag{7.68}$$

According to the result of study on Stokes' second problem (flow near the vibrating flat plate[255], the length of the wave in the viscous fluid is:

$$\lambda_2 = 2\pi\sqrt{\frac{2\nu}{\omega}} \tag{7.69}$$

where ω is the angular frequency of wave; ν is kinematic viscosity coefficient.

The thickness of the fluid layer caused by the pipeline wall vibration is:

$$\delta_2 = \sqrt{\frac{\nu}{\omega}} \tag{7.70}$$

Within the range of δ_2 fluid body is mainly born the viscous shear and has the character of laminar boundary layer. So δ_2 is thought as the thickness of the laminar boundary layer in the vibrating pipeline flow. When the kinematic viscosity coefficient ν decreases or angular frequency of wave ω increases, δ_2 will decrease.

Dividing expression (7.70)by expression (7.69) gives:

$$\frac{\delta_2}{\lambda_2} = \frac{\sqrt{\nu/\omega}}{2\pi\sqrt{2\nu/\omega}} = \frac{1}{2\pi\sqrt{2}} = 0.1125 \tag{7.71}$$

Study shows[255~257] that $\lambda_2 > \lambda_1$. From Eq. (7.68) and (7.71) it can be known that:

$$\delta_2 > \delta_1 \tag{7.72}$$

The above expression shows that the pipeline vibration makes the thickness of the laminar boundary layer increase. According to the boundary layer theory, the velocity distribution of the transported slurry in the vibrating pipeline is:

$$u = u_1 + u_2 = u_1 + Ak\frac{I_0(kr)}{I_0(kR)}\left|\mathrm{e}^{i\left(\xi+\frac{\pi}{2}\right)}\right| \tag{7.73}$$

Therefore the expression of velocity distribution in laminar boundary layer before and after vibrating drag reduction is:

$$u_{\delta_2} = u_{\delta_1} + Ak\frac{I_0(kr)}{I_0(kR)}\left|\mathrm{e}^{i\left(\xi+\frac{\pi}{2}\right)}\right| \tag{7.74}$$

So $u_{\delta_2} > u_{\delta_1}$. Therefore when the pipeline vibration makes the thickness of the laminar boundary layer increase, the neutral stable Reynolds number of laminar boundary layer also increases, so that:

$$Re_2 = \frac{u_{\delta_2} \cdot \delta_2}{\nu} > Re_1 = \frac{u_{\delta_1} \cdot \delta_1}{\nu} \tag{7.75}$$

where Re_1, Re_2 are the neutral stable Reynolds numbers before and after the drag reduction respectively.

The increment of the neutral stable Reynolds number prevents the change of the flow state in the laminar boundary layer, which provides the necessary condition for the vibrating drag reduction.

8

Fractal Behavior of Saturated Granules

8.1 Introduction of Fractal

J. A. Wheeler (1911-), a well-known theoretical physical scientist, has said that in the past if a person does not know entropy, he is not proficient in science; in the future if a person does not know fractal well, he can not be regarded as a cultured person in science[267~269]. Fractal describes not only the essence of chaos and noise, but also a big range of a series of natural things, which cannot be described by using other methods for a long time in the past, or which are deemed to be unworthy studying in the distinguished field of science. They include coastline, tree, mountain range, galaxy distribution, cloud, polymer, weather, pallium, bronchus of lung, microcycle pipeline of blood, etc[267~283]. Fractal exists in nature widely. Thus, it is very convenient and feasible to use the fractal language to describe the rich and colorful appearance of nature.

Since 1950s Mandelbrot B. B. researched deeply on a new geometry day and night. He tried to use this geometry to describe all kinds of ubiquitous irregular phenomena in the society and nature in a unified way, such as the turbulent motion of fluid, the sinuous coastline, the varied weather, the unsteady stock market, the distribution relation of earning, the price fluctuation, etc. Strictly speaking, in those days he did not know what he wanted to find, even he was not aware what he was looking for was a new geometry[280~301].

One day, in 1975, Mandelbrot was reading his son's Latin textbook, and suddenly he had an idea and decided to create a new word "fractus". So the English word "fractal" was also created at the same time. In the sequel, it is spelled the same in French and German, and the noun and the adjective form are also the same. In the same year, his monograph on fractal was published in French version, and in 1977 he published his English version *Fractals: form, chance and dimension.* In 1982 he published the supplementary work *The fractal geometry of nature*[302~310].

In 1958 Mandelbrot had already been a professional researcher; in 1974 he held a position at the Thomas J. Watson research center of IBM in New York. At the same time a kind of new geometry developed in his brain, and it was different from any other geometry[297~316]. Thus Mandelbrot created the fractal theory. In early days he used fractal to describe the stock price. Unexpectedly a mathematical simulation, which can fool the expert in this field, was created. His fractal geometry shows that the whole market has self-similarity, such as the price fluctuation every day or every month.

According to the book *Turbulent Mirror*, although Mandelbrot affixed his enthusiasm in his fractal geometry, at that time the concept of fractal was still not attracted much attention by others. In the middle of 1980s all kinds of mathematical and physical science nearly simultaneously recognized the value of fractal. In addition, people found in surprise that where there were chaos, turbulent motion and disorder, there was fractal geometry.

8.1.1 *Euclidean geometry and fractal geometry*

The common geometric objects have integral dimension, such as zero-dimensional point, one-dimensional line, two-dimensional plane, three-dimensional solid and four-dimensional space-time[267~283]. However, in the recent decades the fractal dimension, which can be non-integral dimension, has attracted attention widely. The main value of fractal geometry is that it offers a kind of important transition zone between the extreme ordered things and the real chaos. The most remarkable characteristic of fractal is that the complex things can be actually described by simple formulae with only a few parameters.

Dimension is a very important characteristic quantity of geometric objects. Generally speaking, dimension is the number of independent coordinate or the number of independent direction, which can identify the position of a point on the geometric objects. In the Euclidean geometry dimension can be obtained naturally: the point of atlas has two coordinates, which are the longitude and the latitude; a container has three sizes, which are the length, the width and the height. They are two-dimensional and three-dimensional objects respectively. This kind of dimension in Euclidean geometry is topologic dimension, and it is expressed by the letter d in this chapter. The integral dimension is an important principle of Euclidean geometry.

Let' s extend the dimension definition of Euclidean geometry now. If every length of foursquare side increases 3 times, a bigger square is obtained and it is equal to $3^2=9$ times of the original square. Analogously, if every length of cubic side increases 3 times, a bigger cube is obtained and it is equal to $3^3=27$ times of the original cube. Deductively, every independent direction of a d-dimensional geometric object increases l times, as a result an object which is N times of original object is obtained. The relation of these three symbols is $l^d=N$, and the logarithmic expression of this applicable equation can be expressed as:

$$d = \frac{\ln N}{\ln l} \tag{8.1}$$

For Euclidean geometry the topologic dimension d of formula (8.1) is integral. If the dimension of formula (8.1) is not confined by the integer, this kind of dimension is defined as the fractal dimension that is expressed by the capital letter D:

$$D = \frac{\ln N}{\ln l} \tag{8.2}$$

The common functional relations are the linear relation, the exponential relation and the power exponential relation, namely:

$$N \sim cl + d$$

$$N \sim c^l$$

$$N \sim l^c$$

where both c and d are constants.

The functional relation related to the definition of fractal dimension is the power exponential relation, for short, is called the power law. When the linear relation, the exponential relation and the power exponential relation are studied, the linear coordinate system, the semi-logarithmic coordinate system and the double logarithmic coordinate system are the optimum coordinate system respectively. When the fractal and fractal dimensions are studied, the double logarithmic coordinate is often used.

8.1.2 *Self-similarity*

Self-similarity of a system is that the characteristics of certain structure or process are similar for different space and time scale. The part of certain system or structure also has self-similarity[267 ~ 283]. In general, self-similarity has more complex behavior, and it is not the simple superposition after the part is magnified by some figures. However, the quantitative properties of the self-similarity system or structure, such as the fractal dimension, are unchangeable with the operation of zoom-out or zoom-in. This property is called dilation symmetry. The change is only manifested by the external behavior.

In Euclidean geometry the regular bodies, such as point, line, plane and solid (e.g., cube, globe, cone, etc.), are purely abstract things of nature, and these geometrical bodies are strictly symmetrical. In a range of certain precision the two completely identical geometrical bodies can be made. However, in nature there are various kinds of irregular bodies, such as the mountain range, river, coastline, etc. These bodies generated by the nature have the self-similarity and are not strictly symmetrical. So there are not two completely identical bodies. When the nature is observed and studied, it can be known that the self-similarity exists in many subjects, such as physics, chemistry, biology, astronomy, economics, materials science, social science, etc. It also exists in many levels of objective physical system, and it is a kind of universal manifestation of substance's motion and development. It is one of the universal laws in nature.

Scientists have designed many kinds of irregular geometrical figures. For example, H. Von Koch, a Swedish mathematician, firstly put forward the Koch curve in 1904. Koch curve is a kind of fractal figure, and has the self-similarity. It is generated according to a certain mathematical theorem so that it has a strict self-similarity. This kind of fractal in general is defined as the regular fractal[267~273]. However, in nature the fractal does not have the strict self-similarity, but the statistical self-similarity, such as the coastline. The fractal which obeys the statistical self-similarity is defined the irregular fractal, so the coastline belongs to the irregular fractal and the shape of the cloud also belongs to it. They both have no strict self-similarity, but statistical self-similarity[278~281].

Looking down a coastline from the airplane, it will be found that the coastline is not a regular smooth curve, but comprises many peninsulas and bays. With the decrement of observation height, i.e. the increment of the amplification, it is found that the original peninsulas and bays also comprise many smaller peninsulas and bays. Walking along the coastline, the coastline is observed again, one can find much finer structure, i.e., the coast comprises finer peninsulas and bays which have self-similarity. Therefore, a general problem is put forward, "Can the length of a coastline be measured precisely?" The answer is no. The length of a coastline cannot be measured precisely. The reason is that with the decrement of the length of ruler the length of coastline will gradually increase. Using the 1 dm ruler to measure the length of coastline is more accurate than using the 1 m ruler. In 1967 Mandebort firstly published his paper "*How long the British*" in Science, and the academic world was astounded. Utilizing the fractal theory, people find that the length of the coastline is uncertain, and it depends on the measurement unit.

Contrasting the structure of the solar system with the atomic structure, it is found that the two systems have striking similarity in some respects. Why is there the self-similarity among the substance's system whose scales have great disparity in universe? It is not clear, and it probably relates to the dynamic characteristics of the universe's evolution. Moreover, in social science the human's history often has the striking similarity (but not the simple recurrence), which can be regarded as the lively manifestation of self-similarity during the course of the human's development[278~283].

The self-similarity of a substance's system also exists widely in the living nature. For example, the human is the form of the anthropoid evolved to a certain degree. The human's brain, nervous system, respiratory system, digestive system, blood vessel, etc. also have high self-similarity in structure.

8.1.3 *Scale invariance*

The scale invariance is that when any part of the fractal figure is zoomed in, the amplified figure will also show the characteristics of the original figure[278~284]. Therefore, for the fractal whether it is zoomed out or zoomed in, its shape, complexity, irregularity and other properties will not change. So the scale invariance is also called as the dilation symmetry. For example, the cloud is a fractal. When the cloud is observed by using a certain multiple telescope, some complex irregular shapes can be observed. If a high-multiple telescope is used to observe the part of the cloud, the same complex irregular shape can be observed. Even though the much higher one is used, the result is the same.

Besides strict mathematical models, such as Koch curve, the scale invariance can only be applicable to a certain scope for the actual fractal bodies. In general,the lowest boundary is the atomic scale, and the uppermost boundary is the macroscopic body. For the common body, the scope of the scale transformation can include several orders of magnitude. In general, the application range of the scale invariance is called the fractal scale space. For example, the projection of cloud only has the self-similarity in the range of $1 \sim 10^6$ km^2, and its fractal dimension is 1.35. Beyond this scope it is not fractal.

Fig. 8.1 is a projection figure of a self-similarity surface, and Fig. 8.1b is the enlarged drawing of a protrusion in Fig. 8.1a. Fig. 8.1b also shows the basic geometric characteristics of Fig. 8.1a. From these two figures, their multiple of magnification can not be ascertained, that is to say, this self-similarity face obeys the scale invariance.

According to the fractal classification, the self-similarity face of Fig. 8.1 belongs to the surface fractal, and it can be expressed by the following formula:

$$S \sim R^{D_S} \tag{8.3}$$

where S is the surface area; D_S is the surface fractal dimension; R is the surface scale. For the common compact plane, $D_S=2$; for the fractal surface, D_S can be the non-integer between 2 and 3. In fact, D_S also describes quantitatively the surface roughness.

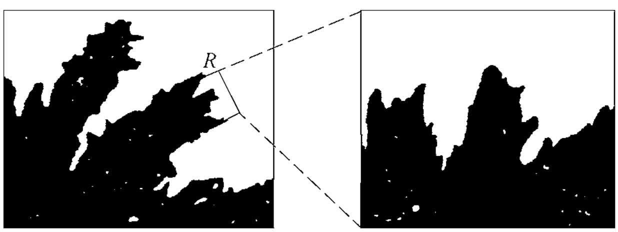

(a) (b)

Fig. 8.1 A projection figure of a self-similarity surface

(a) Before enlargement; (b) After enlargement

8.1.4 *Fractal and complexity*

Most of figures in the nature are very complex and irregular. In fact, the complexity of natural phenomena has been known for a long time, and the ancients showed their understanding of complexity in the description of natural phenomena, such as the cloud's description of China's Tibetan fresco in the 10th century and Japan's early description of ocean wave. The granular media studied in this book also have complexity. Different kinds of granular media (e.g. broken rocks, sandy soils,tailings, etc.) have different formative phenomena, but granules and pores have irregularity, self-similarity, fuzziness, non-linearity, complexity, etc. The main factors of granular structure are the size, shape and distribution of granules and pores, and the interaction among the gas, liquid and solid, etc. The granules and pores are not the regular geometric bodies, so the granular medium can't be described by using one characteristic length. Therefore, the ordinary method cannot precisely describe the granular structure.

In addition, under the action of dynamic force the saturated granules will probably be liquefied. Liquefaction of saturated granules is a phenomenon that granular media show similar to liquid characteristic and lose their carrying capacity completely under the action of dynamic force. Seismic wave, vehicle running, machine vibration, piling, and explosion, etc. can probably cause the liquefaction of saturated granules. In engineering the manifestations of granular liquefaction are mainly the eruptions from the ground, the instability of foundation, the landslide, the settlement of buildings, etc. During the course of vibration, the time series, the power spectral density, the frequency, etc., also have complexity. The steady process of vibrating liquefaction obeys the scaling form, and shows self-organized criticality in the course of vibration. With the increment of the cyclic-index, the stress of saturated granules will decrease rapidly until losing completely, and the strain will increase rapidly, so that the granules cannot sustain load. Consequently the "avalanche" phenomenon takes place.

It is difficult to describe the complexity by using the ordinary geometric methods, so many people are continuously looking for new geometric methods. Since its early introduction by Mandelbrot (1967), the fractal concept has been widely applied[1,2]. It has deeply penetrated into many fields of natural and social sciences. The fractal geometry is a new subject that can describe quantitatively the geometrical body's complex degree, the space filling ability, and also can express the complexity and self-similarity.

The word "fractal" derived from the Latin word "fractus", and its original meaning is "irregular or bitty body". After 1975 the word "fractal" firstly can be found in English dictionary. However, there is a Qing Dynasty epigraphy with carved murals in Nanshan temple, Wutaishan Mountain, Shanxi Province, China, which has the fractal meaning[269].

In nature there are many systems, phenomena and processes with the fractal characteristics, such as the galaxy's distribution, the coastline's shape, the profile of a mountain, the river system, the stock market, the lung's structure, the turbulent flow, the phase change, the city noise, etc.

The fractal has two branches: mathematical fractal and statistical fractal. The mathematical fractal strictly obeys to the self-similarity, such as Cantor aggregate, Koch curve, etc. The statistical fractal is more common in nature and its similarity is only approximate or statistical, such as the coastline, the profile line of mountain, etc.

8.2 Fractal Behavior of Granules and Pores

8.2.1 *Fractal dimension of granularity distribution*

The relation of granularity and granular frequency obeys Weibull distribution[268~273]:

$$\frac{m(<r)}{m_0} = 1 - \exp\left[-\left(\frac{r}{r_0}\right)^n\right] \tag{8.4}$$

where $m(<r)$ is the sum of the mass of granules whose size is less than r; m_0 is the sum of the mass of all granules; r_0 is the average size of all granules; n is the constant power exponent. If $(r/r_0)^n$ is very small, the power function can be expanded according to Taylor series with leaving out a high-order term, then the following equation can be obtained:

$$\exp\left[-\left(\frac{r}{r_0}\right)^n\right] = 1 - \left(\frac{r}{r_0}\right)^n \tag{8.5}$$

Combining Eq.(8.4) with Eq.(8.5) gives:

$$\frac{m(<r)}{m_0} = \left(\frac{r}{r_0}\right)^n \tag{8.6}$$

Many granular statistical data show that the relation of the number of granules N, whose characteristic size is more than r, and r obeys the following expression:

$$N = \frac{C}{r^{D_g}} \tag{8.7}$$

where C is the proportionality constant; D_g is the fractal dimension of granularity distribution.

If Eq.(8.6) and Eq.(8.7) are differentiated the following can be obtained:

$$\mathrm{d}m \sim r^{n-1}\mathrm{d}r \tag{8.8}$$

$$\mathrm{d}N \sim r^{-D_g-1}\mathrm{d}r \tag{8.9}$$

In addition, the relation of the increment of N and the increment of m is:

$$\mathrm{d}N \sim r^{-3}\mathrm{d}m \tag{8.10}$$

From Eq. (8.8), Eq. (8.9) and Eq.(8.10), the fractal dimension of granularity distribution is obtained:

$$D_g = 3 - n \tag{8.11}$$

A considerable amount of experimental studies about granular size and frequency distribution show that granularity distribution has fractal behavior. For example, Hartmann tested that the fractal dimension of granularity distribution of sandy soil is 2.61, that of broken coal is 2.50 and that of gravel is 2.82, etc[268].

8.2.2 *Fractal dimension of granular pore distribution*

The pores among the fractal granules also have fractal characteristic. Suppose that the characteristic radius of pores is R and the number of pores whose radius is more than R is $N_f(>R)$, then:

$$N_f(>R) = \int_R^{\infty} P(R_i)\mathrm{d}R_i \sim R^{-D_f} \tag{8.12}$$

where D_f is the fractal dimension of pore distribution; $P(R_i)$ is the distribution function when the radius of pores is R. Supposing that $V(R)$ is the volume of pores whose radius is more than R, V is the total volume of pores and b is a constant power exponent, then:

$$\frac{V(R)}{V} \sim R^b \tag{8.13}$$

If Eq.(8.12) and Eq.(8.13) are differentiated, according to the following equation:

$$\mathrm{d}N_f \sim R^{-D_f - 1}\mathrm{d}R \tag{8.14}$$

then the fractal dimension of pores distribution is:

$$D_f = 3 - b \tag{8.15}$$

In addition, with the fractal dimension characteristic of pores and granularity fractal distribution of granules, it can be obtained that[272]:

$$D_f = \frac{2D_g}{D_g^2 - D_g + 2} \tag{8.16}$$

The above expression shows that when the fractal dimension of granularity distribution is bigger, the smaller will be the granules. Small granules will fill the pores among the big granules and thus make the porosity and the irregularity of pores decrease. Therefore fractal dimension of pores distribution will become smaller.

The fractal characteristic of pores can be simulated by Sierpinski-gasket model, and the following is the main section of the program, which is successfully debugged in the Visual C++ 6.0 (other programs in this chapter use the same language).

Program 1—the fractal dimension of pores (Sierpinski-gasket)

```
public:
    int x;
    int y;
```

```
// CSierpinskiView drawing

void CSierpinskiView:: OnDraw(CDC* pDC)
{
    CSierpinskiDoc* pDoc = GetDocument();
    ASSERT_VALID(pDoc);
    for (y=0; y<256; y++)
    {
        for (x=0; x<256; x++)
        {
            if (((y-x)&x)==0)
            {
                pDC->SetPixel(x+100, 300-y, RGB(255, 0, 0));
            }
        }
    }
}
```

The running result of the program is shown in Fig.8.2:

The fractal characteristic of pores can also be simulated by Sierpinski-carpet model, and the following is the main section of the program.

Program 2—the fractal dimension of pores 2(Sierpinski-carpet)

```
    public:
    int i, k, MaxY;
    double x, y;
    double d [8] [6];
// CSiercarpetView drawing

void CSiercarpetView:: OnDraw(CDC* pDC)
{
    CSiercarpetDoc* pDoc = GetDocument();
    ASSERT_VALID(pDoc);
    MaxY=200;
    for(i=0; i<8; i++)
    {
        d [i] [0] =0.33333333;
        d [i] [1] =0;
        d [i] [2] =0;
        d [i] [3] =0.33333333;
    }
    d [0] [4] =1;
    d [0] [5] =1; //MaxY;
    d [1] [4] =MaxY;
    d [1] [5] =1;
    d [2] [4] =1;
    d [2] [5] =MaxY;
    d [3] [4] =MaxY;
    d [3] [5] =MaxY/1;
```

```
    d [4] [4] =MaxY/2;
    d [4] [5] =1;
    d [5] [4] =MaxY;
    d [5] [5] =MaxY/2;
    d [6] [4] =1;
    d [6] [5] =MaxY/2;
    d [7] [4] =MaxY/2;
    d [7] [5] =MaxY;

    srand(1);
    x=0;
    y=0;

    for(i=0; i<300000; i++)
    {
        k=rand()%8;
        x=d [k] [0] *x+d [k] [1] *y+d [k] [4];
        y=d [k] [2] *x+d [k] [3] *y+d [k] [5];
        pDC->SetPixel(int(2*x/3)+50, int(2*y/3)+50, RGB(255, 0, 0));
    }
}
```

The running result of program is shown in Fig.8.3:

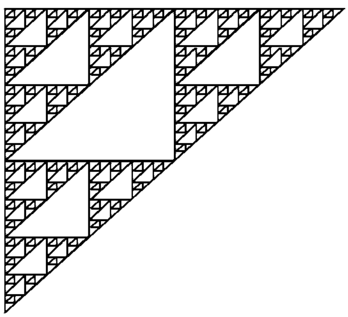

Fig. 8.2 Figure 1 of the pores' fractal dimension (Sierpinski-gasket)

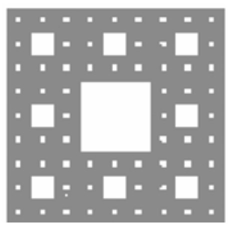

Fig. 8.3 Figure 2 of the pores' fractal dimension (Sierpinski-carpet)

8.2.3 *Fractal dimension of granular surface-to-volume specific surface area ratio*

Granular specific surface area ratio (surface area of unit mass or unit volume) is widely applied to measure granular size. If the roughness of the surface is taken into account, the specific surface area ratio of fine powders is very large. The roughness of granular surface can be described by using the fractal model of Koch curve. The main program of this model is shown in Program 3. Granular fractal surface area can be expressed as follows:

$$S = S_0 r^{2-D_S} \tag{8.17}$$

where D_S is the fractal dimension of the surface, $D_S \in (2.0, 3.0)$; S_0 is the surface area of smooth granules. It can be seen from equation (8.17) that when the granular surface is smoother, the smaller fractal dimension will become, namely $D_S \to 2.0$. So specific surface area ratio S_V can be obtained:

$$S_V = S/(K_V r^3) = K_S r^{1-D_S} / K_V = K_{SV} r^{1-D_S} \tag{8.18}$$

where K_{SV} is the shape factor of specific surface area ratio; K_V is the shape factor of volume.

Program 3—the granule's surface(Koch curve)

```
public:
    double pi;
    double x [8192], y [8192];
    int n;
    double a, a1, a2, a3, a4, b, b1, b2, b3, b4;
    int m, k, l1, l2, l3;
// CKochView drawing

void CKochView:: OnDraw(CDC* pDC)
{
    n=12;

    pi=3.14159;
    CKochDoc* pDoc = GetDocument();
    ASSERT_VALID(pDoc);
    a=sqrt(0.3333)*cos(pi/6);
    b=sqrt(0.3333)*sin(pi/6);
    a1=a;
    a2=b;
    a3=b;
    a4=-a;
    b1=a;
    b2=-b;
    b3=-b;
    b4=-a;
    x [0] =0;
    y [0] =0;
    double x0, y0;
    for (m=1; m<=12; m++)
    {
        l2=int(pow(2, (m-1)))-1;
        l1=l2*2+1;
        l3=l1*2;
        for(k=0; k<=l2; k++)
        {
            x0=x [l2+k];
            y0=y [l2+k];
```

```
                y [l1+k] =a3*x0+a4*y0;
                x [l1+k] =a1*x0+a2*y0;
                x [l3-k] =b1*x0+b2*y0+1-b1;
                y [l3-k] =b3*x0+b4*y0-b3;
        pDC->SetPixel(int(x [l1+k] *500)+50, -int(y [l1+k] *500)+200, RGB(0, 0,
255));
        pDC->SetPixel(int(x [l3-k] *500)+50, -int(y [l3-k] *500)+200, RGB(0, 0,
255));
            }
        }
}
```

The running result of the program is shown in Fig.8.4.

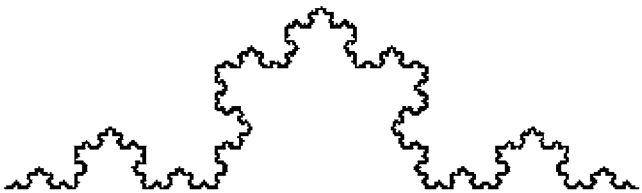

Fig. 8.4 Granule's surface (Koch curve)

8.3 Fractal Behavior of Seepage

8.3.1 *Simple introduction of renormalization group*

The renormalization group method is put forward from the quantum field theory. Recently, it is applied to the study of the high energy asymptotic behavior. Kenneth G. Wilson utilized the renormalization group method to study the critical phenomena and put forward that the renormalization group ascertained the critical behavior of the system at the stationary point. He established the critical theory of the phase change. It was an important breakthrough in the study of critical phenomena, so Wilson had the honor to win the 1982' s Nobel physical prize[278~283].

The aim of the renormalization group method is to gain quantitatively the change of physical quantity when the scale is changed during the course of observation. For example, in a certain scale one physical quantity is measured and marked with p, then it is measured again in another scale which is the double of the former and marked with p' Utilizing a certain scale transformation f_2, the relationship between p' and p is:

$$p' = f_2(p) \tag{8.19}$$

where the subscript of f denotes the double scale transformation. If the scale is doubled again, the following relation will be obtained:

$$p'' = f_2(p') = f_2 \cdot f_2(p) = f_4(p) \tag{8.20}$$

If the above formula is transformed into a common form, the following property of f can be obtained:

$$\begin{cases} f_a \cdot f_b = f_{ab} \\ f_1 = 1 \end{cases} \tag{8.21}$$

where 1 denotes the identical transformation. Because the scale of the transformation f is changeable under the certain given situation, it does not have the inverse transformation f^{-1} generally. On the other hand, if the condition is transformed in advance, its original state cannot be restored. In mathematics this transformation is termed as the semi-group; but in physics it is termed as the renormalization group.

From the definition, this renormalization group closely relates with the fractal. The unchangeable state, which is transformed by f of the renormalization group, is fractal. The renormalization group is the most powerful tool to study the critical phenomena of phase difference.

8.3.2 *Seepage flow model*

Simply speaking, seepage flow is a kind of fluid flow in the random medium. The seepage phenomenon exists in nature widely. For example, the stem, branch of a tree, root and leaf of vegetable are all porous structures where the liquid is transported; in the human's or animal' s tissues and organs, such as lung, heart, liver and kidney, the body fluid is flowing to maintain the common vital activity; in the cell wall of living cell the liquid is continuously seeping; in the porous rocks and sands the petroleum and water are flowing etc. All these belong to the seepage phenomena. The disordered system described by the seepage model is called the seepage system. This kind of system exists widely,such as smoke, dust, virus, amicron, porous medium, random network, forest fire, ect.

In order to know how the liquid flow in the porous granular medium begins, the renormalization group is used as the analysis method. The two-dimensional model of seepage flow is shown in Fig. 8.5a. A square matrix comprises many square boxes, and each box is a unit that may be permeable or impermeable. There are n =256 units in Fig. 8.5a. The seepage probability of each unit is P_0; so the non-seepage probability is $1-P_0$. The definition of the seepage flow is that there is a continuous seepage path from the left to the right. In fact, the seepage or non-seepage of each unit is random, so the problem of seepage flow is a statistical problem. For a given value of P_0, the seepage probability of the square matrix comprised several units is P. If P^* is the critical probability of seepage threshold value, for a bigger square matrix when $0<P_0<P^*$, P will be very small. But when $P^*<P_0<1$, P will be approximate to 1 (Stinchcombe and Wilson, 1976). Therefore, for P_0 there is a critical value P^*, and when $P_0=P^*$ the seepage flow begins. If $P_0<P^*$, for a bigger square matrix, it nearly has no seepage flow; but

when $P_0>P^*$, the square matrix always has seepage flow.

Fig. 8.5a is a 16×16 square matrix, and the total number of units is 256. Supposing that $P_0 = 0.5$, that is to say the seepage flow of a unit is random. There are no horizontal or vertical continuous paths for liquid flow. Using the Monte Carlo method to compute a large number of random behaviors, the seepage probability or non-seepage probability of this square matrix P_0 can be obtained. For the two-dimension square matrix, if n is very big, the result of the numerical simulation is $P^* = 0.59275$ (Stauffer, 1985) when the liquid begins to flow.

For the critical condition $P_0=P^*$, the statistical relationship of frequency in the concentrated area of seepage is very meaningful. The concentrated area of seepage is the number of interconnecting seepage units when the seepage flow starts in the square matrix. The number of units n^*_0 can be obtained from the function of n. For the two-dimensional square matrix, the formula is (Stauffer, 1985) [268,269]:

$$n_c^* \sim n^{91/96} \tag{8.22}$$

Supposing that the reserved squares are the concentrated area of seepage, the result is comparable to the Sierpinski carpet. For the Sierpinski carpet, when n= 9, n_0=8; when n=81, n_c=64. Therefore,

$$n_c = n^{\ln 8/2\ln 3} = n^{D/2} \tag{8.23}$$

Comparing formula (8.22) with (8.23), the fractal dimension of seepage concentrated area under the critical conditions is D=91/98=1.896. The value is approximate to the fractal dimension of Sierpinski carpet D=ln8/ln3=1.893.

If the number of unit n is very large, many random behaviors need to be computed. So much time will be wasted if the direct statistical method is used to study the seepage flow. Another method is shown in Fig. 8.5b. The first-degree layer comprises a square matrix of 4 units. According to the seepage probability P_0 of each first-level unit, the seepage probability P_1 of the first-level primary cell comprising 4 first-level units can be computed. If there is a continuous seepage path from the left to the right in the primary cell, it is believed to be penetrable. The problem is renormalized. The 4 first-level primary cells are turned into 4 secondary-units of the second-level of primary cells. The seepage probability P_2 of the second-level primary cell is ascertained by the seepage probability of the second-level unit (i.e. the first level primary cell). This process is repeated continuously, and then it gradually reaches a high level. This method is called the renormalization group method.

Fig. 8.6 shows all possible cases that the first-level primary cell comprises four first-level units. The probability that all 4 units are impermeable is $(1-P_0)^4$ as shown in Fig. 8.6a. In this situation the primary cell is obviously impermeable. The probability that 1 unit is permeable and other 3 units are impermeable is $P_0(1-P_0)^3$ as shown in Fig. 8.6b, this case has 4 combinations. The permeable unit can exist in any place of primary cell. No matter where the unit is, the primary cell is impermeable. The probability that 2 units are permeable and other 2 units are impermeable is $P^2_0(1-P_0)^2$ as shown in Fig. 8.6c, this case has 6 combinations. The No.1 and No.6 combination have a path through which the liquid can flow from the left to the right, so these 2 primary cells are permeable, but the other 4 primary cells are impermeable. The probability that 3 units are permeable and other 1 unit is impermeable is $P^3_0(1-P_0)$ as shown in Fig. 8.6d, this case has 4 combinations. All the 4 primary cells are impermeable. The probability that all the units are permeable is P^4_0, and this case only has one combination, and it is shown in Fig. 8.6e. Here the primary cell is also permeable.

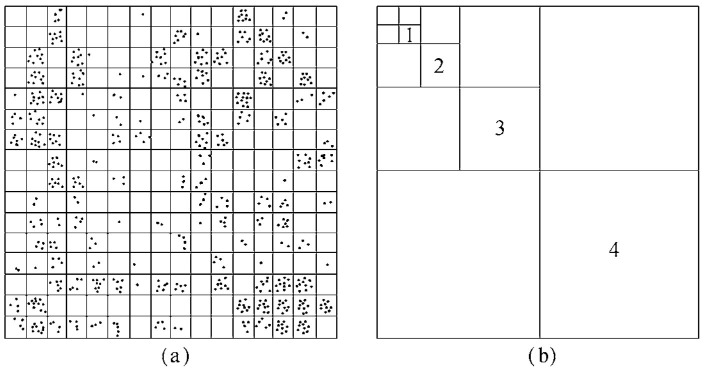

Fig. 8.5 Two-dimensional model of seepage flow

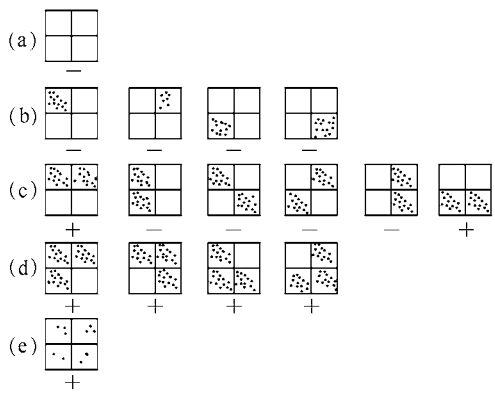

Fig. 8.6 Primary cell comprising 4 units

If there is a continuous path from the left to the right, the primary cell is permeable. The "+" notes that it is permeable, but the "-" notes that it is impermeable

8.3.3 *Fractal analysis of seepage flow*

One of the basic characteristics of seepage system is that there is at least one threshold value or critical value. Therefore, the key problem is that whether it can reach the critical value under the given conditions[278~284]. Considering seepage flow, the point occupation probability has a critical threshold value P_c, and when the point occupation probability $P<P_c$, there is a finite group in the grid points. When $P>P_c$, there is an infinite group in the grid points; when $P=P_c \to 0$, namely the value which is less than P_c but approaches to P_c, there is an initial infinite group in the grid points. As long as the infinite group appears, the grid system reaches the seepage state. In other words, it generates the phase change of seepage. The phase change of seepage is a secondary phase change and its important physical quantity is the seepage probability. When the occupation probability is P, the probability that any grid belongs to the infinite group is called the seepage probability and marked with $\rho(P)$. According to this definition, from P=0 to $P=P_c$ the seepage probability is identically equal to zero, i.e. $\rho(P) \equiv 0$. When $P>P_c$, the seepage probability $\rho(P)$ will increase rapidly with the increment of P, and $\rho(P)$ is the steady increasing function of P. Finally, when P approaches to 1, $\rho(P)$ also approaches to 1, that is to say, the infinite group merges with other finite groups and the whole lattice are held by an infinite group. Therefore, when the phase change of seepage occurs the most important problem in the seepage system is the seepage probability $\rho(P)$. Similar to the common phase change, $\rho(P)$ also has peculiarity at the point P_c. According to the general law of phase change, $\rho(P)$ obeys to the scale law:

$$\rho(P) \sim |P - P_c|^{\beta} \tag{8.24}$$

or:

$$\lim_{P \to P_c} \rho(P) \cong A_{\rho} |P - P_c|^{\beta} \tag{8.25}$$

where β is the critical exponent of seepage probability; A_{ρ} is termed as the critical amplitude of seepage probability.

For a value that is less than P_c, but approaches to P_c, the seepage probability $\rho(P)$ is:

$$\rho(P)\big|_{P=P_c \to 0} = 0 \tag{8.26}$$

In order to describe the seepage process, the incidence function between two points $G(x)$ is also used. It is the probability that when the origin is occupied, the point x away from the origin is also occupied by the same group occupying the origin. For a one-dimensional case, when x = 0, obviously $G(0)$=1; when the nearest point is also occupied, this point certainly belongs to the same group, so $G(1)$ =P. For a incidence point x away from the origin, the point x, $(x-1)$, $(x-2)$, $\cdots$, x = 0 all must be occupied, therefore,

$$G(x) = P^x \tag{8.27}$$

When $P<P_c$=1, the one-dimensional incidence function will approach to zero in terms of the exponent with x:

$$G(x) \sim \exp(-\frac{x}{\zeta}), \quad P < P_c = 1 \tag{8.28}$$

Then utilizing the formula (8.27), ζ can be obtained by:

$$\zeta = -\frac{1}{\ln|P|} = \frac{1}{|1-P|} \quad (\text{if } P\to 1) \tag{8.29}$$

where ζ is termed as the incidence length, and it is the characteristic length of seepage group.

The formula (8.29) shows that when $P\to 1$, the incidence length $\zeta\to\infty$, and the group becomes an infinite group. This state is just the seepage state.The value $P_c = 1$ is termed as the critical value of one-dimensional seepage system. The formula (8.29) also shows that when $P\to 1$, ζ will diverge according to the expression $|1-P|^{-1}$.

For higher dimensional cases, such as the dimension $d=2$ and 3, the value of P_c will not be equal to 1; at that time the incidence function $G(x)$ will obey the following expression:

$$G(x) \sim \begin{cases} \exp(-x/\zeta) & P < P_c \\ (1/x)^{d-2+\eta} & P \to P_c \end{cases} \tag{8.30}$$

where d is the dimension, η is the critical exponent. For the one-dimensional case, $\eta=1$; for high dimensional case, the incidence length ζ obeys:

$$\zeta \sim \frac{1}{|P_c - P|^{\gamma}} \tag{8.31}$$

where γ is another critical exponent, and it only relates to the dimension d. For the one-dimensional case, $d=1$, $r=1$; for the two-dimensional case, $d=2$, $\gamma = \frac{4}{3}$.

The following utilizes the scale characteristics of the initial infinite group to ascertain the relation between the fractal dimension of group D and the critical exponent of the seepage flow. Supposing that there is an initial infinite group in the system, the dimension of group is $R-\zeta(P_c)\to\infty$. Choosing the origin 0 in the initial infinite group, $P_\infty(r)$, the probability of another point $r(r\lesssim\zeta(P_c))$ that is also occupied in this group, becomes:

$$P_\infty(r) - \frac{N(r)}{V(r)} - \frac{r^D}{r^d} = r^{D-d}, (r \ll \zeta(P_c)) \tag{8.32}$$

In order to obtain the common expression of $P_\infty(r)$, it should be multiplied by the scale function $f\left(\frac{r}{\zeta}\right)$, namely:

$$P_\infty(r) = r^{D-d} \cdot f\left(\frac{r}{\zeta}\right) \tag{8.33}$$

The scale function $f(x)$ can be ascertained by the following analysis. In fact, when $x \ll 1$, i.e. $r \ll \zeta$, according to the formula (8.32), $P_\infty(r) \sim r^{D-d}$, so $f(x)$ is a constant and independent of x; when $x \gg 1$, i.e., $r \gg \zeta$, the point r does not belong to the initial infinite group. Therefore, when $r \gg \zeta$, $P_\infty(r)$ is independent of r. So:

$$f(x) \sim \begin{cases} x^{d-D} & x \gg 1 \\ \text{constant} & x \ll 1 \end{cases} \tag{8.34}$$

and

$$P_{\infty}(r) \sim \begin{cases} r^{D-d} & r \ll \zeta(P_c) \\ \zeta(P_c)^{D-d} & r \gg \zeta(P_c) \end{cases} \tag{8.35}$$

According to formula (8.25), obtain:

$$P_{\infty}(P) \sim |P - P_c|^{\beta} \tag{8.36}$$

while according to formula (8.31), obtain:

$$|P - P_c| \sim \zeta(P_c)^{-\frac{\beta}{\nu}} \tag{8.37}$$

therefore,

$$P_{\infty}(P) \sim |P - P_c|^{\beta} \sim \zeta(P_c)^{-\frac{\beta}{\nu}} \tag{8.38}$$

Contrasting formula (8.35) with formula (8.38) gives:

$$D = d - \frac{\beta}{\nu} \tag{8.39}$$

According to formula (8.39), using the critical exponent β and ν, the fractal dimension D of the seepage system can be obtained. Table 8.1 is the computing results according to formula (8.39)[278].

Table 8.1 Relation between the critical exponent and fractal dimension

Model	β	ν	D
Average field (six-dimensional)	1	1/2	4
Two-dimensional seepage model	5/36	4/3	1.896
Two-dimensional Ising model	1/8	1	1.875
Three-dimensional seepage model	0.44	0.88	2.50
Three-dimensional Ising model (progression)	0.312±0.003	0.642±0.003	2.507–2.52
Three-dimensional Ising mode (renormalization)	0.340	0.630	2.46

Fig. 8.7 is the fractal figure of saturated granular medium, including the granules, pores and seepage flow. It is automatically formed by computer and its main program is listed as below:

Program 4—the fractal figure of saturated granular medium (including the granules, pores and seepage flow)

```
public:
    int q;
    int scale;
    int width;
    int i;
    int nx, ny;
    long kcolor;
    double H, r, x0, y0, x, y;
```

```
    double xmin，ymin，xmax，ymax，deltax，deltay;
    char ch;
// CCirclecarpetView drawing
void CCirclecarpetView::OnDraw(CDC* pDC)
{
    CCirclecarpetDoc*pDoc = GetDocument();
    ASSERT_VALID(pDoc);
    q=5; //2，3，4，5，6，7
    scale=64; //4，16，32，64，128
    width=450; //150，200，300，400，500
    xmin=10;
    ymin=10;
    xmax=xmin+scale*3.14159;
    ymax=ymin+scale*3.14159;
    deltax=(xmax-xmin)/width;
    deltay=(ymax-ymin)/width;
    for(ny=0; ny<=width; ny++)
    {
        for(nx=0; nx<=width; nx++)
        {
        x=xmin+nx*deltax;
        y=ymin+ny*deltay;
        H=0;
        for(i=1; i<=q; i++)
        {
            H=H+cos(x*cos(2*3.14159*i/q)+y*sin(2*3.14159*i/q));
        }
        if( (H>-9)&&(H<=-5))
        {
            kcolor=RGB(255，0，0);
        }
        if( (H>-5)&&(H<=-4))
        {
            kcolor=RGB(0，255，0);
        }
        if( (H>-4)&&(H<=-3))
        {
            kcolor=RGB(0，0，255);
        }
        if( (H>-3)&&(H<=-2))
        {
            kcolor=RGB(255，100，0);
        }
        if( (H> -2)&&(H<=-1))
        {
            kcolor=RGB(100，255，0);
        }
        if( (H>-1)&&(H<=-0.5))
        {
```

```
    kcolor=RGB(100, 0, 255);
}
if( (H>-0.5)&&(H<= -0.2))
{
    kcolor=RGB(255, 0, 0);
}
if( (H> -0.2)&&(H<= -0.1))
{
    kcolor=RGB(0, 255, 0);
}
if( (H>0)&&(H<=0.1))
{
    kcolor=RGB(0, 0, 255);
}
if( (H>0.1)&&(H<=0.2))
{
    kcolor=RGB(255, 100, 0);
}
if( (H>0.2)&&(H<=0.3))
{
    kcolor=RGB(100, 255, 0);
}
if( (H>0.3)&&(H<=0.5))
{
    kcolor=RGB(100, 0, 255);
}
if( (H>0.5)&&(H<=1))
{
    kcolor=RGB(100, 0, 100);
}
if( (H>1)&&(H<=3))
{
    kcolor=RGB(250, 250, 250);
}
if( (H>3)&&(H<=5))
{
    kcolor=RGB(100, 100, 0);
}
if( (H>5)&&(H<=7))
{
    kcolor=RGB(255, 255, 255);
}
if( (H>7)&&(H<=9))
{
    kcolor=RGB(0, 0, 0);
}
if( (H>9)&&(H<=11))
{
    kcolor=RGB(100, 100, 100);
```

```
                }
                pDC->SetPixel(nx+10, ny+10, kcolor);
            }
        }
    }
```

The running result is shown in Fig. 8.7.

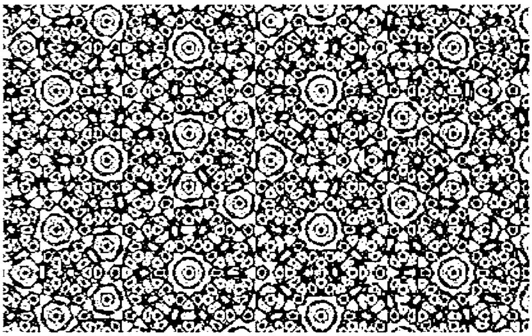

Fig. 8.7 Fractal figure of saturated granular medium

8.4 Fractal Behavior of Granules with Vibration

The fractal of Brownian motion and generalized fractal, which are mathematical models, were put forward by Mandelbrot and Ness in 1968. They are mainly used to describe the mountains, coastline, land formation, and other irregular shapes, and to simulate the time track of all kinds of fractal noises. At present, the fractal of Brownian motion has become a new method to establish mathematical models of random processes[287~292]. Under the action of vibration the granules have irregular and random motion due to the excitation response and wave action, so the fractal behavior of the vibrated granules can be simulated by it.

8.4.1 *The fractal Brownian model*

Brownian motion process is also called as Wiener process. This term derives from the physical terms "Brownian motion". It is a kind of irregular and complex motion.

The random process $\{B(t), t \geqslant 0\}$ is called the Brownian motion process. Supposing that:

(i) $B(0)=0$;

(ii) $\{B(t), t \geqslant 0\}$, and has a steady independent increment;

(iii) For every $t>0$, $B(t)$ obeys the normal distribution, the mean is 0 and the variance is $\sigma^2 t$.

According to the above definition,then:

$$B(t+\tau)-B(t)\sim N(0,\tau\sigma^2),\tau>0 \tag{8.40}$$

where $\sigma^2=\mathrm{var}[B(t+1)-B(t)]$.

If the Brownian motion process is extended, namely the Brownian motion process has been fractional integrals, a new random process termed as the fractal Brownian motion $B_H(t)(0<H<1)$ is generated:

$$B_H(t)=I^{H-(1/2)}[B(\lambda)]=\frac{1}{\Gamma(H+(1/2))}\int_{-\infty}^{t}(t-\lambda)^{H-(1/2)}\mathrm{d}B(\lambda) \tag{8.41}$$

It is similar to the Brownian motion, which is:

$$B_H(t+\tau)-B_H(t)\sim N(0,\ \tau^{2H}\sigma_H^2)\quad(\tau>0) \tag{8.42}$$

where $\sigma^2{}_H=\mathrm{var}[B_H(t+1)-B_H(t)]$. H is called Hurst exponent of $B_H(t)$, when H=1/2, $B_H(t)$ is the Brownian motion. The relation between Hurst exponent and the fractal dimension D is: $D=TD+1-H$, TD is the topologic dimension of $B_H(t)$. Only considering the one-dimensional time series, TD=1, therefore, $D=2-H$.

Suppose $\sigma^2(\tau)=E\{[B_H(t+\tau)-B_H(t)]^2\}$, then:

$$\sigma^2(\tau)=\tau^{2H}\sigma_H^2,\quad \sigma^2(1)=\sigma_H^2 \tag{8.43}$$

therefore $\sigma^2(\tau)=\tau^{2H}\sigma^2(1)$,

$$\log\sigma(\tau)=H\log\tau+\log\sigma(1)\quad(\tau>0) \tag{8.44}$$

where $\log(\tau)$ is the linear function of $\log\tau$. Geometrically, H is the slope of the line $\{(\log\tau,\log\sigma(\tau))\}$.

H can be expressed in another way:

$$\frac{\mathrm{d}\log\sigma(\tau)}{\mathrm{d}\log\tau}=H \tag{8.45}$$

The differential coefficients in any points of the line $\{(\log\tau,\log\sigma(\tau))\}$ are constants.

8.4.2 *The composite model of two fractal Brownian motions*

Supposing that the random process $x(t)$ is the composite of two fractal Brownian motions $B_{H_1}(t)$ and $B_{H_2}(t)$ whose Hurst exponents are H_1 and H_2 respectively ($0<H_1, H_2<1$), so:

$$x(t)=B_{H_1}(t)+B_{H_2}(t) \tag{8.46}$$

According to the properties of Brownian motion, suppose:

$$\begin{cases} B_{H_1}(t+1)-B_{H_1}(t)\sim N(0,\sigma_1^2) \\ B_{H_2}(t+1)-B_{H_2}(t)\sim N(0,\sigma_2^2) \end{cases} \tag{8.47}$$

and the related coefficient between the random variables $B_{H_1}(t+1)-B_{H_1}(t)$ and $B_{H_2}(t+1)-B_{H_2}(t)$ is ρ, namely, $\mathrm{cov}(B_{H_1}(t+1)-B_{H_1}(t)$, $B_{H_2}(t+1)-B_{H_2}$

$(t)) = \rho\sigma_1\sigma_2$.

Suppose $\sigma_1 = 1$, $\sigma_2 = \sigma$, then:

$$B_{H_1}(t+1) - B_{H_1}(t) \sim N(0,1) \tag{8.48}$$

$$B_{H_2}(t+1) - B_{H_2}(t) \sim N(0,\sigma^2) \tag{8.49}$$

therefore:

$$\sigma_x^2(\tau) = \tau^{2H_1} + \tau^{2H_2}\sigma^2 + 2\tau^{H_1+H_2}\sigma\rho \tag{8.50}$$

Formula (8.50) is the variance relation of two fractal Brownian motions. Suppose $H_1 \leqslant H_2$, the logarithm of formula (8.50) is:

$$2\log\sigma_x(\tau) = \log\left(\tau^{2H_1} + \tau^{2H_2}\sigma^2 + 2\tau^{H_1+H_2}\sigma\rho\right) \tag{8.51}$$

Assuming $f(\tau) = \log\sigma_x(\tau)$, therefore:

$$\begin{aligned}\frac{\mathrm{d}\log\sigma(\tau)}{\mathrm{d}\log\tau} &= H_1 + \frac{H_2 - H_1}{1+\tau^{2(H_2-H_1)}\sigma^2 + 2\tau^{H_2-H_1}\sigma\rho}\left[\tau^{2(H_2-H_1)}\sigma^2 + \tau^{H_2-H_1}\sigma\rho\right] \\ &= H_2 - \frac{H_2 - H_1}{1+\tau^{2(H_2-H_1)}\sigma^2 + 2\tau^{H_2-H_1}\sigma\rho}\left[1 + \tau^{H_2-H_1}\sigma\rho\right]\end{aligned} \tag{8.52}$$

8.4.3 *The composite model of multiple fractal Brownian motions*

Suppose that the random process $x(t)$ is the composite of N fractal Brownian motions $B_{H_i}(t)$ whose Hurst exponents are H_i (i=1, ⋯, N, $0 < H_i < 1$) respectively, then:

$$x(t) = \sum_{i=1}^{N} B_{H_i}(t) \tag{8.53}$$

Suppose that:

$$B_{H_i}(t+1) - B_{H_i}(t) \sim N(0,\sigma_i^2) \tag{8.54}$$

and the related coefficients between the random variables $B_{H_i}(t+1) - B_{H_i}(t)$ and $B_{H_j}(t+1) - B_{H_j}(t)$ are $\rho_{ij} = 0 (i \neq j)$, $\rho_{ii} = 1$, so:

$$\sigma_x^2(\tau) = \sum_{i=1}^{N}\sum_{j=1}^{N} \rho_{ij}\sigma_i\sigma_j\tau^{H_i+H_j} \tag{8.55}$$

$$\frac{\mathrm{d}\log\sigma_x(\tau)}{\mathrm{d}\log\tau} = \frac{\sum_{i=1}^{N}\sum_{j=1}^{N}\left(H_i + H_j\right)\rho_{ij}\sigma_i\sigma_j\tau^{H_i+H_j}}{2\sum_{i=1}^{N}\sum_{j=1}^{N}\rho_{ij}\sigma_i\sigma_j\tau^{H_i+H_j}} \tag{8.56}$$

When $\rho_{ij} = 0$ (i, j=1, 2, ⋯, N, $i \neq j$), the formula (8.55) becomes:

$$\sigma_x^2(\tau) = \sum_{i=1}^{N}\sigma_i^2\tau^{2H_i} \tag{8.57}$$

8.4.4 *Fractal analysis of the power spectrum density*

Suppose that the time series $x(t)$ of vibration is in a certain time quantum T, so the mean value of its signals is:

$$\overline{x}(T) = \frac{1}{T}\int_0^T x(t)\mathrm{d}t \tag{8.58}$$

The covariance $V_a(T)$ of signals can be defined as:

$$V_a(T) = \frac{1}{T}\int_0^T [x(t) - \overline{x}]^2 \mathrm{d}t \tag{8.59}$$

If the time series has fractal characteristic, the relation between covariance $V_a(T)$ and T is the power exponential (Voss, 1985) which is expressed as:

$$V_a(T) \sim T^{2H} \tag{8.60}$$

where H is the fractal dimension of the time series.

A time series can be described with $x(t)$ in the physics domain. In the frequency spectrum domain it can be described with spectrum amplitude $V(f, T)$ (f is frequency). $V(f, T)$ is usually a complex number. For $x(t)$ in the time domain $0<t<T$, the amplitude $V(f, T)$ in its frequency domain can be solved by Fourier transformation. It can be expressed as:

$$V(f,T) = \int_0^T x(t)\mathrm{e}^{2\pi i f t}\mathrm{d}t \tag{8.61}$$

The equation with $x(t)$ and $V(f, T)$ is a Fourier inverse transformation. It can be expressed as:

$$x(t) = \int_{-\infty}^{\infty} V(f,T)\mathrm{e}^{-2\pi i f t}\mathrm{d}t \tag{8.62}$$

$|X(f,T)|^2$ is the energy generated by the $x(t)$ component whose frequency is in the interval $(f, f+\mathrm{d}f)$. So the power spectrum of $X(t)$ is:

$$S(f) = \frac{1}{T}|V(f,T)|^2 \tag{8.63}$$

For the time series of fractal, the relation between power spectrum density and frequency is the power exponential (β is power exponent) which can be expressed as:

$$S(f) \sim f^{-\beta} \tag{8.64}$$

If two time series $x_1(t)$, $x_2(t)$ are taken into account, because $x_1(t)$ and $x_2(t)$ have the same statistical property the relation of them is:

$$x_2(t) = \frac{1}{r^H}x_1(rt) \tag{8.65}$$

Fourier transformation of $x_2(t)$ is:

$$V_2(f,T) = \int_0^T x_2(t)\mathrm{e}^{2\pi i f t}\mathrm{d}t \tag{8.66}$$

If equation (8.65) is substituted into equation (8.66) and the variable transformation $r' = rt$ has been done, the following can be obtained:

$$V_2(f,T) = \int_0^{rT} \frac{x_1(t')}{r^H}\mathrm{e}^{2\pi i f t'/r}\frac{\mathrm{d}t'}{r} \tag{8.67}$$

Comparing formula (8.67) with formula (8.61) gives:

$$V_2(f,T)=\frac{1}{r^{H+1}}V_1(f/r,rT) \tag{8.68}$$

According to the formula (8.63), then:

$$S_2(f)=\frac{1}{T}\left|V_2(f,T)\right|^2=\frac{1}{r^{2H+1}}\frac{1}{rT}\left|V_1(f/r,rT)\right|^2=\frac{1}{r^{2H+1}}S_1(f/r) \tag{8.69}$$

Because x_2 is obtained by properly transforming the scale of x_1, the power spectrum density has inevitably scale law. So:

$$S(f)=\frac{1}{r^{2H}}S(f/r) \tag{8.70}$$

From the expression (8.62), the relation between the power exponent and the fractal dimension can be obtained, namely:

$$\beta=2H+1 \tag{8.71}$$

The fractal behavior of the granules can be simulated with Brownian motion. The main program is shown in Program 5.

Program 5—the fractal behavior of the granules when vibrating

```
public:
    double x [100];
    double Gauss();
    int Arand;
    int Nrand;
    double GaussAdd;
    double GaussFac;
    void InitGauss(int seed);
// CGaussView drawing

void CGaussView:: OnDraw(CDC* pDC)
{

    CGaussDoc* pDoc = GetDocument();
    ASSERT_VALID(pDoc);
    x[0] =0;
    InitGauss(5);
    for(int i=1; i<100; i++)
    {
      x[i] =(i-1)+Gauss()/99;
    }
    CPen* pOldPen;
    CPen pen;
    pDC->MoveTo(50, 110);
    pDC->LineTo(560, 110);
    pDC->LineTo(554, 108);
    pDC->MoveTo(560, 110);
    pDC->LineTo(554, 112);
    pDC->MoveTo(50, 10);
```

```
        pDC->LineTo(50, 210);
        pDC->MoveTo(50, 10);
        pDC->LineTo(48, 16);
        pDC->MoveTo(50, 10);
        pDC->LineTo(52, 16);
        pen.CreatePen(PS_SOLID, 1, RGB(120, 0, 250));
        pOldPen=pDC->SelectObject(&pen);

        pDC->MoveTo (50, 110);
        for(i=1; i<100; i++)
        {

          //pDC->TextOut(0, i*50, string(x [i] ));
          pDC->LineTo(50+i*5, int(-x [i] /10));
        }
        pDC->SelectObject(pOldPen);
    }
```

The running result is shown in Fig. 8.8.

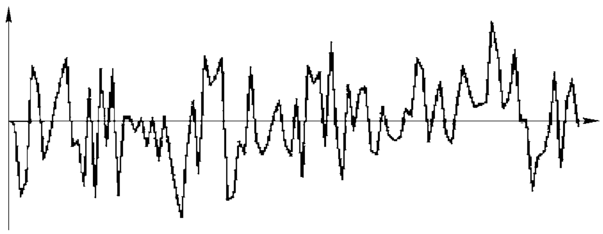

Fig. 8.8 Fractal simulation of the granules when vibrating

8.5 Self-organized Behavior of the Granular Pile

8.5.1 *The cellular automaton*

The cellular automaton was firstly put forward by J. Von Neumann[312~318], and was used to simulate the self-reproduction of biotic system. Besides this it was also used to simulate the other physical systems and natural phenomena.

Suppose that there is a series of identical cells distributing on a line with equal interval. Abstractly speaking, here each cell is an automaton. Each cell has only finite state. For the one with two states, they are denoted by 0 and 1 respectively in the following.

Suppose that the line has no confinement in the two directions, so there are infinite cells. The modes of all cells can be denoted by the symbol sequence with no confinement in both sides. This kind of sequence is termed as a configuration of cellular automaton. Conveniently, the cellular positions distributing in the line correspond with the integers. In particular, the position corresponding to the integer 0 is called the basic point. If the configuration is noted for a, then:

$$a = (\cdots a_{-1} a_0 a_1 \cdots) \tag{8.72}$$

where a_0 is the cellular state in the basic point, the others are analogical.

Suppose that the time is also discrete, and is denoted by t which is chosen for an integer. The t = 0 is called the initial time. Subsequently they are t =1, 2, 3, ⋯. The state changes of all cells are simultaneous. Suppose that the configuration of the time t is a^t, so the configuration a^{t+1} of time t +1 is entirely determined by a^t. At the same time, the state of the i th cell in the time t +1 is determined by the state of the i th cell in the time t and the neighboring $2r$ cells whose distances are no more than r. Namely,

$$a_i^{t+1} = f\left(a_{i-r}^t, \cdots, a_{i-1}^t, a_i^t, a_{i+1}^t, \cdots, a_{i+r}^t\right) \tag{8.73}$$

where the mapping f has no connection with i and t. The r is called neighborhood radius, and the f is called the partial mapping.

Note that S is the finite aggregate, so one cellular automaton can be determined by S, r and f. For a given initial configuration a, which should be noted that a^0 =a, the a^1, a^2, ⋯ can be obtained.

8.5.2 *The cellular automaton simulation of granular pile*

In this section the self-organized criticality of a one-dimensional granular pile is studied with the cellular automaton, such as a simple "pile of sands". Suppose that the pile is built by randomly adding sand. Eventually, the slope will reach a critical value (called the "angle of repose"); if more sand is added it will slide off. Alternately, if the pile is started from a situation where it is too steep, it will not collapse until it reaches the critical state. Such situation is just barely stable with respect to further disorder. The critical state is an attractor for the dynamics. Therefore, the pile will evolve into a critical state at last. As it is built up, the characteristic size of the largest avalanche grows. When the critical point reached, there are avalanches of all sizes up to the size of the system, analogous to the domain distribution of a magnetic system at a phase transition. The energy is dissipated at all length scales. Once the critical point is reached, the system becomes steady. The behavior of all systems at the self-organized critical point is characterized by a number of critical exponents, which are connected by scaling relations, and the systems obey "finite-size scaling", just as equilibrium statistical systems at the critical point.

Fig. 8.9 shows a model of a one-dimensional sand pile with length N. The boundary conditions are such that sand grains only can leave the system at the right-hand side. This arrangement is thought as half of a symmetric sand pile with both ends open. The $h(n)$ is the height of the sand pile where $x = n$, and the height of every sand grain is 1.The number Z_n represents the height differences between the successive positions on the sand pile,

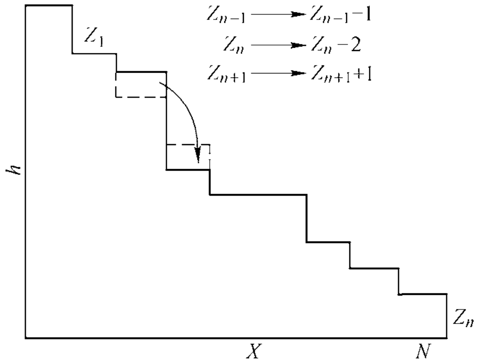

Fig. 8.9 One-dimensional sand-pile model

$$Z_n = h(n) - h(n+1) \tag{8.74}$$

From Fig. 8.9 it can be known that sand is added at the n th position. following the process:

$$\begin{aligned} &Z_n \to Z_n+1 \\ &Z_{n-1} \to Z_{n-1}-1 \end{aligned} \tag{8.75}$$

When the height difference becomes higher than a pre-determined critical value Z_n, one unit of sand tumbles down to the lower level, i.e.,

$$\begin{aligned} &Z_n \to Z_n-2 \\ &Z_{n\pm 1} \to Z_{n\pm 1}+1 \qquad \text{for} \quad Z_n > Z_c \end{aligned} \tag{8.76}$$

where closed and open boundary conditions are used for the left and right boundaries respectively,

$$\begin{aligned} &Z_0 = 0 \\ &Z_n \to Z_{n-1} \\ &Z_{n\ 1} \to Z_{n+1}+1 \quad \text{for} \quad Z_n > Z_c \end{aligned} \tag{8.77}$$

Eq. (8.76) is a nonlinear discretized diffusion equation (nonlinear because of the threshold condition). The process continues until all Z_n are below the threshold value. (8.75). The pile becomes a cellular automation where the state of the discrete variable Z_n at time t +1 depends on the state of the variable and its neighbors at time t.

The condition for stability is:

$$Z_n \leqslant Z_c \quad (n=1,\ 2,\ 3,\ \cdots,\ N) \tag{8.78}$$

So the total number of stable states is Z_c^N.

If sand grains are added randomly from an empty system, the pile will build up. Eventually it reaches the point where all height differences Z_n achieve the critical value Z_n=Z_c. This is the minimum stable of all stationary modes, i.e. the self-organized criticality.

8.5.3 *The fractal analysis of granular pile's self-similarity*

Suppose that s represents the slide size and $P(s)$ is its distribution function. Fig. 8.10a shows the log-log plot, and it can be seen that they obey the power law:

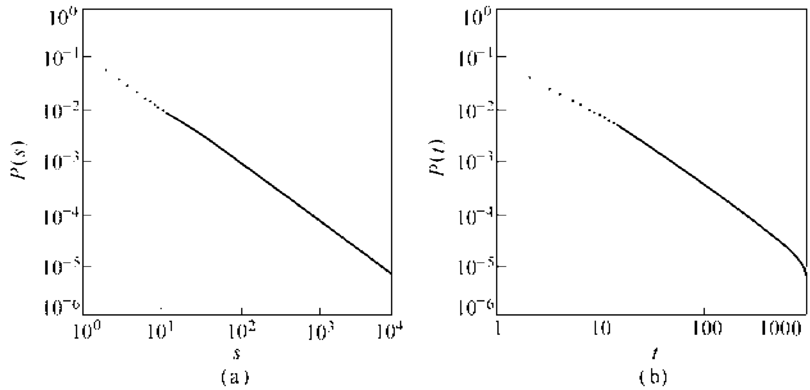

Fig. 8.10 The log-log plot of pile

$$P(s) \sim s^{1-\tau}, \quad \tau \approx 2.1 \tag{8.79}$$

The random distribution at any point Z_n will probably lead to a chain reaction. Adding a sand grain will generate two probable results. One is subcritical in this case the avalanche will disappear after several steps, the probability of a big avalanche is very small; another result is supercritical, in this case the avalanche will lead to the collapse of the whole system[319~322]. Eq. (8.79) shows that the system is critical because of the power law. At this moment it has no characteristic length scale as well as characteristic time scale.

Besides Eq. (8.79), there are several other quantities obeying the scale law of fractal. Suppose that t represents the time when the sand pile begins to collapse. Its distribution of probability is:

$$P(t) \sim t^{1-\tau_t}, \tau_t \approx 2.14 \tag{8.80}$$

and Fig. 8.10b is its log-log plot.

There is also a power relation between s and t:

$$t \sim s^{\gamma_{ts}}, \gamma_{ts} \approx 0.61 \tag{8.81}$$

For a certain collapse point, it is different from the total collapse because some points probably collapse several times. This situation will also obeys a power law:

$$P(s_d) \sim s_d^{1-\tau_d}, \tau_d \approx 2.07 \tag{8.82}$$

In 1996 Frette et al., found the conditions of the self-organized criticality in a pile of rice. Their experiments are meaningful. It seemed that the relation among the fractal, $1/f$ noise and the power law was established. They described the experiments on a granular system, a pile of rice, in which the dynamics exhibited a self-organized critical behavior in one case (for grains with a large aspect ratio) but not in another (for less elongated grains). The experimental results showed that the self-organized criticality was not as "universal" and insensitive to the details of a system as it had been initially supposed. On the other hand its occurrence depended on the detailed mechanism of energy dissipation. These researchers had studied the dynamics of piles of rice for several size systems. Grains of rice were slowly fed into the gap between two vertical and parallel plates. The mass of grains accumulated in a pile until it reached a quasi-stationary state. Under the continued addition, avalanches redistributed the mass along the surface layer of the heap and transported the mass out of the system, thereby changed the entire profile. The anisotropy of the grains gave rise to a variety of packing configuration. The anisotropy restricted the way the grains moved down the slope, enhanced the frictional contact and, to a large extent, suppressed the inertia effects. The size of an avalanche was defined as the energy dissipated between two consecutive profiles. There was a large variation in the avalanche sizes and an apparent chaotic structure with time.

Based on the experiments with a wide range of complex system, it is reasonable to expect that the probability density $P(E, L)$, where $P(E, L)\mathrm{d}E$ is the probability that an avalanche with energy dissipation between E and $E+\mathrm{d}E$ will occur in a system of size L, will have the form

$$P(E,L) = L^{-\beta} f(E / L^{\nu}) \tag{8.83}$$

where the scaling function f and the scaling exponents β and ν are determined .

From the normalization $\int_0^{\infty} P(E,L)\mathrm{d}E = 1$ it follows that $\beta = \nu = 1$. For rice A with system sizes of $L=16$, 33, 66 and 105, the behavior can be described by a scaling function of the form, $f(x)$ is a constant for $x<1$, and $f(x) \propto x^{-\alpha}$ for $x>1$. The exponent α is estimated from fits in the range $6 \leqslant E/L \leqslant 300$. For rice B with $L=26$, 52 and 104, the probability densities are consistent with a stretched-exponential scaling function, $f(x) \propto \exp(-(x/x')^{\nu})$ with $x' \approx 0.45$, and $\nu \approx 0.43$. A characteristic avalanche size $E' = x'L$ for the dynamics of rice B appears which is consistent with the idea of the self-organized criticality.

8.6 Self-organized Criticality of Saturated Granular Liquefaction

8.6.1 *Opening system*

The classic thermodynamics has successfully interpreted these behaviors approaching an equilibrium and disorder. However, it is not the general law that all systems approach an equilibrium and disorder. For example, seeing from Darwinian biological evolutionism, the results of evolution always lead to the species diversity and the complexity of structures, namely the ordered increase. Thereby, biologists believed that the order in space and function is the basic characteristic of lives. However this kind of spatial order in the macroscopic scope can only be maintained through the exchange of substance and energy with external surroundings under the conditions of non-equilibrium. This system is called the opening system. The biotic system obviously belongs to the opening system because the organisms continuously exchange their substance and energy with the surrounding. Besides the biotic system, the opening systems also exist widely in the non-life system; thus the phenomena of self-organized criticality exist in a wide range.

Any new ordered structure is always the result of instability of a certain disordered state, which is the enlarged result of fluctuation after the instability. Thus, in a certain situation the disordered state probably loses the stability when the system continuously exchanges the energy with the external surrounding. Some fluctuations probably are enlarged, leading up to the ordered state of system. Prigogine, a Belgian scientist called this ordered state dissipative structure.

In non-equilibrium system, all states are the function of time t and spatial position r. Assuming that this function exists and is continuous in any given spatial point, then the one conservational quantity should obey the following general equation of continuity,

$$\frac{\partial \rho_Q(r,t)}{\partial t} = -\nabla \cdot j_Q(r, t) \tag{8.84}$$

where the subscript Q is a certain extensive quantity, and is a conservation quantity; When the system at the time t and in the position r, the Q density is $\rho_Q(r,t)$ and the current density is $j_Q(r, t)$.

And the energy conservation equation becomes

$$\frac{\partial}{\partial t}(\rho E) = -\nabla \cdot j_\varepsilon \tag{8.85}$$

where j_ε is the density of the energy flow (the passing energy at unit time in unit area); ρ is the mass density; ε is the total energy of unit mass of the granular media.

8.6.2 *Evolvement analysis of liquefaction*

Firstly according to the dissipative structure theory, the concept of entropy should be introduced in order to describe the self-organized criticality of vibrating liquefaction. σ is defined as the entropy at the unit time in the unit area, and is also called the local entropy. The general expression is

$$\sigma = \sum J_k \times X_k \geq 0 \tag{8.86}$$

where J_k represents the k th irreversible flow, X_k represents the k th irreversible force.

Generally speaking, the macroscopic physical quantity can be divided into two kinds. One is the extensive quantity relating to the general mass of the system, such as volume, total energy, force, etc.; the other is the intensive quantity, and is also called the " field ", such as temperature, displacement, stress, etc. Corresponding to this, during the course of vibrating liquefaction, J_k is an intensive quantity. The displacement, the offset, the destabilization of the granular framework, and the deformation are irreversible flows. These also can predict the vibrating liquefaction as the static parameters of vibrating liquefaction. The irreversible forces X_k in this system mainly represent the granular friction, the viscous resistance, the power of pore water, the acting force of vibration to granules, etc.

The total entropy of the system is

$$P = \int_V \sigma \mathrm{d}V \geqslant 0 \tag{8.87}$$

where V represents the granular total volume.

When granules are in equilibrium state, there is

$$\sigma = 0; \ J_k = 0; \ X_k = 0 \tag{8.88}$$

Namely, there is no irreversible flow or irreversible force in the equilibrium state. Once the system is not in an equilibrium state, a macroscopic irreversible process will occur. This time the irreversible flow and the irreversible force are no longer zero. The irreversible force is the resource of the irreversible flow, wherever there is the irreversible force, there will be the irreversible flow. In other words, when the granules are still in the non-vibrating state, any granule will be in a steady state, and the resultant force is zero. Certainly, there is not any irreversible flow, such as the granular deformation or displacement. Therefore during the course of steady vibration the granules will be in a non-equilibrium state because of the action of force. Namely, the so-called local non-equilibrium and the irreversible force will be generated.

From the above analysis, it can be known that the irreversible flow is a certain function of the irreversible force. Suppose that a certain irreversible flow J_k is the function of all irreversible forces $\left(\{X_l\} = X_1, X_2, \cdots, X_n\right)$:

$$J_k = J_k\left(\{X_l\}\right) \tag{8.89}$$

Eq. (8.86) is expanded by Taylor' s series and simplified,then:

$$J_k = \sum_l L_{kl} X_l \tag{8.90}$$

where

$$L_{kl} = \left(\frac{\partial J_k}{\partial X_l}\right)_0 \tag{8.91}$$

During the course of the formation of vibrating liquefaction, because of the continuous vibration the granular mechanical energy will increase, that is the irreversible forces will increase; at the same time the granular frictional resistance and viscous force will decrease gradually with the change of the granular framework. These two aspects will certainly lead to the increment of the irreversible forces during the course of vibrating liquefaction. When the irreversible forces increase to a certain value, there is a nonlinear relation between the irreversible forces and the irreversible flows, and the system will transform into a far-from-equilibrium state. The non-equilibrium zone obeying the nonlinear relation is called the non-equilibrium nonlinear zone, where an ordered structure will probably occur.

8.6.3 *The evolutional equation of vibrating liquefaction*

The synergetics believe that the nonlinear system with any complex structure is a kind of evolutional self-organized system[315~322].

According to the synergetics, the evolutional process of liquefaction can be described by only two variables (y, s), where y represents the slow variable and s represents the quick variable. The system' s evolutional equation can be expressed as Langevin equation:

$$\dot{y} = K(y,s) + F(t) \tag{8.92}$$

where $K(y, s)$ is the linear function including the slow variable and the quick variable; $F(t)$ is the fluctuation force.

On one hand, the evolution of any nonlinear system is controlled by the inner factors of the system, i.e. the nonlinear interaction among all subsystems, which can be expressed by the nonlinear function $K(y, s)$. On the other hand, it will also be influenced by the external factors which can be expressed by the fluctuation force $F(t)$. The internal cause is an essential one, but the external actions mainly urge the change of internal cause and drive the qualitative change at the critical points. Therefore, in a simple situation the external factors such as the fluctuation force $F(t)$ can be ignored.

For the two-dimensional system, Eq. (8.92) will become:

$$K(y,s) = ay - ys \tag{8.93}$$

Combining Eq. (8.92) and (8.93) gives:

$$\dot{y} = ay - ys \tag{8.94}$$

Generally, s can be expressed by:

$$\dot{s} = -\beta s + y^2 \tag{8.95}$$

Moreover, s can be expressed by y, that is:

$$s(t) = \int_{-\infty} \mathrm{e}^{-\beta(t-\tau)} y^2(\tau)\mathrm{d}\tau \tag{8.96}$$

Using integration by parts, the function $s(t)$ can be transformed into the function $y(t)$, namely,

$$s(t)=\frac{1}{\beta}y^2(t)-\frac{1}{\beta}\int_{-\infty}\mathrm{e}^{-\beta(t-\tau)}2(y\dot{y})_\tau\,\mathrm{d}\tau \tag{8.97}$$

When y becomes small, the integral term in the above equation can be ignored, then:

$$s(t)\approx\frac{1}{\beta}y^2(t) \tag{8.98}$$

Combining Eq. (8.98) and (8.94) gives:

$$\dot{y}=\frac{\mathrm{d}y}{\mathrm{d}t}=ay-by^3 \tag{8.99}$$

where a, b are the control parameters; $b=\frac{1}{\beta}$.

Eq. (8.99) shows that the quick variable can be expressed by the slow variable, namely the quick variable changes with the slow variable; thus the former is in service to the latter. Eq. (8.89) is the evolutional equation of liquefaction.

8.6.4 *The dynamic action analysis of vibration on liquefaction*

Considering the influence of vibration on liquefaction, the control parameter a in Eq. (8.99) is regarded as a random variable $\lambda(t)$, so Eq. (8.99) is turned into the following random differential equation,

$$\frac{\mathrm{d}y}{\mathrm{d}t}=\lambda(t)y-by^3 \tag{8.100}$$

where $\lambda(t)$ can be expressed as:

$$\lambda(t)=\bar{\lambda}+\xi(t) \tag{8.101}$$

where $\bar{\lambda}$ is the mean value of $\lambda(t)$; $\xi(t)$ is the fluctuation term.

The general form of Eq. (8.100) is:

$$\frac{\mathrm{d}y}{\mathrm{d}t}=f(y)+\lambda(t)g(y) \tag{8.102}$$

where $f(y)=-by^3$, $g(y)=y$. After some mathematical operations, the following is obtained:

$$\frac{1}{2}\sigma^2\frac{\partial g^2(y)}{\partial y}=f(y)+\bar{\lambda}g(y) \tag{8.103}$$

where σ^2 is the variance of fluctuation.

By solving Eq. (8.103), then:

$$y_1=0;\ y_{2,3}=\pm\sqrt{\frac{\bar{\lambda}-\sigma^2}{b}} \tag{8.104}$$

and the solution of Eq. (8.100) are:

$$y_1'=0;\ y_{2,3}'=\pm\sqrt{\frac{\lambda}{b}}\quad(\lambda=a) \tag{8.105}$$

Eq. (8.105) shows that there is a steady point $y'=0$ when $\lambda<0$; $y'=0$ is critical unstable when $\lambda = 0$; $y' = 0$ becomes unstable when $\lambda > 0$, and two new stable solutions $y = \pm\sqrt{\frac{\lambda}{b}}$ and a bifurcation are generated. Eq. (8.104) has the similar law. The bifurcation occurs at $\lambda = \sigma^2$ ($\sigma \neq 0$) but not at $\lambda = 0$, namely, the external fluctuation makes the bifurcation generate a "dislocation". Therefore, the external fluctuation probably changes the evolutional progression of the system, even the evolutional method.

8.6.5 *The fractal analysis of vibrating liquefaction*

Fig. 8.11 is the vibratory impulse integrated distribution N (V), i.e., the number of events N (V) whose amplitude is greater than V. After the subtraction of k_2, the double logarithmic graph shows an example of the resulting distributions. It is worthwhile to note that there is a slight departure from the scaling behavior at low and high amplitudes. Therefore, the relation between N (V) and V is expressed by:

$$N(V) \approx k_1 V^{\gamma} + k_2, \quad \gamma = 1.7 \pm 0.2 \tag{8.106}$$

where k_1, k_2 are constants.

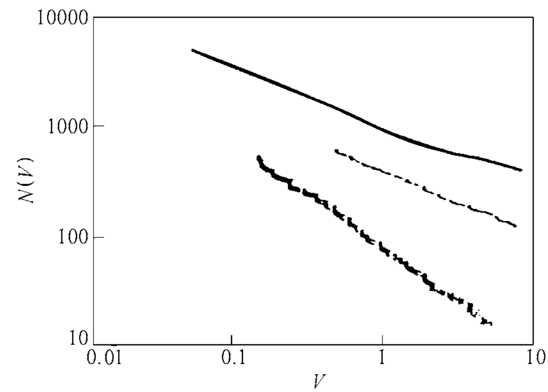

Fig. 8.11 Relation between N (V) and amplitude V

Both the autocorrelation function and the power spectrum of the vibratory impulse signal time series have been analyzed, and Fig. 8.12 shows the autocorrelation function for these two typical data sets. The behavior is an algebraic decay over almost 2 orders of magnitude, and the data fit gives:

$$C_V(t) \sim t^{-\alpha}, \alpha = 0.4 \pm 0.1 \tag{8.107}$$

This corresponds to the following power spectrum,

$$S_V(f) \sim f^{-\beta}, \quad \beta = 1 - \alpha \tag{8.108}$$

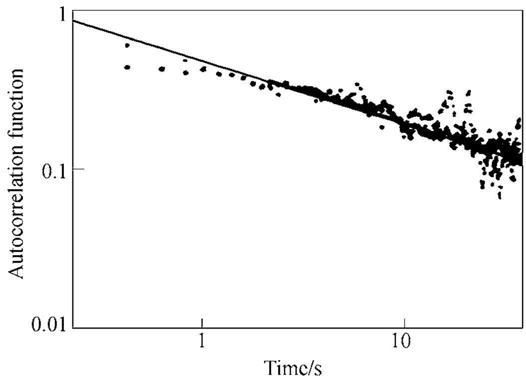

Fig. 8.12 Autocorrelation functions of the vibratory signals time series

Fig. 8.13 shows the experimental results of saturated granules' (silty sand) liquefaction. It can be seen from the relation curve of periodic deviation stress δ_d, dynamic strain ε_d, pore water pressure u_d and cyclic index n that although deviation stress alters within a small range, a certain residual pore water pressure will remain after every stress cycle. With the increment of the stress cycle index, pore water pressure will be continually accumulated and gradually increase, but the effective stress will progressively decrease. Finally when the effective stress is close to zero, granular intensity will suddenly reduce to zero, so the test sample generates liquefaction. Consequently the "avalanche" phenomenon takes place. At the beginning the straining changes slightly, the dynamic stress maintains an equiamplitude cycle, and the pore water pressure gradually increases. After a certain number of cycles, the pore water pressure will sharply increase, so dose the straining. The amplitude value of the dynamic stress will begin to reduce and the granular load capacity will progressively disappear. The above phenomena indicate that liquefaction is in the process. When the pore water pressure is approximately equal to the consolidation pressure, the granules will not be able to bear any load, then the straining will rapidly increase and the dynamic stress will finally reduce to zero. Subsequently the granules will be in the liquefaction and lose the load capacity completely.

The above analysis shows that the steady state developing process of vibrating liquefaction obeys the power law; saturated granules have self-organized criticality which makes the space and time scale invariability of the vibrating liquefaction possible. During the course of vibration, with the increment of cycle index, the granules only have slight adjustment. But after the cyclic index reaches a certain value, at some instant the "avalanche" phenomenon will take place. The granular stress decreases rapidly or loses completely and the straining increases rapidly. The granules have a typical wholeness characteristic rather than part freedom adjustment. Namely, the granules have an obvious self-organized criticality.

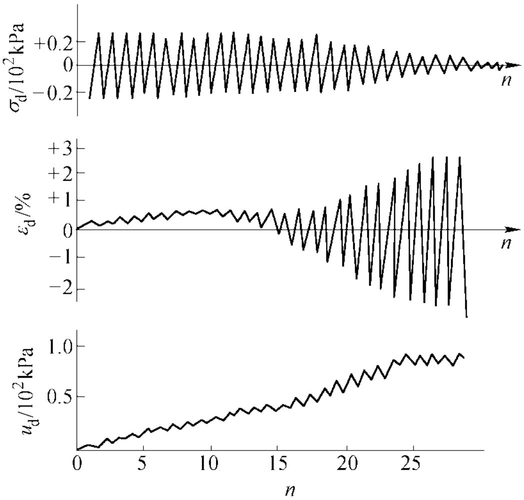

Fig. 8.13 The liquefaction experiment of saturated granules

8.6.6 *The dynamic analysis of vibrating liquefaction*

The difference form of the Eq. (8.99) is:

$$y_{n+1} = (a+1)y_n\left(1-\frac{b}{a+1}y_n^{\,2}\right) \tag{8.109}$$

Suppose $u = a + 1$, $x_n = \sqrt{\dfrac{b}{a+1}}y_n$, then Eq. (8.109) will be

$$x_{n+1} = ux_n(1-x_n^{\,2}) \tag{8.110}$$

Eq. (8.110) is similar to the Logistic equation, and the following steps will analyze this equation:

(1) $0<u<1$

Suppose $x = u\,x(1-x^2)$, then:

$$x_1 = 0 \qquad x_{2,3} = \pm\sqrt{\frac{u-1}{u}} \tag{8.111}$$

Because $u<1$, x_2 is the complex root, so it can be ignored. At this time there is only one stationary point $x_f=x_1=0$.

Suppose $F_u(x)=u\,x(1-x^2)$, so

$$\left|\frac{dFu}{dx}\,|\,x_f\right| = u-3ux^2\,|\,x_f = u < 1 \tag{8.112}$$

and its Lyapunov exponent (L.E.)

$$\lambda = \lim_{n\to\infty}\frac{1}{n}\ln\left|\frac{dFu^n}{dx}\,|\,x_f\right| = \lim_{n\to\infty}\frac{1}{n}\sum_{i=0}^{n-1}\ln\left|Fu'(x_i)\right| = \ln u < 0 \tag{8.113}$$

therefore, $x_f=0$ is the stationary point.

(2) $u=1$

The stationary point is still $x_f=0$, but because

$$\left|\frac{\mathrm{d}Fu}{\mathrm{d}x} | x_f\right| = u = 1 \tag{8.114}$$

$$\lambda = \ln u = \ln 1 = 0 \tag{8.115}$$

therefore, at this time x_f will be transformed into the critical stable state.

(3) $1<u<2$

At this time there are two stationary points:

$$x_f = 0 \qquad x_* = +\sqrt{\frac{u-1}{u}} \quad (\text{discard} -\sqrt{\frac{u-1}{u}}) \tag{8.116}$$

$$\left|\frac{\mathrm{d}Fu}{\mathrm{d}x} | x_f\right| = u > 1 \tag{8.117}$$

$$\left|\frac{\mathrm{d}Fu}{\mathrm{d}x} | x_*\right| = |3-2u| < 1 \tag{8.118}$$

therefore, x_f becomes the unstable stationary point. x_* is the stable stationary point. These indicate that the state and the number of the stationary point will change when the value of u through 1. So $u=1$ is the bifurcation point.

(4) $u=2$

$$\left|\frac{\mathrm{d}Fu}{\mathrm{d}x} | x_f\right| = u = 2 > 1 \tag{8.119}$$

x_f is still the unstable stationary point.

$$\left|\frac{\mathrm{d}Fu}{\mathrm{d}x} | x_*\right| = |3-2u| = 1 \tag{8.120}$$

and

$$\lambda(x_*) = 0 \tag{8.121}$$

At this time x_* is critical unstable again.

(5) $u>2$

For $u>2$, its evolutional state will be transformed. Eq. (8.110) will generate a doubling period bifurcation with the increment of u. For $u \to u_\infty (u_\infty \approx 2.3)$, the period 2^∞ occurs, namely the evolution of the system will transit from the period area to the chaos area. Therefore, the evolution of the vibrating liquefaction is a process from a doubling period bifurcation to the chaos. This process is the dynamic evolutional process of vibrating liquefaction, and can be simulated by computers. Its main program is Program 6.

Program 6—the dynamic evolution simulation of vibrating liquefaction

```
public:
    int n, j, AA, XX;
    double Miu, X, CoefMiu, CoefX, XInitial, MiuMax, MiuMin, MiuStep;
// CHundunView drawing
void CHundunView::OnDraw(CDC* pDC)
{
      CHundunDoc* pDoc = GetDocument();
```

```
        ASSERT_VALID(pDoc);
        MiuMin=1.0;
        MiuMax=4.0;
        pDC->Rectangle(1, 1, 640, 480);
        CoefMiu=280;
        CoefX=440;
        MiuStep=0.001;
        XInitial=0.4;
        Miu=MiuMin;
        while(Miu<MiuMax)
        {
          AA=int((Miu-MiuMin) *CoefMiu);
          X=XInitial;
          n=0;
          while(n<=200)
          {
            X=Miu*X* (1-X*X);
            n=n+1;
          }
          j=0;
          while(j<=100)
          {
            X=Miu*X* (1-X*X);
            j=j+1;
            XX=int(X*CoefX);
            pDC->SetPixel(AA+2, -XX+450, RGB(0, 255, 0));
          }
          Miu=Miu+MiuStep;
        }
}
```

The running result is shown in Fig. 8.14.

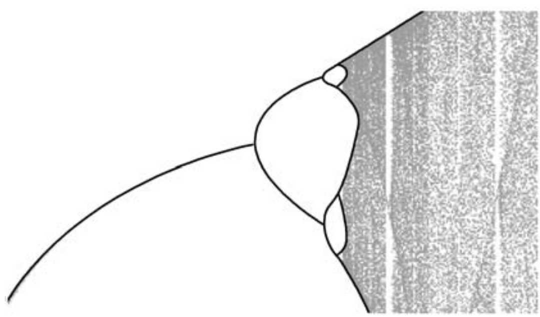

Fig. 8.14 The dynamic evolution simulation of vibrating liquefaction

9
Vibrating Ore-drawing Technology

9.1 The Influence of Vibration on Ores

Vibrating ore-drawing technique is a new mining approach, which uses the efficient action of powerful vibration machine in strengthening the ore-drawing process, perfecting mining methods and promoting an innovation in technological system[323]. After many caving methods were applied widely, it was invented to solve the apparent contradiction between the high efficiency of ore-breaking and the low efficiency of gravity ore-drawing. The invention of the vibrating ore-drawing technique brought important revolution to the development of underground mining technique, and consequently it became a focus in mining field.

At the beginning of 1970s, the research on the vibration ore-drawing technique was started at Central South University in China. "Fluctuating Vibrating Ore-drawing Machine (VOM)" was manufactured successfully in 1974, which enabled the development of China's vibration ore-drawing technique to enter a new stage. For several decades, especially from 1980, the vibration ore-drawing technique has achieved significant development. A series of important research achievement have been acquired with the combination effort of various research institutes and mining companies. Some of the examples are fluctuating VOM, ZGSJ type sieving machine of vibrating feeder, light-duty VOM, FZC series of VOM for gravity shaft, VOM with double bedplate, vibrating transportation train of movable type segment, etc. Because the vibration ore-drawing technique that adapted to China's condition has been a new approach, it attracted the attention of the mining field in China. From 1984, this new technique has been commonly accepted in many industries, such as nonferrous metal department, metallurgy department, chemical engineering department, manufacture of building materials department as well as disposal of granular material department. The speed of general acceptance of this mining research achievement is unprecedented. The practice proves that the vibration ore-drawing technique is a safe, highly effective and economical mining technique. It is being perfected and developed continuously for future several decades.

9.1.1 *The influence of vibration on ores' discharge capacity*

The ores, which are broken down in a stope, are different from each other in lump size and shape. Generally, the sizes of the ores are calculated by their nominal diameter, namely, using the arithmetic mean of the maximum sizes d_1, d_2 and d_3, which is measured on three approximate orthogonal axes in order to calculate.

According to the requirement of ore-drawing techniques, the lump size of loose ores should not be too big or too pulverized, because these conditions affect the ore-drawing efficiency directly. In working practice, there is an allowable maximum size for the lump ores, namely the approved lumpiness. Because the throughput of mines, and mining methods, etc. are different, the value of approved lumpiness vary from 350 to 600 mm. Any ore with size over the approved lumpiness is called unapproved lump ore. The percentage of unapproved lumpiness in caved ores is named boulder yield. Its value determines the discharge capacity of the ores at discharge opening to a great extent. The milled ores, with particle diameter ranging from 0.25 to 5 mm, are called coarse milled ores; meanwhile those with diameter less than 0.25 mm are called clayish ores. With the increase in humidity and the quantity of coarse milled ores with clayish ores, the loose ores will be consolidated under pressure. Consequently, their adhesion will be increased and its flowability will be reduced. So the quantity of milled ores from the caved ores has great effect on the discharge capacity of ores at discharge opening.

The discharge capacity of the ores indicates the ability of loose ores passing the discharge opening or the ore path. There are two parameters to indicate the discharge capacity of ores, one is ore-drawing output of discharge opening in unit time, and the other is the average block-up time of certain ores. For lump ores, the discharge capacity is expressed by the discharging coefficient of the ores.

The discharging coefficient of the ores is the ratio of the effective height of the discharge opening (or the length of ore path's short side) to the size of approved lumpiness:

$$k = \frac{h_0}{d} \tag{9.1}$$

where k is the ore's discharging coefficient at discharge opening, h_0 is the effective height of discharge opening, and d is the size of approved lumpiness.

For the gravity ore-drawing, some researchers show that: k must be more than 3～5 so that the lump ores can flow freely[5]. When k is between 2～3, it is not certain whether or not the ores at the discharge opening (or the ore path) will be blocked. Blockage will often happen if k is less than 2.

Only under the circumstance that the boulder yield is zero, the free flowing can be achieved when k is more than 3～5. However, because the unapproved lump ores exist objectively and the size of the discharge opening (or the ore path) is limited, the blockage cannot be avoided even k is more than 3～5.

There are two blockage types during the process of ore-drawing. One is coarse ores, when they appear as the lump ores blockage and building-up an arch; the other one is milled ores, when they appear as the formation of the milled ores arch or pile-up at the discharge opening.

Experiences indicate that ores blockage is a great disadvantage for the gravity ore-drawing technique and the basic reason for poor ore-drawing performance[5]. The vibrating ore-drawing is an effective technology to avoid blockage and to improve the unloading capacity of the ores at discharge opening.

Firstly, when using vibrating ore-drawing, the effective height of the discharge opening, which is shown in Fig. 9.1, will be increased significantly.

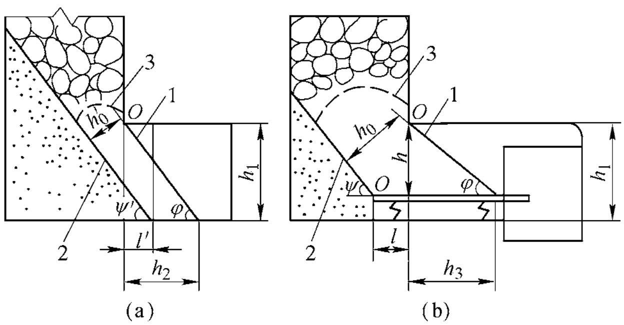

Fig. 9.1 Contrast diagram of ore-drawing ways

(a) Gravity ore-drawing; (b) Vibrating ore-drawing

1—Caved slope; 2—Stagnant ores heap's slope; 3—Arch profile; O—Protecting brim's brow line; h_1—The height of the ore path; h_2, h_3—Fall height of gravity ore-drawing and vibrating ore-drawing; ψ'—Repose angle of gravity ore-drawing; ψ—Repose angle of vibrating ore-drawing; l'—Sweeping length for the electric scraper; l—Burial depth of the VOM; φ—Fall angle of the ores; h—Height of the brow line of vibrating ore-drawing; h'_0, h_0—Effective height of the discharge opening of gravity ore-drawing and vibrating ore-drawing respectively

When gravity ore-drawing is used, the minimum thickness of the ores flowing area in its path (or the effective height h'_0 at discharge opening) is limited by the protecting brim's eyebrow line O and the stagnant ore heap's slope. It is determined with the depth of ores removal h_2-l' (or the sweeping width of the scraper, the length of effective part of the bar screen or shovel depth of the carrying scraper). When using the vibrating ore-drawing, the effective height of the discharge opening h_0 is mainly determined by the burial parameter of VOM. Because the ore-drawing machine has a burial depth l, the stagnant ore-heap's slope shifts outwards from the brow line, so the effective height of the discharge opening is increased excessively. According to the geometric relation in Fig. 9.1 the calculating formula for the effective height of the discharge opening is obtained by:

For the gravity ore-drawing:

$$h_0' = h_1 \cos\varphi' - l' \sin\psi' \tag{9.2}$$

For the vibrating ore-drawing :

$$h_0 = h\cos\varphi + l\sin\psi \tag{9.3}$$

The meanings of these symbols in previous two formulae are shown in Fig.9.1. Supposing that h_1 =2.2 m, l' =0.6 m, ψ' =66° , ψ=62° , l=0.7 m and h= $0.4h_1$, using the formula the following dimensions are obtained: h_0' =0.35 m, h_0 =1.03 m, namely, for the vibrating ore-drawing the effective height of the discharge opening where the ores flow is three times more than the gravity ore-drawing. Although there are many factors affecting the effective height of the discharge opening, its increase should not be questioned.

The discharge capacity of the lump ores will be improved with the increase of the effective discharge opening. It is one of the reasons that the vibrating ore-drawing can decrease the blockage. However, the most important factor is the vibration produced by the VOM's table-board, it can increase the flowability of the ores, so that the ore-drawing condition is improved.

Due to the increase of vibrated ores' flowability, the milled ores and small lump ores in the discharge opening flow continuously along the vibration table-board. The lump ores are closed out following the small ores, as a result, the possibility of lump ores causing blockage is decreased greatly. When some lump ores are blocked occasionally in the brow line, the VOM, which is still working, will reduce the thickness of the ores flowing area on the table-board or even make the surface clear. In this way, on one hand the buttress of the blocked ores are weakened, on the other hand, because the vibration of the table-board is augmented with the reduction of load, the vibration effect of the blocked ores is further strengthened. Consequently, the blocked ores will vibrate continuously with a change of orientation. Once the size of the lump ores at the direction of ore-drawing is slightly less than the size of discharge opening's cross-section the lump ores can be discharged (as showed in Fig. 9.2). The size of the discharged ores can reach 0.9～1.2 m in many mines where vibrating ore-drawing is used. Some working practices indicate that the discharging coefficient of lump ores reduce from 3～5 m (the coefficient for the gravity ore-drawing) to 1.2～2 m. It is said that the effective cross-section of the discharge opening with size 1 m×1 m can make the lump ores with size 0.50～0.83 m pass, so blockage incidents decrease significantly.

With the decrease of internal and external frictional coefficient, the motion resistance of ores' flow (including internal and external resistance) decreases and the flowability increases at the same time. It is so adjusted that the movement of the longer lump and the shaft shape material (such as shaft bar and mine timber) are inhibited. This will avoid the long shape material falling to cause blockage.

During the process of ore-drawing, lump-forming arch is another reason causing the ores' blockage. It is easy to produce a steady balanced arch if the fragmentation degrees of the discharged ores are not unequal. Consequently, the content of the milled ores among lump ores are quite big and the temperature is also high. As a result, the arch buttress support the weight of the ores upside and the ores' flow breaks off suddenly. This phenomenon occurs in gravity ore-drawing frequently, even under the circumstance of the discharge coefficient k between $3\sim5$. There are some ores' arches which are composed of three to five lump ores.

Experiences have made it clear that a firm arch of ores is often formed at the border of the discharge opening which shrink abruptly. Because the flowing cross-section of the ores decrease, as well as the ores have the sideway motion, the ores' arch take place easily (shown in Fig. 9.3). One part of the arch lies on the wall of the ore path, and the other part lies on the slope surface of dead ores' heap. It is very difficult and dangerous to deal with such firm arch.

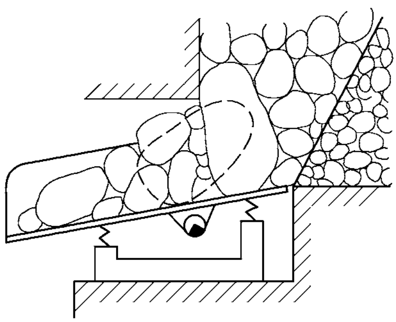

Fig. 9.2 The withdrawal of vibrated lump ores

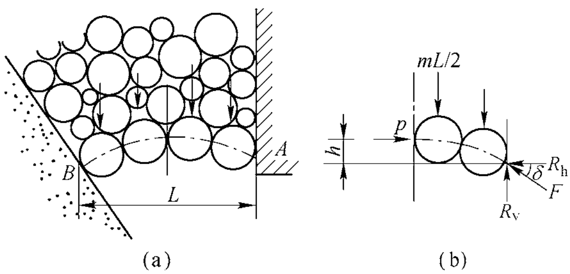

Fig. 9.3 The analysis diagram of ore's arch

The stability of the arch depends on the arch span, arch height and the load. There are only two ways which cause the arch to collapse. One is that the carrying capacity of the arch diminishes because the fragmentation of the contact surface among lump ores. The other is that the frictional force among the lump ores or the interface between the lump ores and the ore path's wall is not enough to resist the shear force acted on the arch by overlying broken ores.

The possibility that the arch cannot form because of the sliding of the arch abutment can be analyzed as follows in Fig. 9.3, where L is the arch span, h is the arch height and w is the mass for the unit length. Considering the moment at the action point of counterforce R and supposing that $R_h=p$, the horizontal component R_h, can be obtained as follows:

$$R_h h = \frac{mL}{2} \times \frac{L}{4} \tag{9.4}$$

$$R_h = \frac{mL^2}{8h} \tag{9.5}$$

Because all resistances on the arch abutment A are frictional resistances, the vertical component of counterforce R_v is:

$$R_v = R_h \tan\delta = \frac{mL^2}{8h} \tan\delta \tag{9.6}$$

The maximum of R_v is a half of the vertical load, *viz.*, $mL/2$; therefore, the condition of arching formation is:

$$\frac{mL^2}{8h} \tan\delta \leqslant \frac{mL}{2} \tag{9.7}$$

$$viz., k \leqslant 4h / \tan\delta \tag{9.8}$$

When the vibrating ore-drawing technique is used, the effective size of the discharge opening and the arch span are increased. As a result, the possibility of the formation of coarse ores' arch decreases greatly. Even though after the arch is formed, transmission of the vibration energy can decrease the internal frictional coefficient of the ores and the external frictional coefficient between the ores and the ore path. Consequently, the arch abutment will be weaken, even be destroyed; so it will be very difficult to form a firm arch.

In addition, comparing with gravity ore-drawing, the falling speed of each coarse ore is almost the same as in the vibrating field. The difference of relative velocity is little and the possibility of arch formation with two or more coarse ores caused by the falling velocity difference is also small.

In fact, during the falling process of vibrated ores, there may be an arching tendency among the coarse ores which interlock each other. But the arch cannot form or only exist transiently because of the transmission action of the vibrating energy.

The lump ores' arch is caused by the random interaction between the lump ores during the course of ore-drawing, but the characteristic of the milled ores' arch is not the same. The latter is greatly affected by the physical mechanical characteristics, such as the humidity, cohesiveness, granularity, compaction degree of ores, shear strength, etc. First of all, the shear strength is the main factor.

The cohesiveness of the milled ores behaves having original shear strength, *viz.*, the cohesion C. When the milled ores are subjected to bigger pressure from top, its consolidation degree increases, as well as shear strength.

Some studies indicate that the withdrawal of the milled ores travel from one layer to another in those ore-paths (such as chute raise and hopper)[5]; hence, they will form an arch at the same time as ore-drawing in each layer. Because the formed arch span is bigger than the balance span, all ore layers will fall down at the same time. However, the drawing process of milled ores is a dynamic one causing formation of unstable arch and its collapse takes place in turn. When shear strength of the loose ores is bigger and the effective cross-section size of discharge opening is smaller, it is very easy to form a stable arch. Different milled ores have both different internal frictional angle and different cohesion *C*, so the span of each stable arch formed is not the same as well.

During the process of milled ore-drawing, those unsteady arches over the discharge opening fall down in succession. Under the circumstance the vertical pressure from the surface that is tangent with the arch line is zero, *viz.*, the minimum principal stress is zero, the arch will be a steady balanced arch. The pressure on the surface that is vertical to the arch line of the steady balanced arch is larger. It increases gradually from the center to the arch abutment along the tangent direction of the arch and reaches its maximum at the point *A* and *B* of the arch abutments. The stress circle is $(\sigma_1,0)$, the stress diagram of the central arch point is$(\sigma_n,0)$(as showed in Fig. 9.4).

Showed in Fig.9.4 is a circular discharge opening, whose diameter is *D*, the bulk density of milled ores is γ . By choosing a separate body $AA'\,B'\,B$, the mechanical equilibrium is analyzed by the following:

The weight of the separate body is

$$G = \frac{\pi D^2}{4}\Delta h \gamma g \tag{9.9}$$

Assuming the shear upward force that separates the body is:

$$F_s = \tau_n \pi D \Delta h \tag{9.10}$$

$G=F_s$, so

$$D = \frac{4\tau_n}{\gamma g} \tag{9.11}$$

From Fig. 9.4b, obtain that:

$$\tau_n = C(1+\sin\varphi_n) \tag{9.12}$$

By substituting Eq.(9.12) into Eq.(9.11), obtain that:

$$D = \frac{4C(1+\sin\varphi_n)}{\gamma g} \tag{9.13}$$

D is the limiting diameter of the ores' arch at the discharge opening. In fact, it is the span of the steady arch, which is formed during the course of the milled ores' drawing. If the size of the discharge opening is larger than *D*, the arch will be destroyed by itself, so the withdrawal milled ores will flow freely. Depending on whether the arch span is equal to it or less, the arch will be stable or the ores' flow will break down. Therefore, the horizontal span of the effective cross-section of the discharge opening (or the chute raise's diameter of bin for milled ores) should be ensured to be larger than *D*.

Accordingly, the vibrating ore-drawing can increase the effective cross-section of the

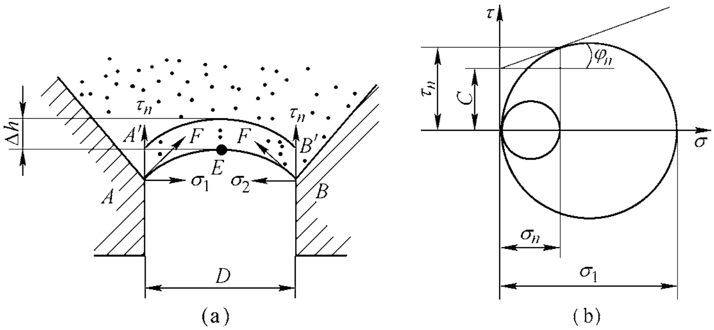

Fig. 9.4 The diagram of milled ores' arch

(a) Hopper's cross-section; (b) Stress circle's diagram

discharge opening; it can reduce the stability of an arch also. In addition, with the vibration of milled ores, the internal frictional coefficient decreases, and the holding power of the ores which form the arch also weakens. Therefore, the withdrawal powdery ores do not all depend on the gravity to overcome the shear strength which does not assist in forming a continuous ores' flow. So the possible distortion of the ore's arch, the ore's hang-up and the milled ores' pile-up are reduced.

Vibration can also improve the discharge capacity of the lump ores and the milled ores at the discharge opening. It ultimately indicates some advantages of vibrating ore-drawing. Furthermore, it not only brings the change for ore-drawing techniques but also promotes it to develop and to be perfect.

9.1.2 *The formation of continuous ores flow in the vibrating field*

Vibrating ore-drawing is a compelling ore-drawing method, which partially depends on the gravity potential energy. The combining action of the gravity and the exciting force makes the ores drawn.

A study indicates that the pressure from upside which the loose ores transmit on vibrating table-board is very big. Under the action of the load q which is regarded as the continuous and averagely distributing force, the loose ores with the shape of a similar cuboid *OMNAB* under the level of the ore path's roof will produce a horizontal thrusting force (showed in Fig. 9.5). This will act on the imaginary retaining wall *OBC* with the shape of a triangular prism (it is called *OBC* for short thereinafter).

Supposing that there is no friction on the surface *OB*, its stressed state is similar to the vertical, and forming a smooth retaining wall. Under the action of the horizontal thrusting force, if *OBC* moves a little ahead, the triangular prism *OBE* (it is called *OBE* for short thereinafter) will slide downwards accordingly. At the same time as the active limiting equilibrium *OBE* will glide downwards. Thus, according to the earth-pressure theory, the total active pressure p in unit

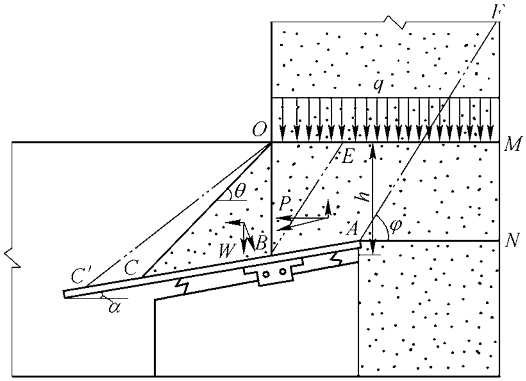

Fig.9.5 The ores' limiting state of equilibrium on vibrating table-board

width on surface OB is:

$$p = \frac{1}{2}\gamma H^2 \tan^2\left(45° - \frac{\varphi_n}{2}\right) + qH\tan^2\left(45 - \frac{\varphi_n}{2}\right) \tag{9.14}$$

This force acts between $H/3 \sim H/2$ above the point B.

Assuming that the ores have no cohesiveness, so the gliding surface BE is a plane, which has an included angle of $45° + \varphi_n/2$ with the horizontal plane.

By dividing the force p into two components, where one is parallel to the surface BC, and the other is vertical to the surface BC. The former is $p\cos\alpha$, which makes OBC to slide forward; the later is $p\sin\alpha$, which is upwards. Supposing the deadweight of OBC is W, it can be divided in two: a sliding force $W\sin\alpha$, which is parallel to the surface BC, and a force $W\cos\alpha$, which is vertical to the surface BC. The product of the vertical force and $\tan\varphi_n$(φ_n is the external frictional angle between the ores and the vibrating table-board) is a skid resistance.

Suppose the width of the vibrating table-board is b, when OBC becomes a static equilibrium state, an equation can be formulated as follows:

$$bp\cos\alpha + W\sin\alpha = (W\cos\alpha - bp\sin\alpha)\tan\varphi_n \tag{9.15}$$

$$W = p\frac{b\cos\alpha + b\sin\alpha\tan\varphi_n}{\cos\alpha\tan\varphi_n - \sin\alpha} \tag{9.16}$$

Obviously, W is a function of p. When the value of p increases, OBC will also increase correspondingly (namely, the point C on the vibrating table-board moves outside), or the bearing repose angle θ on the vibrating table-board will certainly decrease.

Therefore, when the ores on the vibrating table-board are in an equilibrium state, the retaining wall OBC is a ores' triangular prism which falls down from the brow line O with angle θ, and the slope bottom is the fixed point C.

However, if the static vibrating table-board enters into the vibrating state with certain intensity, OBC will be transformed due to the dynamic effect.

As mentioned above, the transmission of the vibrating energy can help to reduce the internal frictional angle of loose ores. Hence, the total active pressure p in Eq.(9.14) will increase significantly, and the external frictional coefficient tan δ will also be smaller due to the vibration of the table-board. Therefore, the static equivalent state, shown in Eq. (9.15), will end. As a result, OBE will slide along the surface BC, and OBC will move towards the discharge end. Finally, the slope bottom C of OBC will extend to C' .

If the coefficient of VOM's working state is more than or approximately equal to 1 and the vibration of the table-board is continuous, the triangular prism of ores will slide with a dynamic and continuous process. At this time, the ores' flow along the full cross-section will take place and the sliding surface will develop from BE to AF. As a result, a continuous vibrating ore-drawing process will come into being.

The upward pressure of the loose ores on the table-board and the vibrating force together will result in the vibrated ores' transition from static to movement state.

For a continuous flow of ores, the transporting velocity of the ores on the vibrating table-board varies in layers with different thickness. The ores on the bottom layer are always in the state of jumping or sliding, so the vibrating energies transferred from the bottom to the top. The ores on the vibrating table-board that move in the horizontal direction are regarded as a number of very thin beds with height of Δh. These beds have no deformation but have cohesive frictional action. The force acting on the beds are: the frictional force between adjacent beds, the side frictional force of each bed, the component of the inertial force on beds caused by the vibrating acceleration and the component of gravity on the beds. When the inertial force is a component of gravity on any one of the beds and is in excess the critical value of the frictional resistance, the ores' layers under this bed will move out along the table-board. This bed is called motive layer (shown in the Fig. 9.6).

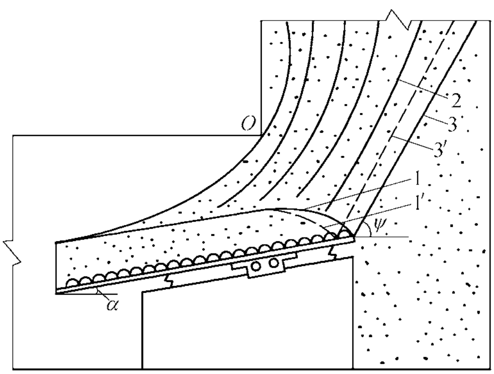

Fig. 9.6 The withdrawal of ores in vibrating field

1′,1—Interface between moving layers;2—Sliding line with downward flow whose velocity is nearly a constant;3′,3—Vibrating sliding surface

Obviously, the formation of this moving layer is the result of combined action of the inertia force and the gravity. Hence, the vibration acceleration and the tilt angle of the vibrating table-board that is related to the two forces are the main factors. These determine the thickness of the moving layer and the buried depth of the ores' pile.

As above, the loads of the vibrating table-board buried under the caved pile are different greatly between the ends of the inlet and outlet. Therefore, the vibrating amplitude and the acceleration of every point along the table-board are different. To a certain point, if its vibration acceleration and the required critical acceleration to form moving layer are the same, the ores will flow freely at the discharge end. There will be a moving layer from the point to the discharge end along the vibrating table-board. If the vibration acceleration of the table-board is smaller or the pressure acquired at the end of the inlet is larger, the thickness of the moving layer will reduce and its starting point will shift in the direction of the smaller pressure along the vibrating table-board. It is showed in Fig. 9.6. Obviously, it is advantageous to increase the vibration acceleration. However, the increment of vibration acceleration of the table-board will lead to the significant increment of the power of equipment, and the requirement of high extra structural strength. Hence, generally the vibration acceleration of the table-board should be less than 60 m/s^2.

The increment of the tilt angle of vibrating table-board means increasing the skidding force of ores along the table-board, and it will invariably increase the thickness of moving layer, and its depth approaches the ores' heap. However, the tilt angle of the table-board is finite, generally which varies between $0° \sim 25°$. If the angle is too large, it is necessary to increase the length of the vibrating table-board so as to avoid ores' falling by itself.

When the vertical distance from the brow line to the vibrating table-board is long and the thickness of ores layer on the table-board is more than the height of the moving layer, the part of the ores on the moving layer near the brow line will glide out by the moving force of the movement and the vibration of ores.

When the vibrating ore-drawing is used, the moving layer moves out continuously and the upper layer ores join it unceasingly at the same time. As a result, the activated ores in the vibration field will be sheared along the sliding line and will flow downwards continuously (as showed in Fig. 9.6). Its flowing velocity is greatest near the brow line, and it approaches to zero with the increment of the horizontal distance from brow line. Because the flowing velocity of the ores decreases and some ores of fine granularity percolate downwards, there will be a compacted steady slope (*viz.*, the vibrating glide plane) at the rim of the inlet end. The vibrating glide plane has a tilt angle ψ to the horizontal surface, which is called the repose angle of the vibrating ore-drawing. Its value depends on the physical and mechanical characteristics and the vibrating strength of the table-board, and it is less than the repose angle ψ' of gravity ore-drawing. It can be expressed as follows:

$$\psi = \psi' - \Delta\psi \tag{9.17}$$

where ψ is the repose angle of the vibrating ore-drawing, ψ' is the repose angle of the gravity ore-drawing, which can be calculated by the equation $\psi' = 45° + \varphi_n/2$, and $\Delta\psi$ is the difference between these two angles for the same type of ores, and this difference varies between $4° \sim 7°$.

9.2 Vibrating Ore-drawing Machine (VOM)

Many kinds of vibrating equipments are invented to meet the demands of the different working conditions, the vast range of applications and the occurrence of new techniques. At present, the equipments that have been applied in mines are classified on the basis of their functions. They are VOM, vibrating transporting machine, vibrating ore-feeder, vibrating loading machine, vibrating arch-destroyer, vibrating feeding and washing machine, vibrating belt screen, vibrating chute, and vibrating cleaning machine, etc. They mostly belong to the vibrating equipment with mid-frequency homogenous system and the inertia of hyper-resonance.

These equipments have different models and vibrating parameters. They can be compatible to the ores with different characteristics, such as the lump ores, the milled ores and the cohesive ores. Also they can satisfy different working conditions with different process requirements, such as ore pass, ore bin, and stope, etc. During the process of strengthening mining production these equipments are extensively used by their vibrating effect. Practical experience indicates that there will be a bright future to develop and utilize these vibrating machines, because they have many advantages comparing to other type of machines, for example, their structures are simple.

Generally, most of them consist of three parts, operating mechanism, elastic system and exciting system. They have no transmission device and can work under heavy load. They are easy to maintain, and can achieve a remote and auto control system. In the industrial application, it is safe, economical and efficient. The special effect of the vibration on the ores brings about new possibility of improving the mining methods and techniques fundamentally. It is the main reason for the vibrating machine to achieve such a great development in the mining industry for the last twenty years.

9.2.1 *The main characteristics of VOM*

Vibrating ore-drawing is a necessary ore-drawing way with stable, continuous and easily controlling ores flow. This is achieved by a strong vibration from the VOM and the partial gravitational potential of ores. Hence, VOM is the key equipment in the vibrating ore-drawing system.

The first VOM machine in China was successfully developed by Central South University together with Tongcheng Feldspar Mine in Hubei province. At the beginning, it was used in collecting ore pass and the stage ore pass in the stope, replacing the air-operated gate or the timber chute. Now, it is being used widely in the stopes, main ore passes, ore bins and mineral processing plants, and in other relative industry departments. The characteristics of VOM are as follows:

(1) Having the role of destroying arch, ore-drawing and shutting down. There is a blockage phenomenon during the process of gravity ore-drawing, so the ore-drawing is always affected. According to the statistics, dealing with the blockage in the hopper takes generally about 25%～35% of the total working time. However, adding to the wasted time in moving and waiting for the vehicle during the course of ore-drawing, the ore loading time is actually only 1/3～1/4 or even less of the whole working time for every shift. For example, using electrical rake for ore-drawing, production of each equipment is only 150～300tons per day.

VOM achieves the arch eliminating and ore-drawing by vibrating action. Once the vibration stops, ores will stop flowing immediately. It integrates three functions, arch eliminating, ore-drawing and shutting down. Neither does it need to have extra equipment to aid flowing by arch eliminating, nor is it required to install a lock gate for the hopper. As a result, the quantity of equipments is reduced, the energy consumption is decreased, and the operation becomes simple.

(2) The ores' flow is loose, continuous and uniform. Vibrating ore-drawing activates the loose ores in the ore pass to flow freely by vibration, so as to increase ores fluidity and discharge capacity of lump ores at the discharge opening. Also it can make ores to be discharged continuously and evenly in a state of mass flow after the expansion of the ores until the machine is stopped or the ores are withdrawn completely. Hence, the ores' flow is continuous, uniform and easily controlled.

(3) It has strong ability to aid flow by arch destroying. VOM transfers the vibration to those ores in ore pass; it can induce the ores to be activated under a suitable vibration frequency. The frictional and cohesive forces between the grains, which create the arch and hinder the ores to flow, are decreased. The ores can move downwards smoothly and ores' arching tendency seldom takes place. In addition, vibration can eliminate those existing arches.

(4) VOM mechanism can be achieved by installing an exciter (which is driven by an electric motor through a cone belt) or by a vibrating electric machine at the bottom surface of the vibrating table-board by bolts. It has no transmission device, such as the reducer. Since its structure is very simple, its production is easy, its cost is low, and its installation is simple and convenient. Moreover, its operation is reliable, and maintenance is simple.

(5) Generally, the mass of a VOM is about several hundred kilograms, and its power consumption is low. Its installed power is about 1.5～3 kW.

Practice testified that the VOM has many significant advantages comparing to those traditional equipments, such as an air-operated gate, the apron feeder, the electric-operated gate, etc. In addition, it has its special advantages over LHD. However, VOM has such disadvantages as poor mobility, a large number of units needed in a stope, much installation work involved and limited applications. But its cost is low, and maintenance is simple, so it can exert its efficiency fully under the circumstance of ore-drawing at a fixed point. The ores' flow is continuous, uniform and easily controlled, so a continuous performance techniques is achieved. Also it is easy to take effect and to generalize it. For instance, in Tongkeng Mine, where the ore-drawing system of VOM and automobile are adopted, its comprehensive ore-drawing ability reaches 620 t/ shift. It reaches or exceeds the productivity by using carry scraper in China.

9.2.2 *The basic structure of VOM*

VOM is a machine buried under the loose ores. The VOM's outline sketch of structure and the installation for the TZ type is shown in Fig. 9.7, which was used in early days in China. Its technical specifications are shown as follows:

Expected productivity	340～400 t/h
Length of vibration table-board	2500 mm
Width of vibration table-board	1350 m
Tilt angle of vibration table-board	12°
Amplitude	2～4 mm
Vibration frequency	24 Hz
Power	7.5 kW
Type of exciter	monoaxial inertia exciter
Exciting force	27～40 kN
Mass of VOM	1043 kg

According to the characteristics of the mine rock, the working condition of the mine and different requirements of productivity and technical effectiveness, varieties of vibrating ore-drawing machines can be designed. However, the basic structure of all the ore-drawing mechanism used in metal mines are similar, they consist of four parts, namely, a vibrating table-board, a frame, an exciter and a series of spring system.

(1) Vibrating table-board. It accepts the pressure from the top ores and transmits the vibration energy to those ores on the table-board. It can activate ores and make them to obtain good fluidity so as to achieve a steady flow of ore-drawing with high efficiency.

(2) Frame. It is the understructure of the whole machine. It supports the vibrating table-board by the springs element and provides space and position for the vibration electric machine or exciter under the vibrating table-board. It can make

their maintenance easy as well.

(3) Exciter. It is the drive source of the vibrating table-board for generating vibration. Also, it is one of the main units, which can ensure a good operation and ore-drawing efficiency of the VOM. It can be classified into two kinds, the monoaxial inertial exciter and the dual-axle exciter.

1) Monoaxial inertial exciter. It is used most installations. The structure is simple. The required vibration frequency can be achieved by changing the gear ratio through cone belt to drive. In order to simplify the structure further, now there are many ore-drawing machines which have adopted the vibration electric machines. These consist of an electric motor and an eccentric body of exciter. So the transmission drive is omitted in order to increase the mechanical efficiency, but the vibration frequency is only determined by the rotating speed of the vibration electric machine.

2) Dual-axle exciter. This type of exciter is used in a large-scale ore-drawing machine. Its structure is complex. Generally, it consists of case, axle, bearing, gear wheel and eccentric body. Because the rotating speed is very high, the gear wheel in the case needs to be lubricated so as to drive freely, and the maintenance is more extensive. Using two sets of vibration electric machines can operate synchronously by the dual-axle inertial exciter. In this way, the structure can be simplified and it is convenient to use.

(4) Spring system. It consists of some elastic elements and is located suitably between table-board and frame. It has the buffering and isolation action for the frame so as to avoid rigid crashing between the frame and the surface of the table-board. It has the action of storing up energy and assisting vibration for the table-board and providing conditions for providing steady amplitude. Metal springs and rubber strips can be used to provide rebounding action. Generally, metal spring is easily fractured, and the pressure on the table-board is large, so it is very difficult to renew. So currently the rubber strips are extensively used. They are located continuously on two sides of the table-board and the undersurface of the end of inlet. These rubber strips also have the function of sealing and can be used for a long time.

In addition, the brow line must be high and the table-board must be wide for those ore-drawing machines that are designed for large productivity and drawing lump ores. If an ore-drawing machine with single table-board and its width of the table-board is more than 1.4 m is used, then its motive power will concentrate excessively, and the power consumption will be high. So it requires a strong structure; both the frame and the table-board need to be made of heavy-duty steel as well. As a result, the equipment is very unwieldy, the haulage and installation become cumbersome. Therefore, using those ore-drawing machines to deal with lump ores for large productivity, they should be designed with double bedplates type.

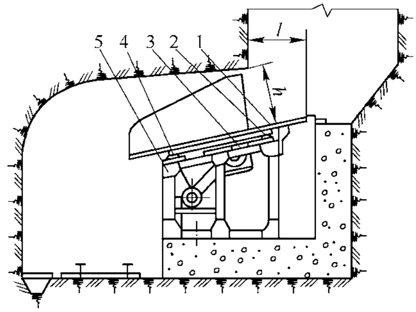

Fig.9.7 The outline sketch of the structure and installation of ore-drawing machine of TZ type

1—Vibration table-board; 2—Elastic element; 3—Inertial exciter;
4—Base of electric motor and rebounding electric machine; 5—Frame

9.2.3 *The development of VOM*

In all vibration equipments, VOM has developed rapidly in the recent ten years as the main equipment of ore-drawing techniques. In China, the fluctuating VOM of FZC type as the representation has been extensively used; in addition, it has been applied widely in stopes and ore passes. However, it is worth pointing out that the light combined-type ore-drawing machine has attracted people's attention, and it has also been commonly used in ore passes with large production and in stopes.

The characteristic of the light combined-type ore-drawing machine is integrating the use of two sets of light type vibration ore-drawing machines as vibration source by replacing a set of heavy type machine with high vibration force. The combined-type machine has many advantages over the heavy machine to achieve the same ore-drawing productivity. For example, its weight is small, its power is little, its distribution of force is uniform and the reliability is high. Because the table-board width of the light combined type ore-drawing machine increases once than the common type, so the discharging cross-section of the ores flow is enlarged, and the span of the ores arch is increased. As a result, the lump ores with the size of 1.2 m and the milled ores with cohesiveness can be drawn out freely. This type of machine is suitable to the mining method of bulk caving system and has the main chute with large productivity; so it has a good future application.

Making a comprehensive review of the development of the ore-drawing machine in recent years, the principle trends can be obtained as follows:

(1) Machine's type is numerous, but most of them belong to the simple hyper-resonance inertial ore-drawing machine, which has simple structure. Also it has steady working condition under the situation of variable load, so it is suitable for the poor underground working conditions.

(2) Commonly using inertial exciters to activate, basically the monoaxial inertial exciter has been replaced by the vibrating electric machine. The dual-axle

inertial exciters are also applied for the mines with much more fine ores and for large production, but the quantity is low. The structures of tri-axle and four-axle types are very complex and have never been introduced in China.

(3) Now most of the vibration ore-drawing machines adopt rubber elastic element so as to increase the reliability of the facilities and simplify their structure, and a few of them use steel spring element. Most of the types in China combine the rubber elastic element with the sealing system together. In this way, their structures become close fitting, installation becomes convenient and all of them have their own specialty.

(4) The welded structure of the vibrating table-board reinforces the rigidity of installing position of the exciter and the whole longitudinal rigidity, enhances the conveyance effect of ores, and the service life of the ore-drawing machine.

(5) The new type has been designed with some low frame and compact structure in order to reduce the overall size, reduce the weight of the machine and to make it easy to remove and install.

(6) Since the knowledge of the vibrating ore-drawing mechanism had enhanced at large, the phenomenon of using high power (that is 7 kW and 10 kW) ore-drawing machine has dropped off increasingly. The ore-drawing machines powered by exciting motors of 4 kW, 3 kW and 1.5 kW which are suitable for the relevant conditions have been used widely, and the power matching of equipment become more reasonable.

(7) The light combined type ore-drawing machines have been commonly installed in ore passes and stopes step by step. Using the combined type to replace the heavy type allows for reducing setup power and enhancing the working reliability of equipment. This reflects on the suitability of the ore-drawing machines with large production in China going the way towards the light combined type.

(8) The normalization of ore-drawing machines has obtained notable achievements. In China, the standard type is the fluctuating type, which uses vibrating motor to excite to adopt rubber as the elastic elements. Its structure is compact and the weight is small. Comparing with the type used by the former Soviet Union, it embodies China's characteristic in structure and its function has reached a high level. At present, the production of the ore-drawing machines and the vibrating motors matching them has been widely spread and the quality of their products has been enhanced much. All of these provide a good foundation substance for the extension of the vibrating ore-drawing technique.

VOM has been used in ore passes and stopes widely, and is used gradually in ore-bins. At the moment, besides the simple vibrating feeder, the type with frame for destroying arch, vibrating feeding and washing screen type also have good development prospect in ore bins.

The VOM with destroying arch frame characteristics has function which destroys arch in ore bins directly and allows ore-drawing. It has two machine modes and they are suspension type and seat type. It has been successfully used in powder bins and rude ores bins with high content of milled ores. This type of machine adopts vibrating motor to excite. The vibrating frame on vibrating table-board can directly break the milled ores arch in ore bins, so the milled ores can be drawn out in full cross-section. This ore-drawing machine had been applied in many mines, such as LingXiang Iron Mine, LaoChang Tin Mine, etc.

Vibrating feeding screen machine is used to feed, screen and wash broken ore for ore bins. It adopts dual-axle inertial exciter, is driven by a speed-regulating motor, and incorporates rubber spring as the elastic element. All the crude ores from the ore bins are handled by this machine, the washed lump ores remain on the screen and are sent to the crusher. While the ore powder ore mud goes under the screen and is concentrated before it is sent into the ore mud processing workshop. This machine can prevent not only blockage and ore-spillage in crude ore bins but also can complete feeding, screening and washing, so it is multifunction equipment with some originality. In another words, it has a new technique for dealing with the ores with more lumps, with high content of powdery ores and ore mud, with strong cohesiveness and with bad water permeability. This machine achieved a very good technical performance in Yichun Tantalum and Niobium Mine.

In addition, there are many successful cases of using the vibrating ore-drawing technique. For example, the ground ore bins adopt the ore-drawing machine for the completely buried form in FanKou Lead and Zinc Mine, the crude ore bins in Yichun Tantalum and Niobium Mine use the vibrating type of ore-loosening equipment, Malanzhuang Iron Mine uses two vibrating chute.

9.2.4 *The problems of vibrating ore-drawing*

At present, the number of types of VOM used in China is large, however they are all simple design, and cannot satisfy the requirements of various kinds of technological conditions. The main problems are as follows:

(1) Taking the kind of VOM as an example, at present, although the number of type is large, it still has not break away from the single mode. Generally, all adopt the similar structure and parameter without considering the magnitude of productivity, the diversity of material's characteristics and the difference of technological conditions.

(2) Considering the current structure of VOM, it basically uses only one mode of FZC series. There are no types available with special function, such as the self-moving ore-drawing machine, the disassembled ore-drawing machine, the segmentation of VOM combining the directional vibrating table-board and chute plate, the VOM with adjustable tilt angle of the table-board, etc.

(3) Considering the applied range of VOM, currently all machines are only suitable for local working condition (*viz.*, the fixed ore-drawing point), but the

machines for working condition at the end phase of the ore-drawing (*viz.*, the moving ore-drawing point) have not emerged.

9.3 Assembly Set of Continuous Operation

In order to increase the labor productivity of underground metal mine remarkably, one of the important approaches is continuous operation. Because the vibrating ore-drawing technique was introduced in stopes, the size of lump ores drawn out is 2～3 time as much as the one using gravity ore-drawing, the phenomenon of blockage by lump ores has decreased sharply and the flow of ore-drawing is continuous, uniform and easy to control, so the continuous operation can be achieved. There are three procedures during extraction chain, which are ore-breaking, ore-drawing and ore-carrying. Ore-drawing is the intermediate link, so its continuous operation will interlink another two procedures organically and form a continuous mining system. In a word, it is the vibrating ore-drawing technological development reaching a certain degree by the assembly a set of continuous operation of drawing, loading, carrying in underground metal mine was achieved.

The China's national key project *The Study on Techniques and Equipments of Underground Continuous Mining* was completed at Shizishan Copper Mine of Tongling Nonferrous Metals Company in 1990. This project has successfully developed equipments for continuous ore-drawing, ores carrying and crude ores screening which are typical characteristics of China. A set of indigenous facilities for the continuous operation of ore-drawing and ore-carrying in stope has been developed. In addition, there are two continuous production lines of ore-drawing and ore-carrying, and the ore-drawing of high intensity for the bulk caving mining system.

The continuous production line of the assembly set A is formed as follows: the light-duty vibrating machine in the stope →the vibrating transportation train of moving segments → the crude ores vibrating bar screen → the ore pass in the stope. The allowed conveying boulder is limited to 1100 mm. The measured average productivity is up to 828 t/h, with the maximum up to 1064 t/h. In addition, it only takes ten man shifts to install eleven segments of vibrating conveyors.

The continuous production line of the assembly set B is formed as follows: vibrating bar screen assisting flow in the stope→VOM→the belt conveyor with rope support for crude ores→ore pass in the stope. Allowed conveying boulder is 800 mm. The measured average productivity is 503 t/h while the maximum is 751 t/h. This machine has advantages of low energy consumption, low noise pollution and low transportation cost.

The key equipment of the assembly set A is the vibrating transportation train of moving segments. Compared to the underground mine vibrating conveyors abroad, such as KP type, BK-2 type, BKBC type and BP-80, the synchronous excitation of vibrating motor has higher operational reliability and is better than the driving of crank connecting rod. The excitation of segmentation will result in a more uniform kinetic distribution on the whole transporting distance. In addition, using the running gear it is easy to install, disassemble and transfer the transportation train.

The key equipment of the assembly set B is the belt conveyor with rope support for crude ores. Compared with the underground mine adhesive tape conveyor abroad, such as КПТ-120 type and КПТ-160 type, its structure is simplified more by adopting the rope support to replace the guide rail and abandoning the chain tension apparatus. Hence the energy consumption and the noise level are decreased, and also the operational reliability is enhanced.

The two assembly set of continuous operation developed in China, especially the two kinds of continuous transporting devices of crude ores, and achieved good technical and economic effectiveness in the industrial practice. The performances of those equipments are examples of the advance level of achievement in the world. It provides a set of indigenous facilities for the underground metal mine to strengthen mining activity in China, and it will bring profound influence to drive the advancement of mining technology in China.

The key project of the Ninth Five-Year Plan *The Study on the continuous mining method in underground metal mine without pillars* has been completed. This project further advances the development of assembly set of continuous operation, and it is introduced as follows.

9.3.1 *The main improvement in design of new generation continuous operation assembly set*

The main equipments of assembly a set of continuous operation for ore-drawing in stope were developed successfully by Central South University. Then an industrial application of testing was carried out for a long period at Fenghuangshan Copper Mine of Tongling Non-ferrous Metal Company. The continuous operation of ore-drawing and ore-carrying in the No.2 stope zone of Fenghuangshan Copper Mine belongs to an well proven machine of new generation, whose internal property, external dimensions, linkage and sealing structure etc. have been optimized.

The main improvements in the design are:

(1) The whole VOM adopts integral structure, and the side plate of the VOM can not be vibrated. At present, the vibrating motor is installed and fixed directly in the reverse direction on the vibrating bedplate of the VOM, which activates vibrating motor as a vibration source. These machines have some disadvantages. Firstly, because the difference of welding technology and the excessive

concentration of exciting force, the bedplate is liable to break; secondly, because the vibrating motor is fixed on the bedplate inversely, the installation process is not convenient and the fastening bolts of vibrating motor are liable to loose and fall down. To overcome these two disadvantages mentioned above, when the VOM of FSZ-II is used, the base of motor and the bedplate is linked during the installation process. Then the vibrating motor is placed under the bedplate horizontally in forward direction. The distribution range of vibrating force on the bedplate of this structure is more reasonable, and the effect of vibrating ore-drawing is much better. In addition, this structure makes the vibrating motor is much easier to install, maintain and renew.

(2) The whole vibrating transportation train adopts the integral structure of segments. In order to enhance the function of the train further, there are some effective improvements are designed as follows:

1) The cross-section of the trough is changed from ladder-type to rectangle, and the rigidity and strength of the trough is increased.

2) The elastic elements adopt compound spring of metal and rubber which has been practiced and produced successfully by Central South University researchers. In addition, the layout is changed, and the structure of the elastic system is simplified further. The transverse swing of the equipment in the resonance zone is basically eliminated, and the working noise is reduced effectively.

3) The frame is changed from a mobile installation structure of running gear to a fixed installation, which not only simplifies the structure but also makes the installation and fixing easier and reliable.

4) The installation position of the vibrating motor is moved from the bottom of the trough to two sides of it, which lowers the height of the train further.

The practice indicates that the new generation of assembly equipment which has been improved has many advantages. Its structure is more finished and its working function is more stable and reliable. The joint of the internodes does not affect the discharge velocity of the material, and the whole machine without load or with heavy load can operate smoothly with little noise. The single-section structure of the new generation of vibrating transportation train is shown in Fig. 9.8.

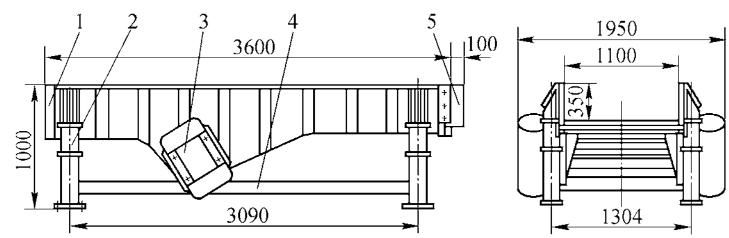

Fig. 9.8 The single-section structure of HZY vibration transportation train

1—Transporting trough; 2—Elastic system; 3—Exciter;
4—Frame; 5—Connecting structure

The motor power of each section of HZY vibrating transportation train shown in Fig. 9.8 is 4.5 kW, its maximum exciting force is 100 kN. To make sure the working exciting force is suitable for transporting ability, and the exciting force is adjusted to 70 kN, 80 kN and 90 kN. Also, the conveying velocity of ores of different degrees of fragmentation and the current consumption are measured respectively under the condition of these three grades of forces. The result is shown in Table 9.1.

Table 9.1 The conveying velocity in different exciting force condition

Order number	Exciting force /kN	Fragmentation degree	Conveying distance /m	Needed time /s	Conveying velocity /m • s^{-1}	Working current /A
1	70	Middle	3.6	31	0.116	
2	70	Large	3.6	37	0.097 0.099	4.8
3	70	Small	3.6	42	0.085	
1	80	Middle	3.6	17	0.211	
2	80	Large	3.6	19	0.189 0.183	4.8
3	80	Small	3.6	24	0.150	
1	90	Middle	3.6	14	0.257	
2	90	Large	3.6	15	0.240 0.323	5.0
3	90	Small	3.6	18	0.200	

Notice:The large fragmentation is from 0.65 m to 1.1 m, the middle one is from 0.01 m to 0.65 m and the small one is less than 0.01 m.

Considering the requirement of the ore-drawing ability and the operating reliability of the equipment for long time working, the exciting force of every section of the vibrating transportation train is adjusted to 80 kN as the working vibrating force of the continuous vibrating ore-drawing. Not only does it ensure the vibrating transportation train with larger conveying ability (the maximum can reach 554 t/h), but also only 80% of the maximum exciting force is used, so the service life of the equipment can be prolonged.

Ore-drawing and ore-carrying ability of stope mainly depend on the transporting ability of vibrating transportation train. Under the circumstance that the working exciting force of the train is determined as 80 kN, the ability of the ore-drawing and ore-carrying in stope according to different trough load condition are measured, and the result is shown in Table 9.2.

Table 9.2 The technical productivity according to the trough load coefficient

Exciting force of single section /kN	Measured average transporting velocity /m • s^{-1}	The density of loose ores /t • m^{-3}	Measured productivity of continuous ore-drawing and ore-carrying according to trough load coefficient /t • h^{-1}						
			1.0	0.9	0.8	0.7	0.6	0.5	0.4
80	0.182	2.2	554.8	199.4	443.9	388.4	332.9	277.5	221.7

From Table 9.2 if the trough load coefficient increases by 0.1, the transporting ability can averagely increases by about 15% correspondingly. Furthermore, the trough load coefficient of the train is enhanced, its energy consumption does not increase with it and the measured current consumption is 0.073 kW • h/t. That is to say, the trough load coefficient should be increased more during the ore-drawing operation, so the ore-drawing productivity can be enhanced. In addition, it can further reduce the energy consumption of unit ores drawn and reduce the cost of ore-drawing. In fact, the ore-drawing cost of vibrating continuous operation in the trial stope is 1.05 yuan/t, which is about one third of Fenghuangshan Copper Mine usual cost of 3.15 yuan/t by using T_4G for ore-drawing.

With the same exciting force, the ores can be discharged by VOM without the consideration of the degree of fragmentation, except for the cohesiveness milled ores with large humidity. This method can also be used to the discharge opening of the ore pass with uniform continuous flow by the train. It means that the effect of fragmentation on transporting effectiveness is not significant. The industrial practice indicates that the discharge capacity of lump ores of GZY vibrating transportation train is very high. In addition, from the measured results it can be seen that the discharge velocity has the trend to rise in a straight line with the increase of exciting force. Also, it can completely meet the requirement of continuous ore-drawing for high productivity in the stope with mass ores.

9.3.2 *The main technical parameters of new generation assembly set*

The main technical parameters of the improved new generation of vibrating assembly set with continuous operation are shown in Table 9.3.

Table 9.3 The main technical parameter of vibrating continuous working assembly set

Main Parameter	Assembly Set		
	FSZ- II type of VOM	HZY type of vibrating transportation train	Vibrating bar screen for crude ores
Technical productivity/t • h^{-1}	>200	200～800	>800
Vibrating frequency/ Hz	15.7	24.7	23.8
Vibrating amplitude /mm	2～5	2～4	1～3
Vibrating angle / (°)		30	30
Exciting force/ kN	(0～20)×2	(0～50)×2	(0～10)×2
Installed power / kW	3×2	2.25×2	1.5×2
Mass of equipment/ kg	2518	1889	1198
Length of equipment / mm	3800	3600	2800
Width of equipment / mm	2200	1950	1920
Height of equipment / mm	2030	1000	
Width of bar screen / mm			570～600
Installed tilt angle / (°)	20	0	21
Allowable flowing boulder size / mm	≤1100	≤1100	≤600

Notice: Because the storage of ores in ore passes is small, the vibrating bar screen is not installed.

9.3.3 *The main technical characteristics of new generation assembly set*

(1) For the combined type VOM with big discharge opening of 1.3 m×2.3 m, it is suitable for the crude ores in stopes, and its discharge coefficient is large. Generally, the boulders (less than 1.1 m) can be discharged smoothly, and the recrushing work at discharge opening is reduced considerably.

(2) Taking biaxial vibrating motor as an exciter for vibrating in synchronism. Its structure is simple, the directionality is good and the performance is stable.

(3) Using the open-wide rectangle transporting trough, it is advantage for the crude ores passing and enhancing the transporting effect of crude ores.

(4) The vibrating motor installed at both sides of the trough. It makes the installation easy to renew and simplifies the structure of the whole equipment. In addition, it further reduces the height of the whole equipment and enhances the stability of the trough body during operation.

(5) The vibrating transportation train belongs to a combined segment type, the train is assembled by connecting several VOM units in series to meet the needs of different haul distance. This kind of transportation train is flexible, with good adaptability and robust. It is compact in overall size, so it can work in a small cross-section drift. Furthermore, the components in the whole equipment will not be damaged easily, so there is little maintenance work.

(6) The combined metal and rubber spring has been developed successfully and was introduced into the new type machine firstly as elastic elements. It effectively reduces the vibrating amplitude of the equipment in the super-resonance zone so the working noise is low. The elastic system is allocated at both sides of the transporting trough, which improves the stability of the equipment and basically eliminates the transverse oscillation which is a disadvantage to the equipment and transportation. Moreover, it strengthens the built-in properties of the equipment greatly.

(7) When the exciting force of the middle segments are the same, the materials transported by the rough will be continuous and uniform, so the ore-carrying velocity will be basically uniform. Furthermore, conveying lump crude ores has no effect on the discharge velocity, also the installed power rating of the assembly equipment is small and the energy consumption is low so as to reduce the ore-drawing cost considerably.

(8) The assembly equipment are all controlled by electricity, which can reduce ore-drawing labor force significantly and improve the working environment of the ore-drawing effectively.

9.3.4 *The evaluation of continuous operation assembly set*

It took 15 years from the rewarding development of the assembly set of continuous operation for ore-drawing and ore-carrying in stopes to the successful industrial application of this new generation machine in Fenghuangshan Copper Mine. It became perfect just after three times of substantial design modifications. From the testing result of industrial application in Fenghuangshan Copper Mine, some advantages are listed as follows:

(1) The assembly equipment provides stable working conditions, large productivity and strong adaptability. The industrial testing results indicate that the assembly set of continuous operation increases the ore-drawing productivity in stopes significantly, reduces the ore-drawing cost, resolves the contradiction between the high efficiency of blast-hole block caving system and the low efficiency of ore-drawing in stopes. The arrangement of this kind of continuous ore-drawing system in stopes is a novel technique of block caving system in the underground mine. This makes the level of continuous mining technique in the underground mine in China to a further step under the circumstance of low investment to equipment.

(2) The ore-drawing and carrying performance of the assembly set of vibrating continuous operation are stable and reliable. During the industrial testing in Fenghuangshan Copper Mine, the quantity of discharged ores by vibrating continuous operation assembly set is about 80000 tons. When the exciting force of the single segment of vibrating transportation train is 80 kN, the highest technical productivity can reach 554 t/h. Influenced by everyday ore-drawing quantity at sublevel, and ore grade, etc., the actual average productivity of ore-drawing is 185 t/h, and the highest quantity of ore-drawing is 486 tons per shift. Even with the unfavorable circumstance of the recrushing of boulders and high moisture in underground, the vibrating assembly equipment can sustain a working performance. Its ore-drawing productivity is 3～4 times as much as T_4G type ore-drawing machine in the same condition. It reaches or even exceeds the highest level by using a carry scraper for ore-drawing in China and its cost of ore-drawing is only one-tenth of the carry scraper. In addition, its maintenance is easier and simpler than LHD, and it is much easier to install and operate on.

(3) The ore-drawing continuous operation assembly set in stopes has strong adaptability to crude ores and has strong discharge capacity for lump ores. The allowable transporting fragmentation of assembly set is less than 1.1 m, sometimes even the lump ores with the weight more than one ton can be discharged smoothly and transported continuously during the ore-drawing process. This reduces the blockage phenomenon of arch formation of lump ores in discharge opening and the working capacity of destroying this arch by explosive. As a result, the working condition of ore-drawing in stopes has improved effectively and labor force is

alleviated. The practice proved that the assembly set of vibrating continuous operation is an effective key equipment to achieve the continuous lump ore-drawing and ore-carrying in stopes. Its stable and reliable working performance and long period of good working condition show that this newly developed equipment and technique have tended to become perfect.

(4) The assembly set of vibrating continuous operation in stopes uses the electric energy directly, and installed power is small. After testing and checking, the current consumption of assembly set for the ores unit volume is 0.073 kW • h/t. When it is converted into the cost of energy consumption, it is 0.04 yuan/t; and converted into the checked ore-drawing cost, it is 1.05 yuan/t. The assembly set has such advantages as easy operation, safe working condition and high efficiency; so that it is a new type of equipment with great economic effect for continuous operation of ore-drawing and ore-carrying in stopes.

(5) The assembly set of vibrating continuous operation in stope is the indigenous equipment developed successfully in China. It has such advantages as low cost, simple structure and easy production. So it can combine with the original ore-drawing transporting system and emerge being a continuous working system of ore-drawing and ore-carrying with high efficiency. In addition, the main equipment of this system has low investment, convenient operation and maintenance, so it provides an important technological approach to achieve continuous mining techniques in underground metal mine.

(6) Industrial testing results also indicate that the process system of continuous ore-drawing and ore-carrying has reasonable combination, simple and reliable techniques. Especially, the assembly set of the improved new generation vibrating operation has reliable operating characteristics and better outline structure. Compared with the initial type, it has further prominent characteristics as follows:

1) The motor of VOM is much easier and more convenient to install, remove and maintain.

2) The whole structure of vibrating transportation train is much compact and easier to handle. The center of gravity of the trough is lower, so it will not upset while shocked by lump ores, and it can operate smoothly without load or with heavy load.

3) The equipment is easily operated, operation is safe, the labor force for ore-drawing is low and the working circumstance is comfortable.

4) It is new equipment for continuous ore-drawing and ore-carrying in stopes with obvious economic effect and social benefit, so it is worth to generalize and apply.

The industrial application for a long period suggests that the application of continuous working system of ore-drawing and ore-carrying in stopes and its matching equipment are successful, and vibrating ore-drawing assembly set is reliable. However, VOM and vibrating transportation train both need further improvement in following aspects:

1) When the vibrating transportation train was installed and fixed near the floor, the lap joint structure should be used for the inter-segments. This not only can eliminate radically the phenomenon of fine ore production in the inter-segments, but also can further simplify the connecting way of inter-segment.

2) In order to prolong the service life of the equipment, an antifriction layer on the baseplate of the train should be used.

3) An automatic dust extractor should be installed at the discharge opening of the VOM, so the dust loading during the process of ore-drawing is reduced and the ore-drawing circumstance is improved further.

9.4 The Application of Vibrating Ore-drawing in Ore Pass

Ore pass takes a leading part in the production of a mine. Comparing to the power lifter, it has many advantages, such as large throughput, balanced production, low energy consumption, low production and working expenditure, and low cost of ore-carrying, etc. So the ore pass has been introduced broadly in the vertical haulage in many non-coals mine.

There are different materials transported by ore pass in mines, such as ores, waste rock and filling material. The characteristics of the materials are different, such as cohesive or non-cohesive, massive or powdered, etc. Some of these chutes are used in open-pit mine, but most of them are used in underground mine. In addition, they have different structural forms and varied productivity. Taking the ore pass of Nanfen Open-pit Iron Mine as an example, its vertical height is more than 300 m, the total sectional area is over 45 m^2, and the discharged quantity of ores is up to 100 million tons per year. While the minimum vertical height of the stope ore pass in underground mine is only 5 m, the amount of ore-drawing every year is only about 20000 tons.

According to its serving arrangement, the ore passes in underground mines can be classified into two kinds: (1) the stope ore pass. It carries from 20 to 50 thousand tons of discharged ores per year. Generally, its height is from 5 to 20 m, the cross-section is 2 m$\times$2 m. (2) The stage ore pass. It carries 50 to 150 thousand tons of discharged ores per year. Its height is from 40 m to 60 m and diameter is more than 2.5 m. According to the operating mode and external appearances, the ore pass can be divided into single-stage straight ore pass, multi-branched straight ore pass, multi-stage controlling ore pass, vertical stage ore pass, single level unloading tilted ore pass, etc.

The research on vibrating ore-drawing technology in China has started from ore pass. For several years, great achievements in the research of VOM type and techniques have been obtained. Moreover, rich experiences have been accumulated.

At present, vibrating ore-drawing has become an important technology of ore-drawing for ore pass in China.

9.4.1 *The flowing law of ores in ore pass*

The flowing rule of ores during the process of ore-drawing is showed in Fig. 9.9.

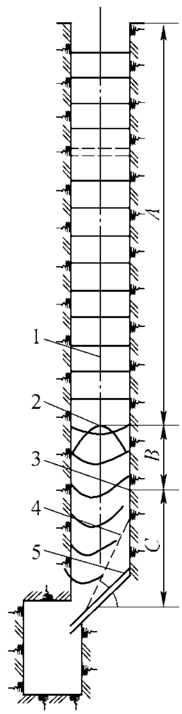

Fig. 9.9 The flowing laws of ores in the ore pass

1—Flowing axis; 2—Top of loose ellipsoid; 3—Vertex of accumulation line of milled ores; 4—Milled ores accumulation line; 5—Milled ores' pile

The test indicates that according to the vertical falling velocity of ores the cross-section of a ore pass can be divided into the free-flowing zone A, the transition zone B and the stagnation zone C[5,324].

The free-flowing zone, where the sidewall friction can be ignored, is located at the axis of the flowing zone. The ores in this zone fall vertically without displacement in horizontal direction. If the dimensions of ore pass and lump ores can be fixed accurately, the ores will not be blocked in this zone generally.

The transition zone is a whole flowing zone. Because the discharge opening is located at the side of the ore pass, the flowing axis will be deflected. The flow speed of the ores along the axis will be higher when the speed of the ores near the sidewall becomes gradually slower. As a result, the ores will have vertical and horizontal displacements and have a moving balanced arch, so generally there are no blockage phenomena.

In the stagnation zone the smaller ores or fine ores pass though among the bigger ores during the flowing process, so an accumulated body of fine ores comes into being out of the borderline of the ore-drawing ellipsoid above the discharge opening. Because of the existing of an accumulated body, the flowing cross-section of the falling ores reduces gradually, the resistance of ores flow increases, the straight falling velocity of the ores near sidewall decreases and the movement in horizontal direction intensifies. As a result, the lump ores can be classified themselves and are concentrated to the axis line. With the decrease of height, this phenomenon will be more obvious, and the probability of forming lump ores arch and small ores will be much larger, so the discharge opening of the ore pass will be blocked continuously.

9.4.2 *The ore-drawing by ore pass in the stope*

The stope ore pass is a passage for ores transportation in the stope. Generally, there are many stope ore passes in a mine. Taking Taolin Lead Zinc Mine as an example, its production is nearly 10 thousand tons per year while the quantity of stope ore passes is more than one hundred.

VOM has been used widely in Taolin Lead Zinc Mine for the stope ore passes of the stage forced-caving system. Its structure and installation sizes are shown in Fig. 9.7.

The favorable technical and economical effectiveness have been achieved in the application of vibrating ore-drawing in the stope ore passes of Taolin Lead Zinc Mine. After adopting vibrating ore-drawing, there is little blockage, and technical productivity of ore-drawing is enhanced by 1 to 2 times, also it lowered the labor intensity and decreased the number of workers employed for ore-drawing. The No. 3 work area needed 13 to 15 persons for ore-drawing in the past, but it only needs 6 to 8 persons now.

9.4.3 *The ore-drawing of main chute*

It is a progressive move to use VOM in the main chute for ore-drawing. This dual table-board parallel vibrating machine has been developed successfully in China, and it is now possible for the main chute to achieve vibrating ore-drawing with large transportation volume. Its installation and layout are shown in Fig. 9.10.

The dual table-board parallel vibrating machine consists of two sets of vibrating machines installed side by side. For each of them, a shield board which is originally located at middle place is eliminated, and there is a gap of 20 mm sealed by rubber board and layer between them. The technical property of a dual table-board parallel vibrating machine used in the main chute is shown in Table 9.4.

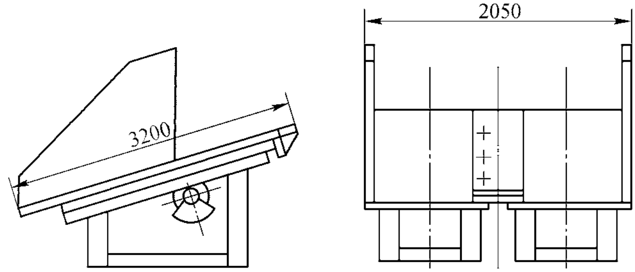

Fig. 9.10 Sketch diagram of the dual table-board parallel vibrating machine

Table 9.4 The technical property of a dual table-board parallel vibrating machine used in the main chute

Item	Parameter	Item	Parameter
Technical productivity/t • h^{-1}	1200～1600	Power/kW	5.5×2
Width of vibrating table-board /mm	1100×2	The maximal exciting force/kN	38±2
Length of vibrating table-board /mm	3500	Inner burial depth/mm	1260
Tilt angle of vibrating table-board /(°)	16	Height of brow line/mm	1100
Type of vibrating machine	2DJ5.5-6	Tilt angle of brow line/(°)	41

This machine is used in the ore pass with diameter of 3.6 m. Because the table-board is increased to 1100 mm×2 mm, the flowing cross-section of ores at the discharge opening is increased up to 27%～32% in the ore pass cross-section. So the span of ores' arch is increased and the blockage phenomenon is basically eliminated. The VOM can load two vehicles of ores each time and the trough load coefficient is expanded up to 0.9. Its ore-drawing productivity is more than three times of a single set vibrating machine, and even it approaches the ore-drawing ability of heavy type vibrating machine. The successful application of dual table-board parallel vibrating machine provides some rich experience for the light-duty VOM in China. At present, this type of machine has been applied in Fenghuangshan Copper Mine, Dachang Tin Mine, etc.

9.4.4 *The application examples of ore-drawing in the ore pass*

The research on vibrating ore-drawing technology in China originated firstly with the ore-drawing in the ore pass. It has been then generalized to all kinds of ore passes in underground mines and open-pit mines for more than twenty years. It is not only successfully used in common ore pass, but also efficaciously used in those ore passes discharging ores with large amount of mud and cohesive ores. It is also used in the main chute with strict requirement of high productivity. In addition, rich experiences were accumulated and notable technical and economical benefit were gained in this aspect. Now vibrating ore-drawing technology becomes an important technology for ore pass ore-drawing in China. The following are some examples which introduce the experience of applying vibrating ore-drawing technology in various ore passes under different conditions.

9.4.4.1 The application of VOM in the common ore pass

The common ore pass is the one that has no special requirement to the characteristics of discharged ores, productive output and a specific control to ore-drawing process.

Example 1: The vibrating ore-drawing of stope ore pass in Taolin Lead Zinc Mine

(1) Basic technology conditions. Taolin Lead Zinc Mine in Hunan province is one of main lead zinc mines in China, which belongs to the hydrothermal fissure filling deposit of middle or low temperature. The average thickness of the main ore body is from 15 to 20 m. The rock of the hanging wall is unstable phyllite while the rock of the foot wall is quartzite and granite. The mining method is the induced block caving.

(2) Technical properties of VOM. As early as the end of 1970s in the 20th century, the TZ type VOMs were introduced widely in stope ore passes. The structure of the machine is shown in Fig. 9.10 and its main technology parameters are shown in Table 9.5. Because of the light mass, small power and stable working property, the TZ type VOM is one type of machine relatively suitable for the stope ore pass. Its working condition coefficient reaches from 2.188 to 3.249, which indicates that its kinetic parameter can fit its actual burial parameter.

Table 9.5 The measured data of Taolin Lead Zinc Mine

Item	Unit	Designed data	Measured data
Technical productivity	$t \cdot h^{-1}$	587	340～400
Exciting force	kN	26.17～37.03	26.03～28.29
Vibrating frequency	time/min	1410	1225～1410.7
Amplitude	mm	2.1	1.87～3.26
Working condition parameter		2.38	2.69～5.41
Tilt angle of vibrating table-board	(°)	12	2.188～3.294
Power of motor	kW	7.5	12
Mass of ore-drawing machine	kg	1040	8.2～11.5
Burial depth	m	0.7	1.1
Height of brow line	m	0.8	0.75
Width of discharge opening	m	1.35	1.3

(3) Experience and effect. The practice proves that the vibrating ore-drawing technique, which was adopted in Taolin Lead Zinc Mine in the stope ore pass, has many advantages and obtains preferable technical and economical effect. The quantity of ore-drawing of the stope ore pass is somewhat small. The hopper of gravity ore-drawing is cheaper, and the initial investment of vibrating ore-drawing

is relatively high. However, the VOM can be removed and used repeatedly; so although its average cost of using for the first time is higher than concrete or wood hopper, it is lower than the air-operated hopper about by 37%. Furthermore, if taking into account that the vibrating ore-drawing can enhance the productivity, it reduces the number of ore-drawing worker, especially can significantly improve the safety condition and reduce the labor force markedly, its technical and economical benefit will be more distinct. The measured technical and economical indexes are listed in Table 9.6.

Table 9.6 The technical and economical index of vibrating ore-drawing in the stope ore pass for Taolin Lead Zinc Mine

Item		The vibrating ore-drawing	Gravity ore-drawing		
			Air-braked hopper	Concrete hopper	Wood hopper
Condition of blockage and ores arch		Very little	Much	More	More
Labor strength of ore-drawing		Very low	Higher	High	High
Working safety		Very good	Better	Worse	Worse
The number of ore-drawing workers		1	2	2～3	2～3
Working capacity of cleaning laneway		Very little	Less	Much	Much
Filing coefficient of ore car		0.9～1	0.7～0.8	0.7～0.8	0.7～0.8
Technical productivity/$t \cdot h^{-1}$		340～400	250～350	80～120	80～120
Material	Steel material/kg	1593	1395	474	72
	Timber/m^3	0.48①	0.48①	0.48①	6②
	Cement/t	2.5	2.5	2.5	
Cost	Cost of equipment/yuan	2468.10	1703.10		
	Installed cost/yuan	169.00	164.60	129.81	11.75
	Others/yuan	772.60	622.30	520.26	582.00
	The Total/yuan	3389.50	2489.80	650.07	593.75
Using(repeated) times		Four times	Once	Once	Once
Average expenditure of using once/yuan		1558.60	2489.80	650.07	593.75

① Used as the concrete back plate;

② The timber consumption from installing to finishing using the hopper.

Example 2: The vibrating ore-drawing of stage chute in Jinchangyu Golden Mine

(1) Basic technical conditions. Jinchangyu Golden Mine belongs to the mesothermal fissure filling gold deposit with narrow vein or lenticular shape. The stability of its ore-body and surrounding rock are good. The ores has no oxidizability, spontaneous combustibility and cohesiveness, and its mud content is also small. The main mining method is short-hole shrinkage stoping with the floor structure of electrical scraper and hopper. The sublevel drilling stage working is the second method. In addition, there is VCR method with long blast-hole mining with large holes. The ores and rock are discharged through the stage chute, and its mesh size of chute screen is 400 mm×400 mm. Before 1980, the gravity ore-drawing with wood hopper and iron

gate were used except two chutes in which the air-operated sector gates were installed. For this type of ore-drawing method the blockage was more serious and its ore-drawing efficiency is very low. In addition, the incident of ore-spillage was very frequent, and the workers were always in danger.

(2) Technical properties of VOM. From 1980s, the vibrating ore-drawing in ore passes has been tested in Jinchangyu Golden Mine, and this method gradually replaced the traditional gravity ore-drawing. The ZZ-5 type VOM have been used in the mine and its main technical properties are showed below:

Length of vibrating table-board	2500 mm
Width of vibrating table-board	1200 mm
Tilt angle of vibrating table-board	10°
Amplitude	2～3 mm
Vibrating frequency	16 Hz
Type of exciter	ZDJ5.5-6 type vibrating motor
Exciting force	19.6～39.2 kN

(3) Experience and effect. This mine gained profound technical and economical effectiveness after the VOM was introduced for ore-drawing in ore passes. Its ore-drawing efficiency was increased over four times than the former gravity ore-drawing with wood hopper, and the transporting ability was boosted by 20%～30% with the filling coefficient of ore car changing from 0.7～0.8 to more than 0.95. In addition, the working condition was greatly improved, not only the dust was kept down, but also the industrial incident decreased. Table 9.7 is the compared results for the economical effect of these two ore-drawing methods before 1991.

Table 9.7 The compared results for the economical effect of these two ore-drawing methods before 1991

Item	Vibrating ore-drawing	Wood hopper ore-drawing	Difference	Remark
One-off investment /yuan	19200×11 = 211420	1617×11×5 =88935	122485	Each of the eleven wood hoppers needs to be renewed its buckets for five times, not including the normal maintenance
Economical difference of the two ore-drawing methods caused by the different filling coefficients/yuan	8198250	10141187	−1942937	
Economical difference of the two rock-drawing methods caused by the different filling coefficients /yuan	3444470	4306869	−862399	
Total/yuan	11854140	14536991	−2682851	The average of every year is about 2236 ten thousand yuan

Note: One-off investment of VOM is 19200 yuan, but that of wood hopper is 1617 yuan.

9.4.4.2 The application of VOM in the ore passes for discharging ores with large water and silt content

During the process of ore-drawing, there are some special requirements of technology and equipment to meet the ores with large water and silt content. The traditional gravity ore-drawing could not cope with this, and the ore-drawing efficiency was influenced greatly. Sometimes, the ore pass was even discarded due to serious blockages. To these special conditions, some of the mines in China took appropriate measures for the vibrating ore-drawing of ore pass and suitably solved the problems of chute using vibrating to draw the ores with large water and silt content.

Example 1: The vibrating ore-drawing of stage ore pass in Tongguanshan Copper Mine

(1) Basic technical conditions.The No.2 ore pass in Tongguanshan Copper Mine is a stage ore pass from 5 to –55 m, and it is also the main ore-drawing ore pass underground. The height is 60 m and cross-section is 2 m×2.2 m. The original design used the sector air-operated gate for ore-drawing. It transported the ores to the ore bins of the main shaft, where the ores are carried come from the deep stages. The average ore-drawing content is 25 thousand tons per month. The ores include chalcopyrite, pyrite, magnetite, granite and the yellow earth with blends during the mining. The fragmentation of ores varies from 0.1 to 650 mm. The types are very complicated, and the water and mud contents are large as well. The ores are often changed into slurry due to many times pouring into the ore pass, and the incident of ore-spillage often takes place there. Ensuring the safety of ore-drawing workers, the operating valve of air-operated gate was always installed in the safety zone, and the distance between the safety zone and the ore pass is usually more than 10 m. Because of the inconvenience of operation, the incident of ore-spillage became more frequent and serious. And the ores were not allowed to be stocked in the ore pass. As a result, it has been in the straight-way working condition for several years so that when an ore-car dumps the ores above ore pass then other ore-car received the ores under ore pass. The ores strike the gate directly from the height of about ten meters. If these are dry ores, these will be flying of dust, while if these are water-bearing ores, it will lead to slurry spattering. Sometimes the flying ores will injure the workers. The safety condition was poor and the dust qualification rate is only 66%. Generally, because of the incident which occurred in the ore pass and the influence of other working areas to complete the tasks, the productivity of the mine was low.

(2) Technical properties of VOM. In order to solve these problems as mentioned above, a set of VOM was installed under the original air-operated gate in the mine. The installation parameters of the air-operated gate were not changed, the tilt angle of the table-board is 45°, the discharge opening is 700 mm×970 mm.

The main technical properties of VOM are shown as follows:

Length of vibrating table-board	2300 mm
Width of vibrating table-board	1300 mm
Tilt angle of vibrating table-angle	15°
Power of motor	3 kW
Fall length of ores	2300 mm
Height of brow line	2300 mm

(3) Experience and effect. In practice, Tongguanshan Copper Mine controls the height of air-operated gate at a fixed point according to the flowability of ores, and we can only operate the VOM when drawing. While not drawing the ores, the air-operated gate is closed so as to avoid ore-spillage. The combined outline diagram of ore-drawing of an air-operated gate and VOM is shown in Fig. 9.11.

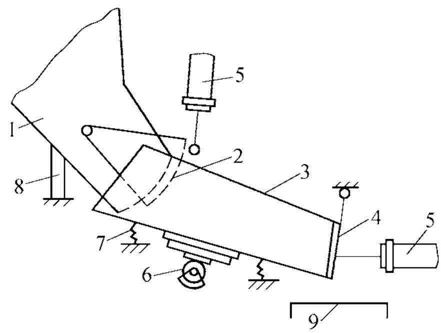

Fig.9.11 The combined outline diagram of ore-drawing of an air-operated gate and VOM
1—Hopper;2—Air-operated gate;3—VOM; 4—Air-operated flashboard;5—Cylinder;
6—Vibrating motor; 7—Support spring; 8—Stiff bracket; 9—Ore car

After the VOM of No.2 ore pass was put into service, the operation has been normal and the effectiveness has been satisfactory. With the combination of air-operated gate and VOM, there are many advantages, such as a good method of ore-controlling, a strong ore-drawing continuity and the stable ores flow. Hence the discharge capacity of the ore pass is enhanced greatly to 150 t/h, which can satisfy the requirement of ore pass with the quantity of more than 300 thousand tons ores per year. In addition, the ore-spillage incident is eliminated, working condition is improved significantly and the transportation efficiency of locomotive is also increased with the filling coefficient of ore car that is improved from 0.6 to more than 0.85. Furthermore, because the direct impact of ores to the gate and to the ore car is basically eliminated, and the opening times of the air-operated gate is reduced substantially, so the period of maintenance for the cylinder, gate and ore car are prolonged. Thus the influence of frequent maintenance during the production and the maintenance cost are decreased considerably. Now, the vibrating ore-drawing technology is used in four ground ore passes and three underground ore-drawing main chutes in the mine. They all proved a sound effectiveness.

Example 2: The vibrating ore-drawing of main chute in Liangshan Iron Mine

(1) Basic technical conditions. Liangshan Iron Mine is the major raw material base of ironstones of Xinyu Iron and Steel Company in Jiangxi province, which locates in the east of iron ores field in the middle of Jiangxi. It has sedimentary-metamorphic magnetite ore deposits caused by undersea volcano erupting during Precambrian period. The ores include banded magnetite quartzite and striped (or stria shape) chlorite magnetite piezoid rock. The hardness of original ores is from 12 to 16, and that of the oxidized ores is from 4 to 6. The density of the former varies from 3.25 to 3.3 t/m^3 while the latter is 3.2 t/m^3. The loosening coefficient of ores is 1.6 and the natural angle of repose is 42° . The water content of crude ores is 10.4% and the amount of water absorption after expansion is 15. 6%. The design scale of this mine is that the production of iron ores per year is 1. 2 million tons. This mine is divided into three mining areas, such as Hushan, Taiping and Xiafang. According to the occurrence deposit of the orebody and the topographic condition, Taiping mining area adopts both open-pit mining and underground mining, while Liangshan mining area adopts open-pit mining during prophase and changes into underground mining during anaphase. Now, the preliminary underground construction of Liangshan mining area has been completed and starts to enter the transition stage from the open-pit mining to underground mining. The two mining areas will adopt the development method of level gallery together with ore pass, and will build ten main ore passes for ore-drawing. Excepting the two ore passes which are located in east zone of 320 m underground in Liangshan mining area and at south zone of 200 m underground in Taiping mining area respectively, the bank of another eight ore passes are all exposed which both used to underground and surface (namely, the former is underground, the latter is surface) mining. The vertical heights of the ore pass are limited by their elevation; the highest is 130 m, the lowest is 30 m and the average is 91.4 m. The diameter of the chutes is 2.5 m. Some of the ore passes has its underneath segment allocated for storing ores, whose height varies from 10 to 20 m and diameter varies from 3.5 to 5 m. These ore passes were mostly built before 1970 and the tilt chutes on the bottom were built in 1970s or before. Air fingered gate with tilt drifting mouth for ore-drawing on the bottom is used in these chutes. The used ore-cars are side-unloading of 2 m^3 and 2.5 m^3 (or the types of 1 m^3 and 1.6 m^3 for transportation at sublevel underground). Because of the blockage of ore pass, there always were some ores arches, the incidents of ore-scattering and ore-spillage. This resulted in bad working condition of ore-drawing at the pit bottom, large labor force, low work efficiency and low safety; hence the development of the mine was restricted greatly.

(2) Technical properties of VOM. To resolve the problem as mentioned above, the VOMs are introduced gradually into six ore passes in this mine for ore-

drawing from 1982. Fig. 9.12 is the outline diagram of vibrating ore-drawing in the ore pass of 320 m. The used VOM belongs to LZ-12 type. Its main technical properties are showed as follows:

Length of vibrating table-board	3150 mm
Width of vibrating table-board	1800 mm
Power of motor	2×5.5 kW

(3) Experience and effect. The LZ-12 type of VOM is based on LZ-1 and LZ-2 types and is improved in structure and material, so it has no such phenomena as table-board fragmentation and welded seam cracking as experienced by those traditional machine types. In addition, it basically eliminated the problems of bolt breaking, bedplate sliding downward and the sealing becoming ineffective. Furthermore, it obviously resolves the problems of short service life, shipping underfill due to narrow trough platform and ore-spillage when discharging the oxidized ores.

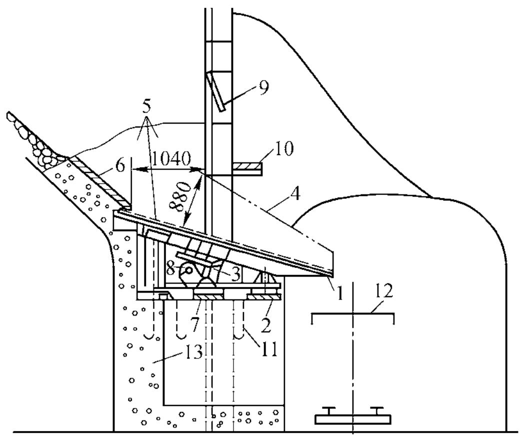

Fig. 9.12 The vibrating ore-drawing outline diagram of the ore pass in Liangshan Iron Mine at 320 m level

1—Vibrating table-board;2—Vibrating base;3—Skidproof facility;4—Side plate;5—Sidewall scaleboard; 6—Pit-bottom buried scaleboard;7—Rubber spring;8—Vibrating motor; 9—Access eye; 10—Small inspection platform;11—Foot screw; 12—Ore car; 13—Groundwork

Example 3: The Applications of VOM in the ore pass discharging the ores with a large amount of mud and water in Daye iron Mine

(1) Basic technical conditions. Daye Iron Mine in Hubei province is located in the south of Changjiang River, which is a deposit with abundant underground water. Especially, for the Jianlinshan underground mining shaft, it has a plenty of groundwater in the rainy season. Hence, the ore-drawing parts of ore passes are designed to adopt the combined structure of slide plate, cylinder and application valve.

When there is no discharging ores, the slide plate is closed so as to avoid mud and sand flowing-out, and also it can avoid the incident caused by the ores rushing out when discharging again after the ore pass was emptied. When discharging ores, the controlling switch should be operated first so that the cylinder can lift the slide plate, then start-up the vibration motor for ore-drawing. There are some advantages by using the structure, such as the sound effect, the high ore-drawing efficiency, no blockage and leakage, the low labor strength, etc. However, because of the large amount of groundwater in the rainy season, the mud sand and ore slurry in the ore pass will overflow from the slide plate, which will add to the working capacity of cleaning slurry and influence the vehicular traffic and the ore-drawing. While in the dry season, there will be much more dust in the air during the ore-drawing process, which will contaminate the environment.

(2) Technical properties of VOM. According to the shortcomings of the original VOM, this mine had developed successfully sealed VOM so as to further improve the working condition of vibrating ore-drawing in ore pass and to ensure the safety of ore-drawing with plenty of mud and water. Its main characteristics are shown as follow:

1) The discharge opening of ore pass is closed fully. There is a steel plate on the right side of the ore-drawing equipment to seal its top while there is an ore-drawing external shield welded with pillar underneath to cover the two side dampers of vibrating bedplate. Because the gap of the shield on each side of the bedplate is bigger than the nominal amplitude of vibrating motor, it can avoid ore crashing each other during the ore-drawing process. There is a sector gate at the lower end of the external shield which uses the cylinder to control the switch-on or off of gate. Hence, looking from the appearance, the VOM and the underneath discharge opening of the ore pass are closed completely. This has the advantage of fitting of the vibrating ore-drawing in the ore pass with plenty of groundwater and the fitting of dropping the ores with much dust. To ventilate air freely under this situation in the ore pass which has hanging arch, a vent-pipe is used at the side of the discharge opening, whose lower end is inserted in water-drain at the side of the laneway. While its top end is inserted in the shaft, so as to the dust can be removed by the sealing water. As a result, the flying dust upwards is reduced and the working condition is improved due to the good sealing property.

2) Renew sealing adhesive tape of open VOM. When the ore pass need to be empty, the sealing adhesive tape of the sealing equipment is installed in the underside of the vibrating bedplate and the fixed base plate, which are sealed by means of hanging bolt or thumb latch so as to avoid ore-leaking. The sealed VOM not only provides good effect in the sublevel chute, but also is helpful to the productivity in the main ore pass.

9.4.4.3 The application of VOM in the ore pass for drawing cohesive ores

The flowability of the cohesive ores is very poor and will affect the ore-drawing procedure badly. Some mine's successful examples of drawing cohesive ores by vibrating in ore passes in China are shown below:

Example 1: The vibrating ore-drawing technology of sublevel ore pass in Jinshandian Iron Mine

(1) Basic technical conditions. The percentage of fine ores in Hubei Jinshandian Iron Mine is 30%, where the fines with particle size less than 0.15 mm constitutes 40%~54%. Under the circumstance of natural temperature, the ores with high cohesiveness can pile up to an angle of 90° , especially when the moisture content of the ores is increased to 12%~15% after blasting and conveying. As a result, it is very difficult to draw the ores and has to depend on pressured wind to blow and the workers to dig up by hand to a great extent. Hence, the ore-drawing efficiency is low and labor strength is heavy.

(2) Technical properties of VOM. The mine uses the SZKJ type of VOM developed by Central South University to replace the original air-operated gate of sublevel ore pass. The SZKJ type of VOM and its installation parameters are shown in Fig. 9.13. Technical properties are listed as follows:

Technical productivity	600 t/h
Length of vibrating bedplate	2520 mm
Width of vibrating bedplate	1200 mm
Tilt angle of vibrating bedplate	15°
Amplitude	2~4 mm
Vibration frequency	17 Hz
Type of vibration motor	dual axis exciter
Power	17 kW
Exciting force	37~51 kN
Mass of VOM	1408 kg

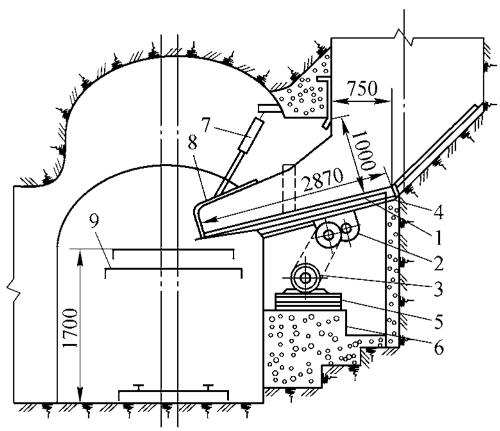

Fig. 9.13 The SZKJ type of VOM and its installation

1—Vibrating bedplate;2—Dual axis inertia exciter;3—Electrical motor;4—Rubber strip; 5—Elastic electrical bed;6—Concrete groundwork;7—Cylinder;8—Gate;9—Ore car

(3) Experience and effect. The SZKJ type of VOM utilizes the dual inertia exciter to drive and utilizes rubber belt as the sealing of the spring system, and a portion of its partial vibrating bed is buried in the ores. The purpose of this design is to take the advantage of large adjustment range of dual inertia exciter (including the exciting force, the exciting angle and the motional track of vibrating bed) to suit the condition of drawing cohesive ores so as to achieve larger productivity. Since the moisture content of cohesive ores is up to 16% and has obvious fluidity, an air-operated gate is placed near the vibrating bed to prevent the dust overflowing after stopping so as to avoid ore-spillage. This type of machine uses a concrete bed.

After installing the SZKJ type of VOM in stage ore pass, the ore-drawing condition has improved significantly. With the reasonable kinetic parameters of the VOM, there is no phenomenon of more cementation with more vibration and the incidents of congestion and arching are reduced. This machine has such advantages as high ore-drawing efficiency and good controllability. To get reasonable technical productivity, the means of adjusting exciting force and exciting angle were always applied to control the ore-drawing velocity. According to the measurement, when the force is 37 kN and the angle is 60° , it takes twenty minutes to fill up a train (consisting of six ore cars with volume of 6 m^3) , however it only takes five minutes to do it when the force is 51 kN and the angle is 45° . The technical productivity of VOM is increased from 400 to 750 t/h, which is increased from three to four times than by using air-operated fingered gate. In summary, not only does this machine have technical advantages, but also it has considerable economical benefit. Table 9.8 shows the statistical data of one stage ore pass in this mine.

Table 9.8 The comparison of vibrating ore-drawing indexes of stage ore pass in Jinshandian Iron Mine

Item	Unit	VOM	
Size of discharge opening	mm	1600×1000	1600×1000
Blockage		No	Often
Time of filling one ore-car(6 m^3)	min	0.5～2	2～3
Time of filling one train (six ore-cars)	min	5～20	15～50
Filling coefficient		0.9～1	0.7～0.8
Quantity of ore-drawing workers		1	8
Weight of equipment	t	1.4	10
Cost of equipment	yuan	3300	19500
Room excavation (not including transportation drift)	m^3	34	118
Cost of room excavation	yuan	2600	9100
Installation	man shift	34	100
Total cost	yuan	6007	28850
Difference of cost	yuan	22843	

Example 2: The vibrating ore-drawing of main ore pass in Nichun Tantalum Niobium Mine

(1) Basic technical conditions. Nichun Tantalum Niobium Mine is a hillside open-pit mine with chute system. Its yearly ores output is 80000 tons. The ores are drawn only through a major ore pass, whose depth is 290 m and diameter is 2.5 m. Formerly, a big air-operated fingered gate was used for gravity ore-drawing. The sub-structure of the ore pass is shown in Fig. 9.14. Because the content of lump ores with boulder size more than 500 mm in the open-pit mine is very large, the milled ores with size less than 2.3 mm in the broken pile always increased about 40%. In addition, because there are much secondary fine ores (the powder less than 10 mm constitutes 27.4%, where the ores less than 2.3 mm constitutes 11.6%) during the process of ore-drawing in the shaft. In addition, the rain water makes the fine ores wet into the chute, the cohesive force of ores increases considerably when the moisture content of powder is 11.9%. As a result, the blockage often takes place at the discharge opening during the ore-drawing of ore pass, and even ores arch occurs in the well, the ores cannot be stored in the ore pass. If the moisture content is up to 15%, the cohesive force of the ores will decrease greatly, so the ore-spillage is easy to happen.

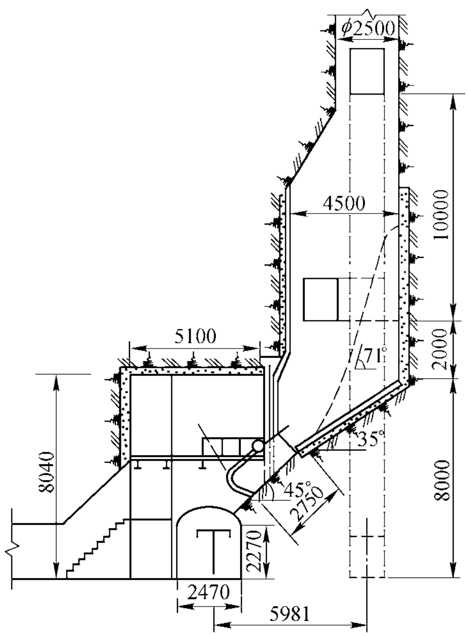

Fig. 9.14 The sub-structure of the main ore pass in Nichun Tantalum Niobium Mine

(2) Technical properties. To eliminate the above-mentioned problems, the main ore pass has been improved by Nanchang Non-ferrous Metallurgy Design and Research Institute. Because the consolidated condition of blockage is mainly caused

by cohesive milled ores, the device that destroys the ores arch by vibration is adopted, and this is shown in Fig.9.15. The formerly installed grill gate is kept down and relative position between the gate and the ore car is not changed, but a vibrating board is positioned on the baseboard. By this way, not only is the cost very low but also the adopted measure is very reliable, and even in the worst condition when the vibrating equipment does not work, it still can continue the production level by using the original gravity ore-drawing method. This ensures production going on normally.

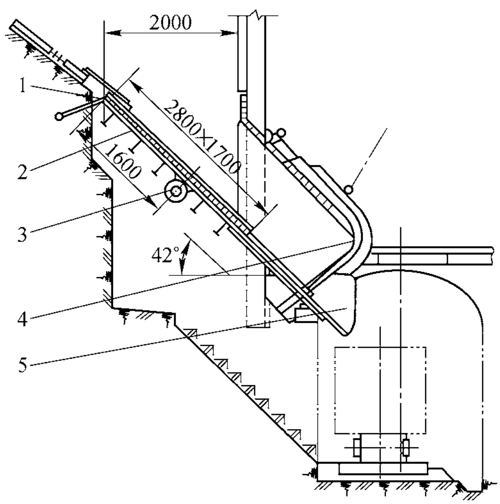

Fig. 9.15 The BZ-1 type of vibrating board for eliminating the blockage at the discharge opening of ore pass

1—Hanging axis; 2—Vibrating board; 3—Vibrating motor;4—Grill gate; 5—Active dipper tongue

(3) Experience and effect. The vibrating board is completely buried under the baseboard of the ore bin. Both the burial depth and the installation angle are large. So the loosening arrange of ores near the discharge opening is increased, and the pile line of milled ores in the bottom hole can move backwards, so as to form a larger passing cross-section of the ores flow. Increasing the angle of the installation of the vibrating board not only can destroy the milled ores arch but also can reduce the required vibrating energy and to gain a larger burial depth by small exciting force.

The vibrating board (2800 mm × 1700 mm) of vibrating equipment is constructed by steel plate of 20 mm thickness. On its top there is a pre-embedded pole for hanging hook of vibrating board, while under the bottom there is a rubber plate, whose tilt angle is 42° . The ZW-500 type of vibration motor with power of 5.5 kW is used to excite. The base of the vibration motor is welded on the vibrating board.

The ore-drawing effect has been clearly improved obviously after the vibrating equipment was used. When there are milled ores arching and the blockage at the discharge opening, these can be immediately eliminated after the exciter is switched on. Once the exciter is switched on, the ores of one car is discharged once, so the ore pass's ore-drawing has become an integral part of the vibrating ore-drawing.

9.4.4.4 The application of VOM in the main ore pass with large output

The main ore pass is the throat of the ore-drawing system of mine. The main ore pass is required a large amount of output, hence if there are troubles during ore-drawing, the ore-drawing efficiency will be influenced. If there are places of severe blockage and ore-spillage, the mine even has to stop working.

The practice of using vibrating ore-drawing technology for more than twenty years in the ore pass indicates that there are many main ore passes with large output in different mines have achieved notable technical and economical effectiveness and accumulated rich experiences by using vibration ore-drawing technology successfully, including the branch main ore pass. The following are some cases.

Example 1: The vibrating ore-drawing of the main ore pass in Shouwangfen Copper Mine

(1) Basic technical conditions. Shouwangfen Copper Mine is a big non-ferrous metal mine. It belongs to copper and iron intergrowth skarn deposit. Its thickness varies from 10 to 50 m. Its rigidity coefficient f varies from 8 to 14. The adopted mining method is sublevel-drilling open-stope mining, whose sublevel height is 60 m. The bottom structure has a hopper with electric scraper. The section of the ore pass is 2 m×2 m and its height varies from 8 to 120 m. The main shaft is a mixed shaft. All ores in the mine are hoisted through the main shaft equipped with twin-skip. The ores from each sublevel are discharged into the main ore pass by stage car-dumper through the tilt chute, and then are discharged into the measured ore bins under No. 5 sublevel. The height of the main ore pass is 220 m. The original ore-drawing gate is air-operated sector gate with double cylinder. First the metering device is put into it, and then the skip is put into it. The designed crushed ores should not be larger than 600 mm.However, because the hardness of the ores lumps are very large, consequently there are many large boulders entering into the ore pass. This brings many difficulties for ore-drawing operation and is required to deal with the lump ores by blasting many times in every shift.

(2) Technical properties. To improve working condition in the mine, the measured ore-drawing gate in the main ore pass has been remodeled and two sets of VOMs of ZZ-6 type are installed. The metering device has been withdrawn and the ores are loaded into skip by VOM directly. The technical properties of ZZ-6 type VOM are shown below:

Technical productivity	500～600 t/h
Length of vibration table-board	2650 mm
Width of vibration table-board	1500 mm

Tilt angle of vibration table-board	10°
Amplitude	2～4 mm
Vibration frequency	17 Hz
Power	13 kW
Exciter type	the single axle inertia exciter
Exciting force	30～60 kN
Mass of VOM	1860 kg

(3) Experience and effect. The depth of the main ore pass in this mine is more than 200 m and the quantity of discharged ores is about million tons per year. After the first year of installing vibrating ore-drawing technology, the ore-drawing quantity is increased by 940 thousand tons. Also these are reduced shock of ores to the skip so the skip service life is prolonged. From 1986 to 1992, the total quantity of ores drawn is about 50 million tons and the services of the VOMs have continuous. It proves that vibrating ore-drawing can meet the requirement of the ore passes with large output in this mine. In addition, this mine has accumulated valuable experiences about the VOM with large output capacity in the aspects of maintenance, structure and installation, etc.

1) Maintenance of the VOM with large output. The experience indicates that the VOM used in the ore pass with large output should be frequently maintained. The main measure is to add scaleboards on the table-board of VOM and its side plate, and to add the spring on its bottom. The VOMs of main ore pass and ore bins in this mine all have steal scaleboards with 10 mm thickness. It is linked tightly with the vibrating bed and its side plate, and should be renewed after the machine draws 400～500 thousand tons. The spring elements are fast wearing parts, and it is very difficult to renew these during the continuous mining. There are other ten springs on the VOM of the main ore pass with large output; so the service life of each spring increases two to three times than the original springs, hence the work of maintenance decreases.

2) Improve the motor base. The original base of the motor was fixed, so when the table-board moves upward during vibration process, the belt would be tightened; when the table-board moves downward, the belt will slip, jump out of the trough and break off. Consequently, the motor is easy to destroy and the belt consumption is very high. To resolve these problems as mentioned above, the base is displaced by an elastic hinge joint, so the tension force of the belt can be adjusted by dead weight of the motor. Hence, even while using only one belt the normal production of the mine can be assured which saves belts by 90% and the motor is not easy to be damaged.

3) Fix the exciter. To avoid the connecting bolt being loose and the exciter falling off, the exciter and table-board is welded together before installation.

Example 2: The vibrating ore-drawing of stope box in Meishan Iron Mine

(1) Basic technical conditions. Meishan Iron Mine is a large underground mine

in China. Its designed output in first stage is 2.5 million tons per year. The development is shafts and the mining method is sublevel caving system without pillars. At present, the stoping is in the level of −200 m and the equipment used for ore-drawing is motor scraper of 2 m^3 and air-operated carrier-loader. The transportation equipment in the roadway is the electric locomotive of 14 t capacity and the side-dump ore-car of 6 m^3 volume. The height of the present ore pass varies from 36 to 60 m, and its diameter is 2.5 m. Both the link gate and the inverse sector gate are used for ore-drawing. The underground crusher for the coarse ores is used and the approved fragmentation is 650 mm.

At present, Meishan Iron Mine is expounding. The new transportation level is at the elevation of −330 m and the stage height is 132 m. The motor scraper of 3.8～6 m^3 for ore-drawing is adopted in the stope, and the height of the stage will be increased to 15 m. There are electrical locomotives of 20 t, a bottom-dump ore-car of 10 m^3 for conveyance in the roadway, and a jaw crusher of 1500×1200 for the underground ore-crushing. The approved fragmentation is 800 mm. There are 43 stope chambers, whose height varies from 42 to 156 m and its diameter is 3 m. The original designed gate for ore-drawing is a chain gate. For the new transport level, the extracted ores will be up to one hundred million tons. If the produced ores is 2.50 million tons per year, the mining life will be forty years. The total quantity of drawn ores from each ore pass, which are all large output ore pass type, varies from 1.2 to 5.5 million tons and the average is 2.8 million tons.

(2) Technical properties. To reduce the engineering work load of underground construction and the investment of the extended shaft in Meishan Iron Mine, to quicken the constructing speed and to avoid the existing shortage of ore-drawing capacity by the chain gate at the same time, a stope chamber at the new transport level of −330 m utilize the vibrating ore-drawing technology to replace the original means of using the chain gate. This experiment was done in the No. 6 and 7 stope chamber situated at the productive transport level −200 m. The original chain gate is firstly dismantled, and then the ore-drawing room is rebuilt for installing the VOM. This is the large dual table-boards VOM designed and produced jointly by Anshan Negritude Metallurgical Mine Institute and Meishan Iron Mine, according to the characteristics, such as the big output, lump sizes, high density, considerable hardness, etc. The technical properties of VOM are listed below:

Technical productivity	2340 t/h
Length of vibration table-board	4115 mm
Width of vibration table-board	1200×2 mm
Tilt angle of vibration table-board	15°
Exciter type	ZDJ-10-6 type of vibration motor
Power	10×2 kW
Eexciting force	(37～74)×2 kN
Mass of VOM	4700 kg

To meet the ore-drawing requirement of ore pass at the new transport level of −330 m, Meishan Iron Mine also designed the larger VOM, whose technical properties are shown as follows:

Technical productivity	2600 t/h
Length of vibration table-board	4300 mm
Width of vibration table-board	2500 mm
Tilt angle of vibration table-board	15°
Exciter type	the vibrating motor
Power	10×2 kW
Exciting force	$(37\sim74)\times2$ kN
Mass of VOM	5000 kg

(3) Experience and effect. The test achieved the desired effect. During experiment for five months, the equipment worked normally and the lump and milled ores can be discharged freely. In addition, there were no incidents of blockage and ores-running and even the lump ores of 1400 mm×600 mm×700 mm could be discharged.

To test the adaptability of VOM, water was added to the lower quality ores with much powder in the ore pass so as to artificially form slurry ores, and then the ores of thirty ore-cars were discharged continuously. During the ore-drawing process, there was good slurry ores outflow with high flow velocity. When the VOM stopped, the mud water kept on outflowing with fine ores, but there were no ore-spillage. The experiment indicates that the VOM still can work regularly for those poor grade ores with high water content.

9.5 The Application of Vibrating Ore-drawing Technology in Ore Bins

There are two kinds of ore bins: the shallow bin and the deep bin. Except for the shallow bin, the bin bodies of other bins all consist of the upper discharge opening, the middle bin body and the bottom bunker. There are two types of bin body: (1) the storage bin. Its full length belongs to the same cross-section and it is only used to store ores. It is mainly used under the condition when the difference of elevation between the upper discharge point and the lower loading level is smaller; (2) the other bin is the one whose upper part is a ore pass with small cross-section and the lower part is a storage bin with large cross-section. Only the lower part is used for storing ores. It is mainly used under the condition when the difference of elevation between the upper discharge point and the lower loading level is large.

The size of the ore bins depends on its capacity. Generally, the bin body has three kinds of cross-sections, namely round, square and rectangle. The shape of the cross-section has no effect on the productivity, but it affects the type of ores'withdrawl.

When the cross-section is round and the size of bin body is built in terms of the ores flowing using the whole cross-section (not the central flowing), this bin body should be slim and high or be replaced by a bunker with large tilt angle. Only this can assure each ore layers in bin body flow downward freely at the same time. If the cross-section is square or rectangle, the speed of the ores at the four corners will be lowered and they even will be stagnant, so the effect on flowing will be poor.

With the advancement of the degree of production centralization, the ore bin has become an important element to link all production departments. If there are some incidents, a few of the departments will stop working, even all the operations in the mine will terminate. The main incident with ore bins during the working is blockage. If there is blockage at the box hole repeatedly, the intermittent ores' flow will affect the ore-drawing efficiency. In addition, the serious blockage in the bin will cause to stop production and ore-spillage incidents, which are dangerous to workers.

Through many observations and the analysis of the incidents of blockage in ore bins, it is found that the focusing on the multi-happening area of the blockage is at the underpart of the bin-body and near the box hole. The common blockage is listed as follows:

(1) Blockage.Fig. 9.16 a and Fig. 9.16 b show that the blockage generally takes place near the discharge opening, which caused by the mechanical joining between three to five lump ores. Because they tend to wedge each other tightly, the ore arch they formed is very rigid. The reason of this phenomenon is that the lump ores are too large or the cross-section size of the discharge opening is too small.

(2) Ore arch. Generally, the ore arch takes place in the following zone: 1) the discharge opening with reduced cross-section, as shown in Fig. 9.16 c; 2) at the lower part of the vertical bin, which is shown in Fig. 9.16 d; 3) the elbow of a bent bin which is shown in Fig. 9.16 e and 4) at the area when the slope of storage bin vary abruptly. The arch is caused by the compaction of the impact load during the discharging process and the dead weight of the stored ores in those bins as mentioned above. It is much tenacious than the blockage. With the passing of time, the arch will become thicker and resilient. The ore-arch is often formed by the ores in the whole section in a large range, while the blockage is only formed by the arch's external shape. Generally, the stored granular material is easy to cause the blockage, while the stored fine clayish material is easy to cause the arch. The arch at the discharge opening is easy to deal with, while the arch at the lower part of the bin body is difficult to dispose, and is very dangerous.

(3) Adherence and connecting pipe. Fig. 9.16 f shows that when the milled ores contain some water, some of these ores near the walls of the bin or at the discharge opening will be squeezed and be adhered to the walls tightly due to the compaction of the stored ores. With the phenomenon being accumulated gradually, there will form a small compressed hopper near the bunker, so the cross-section of the bunker is reduced, and this will cause the connecting pipe phenomenon.

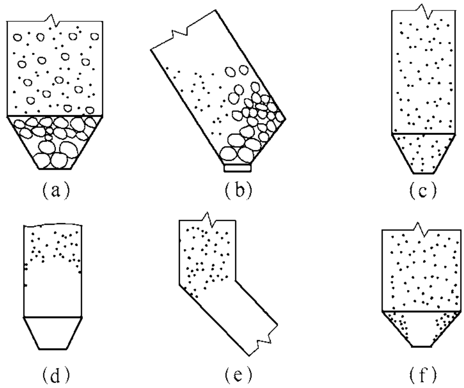

Fig. 9.16 Several kinds of blockage phenomena in ore bins
(a), (b) Blockage; (c), (d), (e) Ore arch; (f) Adherence

A little of adherence has certain advantage of protecting the bin wall, but it is difficult for the serious adherence to be dealt with. Hence, it is important to take appropriate measure to avoid the adherence when dealing with the ores with much fine, yielding materials and some water.

(4) Shed cover phenomenon. The shed cover phenomenon of storage bins often takes place after the protection of internal bin is destroyed. For example, the bin wall drops off wholly due to improper protection; the steel rail comes off due to unsuitable fixation, the reinforced steel bar protrudes outwards causing the clog effect due to the protective layer of ferroconcrete partition being worn out and so on. Sometimes, the discarded mine prop, sleeper and other lumber loaded from the upper mouth also can cause the dead shed. It is very difficult to deal with the hazards of dead shed in the bin; as a result, the production will be stopped for a whole shift or for several days. In addition, it is very dangerous to deal with; therefore, some methods should be used to avoid it.

The ore feeder at the discharge opening is one part of the feeder system of the ore bins, which has the function of adjusting and transporting mineral. The type of the ore feeder has significant effect on the ores' discharging efficiency.

For recent years, with the development of vibrating ore-drawing technology, there are many inertia-type vibrating feeders suitable to conveying the lump ores, the milled ores and the sticky ores. There is other effective equipment for eliminating the blockage, which advances the development of ore-feeding technology of ore bins.

The application of vibrating ore-drawing technology in ore bins solves the blockage effectively, enhances its packing coefficient and improves the feeding work condition. China has accumulated some rich experiences in the production practice and developed many kinds of inertia vibrating equipments in term of different technical requirements.These equipments have strong adaptability to the different types of ores and have high feeding efficiency. In addition, due to many beneficial technical conditions they have advantage in the technology over the electromagnetism vibration feeder, the swing feeder, the plate type feeder and so on; hence it is being applied more and more widely.

9.5.1 *The flowing rule of ores in ore bins*

When the ores are discharged from the discharging opening of ore bins, they flow out from the geometric body with approximate ellipsoid shape. In another words, the original space in the bin occupied by the discharged ores is an ellipsoid of revolution.

From the study of the ore-drawing process, it can be seen that the ore-drawing process can be divided into four stages, and these are the crook hopper, the filling hopper, the withdrawal hopper and the caving hopper. They are shown in Fig. 9.17.

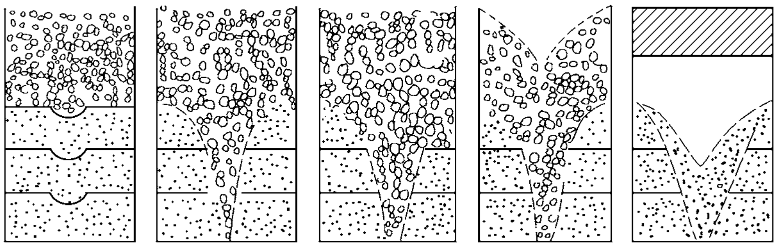

Fig. 9.17 The ore-drawing process under the cover rock

In ore-drawing process in an ore bin, the crook hopper and the caving hopper at the interface of mineral ores and waste rock become one body gradually (as shown in Fig. 9.18).

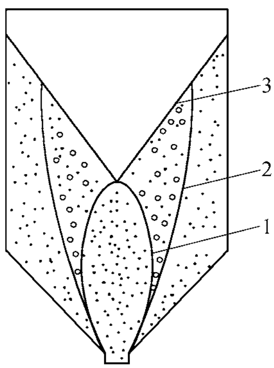

Fig. 9.18 The flowing law of the ores in ore bins

1—Withdrawal ellipsoid; 2—Loosening ellipsoid; 3—Flowing caving hopper

The ideal situation is when the granules flow with full aperture in the ore bin. Whether the ores close to the bin wall can be discharged freely or not depends on the fluidity of the ores. If the fragmentations of ores are uniform and the fluidity is good, the ores will be discharged from the top layer to the bottom layer by falling at the mobile caving hopper. Only if the tilt angle of the bottom of the bin is more than the frictional angle between the ores and the wall of the ore bin, the ores in the bin can be discharged completely.

9.5.2 *The Vibrating ore-feeding in ore bins*

The application of VOM in the ore bin is a new technical approach to eliminate the blockage at the discharge opening of the ore bins, increasing the packing coefficient of the ore bins and improving the work condition of ore-feeding.

Discharge the lump ores from ore bins

Discharging lump ores from the ore bins is similar to the ore pass, so the VOMs that used in the ore passes can be used directly to lump ore bins in many mines and to achieve the same effectiveness. For instance, the waste rock bin with a volume of 15 m^3 at the mouth of main shaft in Wugang Jinshandian Iron Mine, adopts the combined equipment of the ore pass VOM and the belt conveyer, refer to Fig. 9.19. After this mine started using the VOM for ore-feeding, the waste rock can be discharged freely and the effectiveness has been improved.

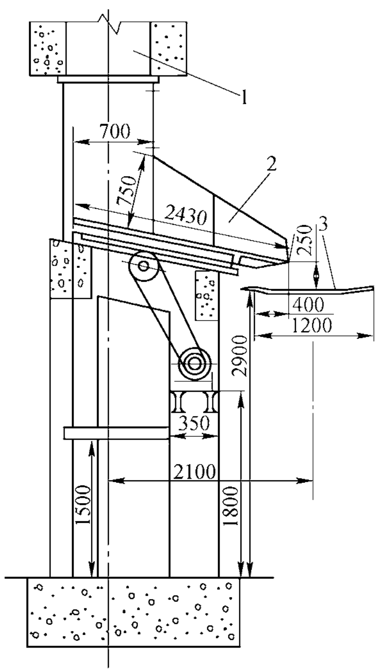

Fig. 9.19 The transportation program of VOM and tape conveyor in the waste rock bin

1—Waste rock bin; 2—VOM; 3—Tape conveyer

Discharge of the fine ores

In all mines, there are the operations of storing and discharging fine ores in the workshops of mineral dressing, sintering, coking, fireproofing and so on. However, during these operations, there are often blockages in the vibration machine with the frame for destroying arch, which is used in the powder bin. The problem becomes more serious and even affects the normal production the milled ores with much mud. Taking the ore bin with a high frame in Lingxiang Iron Mine as an example, firstly the air-operated gate is used to discharge the fine ores, because the fine ores are easy to be compacted and can form an arch. The packing coefficient of the ore bin was very low and there are often blockages at the discharge opening, furthermore, even use of explosive cannot eliminate the arch, hence the production cannot go on normally.

To resolve the problem of discharging fine ores, the vibrating feeder with the frame for destroying arch is adopted. There is a welded arch-destroying frame consisting of channel steels on the table-board. This vibrating feeder is effective equipment for discharging fine ores and provides sound technical and economical effect during its practical application. The discharging capacity of fine ores bin can reach from 500 to 900 t/h. Comparing with the non-vibrating ore-drawing, the productivity is increased by three to four times and the number of operating workers is reduced significantly. The labor force now is only one-fifth of that of the original, in addition, the labor force and the working conditions are improved obviously.

Screen and wash the crude ores by vibration

In the industrial departments of mining and mineral dressing, the crude ore bin and its ancillary equipment for feeder are important to the production. The feeder that often used in the crude ore bin is electromagnetism vibrating feeder or plate feeder. The practice proves that the lump ores with copious amount of mud has disadvantages to electromagnetism feeder. While the working condition of plate feeder will be deteriorated and the production will be influenced when it deals with the lump ores with much water, although it has large feeding capacity and can endure the shock well. The mineral dressing requires the ores be screened and deslimed before crushing, but the two equipments mentioned above, with single function of feeding ores cannot meet the requirement. To resolve this problem, the ZGSJ type of vibration feeding screener is the best choice, which is a single hyper-resonance sturdy VOM and is a typical equipment for ores sieving and desliming.

The vibration table-board is designed with two segments. The ore-accepting segment buried in loose ores on the bottom of the bin is a closed flat-plate, while the ores' discharging segment is a trapezoid grizzly, where a side plate is fixed on a bearing carrier during the installation so that it does not participate with vibration. The dual inertia exciter is placed on the bottom surface of the ore-receiving segment and is driven by the electromagnetism type adjusting asynchronous motor, which can make the table-board to vibrate in a steady state with perfect efficiency. The technical properties of the vibrating ore-feeding screener are listed in Table 9.9.

Table 9.9 The technical properties of vibrating ores-feeding screener

Item	Parameter
Technical productivity / t • h^{-1}	250
Vibration frequency / time • min^{-1}	120～1200
Amplitude / mm	0～4
Exciting force / kN	0～175
Length of vibrating table-board / mm	6750
Width of vibrating table-board / mm	1414
Tilt angle of vibrating table-board / (°)	14
Length of screen's face / mm	3600
Width of trough of trapezoid screen / mm	104～144
Height of the equipment / mm	2312
Power of motor / kW	22(The speed-regulating motor)
Mass of the vibration ores-feeding screener / kg	5294

By simplifying the bottom structure of the stope so that the ore-drawing level and transport level can be the same, not only reduces the volume of mining and cutting work, but also improves the level of mechanization and shortens the preparation cycle for ore blocks. In addition, because of the vibrating action, the volume of the ore-drawing ellipsoid is increased and the quantity of ore-drawing is controlled effectively; thus the ores fall downwards smoothly. As a result, the dilution of the ores is reduced, the recovery of ores is increased; furthermore, the continuous operation of ore-drawing, ore-carrying and ore-loading is achieved.

9.5.3 *The applied examples in ore bins*

Example 1: The ore-feeding by vibrating chute of coarse-crushing plant in Guimeishan Tungsten Mine

The coarse-crushing plant in Guimeishan Tungsten Mine adopted is a combined equipment of the plate feeder and the jaw crusher. The small and fine ores which are transported by feeder fall into the vertical hopper through the belt screen, and the lump ores also enter into it after being broken. There is a gravity chute with the tilt angle of 55° at the underside of the hopper; which transports the coarse-crushing ores to the conveying belt. Since the amount of sticky mud in ores is up to 16%～18%, often there are blockages in the chute. There will be ore-spillage in the following process if using water to wash. To resolve the problems as mentioned above, a new vibration chute is designed to replace the original gravity chute. Fig.

9.20 shows the structure of the new vibration chute. It is excited by a ZDJ3-6 type of vibration motor with the exciting force of 9.8～19.6 kN and the vibration frequency of 16 Hz. The vibration motor is installed at the top of the chute near the discharge opening, which is convenient for installation and maintenance. The ore-receiving end of the chute is supported by a concrete foundation with an elastic hinge so as to avoid the foundation from being damaged. The discharge opening of the chute is supported by a rectangle rubber block, which is positioned longitudinally. Because the ores-receiving end is far away from the vibration source, so its amplitude is small. Hence it is necessary to increase the tilt angle of the chute and increase the discharge velocity by taking advantage of the gravity so as to assure the transportation efficiency of the ore-accepting segment and the ore-drawing segment remains the same.

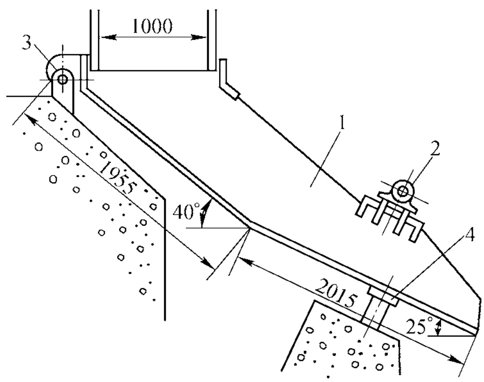

Fig. 9.20 The vibrating chute

1—Chute body; 2—Vibrating motor; 3—Elastic support; 4—Rubber block

The width of the vibrating chute is 720 mm, and the vibrating motor is placed on the chute. The exciting force is transmitted to the chute through the base and the side plates of the motor. This requires that the base have enough rigidity so as to avoid the forming of cracks due to stress concentration.

The experience indicates that the vibrating chute has simple structure and requires small energy consumption. Generally, it can feed ores smoothly with high efficiency. However, the conveying velocity will fluctuate greatly to the ores with much mud with the change of content of water.

Example 2: The vibrating ore-feeding in the ground ore bin of the main shaft in Fankou Lead Zinc Mine

The original design of the ground ore bins for the main shaft of ore-loading station in Fankou Lead Zinc Mine is to use two discharge openings. There are joined with the ore-loading measuring hopper by a tilt chute whose length is 5 m. After it was put into service, the ores were drawn successfully for a long time. However, after 1983, there were blockages and formation of arch on the bottom plate of the ore bin causing the ore-drawing chute to break. At the end of 1984, the bottom structure of the ore bin and chute was redesigned when the production is stopped due to the main shaft needing extension. The tilt angle of the bottom plate was changed to 53° ~82° and manganese steel plate was added. However, after production was resumed in 1985, the characteristics of the ores changed due to the extension of mining level. As a result, the discharged ores from the stope contained much fine ores, where the content of fine ores of less than 2 mm was even increased to 21.32%. In addition, both its water content and cohesiveness increased, which led to more serious blockage and ore-spillage incidents. Furthermore, the incidents caused the chute to break and the ore-turning machine frequently failed under the excessive pressure, which had serious effect on the normal production of the mine.

To reduce this situation as soon as possible, the mine cooperated with Central South University to redesign the ground ores bin of the main shaft, and the project of using vibration forced ore-feeding to replace the gravity ore-drawing was adopted. Taking into consideration of the need to recover the production as soon as possible, the bottom of the bin is not changed much and only several manganese steel plates at the internal side of the discharge opening are removed so as to form a platform for installing a set of fully buried fluctuating inertia VOM, as showed in Fig. 9.21. Then a decompression chamber with roof is installed at the discharge opening, the original chute is not changed. The air-operated measuring gate that is used to load the cable carrier bucket is replaced by the vibrating ore-feeder to load the carrier bucket. The main technical parameters of the vibrating ore-feeder are listed in Table 9.11.

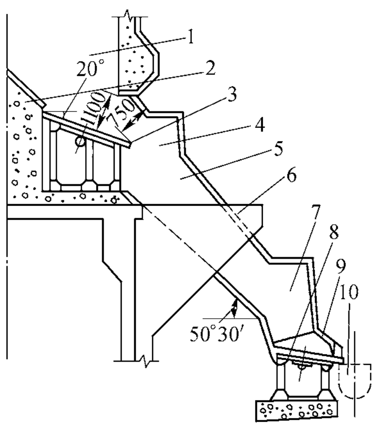

Fig. 9.21 The vibrating feeder of ground ore bin of the main shaft in Fankou Lead Iron Mine

1—Ground ore bin of skip; 2—Manganese steel plate; 3—QM-1 type VOM that is wholly buried at the bottom of the bin; 4—Upper decompression chamber; 5—Chute; 6—Buttress wall; 7—Lower decompression chamber; 8—VOM; 9—Electrical finger gate; 10—Cable carrier bucket

Table 9.10 The reconstruction cost of the chute of the main shaft's ore bin

Item	The upper vibration machine	The lower vibration machine
Vibration motor / yuan	1900×2=3800	890×2=1780
Rubber strip / yuan	450	350
Steel material / yuan	3730	2200
Electrical control system / yuan	1000	500
Electrical gate / yuan		1000×2=2000
Other materials / yuan	400	
Installation cost / yuan	1440	700
Summation / yuan	10820	7530
Total / yuan	18350	

Table 9.11 The main technical parameters of the vibrating feeder

Item	The upper vibration machine		The lower vibration machine	
	1# chute	2# chute	1# feeder	2# feeder
Tilt angle of the bed /(°)	20	22	10	12
Height of the brow line / mm	760	790	800	600
Depth of burial / mm	1630	1650	1100	1100
Exciting force / kN	22.5	22.5	21or22.5	21or22.5
The maximal exciting force / kN	31.3	31.3	29.4	29.4
Vibrating frequency / Hz	16	16	23	23
Type of motor	ZDJ7.5-6	ZDJ7.5-6	ZDJ4-4	ZDJ4-4
Width of the bed / mm	920	920	900	900
Length of the bed / mm	1820	1840	2600	2600
Starting current / A	>50	>50	37	37
Nominal current / A	9～10	9～10	9.4	9.4

Note: If the stickiness of the ores were very pronounced, the exciting force should be 22.5 kN; if the ores contain much water, it should be 21 kN.

The fully buried vibrating feeder has no side plate and the vibration source is closed in its frame. Its main functions are to loosen the ores at the bottom of the bin and to eliminate the blockage at the discharge opening in order to avoid forming a stable balance arch in this throat part. The practice indicates that after this reconstruction project was adopted, as long as the upper vibrating ore-feeder is started up, the blockage and arch can be eliminated. Even the ores with a large quantity of cohesive powder can also be discharged; it assures that the ores flowing freely at the discharge opening. However, for the ores with much water there still is the possibility of ore-spillage, but generally it is caused by the blockage at the discharge opening; it can be avoided with the elimination of the blockage at the discharge opening. In a word, after the vibrating ore-feeding was adopted in the ground ore bin of the main shaft, the production condition is sound in this mine and the ores can be discharged evenly and steadily, which fulfills the requirement of the design. From the time of the installation to the present time, there were no serious blockages and ore-spillage and the ores can be transported freely. In addition, the working condition has been safe, which assured the conformity of mining and mining processing, and the transportation capacity of cable from the ore bin to the dressing plant has been increased, which has significant effect for the mine to attain its production task.

Example 3: The vibrating ore-feeding of the ore bin with high frame in Guangxi Vinylon Mine

This factory needs to produce 300 thousand tons limestone as the raw material every year. The ores from stope are transported to the branch factories' ore bin with high frame, and then are fed to the jaw breaker of 900×600 mm by a plate feeder. Because there are blockages and arch formations at the discharge opening, the idle running of the plate feeder often takes place. In addition, there are industrial incidents due to using explosives by workers to destroy the arch which are formed frequently. Furthermore, since the plate feeder cannot function smoothly, it induces blockage in the breaker and thus damages it at the end.

To resolve the problem mentioned above, the mine and Hengdian Metallurgical Maintenance Plant have designed a vibrating feeder to replace the plate feeder. Moreover, it adopted the continuous vibrating feeder according to the following characteristics of the limestone in the ore bin: (1) its density is 1.4 t/m^3; (2) its fragmentation is large (the ores of 500 mm×700 mm take up 20%, while the ores of 400 mm×400 mm constitute 70%); (3) It contains a small amount of mud and water and (4) it is easy to develop blockage and arch at the discharge opening of the ore bin. This type of feeder is shown in Fig. 9.22 and its technical properties are listed in Table 9.12.

Table 9.12 The technical properties of the bed continuous vibrating feeder

Item	Parameter	Item	Parameter
Length of table-board/mm	3480	The vibration motor	ZDJ5.5-6
Width of table-board /mm	1110	The exciting force/kN	14.7～29.4
Tilt angle of table-board /(°)	7	The vibration frequency/Hz	16
Height of the brow line/mm	750	The amplitude/mm	1～2.2
Angle of the brow line/(°)	43	The productivity/$t \cdot h^{-1}$	100～282

When the vibrating feeder is running, the vibrating table-board derives the ores to move forward with leaping movement like jumping so as to complete feeding process. Since the distance between the ore bin and the breaker is very far and the table-board of the vibrating feeder is somewhat long, not only the frame should have enough strength and rigidity, the table-board should also be rigidly reinforced for rigidity towards the machine. Hence, some formed steel and stiffening ribs are welded under the table-board so as to provide enough integral rigidity. During the welding process, it is necessary to meet length of the welding line that is figured out according to the strength and not to use transverse welding, but to use the longitudinal intermittent welding as possible as in order to assure the table-board having no transversal fracture.

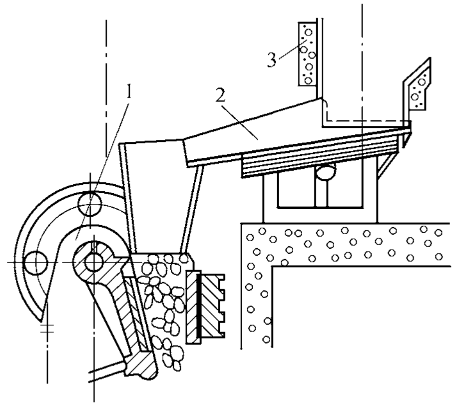

Fig. 9.22 The arrangement diagram of the continuous vibrating feeder

1—Jaw breaker; 2—Vibrating feeder; 3—Ore bin

The experience shows that the continuous vibrating feeder can replace the plate feeder completely. The new type of feeder can be installed on the base of the original plate feeder without expelling the original ore bin and its base; thus the installation working time is very small.

After the continuous vibrating feeder is brought into production, there is a good ore-drawing efficiency with little blockage. Comparing with the plate feeder, it has many advantages, such as the safe feeding condition, low energy consumption, low labor force, large ore-feeding fragmentation, and it also reduces the cost of mining and maintenance of equipments with obvious technical and economical benefit as shown in Table 9.13. Since it can feed ores smoothly, the service life of the breaker and the conveying belt are lengthened. For the ore bin which is easily blocked and whose fragmentation of ores is large, the superiority of using vibrating feeder to replace the plate feeder to feed ores into the breaker directly will be more apparent.

Table 9.13 The comparison of the technical and economical effect

Item	Vibrating feeder	Plate feeder
Number of ore-drawing workers / number	1	2~3
Power of motor / kW	5.5	7.5
Fragmentation of the ores / mm	450×500	300×400
Price of the equipment / $\times 10^4$yuan	1	5
Ratio of the maintenance cost every year /%		25
Safety condition	Safe and no incident	Unsafe, has casualty
Blockage condition	Little blockage	Much blockage
Working hours for maintenance	Few	Many
Technical productivity /t·h^{-1}	100~282	80~300

Example 4: The vibrating ore-feeding of waste rock bin in Mayang Copper Mine

The inclined shaft of Mayang Copper Mine is a secondary shaft. The waste rocks are loaded into the skip at the bottom of the inclined shaft directly by manpower, while the waste rocks which are transported from the level drift are discharged to material bin and then loaded into the skip by the vibrating feeder. There is a groundbased material bin at the shaft top and the waste rocks lifted by the skip are discharged into it. In addition, the vibrating feeder is also installed in this material bin.

To reduce the number of loading point for the inclined shaft, it is designed to cut a room for ore-drawing and install a vibrating feeder at every two levels. The section of the material bin is 2 m×2 m and the upside bin, and the lower bin are allocated on the same vertical line. The material bin at the above level is 30 m deep. It is installed with a grilled gate and through it the waste rock can enter into the material bin at the next level, whose depth is 13 m. A vibrating feeder of MZ-3 type is installed here and its technical parameters are shown in Table 9.14.

Table 9.14 The technical parameters of MZ-3 type of vibrating feeder

Item	Parameter	Item	Parameter
Length of vibrating bed / mm	2100	Burial depth / mm	890
Width of vibrating bed / mm	1150	Vibrating frequency / Hz	16
Tilt angle of vibrating table-board / (°)	15	Power of the motor / kW	7.5
Length of active hopper tongue / mm	420	Technical productivity / $t \cdot h^{-1}$	450
Width of active hopper tongue / mm	1150		

The vibrating feeder is installed in the vibration room of the stock bin, and the room is wholly constructed by concrete. In order to make it convenient to dismantle and maintain, the vibrating feeder is fixed in the room by the timber cleat. The gap between the vibrating feeder and the hopper of the stock bin is sealed off with an iron plate, and the active hopper chute extends into the skip and exceeds its rim for 200 mm. Because the tilt angle of the inclined shaft is 32° , the skip can be filled up without any aid, and the filling coefficient is more than 0.83. The average time for filling up a skip is 20 s.

The experience in this mine indicates that applying vibrating feeder in the ore bin of the inclined shaft has such advantages as given below:

(1) High efficiency. Since the lump discharge capacity of the vibrating feeder is large and with little blockage, the average time for filling up a skip of 1.2 m^3 capacity is only 20 s and the theoretical productivity reaches 450 t/h, which is 2～3 times as much as manual ore-drawing by wood hopper.

(2) Uniform loading with large filling coefficient. The cohesiveness of the waste rock in the mine is very strong, so it is difficult to discharge the ores through

an air-operated device or gate, while it is easy to cause ore-spillage incidents which are difficult to control. As a result, the loading is not uniform and the filling coefficient is low.

(3) Safe working condition.

(4) Fewer number of workers.

(5) Low production and installation cost. According to the data of this mine (in1981), the cost for producing a set of vibrating feeder of MZ-3 type is 2200 yuan, while the corresponding cost for a set of air-operated gate is 4000 yuan. The cost for installing a vibrating feeder is 500 yuan, while an air-operated gate is 2200 yuan. In addition, the energy consumption of the vibrating feeder is much lower than the air-operated gate during their utilization.

Example 5: The ore-feeding of ore bin with high frame in Lingxiang Iron Mine

Lingxiang Iron Mine is one of the ore sources for Wuhan Iron Company. Its annual output of ironstone is 800 thousand tons, where 50%～60% of the ores will be stored and transported out by using a high frame ore bin. The structure of the bin is a U trough type structure of reinforced concrete and the angle of the bin wall on two sides is 40° . Its volume is 3120 m^3 and can store 6500 t ores. The type of ores is blast-furnace enriched iron powder, whose density is less than 2.146 t/m^3. The granularity of the ores is less than 10 mm and its water content is 1%～6.62%, while the maximum mud content is up to about 20%. The maximum size of the ores that can be discharged is 750 mm×750 mm. Originally the fine ores are discharged form the air-operated gate to the railway carriages in this mine. During the discharging process, the fine ores were liable to form arches due to the compaction process. In addition, the volumetric efficiency of the ore bin was very low, and there were always blockage which were difficult to eliminate even by explosion, so the normal production would be frequency interrupted.

To eliminate the above-mentioned problems, this mine redesigned the discharging technology of fine ores and developed the vibrating feeder with an arch-destroying frame, the gravity ore-drawing through the air-operated gate was replaced by the vibrating ore-feeding.

The suspended vibrating feeder depends on the forced pulsating principle of single particle, and it vibrates through the suspended support at the bottom, so it has such functions as destroying arch directly and forcing the ores to discharge out. The suspended structure can transmit the vibration for destroying arch, which has obvious efficiency in destroying the arch formed by the fine ores with high large moisture content.

The Fig. 9.23 shows the FZC-2.3/0.9x-3 type of suspended vibrating feeder with frame for arch-eliminating. It is placed at the bottom of the ore bin. According to the practical situation of the bin, a rubber support is incorporated on the inclined wall of the bin, and some rubber elastic elements are installed, so the whole machine is suspended. Because the rubber support is placed at the middle of the machine which approaches its center of gravity, the vibration of the arch-destroying frame is balanced, without any swinging either in front or behind.

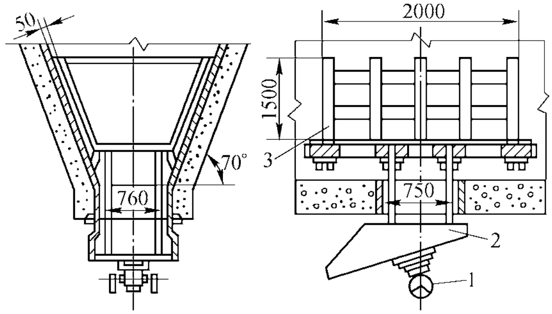

Fig. 9.23 The FZC-2.3/0.9x-3 type of suspended vibrating feeder with an arch-destroying frame

1—Vibrating motor; 2—Vibrating trough; 3—Arch-destroying frame

The arch-destroying frames are the two rows of bent frames placed parallel to the bin wall. They are located at the two sides of the bin and are 50 mm apart from it to avoid damage. The two bent frames are 2 m long and 1.5 m high. There is a rigid connection between the vibrating table-board of the vibrating feeder and the arch-destroying frame. The arch-destroying frame is situated at the position of the arch foot directly, where the arch is easy to form. When the vibrating feeder vibrates, the bent frames will immediately vibrate with it and cut the arch foot continuously along its vertical direction. In this way, the stickiness of the ores is damaged and bearing force of the arch foot is weakened (the reason is that the bent frames are installed in the vertical direction of the arch-forming), as a result, the middle part of the ores leads to an arch avalanche. At the same time, the ores are discharged out continuously with the vibration of the table-board.

After the suspended vibrating feeder was introduced in Lingxiang Iron Mine, it has achieved a sound technical and economical effect. The discharging capacity of the bin of fine ores is up to 800 t/h, and the ores are discharged smoothly. When switching on four sets of vibrating ore-feeder at one time, it only needs 2～2.5 hours to fill up a train consisting of forty-two mine cars. However, while using gravity for ore-drawing, it needs more than eight hours. So the discharging capacity is increased 3～4 times, and the production target is achieved in advance. In addition, the work force is reduced by as much as 75%～80%, and it only needs 2-3 persons to operate ten vibrating feeders, while it needs 8～10 persons each shift for using gravity with large labor strength and unsafe working condition. Moreover, the energy consumption is decreased. The power consumption of feeding 187.6 t ores by vibrating feeder is 1 kW • h. But for using gravity, it needs to operate a set of air compressor with the volume of 6 m^3 and motor power of 40 kW in sixteen discharging opening every time. Therefore, the power consumption is high, the air leak of the air-operated equipment is serious, and the maintenance is not convenient.

9.6 The Application of Vibrating Ore-drawing Technology in All Kinds of Mining Methods

To advance the mining efficiency further and to perfect various mining methods, the VOMs have been generalized and used in stope gradually. It changed the original sluggish condition of ore-drawing in the stope, enhanced its quality and output of ore-drawing. In addition, by adopting vibrating ore-drawing technology in the mining methods brings in revolution in mining method and expedite the development of stoping technology.

The experience proves that there are many distinct advantages by using vibrating ore-drawing in the mining method. The efficiency of vibrating ore-drawing in stope can reach 400～1400 t/shift, which is helpful to achieve the concentrated forced mining. The vibrating ore-drawing technology increases the distance between the levels, enlarges the amount of the ores in each room and reduce the mining cost. In addition, it can considerably advance the discharge capacity of the lump ores, reduce the blockage, lower the explosive consumption of recrushing and improve the ore-drawing condition. Comparing with the scraper, the labor productivity of the vibrating ore-drawing is increased 2～4 times, the transportation cost is reduced by half and also the vibrating ore-drawing capacity is improved greatly.

9.6.1 *The requirement in the bottom structure of stope provided by vibrating ore-drawing*

In the design of mining methods, one of the important contents is to choose a reasonable bottom structure with rational parameters for the stope. The bottom structures are those roadways and rooms laid in the stope from the floor of transport level to the floor of the undercutting level. The bottom structure of the stope and its matching haulage system have significant effect on the technical and economical efficiency of the mining methods, such as the ratio between mining and cutting, the cost and the productivity between mining and cutting, the labor productivity, the loss coefficient and the dilution ratio of the ores, the cost of stoping, the safety degree of mining operation, etc. Generally speaking, the needed labor consumption to form the bottom structure is about 15%～20% of the total labor consumption of per ton ores; the content of ores in the floor pillar takes the content of the whole block as much as 15%~20% and the ore loss factor of mining floor pillar is up to 30%~60%; the cost of ore-drawing and conveying in the stope accounts 10%~15% of the direct cost of mining, and the maximum can reach 50%. The types of bottom structure and correction of parameters have significant influence on the loss factor and dilution ratio. The incidents near the bottom structure of the stope and the corresponding ore-conveying accounts as much as 60% of the total incidents.

It has been twenty years since the vibrating ore-drawing technology was introduced in China. Now it has entered into a stage that can be used to all kinds of mining methods. The vibrating ore-drawing technology is an advanced facility that can assist ore-drawing process by virtue of its effective action of its strong vibration mechanism to loose ores, and help perfect mining methods and mining technical system. In the past, the bottom structure of vibrating ore-drawing was always designed according to the principle of gravity ore-drawing and continues to use its simplified stope bottom structure in the site. This can increase the fragmentation of the ores, reduce the volume of mining and development work, and decrease the loss and dilution of the ores. However, this process does not compare fully to the superiority for increasing the strength of mining in relation to the mining method using vibrating ore-drawing technology. The old system cannot achieve the optimum technical and economical efficiency.

9.6.2 *The main technical characteristics of the vibrating continuous ore-drawing in the stope*

It is a significant change for the conveying system by introducing vibration technology into ore-drawing in the stope, to transport the ores continuously and to apply vibrating ore-drawing to replace the gravity ore-drawing. Comparing with the traditional gravity ore-drawing, the vibrating ore-drawing technology has the following three main features: (1) it can positively increase the fluidity of the ores to facilitate effective action of vibrating ore-drawing equipment for bulk ores, (2) the discharge capacity of the lump ores is increased significantly, and (3) the ores flow is continuous, uniform and easy to be controlled.

9.6.2.1 The flowability of the ores is increased

The bulk ores has both the solid and liquid characteristics. A single ore particle has the property of solid, whereas the whole bulk has the fluidity of liquid. The internal frictional angle is the basic physical quantity to express the fluidity of the bulk ores, and it depends on the constitution and shape of the block, porosity, humidity, shear velocity of the bulk ores, etc. With the effect of the vibration wave, the internal frictional angle will change, so that the flowability of the vibrated ores will increase.

Under the influence of the vibration field, the number, magnitude and direction of interactive ores particles have randomness. Since the acting force to an ores particle is three-dimensional, and it cannot keep balance. Since most of the ores particle in the bulk loss balance, there will be a relative movement, and the static friction transformed into to kinetic friction. As a result, the shearing strength of the bulk ores is decreased while its fluidity is increased.

In addition, the vibrating energy spreads in the form of wave. With the action of the vibration wave, the bulk ores will have deformation due to shearing and pressing, which will result in a new stress field at the contact points among particles. Therefore, the shearing strength of bulk ores will decrease, and the frictional force and internal frictional angle among the ores particles will decrease, too. Similarly, the external friction angle between the ores particles and the fixed border of mine rock will decrease, thus the fluidity of the discharged ores increases effectively.

9.6.2.2 The discharge capacity of the lump ores at the discharge opening is enhanced

The ores discharge capacity describes the degree of difficulty of the loose ores pass through the discharge opening and virtually it reflects the ability of the ores pass through the discharge opening.

There are many differences between using vibrating ore-drawing in stope and other systems, because the ores in the stope are crude ores without being recrushed. The main factor affecting the ore-drawing efficiency during the process is the blockage due to the lumps. This condition can be improved by using vibrating ore-drawing technology from the following two aspects so as to increase the discharge capacity of the lumps at discharge opening.

(1) The vibrating ore-drawing is a controllable initiative ore-drawing method based on the gravity ore-drawing, and the size of the discharge opening can be increased so as to enlarge the block size and reduce blockage.

(2) Since the VOM is buried under the caved ores in the stope, the repose angle of the vibrated ores is less than the one of the gravity ore-drawing, hence, the probability of ores forming balance arch in the discharge opening is decreased significantly and therefore the discharge capacity at the discharge opening is enhanced effectively.

9.6.2.3 The ores flow is continuous, uniform and easy to control

The vibrating ore-drawing is an innovative ore-drawing method controlled by the mechanical vibration energy, so it can achieve ore-drawing with uniformity and continuity. From the analysis of the vibrating ore-drawing process, it can be seen that the jumping motion of the ores on vibration bed not only has the function of transporting ores but also can prevent and eliminate blockage. This avoids the problem of the ores flow discharged out being disrupted by the blockage and assures its continuity. Since the vibrated ores has good fluidity, uniformity and balance, the ores flow is easy to be controlled, unlike to the gravity ore-drawing with discontinuous ores flow.

A good ores fluidity not only can increase the ore-drawing efficiency but also can bring about other sound technical effect. The repose angle of vibrating ore-drawing is less than the gravity ore-drawing by as much as 4° ~8° , which provides a precondition to reduce the loss of the hopper ridge in the stope or to increase the bearing area of the ores entrance. In addition, the increase of the ores' fluidity can develop the withdrawal ellipsoid. When drawing under the rock cover, the contact surface between the rock and ores is smooth, and the quantity of ores drawn out from each discharge opening can be controlled effectively by vibration. Thus it can organize the ore-drawing according to an organized scheme so as to reduce ores loss and dilution.

The enhancement of the lump discharge capacity at the discharge opening makes it possible to increase the allowable block size, reduce the explosive consumption of recrushing, reduce the times of blockage, assure the ore-drawing condition safe and increase the stope productivity considerably.

The ores flow is continuous, uniform and controllable, which displays the prospect of the ore-drawing system underground achieving the continuous operation. It is also very significant to promote the mining mechanization, technical advancement continuity, production centralization and scientific management.

9.6.3 *The design of the bottom structure of vibrating ore-drawing in stope*

9.6.3.1 The principles of design

According to the factual geological condition and the requirement of the vibrating continuous ore-drawing, it is very important to choose a reasonable bottom structure so that the vibrating continuous operation of assembly set can provide its advantages fully. Hence, one must abide by the following principles in designing a bottom structure:

(1) During the entire ore-drawing process, the roadways of bottom structure should be stable enough so as to endure the effect of kinetic load caused by ores caving, ore-drawing and recrushing. This will assure the ores be discharged completely on schedule. Thereby, the goal of recovering resources fully can be reached

(2) The amount of the roadways in bottom structure and their arrangement must meet the requirement of ore-drawing, recrushing, conveying and ventilation. There should have sound safety condition so as to assure the volume of roadway work as little as possible, and their structure be simple, which is helpful to install and detach the assembly set.

(3) The relevant dimension of the room for installing the VOM should be compatible with the geometric parameter and burial depth of the VOM. Also it is helpful to enlarge the transmission range of vibration energy, draw the lump ores and recrush the exceptional by large boulders.

(4) With the precondition of the bottom structure with sufficient stability, the ores amount on the bottom pillar should be reduced as much as possible so as to increase the recovery of the ores block.

(5) Because the ore-drawing ability of the assembly set of vibrating continuous ore-drawing is very high, it is very important to assure that the ores feeding process is continuous.

9.6.3.2 The choice of bottom structure model

Kinds of stope bottom structure

The developing trend of stope bottom structure is changing from multi-levels to one level, from multi kinds of roadways to one level roadway. According to the shape of the ores roadways, the bottom structure can be classified into three types, namely flat-bottom type, trench type and hopper type.

The structure of the flat-bottom or trench type connects all the hoppers in longitudinal direction, makes the level of undercutting and recrushing at the same height, and rescind the mining and cutting roadways that are difficult to excavate, such as the hopper neck. The main advantages of these two types of bottom structures are listed as follows: the condition of mechanization work for undercutting is very good; the productivity of development work is high, the cost is low and the labor consumption is low; the blockage is uncommon and easy to be eliminated, in addition, the ore-drawing productivity is high; and the bottom pillar is short and have a small amount of ores. However, because the pillars of the two structures are heavily cut, causing decrease in their sturdiness, they are only suitable for the hard and competent orebody. The hopper bottom structure appeared at the earliest slope and used most widely. Its advantages and disadvantages are contrary to the two bottom structures as above-mentioned.

Determining the distance between the vibrating machines

Starting from the effective active zone of the vibration wave, the distance of the vibrating machines can be calculated from the following formula:

$$D = b + 2h / \tan\theta \tag{9.18}$$

where D is the distance of the vibrating machine, m; b is the width of the bed of the VOM, m; θ is the repose angle of vibrating ore-drawing, m; h is the effective acting height of vibration wave, m.

$$h = \frac{1}{\varepsilon}\ln\frac{a_0}{a_{\mathrm{m}}} \tag{9.19}$$

where ε is the attenuation coefficient of vibration wave in mine rocks, ε =0.8～

1.23; a_m is the vibration acceleration of discharged ores, a_m=(0.04～0.03) g, where g is the gravitational acceleration, m/s^2; and a_0 is the vibration acceleration caused by the VOM, m/s^2.

9.6.4 *The application instances of vibrating ore-drawing technology in all kinds of mining methods*

Example 1: The stage forcing caving method with vibrating ore-drawing technology at No.29 orebody in Yimen Copper Mine

(1) Mining technical conditions. The length of No.29 orebody is 350 m in north-south strike direction, its average thickness is 26 m and vertical depth is up to 445 m. It inclines towards west with the tilt angle of 65°～70°. The hanging wall rock of the orebody over the 1200 m level is the caesious dolomite, while the rock under the 1200 m level is the interbed fractured zone of purple dolomite (the hardness f is 4～6), which is unsteady and easy to collapse. The foot wall is stable caesious dolomite (f=6～8). The rock including the caesious dolomite and purple breccia, has a density of 2.78 t/m^3. The orebody is contained between the faults of F_{26}, F_{28}. Its joint fissure developed well by their induced faults, so it is easy to collapse along the bedding plane.

(2) The characteristics of the mining method. The composition elements of the mining method used in No.29 orebody are given as: the layout of stope is vertical to the strike direction, and the space between the stopes is 15 m; the length of the stope is equal to the thickness of the orebody, its height is 50 m, and the bottom pillar is 8 m; the VOMs are placed in alternative stopes and the space between two VOMs at the same side is 7.5 m; the VOMs adopted is the type of homemade ZY-1, whose installation parameters are: the brow line is 0.8 m high, the burial depth is 0.8～1.0 m, the tilt angle is 15°～20°, the length of bedplate is 3.5 m, the width is 1.2 m, the motor power is 3～7.5 kW and the theoretical productivity is 400～650 t/h.

The development work consists of a room for the vibration machine and three raise shafts. According to the stage height, the shafts are connected by crosscuts, and the walking, conveying, ventilating and residue-discharging systems can be set up.

The cross-cutting includes undercutting, excavating the hopper neck and the stage drill drift. Undercutting must make sure that the hopper neck of each vibrating machine is connected to the stope so as to avoid the damage due to explosions at the bottom structure and provide enough blasting room. Hence, two undercutting drifts are arranged in the stope direction to connect all vibration machines, and the additional two drill rooms are excavated in the vertical direction of the stope. The method of sublevel caving is used and the stope is divided into five sublevels with vertical intervals of 8 m, 10 m and 12 m. There are two sublevel drilling drifts at each sublevel. Firstly, a main line of 2.0 m×1.8 m is formed, and then it is enlarged to a drill room of 15 m×3.6 m×3.2 m according to the mining sequence and caving stage distance. The drifts outside the mining stage distance are not enlarged to become a room temporarily. The steel cords are buried there and are used for hanging electrical scraper sheaves in advance so that the ores excavated by explosion can be dealt with freely.

Undercutting, excavating hopper neck and sublevel drill drifts are two parallel working lines. Undercutting and excavating hopper neck can keep alternative parallel working, while the sublevel drill drifts are constructed from the top to bottom generally.

The shape of "T" is adopted by belling. In the area about 400 m over the brow line of VOM, the hopper wall along its two sides and frontage is excavated 2 meters. And then in the formed drifts, the hopper neck is enlarged with using short holes blasting. In this way, the lump ores can fall near the brow line and can be blasted, which eliminates the drifts for recrushing. The advantages of the method are: (1) the hopper neck can be substantially enlarged without destroying the steadiness of the bottom structure; and (2) it is helpful for recrushing.

After the sublevel drilling room is enlarged completely, one can go on stoping with the YQ-100 type of rock ripper to drill vertical sector deep hole, and the multi-rows lateral compression explosion is used to blast rock. The hole distance varies from 5.5~6 m, the burden varies from 1.2~1.5 m, the concentration coefficient varies from 3.5~5 and the pace length of ore-breaking is 15 m. According to the production condition, the whole stope can be blasted from the top layer to bottom layer gradually.

To keep the stability and to avoid the removal of the mine rock in the contiguous stopes without ground movement, it is ensured that the holes are not damaged and the workers are safe. From the beginning of the first unit to the middle of the stope there is an additional excavation of 7.5 m to the direction of contiguous stope. This process is continued until the room comes into being. The ore-drawing operation can be carried out under the instruction of an authorized ore-drawing scheme after the stope was blasted from the top layer to the bottom layer. It contains four steps. Firstly, it is the loose ore-drawing. It requires the ores be drawn from the foot wall to the hanging wall freely and the amount of ores in each VOM is 32 tons. Secondly, cut the peak. Until the amount of the ores drawn in the first step is up to 1500~2000 tons, the rocks of the stope in a certain area of the explosion become basically loose. So the second step of ore-drawing can be carried through, that is peak-cutting. According to the geological condition and the ore-drawing condition of the contiguous stope, the contact surface of the ores and the waste rock is adjusted, so all VOMs are towards the same direction being similar to the level surface, and the tilt angle between the VOM and the stope should be 45°. Thirdly, recover isometric pure ores. It requires every VOM with the ore-drawing descending line limited to 5 m. The last step of ore-drawing should be at the maximum height.

During the excavation of sublevel drilling drift, the walkway serves as ventilation inlet and a ventilator at level gallery is installed. The exhaust fan is combined with pressure fan for air circulation. The lower subsection of the lashing raise is used to lash, while the upper subsection used for return air. The ventilation of the stope consists of intake through the drifts of the bottom wall and the air return through the drifts of the upper wall. The return airway is higher than transport drift by as much as 8m, and every stope is connected with return airway by raise. In addition, a air sheet is installed as a boosting measure near the mouth of the drift at the bottom wall, so that foul air can be avoided entering into the transport drifts at the bottom wall to cause short circuiting of the wind current in the bottom wall.

The application of stage forcing caving method with vibrating ore-drawing in Yimen Copper Mine has produced good technical and economical effectiveness and achieved the goal of high speed, low powder consumption and large output. In addition, the production and management system have been improved, which is very important for completing the production task and decreasing the productive costs. Moreover, the mine has accumulated much experience in this aspect.

Example 2: The test of the stage forcing caving method with vibrating ore-drawing in Sichuan Asbestos Mine

(1) Mining technical condition. The average thickness of the orebody is 52 m, and the ores has medium hardness (f=6～8). The induced cracks are developed so generally the orebody is easy to be caved. The average tilt angle of the orebody is 80° . The surrounding rock of both the foot wall and the hanging wall is serpentinite, which is easy to cave. The border-line of the surrounding rock and the orebody is not obvious.

(2) Characteristics of the mining method. There is an ore block in the vertical trend. Its width is 20 m and the length is 40 m (that is equal to the thickness of ore block). The height of the stage is 50 m, but the height of floor pillar is 14 m. There is a haulage roadway along the direction of the orebody's length. There are two rows of symmetrical ore-drawing hoppers are arranged in the haulage road, as well as ten sets of VOM are installed (there were only five sets during testing), a conveying belt and a recrushing machine for every other ten meters. In the direction of the height of the ore block, there are two drill drifts in the strike direction for every other 10～12 meter. The YGZ-90 type of drilling rig is used to drill vertical deep fan-holes, whose depth varies from 10 to 15 m. The used explosive is ammonium powder, and the explosion method is compression blasting. The flowing direction of the ores is: VOM→conveying belt→recrushing machine→vibrating feeder→conveying belt→ore pass. The whole transporting equipment for ore-drawing is regulated by the underground control cabin and supervised by an industrial television. This achieves automatic remote control of the ore-drawing equipment and to form a

productive line of mechanization, continuity and automation.

(3) Effect.The effect of the testing is good. The productivity of the stope is up to 1000 t/shift, which is increased 9～10 times as much as before. The labor productivity of the ore-drawing workers is up to 300 t/shift that is enhanced more than 40 times as much as before.

Example 3: The test of floor pillared sublevel caving mining with vibrating ore-drawing in Guizhou Lindai Aluminum Mine

(1) Technical condition of mining. The thickness of the orebody varies from 5 to 6 m, and the tilt angle is more than 75° . The mine rock is of middle hardness (f=5～11). The stope is the experimental one from open-pit mining to underground mining, whose top is the bottom of the open-pit cavity, where some development work have been prepared according to the requirements of the horizontal sublevel filling mining.

(2) Characteristics and effect of the method. Fig. 9.24 shows the development and holing arrangement diagram of the floor pillared sublevel caving mining with stage vibrating ore-drawing in Lindai Aluminum Mine. The stoping area is arranged along the orebody's strike direction. The length of each room is 54 m and the width is 5～6 m. The height of sublevel is 7.5 m, the height of floor pillar is 7m and the space between the VOMs varies from 6 to 8 m. There is no recrushing level, and the JZ-1 type of VOM is installed in the room for vibrating machines.

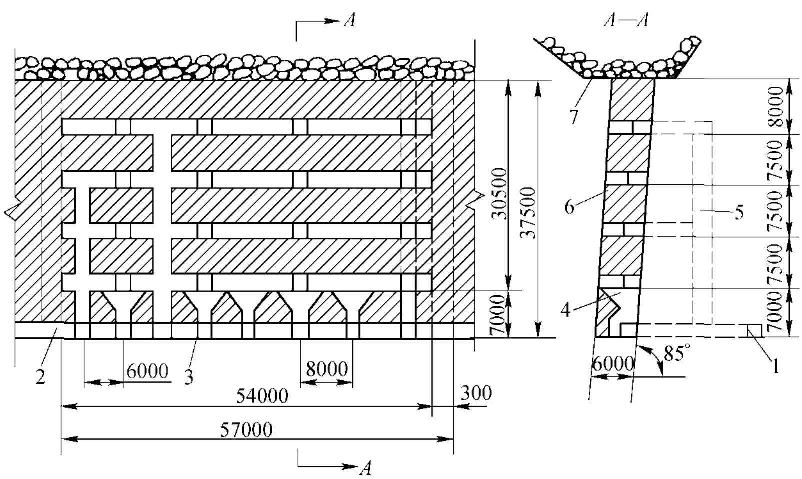

Fig. 9.24 The development and holing arrangement diagram of floor pillared sublevel caving mining with stage vibrating ore-drawing

1—Footwall haulage roadway; 2—Reef haulage roadway; 3—VOM;4—Hopper; 5—Rock raise; 6—Sublevel drill drift; 7—Flexible false roof

To ensure the quality of the ores mined, there is installed a wire netting false roof at the bottom of the open-pit so as to isolate the top waste rock. It adopts short sublevel for drilling and moderate deep fan-hole for ground breaking so as to ensure good blasting effect. There is left skin ores of 0.5 m deep and 0.3 m deep at upper wall and bottom wall separately so as to avoid dilution from the rock in the walls. The ores brought down are drawn out centrally by the VOMs at the bottom with the conveying of false roof so as to achieve continuous and uniform ore-drawing according to the plan. This is to assure that the false roof go down horizontally and isolate waste rock effectively.

Since the blasted aluminum has a few lump ores and more fine ores, there is little blockage. Hence, when adopting floor-pillared sublevel caving method to aluminum mine, it is effective of using VOM for ore-drawing in the stope and not arranging recrushing level, which has been proved by practice.

Example 4: The tested vibrating ore-drawing mining method of VCR in Fankou Lead Zinc Mine

(1) Mining technical conditions. The tested ores block is the No. 15 stope at stage of –200 m of Shiziling. The tilt angle of the orebody varies from 70° ~85° . The ores are high-grade and dense block iron pyrites and lead zinc ores, whose sulfur content is 20%, lead and zinc content is 14.8%. The caved ores has the tendency of oxidization and spontaneous combustion. The form of the orebody is very complex and there is limestone in the stone-band. Both the ores and the wall rock are stable in character (f=8~10) and their boundary is very clear, where is the strip nodular limestone in foot wall and the graniphyric limestone in hanging wall. The hanging wall of the orebody along the entire height of the stope is controlled by the fault F_3.

(2) Characteristics of the method. The tested vibrating ore-drawing mining method of VCR in Fankou Lead Zinc Mine is shown in Fig. 9.25.

The full height of the stope is 84.2 m (where two stages are mined continuously). There are two drill levels and the stope whose length is 25 m and the width is 10 m. The height of the floor pillar is 7 m, and the height of undercutting layer is 2 m. The height of the drill room is 4.2 m and the tilt angle of the wing of the hopper varies from 47° ~65° . The height of the discharge opening is 800 mm and its width is 1200 mm.

The stope adopts the vertical deep holes spherical charge of large diameter to cave the ores from upper layer to lower layer. The ores caved are loaded to ore cars by VOMs and carried away by electric locomotive after passing the bottom structure of the hopper without recrushing level.

(3) Effect. The VOM is used in the stope with VCR method and combined with the advanced drilling equipment for deep hole and blasting technology. All kinds of equipment have worked well, and obviously technical and economical efficiency are gained. The average productivity of the stope is 525 t/d, and the maximum is up to 1020 t/d, which is higher than the work efficiency of the scraper by as much as 2.5 times. The ore-drawing cost of the VOM is 0.8 yuan/t that is 25% of the cost of the scraper (that is 3.317 yuan/t) in the testing stope during

the corresponding period. The vibrating ore-drawing technology not only reinforces ore-drawing work, heightens labor productivity but also has safe and comfortable working condition. Hence scraper ore-drawing and wooden hopper ore-drawing have been proved to be very poor.

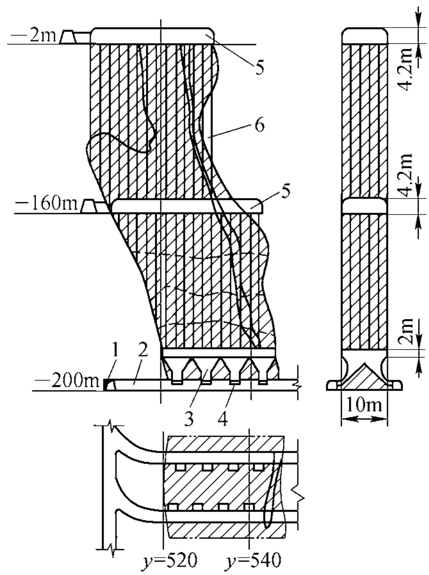

Fig. 9.25 The vibrating ore-drawing mining method of VCR in Fankou Lead Zinc Mine

1—Haulage drift; 2—Ore-drawing drift; 3—Hopper;4—VOM; 5—Drilling room; 6—Deep hole

Example 5: The sub-level open stoping with vibrating ore-drawing in Huitongshan Copper Mine

(1) Technical conditions of mining. Huitongshan Copper Mine is a skarn copper iron ore deposit. The ores bed lies in the skarn strip of the skarnization marble rocked. The orebody is more regular and hard (f =10～12), its average thickness varies from 8 m to 10 m and the tilt angle varies from 70° to 90° . The surrounding rock that is comparatively stable (f =12～14) includes the skarnization marble rock bed and the skarn.

(2) Characteristics of the method. The sub-level open stoping with vibrating ore-drawing is adopted by the mine, which is shown in Fig. 9.26. The length of the stoping area is 45～50 meters, the height of stage is 60 m and the width of the intervening pillar is 8 m. The height of the floor pillar is 11 m (that is a hopper floor pillar with recrushing level) and the sublevel height varies from 10 to 11 m.

The stoping operation begins from central trough to two sides, where the YG-80 type of rock ripper is used to drill holes in the sublevel. The row span is 3 m and two rows are caved every time. The caved ores can reach the recrushing drift after passing through the hopper, and the lump ores crushed will slide to underneath the chute mouth. The upside hopper and the underneath chute mouth are arranged alternatively. Three sets of VOM of 13 kW are installed at the underneath chute mouth, and every VOM should deal with the ores drawn by two hoppers. The correlative position of the VOM and the hopper neck is shown in Fig. 9.26b.

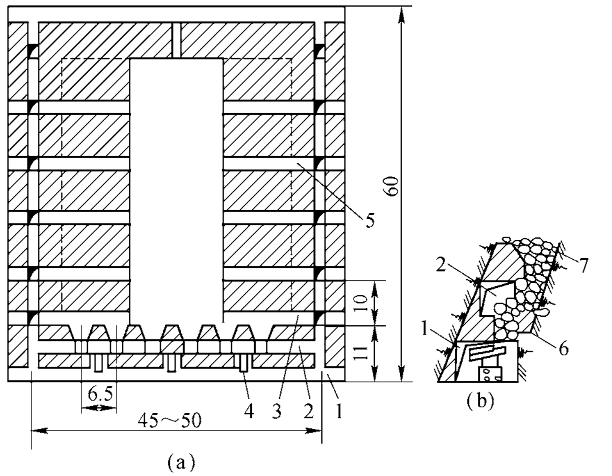

Fig. 9.26 The sub-level open stoping with vibrating ore-drawing

1—Haulage drift; 2—Recrushing drift; 3—Caving drift; 4—VOM; 5—Sublevel drift;

6—Underneath chute mouth;7—Hopper of stope

(3) Effect. Previously the mine adopted electrical scraper for conveying and the chute air-operated gate for ore-drawing. In this way there are always blockages due to the lump ores, and every shift can blast hoppers only six or seven times. After the vibrating ore-drawing technology was introduced, there are few blockages and even the lump ores of 0.8 m$\times$1.2 m can be drawn out. The carrying capacity of ore car of 0.75 m^3 has been increased from 1.13t to 1.4t, and the haulage efficiency has been enhanced by as much as 15%~18%. The original ore-drawing operation by air-operated gate needed five workers (where two workers for recrushing, three workers for ore-drawing in haulage drift). However, the vibrating ore-drawing only needs three workers (where two for recrushing and one for ore-drawing in haulage drift), so the labor productivity has increased greatly. In addition, the ore-drawing capacity of stope has been improved from the original 300~350 t/d to nowadays 350~500 t/d.

Example 6: The benching room mining with vibrating ore-drawing in Dajishan Tungsten Mine

(1) Technical condition of mining. Dajishan Tungsten Mine belongs to postmagmatic hypothermal fissure-filling tungstenic quartz vein deposit and the orebody hosts among Cambrian epizone metamorphism sandstone, slate and diorite. According to the prevailing condition, the mine adopts both the stage room mining and short-hole shrinkage mining, where the ores mined by the former mining

method is 60% of the total ores of the whole mine. Since the original bottom structure completely depended on the gravity ore-drawing, the efficiency was very low and the labor force was high. In addition, it has high energy-consumption, large maintenance cost and ore-drawing cost, etc. Hence, the vibrating ore-drawing technology is introduced in the grade room mining.

(2) Properties of the method. The following Fig. 9.27 shows the bottom structure of the benching room mining with vibrating ore-drawing of the mine.

Since the types of ore car used in the mine are the dump truck of 0.75 m^3 and the fixed type ore car of 2 m^3, the DZJ-Ⅰ type and DZJ-Ⅱ type of VOM are adopted to match them respectively. The main technical properties of the two types of VOMs are shown in Table 9.15.

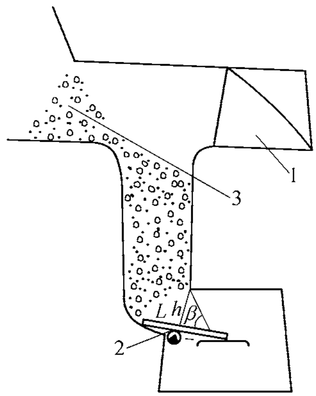

Fig. 9.27 The bottom structure of the benching room mining with vibrating ore-drawing in Dajishan Tungsten Mine

1—Recrushing drift;2—VOM;3—Ore-feeder head

Table 9.15 The main technical properties

Types of machine	DZJ-Ⅰ type	DZJ-Ⅱ type
Vibration amplitude / mm	0.9	2.2
Vibration frequency / time • min^{-1}	1400	940
Maximum exciting force / kN	10	20
Applicable exciting force / kN	7	14
Elastic element / mm	50×60×950 50×60×1200	50×60×1300 50×60×1400
Size of the bed / mm	2000×1000	2400×1350
Power / kW	1.5	3.0
Height of brow line h / mm	720	800
Angle of brow line ψ/(°)	41.5	41.5
Installation tilt angle α /(°)	15	15
Built-in length L / mm	720	800
Upward extending length in ore car b / mm	200	300

Note: The practice suggests that the parameters as above-mentioned are reasonable.

(3) Effect. This mine has an output of more than 1000 thousand tons by using vibrating ore-drawing benching room mining. Here the vibrating ore-drawing has obvious advantages against other ore-drawing methods. Table 9.16 shows the main technical economical indexes of three different ore-drawing methods.

Table 9.16 Comparison of technical economical indexes of the three ore-drawing ways

Item	Vibrating ore-drawing	Muck loader ore-drawing	Gravity ore-drawing
Productivity (the highest)/t • machine-team^{-1}	562	189	178
Productivity (the average)/t • machine-team^{-1}	219	80	108
Labor productivity/yuan • t^{-1}	54.8	26.7	18
Material cost of recrushing/yuan • t^{-1}	0.14	0.17	0.21
Power cost/yuan • t^{-1}	0.002	0.84	
Maintenance cost/yuan • t^{-1}	0.01	0.30	0.02
Salary of worker/yuan • t^{-1}	0.08	0.14	0.21
Direct cost of ore-drawing/yuan • t^{-1}	0.36	1.49	0.44

Example 7: The shrinkage stoping method with vibrating ore-drawing in Huibei Fengjiashan Copper Mine

(1) Technical conditions of mining. Fengjiashan Copper Mine belongs to contact-metasomatic deposit and the ores (f=12～18) mainly include copperish skarn and copperish magnetite. The average depth of the orebody is 3～4 m and its tilt angle is about 70° . The short hole shrinkage stoping method with gravity ore-drawing was adopted before, but the ore-drawing in the stope was very difficult because the ores are hard and with many boulders. The common hopper, platform ore-drawing and scraper lashing have been used in the past. Then these were replaced by the muck loader ore-drawing, but there were still many problems. Hence, finally the shrinkage stoping method with vibrating ore-drawing was adopted.

(2) Properties of the method. Fig. 9.28 shows the shrinkage stoping method with vibrating ore-drawing of the mine. The haulage roadways are excavated along the foot wall of the orebody and there is a hopper throat with trench bottom structure at every other 6～7 m.

(3) Effect. After the vibrating ore-drawing technology being introduced, the discharge capacity of lump ores has significantly increased and also there has been significant improvement in the working condition. Comparing with other methods, it has obvious advantages. The following Table 9.17 shows its main technical economical indexes.

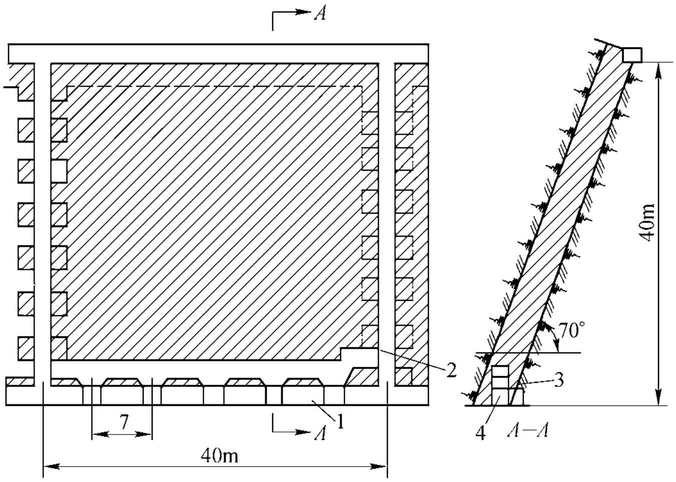

Fig. 9.28 The shrinkage stoping method with vibrating ore-drawing of Fengjiashan Copper Mine

1—Haulage roadway; 2—Raise; 3—Hopper neck and trench;4—Installation room for VOM

Table 9.17 The main technical economical indexes

Item	VC-1 type of VOM	Muck loader ore-drawing	Gravity ore-drawing hopper	
			The iron hopper	The wooden hopper
Technical productivity / t • h^{-1}	190～280	33～40	10～15	10～15
Filling coefficient of ore car	0.9～0.95	0.8～0.85	0.8	0.8
Number of blockage and arch in the hopper	little	much	Very much	Very much
Labor strength of worker	very low	high	very high	very high
Safety of ore-drawing operation	very good	good	bad	bad
Number of ore-drawing workers / person	1～2	2～3	3～4	3～4
Investment of each equipment / yuan	2350	23000	800	300
Service times of every installation/time	4		1	1
Average depreciation expense of using one time / yuan	587.5		800	300
Wooden material consumption / m^3	0	0.6	0.067	2～2.5①
Number of equipment in a stope	6	1	6	6
Power cost of every ton ores / yuan	0.0028	0.063		
Excavation volume of bottom structure / m②	64	82	7	76

① The whole consumption from installing to finishing usage; ② The standard meter converted.

Example 8: The application of vibrating ore-drawing technology in the back-filling method in Tonglushan Copper Mine

(1) Technical conditions of mining. Tonglushan Copper Mine is a skarn multi-

metal declining thick ores deposit with high grade of copper and iron. The ores include copperish magnetite, copperish marble and copperish skarn. Generally, the ores are stable and not liable to spontaneous combustion and blocking, while the surrounding rocks are not stable. In order to increase the recovery of the ores, hydraulic cut and fill method, as shown in Fig. 9.29, was adopted. In this method the filling materials are water and sand, and the height of each sublevel is about 2～2.5 meters.

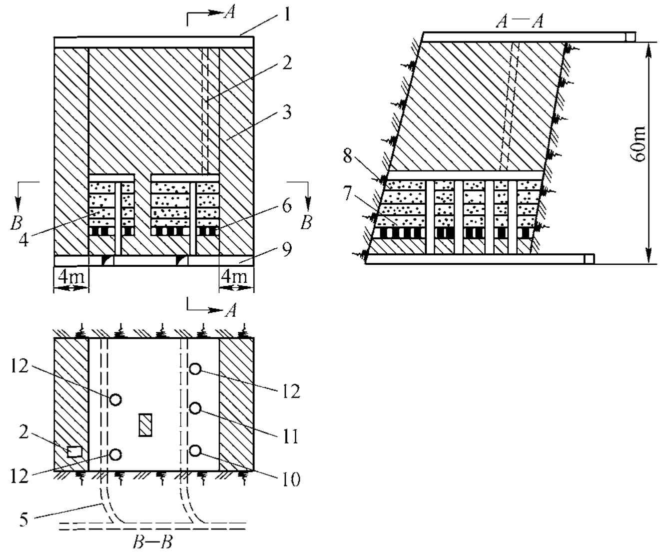

Fig. 9.29 Filled flat-back stull stope method

1—Return airway;2—Raise;3—Barrier pillar;4—Point pillar;5—Transverse gallery; 6—Artificial floor pillar;7—Cinder;8—Cementation plane;9—Horizontal gallery; 10—Haulage shaft; 11—Ore pass; 12—Filter well

The height of its stage is 60 m, and the width of the ores block is 28 m or 44 m (when it is arranged along the strike direction). The length of the ores block is equal to the depth of the ore body (it is generally 50 m and the maximum is 100 m). There is a permanent pillar of 4 m thick between two blocks of ores, and the top pillar is 3～4 m high, while the height of floor pillar is 6 m, of which 0.8 m is manual ferroconcrete pillar. In each stope, there are two fill raises (they is also used for ventilation), two or three ore passes, two or three infiltration walking wells and two sets of ZYQ-14 type of air carrier-loaders for ore-drawing are arranged. Also there are one or two pointed prop of 5 m×5 m. Both the ore passes and infiltration wells are composed of the steel tanks welded.Generally, the area of stope varies from 500 to 1500 m^2, the maximum being 1800 m^2 and the average is 700 m^2. There is an air-operated gate for ore-drawing at the lower mouth of each ore pass.

The practice indicates that using the air-operated gate for ore-drawing has many disadvantages: there are many places where compressive air leaks, and the air consumption is high, there are many blockages. The work efficiency is low, the production cost is high and many occupational incidents take place. In order to improve the conditions, the mine tested the back-filling method with vibrating ore-drawing in stope ore pass. Taking into consideration of large amount of drainage during filling the stopes, the ore pass must be emptied before cementation fill, so the bottom hole has to possess big shock resistance. In this way, not only does it avoid the vibrating bed being destroyed due to empty ore pass unloading ores, but also it assures the VOM has a reasonable built-in depth, which is helpful to seal the vibrating bed well.

(2) The effect. Tonglushan Copper Mine has adopted the vibrating ore-drawing technology fully in every stope chute. The work of driving, and permanent lining and the cost of equipment has decreased greatly, the work efficiency of ore-drawing is increased 1.5～2 times, and the safety condition of the operation also has improved considerably.

References

1. Wu Aixiang (1991). A study on the characteristic of bulk solids and the theory of dynamics in vibrating field, PhD Thesis. Central South University of Technology (in Chinese).
2. Dai Xingguo (1990). A study on the theory of Ore Pressure and Flowing Mechanism in Storage of Ore, PhD Thesis, Central South University of Technology (in Chinese).
3. Guan Shurong (1997). Railway Gravels. China Railway Press, Beijing.
4. Gu Desheng, Wang Huiying and Li Juexin (1989). Vibrating Ore-drawing Technology. Central South University of Technology Press, Changsha.
5. Wu Aixiang, Gu Desheng and Sun Yezhi, et al. (2001). Experiment and mechanism of vibration liquefaction and compacting of saturated bulk solid, *Journal of Central South University of Technology*, 1, pp. 34-39.
6. Liu Songyu, Zhu Zhiduo and Fang Lei, et al. (2001). On the standards and suggested methods of improvement against liquefaction of ground in highway engineering, *Chinese Journal of Geotechnical Engineering*, 2, pp. 135-138 (in Chinese).
7. Xie Dingyi (1988). Soils Dynamics. Xi'an Jiaotong University Press, Xi'an.
8. Luo Wenhai (1985). Stress Wave in Soils and Its Measurement. China Railway Press, Beijing.
9. Wang Zhongqi (1988). Measuring and Testing Techniques in Geotechnical Engineering. China Building Materials Industry Press, Beijing.
10. Zhang Sumin (1982). Engineering Geology Handbook. China Construction Industry Press, Beijing.
11. Wu Aixiang, Sun Yezhi and Li Jianhua (2001). Characteristic of elastic wave propagation in granular media, *Chinese Journal of Geotechnical Engineering*, 6, pp. 1121-1123 (in Chinese).
12. Gu Kouxiu (1986). Vibration Engineering. Mechanical Industry press, Beijing.
13. Qu Zhijiong (1987). Plastic Mechanics in Soils. Chengdu Science and Technology University Press, Chengdu.
14. Zhang Guofu (1983). Coal Bunker and Ore Bin in Underground Mines. Coal Industry Press, Beijing.
15. Reisner, W. (1978). Bunker. China Building Industry Press, Beijing.
16. Dai Xingguo, Gu Desheng and Wu Xianzhen (2000). The loosening and concentrating phenomena of fine materials under vibration, *Journal of Central South University of Technology*, 3, pp. 202-204.
17. Li Jianhua, Sun Yezhi and Wu Aixiang, et al. (2001). Excited response of granular ores in vibrating field, *Journal of Central South University of Technology*, 2,pp. 120-124.

18. Sun Yezhi, Wu Aixiang and Li Jianhua (2001). Wave propagation characteristics in granular media, *Mining and Metallurgical Engineering*, 2, pp. 12-14 (in Chinese).
19. Tan Luorong (2001). Discussion on mechanisms of disintegration and argillization of clay-rock, *Rock and Soils Mechanics*, 1, pp. 1-5 (in Chinese).
20. Shi Shaoqiu and Wang Lili (2001). Discussion on dynamic mechanical behaviors of cement mortar under quasi-one and one dimensional strain states, *Chinese Journal of Geotechnical Engineering*, 3, pp. 321-327.
21. Li Jianhua, Yan Ronggui and Chen Shouru, et al. (2001). Mechanism and control method of complex landslide of steep cut slope with brandy-inclined joints in high-grade highway, *Chinese Journal of Geotechnical Engineering*, 3, pp. 415-418 (in Chinese).
22. Shou Peijie (1982). Application of Seismic Wave in Engineering. Seism press, Beijing.
23. Gong， J. C. and Malvern， L. E. (1990). Passively confined tests of axial dynamic compressive strength of concrete, *Experimental Mechanics*, 3, pp. 45-49.
24. Huang Wenxi (1983). Engineering Properties of Soils. Water Conservancy and Electric Power Press, Beijing.
25. Wang Zhendong (1988). Applied Techniques of Seismic Exploration in the Shallow Layer. Geological Publishing House, Beijing.
26. Xu Youzai and Liu Xingman (1987). New Techniques of Dynamic Measurement for Pile Foundation. China Building Materials Industry Press, Beijing.
27. Zhu Chuanyun, Yu Shengchun and Yi Changping (2001). Analysis on factors effecting stress distribution in rock wall under blasting operations, *Rock and Soils Mechanics*, 1, pp. 22-25 (in Chinese).
28. Zhang Weiping (1989). Mechanical Vibration. Metallurgical Industry Press, Beijing.
29. Roy R. and Craig Jr. (1996). Structural Dynamics. People's Communication Press, Beijing.
30. Wang Duo (1995). New Development of Elastic Dynamic. Science Press, Beijing.
31. Yang Guiyuan and Zhang Shanyuan (1988). Elastic Dynamics. China Railway Press, Beijing.
32. Fakharian, K. and Evgin, E. (2000). Elasto-plastic modeling of stress-path-dependent behavior of interfaces, *International Journal for Numerical and Analytical Methods in Geomechanics*, 1, pp. 183-199.
33. Hohnborg, J. M. (1992). A Joint Element for the Nonlinear Dynamic Analysis of Arch Dams. Birkhaeuser Publishers Basel, Berlin.
34. Ma Hongwu and Wu Bin (2000). Elastic Dynamics and Its Numerical Analysis. China Building Materials Industry Press, Beijing.
35. Li Yaochen, Chen Jie and Zhou Shunhua (2001). Numerical simulation for a foundation reinforcement procedure using dynamic consolidation technique, *Rock and Soil Mechanics*, 1, pp. 6-11 (in Chinese)
36. Chow, Y. K., Yong, D. M. and Lee, S. L. (1992). Dynamic compaction analysis, *Journal of Geotechnical Engineering*, ASCE, 8, pp. 1141-1157.
37. Zuo Ming (1990). Reinforcement of Foundation by the Strong-rammer Method. China Railway Press, Beijing.

38. Deng En (1984). Geotechnical engineering analysis. Geology Press, Beijing.
39. Huang, N. C., Szewczyk, A. A. and Li, Y. C. (1990). Variational principles and finite element method for stress analysis of porous media, *International Journal of Numerical and Analytical Methods in Geomechanics*, 14, pp. 11-26.
40. Liu Changqing (1985). Experimental Methods and Testing Techniques. Coal Industry Press, Beijing.
41. Liao Hongjian, Song Li and Yang Zhen, et al. (2001). Experimental study on shear strength and yield criterion of cohesive soils under repeated loads, *Rock and Soil Mechanics*, 1, pp. 16-20 (in Chinese).
42. Dai Xiongjie (1984). Basic Tribology. Shanghai Science and Technology Press, Shanghai.
43. Jiang Pengnian (1982). Soils Constitutive Relation. Science Press, Beijing.
44. Zheng Yingren (1989). Plastic Geomechanics. China Building Materials Industry Press, Beijing.
45. Huang Yangxian (1988). Stability Analysis of Earth Slope. Tsinghua University Press, Beijing.
46. Qian Ning and Wang Zhaohui (1983). Argillaceous Silt Dynamics. Science Press, Beijing.
47. Zhong Xiaoxiong and Yuan Jianxin (1992). Shearing model of granular materials, *Rock and Soil Mechanics*, 1, pp. 1-10 (in Chinese).
48. Han Qiwei (1984). Statistical Theory of Argillaceous Silt Motion. Science Press, Beijing.
49. Liu Ke (1982). Backfill Theory. Metallurgical Industry Press, Beijing.
50. Wang Changhai (1982). Ore-drawing Technique. Metallurgical Industry Press, Beijing.
51. Liu Xingguo (1995). Ore-drawing Theory. Metallurgical Industry Press, Beijing.
52. Wen Bangchun (1989). Design and Improvement of Vibrating Sift, Vibrating Feeder and Vibrating Transporter. Chemical Industry Press, Beijing.
53. Wu Aixiang, Sun Yezhi and Li Jianhua (2001). Excited response of broken ores drawn by vibration, *Journal of Xiangtan Mining Institute*, 2, pp. 5-8 (in Chinese).
54. Hong Yukang (2000). Foundation Soil Science and Soil Mechanics. People's Communication Press, Beijing.
55. Xie Dingyi (1992). Some problems of saturated sandy soils liquefaction, *Chinese Journal of Geotechnical Engineering*, 3, pp. 90-98 (in Chinese).
56. Wu Aixiang and Gu Desheng (1992). The study on experiments and mechanism of vibration liquefaction and compaction of bulk solid, *Journal of Central-South Institute of Mining and Metallurgy*, 2, pp. 15-20 (in Chinese).
57. Wu Aixiang and Gu Desheng (1992). A research work into the propagation of vibration wave and energy dissipation in broken ore,*Journal of Central-South Institute of Mining and Metallurgy*, 3, pp. 267-272 (in Chinese).
58. Dai Xingguo and Wu Xianzhen (2000). A study on the mechanism of loosening and concentrating of fine material under vibration, *Mining and Metallurgical Engineering*, 1, pp. 12-14 (in Chinese).
59. He Guangna (1994). Some New Theories and Their Applications in Geotechincal

Engineering. Water Conservancy and Electric Power Press, Beijing.
60. Sun Yezhi (1999). A study on drag reduction by vibration of materials in pipeline, M. Eng. Thesis, South Institute of Metallurgy (in Chinese).
61. Wu Aixiang and Gu Desheng (1992). The mechanical models of shear test of bulk materials under vibration, *Journal of Central-South Institute of Mining and Metallurgy*, 2, pp. 136-141 (in Chinese).
62. Wu Aixiang and Gu Desheng (1992). An investigation on the mechanism of dynamic shear strength of broken ore, *Journal of Central-South Institute of Mining and Metallurgy*, 6, pp. 7-14 (in Chinese).
63. Wu Aixiang and Gu Desheng (1991). The research into dynamic characteristics of broken ore under vibration, *Journal of Central-South Institute of Mining and Metallurgy*, 3, pp. 242-248 (in Chinese).
64. Wu Aixiang, Gu Desheng and Dai Xinguo (1994). The influence of water content on the flow property of bulk solid, *Journal of Central-South Institute of Mining and Metallurgy*, 4, pp. 455-459 (in Chinese).
65. Wu Aixiang and Gu Desheng (1993). The characteristics of inner and boundary friction of back solid under vibration, *Journal of Central-South Institute of Mining and Metallurgy*, 4, pp. 459-463.
66. Zhao Pengnian (1995). Mechanism of Granular Media. Seism Press, Beijing.
67. Liu Chengyu (2000). Soils Mechanics. China Railway Press, Beijing.
68. Wang wenshao (1997). Dynamic Strength and Liquefaction Characteristics of Soils. China Electric Power Press, Beijing.
69. Tovey, N. K. and Krinsley, D. H. (1992). Mapping of the orientation of fine-grained mineral in soils and sediments, *Bulletin of IAEG*, 46, pp. 93-101.
70. Ringrose-Voase, A. J. (1987). A scheme for the quantitative description of soil macrostructure by image analysis, *Journal of Soil Science*, 38, pp. 343-356.
71. Smart, P. and Tovey, N. K. (1988). Theoretical aspects of intensity gradient analysis, *Scanning*, 8, pp. 75-90.
72. Hu Ruilin, Li Xiangquan and Guan Guolin (1996). State factors of clayey microstructure and the technique for quantitative analysis, *Acta Geoscientia Sinica*, 6, pp. 229-236.
73. Gutierrez, M., Ishihara, K. and Towhata, I. (1993). Model for the deformation of sands during rotation of principal stress direction, *Soils & Foundations*, 3, pp. 105-117.
74. Wang, Z. L., Dafalias, Y. F. and Shen, C. K. (1990). Bounding surface hypoplastic model for sand, *Journal of Engineering Mechanics*, ASCE, 5, pp. 983-1001.
75. Iai, S., Matsunaga, Y. and Kameoka, T. (1992). Strain space plasticity model for cyclic mobility, *Soils & Foundations*, 2, pp. 1-15.
76. Bhatia, S. K. and Soliman, A. F. (1990). Frequency distribution of void ratio of granular materials determined by an image analyzer, *Soils and Foundations*, 1, pp. 1-16.
77. Tobita, Y. (1989). Fabric tensors in constitutive equations for granular materials, *Soils and Foundations*, 4, pp. 91-104.

78. Nakata, Y., Hyodo, M. and Murata, H., et al. (1998). Flow deformation of sands subjected to principal stress rotation, *Soils & Foundations*, 2, pp. 115-128.
79. Shi Zhaoji and Wang Lanmin (1999). Dynamic Characteristics and Liquefaction Potential of Soils, and Its Hazardness Assessment. Seism Press, Beijing.
80. Japanese Geotechnical Engineering Society (1999). In-situ Compaction of Coarse Granular Materials. China Water Conservancy and Hydroelectricity Press, Hangzhou.
81. Gong Xiaonan (1998). Advanced Soil Mechanics. Zhejiang University Press, Hangzhou.
82. Hu Zhongxiong (1997). Soil Mechanics and Environmental Soil Engineering. Tongji University Press, Shanghai.
83. Guo Qingguo (1998). Engineering Characteristics and Application of Coarse Granules. Huanghe River Water Conservancy Press, ZhengZhou.
84. Oda, M. (1975). On stress-dilatancy relation of sand in simple shear, *Soils and Foundations*, 2, pp. 17-29.
85. Shamoto, Y. and Zhang, J. M. (1998). Evaluation of seismic settlement potential of saturated sandy ground based on concept of relative compression, *Soils and Foundations*, 2, pp. 57-65.
86. Zhang, J. M., Shamoto, Y. and Tokimatsu, K. (1997). Moving critical and phases-transformation stress state lines of saturated sand during undrained cyclic shear, *Soils and Foundations*, 2, pp. 51-59.
87. Pradhan, T. B. S. and Tatsuoka, F. (1989). On stress-dilatancy equations of sand subjected to cyclic loading, *Soils and Foundations*, 1, pp. 65-81.
88. Wu Shiming and Xu Youzai (1998). Status quo and development of soil dynamics, *Chinese Journal of Geotechnical Engineering*, 3, pp. 125-131 (in Chinese).
89. Ma Xiuyuan and Xu Youjian (2000). Behavior of dispersive clay and its limestabilized test in Guanlu reservoir in Qingdao, *Chinese Journal of Geotechnical Engineering*, 4, pp. 441-444 (in Chinese).
90. Zhang Jianfa (2000). Reversible and irreversible dilatancy of sand, *Chinese Journal of Geotechnical Engineering*, 1, pp. 12-17 (in Chinese).
91. Zhang, J. M., Shamoto, Y. and Tokimatsu, K. (1999). Cyclic critical stress states of sand with nonfrictional effects, *Journal of Engineering Mechanics*, 10, pp. 1106-1115.
92. Liu Sihong and Lu Tinghao (2000). Microscopic shear mechanism of granular materials in simple shear by DEM, *Chinese Journal of Geotechnical Engineering*, 5, pp. 608-611.
93. Wu Heng, Zhang Xingui and Yi Nianping, et al. (2000). Research on water-soil interaction and meso-structure of soil mass, *Chinese Journal of Geotechnical Engineering*, 2, pp. 199-204 (in Chinese).
94. Fu Lei, Wang Hongjin and Zhou Jingxing (2000). Effect of the initial rotation angle of principal stress on the dynamic properties of soil, *Chinese Journal of Geotechnical Engineering*, 4, pp. 435-440 (in Chinese).
95. Li Shihai, Xu Yihong and Zhang Junfeng, et al. (2000). Simplified mechanical model and analysis on the characteristic of saturated soils under impact load, *Chinese Journal of Geotechnical Engineering*, 3, pp. 321-325 (in Chinese).

96. Yasuhara, K., Hirao, K. and Flhyde, A. (1992). Effects of cyclic loading on undrained strength and compressibility of clay, *Soils and Foundations*, 1, pp. 100-116.
97. Li Hongnan. (1998). Structural Multidimensional Anti-seismic Theory and Design Methods. Science Press, Beijing.
98. Zhu Hehua, Chen Qingjun and Yang Linde (1997). Boundary Element Method and Its Application in Geotechnical Engineering. Tongji University Press, Shanghai.
99. Tonosaki, A., Liao, H. J. and Akaishi, M. (1995). Shear strength characteristics of Kanto Loam subjected repeated loads, *Proceedings of the School of Engineering Tokai University*, 1, pp. 181-191.
100. Lien Kwei Chien, Shan Jin Chang and Yan Nam Oh (1999). Initial shear stress effects on dynamic properties of reclaimed soil in offshore area, *Chinese Journal of Geotechnical Engineering*, 4, pp. 420-426 (in Chinese).
101. Fourney, W. L., Barker, D. B. and Holloway, D. C. (1981). Model studies of explosive well stimulation technique, *Int. J. Rock Mech.Min. Sci. & Geomech. Abstr.*, 2, pp. 113-127.
102. Perkin, R. D., Green, S. J. and Friedman, M. (1970). Uniaxial stress behavior of porphritic to nalite at strain rates to 10^3/sec, *Int. J. Rock Mech. Min. Sci.*, 7, pp. 527-535.
103. Hauser, F. E. (1966). Techniques for measuring stress-strain relations at high strain rates, *Experimental Mechanics*, 8, pp. 395-402.
104. Blanton, T. L. (1981). Effect of strain rates from 10^{-2} to 10 sec^{-1} in triaxial compression tests on three rocks, *Int. J. Rock Mech.Sci. & Geomech.Abstr.*, 1, pp. 47-62.
105. Lindholm, U. A. (1964). Some experiments with the split Hopkinson pressure bar, *J Mech Phys Solid*, 12, pp. 317-385.
106. Baker, W. E. and Yew, C. E. (1966). Strain-rate effects in the propagation of torsional plastic waves, *Journal of Applied Mechanics*, 33, pp. 117-127.
107. Nilson, R. H., Proffer, W. J. and Duff R. E. (1985). Modelling of gas-driven fractures induced by propellant combustion within a borehole, *Int. J. Rock Mech. Min. Sci. & Geomech. Abstr.*, 1, pp. 3-9.
108. Nicholas, T. (1981). Tensile testing of materials at high rate of strain, *Experimental Mechanics*, 5, pp. 177-185.
109. Cristensen, R. J., Swanson, S. R. and Brown, W. S. (1972). Split-Hopkinson bar tests on rock under confining pressure, *Experimental Mechanics*, 11, pp. 508-513.
110. Lewis, J. L. and Campbell, J. D. (1972). The development and use of a torsional Hopkinson-bar apparatus, *Experimental Mechanics*, 11, pp. 520-524.
111. Kumar, A. (1968). The effect of stress rate and temperature on the strength of basalt and granite, *Geophysics*, 3, pp. 501-510.
112. Bogy, D. B. and Gracewski, S. M. (1983). Reflection coefficient for plane waves in a fluid incident on a layered elastic half-space, *Journal of Applied Mechanics*, 50, pp. 405-414.
113. Clay, R. B., Cook, M. A. and Keyes, R. T. (1962). Shock waves in solids and

rock mechanics, *Mining Research*, 2, pp. 681-712.

114. Zhou, D. H. and Miller, H. D. S. (1991). Simulation of microseismic emission during rock failure, *Int. J. Rock Mech. Min. Sci. & Geomech. Abstr.*, 4, pp. 275-284.
115. Grady, D. E. and Kipp, M. E. (1979). The micromechanics of impact fracture of rock, *Int. J. Rock Mech.Min. Sci. & Geomech. Abstr.*, 16, pp. 293-302.
116. Goldsmith, W., Sackman, J. L. and Ewert, C. (1976). Static and dynamic fracture strength of Barre granite, *Int. J. Rock Mech. Min. Sci. & Geomech. Abstr.*, 13, pp. 303-309.
117. Lankfork, J. (1981). The role of tensile microfracture in the strain rate dependence of compressive strength of fine-grained limestone-analogy with strong ceramics, *Int. J. Rock Mech. Min. Sci. & Geomech. Abstr.*, 18, pp. 173-175.
118. Campbell, J. D. and Dowling, A. R. (1970). The behaviour of materials subjected to dynamic incremental shear loading, *J. Mch. Phys. Solid*, 18, pp. 43-49.
119. Goldsmith, W. and Wu, W. Z. (1981). Response of rock to impact loading by bars with pointed ends, *Rock Mechanics*, 13, pp. 157-184.
120. Rogers,C. O., Pang, S. S. and Kumano, A., et al. (1986). Response of dry- and liquid-filled porous rocks to static and dynamic loading by variously-shaped projectiles, *Rock Mechanics and Rock Engineering*, 19, pp. 235-260.
121. Kabo, M., Goldsmith, W. and Sackman, J. L. (1977). Impact and comminution processes in soft and hard rock, *Rock Mechanics*, 9, pp. 213-243.
122. Shockey, D. A., Curran, D. R. and Seaman, L., et al. (1974). Fragmentation of rock under dynamic loads, *Int. J. Rock Mech. Min. Sci. & Geomech. Abstr.*, 11, pp. 303-317.
123. Kumano, A. and Goldsmith, W. (1982). Projectile impact on soft, porous rock, *Rock Mechanics*, 15, pp. 113-132.
124. Kumano, A. and Goldsmith, W. (1982). An analytical and experimental investigation of the effect of impact on coarse granular rocks, *Rock Mechanics*, 15, pp. 67-97.
125. Zhou Guangquan and Liu Xiaomin (1996). Viscoelasticity Theory. China Science and Technology University Press, Hefei.
126. Guo Ziqiang (1982), Wave in Solids. Seism Press, Beijing.
127. Wu Aixiang, Sun Yezhi and Li Jianhua (2001). Wave propagation and mechanism of aided flow by vibration in granular flow field, *Chinese Journal of Nonferrous Metals*, 4, pp. 661-665.
128. Xia Tangdai, Zhang Zhongmiao and Wu Shiming (1996). Numerical simulation of Raileigh surface wave principle (in Chinese), *Journal of Zhejiang University*, 3, pp. 277-285(in Chinese).
129. Vardoulakis, L. and Vrettos, C. (1988). Dispersion law of Rayleigh-type waves in a compressible Gibson half-space, *Int. J. Numer. Methods Geomech.*, 12, pp. 639-655(in Chinese).
130. Xia Tangdai, Cai Yuanqiang and Chen Yunmin (1996). Study on the computation of dynamic response utilizing the Reileigh wave's characteristics, *Chinese Journal of Geotechnical Engineering*, 3, pp. 28-34 (in Chinese).

131. Chen Yunmin and Wu Shiming (1991). Solution of characteristic equation of Rayleigh wave in laminated foundation, *Journal of Zhejiang University*, 1, pp. 40-52 (in Chinese).
132. Xia Tangdai, Cai Yuanqiang and Wu Shiming, et al. (1996). Dispersive characteristics of Rayleigh wave in the anisotropic layered foundation, *Journal of Vibration Engineering*, 2, pp. 191-197 (in Chinese).
133. Vrettos, C. (1990). In-plane vibration of soil deposits with variable shear modulus: I. Surface wave, *Int. J. Numer. Methods Geomech.*, 14, pp. 209-222.
134. Hu Jiafu (1999). A study on the interpretation procedure of Rayleigh wave in engineering prospecting, *Chinese Journal of Geotechnical Engineering*, 5, pp. 599-602 (in Chinese).
135. Xia Tangdai, Zhang Zhongmiao and Wu Shiming (1996). A study on the computation of dynamic response utilizing the Love wave's characteristics, *Journal of Vibration Engineering*, 3, pp. 281-285 (in Chinese).
136. Wu Shiming (1997). Wave in Soils. Science Press, Beijing.
137. Shen Kuo (1996). Meng Xi Bi Tan (Song Dynasty, in Chinese). Tuanjie Press, Beijing.
138. Liu Huishan, Xu Fengping and Li Pengcheng (1997). Influence of large displacement of ground caused by liquefaction on engineering and its current study, *Anti-seism of Engineering*, 2, pp. 21-26 (in Chinese).
139. Juang, C. H., Rosowsky, D. V. and Tang, W. H. (1999). Reliability-based method for assessing liquefaction potential of soils, *Journal of Geotechnical and Geoenvironmental Engineering*, 8, pp. 684-689.
140. Sasaki, Y., Towhata, I. and Tokida,K., et al. (1992). Mechanism of permanent displacement of ground caused by seismic liquefaction, *Soils and Foundations*, 3, pp. 79-96.
141. Low, B. K. and Tang, W. H. (1997). Efficient reliability evaluation using spreadsheet, *Journal of Engineering Mechanics*, 7, pp. 749-752.
142. Youd, T. L. and Perkins, D. M. (1987). Mapping of liquefaction severity index, *Geotech Engrg*, ASCE, 11, pp. 1347-1391.
143. Seed, H. B., Tokimatsu, K. and Harder, L. F., et al. (1985). Influence of SPT procedures in soil liquefaction resistance evaluations, *Journal of Geotechnical Engineering*, 12, pp. 1425-1445.
144. Bartleit, S. F. and Yould, T. L. (1995). Empirical prediction of liquefaction-induced later spread, *Journal of Geotechnical Engineering*, ASCE, 4, pp. 316-329.
145. Anthony, T. C. (1994). Seismic liquefaction potential assessed by neural networks, *Journal of Geotechnical Engineering*, 9, pp. 1467-1480.
146. Halder, A. and Tang, W. H. (1979). Probabilistic evaluation of liquefaction potential, *Journal of Geotechnical Engineering*, 2, pp. 145-165.
147. Wang Mingwu and Luo Guoyu (1999). Application of optimization on the assessment of sand liquefaction potential, *Chinese Journal of Geotechnical Engineering*, 6, pp. 704-706 (in Chinese).
148. Tokimatsu, K. and Yoshimi, Y. (1883). Empirical correlation of soil liquefaction based on SPT N-value and fines content, *Soils and Foundations*, 4, pp. 56-74.

149. Vaid, Y. P. and Thomas, J. (1995) Liquefaction and postliquefaction behavior of sand, *Journal of Geotechnical Engineering*, ASCE, 2, pp. 163-173.
150. Yoshimine, M. and Ishihara, K. (1998). Flow potential of sand during liquefaction, *Soils and Foundations*, 3, pp. 189-198.
151. Meneses, J., Ishihara K. and Towhata, I. (1998). Effects of superimposing cyclic shear stress on the undrained behavior of saturated sand under monotonic loading, *Soils and Foundation*, 4, pp. 115-127.
152. Towhata, I., Sasadi, Y. and Tokida K., et al. (1992). Prediction of permanent displacement of liquefaction ground by means of minimum energy principle, *Soils and Foundations*, 3, pp. 97-116.
153. Yasuda, S., Nagase, H., and Kiku H, et al. (1992). The mechanism and a simplified procedure of the analysis of permanent ground displacement due to liquefaction, *Soils and Foundations*, 1, pp. 149-160.
154. Kuwano, J. and Ishihara, K. (1988). Analysis of permanent deformation of earth dams due to earthquakes, *Soils and Foundations*, 1, pp. 41-55.
155. Orense, P. R. and Towhata, I. (1998). Three dimension analysis on lateral displacement of liquefied subsoil, *Soils and Foundations*, 4, pp. 1-15.
156. Wang Wenshao (1980). The strength, liquefaction and failure of saturated sand under repeated loading, *Journal of Water Conservancy*, 1, pp. 14-27 (in Chinese).
157. Wang Wenshao (1981). A study on saturated sand under repeated loading, *Chinese Journal of Geotechnical Engineering*, 3, pp. 61-65 (in Chinese).
158. Yoshimi, Y., Tokimatsu, K., Kaneko, O. and Makihora, Y. (1984). Undrained cyclic shear strength of a dense Niigata sand, *Soils and Foundations*, 4, pp. 131-145.
159. Gastro, G. and Poulos, S. J. (1977). Factors affecting liquefaction and cyclic mobility, *Proc. ASCE J. GED*, 103, pp. 501-516.
160. Poulos, S. J., Castro, G. and France, J. W. (1985). Liquefaction evaluation procedure, *J. Ge. ASCE*, 6, pp. 772-792.
161. Wang Wenshao (1981). The mechanism of soils liquefaction, *Journal of Water Conservancy*, 5, pp. 22-34 (in Chinese).
162. Kramer, S. L. and Seed, H. B. (1988). Initiation of soil liquefaction under static loading, *J. Ge. ASCE*, 4, pp. 412-430.
163. Alarcon-Cuzman, A., Leonards, G. A. and Chameau, J. L. (1988). Undrained nomotonic and cyclic strength of sands, *J. Ge. ASCE*, 10, pp. 1089-1109.
164. Castro, G., Poulos, S. J. and Leathers, F. D. (1985). Re-examination of slide of lower San Fernando dam, *J. Ge. ASCE*, 9, pp. 1093-1107.
165. Richardson, A. M. and Whitman, R. V. (1963). Effect of Strain-Rate upon Undrained shear resistance of a saturated remoulded fat clay, *Geotechnique*, 4, pp. 310-324.
166. Wang Wenshao (1980). Some findings of soil liquefaction characteristics, *Chinese Journal of Geotechnical Engineering*, 3, pp. 55-63 (in Chinese).
167. Wang Wenshao, Qin Wenqin and He Changrong (1987). The shear strength and liquefaction characteristics of pulverized fuel ash, *Chinese Journal of Geotechnical Engineering*, 1, pp. 109-112 (in Chinese).

168. Wang Mingwu and Luo Guoyu (2000). Application of reliability analysis for the assessment of sand liquefaction potential, *Chinese Journal of Geotechnical Engineering*, 5, pp. 542-544 (in Chinese).
169. Gong Quanmei, Zhou Shunhua and Fang Zhihua (2000). Analysis on differentiation of two specifications in the assessment of soil liquefaction, *Rock and Soil Mechanics*, 2, pp. 141-144.
170. Gao Yufeng, Liu Hanlong and Zhu Wei (2000). Advances in large ground displacement induced by seismic liquefaction, *Rock and Soil Mechanics*, 3, pp. 294-297 (in Chinese).
171. Zhang Jianmin, Tokimatsu Kohji and Taya Yuhji (1999). Effect of water absorption in shear of post-liquefaction sand, *Chinese Journal of Geotechnical Engineering*, 4, pp. 398-402 (in Chinese).
172. Shen Zhujiang (1999). A granular medium model for liquefaction analysis of sand, *Chinese Journal of Geotechnical Engineering*, 6, pp. 742-748.
173. Sun Gengsheng and Zheng Datong (1987). Yielding soil Foundation and underground engineering. China Building Industry Press, Beijing.
174. Li Xiangwei and Li Xiangyue (1989). The problem of coupling wave in the saturated porous media, *Applied Mathematics and Mechanics*., 4, pp. 309-714 (in Chinese).
175. Men Fulu (1981). The problem of wave propagation in the saturated porous media, *Geophysics Journal*, 1, pp. 65-76 (in Chinese).
176. Zhang Dean (1989). Influence of natural anisotropy on the dynamic shear modulus. *Chinese Journal of Geotechnical Engineering*, 2, pp. 75-81 (in Chinese).
177. Wu Shiming and Chen Longzhu(1989). Poisson's ratio of saturated soil and influence of gas content on it, *Journal of Water Conservancy*, 1, pp. 37-43 (in Chinese).
178. Mei, C. C and Foda, M. A. (1981). Wave induced responses in a fluid poroelastic solid with a free surface, *Geophy. J. Roy. Astr. Soc.*, 66, pp. 597-631.
179. Philippacopoulos, A. J. (1987). Waves in a partially saturated layered halfspace: analytic formulation, *Bull. Seism. Soc. Am.*, 77, pp. 1838-1853.
180. Plona, J. (1980). Observation of a second bulk compressional wave in a porous medium at ultrasonic frequency, *Appl. Phys. Lett.*, 36, pp. 259-261.
181. Philippacopoulos, A. J. (1988). Lamb's problem for fluid-saturated porous media, *Bull. Seism. Soc. Am.*, 2, pp. 908-923.
182. Stoll, R. D. (1979).Experimental studies of attenuation in sediments, *J. Acoust. Soc. Am.*, 66, pp. 1152-1160.
183. Stoll, R. D. and Kan, T. K. (1981). Reflection of acoustic waves at a water-sediment interface, *J. Acoust. Soc. Am.*, 70, pp. 149-156.
184. Seed, H. B. and Chan, C. K. (1966). Clay strength under earthquake loading conditions, *Pro. ASCE J. SMFD*, 92, pp. 53-78.
185. Anderson, K. H, Pool, J. H. and Brown, S. F, et al. (1980). Cyclic and static laboratory tests on drammen clay, *Proc. ASCE J. Ged*., 106, pp. 499-529.
186. Yang Jun, Wu Shiming and Cai Yuanqiang (1996). Elastic wave propagation in saturated soil, *Journal of Vibration Engineering*, 2, pp. 128-137 (in Chinese).
187. Chu Guozhen (1994). Sound wave in saturated porous media. *Applied Acoustics*, 4, pp. 1-6 (in Chinese).

188. Abo-Zena, A.(1979). Dispersion function computation for unlimited frequency values, *Geophys. J. R. Astr. Soc.*, 58, pp. 91-105.
189. Bardet, J. P. (1992). A viscoelastic model for dynamic behavior of saturated poroelastic soils, *Transactions of the ASME, J. Appl. Mech.*, 59, pp. 128-135.
190. Berrman, J. G. (1980). Confirmation of theory, *Appl. Phys. Lett.*, 37, pp.382-384.
191. Biot, M. A. (1956). The theory of propagation of elastic waves in a fluid-saturated porous solid: I. Low-frequency range, *J.Acoust Soc. Am.*, 28, pp.168-178.
192. Chen, J. (1994). Time domain fundamental solution to Biot's complete equations of dynamic poroelasticity, *Int. J. Solid Stract.* , 31, pp. 169-202.
193. Gatmiri, B. (1992). Response of cross-anisotropic seabed to ocean waves, *Journal of Geotechnical Engineering*, ASCE, 9, pp.1295-1314.
194. Chow, Y. K. and Smith I. M. (1981). Static and periodic infinite solid elements, *Int. J. for Num. Methods in Engrg.*, 4, pp. 501-526.
195. Vrettos, C. (1990). Dispersive SH-surface waves in soil deposits of variable shear modulus, *Soil Dynamics and Earthquake Engineering*, 5, pp. 252-264.
196. Waas, G., Riggs, H. R. and Werkle, H. (1985). Displacement solution for dynamic loads in trasversely-isotropic stratified media, *Earthquake Engineering and structural Dynamics*, 13, pp. 173-193.
197. Zienkiewicz, O. C, Chang, C. T and Bettess, P. (1980). Drained, undrained, consolidating and dynamic behavior assumptions in soils, *Geotechnique*, 30, pp. 385-395.
198. Zienkiewicz, O. C. (1984) Dynamic behavior of saturated porous media: the generalized Biot's formulation and numerical solution, *Int. J. Numer. Meth. Geomech.*, 8, pp. 71-96.
199. Prevost, J. H. (1985). Wave propagation in fluid-saturated porous media: an efficient finite element procedure, *Soils Dynamics and Earthquake Engineering*, 4, pp. 183-201.
200. Xu Zhongda (1997).Seismic Wave Theory. Tongji University Press, Shanghai.
201. Lervin, F. K. (1980). Seismic velocities in transversely media, *Geophysics*, 1, pp. 3-17.
202. Rommel, B. E. (1993). Approximate stacking velocities in a weakly transversely isotropic layer, *Can. J. Expl. Geophys.*, 1, pp. 98-108.
203. Thomsen, L. (1986). Weak elastic anisotropy, *Geophysics*, 10, pp. 1954-1966.
204. Lervin, F. K. (1979). Seismic velocities in transversely isotropic media, *Geophysics*, 5, pp. 818-936.
205. Nickell, R. E. (1971). On the stability of approximation operators in problems of structural dynamics, *Int. J. Solids Struct.*, 7, pp. 301-319.
206. Beltzer, A. I. (1988). Dispersion of seismic waves by a causual approach, *Pure Appl. Geophys.*, 5, pp. 896-917.
207. Wilson, E. L.,Farhoomand, I. and Bathe,K. J. (1973). Nonlinear dynamic analysis of complex structures, *Earthquake Engr. Str. Dyn.*, 1, pp. 241-252
208. Daley, P. F. and Hron, F. (1977). Reflection and transmission coefficients for transversely isotropic media, *Bull. Seism. Soc. Am. BSSA*, 67, pp. 661-675.

209. Crampin, S. (1984). Effective elastic constants for wave propagation through cracked solids, *Geophys. J. R. Astr. Soc.*, 76, pp. 135-145.
210. Buchen, P. W. (1971). Plane waves in liner viscoelastic media, *Geophys. J. R. Astr. Soc.*, 23, pp. 531-542.
211. Byun, B. S. and Cheng, S.W. (1986). Apparent axial properties of transversely isotropic media, *Geophysics*, 4, pp. 1012-1013.
212. China National Seismic Bureau. (1998). Analysis and Application of Seismic Wave. Seism Press, Beijing.
213. Banik, N. C. (1987). An effective anisotropy parameter in transversely isotropic media, *Geophysics*, 12, pp. 1654-1664.
214. Banik, N. C., Lerche, I. and Shuey, R. T. (1985). Stratigraphic filtering, part Ⅰ: derivation of the O'Doherty-Anstey formula. *Geophysics*, 50, pp. 2768-2774.
215. Beltzer, A. I. (1988). Dispersion of seismic waves by a causal approach, *Pure. Appl. Geophys.*, 128, pp. 147-156.
216. Byun, B. S. (1982). Seismic parameters for media with elliptical velocity dependencies. *Geophysics*, 47, pp. 1621-1626.
217. Berryman, J. G. (1979). Long-wave elastic anisotropy in transversely isotropic media. *Geophysics*, 5, pp. 896-917.
218. Buchen, P. W. (1971). Plane waves in liner viscoelastic media. *Geophys. J. R. Astr. Soc.*, 23, pp. 531-542.
219. Buchen, P. W. (1971). Reflection, transmission and diffraction of SH-waves in linear viscoelastic solids. *Geophys. J. R. Astr. Soc.*, 25, pp. 97-113.
220. Byun, B. S. (1984). Seismic parameters for transversely isotropic media. *Geophysics*, 11, pp. 1908-1914.
221. Brennan, B. J. and Smylie, D. E. (1981). Linear viscoelasticity and dispersion in seismic wave propagation. *Rev. Geophys. Space. Phy.*, 19, 233-246.
222. Alkhalifah, T.(1997). Velocity analysis using nonhyperbolic moveout in transversely isotropic media. *Geophysics*, 62, pp.1839-1854
223. Crampin, S. (1984). Suggestions for consistent terminology for seismic anisotropy. *Geophys. Prop.*, 37, pp. 753-770.
224. Crampin, S. (1981). A review of wave motion in anisotropic and cracked elastic-media. *Wave Motion*, 3, pp. 343-391.
225. Crampin, S.(1993). A review of the effects of crack geometry on wave propagation through aligned cracks. *Can. J. Expl. Geophys.*, 29, pp.3-17.
226. Crampin, S. (1991). Effects of singularities on shear-wave propagation in sedimentary basins, *Geophys. J. Int.*, 3, pp. 531-543.
227. Daley, P. F. and Hron, F. (1977). Reflection and transmission coefficients for transversely isotropic media. *Bull. Seism. Soc. Am., BSSA*, 67, pp. 661-675
228. Daley, P. F. and Hron, F. (1979). Reflection and transmission coefficients for seismic wave in ellipsoidally anisotropy media, *Geophysics*, 1, pp. 27-38.
229. Hudsom, J. A. (1981). Wave speeds and attenuation of elastic waves in material containing cracks. *Geophys. J. R. astr. Soc.*, 64, pp. 133-150.
230. Gorich, V. and Muller, G . (1987). Apparent and intrinsic Q: the one-dimensional case, *J. Geophys.*, 61, pp. 46-54.

231. Fryer, G. J. A. (1980). Slowness approach to the reflectivity method of seismogram synthesis, *Geophys. J. R. astr. Soc.*, 63, pp. 747-758.
232. Haskell, N. (1953). The dispersion of surface waves in multilayered media. *Bull Seismol Soc Amer*, 43, 17-34.
233. Helbig, K. (1983). Elliptical anisotropy-It's significance and meaning. *Geophysics*, 7, pp. 825-832.
234. Hudson, J. A. (1980). Overall properties of cracked solid. *Math. Proc. Camb. Phil. Soc.*, 88, pp. 371-384.
235. Kim, K. Y., Wrolstad, K. H. and Aminzaden, F. (1993). Effects of transverse isotropy on P-wave AVO for gas sands, *Geophysics*, 6, pp. 883-888.
236. Kjartansson, E. (1979). Constant Qwave propagation and attenuation, *J Geophys Res*, 84, pp. 4737-4748.
237. Levin, F. K. (1978). The reflection, refraction, and diffraction of waves in media with an elliptical velocity dependence, *Geophysics*, 3, pp. 528-537.
238. Krebes, E. S. (1983). Discrepancieson energy calculations for inhomogeneous waves, *Geophys. J. R. astr. Soc.*, 75, pp. 839-846.
239. Mithal, R. and Vera, E. E. (1987). Comparison of plane-wave decomposition and slant stacking of pointsource seismic data. *Geophysics*, 12, pp. 1631-1638.
240. O'Doherty, R. F. and Austey, N. A. (1971). Reflection on amplitudes. *Geophys. Prosp.*, 19, pp. 430-458.
241. Ostrander, W. J. (1984). Plane-wave reflection coeffients for gas sands at nonnormal angles of incidence. *Geophysics*, 10, pp. 1637-1648.
242. Pelissier, M. A., Betts, A .T. and Vestergouard, P. D. (1991). Azimuthal variations in scattering amplitudes indeced by transverse isotropy. *Geophysics*, 10, pp. 1584-1595.
243. Rokhlin, S. I., Bolland, T. K. and Adler, L. (1986). Reflection and refraction of elastic waves on a plane interface between two generally anisotropic media,*J. Acoust. Soc. Am.*, 4, pp. 906-918.
244. Parscau, J. D. (1991). Relationship between phase velocities and polartzation in transversely isotropic media, *Geophysics*, 10, 1578-1583.
245. Richards, P. G. and Menke, W. (1983). The apparent attenuation of a scattering medium, *Bull. Seis. Soc. Am.*, 73, pp. 1005-1021.
246. Rommel, B. E. (1993). Approximate stacking velocities in a weakly transversely isotropic layer, *Can. J. Expl. Geophys.*, 29, pp. 98-105.
247. Shah, P. (1973). Use of wavefront curvature to relate seismic data with subsurface parameters. *Geophysics*, 38, pp. 812-825.
248. Rommel, B. E. (1994). Approximate polarization of plane waves in a medium having weak transverse isotropy, *Geophysics*, 10, pp. 1605-1612.
249. Shuey, R. T. (1985). A simplification of the Zoeppritz equations. *Geophysics*, 4, pp. 609-614.
250. Trorey, A. W. (1962). Theoretical seimograms with frequency and depth dependent absorption. *Geophysics*, 34, pp. 516-528.
251. Thomsen, L. (1986). Weak elastic anisotropy, *Geophysics*, 10, pp. 1954-1966.
252. Thomsen, T. (1988). Reflection seismoloogy over azimuthally anisotropic media,

Geophysics, 3, pp. 304-313.
253. Thomson, W. (1950). Transmission of elastic waves through a stratified solid medium, *J. Appl. Phy.*, 21, pp. 89-93.
254. Wright, J. (1987) The effects of transverse isotropy on reflextion amplitude versus offset, *Geophysics*, 4, pp. 564-567.
255. Cheng Guangwen (1994). A study on the transportation characteristics of highly concentrated slurry, and the experiment on vibrating drag reduction, PhD Thesis, Central South University (in Chinese).
256. Hou Huichang (1987). Drag Reduction Mechanics. Science Press, Beijing.
257. Han Wenliang (1990). A study on the problem of drag reduction of mine-fills, *Non-ferrous Metal* (*quarterly*), 3, pp. 5-10 (in Chinese).
258. Wang Congyue, Xia Yuanming and Xie Yanning (1998). The reflection and transmission of elastic wave in non-homogeneous thin rods, *Chinese Journal of Applied Mechanics*, 3, pp. 43-50 (in Chinese).
259. Zhang Yuanjun (1987). Two-phase Hydromechanics. Beijing Aviation College Press, Beijing.
260. Sun Xianghai (1987). Computational Hydromechanics. Shanghai Jiaotong University Press, Shanghai.
261. Zhang Benzhao (1986). The Finite Element Method Applied in Hydromechanics. Mechanical Industry Press, Beijing.
262. Liu Chaoqun (1995). The Multigrid Technique and Its Application in Computational Hydromechanics. Tsinghua University Press, Beijing.
263. Lin Yu (1987). Diphasic Flow of Solid-liquid. Jiangxi Metallurgical Institute Press, Jiangxi.
264. Zhou Xueyi (1994). Computational Water Conservancy Science. Tsinghua University Press, Beijing.
265. Fei Xiangjun (1994). Hydromechanics of Transportation of Slurry and Granular Materials. Tsinghua University Press, Beijing.
266. Wuhan Waterpower and Electric Power University (1981). Engineering Science of River Silt. Water Conservancy Press, Beijing.
267. Liu Huajie (1998). Fractal Art. Hunan Science and Technology Press, Changsha.
268. Xie Heping (1992). Fractal geometry and its application to rock and soil materials, *Chinese Journal of Geotechnical Engineering*, 1, pp. 14-24 (in Chinese).
269. Chen Yong and Cheng Ling. (1998). Fractal Geometry. Seism Press, Beijing.
270. Fu Helin, Li Liang and Li lei (2000). The fractal study of structure of expansive soil, *Journal of Changsha Railway University*, 1, pp. 1-5 (in Chinese).
271. Turcotte, D. L. (1986). Fractals and fragmentation, *J Geophys Res*, 91, pp. 1921-1926.
272. Xu Yongfu, Sun Wanyin and Wu Zhenggen (1997). On Fractal structure of expansive soils in China, *Journal of Hohai University*, 1, pp. 18-23 (in Chinese).
273. Bark, P., Tang, C. and Wiesenfeld, K. (1988). Self-organized criticality, *Phys Rev*, A38, pp. 364-374.
274. Long Qiwei (1999). Metal Fractal and Its Complexity. Shanghai Science and Technology Press, Shanghai.

275. Xie Heping (1993). Fractal pores and fractal particles of rock and soil materials, *Advances in Mechanics*, 2, pp. 145-164 (in Chinese).
276. Petri，A. and Paparo, G.，Vespignani, A.， et al. (1994). Experimental evidence for critical dynamics in microfacturing processes, *Phys. Rev. Lett.*, 25, pp. 3423-3426.
277. Ochiai, M., Ozao, R. and Yamazaki, Y. (1992). Self-similarity law of particle size distribution and energy law in size reduction of solids, *Physics A*, 191, pp. 295-300.
278. Zhang Jizhong (1997). Fractal. Tsinghua University Press, Beijing.
279. Lu Chunsheng and Bai Yilong (1990). Application of fractal in damage and fracture of materials, *Advances in Mechanics*, 4, pp. 468-477 (in Chinese).
280. Li Houqiang and Cheng Guanyue (1990). Fractal and Fractal Dimension: New Method to Probe into the Complexity. Sichuan Education Press, Chengdu.
281. Dong Lianke (1991). Fractal Theory and Its Application. Liaoning Science and Technology Press, Shenyang.
282. Wang Fuquan (1993). Fractal Geometry and Dynamic System. Heilongjiang Education Press, Ha'erbin.
283. Xie Heping (1996). Fractals-rock Mechanics. Science Press, Beijing.
284. Petro，M. and Sun Fang-Kuo (1993). Measuring the fractal dimension of signals: Morphological covers and iterative optimization. *IEEE Trans. on SP*, 1, pp. 108-121.
285. Yi Yunmin, Li Zhiheng and Zhang Yanzhong (1999). The fractal characteristics of fracture in expansive soil and its significance, *Chinese Journal of Geotechnical Engineering*, 3, pp. 294-298 (in Chinese).
286. Naokazu，Y.(1989). Fractal-based analysis and interpolation of 3D natural surface shapes and their applications to Terrain modeling, *Computer Vision, Graphics and Image Processing*, 46, pp. 1-8.
287. Smalley, R. F., Chatelain, J. L. and Turcotte, D. L., et al. (1987). Fractal approach to the clustering of earthquakes: application to the seismicity of new Hebrides. *Bull. Seismol. Soc. Am.*, 4, pp. 1368-1381.
288. Zhu Jubo and Liang Diannong (2000). Combinatorial fractal-Brownian motion model, *Science in China* (*Serials E*), 4, pp. 312-319 (in Chinese).
289. Crustzberg, R. and Ivanov, E. (1989). Computing fractal dimension of image segments, Proc. III *Int. Conf. on Computer Analysis and of Image and Patterns*, CAIP, pp. 110-116.
290. Feder，J. (1988). Fractals, Plenum，New York.
291. Turcotte, D. L. (1988). Fractal and fragmentation. *J. of Geophysics*, 132, pp. 1291-1296.
292. Haykin, S. and Li, X. B. (1995). Detection of signals in chaos. *Proceedings of the IEEE*, 1, pp. 95-122.
293. Li Tingjie, Wang Yaohui, Zhang Haiying, et al. (2000). Fractal properties of crack in rock and mechanism of rock-burst, *Chinese Journal of Rock Mechanics and Engineering*, 1, pp. 6-10 (in Chinese).
294. Wang Jinfa, Xie Heping, Tian Xiaoyan, et al. (2000). Scale effect on fractal measurement of rock fracture surfaces, *Chinese Journal of Rock Mechanism and Engineering*, 1, pp. 11-17 (in Chinese).

295. Theodore, R. M. (1983). A renormalizations group approach to the critical phenomena of conduction and failure in crystalline rocks, *J. of Geophys. Res.*, 88 B1, pp. 585-592.
296. Bak, P. and Tang, C. and Wiesenfeld, K. (1987). Self-organized criticality: an explanation of 1/f noise, *Phys. Rev. Lett.*, 59, pp. 381-384.
297. Bak, P. and Tang, C. (1989). Earthquakes as a self-organized critical phenomenon, *J. Geophys. Res.*, 94, pp. 15635-15637.
298. Ito, K. (1990). Earthquakes as self-Organized critical phenomenon, *J. Geophys. Res.*, 95, pp. 6835-6860.
299. Carlson, J. M. and Langer, J. S. (1989). Mechanical model of an earthquake fault, *Phys. Rev. Lett.*, A, 40, pp. 6470-6483.
300. Nakanishi, H. (1990). Cellular-automaton model of earthquakes with deterministic dynamics, *Phys. Rev.* A., 41, pp. 7086-7089.
301. Mandelbrot, B. B. (1997). Fractals: Form, Chance and Dimension. W. H. Freeman and Co, San Francisco.
302. Mandelbrot, B. B. (1982). The Fractal Geometry of Nature. W H Freeman and Co, New York.
303. Mandelbrot, B. B. (1961). Stable Paretian random functions and the multiplicative variable of income, *Econometrica*, 4, pp. 517-543.
304. Shearer, R. R. (1995). From flatland to fractaland: new geometries in relationship to artistic and scientific revolutions, *Fractals*, 3, pp. 617-625.
305. Steinhaus, H. (1954). Length shape and area, *Colloquium Mathematicum*, 3, pp. 1-13.
306. Johnson, P. A., et al. (1991). Magnitude and frequency of debris flows, *J. Hydro.*, 123, pp. 69-82.
307. Xie, H., Wang Jin'an and Stein, E. (1998). Direct fractal measurement and multi-fractal properties of fracture surfaces, *Physics Letters A*, 242, pp. 41-50.
308. Xie H. and Pariseau, W. G.. (1994). Fractal estimation of joint roughness coefficients, *Sciences in China* (*Series B*), 12, pp. 1516-1524.
309. Rice, J. R. and Ruina, A. L. (1983). Stability of steady frictional slipping, *J. Appl. Mech.*, 50, pp. 343-349.
310. Krajcinovic, D. and Silva, M. A. G. (1982). Statistical aspects of the continuous damage theory, *Int. J. Solids. Structures*, 7, pp. 551-562.
311. Huajie, L. and Jun, L. (1996). A method for generation super large fractal image useful to decoration art, *Communications in Nonlinear Science & Numerical Simulation*, 3, pp. 25-27.
312. Henley, S. (1976). Catastrophe theory models in geology, *Mathematical Geology*, 6, pp. 649-655.
313. Cubitt, J. M. and Shaw, B. (1976). The geological implication of steady-state mechanisms in catastrophe theory, *Mathematical Geology*, 6, pp. 657-662.
314. Ruina, A. (1983). Slip instability and state variable friction laws, *J Geophys Res*, 83, pp. 10359-10370.
315. Xie Huimin (1995). Complexity and Dynamic System. Shanghai Science and Technology Press, Shanghai.

316. Odling, N. E. (1994). Natural fractal profiles, fractal dimension and joint roughness coefficients, *Rock Mech. Rock Engng.*, 3, pp. 135-153.
317. Xie, H. (1993). Fractal in Rock Mechanics. A. A. Balkema Publisher, Rotterdam.
318. Qi Siqing (2000). Primary discussion on the mechanism of dissipative structure formation in instability process of rock mass, *Chinese Journal of Geotechnical engineering*, 3, pp. 265-269 (in Chinese).
319. Frette, V. and Christensen K.， et al. (1996). Avalanche dynamics in a pile of rice, *Letters to Nature*, 4, pp. 49-52.
320. Paczuski， M. and Boettcher， S. (1996). University in sandpiles, interface depinning, and earthquake models, *Phys. Rev. Lett.* , 1, pp. 111-114.
321. Bak, P., Tang, C. and Kurt, Wiesenfeld (1988). Self-organized criticality, *Phys. Rev. A.*, 1, pp. 364-374.
322. Caldarelli,G. (1996). Self-organization and annealed disorder in a fracturing process, *Phys. Rev. Lett.*, 12, pp. 2503-2506.
323. Gu Desheng (1992). Development and the prospect of vibrating ore-drawing techniques in China, *China Non-ferrous Metal Industry National Company Symposium for Vibrating Ore-drawing Techniques and Its Equipment*, pp. 1-10 (in Chinese).
324. Wang Huiying and Luo Dianping (1996) .Vibrating Ore-drawing and Its Application. Hunan Science and Technology Press, Changsha.